Conference Proceedings

Graz, March 30th and 31st, 2016

organized by the

Institute of Paper, Pulp and Fibre Technology
Institute of Process and Particle Engineering

TU Graz
Graz University of Technology

process & particle engineering

Program- and Organizing Committee:

Wolfgang Bauer
Wolfgang Fischer
Thomas Gamse
Ulrich Hirn
Peter Loidolt
Jakob Redlinger-Pohn
Stefan Radl
Adela Roller
Kerstin Schefzik

Titlepage Source of Figures:
Campus „Alte Technik“: © Graz University of Technology
Simulated Particles: Loidolt, P., 12th Minisymposium VT, Graz, 2016
Microscopy of Fibre Fines: Mayr, M., 12th Minisymposium VT, Graz, 2016
Suspended Droplets: © Grafschafter, Annika, CEET, Graz University of Technology

U. Hirn (Editor)
Minisymposium Verfahrenstechnik Graz, 2016 Conference Proceedings

Graz, 2016

www.ub.tugraz.at/Verlag

e-ISBN: 978-3-85125-456-3
DOI: 10.3217/978-3-85125-456-3


NAWI Graz
Natural Sciences


BDI


infineon

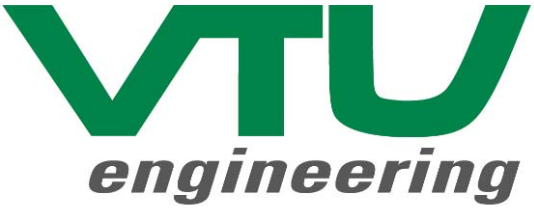
VTU
engineering


natex
PROZESSTECHNOLOGIE


research
center
pharmaceutical
engineering


OMYA

Table of Contents

Gas-Particle Systems

Katja Hüttenbrenner, MU Leoben *"Investigations on the influence of porous material on the ignition behavior of combustible dust/air-mixtures"* 1

Christian Mayerl, MCI *"Laseroptische Evaluierung der Primärstufe eines Kombinationsfilters"* 5

Gerhard Hofer, BOKU *"Heat transfer at immersed tube bundles in bubbling fluidized beds considering Geldart Type B particles"* 9

Liquid-Particle Systems

Thi Huyen Trang Trinh, JKU Linz *"The performance of photocatalysis – submerged microfiltration membrane system for water treatment"* 13

Thomas Senfter, MCI *"Entwicklung einer Versuchsanlage für Fest-Flüssig-Trennversuche an Massenkraftabscheidern"* 17

Bahram Haddadi Sisakht, TU Wien *"Membrane module design optimization using CFD"* 21

Materials

Philipp Biegger, MU Leoben *"Vergleich der Trägermaterialien γ-Al2O3 und t-ZrO2 in der katalytischen Methanisierung von CO2"* 27

Daniel Varga, TU Graz *"Impregnation of Polycarbonate with Copper Nanoparticles in Supercritical Carbon Dioxide"* 31

Melanie Mayr, TU Graz *"Morphological characterization of cellulose pulps with imaging methods"* 35

Pharma

Manuel Berger, MCI *"Investigation of the respiratory flow through the nasal cavity with CFD"* 41

Peter Loidolt, TU Graz *"Multi-particle finite element method of powder compaction"* 45

Michael Martinetz, RCPE Graz *"Feasibility study for turret speed operating points in a rotary tablet press"* 49

Energy

Eva M. Rohringer, JKU Linz *"Influence of the heat transfer and operation time of a coaxial probe for deep geothermal energy"* 55

Florian Benedikt, TU Wien *"The Novel Dual Fluidized Bed Gasifier at TU Wien - Part I: Parameter Variation with Wood Pellets"* 59

Josef Fuchs, TU Wien "*The Novel Dual Fluidized Bed Gasifier at TU Wien - Part II: Gasification of Alternative Fuels"* 65

Poster Presentations A: Energy & Environment

Michael Lammer, TU Graz *"Investigation into thermal runaway of Li-ion batteries"* 71

Ilena Kaltenböck, TU Graz *"Non-precious cathode catalysts for direct liquid fuel cells"* 75

Birgit Pichler, TU Graz *"Design of bifunctional air electrodes for rechargeable zinc/air redox flow systems"* 79

Georg Baldauf-Sommerbauer, TU Graz *"Synthesegas aus Wasserstoff und Magnesit/Dolomit"* 83

Kathrin Kos, TU Graz *"Fuel Surrogate Design and Application to Commercial European Diesel"* 85

Niesenbacher, MU Leoben *"Bilanzierung eines mehrstufigen Prozesses zur Karbonatisierung mineralischer Rohstoffe"* 91

Gernot Voitic, TU Graz "*Pressurized Hydrogen Production by Fixed-Bed Chemical Looping"* 95

Andrea Rollett, TU Graz *"Continuous hydrodeoxygenation of liquid phase pyrolysis oil"* 101

Elisabeth Rammerstorfer, Prozess Optimal Holzer GmbH *"Modeling of fouling in Crude Oil Heat Exchangers"* 105

Chakkrapong Chaiburi, TU Graz *"Study on ethanol-tolerant electrocatalysts for oxygen reduction reaction in alkaline media"* 109

Julius Pirklbauer, TU Wien *"bioCH4.0; Biogas Upgrading zu Biomethan im kontinuierlichen Temperaturwechsel Adsorptionsprozess"* 113

Michael Derntl, AVL List GmbH *"Thermo Chemical Recuperation of diesel exhaust gas"* 117

Ana Roza Medved, MU Leoben *"Methanation of CO2 from biogas for Power-to-Gas application"* 123

Markus Groß, TU Wien *"Hydrogen extraction facilities for utilization in Power to Gas framework"* 127

Thomas Märzinger, BOKU *"GUFO Lastprofile"* 133

Markus Ellersdorfer, MU Leoben *"Charakterisierung natürlicher Zeolithe für die Ammoniumentfernung aus Trübwässern"* 139

Daniel Schwabl, MU Leoben *"Optimierung der Betriebsparameter Versuchsanlage Plastic Reborn"* 143

Mohammad Rezaei, JKU Linz *"Wetting control of Multiscale-Layer Membranes for Membrane Distillation"* 147

Muhammad Ali Samee, TU Wien *"Experimental study of separation performance of nanofiltration process for complex mono and multivalent salts during sugar concentration"* 151

Thomas Laminger, TU Wien *"Regenerierung von staubbeladenen Filtermedien mittels Absaugung"* 155

Nicos Dimitri Tsioutsios, MU Leoben *"Einflussgrößen des Druckverlustes bei der Durchströmung von Sinterbetten"* 161

Werner Rudolf Pollhammer, MU Leoben *"Development of a dust dispersion system for investigations on reduced pressure conditions in the 20 liter SIWEK apparatus using OpenFOAM"* 167

Teresa Schubert, MU Leoben *"Thermogravimetric analysis of pure and additive-commingled polypropylene"* 171

Florian Pöllabauer, TU Graz *"Energy optimization of cross-linked plants on the example of a refinery"* ... 177

Poster Presentations B: Separation, Food & Pharma

Anda Lucia, MU Leoben *"Absorption of oxygen by sodium sulfite droplets"* 181

Miriam Wimmer-Teubenbacher, RCPE Graz *"NIR-based Real Time Release Testing of Printed Orodispersible Films"* 187

Johannes Poms, RCPE Graz *"NIR-Hyperspectral Imaging and Raman Chemical Mapping of Multilayer-Tablets"* 191

Peter Scherübel, TU Graz *"Prozessintensivierung von Batch-Destillationsverfahren zur Herstellung von Spirituosen"* 195

Nélio Drumond, TU Graz *"A rheological method to predict mucoadhesion between dosage form excipients and human saliva"* 199

Surangkana Chaichoowong, KMUTNB Bangkok *"Isolation of valuable components from Acalypha indica using solvent extraction"* 203

Bhumphong Rajcharak, KMUTNB Bangkok *"Modeling of drop sedimentation in liquid-liquid phase separation"* 207

Candela Campos Dominguez, TU Graz *"Continuous Supercritical Fluid Extraction of Liquids Using Micro-Mixers"* 213

Aroonrat Poonyaratanasrikhajon, KMUTNB Bangkok *"O/W-emulsions, production and stability"* 217

Günther Holzer, TU Graz *"Anthocyangewinnung aus der schwarzen Holunderbeere"* 221

Eva Kalvoda, TU Graz *"Mass transfer measurements in extraction under column conditions"* 227

Annika Grafschafter, TU Graz "*TCDC, design and validation"* 231

Robert Macher-Ambrosch, TU Graz *"Turbidity Control"* 237

Daniela Painer, TU Graz *"Prozessintensivierung durch reaktive Trennverfahren in der Lösungsmittel-Rückgewinnung"* 241

Maryam Askarishahi, RCPE Graz *"CFD-DEM Simulation of Wet Fluidized Beds: Evaporation Rates from the Spray and the Particle Surface"* 245

Nuttakul Mungma, TU Graz *"Process development strategies: Lactic acid isolation"* 249

Andreas Toth, TU Graz *"Herausforderungen der Technologie- und Verfahrensentwicklung und Lösungsalgorithmen"* 253

Investigations on the influence of porous material on the ignition behavior of combustible dust/air-mixtures

Katja Hüttenbrenner, Hannes Kern, Harald Raupenstrauch
all: Montanuniversitaet Leoben, Department of Environmental and Energy Process Engineering – Chair of Thermal Processing Technology, 8700 Leoben, Franz-Josef-Straße 18
katja.huettenbrenner@unileoben.ac.at

Abstract

In the process industry major losses are caused by fires and explosions. To cope with these problems, inerting materials are used to reduce the combustibility of combustible dusts. Furthermore, the explosibility gets influenced either. In general two types of inerting are known: Thermal extinction and chemical extinction. The first option, the thermal extinction, is based on the cooling effect caused by the partial evaporation of the dust particle. On the contrast, the inerting effect can be caused by the interaction of the radicals with the particle wall (i.e. the surface of the inerting particle). Therefore, an influence on the explosibility of combustible dust due to the addition of particles with a high specific surface area is expected. The aim of the present work was to identify the impact of inerting material on the ignition behavior of combustible dust/air-mixtures.

Introduction

To cover fire and explosion risks in the process industry two strategies are known: Prevention and controlling. Both strategies predicate on the use of inerting material. In general two types of inerting are known: The thermal extinction and the chemical extinction. The first option, the thermal extinction, is based on the cooling effect caused by the partial evaporation of the dust particle (e.g. silica, cupric oxid, and alumina). On the other hand, the inerting effect can be caused by the interaction of the radicals with the particle wall (i.e. the surface of the inerting particle). The inerting based on the specific surface area reposes on the destruction of the particle wall due to radicals and, therefore, the combustion process gets stopped [1]. Dewitte suggested that both, the cooling effect and the chain termination effect become effective simultaneously. Thereby, one effect predominates the other.

Method

For investigations on combustible dust/air-mixtures, tests on the minimum ignition energy (MIE) were done. Eckhoff describes the minimum ignition energy “as the lowest spark energy that gives at least one ignition in ten trials at the same spark energy” [2]. Trials for the present investigations were done in the so-called MIKE 3-apparatus from the Kühner AG (see Figure 1). According to Kühner AG, the MIKE 3-apparatus is “a modified Hartmann tube made of glass with a volume of 1.2 liters” [3]. “The dust dispersion system at the base of the tube is of the ‘mushroom-shaped’-type on which the sample is loosely scattered. A blast of compressed air at 7 bar is used to disperse the dust in the glass cylinder where it is ignited by a spark between two electrodes” [3]. The two electrodes are made of stainless steel with a diameter of 2 mm and a space between two electrodes of 6 mm [3]. Influential parameters on the testing method are: Inductance in the discharge circuit, turbulence, particle size, product humidity, temperature, dust concentration, as well as oxygen concentration. To get equal conditions for the trials dry dust with a defined

median value is used. The ignition delay time is set to adjust the turbulence during the experiment. High turbulence can be adjust with a short delay time, a long delay time induces a very low turbulence level. Tests are made with time protracted sparks, because these sparks are “clearly more incentive than purely capacitive discharges” [2].

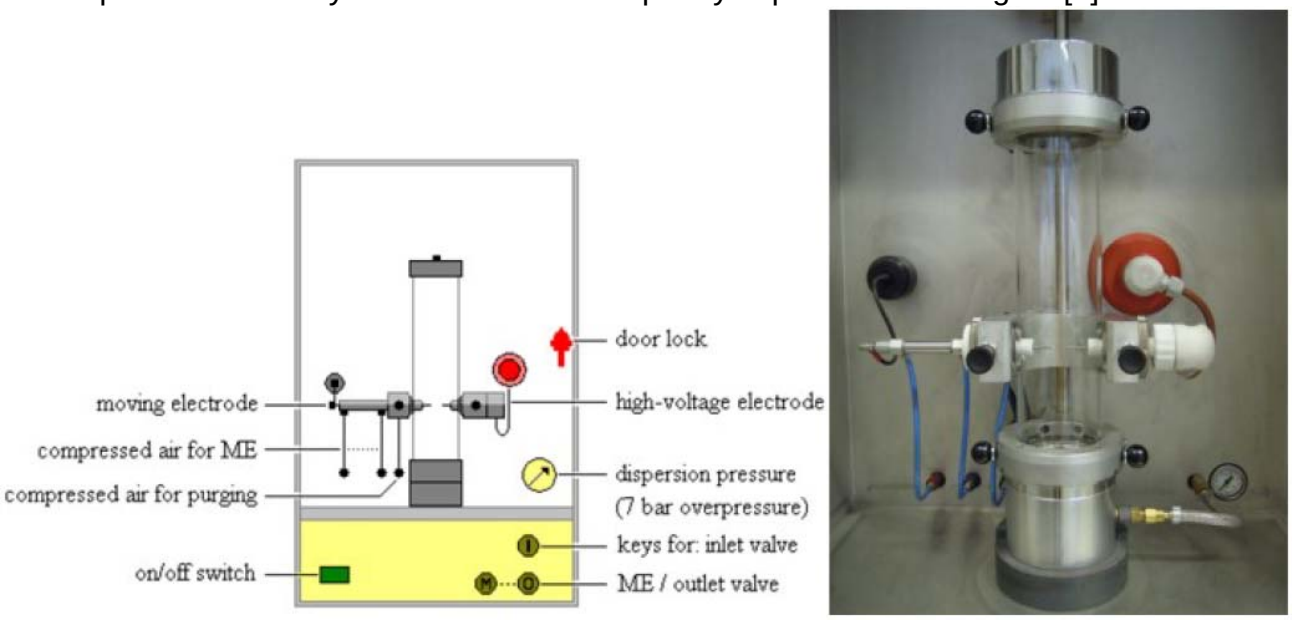

Figure 1: MIKE 3-apparatus [3]

Experimental Investigation

Experiments were done to identify the impact of inerting material on the ignition behavior of combustible dust/air-mixtures. An influence on the explosibility of combustible dust due to the addition of dust particles with a high specific surface area was expected. Therefore, mixtures of lycopodium as combustible dust and inerting materials with various specific surface areas were investigated.

Ceramic beads were used as inerting agent with a low specific surface area and a unique appearance. Caused by the low specific surface value effects on the particle wall should be low, and therefore, the inerting effect low.

The second material used as inerting agent was extinguishing powder, called “ABC-powder”. It is a mixture of ammonium dihydrogen phosphate and ammonium sulphate. The surface area is about 0.1 to 0.4 m²/g and it is used as dry chemical in industrial applications for extinguishing or in portable fire extinguishers in households.

The last used inerting material was zeolite. Zeolite is a crystalline mineral, based on alumina silicates. It is characterized by a three dimensional structure of silicon compound ($[SiO_4]^{4-}$) and alumina compound ($[AlO_4]^{5-}$). One property of this material is the high specific surface area, caused by naturally build cavities [4]. For testing the zeolite “Clinoptilolite” with a specific surface area of about 400 to 600 m²/g was used.

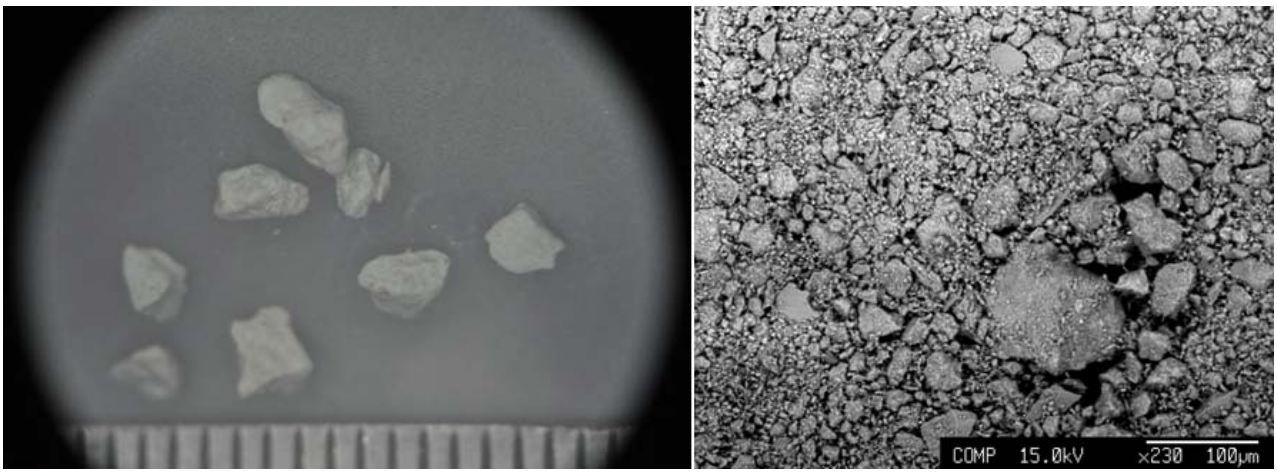

Figure 2: Zeolite

Both the combustible dust and the inerting material were sieved and a particle fraction between 32 and 63 µm was used. According to Harris particles with a median value more than 841 µm will not mix up with air [5]. Finer particles have a higher specific surface area than coarse particles. Therefore, fine particles are the better alternative as extinguishing powder.
The aim of the experimental tests was to identify the way of changing the minimum ignition energy by altering the amount of the inerting material in the dust/air-mixture. Hence, various mixtures with different amounts of inerting material were produced, tests were done and the statistic minimum ignition energy level calculated. The used energy levels alter between three and 1,000 mJ. For providing a proper mixture, the dust was dispersed in an air filled bag of about 0.5 m^3 and mixed for several minutes. This approach prevents a segregation of the combustible dust and the inerting material.

Results

To identify the effect of the inerting based on the interaction of the radicals with the particle wall, so the specific surface area, experimental tests were done. Therefore, investigations on the minimum ignition energy were done in a standardized apparatus as described before. Various samples with different concentrations were tested and different energy levels were used to find out the lowest energy level for igniting the dust/air-mixtures. Figure 3 shows the results of the investigations.
Ceramic beads are characterized by low specific surface area, so only few chain carriers can be attached on the surface. Until an amount of about 70% ceramic beads in the dust mixture no shift can be seen. Thus, the amount of dust with a low specific value has to be very high to reach an inhibition effect by catching combustion radicals.
In contrast the inerting effect of zeolite occurs with a lower amount of zeolite in the dust mixture. Zeolite is a non-combustible dust with a very high specific surface value, and therefore, a perfect inhibition material. With an amount of 55% and more of zeolite in the mixture zeolite – combustible dust, an inerting effect of the combustion can be seen.
ABC extinguishing powder was investigated to get a benchmark. The value of the specific surface area lies between the ceramic beads and the zeolite. The inerting effect of ABC powder occurs faster that of the other materials, because of chemical decomposition reactions. ABC powder not only uses the particle wall for inerting combustible dust mixtures, but also produces endothermic chemical reactions for taking the energy of the flame. With these results of the extinguishing powder no clear statement concerning the influence of the specific surface area can be given, but the results give a good idea which values should be reached.

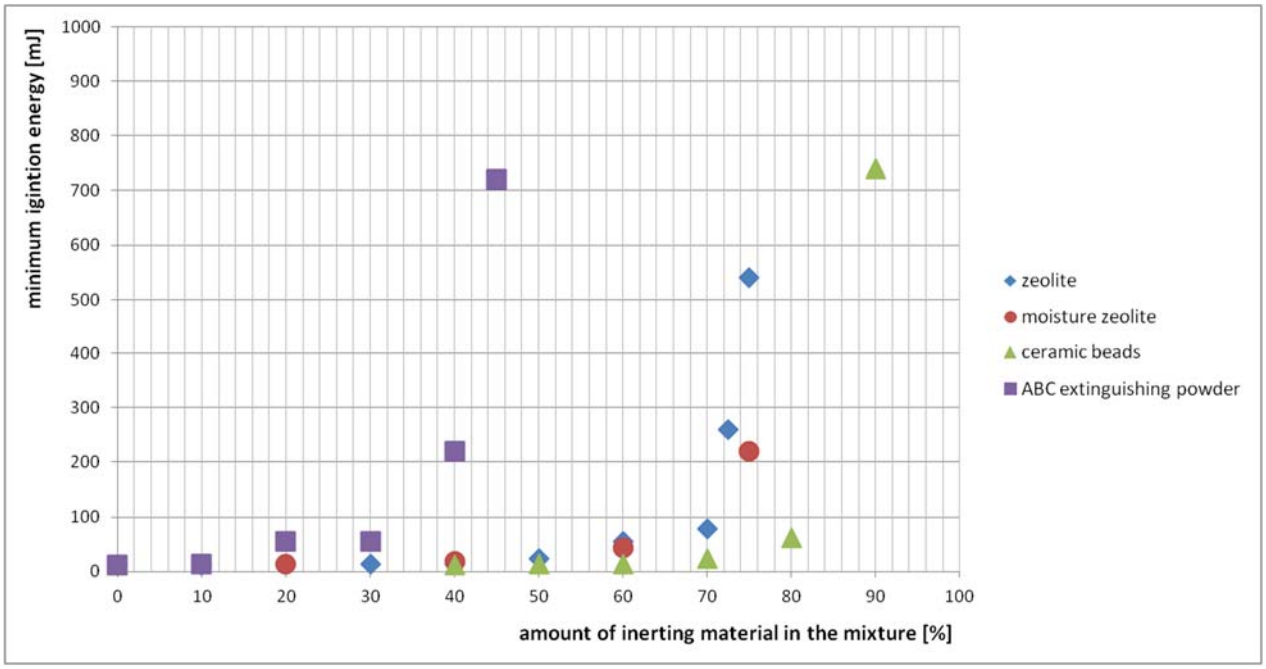

Figure 3: Results minimum ignition energy (MIE)

Conclusions

Purpose of the present investigations was to identify the impact of inerting material with different specific surface areas on the ignition behavior of combustible dust/air-mixtures. Tests on the minimum ignition energy were done with fine particles (between 32 and 63 µm) to receive the highest possible specific surface areas of the material. The overall data shows a correlation between the amount of the inerting material in the dust mixture (combustible dust and inerting material). The higher the specific surface area, the faster the minimum ignition energy is rising.
In summary it can be said, therefore, that the specific surface area of the inerting material has an influence on the ignition behavior of combustible dusts. Furthermore, the inerting effect due to porous materials has an impact on the dust explosibility.

References

[1] Dewitte, M., Vrebosch, J. and van Tiggelen, A., Inhibition and Extinktion of Premixed Flames by Dust Particles, Belgium, 1964.
[2] Eckhoff, R.K., Explosions Hazards in the process industries, Gulf Pup., Houston, TX, 2005
[3] Cesana, C., and Siwek, R., Manual MIKE 3, Kühner AG, Birsfelden, 2011.
[4] Dyer, A., An introduction to zeolith molecular sieves, J. Wiley, Chichester, New York, 1988.
[5] Harris, M.L., Sapko, M.J., Zlochower, I.A., Perera, I.E., Weiss, E.S., Particle size and surface area effects on explosibility using a 20-l-chamber, Jounal of Loss Prevention in the Process Industries 37, Elevier Ltd.: 33-38

Laseroptische Evaluierung der Primärstufe eines Kombinationsfilters

Ch. Mayerl[1], M. Pillei[1], S. Kunze[2] und M.Kraxner[1]
[1]MCI - Departement Umwelt-, Verfahrens- & Energietechnik,
Universitätsstraße 15, 6020-Innsbruck, AT
[2]MANN+HUMMEL GMBH, Advanced Development Filtration Systems CI-AD-FS,
Hindenburgstrasse 45, 71638 Ludwigsburg, DEU
christian.mayerl@mci.edu

Kurzfassung

Die Simulation von Kombinationsfiltern gestaltet sich aufgrund der anspruchsvollen Geometrien und der schwer nachzubildenden porösen Schicht des Filtermediums schwierig. Aus diesem Grund wird in dieser Arbeit ein Kombinationsfilter, mit Hilfe von Particle-Image-Velocimetry-Messungen, strömungstechnisch untersucht, um vorhandene CFD-Simulationen zu validieren bzw. adaptieren. Die PIV-Messungen liefern bei einer Messebene mit einem Strömungsübergang von Axial- auf Radialströmung valide Messergebnisse, welche zur Validierung / Adaptierung der CFD-Berechnungen herangezogen wurden. Die angepassten CFD-Daten stimmen mit den Messergebnissen sehr gut überein. In einer anderen Messebene tritt aufgrund einer normal auf die Messebene stehenden Hauptströmungsrichtung eine sehr hohe *out-of-plane*-Geschwindigkeit auf. Für die Abbildung der identen Partikel auf beiden Frames eines PIV Doppelbildpaares ist für diese Strömungsmessung daher eine sehr kurze Pulsdistanz erforderlich. Limitiert durch die Breite des Laserschnittes können somit örtlich nur sehr kurze Partikelversätze evaluiert werden, was zu messtechnischen Schwierigkeiten und folglich Abweichungen führt. Aus diesem Grund ist eine Validierung der CFD-Berechnungen in dieser Ebene nicht möglich, wobei die Geschwindigkeitsverteilungen der CFD-Berechnung und der PIV-Messung qualitative Ähnlichkeit aufweisen.

Einleitung

Kombinationsfilter bzw. Zwei-Stufenfilter stellen ein mögliches System zur Abscheidung von Störstoffen aus einer fluiden Phase dar. Dies ist nahezu überall erforderlich, in welchen Luft für technische Zwecke wie z.B. für Verbrennungsmotoren verwendet wird. Kombinationsfilter bestehen meist aus einer vorgeschalteten Zyklonstufe und einem filternden Abscheider. Die Zyklonstufe übernimmt dabei die Aufgabe eines Vorabscheiders und soll somit die auf den filternden Abscheider treffende Staubkonzentration minimieren. Dies bedeutet, dass die Standzeit dieser Systeme stark vom Abscheidegrad der Zyklonstufe abhängt und durch eine Verbesserung des Zyklonabscheidegrades deutlich längere Standzeiten erreicht werden können.
Ziel dieser Arbeit ist es, die Zyklonstufe eines am Markt befindlichen Kombinationsfilters strömungstechnisch zu untersuchen. Sowohl die poröse Filterschicht als auch die geometrischen Abmessungen von Kombinationsfiltern stellen erhebliche Herausforderungen für die CFD-Simulation dar. Aus diesem Grund sollen die ermittelten Messdaten zur Validierung und Adaptierung von CFD-Simulationen dienen. Auf Grundlage der Messdaten lassen sich die Randbedingungen der Simulationen anpassen um die tatsächlichen Strömungsbedingungen besser abbilden. Dies lässt sich auch auf neue bzw. geänderte Geometrien anwenden und führt somit zu einer höheren Validität der Simulationen und zu einer schnelleren Optimierung der Zyklonstufe.

Methoden und Verfahren

Als Grundvoraussetzung für die experimentellen Untersuchungen am Kombinationsfilter wurde eine Versuchsanlage gemäß den Vorgaben der ISO 5011:2014 aufgebaut und an den vorhandenen Kombinationsfilter angepasst. Die strömungstechnischen Untersuchungen im Kombinationsfilter wurden mittels 2D/2C-Particle-Image-Velocimetry-Messungen (kurz PIV-Messungen) durchgeführt. Eine schematische Darstellung des experimentellen Aufbaus und der Komponenten ist in Abbildung 1 dargestellt.

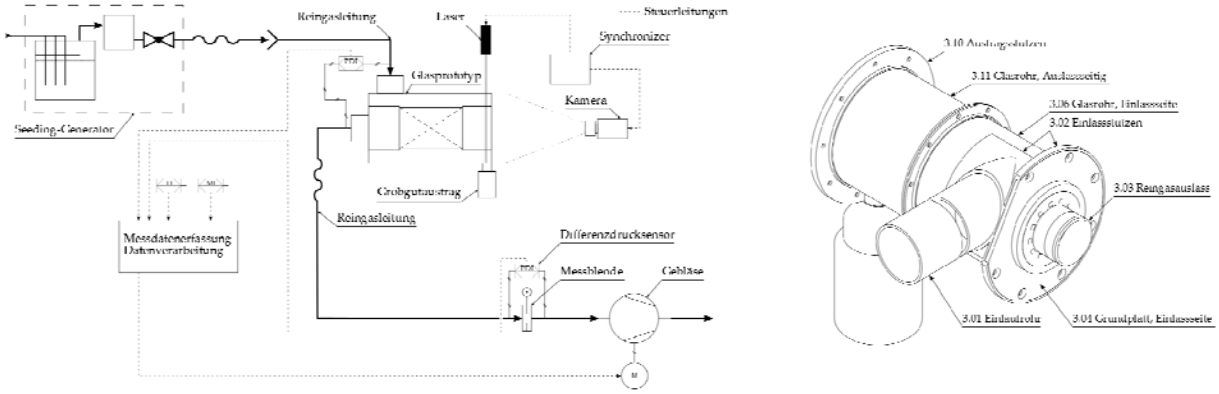

Abbildung 1: Schematische Darstellung des experimentellen Aufbaus und des Glasprototypen

Die für die PIV-Messungen notwendige optische Zugänglichkeit erforderte einen Glasnachbau des Serienkombinationsfilters. Dieser Glasprototyp wurde auf Grundlage der geometrischen Abmessungen des Serienproduktes geplant und angefertigt. Für alle benötigten Glaskomponenten wurden *Simax*®-Rohre (Borosilikatglas 3.3) verwendet. Die Verbindungsbauteile wie Flansche und Anschlussstutzen wurden konstruiert und mittels Rapid-Prototyping aus nicht transparentem Kunststoff hergestellt und mit den Glasbauteilen verklebt. Eine Zusammenbauzeichnung des Glasprototypen ist in Abbildung 1 dargestellt.
Die strömungstechnischen Untersuchungen im Kombinationsfilter wurden mit 2D/2C-PIV-Messungen durchgeführt. Dieses System lässt eine gleichzeitige Erfassung von zwei Geschwindigkeitskomponenten in der Ebene zu. Eine Auflistung der relevanten Spezifikationen ist in Tabelle 1 angeführt.

Tabelle 1: Versuchsspezifikationen und Komponenten

	Parameter	Spezifikation	Einheit
Laser	Type	Nd:YAG	--
	Wellenlänge	532	nm
	Puls Distanz	10 bis 35	µs
Kamera	Type	ILA.PIV.Nano	--
	Auflösung	1392 x 1040	Pixel
Optik	Brennweite	35	mm
	Lichtstärke	F1,8	--
Medium	Luft	20	°C
Seeding-Generator	Tracer-Partikeldurchmesser	Modalwert ca. 1,2	µm

Die Position der untersuchten Messebenen bzw. der Laserlichtschnitte ist in Abbildung 3 dargestellt. Zur Validierung der PIV-Messergebnisse wurde durch die Messebene A ein Schnitt gelegt, der Geschwindigkeitsmittwert eruiert und anschließend daraus der Volumenstrom für den Einlaufrohrquerschnitt berechnet. Die Abweichung des so ermittelten Volumenstromes vom tatsächlich gemessenen Volumenstrom (kalibrierte Normmessblende) beträgt weniger als 1 %.

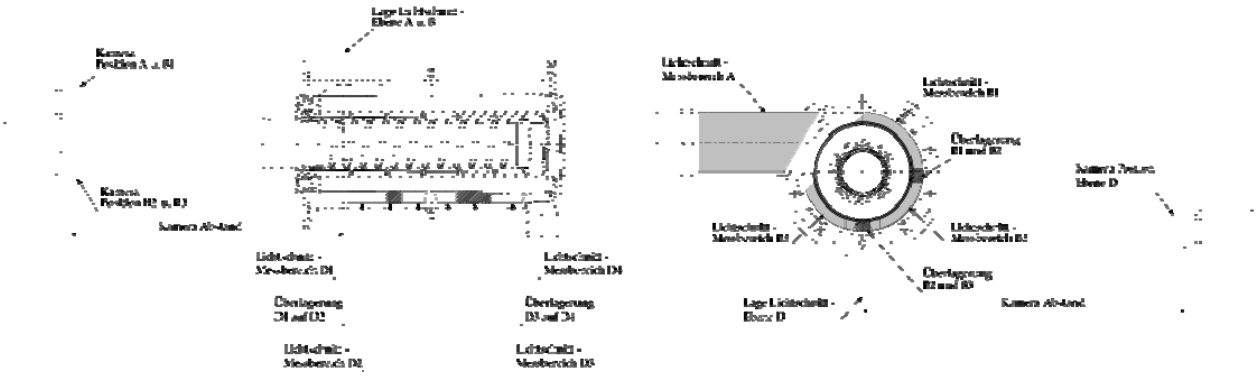

Abbildung 2: Messebenen

Die CFD-Simulationen wurden durch den Kooperationspartner *MANN+HUMMEL*® durchgeführt und für diese Arbeit zur Verfügung gestellt.

Ergebnisse und Interpretation

In der Abbildung 4 sind die normalisierten Geschwindigkeits-Konturdiagramme der Ebenen A und B dargestellt. Sowohl bei den Messergebnissen der PIV-Messungen als auch bei den CFD-Rechenergebnissen ist eine deutliche Einschnürung der Strömung beim Übergang zwischen dem Einlaufrohr und der eigentlichen Zyklonstufe zu erkennen, wobei die höchste Umfangsgeschwindigkeit im Bereich x=0 mm gemessen bzw. berechnet wurde. Im weiteren Verlauf ist eine Abnahme der Geschwindigkeit in der Messebene zu erkennen. Dies liegt einerseits daran, dass sich die Strömung in z-Richtung ausbreitet und andererseits daran, dass sich eine spiralförmige Strömungssträhne in Richtung Austragsbereich ausbildet und sich somit aus der Ebene hinausbewegt. Der Vergleich der PIV-Messergebnisse mit den CFD-Ergebnissen zeigt eine gute Übereinstimmung der Geschwindigkeitsverläufe sowohl im Einlaufrohr als auch in der Zyklonstufe.

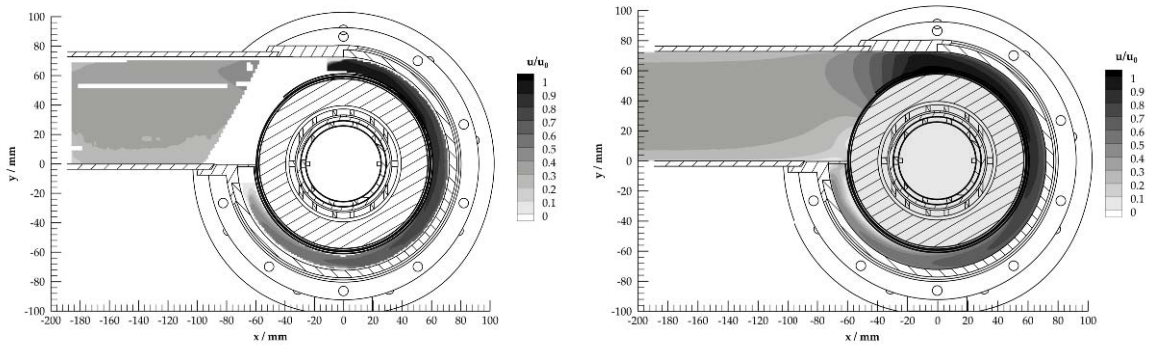

(a) *PIV* *(b) CFD*

Abbildung 3: Normalisierte Geschwindigkeits-Konturdiagramme der Ebenen A und B

Die Ergebnisse der PIV-Messungen bzw. CFD-Berechnungen der Ebene D sind in Abbildung 5 dargestellt. Die Problematik bei der PIV-Messung in der Ebene D liegt in der hohen *out-of-plane*-Geschwindigkeitskomponente (Umfangsgeschwindigkeit) der Strömung, welche um ein Vielfaches (ca. 4-fach) höher ist als die Axialgeschwindigkeit in der Ebene. Durch die hohe Umfangsgeschwindigkeit muss die Pulsdistanz bei der Messung sehr kurz gewählt werden, um dieselben Partikel auf beiden Einzelbildern abbilden zu können. Dies führt jedoch wiederum zu einem sehr bzw. zu niedrigen Partikelversatz in der Messebene [1]. Auf Grund dieses ungünstigen Verhältnisses zwischen Umfangs- und Axialgeschwindigkeit sind die PIV-Messergebnisse in der Ebene D nur eingeschränkt aussagekräftig und können somit nur als Anhaltspunkt dienen. Die

Abweichungen zu den Ergebnissen der CFD-Berechnung können somit auf die schwierigen Messverhältnisse zurückgeführt werden, wobei sich wiederum bei beiden Ergebnissen die qualitative Geschwindigkeitsverteilung nahezu ident darstellt. Deutlich zu erkennen ist die Einschnürung der Strömung in Richtung Filter am Ende der Einlaufzarge im Bereich x=40mm und die Rückströmung entlang der Austragszarge im Bereich x=170mm [2]. Die Einschnürung am Ende der Einlaufzarge deutet daraufhin, dass ein Teil der Strömung direkt nach der Zarge durch den Filter in den Reingasbereich gesaugt wird und somit gar nicht erst zum Austragsbereich gelangt. Über die Rückströmung an der Austragszarge gelangt der bis zum Austragsbereich geführte Volumenstrom in den Reingasbereich.

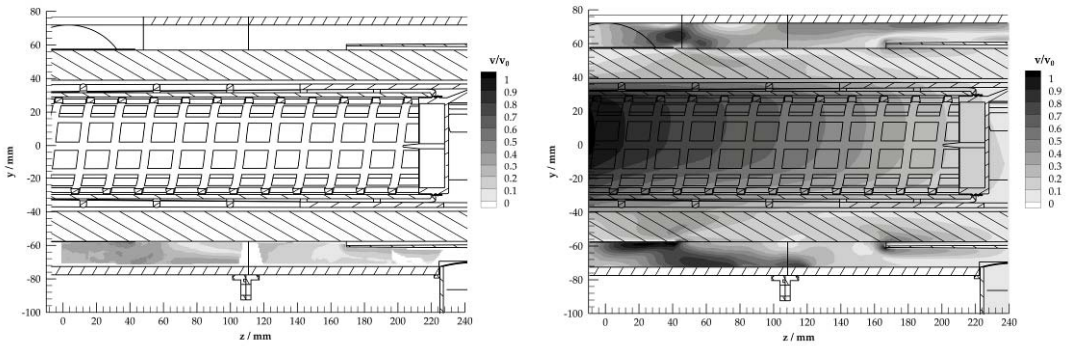

(a) *PIV* *(b) CFD*

Abbildung 4: Normalisierte Geschwindigkeits-Konturdiagramme der Ebene D

Zusammenfassung

Der Vergleich zwischen den PIV-Messergebnissen und den CFD-Berechnungs-ergebnissen zeigt in den Messebenen A und B eine sehr gute Übereinstimmung, wobei eine deutliche Einschnürung der Strömung im Eintrittsbereich in die Zyklonstufe und eine Abnahme der Umfangsgeschwindigkeit über die Messebene in Richtung hin zum Einlaufrohr zu erkennen ist. Dies lässt zusammen mit den Ergebnissen der Ebene D auf eine in Richtung Austragsbereich verlaufende, spiralförmige Strömung schließen, wie Sie bereits bei Standard Gegenstromzyklonen festgestellt worden ist [3]. Die Aussagekraft der PIV-Messergebnisse der Ebene D ist aufgrund der schwierigen Messverhältnisse eingeschränkt, qualitativ stimmen die Messergebnisse jedoch mit den CFD-Berechnungen überein und zeigen eine Einschnürung am Ende der Einlaufzarge und eine Rückströmung entlang der Zarge im Austragsbereich.
Die Ergebnisse zeigen dass eine Validierung der CFD-Berechnungen mittels PIV-Messung aufgrund der Strömungsverhältnisse nicht in allen Messebenen möglich ist. Eine Möglichkeit zur Validierung der Messebene D wäre beispielsweise eine Strömungsuntersuchung mittels Laser-Doppler-Anemometry.

Literatur

[1] J. Kompenhans, M. Raffel, S. T. Wereley, and C. E. Willert, *Particle image velocimetry: A practical guide,* Berlin, Heidelberg: Springer, 2007.

[2] M. Kraxner, *Empirische Ermittlung von Auslegungskriterien für Gleichstromzyklone in Multizyklonblöcken*. PhD thesis, TU München, 2013.

[3] M. Stiess, *Mechanische Verfahrenstechnik*. Springer-Lehrbuch, Berlin: Springer, 3., vollst. neu bearb. Aufl ed., 2009.

Heat transfer at immersed tube bundles in bubbling fluidized beds considering Geldart Type B particles

Gerhard Hofer
University of Natural Resources and Life Sciences, Department of Material Sciences and Process Engineering, Peter-Jordan-Str. 82, 1190 Vienna, Austria
gerhard.hofer@boku.ac.at

Abstract

Heat transfer coefficients regarding single tubes and tube bundles immersed in bubbling fluidized beds can be calculated by a variety of established mathematical models. Regarding Geldart Type A particles, Lechner (2013) has developed the so-called tube bundle reduction factor to predict heat transfer rates at tube bundles with varying tube diameter, spacing and arrangement, such as in-line, staggered or cross-over. The present work focuses on heat exchange measurements concerning Geldart Type B particles at staggered tube bundles. The tube diameter is varied as well as tube spacing and fluidization gas flow, respectively. Therefore, a heat transfer measurement test device (HTMT) has recently been put into operation.

Introduction

Many extensive studies have already been published regarding heat transfer in bubbling fluidized beds (BFB) with regards to immersed single tubes (Mathur et al., 1986; Kunii et al., 1991) and tube bundles (Grewal et al., 1983). Furthermore, the influence of tube alignment (horizontal, vertical) and arrangement (in-line, staggered, crossover) has been investigated. The most convenient calculation models to predict heat exchange coefficients pertaining immersed single tubes in bubbling fluidized beds might be those of Molerus et al. (1995) and Martin (2013), because these models establish a relation to fluidization velocity and bed voidage as well as to gas and particle properties. Since the abovementioned calculation methods of Molerus and Martin merely consider single tubes, Lechner (2013) developed a reduction factor to accommodate the obtained heat transfer rates for particular tube bundle designs considering Geldart Type A particles solely. In order to determine heat exchange coefficients for immersed tube bundles utilizing Geldart Type B particles, a heat transfer measurement test device (HTMT) has been constructed and put into operation. Horizontal and vertical tube alignment is considered as well as the variation of tube diameter and spacing while varying fluidization settings. Future research shall aim the investigation concerning the resistance of immersed heat transfer surfaces to particle movement.

Experimental Setup

Compressed air fluidizes the bulk material the HTMT contains. A rotary displacement gas meter is used to measure the actual gas flow, which can range from 2.5-400Nm³/h. Thereby, the PLC controlled ball valve regulates the gas flow. In order to conduct measurements at thermostatic conditions an air preheater warms the introduced air. The HTMT features a rectangular cross sectional area of 400x200mm and the bubbling bed height can get up to 350mm. Fig. 1 is showing an construction assembly of the HTMT and Fig. 2 the actual device in horizontal tube bundle configuration.
Exchangeable front covers with varying hole pitch (p_h=55, 70 and 85mm) are designed to accommodate dummy tubes with different diameters (d_o=20, 25 and 30mm) for the simulation of various horizontal tube bundles. In order to conduct measurements at vertical

tube bundles an exchangeable distributor plate will be constructed wherein the vertical tubes are fixed.
Four pipe dummies are equipped with resistance thermometers to measure the temperature of the fluidized bed T_{fb}.
The cylindrical heat transfer measurement probes are made of acrylic glass with an electrically heated copper part in the middle of it (Fig. 3). The acrylic glass ensures that the entire amount of introduced heat is transported to the contacting particles of the fluidized bed by isolating the probe from the HTMT casing. The copper cylinder can easily be manufactured with various shapes, such as finned, pinned or threaded. Resistance thermometers determine the temperature of the heated probe T_{hex}. Thereby, the PLC control records the electrical power consumption Q as well as the mentioned temperatures in order to calculate the heat transfer coefficient h with Equation (1).

$$h = \frac{Q}{A_{hex} \cdot (T_{hex} - T_{fb})} \tag{1}$$

Additionally, the HTMT side covers are exchangeable to attach the necessary equipment for the investigation of the resistance time distribution (RTD) inside a moving bubbling fluidized bed. Thus, the resistance of immersed heat exchange surfaces to the crosswise particle movement can be quantified.

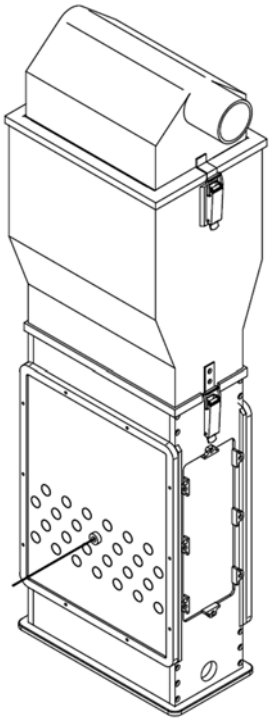

Fig. 1. HTMT construction assembly

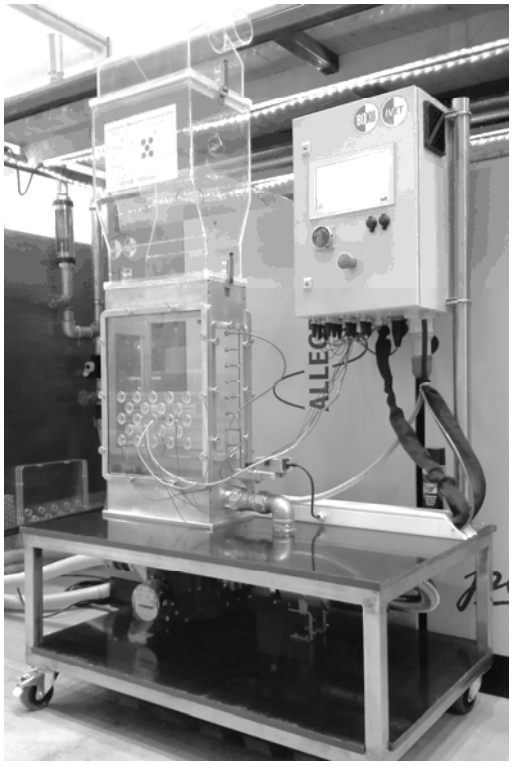

Fig. 2. HTMT in horizontal tube bundle configuration

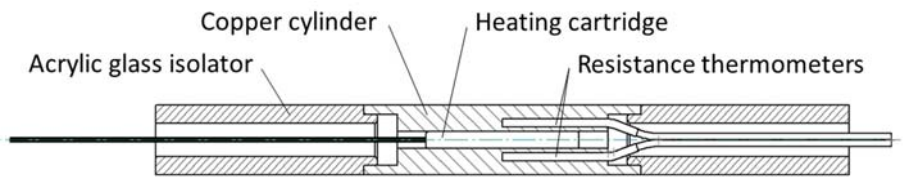

Fig. 3. Construction of the heated pipe dummy with plain surface design

To ensure reproducibility of measurement results the HTMT operation is standardized regarding the variation of the fluidization gas flow $\dot{V}_{gas}$. First tests have shown that it is inevitable to properly fluidize particles before conducting measurements in order to derive accurate results. This is particularly true for low gas velocities. Hence, a certain startup and measurement fluidization pattern has been programmed (Fig. 4).

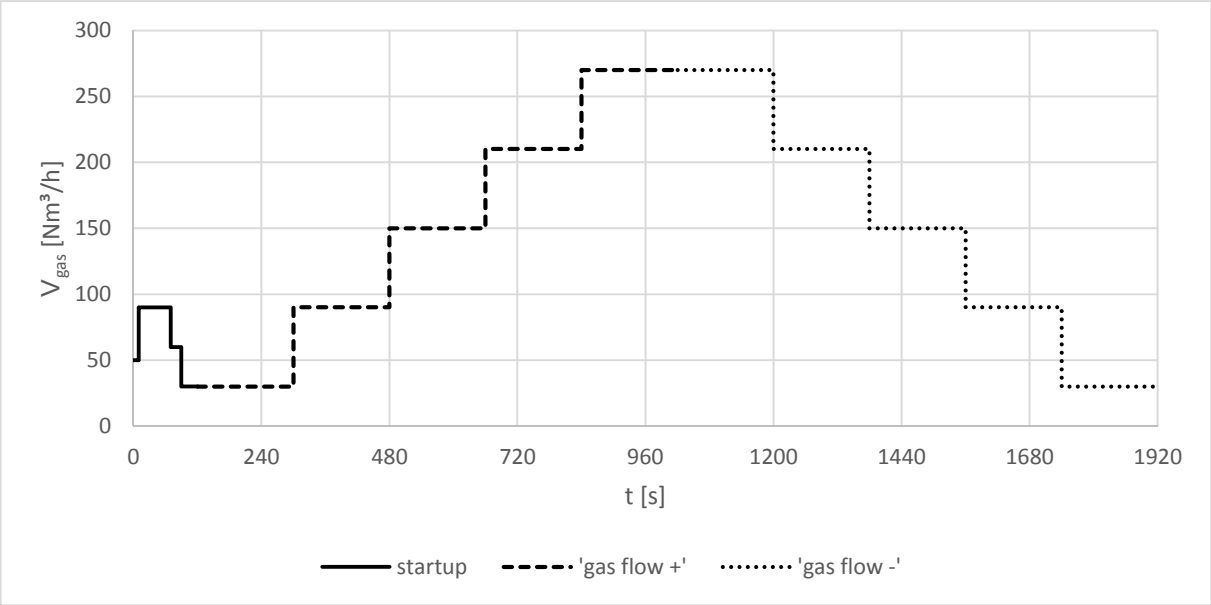

Fig. 4. HTMT standard startup and measurement gas flow pattern

Results

Utilizing the HTMT first tests have been conducted. Thereby, heat transfer at a single tube (d_o=20 and 30mm) and at a tube bundle (d_o=20mm, s_h=3.5) was investigated. The used bulk material (glass beads) has a particle density of ρ_p=2450kg/m³ and the particle diameter ranges from d_p=200-300µm. Fig. 5 is showing the measured heat transfer coefficients as a function of the superficial gas velocity U.

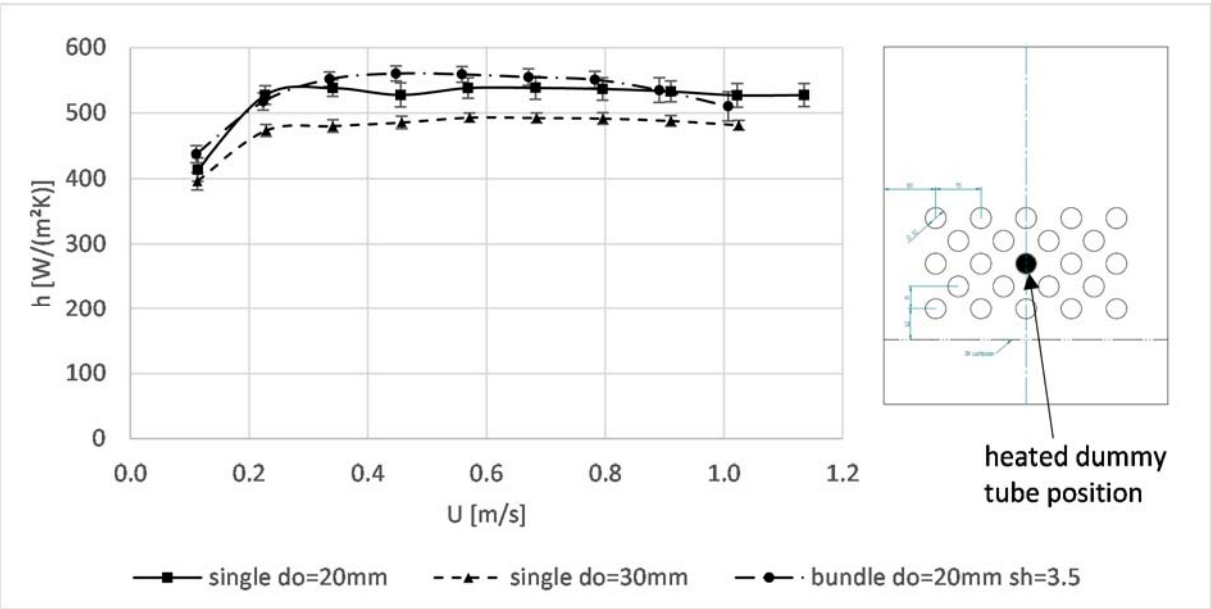

Fig. 5. Measured heat transfer rate as a function of gas velocity

It is shown that heat transfer decreases with increasing tube diameter. Further it can be seen, that heat exchange at the chosen bundle setting (d_o=20mm, s_h=3.5) is more or less corresponding to the d_o=20mm single tube. It can be assumed that a decreasing tube spacing leads to lower heat transfer rates.

Conclusion

A heat transfer measurement test device has been put into operation and first measurements were conducted. The considered particles are Geldart Type B and heat transfer will be measured at single tubes with varying tube diameter and tube bundles with different bundle settings (tube diameter and spacing). The upcoming research shall investigate the influence of immersed heat exchanger surfaces to the retention time distribution (RTD) of particles inside a bubbling fluidized bed with crosswise particle movement.

Notation

Symbol	Description	Unit
A_{hex}	Heat exchanger surface area	[m^2]
d_o	Outer diameter of heat exchanger tube	[m]
d_p	Particle diameter	[m]
h	Heat transfer coefficient	[$W \cdot (m^2K)^{-1}$]
p_h	Horizontal pitch of heat exchanger tubes	[m]
Q	Electrical power consumption	[W]
s_h	Horizontal spacing of heat exchanger tubes	[-]
T_{fb}	Temperature of fluidized bed	[K]
T_{hex}	Temperature of heat exchanger	[K]
U	Superficial gas velocity	[m/s]
V_{gas}	Fluidization gas flow	[Nm^3/h]
ρ_p	Particle density	[kg/m^3]

References

Grewal, N.S., Saxena, S.C., (1983). Experimental Studies of Heat Transfer between a Bundle of Horizontal Tubes and a Gas-Solid Fluidized Bed of Small Particles. Ind.Eng.Chem. Process Des.Dev. 22, 367-376.

Kunii, D., Levenspiel, O., (1991). Fluidization Engineering. Butterworth-Heinemann, USA, 2nd Ed., 1991.

Lechner, S., Merzsch, M., Krautz, H.J., (2013). Heat-transfer from horizontal tube bundles into fluidized beds with Geldart A lignite particles. Powder Technology 253, 14-21.

Martin, H., (2013). Wärmeübergang in Wirbelschichten (chap. M5), VDI Wärmeatlas. Springer-Verlag, Berlin Heidelberg, 11th Ed., 2013.

Mathur, A., Saxena, S.C., Chao, A., (1986). Heat Transfer from an Immersed Vertical Tube in a Gas-Fluidized Bed. Ind.Eng.Chem. Process Des.Dev. 25, 156-163.

Molerus, O., Burschka, A., Dietz, S., (1995). Particle migration at solid surfaces and heat transfer in bubbling fluidized beds 2. Chemical Engineering Science 50 (5), 879-885.

The performance of photocatalysis – submerged microfiltration membrane system for water treatment

Thi-Huyen-Trang Trinh, Wolfgang M. Samhaber
Johannes Kepler University Linz, Institute of Process Engineering,
4060 Leonding, Welser Straße 42
trinhtrangbk@gmail.com, Wolfgang.Samhaber@jku.at

Abstract

Microfiltration (MF) membrane was coupled with UV/TiO_2 photocatalysis aiming to separate catalytic particles from treated mixture. The performance of photocatalysis – submerged MF membrane system was investigated. This paper reports the photocatalytic reactivity of TiO_2 catalyst and the separation performance of ceramic membrane in the coupling system. The results revealed that the combination of MF filtration with photocatalysis enhanced the photocatalytic efficiency as well as the permeate flux through membrane in comparison with the individual application of photocatalysis and MF process.

Introduction

There has been increasing interest in applying UV/TiO_2 photocatalysis for water and waste water treatment due to its ability to degrade and mineralize various organic compounds. Generally, two modes of TiO_2 catalytic particles in the reactor are applied: (i) TiO_2 dispersed in aqueous mixture and (ii) TiO_2 immobilized on support materials (glass, zeolites, membrane, etc.). Obviously, in case of the immobilized TiO_2 on a support the active surface is reduced what usually results in a loss of photoactivity. If the suspension of the catalyst is applied, the active surface is much greater. However, a post-treatment of separation of catalytic particles is necessary required.

A promising approach for separation of suspended TiO_2 is the coupling of photocatalysis with membrane process such as Microfiltration (MF), Ultrafiltration (UF) and Nanofiltration (NF). In the literature, it has been proved that MF is successful to separate nanosized catalysts from aqueous suspensions [1–6]. R. Molinari and co-workers [3] have investigated the performance of not only pressurized but also depressurized (submerged) membranes. The authors concluded that the submerged membrane showed the advantage in term of permeate flux and could be interesting for application purposes. There have been some attempts previously in combination of UV/TiO_2 photocatalysis with submerged membranes [2–4,7,8]. Nevertheless, the literature review reveals that most of papers have focused on the performance of polymeric membranes. Although polymeric membranes have the advantage of lower cost, ceramic membranes exhibit high resistance to UV light and high permeability. In fact, there is little published data on ceramic membranes applied in hybrid photocatalysis-membrane systems [5].

Therefore, the main objective of this study was to investigate the performance of a UV/TiO_2 photocatalyis - membrane system employed submerged ceramic MF membrane. The permeate flux through membrane and the decomposition rate of organic compound in the hybrid system was determined and discussed.

Materials and method

Materials

Aeroxide® TiO_2 P90 (Evonik, Germany) was used in all experiments as the photocatalyst.

For the reaction, oxalic acid (> 97%, Fluka, M = 90 g/mol) was chosen, because it is not only the water pollutant resulting in many processes but also the intermediate of other organic compounds degradation [9]. The concentration of oxalic acid in the reactor was 100 - 110 mg/L (the molar concentration was about 1.2 mmol/L).

A ceramic submerged membrane provided by ItN Nanovation (Germany) with the pore size of 0.2 µm was employed. The effective area of the membrane was 0.075 m^2.

Experimental set-up

Figure 1 shows the schematic diagram of the experimental set-up. The membrane box has a rectangular channel with dimensions of 160 mm in length, 40 mm in width, and 700 mm in height, where a flat sheet membrane was placed at the middle. The volume of suspension in the membrane box was approx. 3.5 L.

A medium pressure UV lamp (UMEX Dresden, Germany) was used to irradiate either the feed tank or directly the retentate compartment of the membrane unit. This paper presents the results obtained in case of photocatalysis followed by MF membrane.

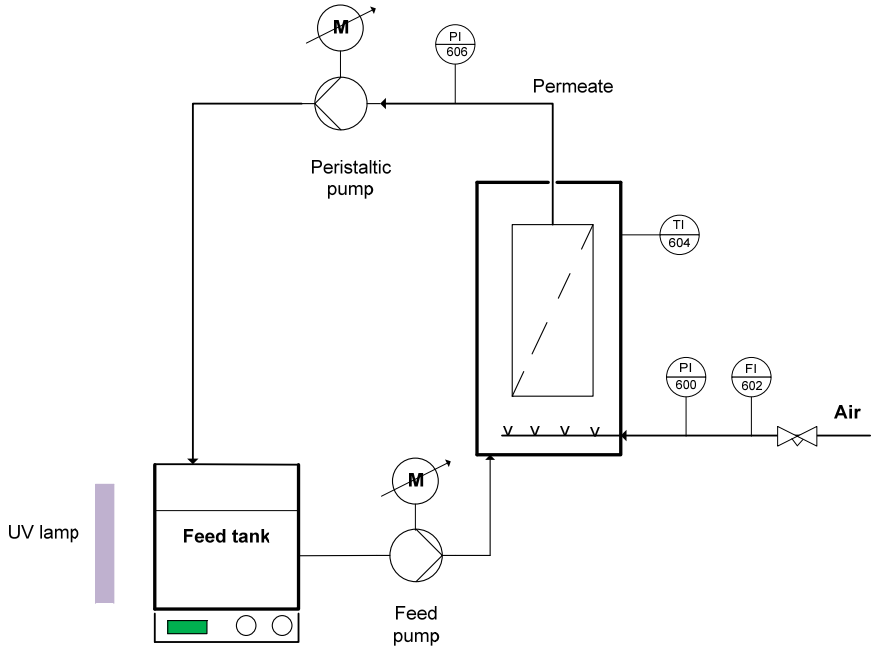

Figure 1: Schematic diagram of the photocatalysis – MF membrane system

Analytical method

The concentration of TiO_2 suspension was determined based on the calibration of turbidity and concentration. The turbidity measurements were done by using turbidity meter (WTW Turb-500, Germany). Electrical conductivity and pH of the reaction mixture were monitored during the irradiation time. The samples were withdrawn with interval time to measure the Total Organic Carbon (TOC).

Results and discussion

Figure 2 compares the changes of TOC concentration in the photocatalysis – MF system with and without membrane performance. It was obtained 95 – 97% of TOC degradation after two hours of UV irradiation in both cases and the reaction rates were comparable.

It can be seen from Figure 3 that the permeate flux was significantly enhanced in the hybrid system in comparison with the performance of MF alone. The result matches the observed in previous study by Mozia et al. [5]. The authors suggested that the abrasion of a membrane skin layer by the photocatalytic particles might improve the permeate flux.

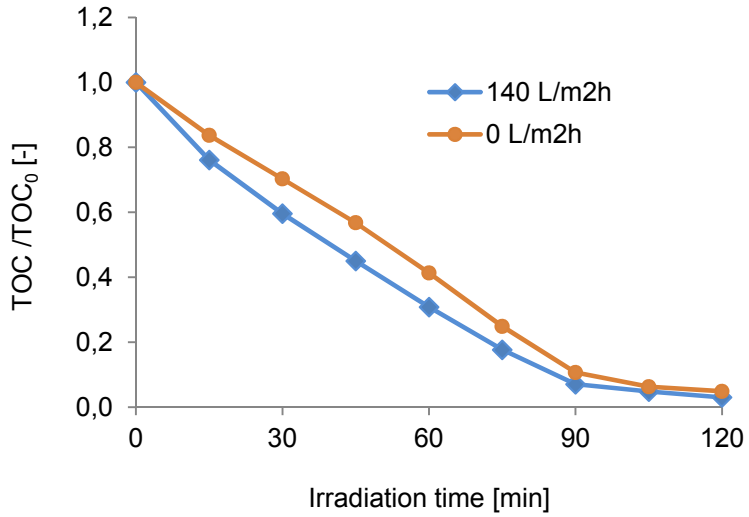

Figure 2: Changes of TOC concentration during irradiation time with and without membrane filtration (C_{TiO2} = 0.5 g/L)

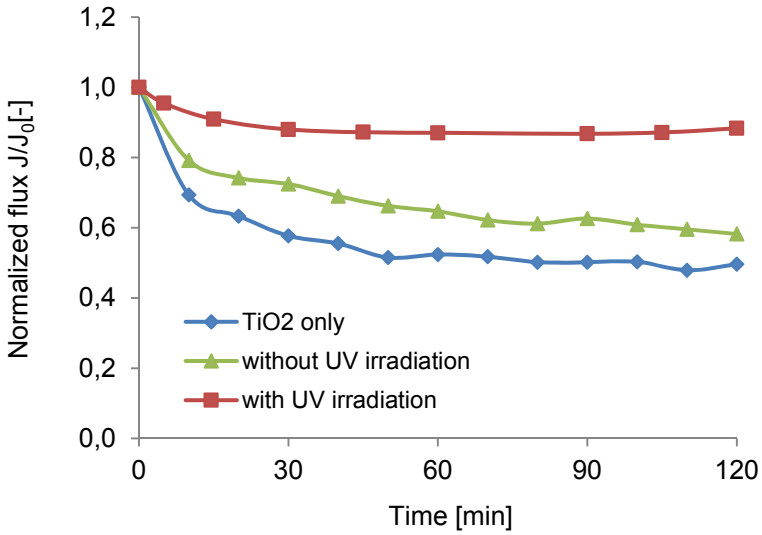

Figure 3: Variation of the normalized flux with different operating modes (C_{TiO2} = 0.5 g/L, Permeate flux J_p = 140-144 L/m^{2}h)

Conclusions

The results have shown that TiO_2 catalytic particles were effectively separated without

loss of photocatalytic activity by the photocatalysis - MF membrane system. Furthermore, the performance of MF membrane coupled with photocatalysis was found to be improved up to 43% in term of permeate flux as compared to MF process alone.

Acknowledgement

The authors gratefully acknowledge financial support of Erasmus Mundus – GATE program and wish to thank ItN Nanovation AG (Saarbrücken, Germany) as well as UMEX GmbH Dresden (Germany) for providing membranes and UV irradiation unit, respectively.

Literatures

[1] W. Xi, S.U. Geissen, Separation of titanium dioxide from photocatalytically treated water by cross-flow microfiltration, Water Res. 35 (2001) 1256–1262.

[2] J. Fu, M. Ji, Z. Wang, L. Jin, D. An, A new submerged membrane photocatalysis reactor (sMPR) for fulvic acid removal using a nano-structured photocatalyst, J. Hazard. Mater. 131 (2006) 238–242.

[3] R. Molinari, a. Caruso, P. Argurio, T. Poerio, Degradation of the drugs Gemfibrozil and Tamoxifen in pressurized and de-pressurized membrane photoreactors using suspended polycrystalline TiO_2 as catalyst, J. Memb. Sci. 319 (2008) 54–63.

[4] R.A. Damodar, S.J. You, G.W. Chiou, Investigation on the conditions mitigating membrane fouling caused by TiO_2 deposition in a membrane photocatalytic reactor (MPR) used for dye wastewater treatment, J. Hazard. Mater. 203-204 (2012) 348–356.

[5] S. Mozia, K. Szymański, B. Michalkiewicz, B. Tryba, M. Toyoda, A.W. Morawski, Effect of process parameters on fouling and stability of MF/UF TiO_2 membranes in a photocatalytic membrane reactor, Sep. Purif. Technol. 142 (2015) 137–148.

[6] G. Zhang, J. Zhang, L. Wang, Q. Meng, J. Wang, Fouling mechanism of low-pressure hollow fiber membranes used in separating nanosized photocatalysts, J. Memb. Sci. 389 (2012) 532–543.

[7] H.J. Szabolcs Kertèsz , Jiří Cakl, Submerged hollow fiber microfiltration as a part of hybrid photocatalytic process for dye wastewater treatment, Desalination. 343 (2013) 106–112.

[8] S.I. Patsios, V.C. Sarasidis, A. J. Karabelas, A hybrid photocatalysis-ultrafiltration continuous process for humic acids degradation, Sep. Purif. Technol. 104 (2013) 333–341.

[9] M.I. Franch, J.A. Ayllón, J. Peral, X. Domènech, Photocatalytic degradation of short-chain organic diacids, Catal. Today. 76 (2002) 221–233.

Entwicklung einer Versuchsanlage für Fest-Flüssig-Trennversuche an Massenkraftabscheidern

Thomas Senfter[1], Mathias Senn[1], Anke Bockreis[2], Wolfgang Rauch[2] und Michael Kraxner[1]
[1] MCI – Umwelt-, Verfahrens- & Energietechnik, Universitätsstraße 15, Innsbruck, AT
[2] Universität Innsbruck, Arbeitsbereich Umwelttechnik, Technikerstraße 13, Innsbruck, AT
thomas.senfter@mci4me.at

Kurzfassung

Für die Untersuchung von Fest-Flüssig-Trennapparaten in Form von Massenkraftabscheidern werden üblicherweise Versuchsanlagen verwendet, bei denen nach dem Trennapparat der partikelreiche sowie der partikelarme Strom in einen gemeinsamen Suspensionsbehälter geleitet werden. Dies ist hinsichtlich der Bestimmung der Leistungsparameter mitunter ungünstig, da die entsprechenden Messungen auf wenig zuverlässige Methoden aufbauen. Deshalb wird in der vorliegenden Arbeit ein alternativer Ansatz verfolgt, bei welchem unmittelbar vor dem Trennapparat die Zudosierung der Partikel in das Versuchsfluid erfolgt. Dem Trennapparat nachgeschaltet wird ein Endabscheider, mit welchem die nicht abgeschiedenen Partikel aus dem Fluidstrom entfernt werden sollen.

Einleitung

In vielen Technologiebereichen ist es notwendig, theoretische Überlegungen anhand von Experimenten zu bestätigen. Dies gilt auch für die mechanische Fest-Flüssig-Trennung bei der Untersuchung von Massenkraftabscheidern. Theoretische Ansätze und Simulationsergebnisse bilden die Grundlage und werden häufig an Versuchsanlagen validiert. Für die Auslegung und Optimierung eines Trennapparats soll eine Versuchsanlage entwickelt werden, welche für einen möglichst vielseitigen Einsatzbereich hinsichtlich Messtechnik, Partikelbeladung und Volumenstrom geeignet ist. Ziel ist es, einen exakt definierten partikelbeladenen Fluidstrom reproduzierbar herzustellen.
In vielen Fällen werden Versuchsanlagen verwendet, bei welchen eine zu Versuchsbeginn hergestellte Suspension direkt dem Trennapparat zugeführt wird. Nach dem Trennapparat werden der partikelarme und der partikelreiche Strom in denselben Suspensionsbehälter zurückgeführt, siehe Abbildung 1. Die Bestimmung der Abscheideleistung erfolgt dabei anhand der Konzentrationsmessungen DI1-2 vor und nach dem Trennapparat. Anwendung findet dieses Anlagenkonzept beispielsweise bei *Braun* [1], *Bohnet* [2] oder *Neeße* [3].

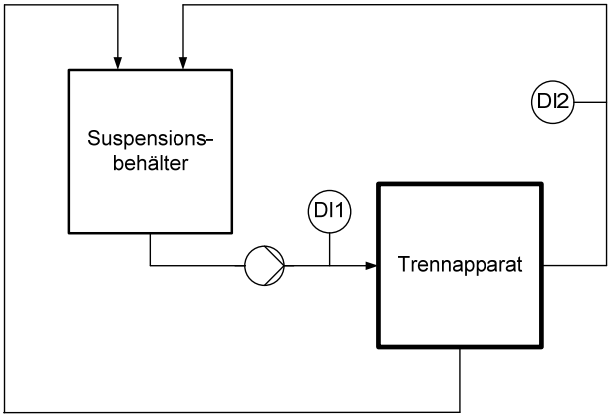

Abbildung 1: Übliches Versuchsanlagenkonzept zur Untersuchung von Trennapparaten

Zur Konzentrationsmessung werden bevorzugt optische Extinktionsmessverfahren angewendet. Hierbei wird jene Lichtmenge gemessen, die das Messobjekt durchdringt [4,5]. Diese Technik ist berührungslos und es wird keine Rückwirkung auf das zu untersuchende System hervorgerufen [6]. Eine wesentliche Einschränkung bei diesem Messverfahren resultiert aus dem relativ großen Einfluss der optischen Partikeleigenschaften auf das Messergebnis. Dies führt dazu, dass bei Verwendung unterschiedlicher Messgeräte oft auch die Messergebnisse unterschiedlich sind [7]. In einigen Anwendungen wird auf die optische Extinktionsmessung verzichtet und Proben aus dem Suspensionsbehälter sowie dem Strom nach dem Trennapparat entnommen. Durch Trocknung und Partikelmassenbestimmung ist somit die Ermittlung des Abscheidegrades möglich. Einschränkend wirkt sich auf diese Methodik aus, dass hinsichtlich der Probenahme die Isokinetik eine wesentliche Forderung darstellt [8]. Dies erfordert spezielle Techniken, wobei trotz aufwendiger Einrichtungen die Fließgeschwindigkeit der Probe von jener in der zu beprobenden Leitung erheblich abweicht und somit meist zu ungenauen Ergebnissen führt [5].
Als unproblematisch gilt in der Praxis die gravimetrische Massenbestimmung. Auf diesen Umstand aufbauend soll im Gegensatz zum üblichen Versuchsanlagenkonzept im vorliegenden Projekt die Partikelzugabe unmittelbar vor dem Trennapparat erfolgen, siehe Abbildung 2.

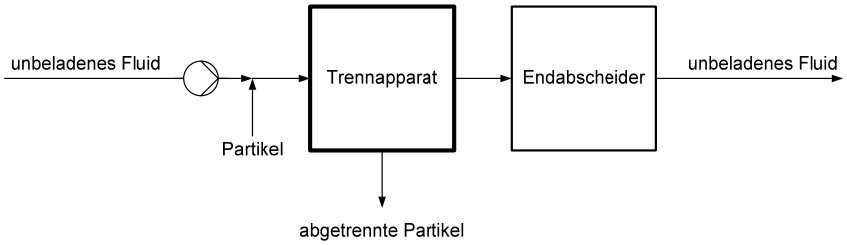

Abbildung 2: Alternatives Versuchsanlagenkonzept zur Untersuchung von Trennapparaten mittels eines Endabscheiders

Die Partikel, welche sich nach dem Trennapparat im partikelarmen Strom befinden, werden mittels eines Endabscheiders aus dem Fluid entfernt. Die Bestimmung der Abscheideleistung erfolgt bei diesem Anlagenkonzept gravimetrisch. Hierbei ist der Abscheidegrad der Quotient aus der Masse der abgetrennten Partikel und jener der zugegebenen Partikel. Diese Werte sind vergleichsweise einfach und zuverlässig zu bestimmen.

Umsetzung Versuchsanlage

Die Versuchsanlage, dargestellt in Abbildung 3, besteht aus einem Vorlagebehälter, in welchem sich das unbeladene Fluid befindet. Dieses wird von der Zirkulationspumpe dem zu untersuchenden System zugeführt. Die Störstoffe werden in die Zirkulationsleitung dosiert und vom Trennapparat abgeschieden. Nicht abgeschiedene Partikel gelangen in ein Sedimentationsbecken bzw. in den nachgeschalteten Endabscheider, dessen Trennverhalten eine nahezu vollständige Abtrennung der Partikel ermöglicht.

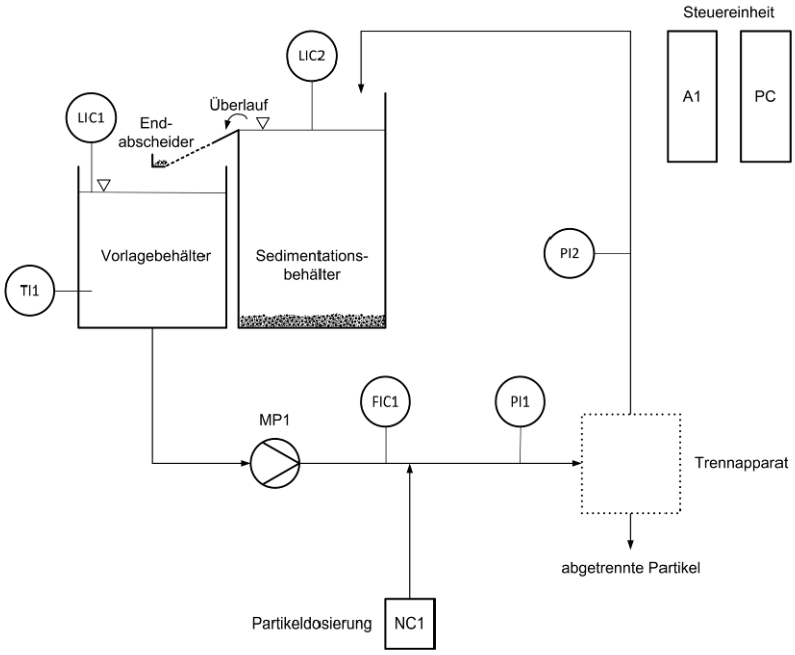

Abbildung 3: Anlagenschema

Der Füllstand wird mittels der Sensoren LIC1 und LIC2 überwacht. Die Erkennung einer Leckage im System sowie eine Not-Abschaltung erfolgt, wenn die Summe aus beiden Messwerten nicht konstant ist. Der Volumenstrom wird mit dem eingebauten Flügelradsensor FIC1 im unbeladenen Fluid ermittelt. Die Drucksensoren PI1 und PI2 liefern den Druckverlust über den Trennapparat. Eine besondere Herausforderung besteht in der Partikeldosierung, da die Partikel in ein Überdruck-System eingebracht werden müssen. Klassische und in vielen Bereichen bewährte Fördereinrichtungen, wie beispielsweise Schneckenförderer, Bandförderer oder Schwingrinnen, sind im gegebenen Anwendungsfall ungeeignet [9,10]. Aus diesem Grund wurde für das vorliegende Projekt eine Kolbendosierung entwickelt. Dabei werden die Partikel vor Versuchsbeginn in das Überdruck-System gebracht und während des Versuches, wie in Abbildung 4 dargestellt, kontinuierlich dem Fluidstrom zudosiert.

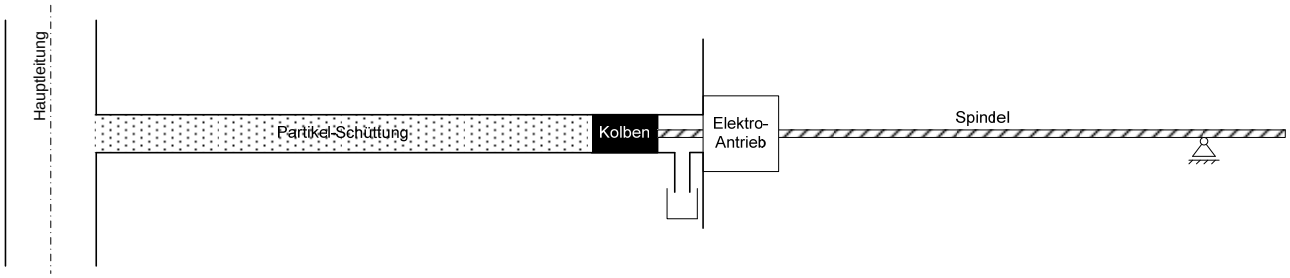

Abbildung 4: Schema Partikeldosierung

Durch die Verwendung eines Schrittmotos als Antrieb für die Partikeldosierung sind die Position des Kolbens sowie die Vorschubgeschwindigkeit beliebig wählbar. Dies ermöglicht die Abdeckung eines großen Partikelmassenstrombereichs.

Ergebnisse

Die ersten Vorversuche an der Anlage bestätigen die modulare und flexible Anwendbarkeit für die angestrebten Untersuchungen von Trennapparaten. Der maximale Volumenstrom

beträgt bei den gewählten Komponenten 40 m³/h. Der dosierbare Partikelmassenstrom liegt zwischen 50 g/h und 100 kg/h. Limitierend auf die mögliche Versuchszeit wirken sich die Abmessungen der Partikeldosierung aus. Durch die Parallelschaltung von zwei baugleichen, hintereinander betriebenen Dosiereinheiten ist jedoch auch ein ununterbrochener Betrieb der Versuchsanlage möglich.

Literatur

[1] Braun, T., Theoretische und experimentelle Untersuchungen des Einflusses der Feststoffkonzentration und der Partikelgrößenverteilung auf das Trennverhalten von Hydrozyklonen, Dissertation, TU Carolo-Wilhelmina, Braunschweig, 1989.

[2] Bohnet, M., Neuere Untersuchungen über die Trennwirkung und den Druckverlust von Hydrozyklonen, Chemische Technik, 20, 1968.

[3] Neeße, T., Schubert, H., Praktische und theoretische Aspekte der Dichtstromklassierung, Aufbereitungstechnik, 32, 459-472, 1991.

[4] Löffler-Mang, M., Optische Sensorik, 1. Auflage, Vieweg+Teubner Verlag, 2012.

[5] Tränkler, H.-R., Reindl, L., Sensortechnik, 2. Auflage, Springer Verlag, 2014.

[6] Steinke, L., Wessely, B., Ripperger, S., Optische Extinktionsmessverfahren zur Inline-Kontrolle disperser Stoffsysteme, Chemie Ingenieur Technik, 81, 735-747, 2009.

[7] Steinke, L., Vetter, A., Ripperger, S., Die Partikelzählung in Flüssigkeiten unter Berücksichtigung der Rückführbarkeit der Messgrößen, Filtrieren und Separieren, 28, 2014.

[8] Stieß, M., Mechanische Verfahrenstechnik – Partikeltechnologie 1, 3. Auflage, Springer Verlag, 2008.

[9] Vetter, G., Handbuch Dosieren, 2. Aufl., Vulkan-Verlag, 2002.

[10] Marthinussen, S.-A., The Effect of Fluid Viscosity on Hydrocyclone Performance, Master Thesis, Process Technology, University of Bergen, 2011.

Membrane Module Design Optimization Using CFD

Bahram Haddadi, Christian Jordan, Philipp Schretter, Tino Lassmann, Michael Harasek
Technische Universität Wien, Institute of Chemical Engineering
Getreidemarkt 9/1662, 1060 Wien
bahram.haddadi.sisakht@tuwien.ac.at, christian.jordan@tuwien.ac.at,
e0717910@student.tuwien.ac.at, tino.lassmann@tuwien.ac.at
michael.harasek@tuwien.ac.at

Introduction

In today's world there is a common agreement on moving from fossil fuels to alternative sources [1]. One of the very promising sources of energy is biogas [2]. A sustainable way of biogas production is anaerobic digestion of organic materials. Usually the product of this process is either methane or hydrogen mixed with carbon dioxide. Membranes are one of the most cost and energy efficient ways of gas separation [3]. Therefore it is important to consider gas permeation for biogas upgrading. In this context computational fluid dynamics (CFD) not only can be used to analyze separation using membrane modules but also to optimize the separation process.

Membrane modeling

Gas permeation through dense membrane is often described by a solution-diffusion mechanism; the process described by this mechanism can be divided into three main steps [4]:

- Sorption of the penetrants at the feed side
- Diffusion across the membrane, and
- Desorption at the permeate side

Mathematically solution-diffusion mechanism is described by the relation between driving force (partial pressure difference of specie i at both sides of the membrane) and the mass flow rate through the membrane:

$$J_i = \Pi_i(p_{i,0} - p_{i,l}) \quad (1)$$

J_i is the specific mass flow rate of specie i through membrane, $p_{i,0}$ and $p_{i,l}$ are partial pressures of specie i at feed and permeate side of membrane and the Π_i is the permeability of specie i divided by membrane selective layer thickness [5]. Permeability shows the membrane ability to permeate gas component i.

CFD methods

Computational fluid dynamics (CFD) is one of powerful methods in analyzing systems including fluid flow, mass transfer and heat transfer. For using CFD a good knowledge of phenomena and also underlying physics of them is required. When a new CFD solver is developed it should be tested and validated, e.g. against lab experiments. After debugging and validation solver can be used for detailed investigation of processes, and also optimizing or scale up of different processes.
OpenFOAM® [6] is a free open source CFD tool which is published under GNU public license and can be used for modeling multitude of flow phenomena. Since it is open

source the source code is available and can be modified to implement functionalities which are not provided in the original release version.

Solver (LTSMembraneFoam)

There is no dedicated solver in the OpenFOAM® package for modeling membranes. Therefore in the current study a new solver for modeling membranes was developed based on the OpenFOAM® platform. This solver can handle multi-region flows and also mass and heat transfer within the regions as well as between regions. The solution-diffusion mechanism was implemented for handing gas permeation through a membrane. Since membranes are usually operated in steady state conditions, the new solver was developed applying the LTS concept for steady state solutions.

Geometry

The simplified membrane module investigated in this study is a hollow fiber membrane module with seven fibers (a commercial membrane module can have up to 10^4 fibers). The fibers are 0.5 m long and 0.001 m in diameter. Flow enters the module from left had side and the retentate exits at right hand side (Figure 1). The geometry and mesh are created with commercial geometry and mesh creation software Ansys GAMBIT®. The module has five outlets at permeate side, and depending on the membrane operation configuration (co-current, counter-current or mixed current) one of the outlets is open and the rest are closed (Table 1).

Figure 1: Seven fiber module geometry and exit positioning at permeate side (scaled 1:10 in length)

Table 1: Investigated geometries based on the permeate outlet position

Case	Case 1	Case 2	Case 3	Case 4	Case 5
Permeate outlet (Figure 1)	Ex 1 100% counter-current	Ex 2	Ex 3 50/50	Ex 4	Ex 5 100% co-current

Simulation settings

The module was used for separation of CO_2 from CO_2, CH_4 and O_2 mixture. The feed has a flow rate of 6.2×10^{-6} kg/s at 316.5 K and exits at pressure of 1.1 bar. The pressure at permeate outlet is 9 bar. The permeances and mass fractions of different species are given in table 2.

Table 2: Species mass fractions and permeances through membrane [2]

Specie	CH_4	CO_2	O_2
Mass fraction	0.406	0.58	0.012
Permeance [$m^3/(m^2$ bar s)]	1.59×10^{-6}	5.91×10^{-5}	1.36×10^{-5}

Validation

The new developed LTSMembraneFoam was validated against a process simulation model which was implemented into Aspen Custom Modeler® (ACM) [7]. Case 1 was used as the base case for this part of study and five different feed flow rates were simulated with it. The five mass flow rates are: 6.2×10^{-7}, 1.2×10^{-6}, 3.1×10^{-6}, 6.2×10^{-6}, 3.1×10^{-5} kg/s. As it can be seen from figure 3, retentate mass fractions at different stage cuts are calculated and compared. The results from CFD are in good agreement with ACM data [8].

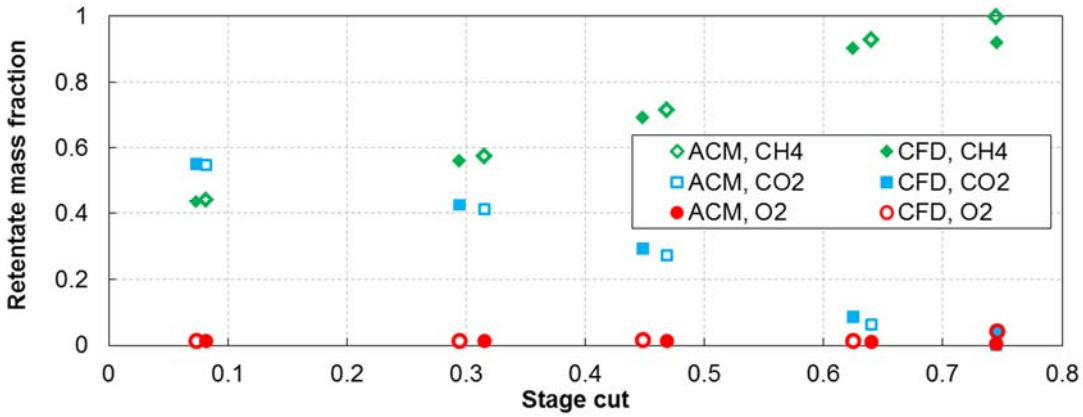

Figure 2: Comparison of ACM and CFD results at different stage cuts for case 1 [7]

Data extraction

In all the evaluations in this study results from permeate side are extracted along the center line of shell side and for retentate side from center line of central fiber. For sake of space just the contour lines of case 3 are shown, since it is a mixed current flow configuration and can describe both configurations.

Pressure results

In figure 3-a the fiber side pressure profile along fibers can be seen, as it is expected the pressure reduces by moving from inlet to outlet. The pressure drop inside the fibers is the same for all cases. But by having a look at permeate side (figure 3-b) it can be seen the case 1 (counter current configuration) has the lowest pressure drop in the shell side, and for all cases lowest pressure happens at the outlet.

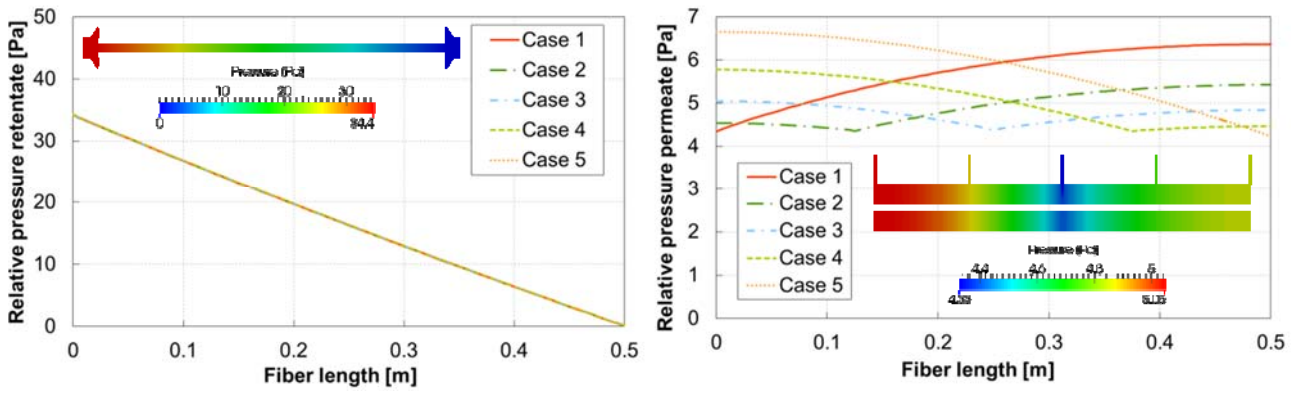

a b

Figure 3: Pressure profiles and pressure contour (case 3) along fiber and shell side

Mass fractions results

As it can be seen mass fraction of CH_4 increases along the membrane at the fiber side (figure 4-a), this is because of lower permeance of CH_4 compared to the other two components. The mass fraction of CH_4 also increases at permeate side along the module length, this is because by moving towards the retentate outlet side of the module the mass fraction of CH_4 at the retentate side increases. According to equation 1 this will also increase driving force for CH_4 permeation. The same trend can also be seen for two other components, but for sake of space they are not listed.

Outlet mass fractions and velocities

As it can be seen from figure 5-a the lowest mass flow of CO_2 occurs at the module with fully co-current flow in there, this shows with this configuration more CO_2 is removed.

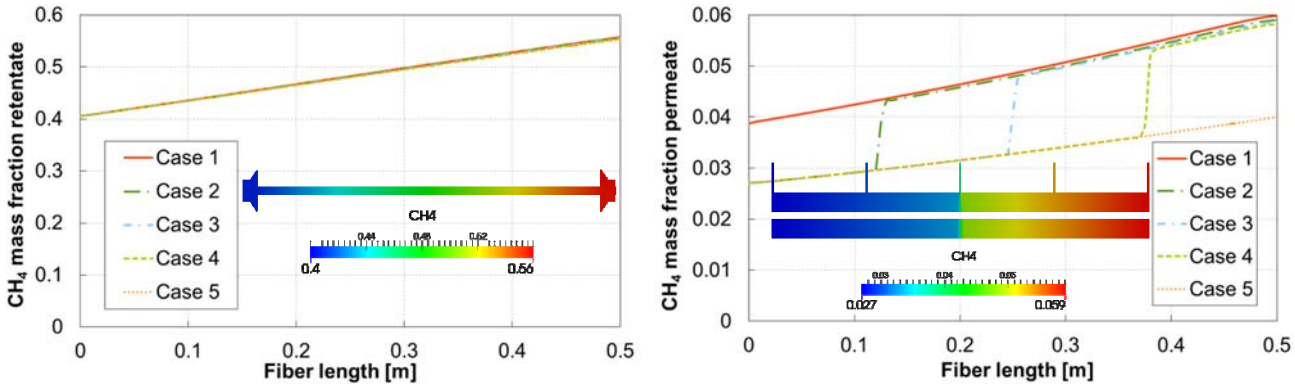

a b

Figure 4: CH_4 mass fraction profiles and contour (case 3) for fiber and shell side

Figure 5-b shows the velocity at the permeate outlet at all cases. As it can be seen the counter-flow configuration has the highest velocity at outlet, in this configuration most gas passes the membrane.

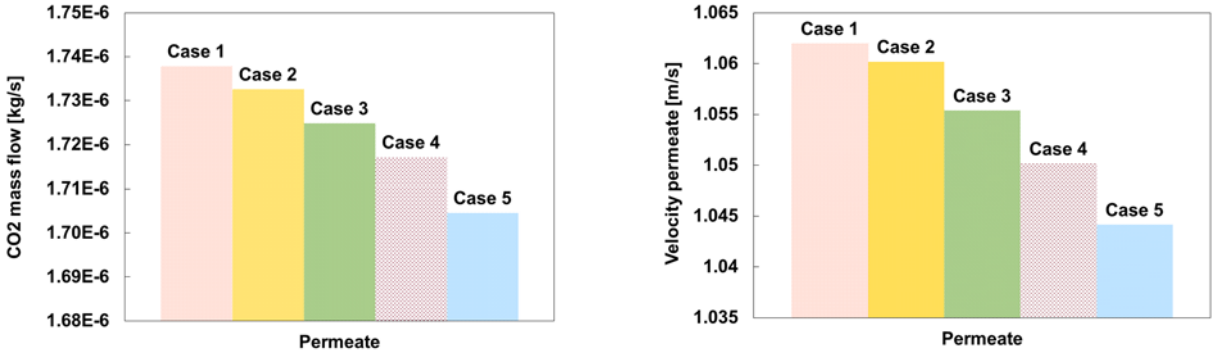

a b

Figure 5: CO_4 mass flow and outlet velocities at permeate outlet for different cases

Conclusion

In this study a new solver was written based on the open source CFD tool OpenFOAM®, LTSMembraneFoam. This solver is used for simulating gas separation membrane modules operating at steady state conditions. It can be applied for detailed analysis of membrane modules behavior and also for design optimization of membrane modules. Therefore a seven fiber hollow fiber module was investigated with the newly developed solver to

investigate the effect of outlet positioning (flow configuration) on the quality and quantity of separation.

References

[1] Turner JA. Sustainable hydrogen production. Science. 2004 Aug 13; 305(5686): 972-4.
[2] Makaruk A, Miltner M, Harasek M. Membrane biogas upgrading processes for the production of natural gas substitute. Separation and Purification Technology. 2010 Jul 30; 74(1): 83-92.
[3] Scott K. Handbook of industrial membranes. Elsevier; 1995 Dec 20.
[4] Shao L, Low BT, Chung TS, Greenberg AR. Polymeric membranes for the hydrogen economy: contemporary approaches and prospects for the future. Journal of Membrane Science. 2009 Feb 5; 327(1): 18-31.
[5] Baker RW. Membrane technology. John Wiley & Sons, Inc.; 2000.
[6] OpenCFD Ltd. United Kingdom: OpenCFD Ltd; 2015 [last visited 2015 May]. Available from: http://www.openfoam.org/licence.php.
[7] Aspen Technology Inc.. ACM V7.3. Burlington: . Aspen Technology Inc.; 2011.
[8] Lassmann T. The purification of fermentatively produced hydrogen using gas permeation: A practical and simulative approach. Vienna: Technische Universität Wien; 2015.

Vergleich der Trägermaterialien γ-Al_2O_3 und t-ZrO_2 in der katalytischen Methanisierung von CO_2

Philipp Biegger, Ana Roza Medved, Markus Lehner
MU Leoben, Lehrstuhl für Verfahrenstechnik des Industriellen Umweltschutzes,
A-8700 Leoben, Franz-Josef-Straße 18
philipp.biegger@unileoben.ac.at, ana.medved@unileoben.ac.at,
markus.lehner@unileoben.ac.at

Kurzfassung

Die Methanisierung von CO_2 erfordert Verbesserungen hinsichtlich Lastflexibilität und Stand-by-Verhalten, um innerhalb der „Power to Gas"-Technologie eingesetzt zu werden. Zentrale Elemente der angestrebten Weiterentwicklungen sind die Verwendung von Wabenkatalysatoren auf Keramikbasis und ein adaptiertes Verfahrenskonzept. An einer Laboranlage wurden die Funktion und der Einfluss verschiedener Katalysatorsysteme auf die Methansynthese untersucht. Dabei konnten neben Auswirkungen auf die erzielten CH_4-Konzentrationen im Produktgas auch der Einfluss auf die Katalysatorstandzeit beobachtet werden.

Einleitung

Methanisierungsverfahren wurden bereits seit den 1960er Jahren im Bereich der Kohletechnik entwickelt, um fossiles Erdgas durch künstlich erzeugtes SNG (Synthetic Natural Gas) zu substituieren. Gemäß der Sabatier-Reaktion kann Methan CH_4 und Wasserdampf H_2O durch die heterogen gaskatalytische Reaktion von Kohlenmonoxid CO bzw. Kohlendioxid CO_2 mit Wasserstoff H_2 hergestellt werden. Die Versorgung mit den Eduktgasen H_2 und CO wurde über die Vergasung von Kohle ermöglicht, dementsprechend wurden die Anlagen dabei als großtechnische, kontinuierlich bei gleichbleibender Last betriebene Apparate konzipiert. [1–3]
Das neue Anwendungsgebiet innerhalb der Power to Gas – Technologie bringt andere Voraussetzungen mit sich, schließlich ist das Hauptziel die Speicherung von elektrischer Energie in einem stofflichen Energieträger. Dazu wird idealerweise überschüssige Energie aus erneuerbarer Erzeugung eingesetzt, um in einem Elektrolyseur Wasser in H_2 und O_2 zu spalten. Um die örtlich und zeitlich sehr volatil anfallende Residuallast optimal nutzen zu können, müssen Umwandlungsprozesse hohe Lastwechselfähigkeit und schnelle Ansprechzeiten vorweisen. Die Wasserelektrolyse ist bereits sehr lastwechselfähig und kann innerhalb von Sekunden angefahren werden. Der optionale, nachfolgende Prozessschritt der Methanisierung hingegen kann diesem Lastprofil nur sehr bedingt gerecht werden, was derzeit über Zwischenspeicher ausgeglichen wird. [4, 5]

Verfahrens- und Katalysatorentwicklung

Das Forschungsprojekt „EE-Methan aus CO_2", welches in der Sonderausschreibung im Rahmen der Energieforschungsinitiative der FFG als Research Studio Austria (RSA) gefördert wird, hat sich die Weiterentwicklung und Anpassung des Methanisierungsprozesses an die Power to Gas – Technologie zum Ziel gesetzt. Wesentliche Neuerungen sind dabei der Einsatz von wabenförmigen Katalysatoren anstelle der handelsüblichen Katalysatorpellets, sowie die Entwicklung eines verbesserten Verfahrenskonzeptes. [6]

Als Grundkörper dient eine keramische Wabe aus Cordierit $Mg_2Al_3[AlSi_5O_{18}]$, ein besonders temperaturwechselbeständiges Material, das häufig in Wärmerückgewinnungsanwendungen zum Einsatz kommt. Auf der Wabe wird zunächst eine Schicht aus γ-Al_2O_3 fixiert, welche in einem nachfolgenden Schritt mit dem katalytisch aktiven Nickel beschichtet wird. Die Aufbringung dieses Washcoats erfolgt durch Infiltration mit einer $Ni(NO_3)_2$-Lösung und einer anschließenden Trocknung. [7] Die gleichmäßige Durchströmung, die einfache Skalierbarkeit sowie die hohe keramische Masse der Wabenkatalysatoren versprechen einen positiven Einfluss auf die Prozessführung innerhalb der Methanisierungsreaktion.

Anstelle der üblichen Ausführung mit mehreren, seriell verschalteten Reaktoren, soll die Mehrstufigkeit in nur einem Hordenreaktor realisiert werden. Dabei werden die Katalysatorschichten (Horden) innerhalb eines Behälters realisiert, die Temperaturkontrolle erfolgt durch Wärmeübertrager oder Kaltgaszufuhr zwischen den Stufen. Des Weiteren sind Unterteilungen der einzelnen Wabenschichten in bis zu vier Kompartimente vorgesehen, welche durch ein Ventilsystem gezielt anströmbar sind. Dadurch kann die Lastflexiblität, v.a. gegenüber niedrigen Belastungen, gesteigert werden.

Im Zuge des Research Studios „EE-Methan aus CO_2“ wurde an der MU Leoben eine Laboranlage zur Methanisierung von CO_2 geplant und gebaut. Die hohe Komplexität eines Hordenreaktorsystems erfordert eine vereinfachte Lösung für die Umsetzung im Labormaßstab. Daher wurde die Anlage mit drei in Serie geschalteten Reaktoren, mehreren Gasvorwärmungszonen sowie Probenahmemöglichkeiten vor und nach jeder Reaktorstufe konzipiert. Das Betriebsfenster sieht maximale Gasdurchflüsse von 50 NL/min bei einem Druck von bis zu 20 bar (abs.) vor.
Mit den ersten Versuchen konnten die Funktion der Laboranlage sowie der Wabenkatalysatoren (Größe 50x50x100 mm, 100 cpsi) eingehend untersucht werden. Durch Vergleichsmessungen mit kommerziellen Katalysatoren wurde ein Verbesserungspotential im Bereich der Katalysatoraktivierung identifiziert. In weiteren Messreihen führte die verbesserte Aktivierungsprozedur zu deutlich gesteigerten CO_2-Umsätzen und CH_4-Konzentrationen. [8]

t-ZrO_2 als Trägermaterial für die Katalyse

Basierend auf den Versuchsergebnissen und einer Literaturrecherche wurde ein alternatives Katalysatorsystem entwickelt und in der Laboranlage untersucht. Als Trägermaterial kam tetragonales ZrO_2 anstelle des zuvor getesteten γ-Al_2O_3 zum Einsatz, welches wiederum mit der katalytisch aktiven Substanz beschichtet wurde. Um eine möglichst hohe Vergleichbarkeit zu gewährleisten, wurden Trägermaterial, katalytisch aktive Substanz, die Wabengeometrie sowie die Versuchsbedingungen nicht verändert. [9, 10]

Das Betriebsverhalten der beiden Katalysatorsysteme zeigte große Ähnlichkeiten, denn es konnten sowohl der positive Einfluss einer Druckerhöhung als auch der Verringerung der Raumgeschwindigkeit GHSV (Gas Hourly Space Velocity $GHSV[\frac{1}{h}] = \frac{\dot{V}_{Gas}[\frac{Nm^3}{h}]}{V_{Katalysator}[m^3]}$ $GHSV[\frac{1}{h}] = \frac{\dot{V}_{Gas}[\frac{Nm^3}{h}]}{V_{Katalysator}[m^3]}$) beobachtet werden. Zudem wurden mit der alternativen t-ZrO_2 Beschichtung höhere CO_2-Umsätze, respektive CH_4-Gehalte im Produktgas erzielt. Ein Vergleich der erzielten CH_4-Gehalte bei der stöchiometrischen Eduktzusammensetzung von H_2:CO_2 = 4,0 ist in Abbildung 1 dargestellt.

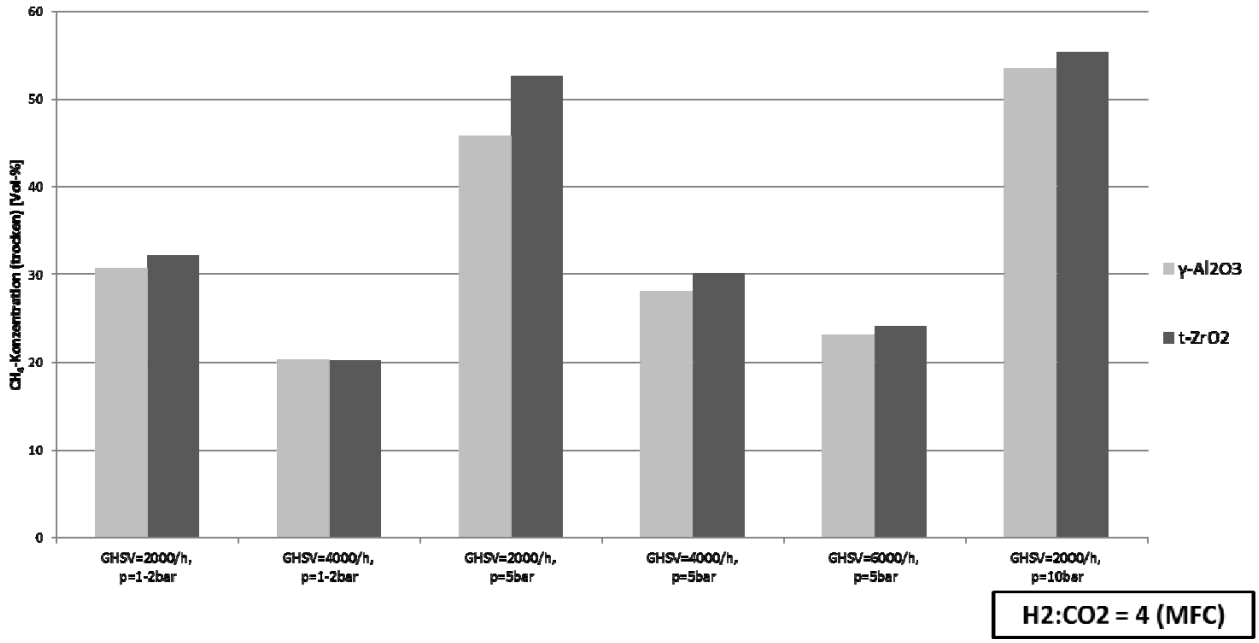

Abbildung 1: Erzielte CH_4-Konzentration bei verschiedenen Versuchsbedingungen in Abhängigkeit des Trägermaterials; Gaszusammensetzung H_2:CO_2 = 4,0

Von einer weiteren Verwendung von t-ZrO_2 als Trägermaterial wurde trotz der sehr positiven Versuchsergebnisse abgesehen, da neben den höheren Materialkosten vor allem die geringe Haltbarkeit der Katalysatoren aufgefallen ist. Nachdem die Katalysatoren in H_2-Atmosphäre aktiviert wurden konnten in zwei Versuchsreihen nur sieben bzw. zwei Versuche bis zur vollständigen Deaktivierung durchgeführt werden. Im Gegensatz dazu wurde beim γ-Al_2O_3-basierten System dieses Verhalten bei ordnungsgemäßem Versuchsbetrieb nicht beobachtet.

Zusammenfassung

Ausgehend von den ersten Versuchsreihen, welche die Funktion der Wabenkatalysatoren nachgewiesen haben [8], wurde eine alternative keramische Beschichtung für die Katalysatorherstellung verwendet. Anstelle des bereits untersuchten γ-Al_2O_3 wurde das vielversprechende t-ZrO_2 auf die keramischen Waben aufgebracht. Der positive Einfluss des Trägermaterials auf die Katalyse schlug sich auf die erzielten CH_4-Konzentrationen nieder, welche im Vergleich zum γ-Al_2O_3-System höher ausfielen. Jedoch wurde im Versuchsbetrieb eine deutlich verringerte Funktionsdauer der Katalysatoren beobachtet, was, kombiniert mit den deutlich höheren Materialkosten, dazu führte, dass weiterhin auf das bewährte γ-Al_2O_3 zurückgegriffen wird.

References

[1] S. Rönsch and A. Ortwein, “Methanisierung von Synthesegasen - Grundlagen und Verfahrensentwicklungen,” (Deutsch), *Chemie Ingenieur Technik*, vol. 83, no. 8, pp. 1200–1208, http://onlinelibrary.wiley.com/doi/10.1002/cite.201100013/pdf, 2011.

[2] J. Kopyscinski, T. J. Schildhauer, and Serge M. A. Biollaz, “Production of synthetic natural gas (SNG) from coal and dry biomass - A technology review from 1950 to 2009,” *Fuel*, vol. 89, no. 8, pp. 1763–1783, http://www.sciencedirect.com/science/article/pii/S0016236110000359, 2010.

[3] F. Ausfelder, C. Beilmann, M. Bertau, S. Bräuninger, A. Heinzel, R. Hoer, W. Koch, F.

Mahlendorf, A. Metzelthin, M. Peuckert, L. Plass, K. Räuchle, M. Reuter, G. Schaub, S. Schiebahn, E. Schwab, F. Schüth, D. Stolten, G. Teßmer, K. Wagemann, and K.-F. Ziegahn, “Energiespeicherung als Element einer sicheren Energieversorgung: Energy Storage Technologies as Options to a Secure Energy Supply,” *Chemie Ingenieur Technik*, vol. 87, no. 1-2, pp. 17–89, http://dx.doi.org/10.1002/cite.201400183, 2015.

[4] H. Steinmüller, G. Reiter, R. Tichler, C. Friedl, M. Furtlehner, J. Lindorfer, M. Schwarz, M. Koppe, P. Biegger, A. Felder, M. Lehner, M. Harasek, A. Makaruk, M. Miltner, M. Fraubaum, M. Haider, S. Begluk, W. Gawlik, C. Maier, R. Haas, and A. Ajanovic, “Power to Gas - Eine Systemanalyse: Markt- und Technologiescouting und -analyse,” Im Auftrag des BMWFJ, 2014.

[5] M. Sterner and M. Specht, “Erneuerbares Methan,” *Solarzeitalter*, no. 1, pp. 51–58, http://www.eurosolar.de/de/images/stories/pdf/SZA%201_2010_Sterner_farbig.pdf, 2010.

[6] P. Biegger, A. H. Felder, and M. Lehner, “EE-Methan aus CO2: Entwicklung eines katalytischen Prozesses zur Methanisierung von CO2 aus industriellen Quellen,” in *Book of Abstracts zum 9. Minisymposium der Verfahrenstechnik*, Leoben, 2013, pp. 105–107.

[7] A. Fuchsbauer, B. Dittert, H. Leichtfried, and H. Außerhuber, “Beschichtungsverfahren zur Herstellung der Wabenkatalysatoren,” interner Bericht, Profactor GmbH, 2014.

[8] P. Biegger, A. R. Medved, M. Lehner, H. M. Ebner, and A. Friedacher, “Methanisierung im Umfeld von "Power to Gas",” in *Kurzfassungsband zum 14. Symposium Energieinnovation*, Graz: Verlag der Technischen Universität Graz, 2016, pp. 463–464.

[9] A. Fuchsbauer, B. Dittert, H. Leichtfried, and H. Außerhuber, “t-ZrO2 - Beschichtung der keramischen Waben,” interner Bericht, Profactor GmbH, 2015.

[10] J. R. Rostrup-Nielsen, K. Pedersen, and J. Sehested, “High temperature methanation: Sintering and structure sensitivity,” *Applied Catalysis A: General*, vol. 330, no. 0, pp. 134–138, http://www.sciencedirect.com/science/article/pii/S0926860X07004206, 2007.

Impregnation of Polycarbonate with Copper Nanoparticles in Supercritical Carbon Dioxide

Dániel Varga, Michael Giebler, Thomas Gamse
Graz University of Technology, Institute of Chemical Engineering and Environmental Technology, 8010 Graz, Inffeldgasse 25/C, Austria
daniel.varga@tugraz.at

Abstract

In this study, copper impregnated polycarbonate was created by supercritical fluid impregnation. This process is an environmentally friendly and cost efficient method for polymer–nanocomposite production. Experiments took place in a high pressure batch vessel and were carried out in the range of 100–300 bar and at 40 °C for various sorption times. Samples were investigated by different analytical methods to study their properties. Experiments resulted in an equally, entirely impregnated polycarbonate pellets with good distribution of the nanoparticles. Their particle size varied between 5 and 400 nanometers.

Introduction

Polymer containing nanoparticles are receiving growing interest in the recent years [1]. Due to their unique properties, they can be used in microelectronics and for optical and catalytic applications. Their properties can be fine tuned by the size and the amount of the incorporated nanoparticles, since the surface of the nanoparticles plays an important role in their catalytic properties [2]. There are several ways to synthesize polymer-supported nanoparticles; however all the conventional techniques have several drawbacks, such as aggregation and dispersing uniformly the particles within the polymer matrix is also difficult.

Supercritical Fluid Impregnation (SFI) is a convenient, environmentally friendly, non-expensive and a promising way to deposit metal nanoparticles into supporting materials (for most of the cases into polymers) by the use of supercritical carbon dioxide ($scCO_2$) as a solvent [2]. As an impregnation solute, mostly a $scCO_2$ soluble complex of the metal is used. This is a batch process which takes place in a high pressure vessel and it is carried out in one single step. After placing the raw materials in the tempered vessel, it is sealed and pressurized up to the desired pressure and being held under pressure for a given sorption time (typically for several hours). During sorption, $scCO_2$ penetrates into the matrix together with the solute. After a controlled decompression, CO_2 leaves the polymer leaving the solute trapped behind in the matrix. Solvent free product can be gathered in solid form [3]. Critical parameters of the process are the applied pressure, temperature, sorption time and the depressurization rate [4]. Since CO_2 is highly non-polar, application of different co-solvents (water, alcohols) also have an influence on the impregnation.

As a comparison, three different $scCO_2$ soluble copper complexes were used. First, a commercially available molecule, Copper(II)-hexafluoroacetylacetonate-hydrate $Cu(hfac)_2$ was used, then two other copper complexes, the primary and secondary copper dithizonate ($Cu(HDz)_2$ and CuDz, respectively, synthesized in our laboratory. CuDz was used only for some preliminary experiments. The results shown here were obtained by the use of $Cu(HDz)_2$.

Materials and Methods

$Cu(hfac)_2$ and dithizone were ordered from Sigma-Aldrich Austria. Carbon dioxide (purity >99.5%) was supplied from Linde Gas GmbH. Polycarbonate (PC) samples (LEXAN 121 resin) were kindly provided by the Saudi Arabian Basic Industries Corporation (SABIC) in pelletized form. Other reagents (such as solvents, washing ethanol) were obtained also from Sigma-Aldrich Austria. All chemicals were used as received. CuDz and $Cu(HDz)_2$ were both synthesized in our laboratory according to Irving and Kiwan [5]. For all the experiments introduced here, 2,0 g of polycarbonate, 0,0150 g of $Cu(HDz)_2$ and 0,0500 g of $Cu(hfac)_2$ were used.

Experimental Apparatus

Batch experiments were carried out in a high pressure vessel having a volume of approx. 150 ml. It is placed in an oven and can be operated up to 250 °C and 690 bar (Applied Separations, USA). Experimental setup also consists of a liquid CO_2 pump (Haskel ASF-100, USA) which was maintained less than 3 °C by a recirculation cooling bath. The vessel was tempered in the oven and when its final temperature was reached, it was filled up with $scCO_2$ to the desired pressure. To enhance the impregnation the supercritical fluid of the vessel was slowly circulated by a gear pump (constructed by ETH Zürich, Switzerland). After the impregnation time (varied between 2 and 4 hours), the vessel was controlled decompressed by using a metering valve (Kämmer KA) within 30 or 60 minutes. The product was washed with ethanol in order to remove the solid particles precipitated on the surface during decompression. Samples were air dried, dissolved in HNO_3/HCl mixture with microwave support and investigated by ICP-OES and ICP-MS in order to determine the overall copper content.

Results

However, $Cu(hfac)_2$ is reported to be used often and successfully in supercritical CO_2 media, we could not achieve successful impregnation with this complex at 40 °C and in the range of 100–300 bar and 2–4 hours of reaction time. According to literature data [6], this complex has an outstanding high solubility in $scCO_2$. This corresponds to our observations in a high pressure view cell, where fast dissolution was observed. Authors suggest that due to the relatively high solubility in the $scCO_2$ phase and to the low solubility in the polymer phase, its diffusion into the polymer matrix is not favored. Because of this high solubility of the solute the complex would leave the matrix with the CO_2 during decompression, even if diffusion took place.
The behavior of $Cu(HDz)_2$ complex was investigated in the view cell on 100 bar and 40 °C. A slow, but fully dissolution of small amount of the solute was observed in the stirred cell after 90 minutes. By the use of $Cu(HDz)_2$, a copper load of 2–6 ppm ($mg_{copper}/kg_{polymer}$) in the PC was achieved (measured by ICP-MS). Higher loadings were obtained at longer impregnation times and by the use of ethanol as a co-solvent.

It has been tried to carry out the impregnation not only via the conventional way, which is dissolving a complex and using this solution as the impregnation solute, but synthesizing the complex during the impregnation, *in-situ* in the polymer phase. Dithizone is often used as a ligand in spectrophotometrical detection, since it has an ability to build chelate complexes with several metallic ions. Therefore, the aqueous solution of copper ions (from $Cu(NO_3)_2$) was mixed with the alcoholic solution of the dithizone and then this solution was used for further experiments. However, successful results were not obtained this way, the

process could be realized in two steps. First, PC pellets were impregnated with dithizone in $scCO_2$ atmosphere. Then, this product, the polycarbonate containing dithizone (DPC) was impregnated with an aqueous solution of copper ions as a second step. Interestingly, by applying this method, 10-20 times higher metal load in the polymer has been achieved than by the use of $Cu(HDz)_2$ or $Cu(hfac)_2$ copper complexes. As a maximum, 110 ppm was obtained. SEM studies confirmed that the impregnation occurred deeply within the polymer matrix (not just close to the surface) and showed that the copper can be found in nanometric scale: relatively big copper clusters (200-400 nm) are surrounded by many smaller particles (5-20 nm).
Since dithizone is capable of building such chelate complexes with several metallic ions, further experiments using different metals are planned to be carry out to study the applicability of our process.

Summary

A copper impregnation of polycarbonate was studied in supercritical carbon dioxide media. Two different copper complexes were compared. By the use of $Cu(hfac)_2$, impregnation was not successful, but with another complex synthesized in our laboratory ($Cu(HDz)_2$) a copper load of the polycarbonate samples up to 6 ppm has been achieved. A novel, two step process has been developed for obtaining copper nanoparticle impregnated polycarbonate. By this method, 110 ppm of copper load in polycarbonate was achieved. Authors suggest that this method can also be used for some other metals and polymers.

Acknowledgements

This work was financially supported by the Marie Curie Initial Training Networks (ITN) via “DoHip – Training Program for the Design of Resource and Energy Efficient Products by High Pressure Processes”; project number PITN-GA- 2012-316959. The authors would like to acknowledge Helmar Wiltsche, Julian Wagner and FELMI Graz for the analytical measurements and Candela Campos Domínguez for her valuable assistance during the experimental work.

Literature cited

[1] Metal-Polymer Nanocomposites, ed. L. Nicolais, G. Carotenuto. John Wiley & Sons, **2005**

[2] Y. Zhang, C. Erkey: Preparation of supported metallic nanoparticles using supercritical fluids: A review. Journal of Supercritical Fluids 38 (2006) 252–267

[3] I. Kikic, F. Vecchione: Supercritical Impregnation of Polymers, Current Opinion in Solid State and Materials Science, Vol. 7 (2003) 399–405.

[4] S. G. Kazarian: Polymer Processing with Supercritical Fluids, Polymer Science, Ser. C, Vol. 42, No. 1, (2000) 78–101.

[5] H. M. N. H. Irving, A. M. Kiwan: Studies with Dithizone, Part XXV. Secondary Copper (II) Dithizonate. Anal. Chim. Acta 56 (1971) 435–446

[6] Solubility in Supercritical Carbon Dioxide, ed. R. B. Gupta and J-J. Shim. CRC Press, **2007**

Morphological characterization of cellulose pulps with imaging methods

Melanie Mayr[1], Wolfgang Fischer[1], Rene Eckhart[1], Wolfgang Bauer[1]
[1]Institute of Paper, pulp and fiber technology, 8010 Graz Inffeldgasse 23/1

Abstract

Characterization of particles of great importance in many fields of research. The morphological characterization of particle shape, size and size distribution is one part of it. Optical particle analyzers are the most common way for this. The advantages of these methods are the availability of the images and a reliable characterization of elongated particles. A disadvantage is the dependence of optical properties. Focus is put on elongated particles namely pulp fibers and fines, which are the organic components of a papermaking pulp. The results obtained in this study show the influence of optical characteristics on the measurement results. Another outcome is that some of the devices cannot be used for elongated particles or heterogeneous mixtures.

Introduction

The constituent parts of a papermaking pulp, fibers and fines, are either produced by chemical or mechanical disintegration of wood. For chemical pulp two main processes are used, namely the sulfite and sulfate process. Defibration is done by chemical cooking of woodchips. In case of mechanical pulps the separation of fibers is done by grinding logs or wood chips. Besides the pulping process, differences in pulp properties can be attributed to the wood species used. Furthermore, subsequent mechanical and chemical treatments such as refining and bleaching influence the pulp properties. These differences can also be observed in the morphology of fibers and fines.
Compared to fibers, which are relatively well studied, fines are often not considered as a specific fraction having particular properties. In general, fines are considered to be any particles that can pass through a 200 mesh screen of a Bauer Mc-Nett classifier [1]. In previous studies fines were also defined as material passing a 100 mesh screen [2], [3]. Besides fractionation methods, fiber analyzers distinguish between fibers and fines according to their length. Fines are defined as particles having a length smaller than 200 µm (ISO 16065). According to the pulping process, fines can be divided into primary and secondary fines. Primary fines are particles which are the result of the pulping process whereas secondary fines are produced by mechanical treatment of the pulp after pulping [5]. Here approximately 15 - 30 wt. % of the pulp are primary fines. In comparison primary fines of chemical pulp almost only include non - fibrillar material such as ray-cells, parenchyma-cells, pith-cells and in case of hardwood vessel fragments. Thus, the amount of primary fines in chemical pulps (~ 5 wt. %) is much smaller than the one in mechanical pulps. In case of mechanical pulps, fines can be subdivided according to their shape into “flour stuff” and “slime stuff” [1] or in general into fibrillar and flake like material [4], [6].
With respect to technological properties of fines the classification into fibrillar and flake like material as well as the size distribution is important. A qualitative classification can be obtained rather easily from micrographs using a standard light microscope. An image analysis method for micrographs was developed by Lukko et al. [6]. Here fines are quantitatively classified into fibrillar and flake like material. Nevertheless a quantitative identification of particle size distribution (PSD) and quantification of the content of fibrillar and flake like material is tedious using a microscope technique. Particle analysers, equipped with a flow cell, would be an alternative. Three different detection principles are available for

these analyzers:

- direct optical methods with image acquisition and analysis software
- indirect optical methods based on the interaction of particles with light
- electrical methods detecting variations of the conductivity depending on the particles mass [5], [7].

Direct optical methods are widely used for particle and fiber analyzers, because of the elongated shape of fibers. Fiber analyzers are specially designed for application in the pulp and paper industry. Analysis routines for all kinds of fiber and fines properties have already been implemented. One drawback of this analyzers is their resolution. The results are strongly influenced by the image analysis routine and by optical properties. In previous studies different fiber analyzers were used to measure fiber properties of various pulps [8], [9]. Although the detection limit is not relevant for the measurement of fibers, the analyzers showed differences in PSD as well as in the mean fiber length and width. Laser diffraction spectroscopy (LDS) was applied for the measurement of fines [4], [10]. The advantage of indirect optical methods (e.g. LDS) is the high resolution compared to direct optical methods. The PSD is determined from the detected scattering pattern of light using the Mie Theory [11]. In this case only an equivalent diameter is calculated which give no information about the particle shape. The technique measuring PSD by electrical properties also cannot describe length and width or shape. Nevertheless, this is the only technique which is independent of the change in size of fines due to swelling in aqueous solution. Because of the detection of conductivity it is independent from optical properties of the particles (e.g. transparency). Drawback are the tedious preparation, measurement as well. Disadvantageous is the effect of the measurement gap, dilution and tedious sample preparation. In the present study different imaging methods and LDS have been used to analyze fibers and fines. Furthermore, the results of the different devices have been compared.

Materials and Methods:

In the present study unbleached pressurized ground wood (P - 1), semi - bleached softwood kraft pulp (P – 2), bleached softwood kraft pulp (P – 3) and bleached sulphite pulp, (P - 4) were used. After removing the primary fines from pulp P – 3, it was refined in a PFI mill at 5000 revolutions in order to produce secondary fines (P – 3,b). The fines material was separated from the pulp using a Britt Dynamic Drainage Jar (BDDJ), which was equipped with a 200 mesh screen (ø=76 µm, round hole). The fines were collected in beakers and allowed to settle. The supernatant water was removed with a tube which was connected with a vacuum pump. The obtained fines fractions will be referred to as F1.

Due to the small quantities that could be produced with the BDDJ method it has been decided to use another separation process for the pulps that were used for the fiber analyzers. Fines were isolated with a dewatering device (developed at the Institute of Paper Pulp and Fiber Technology, TU Graz) which is similar to the wire section of a foudrinier former equipped with a SC - wire. Further components are a head box and two tanks for white water collection. The pulps were diluted to 1 wt% and afterwards dewatered using this device. The white water was collected in the plastic tanks. After sedimentation of the fines the supernatant water was removed with a tube connected to a vacuum pump. The fines fractions will be referred to as F2.

The main specifications of the particle and fiber analyzers are summarized in Table 1. All of these analyzers are equipped with a flow cell and use optical methods.

Particle analyzers			
Name	Mastersizer 2000, dispersion unit: Hydro 2000µP (Malvern Instruments)	MFI 5100 (ProteinSimple)	QICPIC, dispersion unit: MIXCEL (Sympatec)
Resolution	0.02 µm	0.25 µm	1 µm
Measurement principle	Laserdiffraction (Mie Theory), Flow Cell	Image analysis, Flow Cell	Image analysis, Flow Cell
Result: weight/measured value	Volume (Q3)/Equivalent volume diameter (x_v)	Volume (Q3)/ Equivalent circular diameter (x_c)	Volume (Q3)/ Equivalent volume diameter (x_v)

Fiber analyzers			
Name	MorFi Compact	Metso FS5	L&W Fiber tester plus
Resolution	10 µm	6.5 µm	3.3 µm
Measurement principle	Image analysis, Flow Cell	Image analysis, Flow Cell	Image analysis, Flow Cell
Result: weight/measured value	Length (Q1)/ Length (x_l)	Length (Q1)/ Length (x_l)	Length (Q1)/ Length (x_l)

Table 1: Main specification of the particle analyzers

Results:

The main objective of this study was to find suitable methods for morphological characterization of different types of fibers and fines. First the particle analyzers are discussed. Table 2 shows the results (mean equivalent diameters) of particle analyzers.

	Mastersizer	MFI	QicPic
	$\bar{x}_v$ [µm]	$\bar{x}_c$ [µm]	$\bar{x}_v$ [µm]
F1 - 1	39.74	19.82	18.04
F1 - 2	47.95	26.33	20.94
F1 - 4	42.91	24.56	13.11

Table 2: Mean equivalent particle diameter determined from particle analyzers

In comparison to the other analyzers, the Mastersizer 2000 is the only device using laser light scattering. The results show a bimodal PSD for the chemical pulp fines F1-2 and F1-4. This distribution was also observed when using other chemical pulp fines (not discussed in this study). In order to proof that the bimodal distribution is related to the material, spherical and elongated test particles with defined dimensions were analyzed. The mean equivalent volume diameter of the spherical test particles ($\bar{x}_v$ = 50 µm) was provided by the supplier. The one of the elongated particles ($\bar{x}_v$ = 57 µm) was determined from the length (L = 300 µm) and width (W = 20 µm) by assuming a cylindrical shape. Figure 1 shows the PSD of these test particles as well as the 95% confidence intervals.

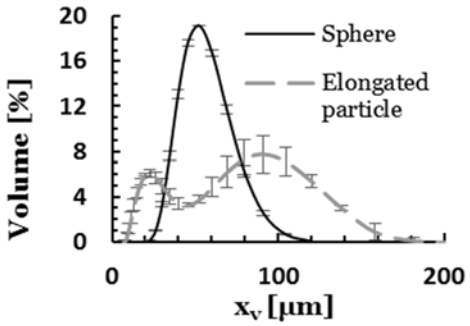

Figure 1: Evaluation of Mastersizer 200 with elongated and spherical test particles

The elongated particles show a bimodal distribution. The measured $\bar{x}_v$ for is 87 µm although for a bimodal curve this number is not meaningful. The spherical particles show a monomodal distribution ($\bar{x}_v$ = 52 µm) and fit well with the specifications. The elongated test particles were also analysed with the fiber analyzer Fiber Tester Plus from L&W, which results in a monomodal distribution. The measurement principle of the Mastersizer 2000 is based on the Mie theory, which assumes that particles do not have an oriented linear expansion, i.e. a high aspect ratio. In the user manual of the Mastersizer 2000 the possibility to measure non-spherical particles is described although there is no evidence how this is applicable when using the Mie theory. The measurement principle of this device is not suitable for elongated particles present in fines.
The Micro Flow Imaging device (MFI) was primarily designed to analyze protein agglomerates. Protein agglomerates as well as fines are relatively transparent and include various shapes. In the present experiments the fines dispersion was not sufficient for the measurement unit, even if the particle concentration was kept low. In the images of the MFI, agglomerates could be observed and PSD was too high.
The QicPic was designed to analyze elongated particles. With this device it is also possible to identify agglomerates. The measurement results show that the transparency of fines leads to errors, because transparent particles are detected as an accumulation of smaller particles. The QicPic is also not suitable for PSD analysis of fines. In comparison to the conventional particle analyzers, fiber analyzers are designed for the application in the pulp and paper industry and even the measurement of fine material is implemented in the software. Nevertheless limitation result from the limited resolution of these devices (compare Table 1) and transparency of fibrillar material. Figure 2 shows a comparison of the length distributions of F2-1 and F2-3,b measured with the L&W fiber tester and the Metso FS5.

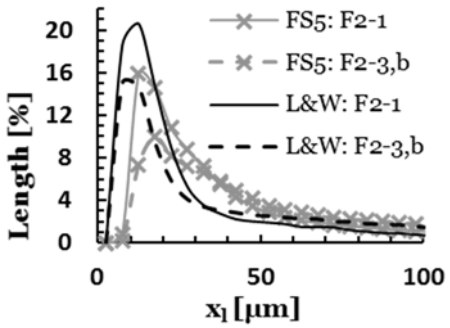

Figure 2: Length - distribution of F2 - 1 and F2 - 3,b fines measured with L&W fiber tester and Metso FS5 analyzer.

Due to the lower resolution of the Metso FS5, small particles are not detected although they have a high contribution to the PSD as shown in the PSD measured with the L&W fiber

tester. The broader distribution obtained with the FS5 might result from an insufficient dispersion. The Morfi Compact device only includes nine data points within the fines range (0 – 200 µm) and has the lowest resolution. All three devices show the same trends when comparing the different fines (Table 3).

	Morfi Compact	FS 5	L&W
	$\bar{x}_l$ [µm]	$\bar{x}_l$ [µm]	$\bar{x}_l$ [µm]
F2 - 1	33.0	45.2	34.8
F2 - 3	47.5	69.9	66.3
F2 - 3,b	37.5	62.1	53.0

Table 3: Mean particle length determined from fiber analysers

Conclusion

After the assessment of all criterions influencing the measurement result, the particle analyzers will not be used for further measurement due to different errors. The L&W fiber tester seems to be the most suitable of all devices, due to the relatively high resolution and reproducibility of results. Nevertheless, fine fibrils cannot be detected because of their high transparency and the limited resolution. A solution for this would be a microscope and subsequent image processing.

Literature

[1] W. Brecht and K. Klemm, “Das Struckturgemisch eines Holzschliffs als Schlüssel für die Kenntnis seiner technologischen Eigenschaften,” *Wochenblatt für Pap.*, vol. 11, pp. 364–370, 1952.

[2] K. Luukko and T. Maloney, “Swelling of mechanical pulp fines,” *Cellulose*, vol. 6. pp. 123–135, 1999.

[3] H. Chen, A. Park, J. a. Heitmann, and M. a. Hubbe, “Importance of cellulosic fines relative to the dewatering rates of fiber suspensions,” *Ind. Eng. Chem. Res.*, vol. 48, no. 20, pp. 9106–9112, 2009.

[4] J. Mosbye, “Fractionation and chemical analysis of fines,” in *27th EUCEPA conference - Crossing the millennium frontier*, 1999, pp. 317–321.

[5] P. J. Ferreira, A. Martins, and M. Figueiredo, “Primary and secondary fines from Eucalyptus globulus kraft pulps - Characterization and influence.,” *Pap. Ja Puu-Paper Timber*, vol. 82, no. 6, pp. 403–408, 2000.

[6] K. Luukko, P. Kemppainen-Kajola, and H. Paulapuro, “Characterization of mechanical pulp fines by image analysis,” *Appita*, vol. 50, no. 5, pp. 387–392, 1997.

[7] H. Kang, T. and Paulapuro, “Characterization of Chemical Pulp Fines,” *Tappi J.*, vol. 5, no. 2, pp. 25–28, 2006.

[8] U. Hirn and W. Bauer, “A review of image analysis based methods to evaluate fiber properties,” *Lenzinger Berichte*, vol. 86, pp. 96–105, 2006.

[9] W. D. Guay, N. Malandri, M. Schneider, N. Sutherland, A. Stephens and R. and K. Mattingly, “Comparison of Fiber Length Analyzers,” in *Practical Papermaking Conference [electronic resource]*, 2005.

[10] Y. Xu and R. Pelton, “A New Look at How Fines Influence the Strength of Filled Papers,” vol. 31. pp. 147–152, 2005.

[11] W. Hergert and T. Wriedt, “The Mie Theory,” in *The Mie Theory: Basics and Applications*, Springer-Verlag, 2012, pp. 53–71.

Investigation of the respiratory flow through the nasal cavity with CFD

Manuel Berger[1], Martin Pillei[1], Andreas Mehrle[1], Wolfgang Freysinger[2] and Michael Kraxner[1]
[1]MCI – Department Environmental, Process & Energy Engineering, Universitätsstraße 15, 6020-Innsbruck, AT
[2]Medical University Innsbruck, Innrain 52, Innsbruck, AT
manuel.berger@mci.edu

Abstract

In the field of operative medicine simulations can help and support surgeries. The objective of this project is to predict the flow through the nasal cavity in order to know whether a surgery is reasonable or not. Therefore, a new simulation technique called *Lattice Boltzmann* (*LB*) will be compared with the state of the art *Finite Volume Method* (*FVM*). At small Reynolds numbers both simulation techniques show qualitatively and quantitatively similar results. However, the big advantage of *LB* in contrast to *FVM* is that it is much simpler to create a mesh for the simulation, so it reduces the preparation time.

Introduction

Breathing in terms of air flow and air turbulences is a very complex procedure within the nasal cavity, attached sinuses and nasopharynx caused by anatomical situation but also by pathologies. Diagnostic identification whether a nose surgery is necessary and successful or not is so far done either by rhinomanometry, radiologic imaging (*CT*) and / or endoscopy. Unfortunately, both methods are rather uncomfortable for the patient. The outcome of surgery cannot be predicted quantitatively. So there is the need to develop a prediction tool for nose surgeries. A *LB* flow simulation technique is used to simulate the flow within the paranasal sinuses, because it is easy applicable for complex geometries. Though, the results needed to be compared by measurements or other simulations. Therefore, the conventional *FVM* within respiratory ducts is compared with *LB*. Furthermore, the development of a test rig will allow *Particle Image Velocimetry* (*PIV*) and *Laser Doppler Anemometry* (*LDA*) measurements in order to validate the numerical simulations.

Methods

Anatomy derived boundary conditions

In order to perform a successful simulation it is necessary to create a 3D model of the fluid domain. With a *computerized axial tomography (CT)* scan a human head dataset will be created slice by slice. The information is an array of voxels (i. e. small volume elements) that show a grey value depending on the physical density of the object that is made up from these elements. Segmentation is a process to get the desired 3D–geometry out of the *CT* dataset. Fig. 1 shows all process steps in chronological order. At the beginning there is a thresholding step in order to detect the air domain in the *CT* dataset, since one is interested in the cavity of the nose (2). So, it is possible to determine the difference between bone, soft tissues and cavities. Especially for the nasal shape it is necessary to find an entrance and exit which is limited by horizontal boundaries (3). As a consequence, the mass flow rate can be simply adapted to this surface. Subsequently, the marching cubes algorithm (4) [1] allows creating a surface geometry which is commonly saved in the

file format STL and later on used for all *Computational Fluid Dynamics (CFD)* simulations. The *CT* scan has a resolution of 0.4 x 0.4 x 0.8 mm³. Therefore, *3DSlicer*, a free and open source software package for visualization and medical image, is used [2].

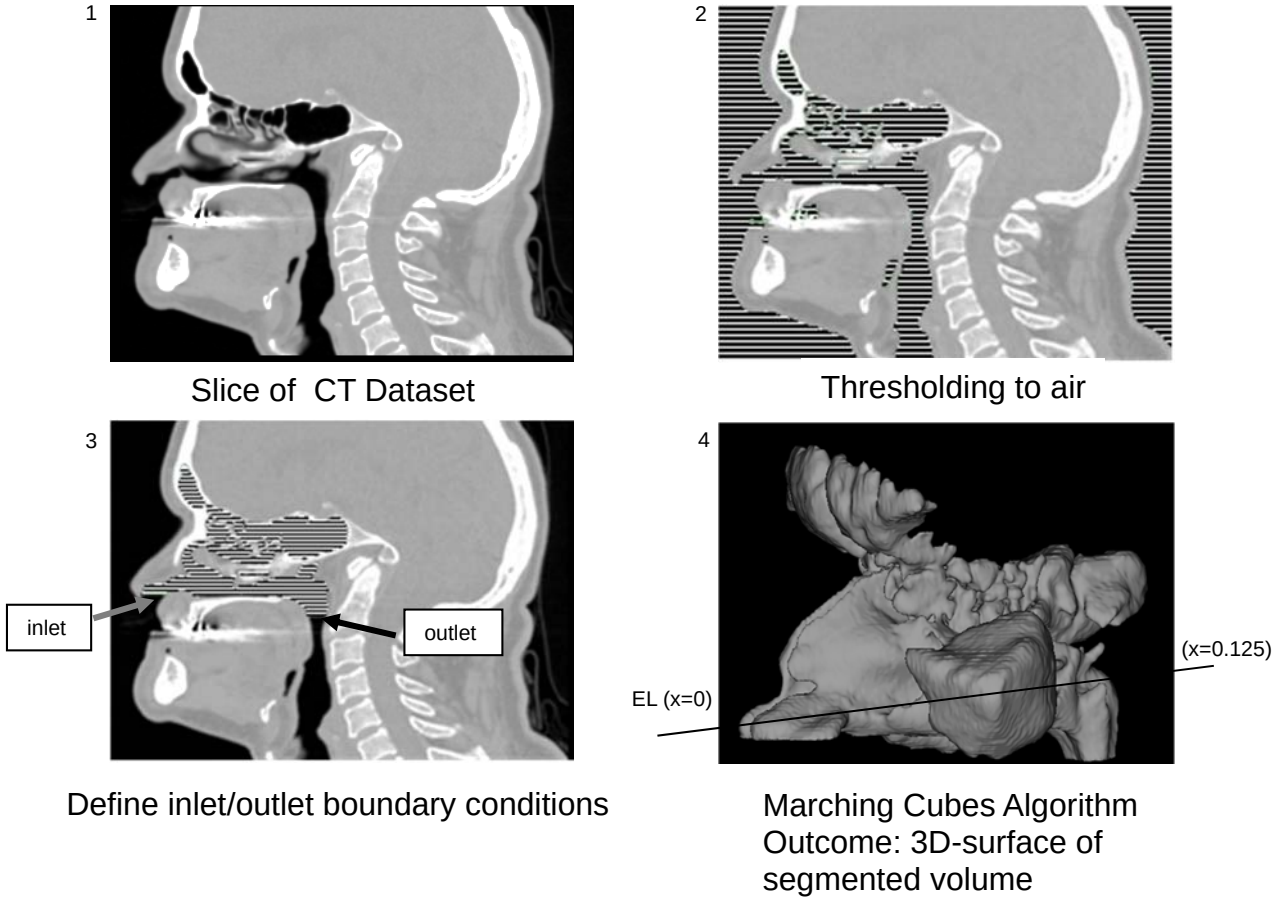

Fig. 1: Segmentation from CT to STL.

FVM Methodology

Simulations based on the *FVM* need a mesh which is generated out of the STL file. *SnappyHexMesh [3]* out of the *openFoam [4]* free fluid flow simulation toolbox allows generating hexahedron based meshes which are very powerful for the *FVM* to solve scalar and vector fields like pressure and velocity very accurate. However, not only one STL file is needed, but one for every boundary condition. In other words, the STL must be separated in inlet, outlet and wall domain. Subsequently, this mesh can be either solved with transient or stationary solvers in *openFoam* and *Fluent [5]*. Since *FVM* simulations still need a huge amount of computational power the user has to be aware of cell size and quality.

LB Methodology

Lattice Boltzmann is a flow simulation technique which tries to estimate the variables with collision models [6]. For all LB simulations the software package *Sailfish CFD* [7] is used. Though, this is limited to flows with small Reynolds numbers [8]. However, the big advantage in contrast to *FVM* is the simpler mesh requirement. The *Boltzmann equation* describes the statistical behavior of the thermodynamics and flow system. The difference from other simulations is that the physical values cannot be used directly. Furthermore, pressure does not appear in the *Boltzmann equation*. The devious route is to calculate this

specific quantity from the density via the ideal gas law. So there is the need to create a unit-less system in the domain that is representing the real physical system accordingly. *LB* works in the following way: the exchange of momentum and energy is achieved through particle streaming and billiard-like particle collision. So particles are moving around with random motions. *LB* works with 2D and 3D geometries for laminar flow, additionally, it is possible to use *LES* [9] for turbulence modelling. Small eddies are modelled with extra formulas. However, there is no turbulence model used, since the Reynolds number is so small that the flow will be laminar.

Results

The comparison between the two software packages *Sailfish CFD* which uses the Lattice Boltzmann method and the conventional *CFD* software package *Fluent*, differ in the range of 10 % even for the complex nasal geometry and small inlet velocity. In other words, the spatial discretization for both is fine for both simulations techniques. In Fig. 2 the velocity contour plots of both simulation techniques are shown. The velocity v_{mag} is the velocity magnitude ($\sqrt{\vec{v}_x^2 + \vec{v}_y^2 + \vec{v}_z^2}$).

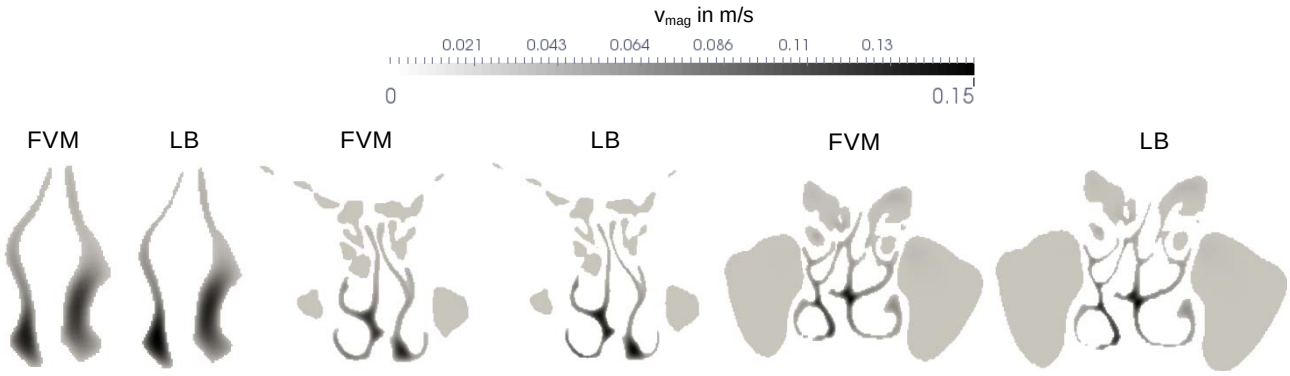

frontal sinus anterior ethmoidal sinus posterior ethmoidal sinus

Fig. 2: Speed given as contour plot at coronal planes.

In Fig. 3 the velocity is shown on an evaluation line (EL). The position of the line is depicted in Fig. 1.

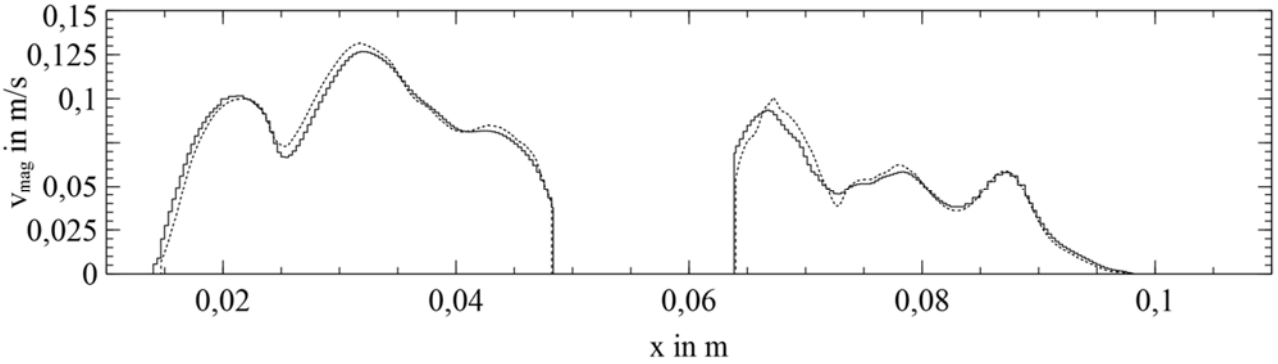

Fig. 3. Speed given on the EL. Solid: FVM, Dotted: LBM.

Discussion

Either *FVM* and *LB* seem to be applicable for medical flow investigations, particularly for

complex geometries and small velocities. The big advantage of LB in contrast to FVM is that it is much simpler to work with voxel based CT datasets, since LB uses the same data format.

Outlook

All simulations are needed to be validated by measurements. In Fig. 4 a schematic of the experimental setup is depicted. The object for the measurement process is the nose (1). Additionally, a fan (3) is creating a negative pressure, so that the desired flow rate can be achieved. However, a flowmeter (2) provides information about the flow rate, so that the fan speed can be adapted accordingly with a closed loop control system (6). Furthermore, a difference pressure gauge (5) is used to measure the pressure drop between inlet and outlet of the nose. The flow measurement techniques *LDA and PIV* are going to be used.

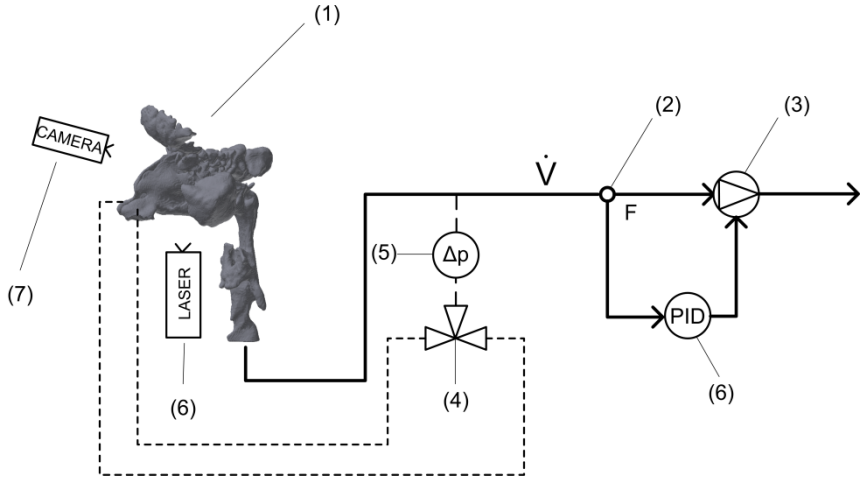

Fig. 4: Schematic of the experimental setup. For details see text.

Literature

[1] T. S. Newman, H. Yi, A survey of the marching cubes algorithm In: Computer Graphics, Vol. 30, Nr. 5, Oktober, p. 854-879, 2006.

[2] Fedorov A., Beichel R., Kalpathy-Cramer J., Finet J., Fillion-Robin J-C., Pujol S., Bauer C., Jennings D., Fennessy F., Sonka M., Buatti J., Aylward S.R., Miller J.V., Pieper S., Kikinis R. 3D Slicer as an Image Computing Platform for the Quantitative Imaging Network. Magn Reson Imaging. 2012 Nov;30(9):1323-41. PMID: 22770690.

[3] Engys Ltd. , A comprehensive Tour of snappyHexMesh, 7th OpenFoam Workshop, 2012

[4] H. Weller, C. Greenshields, B. Santos, R. Jones, P. Edwards, OpenFOAM Free Open Source CFD, Available at: http://www.openfoam.org/.

[5] J. Grievink, J. van Shijndel, European Symposium on Computer Aided Process Engineering, 2012.

[6] A. Mohamad, Lattice Boltzmann Method, Fundamentals and Engineering Applications with computer codes p 72, 2011.

[7] M. Januszewski, M. Kostur, Sailfish: A flexible multi-GPU implementation of the Lattice Boltzmann method, Computer Physics Communications 185/9, 2014.

[8] C. Kleinstreuer, Modern Fluid Dynamics, Basic Theory and Selected Applications in Macro- and Micro Fluidics, 2010.

[9] S. Succi, The lattice Boltzmann equation for fluid dynamics and beyond, p. 138, 2001.

Multi-particle finite element method of powder compaction

Peter Loidolt[a], Manfred H. Ulz[b], Johannes Khinast[a,c]
[a]Institute for Process and Particle Engineering, Graz University of Technology, Inffeldgasse 13/3, 8010 Graz
[b]Institute for Strength of Materials, Graz University of Technology, Kopernikusgasse 24/I, 8010 Graz
[c]Research Center Pharmaceutical Engineering, Graz University of Technology, Inffeldgasse 13/2, 8010 Graz

peter.loidolt@tugraz.at, manfred.ulz@tugraz.at, khinast@tugraz.at

Abstract

In this study a multi-particle finite element method (MPFEM) model is used to determine flow surfaces of compacted powder. A representative volume element (RVE) of spherical particles is compacted in a FEM model with isostatic and closed-die compression. After compaction the yield strength of the compact is probed in the three-dimensional stress space. The obtained yield surfaces for isostatic compaction show isotropic material strength, but the yield strength after closed-die compaction is higher in compaction direction than normal to the compaction direction.

Introduction

Cold compaction of powder is important for many industrial processes, e.g., for the production of green bodies before sintering of metal or ceramic parts in mechanical engineering, production of pellets for mineral or animal food industry or the production of tablets in the pharmaceutical industry. The goal of powder compaction is to reduce the volume of the powder, increase the flowability or to create a part of a certain shape and size.
The final powder compact needs a minimum of strength because otherwise it disintegrates during processing, transportation or storage. The strength of a compact depends on both, material and process parameters. The chemical composition of the particles, as well as the particle size and shape, are important material parameters. The material properties are influenced by the environmental conditions, e.g., temperature and humidity. The process is determined by the geometry of the tools, the compaction stress or the compaction strain, depending on the control of the compaction machine. Experiments can be used to adjust the process to get the desired compact properties. This can be very time-consuming, if some parameters change very often, e.g., the geometry of the parts or the powder properties. Hence, it would be beneficial to have a numerical model available that can predict the properties of the compacts.
The finite element method is widely used for simulations of structural parts but also for the simulation of soil and powders. In the FEM simulation powders are usually described as a continuum, i.e., the discrete nature of the particles is not implemented. This makes the method much more efficient than the discrete element method DEM, where every single particle is tracked. In FEM a material model is required to connect the stress and the strain of the material. In addition to the elastic properties the yield surface has to be provided. Earlier work [1] showed that the Drucker-Prager/Cap model (see Figure 1) can be used to model the yield surface of compacted powders. Since the strength of the powder changes

during compaction, the flow surface has to grow during compaction (Figure 1 right). Hence a huge amount of compression tests is necessary to determine the evolution of the yield surface. This is the motivation for this work. Our aim is to obtain reliable flow surfaces by means of simulation.

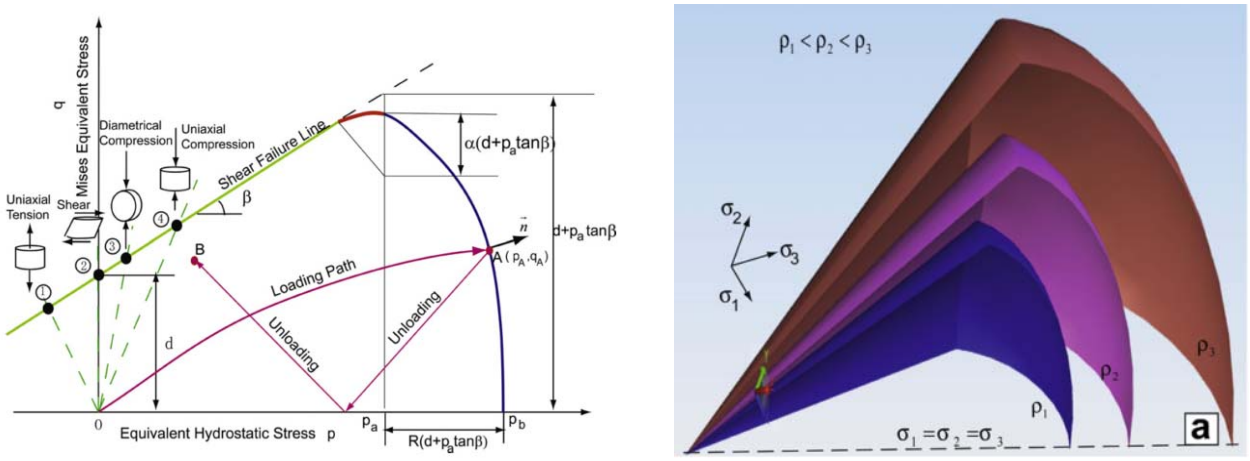

Figure 1: left: Drucker-Prager/Cap model in the hydrostatic stress/ equivalent stress plane showing stress states of common testing methods; right: 3d representation of the Drucker-Prager/Cap flow surface for different powder densities. [1]

Methods

The multi-particle finite element method is used in this work to derive flow surfaces based on a detailed modeling of the particles during compaction. In contrast to DEM particles are deformable in MPFEM which leads to immense numerical costs. Hence, the concept of a representative volume element (RVE) is used to limit calculation time. A RVE is a sample of the whole body which has the same average properties. The size of a RVE has to be much smaller than the whole system to ensure no strain gradients within the RVE. On the other hand the RVE must be significantly larger than the biggest substructure (in this work particle) within the RVE to be representative for the whole body.
In this work the yield stress of the RVE is determined for different compaction strains. For this, a sample of 100 particles (see Figure 2) is compacted in isostatic and closed-die compression for different strains. Isostatic means the compaction strain is equal in all directions ($\varepsilon_{11}=\varepsilon_{22}=\varepsilon_{33}=\varepsilon$). In contrast to that there is only strain in one direction for closed-die compaction ($\varepsilon_{11}=\varepsilon$; $\varepsilon_{22}=\varepsilon_{33}=0$). The diameter of the particles is $d_{Particle}=0.115$m which follows from the particle number and the box size of 1x1x1m.
Periodic boundaries are used to avoid boundary effects. A periodic box filled with randomly closed packed spheres obtained from a DEM simulation is used as initial packing. Particles which are located on the boundary are cut into pieces by the (virtual) wall of the box. The pieces are moved to the appropriate side of the periodic box. Thus, for every node on the boundary of the box there is another node on the opposite side of the box. The displacements of nodes at opposite sides of the box are connected with linear constraint equations which are also used to superimpose the deformation of the RVE.

Each particle is modeled as an elasto-plastic body with a Young's modules of 210GPa and a piecewise linear yield strength of 200, 300 and 400MPa at an equivalent strain of 0, 1 and 5, respectively. These material model properties describe the properties of steel approximately. Since failure of powder mainly occurs at contacts between particles the contact properties are of big importance. The contacts are modeled as hard in

compression direction and cohesive in tension. The coefficient of friction is 0.2.

The cohesion stiffness is chosen to be 100GPa normal to the contact surface and 50GPa tangential to the surface. If the contact stress exceeds the failure stress of 10MPa or 5MPa in tensile or tangential direction, respectively, the cohesive failure is initiated. After failure initiation the cohesion stress decreases linearly with separation until it vanishes at a separation of 0.0003m. The maximal separation of the cohesion model is much larger than the real interaction length of surfaces, because the whole model is scaled up to get a simulation box of 1x1x1m.

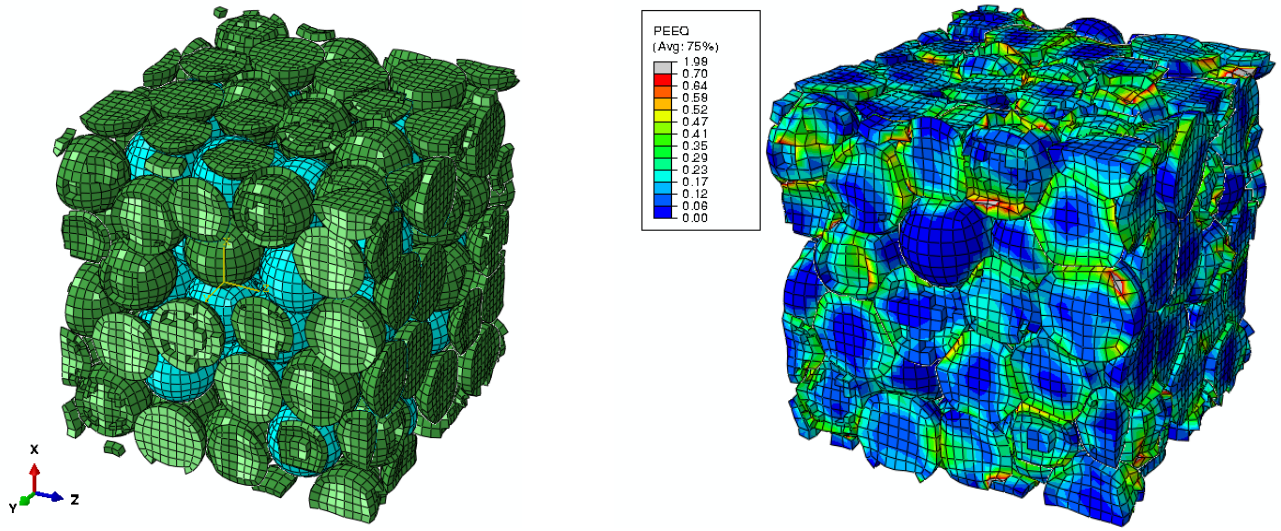

Figure 2: left: RVE of 100 particles with periodic boundary conditions; right: RVE after isostatic compaction (the color gradient shows the plastic equivalent strain of the particles)

The MPFEM simulation is carried out with the commercial FEM package Abaqus and is divided in three steps. In the first step the initial packing is compacted with isostatic or closed die compression. An explicit solver is used for this step, since the implicit solver does not converge due to the severe discontinuities of created contacts during compaction. In the second step the compacted structure is relieved using an implicit solver. In the third (implicit) step the RVE is reloaded again in different directions with ramped force amplitudes to probe the strength of the compact. Due to limitation of the software cohesion is only applied during release and probing.
During post-processing the forces necessary to cause plastic deformation are evaluated and used to calculate points on the yield surface. The procedure in this work is very similar to the procedure in [2] and [3] whereat in contrast to the current work the former uses rigid walls as boundaries and in both no cohesion is considered.

Results

In Figure 3 discrete points of the flow surfaces for isostatic and closed die compaction after different compaction strains are shown. In both cases the yield surfaces are elongated into the sector of negative hydrostatic pressure and they grow with increasing compaction strain. The flow surfaces after isostatic compression is approximately rotationally symmetric around the 111-axis plotted as a black dashed line. This means the strength of the powder is isotropic after isostatic compaction. In contrast to this the flow surfaces are tilted towards the compression direction (σ_1-direction) after closed-die compression. This means the powder compact can resist higher tensile and compression stresses in compaction direction than normal to the compaction direction. Similar results were

obtained in [2] but only for the compression strength, since no cohesion was considered in that study.

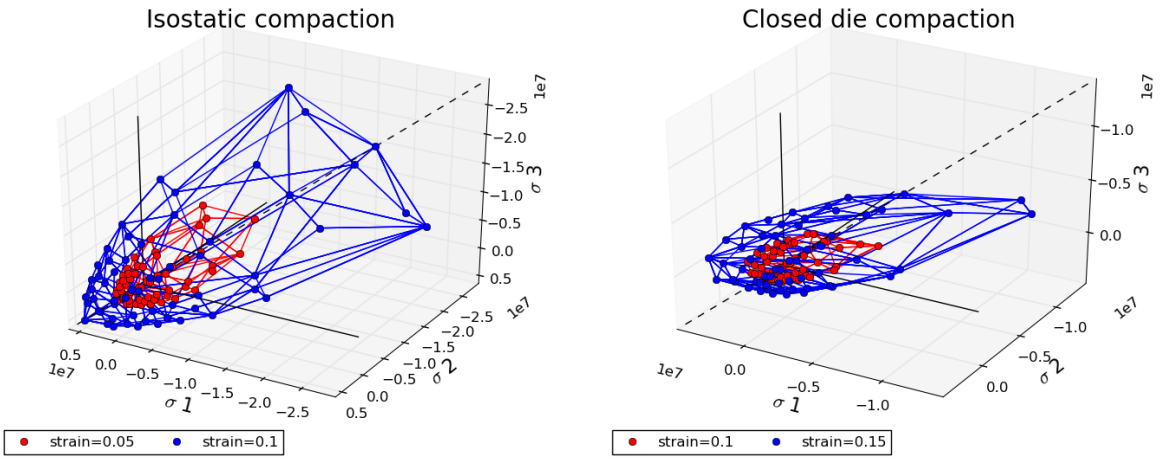

Figure 3: Results for the yield surfaces after isostatic (left) and closed-die (right) compression. The yield surfaces grow with increasing compaction strain.

Conclusion and outlook

This work shows the evolution of the yield surfaces during compaction of a monodisperse powder. In contrast to earlier works in [2] and [3] cohesion is considered in this work what allows to give a statement about the tensile strength after compaction. This is of great industrial importance since failure of compacts is usually to tensile loads.
The Drucker-Prager/Cap model used in other works of powder compaction seems to be useful to describe powders after isostatic compaction approximately, but it is not valid after non-isotropic closed-die compaction. The representation of the flow curves in three dimensional stress space points out the anisotropic behavior after closed-die compaction. This is also seen in experiments e.g. [4].

Although interesting results are obtained in this work, there are still open questions. It is not clear yet how many particles have to be considered to get representative results and how the mesh size influences the results. Furthermore, non-spherical particles should be used to elucidate the influence of particle shapes. Finally, the particles shape, the material and contact properties have to be adjusted to real powders to get results of industrial relevance.

Literature

[1] L. H. Han, J. A. Elliott, A. C. Bentham, A. Mills, G. E. Amidon, and B. C. Hancock, “A modified Drucker-Prager Cap model for die compaction simulation of pharmaceutical powders,” *Int. J. Solids Struct.*, vol. 45, no. 10, pp. 3088–3106, 2008.

[2] B. Harthong, D. Imbault, and P. Dorémus, “The study of relations between loading history and yield surfaces in powder materials using discrete finite element simulations,” *J. Mech. Phys. Solids*, vol. 60, no. 4, pp. 784–801, 2012.

[3] I. Schmidt, A. Trondl, T. Kraft, and A. Wonisch, “Simulation of the material behaviour of metal powder during compaction,” *Proc. Inst. Mech. Eng. Part E-Journal Process Mech. Eng.*, vol. 224, no. E3, pp. 187–194, 2010.

[4] S. Galen and A. Zavaliangos, “Strength anisotropy in cold compacted ductile and brittle powders,” *Acta Mater.*, vol. 53, pp. 4801–4815, 2005.

Feasibility study for turret speed operating points in a rotary tablet press

Michael Martinetz[1], Isabella Aigner[1], Jakob Rehrl[2] Otto Scheiblhofer[3], Stephan Laske[1], Johannes Khinast[1,3]
[1]Research Center Pharmaceutical Engineering GmbH, 8010 Graz, Inffeldgasse 13
[2]Graz University of Technology, Institute of Automation and Control, Inffeldgasse 21/B/I, 8010 Graz
[3]Institute for Process and Particle Engineering, Graz University of Technology, Inffeldgasse 13, 8010 Graz
michael.martinetz@rcpe.at

Abstract

Continuous manufacturing in the pharmaceutical industry needs appropriate solutions to maintain production, even during short-term malfunctions of upstream units or upstream discharge of out-of-specification material. Installation of bigger buffers to compensate for varying mass flow during operation, is not an appropriate solution. This is because of segregation and loss of material during shut down. A more promising approach is the implementation of additional operating points (fast-, normal-, slow- operation), in the sub-units of the manufacturing line, set to react on variations in mass flow up to a certain degree. A variable turret speed allows control of the overall mass flow in a rotary tablet press. In this work, a feasibility study was performed to show that on the rotary tablet press tablets that meet the regulatory requirements can be produced over a wide range of turret speeds.

Introduction/Problem statement

Continuous manufacturing introduces fundamental changes to the pharmaceutical industry, such as rethinking of the batch-based pharmaceutical quality control concept and the implementation of fully automated process units. Consequently, there have been significant steps in the development of continuous manufacturing of pharmaceuticals. With the quality-by-design (QbD) paradigm put into practice and the constant improvement of process analytical technology (PAT), the way has been paved for further development in this field. As a partial development of the continuous production process, the control concept of the pharmaceutical manufacturing standard was adapted from the batch process to a continuous control concept [1].
Tablet production via a rotary tablet press is a well-known process step in the pharmaceutical industry. In recent decades, the output of rotary tablet presses has increased up to several hundred thousand tablets per hour [2]. Often the tablet press is one of the last unit operations in most continuous manufacturing lines. It can be the master of the control concept and determine the overall mass flow through the process [3].
Through the help of an internal hopper variations of upstream units or deviations of the mass flow can be handled, in order to maintain the production of the tablet press. Following this approach, the tablet press continues working with a constant operating speed and the necessary material to bridge the upstream lack of material is obtained from the internal hopper. This approach only works in short continuous production campaigns (i.e., several hours) and/or for very stable processes, due to the limited amount of the material in the hopper. As continuous manufacturing lines have become more complex, with an increasing number of unit operations and more sensible process steps, like wet

and dry granulation, and manufacturing lines which should be kept in operation for longer periods, there is a higher probability of upstream malfunctions in the production line.
The easiest possibility to overcome the aforementioned missing material would be to increase the hopper size, providing a bigger material buffer. During the shutdown of a manufacturing line, often a not negligible amount of material must be removed from the process. This is because production in the predefined conditions can no longer be guaranteed. Following from that, one disadvantage of increasing the hopper size is the larger amount of material removed during shutdown, and therefore a greater financial loss. A further disadvantage is segregation occurring in the hopper during start-up and shut-down procedures [4]. It can be concluded that a more sophisticated process control must be developed to react on upstream malfunctions.
Through the implementation of fast-, normal-, slow- turret speed operating points, it would be possible to react to upstream malfunctions with a slower production speed, so the amount of material in the hopper lasts longer. When refilling the hopper, after an upstream error, the turret speed can be kept slow so that the amount of material in the hopper can accumulate to bridge the next missing mass flow. The fast operation mode can be useful in handling accumulated material in the hopper during a short shutdown of the rotary tablet press. This variation in turret speed causes a change of dwell time. It can be summarized that operating points in turret speed can ensure reliability in plants with smaller buffer tanks. Nonetheless, this variation in dwell time can have an impact on important tablet properties such as variation in weight, basic height, hardness, and disintegration time, depending on the formulation and the materials used.
This feasibility study investigates which turret speed range/dwell time variance for solid dosage forms that fulfill the regulations can be produced with the chosen material. According to Tye, Sun and Amigdon [5], for some known excipients, this impact should be small enough to remain within the product specific design space. Since it is required to remain within the quality target product profile (QTPP) of the product, the range of dwell time independence of the specific formulation has to be determined as a partial development of the specific solid dosage form [6]. In this work a feasibility study with one excipient was performed, to show that with different turret speeds solid dosage forms in accordance to the QTPP can be obtained.

Materials and Methods

The excipient used for the experimental setup and compaction was pure lactose monohydrate (Tablettose® 80 from Meggle GmbH). It was mixed with 1% (w/w) Magnesium Stearate and compacted in a rotary tablet press for industrial applications. Since the main goal is to improve the control system of an industrial continuous manufacturing line, the FETTE 102i was used during the experiments. The FETTE 102i (shown in Figure 1) is a rotary tablet press built for small-quantity industrial campaigns or laboratories. Therefore, results on this machine can be seen as representative for industrial applications

The first objective was to analyze at which process parameters the desired product attributes can be obtained. According to Ritschel [2], the deviations declared to the European Pharmacopoeia are permitted to be ±1 mm in basic height and between ±5% of target weight. Those parameters were analyzed as a part of this work.

In the investigated experimental setup, the turret speed (20 to 100 rpm), as well as the compaction force (1 to 7 kN), were varied in small steps. After a waiting time, which was needed to establish stable production, representative samples of 20-30 tablets were taken. According to the manual of the FETTE 102i, a stable production after changes in turret

speed is reached after two rotations of the turret. It was decided that 20 rotations of the turret ensured a big enough safety factor to guarantee stable production. Following from this information, the waiting time was determined according to the turret speed and ranged from 240s at 5 rpm to 12s at 100 rpm. The produced tablets were analyzed offline, after a relaxation time of 48 hours [2], [7].

Figure 1: FETTE 102i during the experiments

Sample Characterization/Evaluation

After a 48 hour tablet relaxation time, ten tablets were randomly selected from every sample. Their tablet weight and tablet basic height were measured with a lab scale (Sartorius AW-224, Sartorius AG, Germany) and a dial indicator. The arithmetic mean value $\bar{x}$ and the standard deviation s were determined, from the measured values, according to Equation 1 and Equation 2.

$$\bar{x} = \frac{1}{n}\sum_{i=1}^{n} x_i$$

Equation *1*

$$s = \sqrt{\frac{\sum_{i=1}^{n}(x_i - \bar{x})^2}{n-1}}$$

Equation *2*

The following procedure was taken to prove that points determined to be close to the border of the out-of-specification area (see Figure 2 and Figure 3) are representative. The determined standard deviation of the measured values of tablet weight was in the range of 0.001 g. It was assumed that deviations of weight and length are normally distributed. Following on from this, the double standard deviation to fulfill the 95% confidence interval was calculated at 0.002 g. The determined maximal double standard deviation of the tablet basic height was 0.07 mm. Subsequently, it can be concluded that the arithmetic mean value is representative the determined double maximal standard deviations of the measured values are shown in Figure 2 and Figure 3.

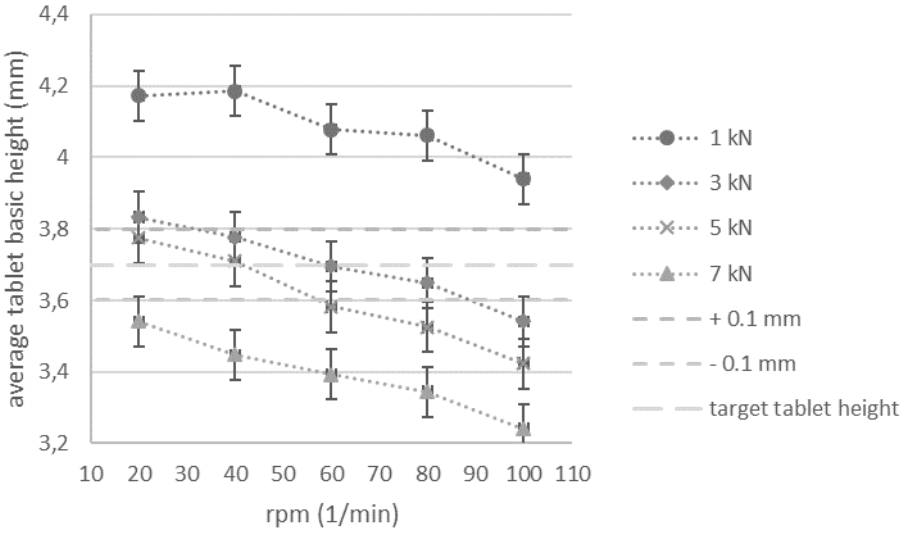

Figure 2: Average tablet basic height at varied turret speed

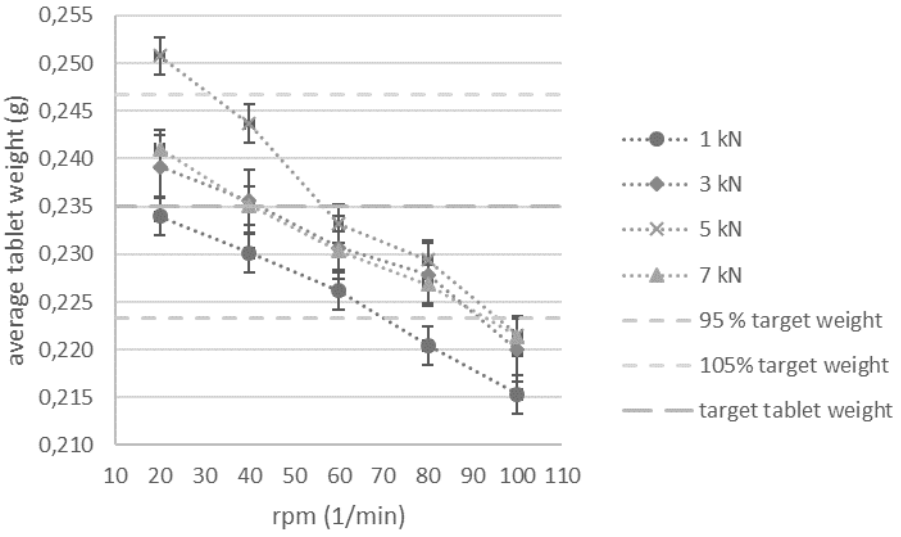

Figure 3: Average tablet weight at varied turret speed

In Figure 2 it is shown that the solid dosage form, with the maximum deviations of ±1 mm in tablet basic height, can be obtained with a compaction force of 3 kN and a turret speed of 40 to 80 rpm. A similarly positive agreement in desired quality attributes for tablet basic height can be reported for the 5 kN experimental run, in the range of 20 to 60 rpm of the turret. In Figure 2, the average weight as well as the double maximal determined standard deviation of 0.07 mm is shown. In Figure 3, the weight derivations of ±5%, which are allowed according to the regulations, are shown over the rpm of turret speed. In Figure 3, the doubled maximal determined standard deviation of 0.002 g, for every sample point, is considered for this analysis. It can be clearly seen that the target weight, including the doubled maximal standard deviation, meets the specifications of ±5% from 20 to 80 rpm of turret speed, and for compaction forces of 3 and 7 kN. At a compaction force of 5 kN, the desired product attributes were obtained between 40 and 80 rpm of turret speed. It can be see that the average tablet basic height as well as the average tablet weight is decreased by an increase of the turret speed. This effect is probably caused by the constant feed frame speed over the whole turret speed range.

Results and Outlook

Clearly, the implementation of turret speed operating points, in a rotary tablet press, would be a step towards continuous manufacturing in the pharmaceutical industry.
In Figure 2 and Figure 3, the investigated parameters of the solid dosage form are shown over the turret speed. It can be seen that over the wide range of 3 kN and 5 kN compaction forces, tablets can be produced which meet the strict regulatory requirements.
Due to the fact that most of the bulk goods used in the pharmaceutical industry are very different in handling and processing, as a next step a variation of processing parameters must be performed with different excipients and additives (microcrystalline cellulose, starch, dicalcium phosphate, lactose, magnesium stearate etc.) [5], [8], [9]. Based on already discovered interactions, other key parameters of a rotary tablet press, such as the impact of the paddle speed in the feed frame and the ratio between feed frame paddle speed and turret speed, should be investigated [10], [11]. As a part of the next steps an online analysis with appropriate PAT tools is planned [12]. It appears that based on these results the variation in tablet properties can be further reduced.

Literature

[1] S. L. Lee, T. F. O'Connor, X. Yang, C. N. Cruz, S. Chatterjee, R. D. Madurawe, C. M. V. Moore, L. X. Yu, and J. Woodcock, "Modernizing Pharmaceutical Manufacturing: from Batch to Continuous Production," *J. Pharm. Innov.*, vol. 10, no. 3, pp. 191–199, Sep. 2015.

[2] W. A. Ritschel and A. Bauer-Brandl, *Die Tablette: Handbuch der Entwicklung, Herstellung und Qualitätssicherung*, 3rd ed. Aulendorf: Editio Cantor Verlag, 2012.

[3] R. Singh, M. Ierapetritou, and R. Ramachandran, "System-wide hybrid MPC-PID control of a continuous pharmaceutical tablet manufacturing process via direct compaction," *Eur. J. Pharm. Biopharm.*, vol. 85, no. 3 PART B, pp. 1164–1182, 2013.

[4] K. Manjunath, S. Dhodapkar, and K. Jacob, "Solids Mixing Part B: Mixing of Particulate Solids in the Process Industries," in *Handbook of industrial mixing: science and practice*, E. L. Paul, V. A. Atiemo-Obeng, and S. M. Kresta, Eds. John Wiley & Sons, Inc., Hoboken, New Jersey., 2004, p. 1377.

[5] C. K. Tye, C. Sun, and G. E. Amidon, "Evaluation of the effects of tableting speed on the relationships between compaction pressure, tablet tensile strength, and tablet solid fraction," *J. Pharm. Sci.*, vol. 94, no. 3, pp. 465–472, 2005.

[6] L. X. Yu, "Pharmaceutical quality by design: Product and process development, understanding, and control," *Pharm. Res.*, vol. 25, no. 4, pp. 781–791, 2008.

[7] J. Ropero, Y. Colon, B. Johnson-Restrepo, and R. J. Romanach, "Near-Infrared Chemical Imaging Slope as a New Method to Study Tablet Compaction and Tablet Relaxation," *Appl. Spectrosc.*, vol. 65, no. 4, pp. 459–465, 2011.

[8] M. Jivraj, L. G. Martini, and C. M. Thomson, "An overview of the different excipients useful for the direct compression of tablets," *Pharm. Sci. Technol. Today*, vol. 3, no. 2, pp. 58–63, 2000.

[9] G. E. Amidon, P. J. Secreast, and D. Mudie, "Developing Solid Oral Dosage Forms," in *Developing Solid Oral Dosage Forms*, Elsevier, 2009, pp. 163–186.

[10] E. Peeters, T. De Beer, C. Vervaet, and J. Remon, "Reduction of tablet weight variability by optimizing paddle speed in the forced feeder of a high-speed rotary tablet press," *Drug Dev. Ind. Pharm.*, vol. 41, no. 4, pp. 530–539, Apr. 2015.

[11] R. Mendez, F. Muzzio, and C. Velazquez, "Study of the effects of feed frames on powder blend properties during the filling of tablet press dies," *Powder Technol.*, vol. 200, no. 3, pp. 105–116, 2010.

[12] P. R. Wahl, G. Fruhmann, S. Sacher, G. Straka, S. Sowinski, and J. G. Khinast, “PAT for tableting: Inline monitoring of API and excipients via NIR spectroscopy,” *Eur. J. Pharm. Biopharm.*, vol. 87, no. 2, pp. 271–278, 2014.

Influence of the heat transfer and operation time of a coaxial probe for deep geothermal energy

Eva M. Rohringer, Wolfgang M. Samhaber
Johannes Kepler Universität Linz, Institut für Verfahrenstechnik,
eva.rohringer@jku.at, wolfgang.samhaber@jku.at

Abstract
For this exploratory study, a 6000 m deep coaxial borehole heat exchanger (CBHE) was investigated. The drilling for this CBHE is carried out at a depth of -1000 m from a cavern to minimize the heat losses. In this depth the surrounding reaches already higher temperatures, while a reduction of the heat extraction occurs caused by higher heat loss. In this study the temperature profile along the probe was calculated to present the influence of operating time and the outlet temperatures. Therefor a triple pipe heat exchanger was installed to control the numerical calculation with the experimental model. In addition, the first 1000 m pipe lengths are isolated in order to achieve higher outlet temperatures. The aim is to achieve high heat extraction rates from the underground.

Introduction
The heat extraction with deep geothermal due a single pipe system, in this case a CBHE, is influenced by various parameters such as thermal properties of borehole wall and pipes, probe design, flow conditions and the operating time. Higher temperatures are reached in a deeper depth as well as higher quantity of heat extraction but also higher heat losses occur along the probe caused by the counter flow process. Another important aspect is the operating lifetime while an increase of the operating time leads to a decrease of heat extraction caused due the non-regenerating surrounding of the borehole wall. To generate an economically efficient heat extraction from this depth, the radial and vertical heat transport around the pipes and the pipe system itself are important. The heat transfer is influenced by parameters such as characteristics of the surrounding, thermal conductivity to the annular gap, borehole diameter, sizing of pipes, possible insulating layers and their thermal conductivity [1] but also the operating parameters such as flow rates and flow regimes [2].
Heat is transported due conduction at the outer pipe cause of direct contact of the pipe itself, the backfilling or the insulation of the pipe with the surrounding. The inner wall of the outer pipe transmits the temperature of the flowing medium of the annular gap. A convective heat transfer occurs from the fluid in the annular gap on the outside of the central pipe or its insulation and from the inner central wall to the flowing fluid, while heat is transferred due conduction through the central pipe material [3]. With increasing depth, an increase in the temperature along the probe is reached and due to the emerging temperature gradient heat is extracted from the surrounding soil [4]. In order to generate a high heat extraction rate, a high outlet temperature of the central pipe, and thus a large temperature difference between inlet and outlet temperature is required. The flow direction of this CBHE is with the fluid inflow into the outer pipe, the annular gap, and is coming out from the central pipe. Theoretically, the flow direction can be adjusted in the reversed direction [5]. The flowing fluid is heated up downwards in the

annular gap and is transported upward in the inner tube [2]. The probe operating in countercurrent thus holds another heat loss for instance from the return to the inflow flux. At a certain height the extracted heat is transferred back from the warmed flowing medium of the central pipe to the cooler forward flowing medium. The aim is to maximize heat extraction and to minimize heat losses [4].

Experimental and CBHE model

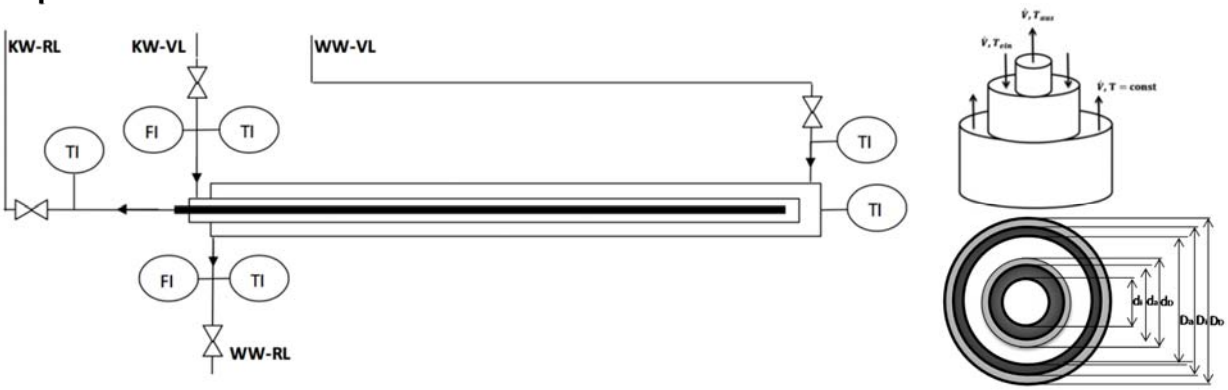

Figure 1: Set-up of the empirical measurements and a cross-section of the CBHE of the numerical model.

A triple pipe system is installed to simulate a CBHE, with a length of 13 m. The outer pipe made of PVC has a diameter of 63 mm and a wall thickness of 3 mm. In this outer annular gap a warm water heat flow is applied. The second pipe made of copper transfers the heat to the inner annular gap with the cold fluid inflow. This heated fluid returns through the central pipe made of PVC. Various measurements under changing conditions have been performed such as different flow rates and temperatures of the outer annular gap and the CBHE as well. These results serve to control the calculations of the numerical model which has been used for the modelling of the deep geothermal CBHE system. According to the calculation the defined dimensioned system is used to simulate the axial temperature profile of the CBHE.

Table 1: Pipe parameters and heat conductions.

	1st -1000 to -2600 m		2nd -2600 to -6000 m		Experimental	
Pipe	**Outer**	**Central**	**Outer**	**Central**	**Outer**	**Central**
D_a / m	0.245	0.0889	0.178	0.0889	0.042	0.016
D_i / m	0.231	0.0794	0.165	0.0794	0.038	0.014
WS_R/ m	0.0138	0.0095	0.013	0.0095	0.002	0.001
WS_{Ins} / m	0.001	0.001	0.001	0.07	0	0
λ_{Pipe}/Wm^{-1}K^{-1}	30.0	0.4	30.0	0.4	400	0.17
$\lambda_{Pipe-Ins}$/Wm^{-1}K^{-1}	30.0	0.40	30.0	0.4	0	0
λ_{Soil} /Wm^{-1}K^{-1}	3.00		3.00			

Results and Discussion

Defined parameters such as pipe dimensions were chosen in advance to guarantee technical requirements which are shown in
Table 1. The calculation of the heat profiles, therefore the heat transfer mechanism and heat transfer coefficient of the central and outer pipe, are calculated separately. Similitudes for instance Nusselt-number are used to calculate the convective heat transfer coefficient and further determine the heat transfer coefficient *k* [W m-2K-1] [2].

The borehole wall is segmented as well as the outer and the central pipe to receive the temperature profile along the probe of the annular gap and the inner tube. The cavern is located -1000 m underneath the surface of the earth from where the actual drilling starts. That implies a higher borehole wall temperature and saves drilling meter and within drilling costs. For this deep heat exchanger a depth of -5000 m is intended. In the first section the pipe consists of a larger diameter than the one in the second section starting at -2600 m. For the heat transfer parameter the changing dimensions need to be taken in account of the calculations. The heat flux Q [W m-1] increases with increasing depth of the borehole caused due the increasing temperature of the underground, shown in Table 2. The central pipe reaches a depth of -5900 m.

Table 2: Heat flux along the pipe with increasing depth.

Depth / m	1000-2000	2000-3000	3000-4000	4000-5000	5000-6000
Q / W m^{-1}	0.1	55	110	170	220

The outlet temperature of the annular gap is determined gradually to the end of the outer pipe at -6000 m by knowing the borehole wall temperature and the different heat fluxes along the pipe of 55-220 W m^{-1}. The outlet temperature and the temperature profile of the annular gap are decisive for the calculation of the temperature profile of the central pipe and its outlet temperature. Therefore to achieve high outlet temperature insulation for the outer and inner pipe from -1000 m to a depth of -2000 m is taken into account. In this case with fix pipe parameters and heat fluxes of the surrounding the temperature profile is mainly influenced by the central pipe isolation and its thickness.

Table 3: Comparison of the outlet temperatures at different operating years with a flux of 3.9 m^3 h^{-1}.

		Annular gap				
		2000 m	**3000 m**	**4000 m**	**5000 m**	**6000 m**
6F	T_{out} / °C _ 0.2	60.0	77.9	95.7	113.5	131.4
7F	T_{out} / °C _ 15	60.0	71.2	82.5	93.7	105.0
8F	T_{out} / °C _ 30	60.0	70.2	80.3	90.5	100.6
Central pipe						
6F	T_{out} / °C _ 0.2	126.9	127.9	128.0	128.4	130.2
7F	T_{out} / °C _ 15	101.6	101.6	101.6	102.7	103.8
8F	T_{out} / °C _ 30	97.3	97.3	97.4	98.5	99.6

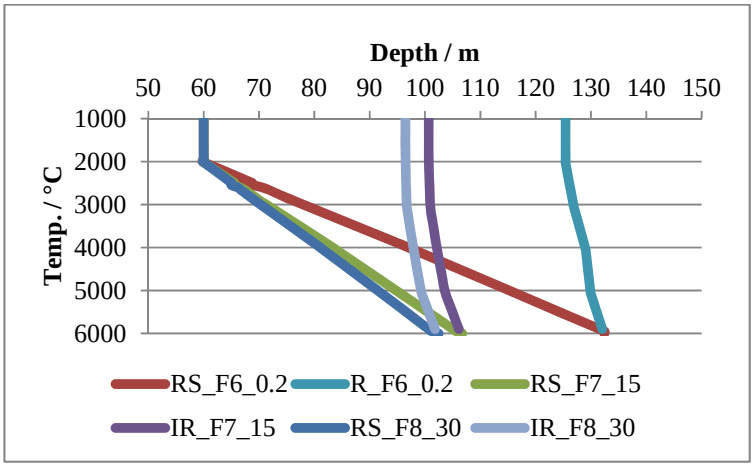

Figure 2: Influence of the operating time: F6 after 0.2, F7 after 15 and F8 after 30 operating years.

Based on the borehole wall temperatures, the heat fluxes are calculated and show with increasing operating time, a decrease of the outlet temperatures and the heat extraction rate from the underground, shown in *Table 3*. This change over the operating time has a significant impact on the economics of such a system. *Figure 2* presents the apparent decrease in the borehole temperature and consequently also the outlet temperature of the return medium caused due the slow regeneration of the surrounding soils. The temperature decreases from 130.2 °C after 0.2 years of operation, to 103.8 °C after 15 years, and to 99.6 °C after 30 years of operation.

Conclusion

The potential of heat extraction, in this case by using a CBHE, mainly depends on the surrounding temperature, the borehole wall temperature, the design and dimension of the pipe system and thermal conductivities of soils and pipe materials. Significant influence parameters of an economic probe system are pipe- and insulation thickness dimensions, thermal conductivity and flow characteristics. The minimization of heat losses to the surrounding soil and in the pipe system itself is of great importance in order to generate high heat extraction rate. The technical feasibility of such a system in deep mountain regions optionally has technical limits. The goal is to minimize the heat losses and to maximize the heat extraction performance. More detailed calculations, including assumptions and consideration of technically feasible pipe systems, and borehole wall temperatures and heat fluxes show the absolute necessity for an insulation of the outer pipe to the environment as well as the isolation of the central pipe in the first 1000 m of drilling. A significant role has within the central pipe insulation and its thermal conductivity under the given pipe dimensions. The heat transfer from the forward medium to the return medium induces an advantage in deep segments while a higher heat loose occurs in shallower segments. Finally an important aspect is the operating time that needs to be considered then with increasing duration a lower heat extraction is achieved. Preliminary calculations such as investment costs, profitability calculation and consideration of the changing heat recovery are therefore advisable.

Literature

[1] P. J. Yekoladio, T. Bello-Ochende, and J. P. Meyer, “Design and optimization of a downhole coaxial heat exchanger for an enhanced geothermal system (EGS),” *Renew. Energy*, vol. 55, pp. 128–137, 2013.

[2] R. a. Beier, J. Acuña, P. Mogensen, and B. Palm, “Borehole resistance and vertical temperature profiles in coaxial borehole heat exchangers,” *Appl. Energy*, vol. 102, pp. 665–675, 2013.

[3] B. Glueck, “Simulationsmodell ‘Erdwämresonden’ zur wärmetechnischen Beurteilung von Wärmequellen, Wärmesenken und Wärme-/Kältespeisern - 1. Ergänzung: Koaxialsonden,” Jößnitz, 2015.

[4] L. Dijkshoorn, S. Speer, and R. Pechnig, “Measurements and Design Calculations for a Deep Coaxial Borehole Heat Exchanger in Aachen , Germany,” vol. 2013, 2013.

[5] S. Javed, P. Fahlén, and J. Claesson, “Vertical Ground Heat Exchangers: A review of heat flow models,” in *11th international conference on themal energy storage, Effstock, Stockholm, Sweden*, 2009.

The Novel Dual Fluidized Bed - Gasifier at TU Wien Part I: Parameter Variation with Wood Pellets

Florian Benedikt*, Josef Fuchs, Johannes C. Schmid, Hermann Hofbauer
TU Wien, Institut für Verfahrenstechnik, Umwelttechnik und Techn. Biowissenschaften
Getreidemarkt 9/166, 1060 Wien, Austria
*florian.benedikt@tuwien.ac.at

Abstract

A new test plant with a novel dual fluidized bed (DFB) steam gasification concept was built at the TU Wien. The improved technology of the test plant enhances gas-solid contact between hot bed material and product gas to minimize the tar content in the product gas. In addition a new particle separator system facilitates the use of softer and catalytically more active bed material.
In this work, two gasification experiments with wood pellets are presented. Thereby, the main product gas composition, tar, dust and char content were investigated, depending on the variation of gasification temperature and bed material composition.

Introduction

The thermo-chemical conversion of biogenous feedstock is a promising option to advance the eco-friendly and efficient production of heat and power, secondary energy carriers and valuable products for the chemical industry based on renewable sources. The basic principle of the DFB process is illustrated in Figure 1. Through the circulation of hot bed material the combustion reactor (CR) supplies heat for the overall endothermic gasification in the gasification reactor (GR). Thereby generated residual char is transported back to the combustion reactor where it is burnt and therefore closes the loop. Steam is serving as gasification agent to convert a solid fuel into the product gas which mainly consists of H_2, CO, CO_2, and CH_4 with a lower heating value of about 12 MJ/Nm³. The utilization of catalytically active bed material, such as olivine or calcite ensures reduced tar contents in the product gas. [1]

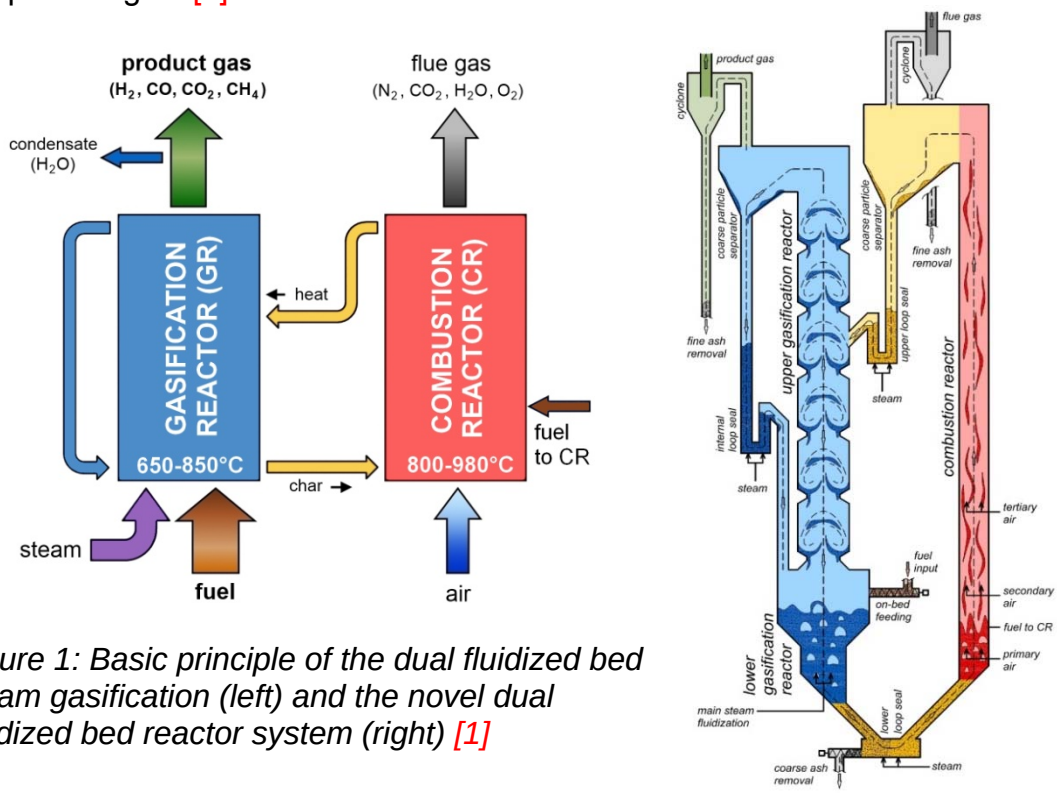

Figure 1: Basic principle of the dual fluidized bed steam gasification (left) and the novel dual fluidized bed reactor system (right) [1]

The gasification reactor in the novel design is divided into a lower part with a bubbling bed fluidization regime including the fuel input and an upper countercurrent part with turbulent zones realized through a cascade structure. Thus an increased gas-solid contact is expected to further reduce the tar content in the up-streaming product gas.

Experimental

In this paper, two parameter variations regarding gasification experiments with wood pellets are presented [2]. During the experiments wood pellets were introduced via on-bed feeding onto the bubbling bed of the lower GR. First results were gathered to describe the influence of temperature variations in the GR, with fresh olivine as bed material only. Subsequently a mixture of fresh olivine and calcite was used as bed material. The influence on the gasification parameters for fresh olivine as bed material only and a mixture of fresh olivine and calcite was compared. To set the gasification temperatures and to compensate heat losses an additional fuel input into the CR was used. During the experiments the process control system of the novel DFB-gasifier at TU Wien continuously measured and recorded data of temperature, pressure, flow rates and gas compositions (Rosemeount NGA2000). C_2H_4 was analyzed every 15 minutes by a gas chromatograph (Perkin Elmer ARNEL – Clarus 500) [3]. Measured data are always presented as mean values. Further an adapted standardized arrangement of sampling equipment is used to analyze the content of dust, char and tar in the product gas stream [4]. Operating parameters for the experiments are given in Table 1. The chemical and elemental analysis of the used wood pellets is presented in Table 2.

Table 1: General operating parameters for presented gasification test runs.

Parameter/name	Unit	Olivine	Olivine and calcite mix
Bed material particle size range & type	µm	100-300 olivine	100-300 olivine, 250-400 calcite
Bed material mixture	wt.-%	100 olivine	90 olivine, 10 calcite
Initial bed material inventory	kg	82-83	97
Fuel mass flow	kg/h	19.0-19.5	20.1
Fuel power into GR	kW	92-94	97
Fuel power into CR	kW	46-53	50

Table 2: Chemical analysis of wood pellets as fuel for gasification.

Parameter/name	Unit	Wood pellets
Water content	wt.-%	7.2
LHV (moist)	kJ/kg	17400
Ash content	wt.-%$_{db}$	0.2
Carbon (C)	wt.-%$_{db,af}$	50.7
Hydrogen (H)	wt.-%$_{db,af}$	5.9
Oxygen (O)	wt.-%$_{db,af}$	43.0
Nitrogen (N)	wt.-%$_{db,af}$	0.21
Sulfur (S)	wt.-%$_{db,af}$	0.005
Chlorine (Cl)	wt.-%$_{db,af}$	0.005
Typical ash deformation temp. (A)	°C	1330-1400
Typical ash flow temp. (D)	°C	>1430

Results and Discussion

Figure 2 shows the influence of the gasification temperature on the product gas composition. The bubbling bed temperature GR6, which is located in the lower gasification reactor (also see Figure 4 for the exact position of GR6 in the near of the fuel input) was varied from 655 to 836°C. Thereby the H_2 content increased from 23.8 to 38.7 vol.-%$_{db}$ whereas CO decreased from 35.3 to 27.1 vol.-%$_{db}$. CO_2 was slightly elevated from 17.1 to 18.5 vol.-%$_{db}$, CH_4 was reduced from 14.9 to 10.1 vol.-%$_{db}$ and C_2H_4 decreased from 4.3 to

1.6 vol.-%$_{db}$. The presented temperature variation and its impact on the main product gas composition is in very good accordance to previous results [5].

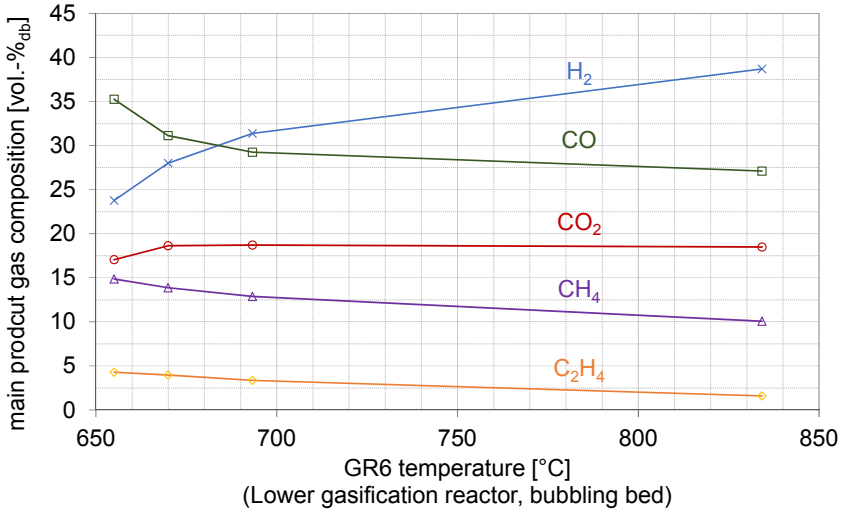

Figure 2: Main product gas composition depending on gasification temperature with fresh olivine as bed material only (no mix).

Figure 3 shows the time averaged temperature profile over the height of the GR and CR for the bed material variation. The temperature profiles for both test runs are well comparable to each other. The lower temperature levels in the lower part of the GR showed the effect of the endothermic gasification reactions, while the upper GR reactor showed quite consistent temperatures over the height. The peak temperature at the CR appeared where additional fuel and the secondary air were introduced.

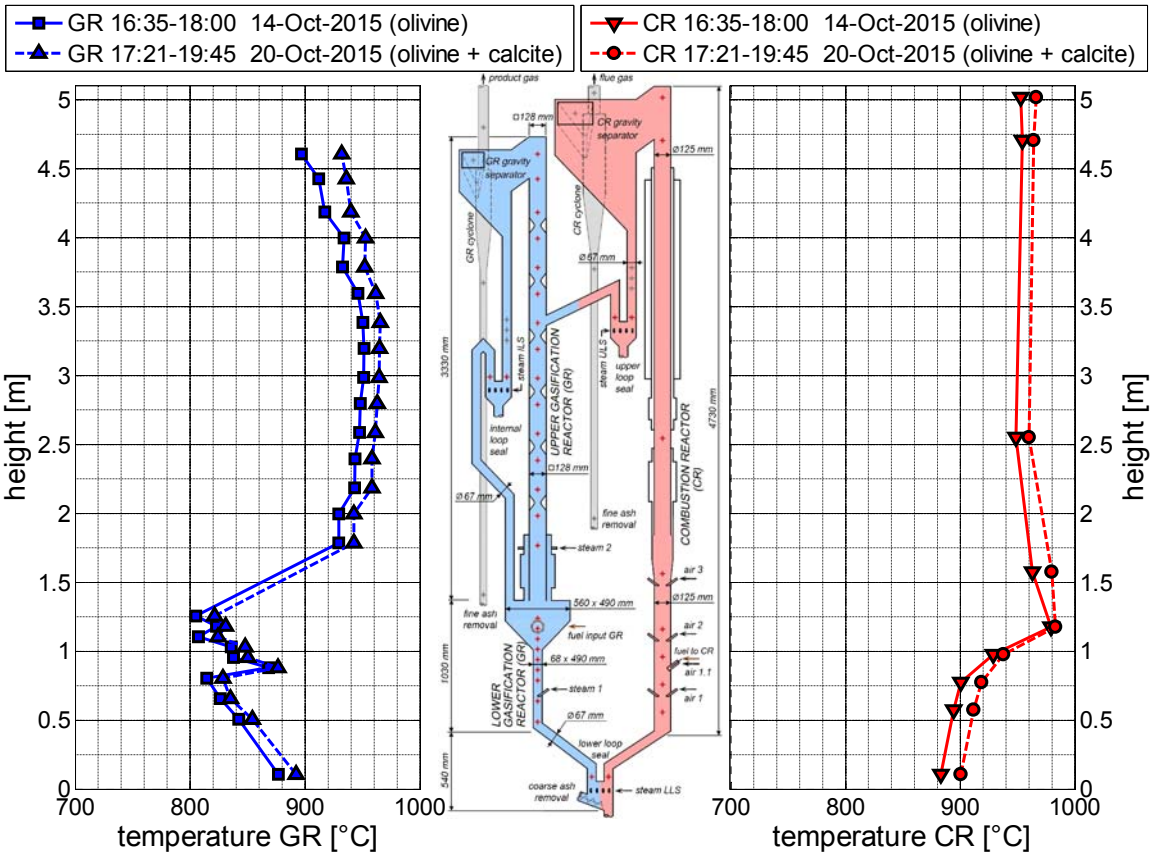

Figure 3: Temperature profile (average values) of GR and CR with fresh olivine and a mixture of fresh olivine and calcite as bed material.

Figure 4 presents the temperature trends of selected measurement points of the GR for the steady-state operation phases of the test plant. Comparison of all temperature measurement points GR6, GR11, GR11 and GR22 were in good agreement for both test runs with an average difference of 12 °C for GR6 near the wood pellet fuel input.

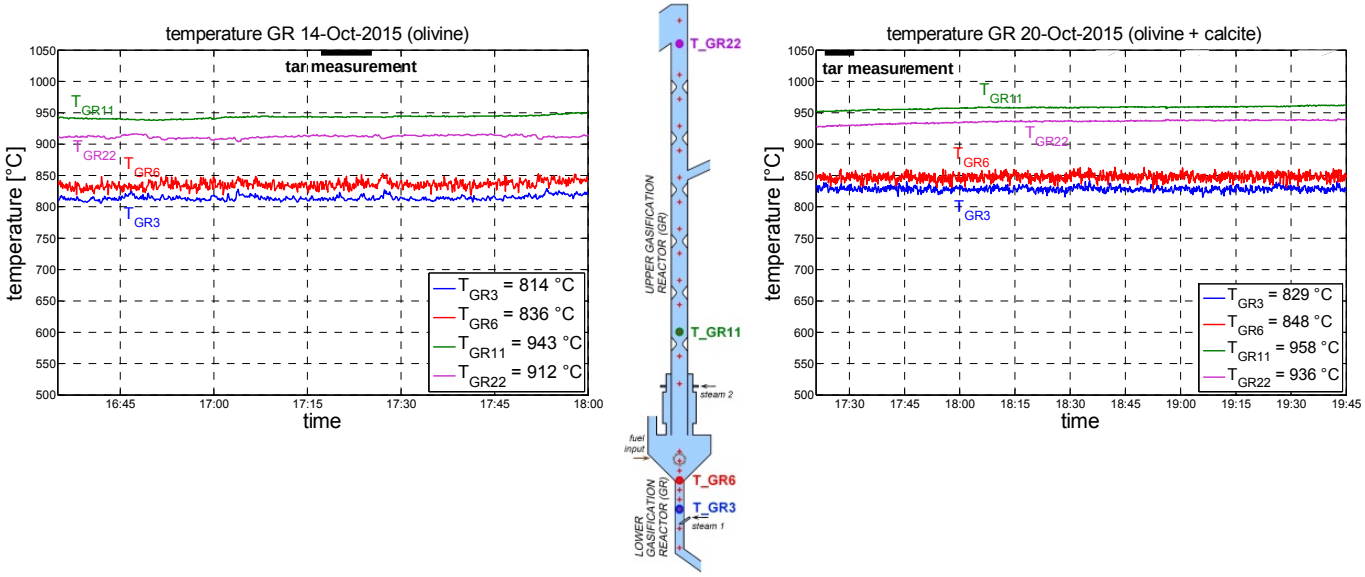

Figure 4: Temperature trend of the gasification reactor for experiments with fresh olivine and a mixture of fresh olivine and calcite as bed material.

Figure 5 displays the difference of the average product gas composition and tar, dust and char content for gasification with fresh olivine and a mixture of fresh olivine and calcite as bed material. When comparing the product gas composition the H_2 content was increased from 38.7 to 43.6 vol.-%$_{db}$ and CO_2 was slightly elevated from 18.5 to 20.6 vol.-%$_{db}$. The CO content was decreased from 27.1 to 21.7 vol.-%$_{db}$, CH_4 content was reduced from 10.1 to 9.1 vol.-%$_{db}$ and C_2H_4 content was halved from 1.6 to 0.8 vol.-%$_{db}$. The strongest impact of change in bed material is seen by the comparison of the tar values. GCMS tar is reduced from 11.2 to 4.5 g/Nm³ and gravimetrical tar from 6.7 to 1.5 g/Nm³. C_2H_4 seems to be an indicator for the GCMS tar content in the product gas. This is in good accordance to previous results [6, 7]. There was no mentionable effect on the dust content which was 0.3 respectively 0.4 g/Nm³. The char content was halved from 2.4 to 1.2 g/Nm³.

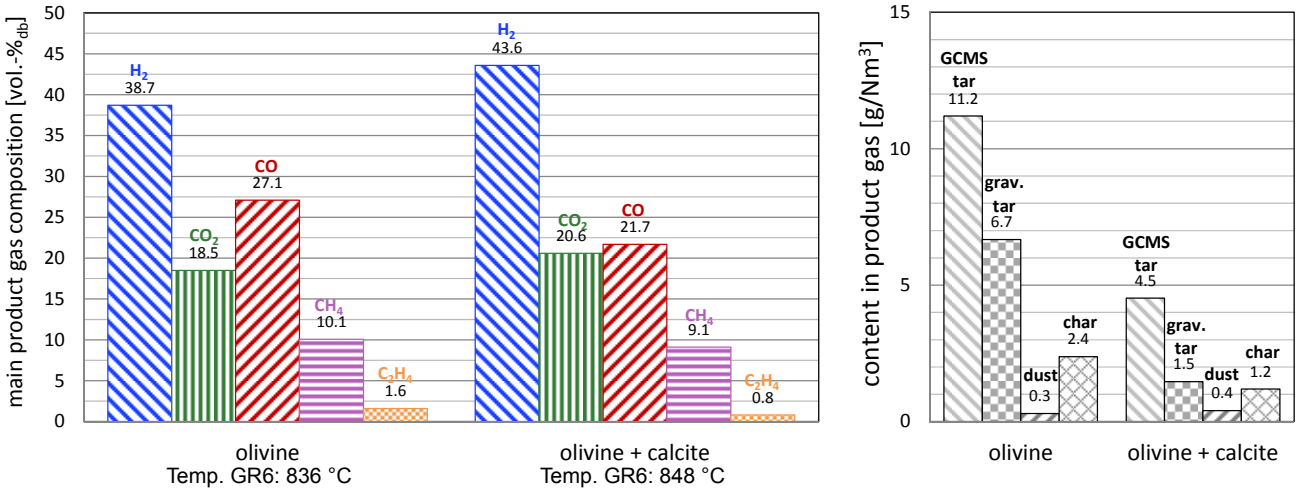

Figure 5: Main product gas composition (left), tar, dust and char contents (right) for experiments with fresh olivine and a mixture of fresh olivine and calcite as bed material.

Conclusion and Outlook

Gasification temperature and bed material variations with wood pellets were carried out at the novel DFB-gasifier at TU Wien. The temperature variation showed great impact on the product gas composition and was in good accordance to former results with other DFB gasifiers. Results from a test run with fresh olivine and a test run with a mixture of fresh olivine and calcite as bed material were compared. Thereby, a change in main product gas composition and tar content was observed. The C_2H_4 content in the product gas was halved from 1.6 to 0.8 vol.-%$_{db}$ and the GCMS tar content was reduced from 11.2 to 4.5 g/Nm³, when the mixture of fresh olivine and calcite was used instead of fresh olivine only as bed material. These results also confirm the direct correlation between C_2H_4 and GCMS tar content in the product gas. The proper feasibility of the novel gasification reactor concept was proven. Future work should focus on further experimental research regarding parameter variations with the novel DFB-gasifier. Thereby, well-known correlations of the DFB gasification process should be verified and ideal operation parameters like temperature and steam to fuel ratio with the novel gasifier should be investigated in detail. In addition experiments with softer and catalytically more active bed material (e.g. only calcite) should be conducted.

Acknowledgement

The present work contains results of the project ERBA II which is being conducted within the “Energieforschung” research program funded by the Austrian Climate and Energy Fund and processed by the Austrian Research Promotion Agency (FFG). The work has been accomplished in cooperation with voestalpine Stahl GmbH, and voestalpine Stahl Donawitz GmbH.

Literature

[1] Schmid, J.C., 2014, "Development of a novel dual fluidized bed gasification system for increased fuel flexibility", doctoral thesis, Institute of Chemical Engineering, TU Wien, ISBN 978-3-9502754-6-9

[2] Kolbitsch, M., 2016, doctoral thesis, Institute of Chemical Engineering, TU Wien, to be published

[3] Schmalzl, M., 2014, "Implementierung der MSR-Technik einer 100 kW DUAL FLUID Versuchsanlage zur Vergasung von Festbrennstoffen", master thesis, Institute of Chemical Engineering, TU Wien

[4] CEN/TS 15439:2006 “Biomass Gasification - Tar and Particles in Product Gases - Sampling and Analysis”

[5] Koppatz, S., Pfeifer, C., Hofbauer, H., 2011, "Comparison of the performance behaviour of silica sand and olivine in a dual fluidised bed reactor system for steam gasification of biomass at pilot plant scale", Chemical Engineering Journal, Vol. 175, pp. 468-483, Date: 15 Nov. 2011, doi:10.1016/j.cej.2011.09.071.

[6] Kitzler, H., 2013, "Zweibettwirbelschicht-Dampfvergasung von biogenen, ascheintensiven Brenn- und Reststoffen - Einfluss der Asche auf den Prozess", doctoral thesis, TU Wien

[7] Kern, S., 2013, "Gasification and Co-Gasification of Coal, Biomass and Plastics in a Dual Fluidized Bed System", doctoral thesis, TU Wien

The Novel Dual Fluidized Bed - Gasifier at TU Wien Part II: Gasification of Alternative Fuels

Josef Fuchs*, Stefan Müller, Cesar J. Aguiari, Johannes C. Schmid, Hermann Hofbauer
TU Wien, Institut für Verfahrenstechnik, Umwelttechnik und Techn. Biowissenschaften
Getreidemarkt 9/166, 1060 Wien, Austria
*josef.fuchs@tuwien.ac.at

Abstract

This work presents two test runs with the novel dual fluidized bed steam gasification test plant at TU Wien. The improved technology of the test plant enhances gas-solid contact between hot bed material and product gas to minimize the tar content in the product gas and meet the requirements for gasification of biogenous alternative fuels. The successful gasification of two different alternative fuel types (sugar cane bagasse and exhausted olive pomace) has been proven. The gasification temperature for exhausted olive pomace differs significantly from usual gasification conditions due to a low ash deformation temperature. Due to a used bed material mixture of olivine and calcite the lower temperature in the gasification reactor is suspected to enable a weak selective transport of CO_2 from the gasification reactor to the combustion reactor, which influences the product gas composition. Furthermore, tar and dust content in the product gas are presented.

Introduction

Facing future challenges in energy supply, gasification of biomass is a reliable technology for gaining syngas. In the range of renewable resources biomass is unique, as it constitutes the only renewable carbon source. The utilization of cheap alternative fuels like residuals and wastes becomes more and more important, since the increasing use of high-grade biomass (like wood chips) leads to increasing fuel prices as well. Due to challenging characteristics of alternative fuels (low ash deformation temperature, high tar contents, etc.) the enhancement of existing technologies is of great relevance. A novel dual fluidized bed steam gasification test plant for handling of various fuels has been designed by TU Wien. This technology enhances gas-solid contact compared to former designs by a new countercurrent-column, which is placed subsequent to the bubbling bed of the gasification reactor and enlarges the range of applicable fuels because of e.g. higher tar conversion rates compared to other dual fluidized bed (DFB) systems. [1]

Experimental

Gasification of two alternative fuels was investigated: Sugar cane bagasse (SCB) [2] and exhausted olive pomace (EOP). For both fuels several pre-processing steps were performed. To guarantee pourability in the fuel hopper and a uniform input into the 100 kW pilot plant by the screw conveyor the SCB had to be milled and pelletized. Due to a low ash deformation temperature of the EOP raw material the EOP pellets had to be mixed with $CaCO_3$ and pelletized again afterwards. During the test runs main product gas components like H_2, CO, CO_2 and CH_4 were analyzed by Rosemeount NGA2000 measurement equipment. C_2H_4 was analyzed by a gas chromatograph (Perkin Elmer ARNEL – Clarus 500). A large number of temperature and pressure sensors guaranteed an effective process control. Further a standardized arrangement of sampling equipment was used to analyze the content of dust, water, char and tar in the product gas stream [3]. Operating parameters for SCB and EOP are given in Table 1. The chemical and elemental analysis of the fuels are presented in Table 2. One can see that the operation parameters for both fuels are similar (fuel power into gasification reactor (GR), fuel into combustion reactor (CR), bed material mixture, etc.).

Table 1: General operating parameters for gasification test runs with SCB and EOP.

Parameter/name	Unit	SCB	EOP
Bed material particle size range & type	µm	100-300 olivine, 250-400 calcite	100-300 olivine, 250-400 calcite
Bed material mixture	wt.-%	82 olivine, 18 calcite	78 olivine, 22 calcite
Initial bed material inventory	kg	86.7	85.1
Fuel mass flow	kg/h	20.0	19.8
Fuel power into GR	kW	90.6	83.8
Fuel power into CR	kW	57	54

Table 2: Chemical analysis of SCB and EOP pellets as fuel for gasification.

Parameter/name	Unit	SCB	EOP
Water content	wt.-%	7.7	11.8
LHV (moist)	kJ/kg	16310	15240
Ash content	wt.-%$_{db}$	2.3	11*
Carbon (C)	wt.-%$_{db,af}$	48.9	52.4
Hydrogen (H)	wt.-%$_{db,af}$	5.9	6.2
Oxygen (O)	wt.-%$_{db,af}$	44.6	40.1
Nitrogen (N)	wt.-%$_{db,af}$	0.41	1.1
Sulphur (S)	wt.-%$_{db,af}$	0.05	0.11
Chlorine (Cl)	wt.-%$_{db,af}$	0.06	0.15
Typical ash deformation temp. (A)	°C	1130 - 1200	750 - 840
Typical ash flow temp. (D)	°C	> 1330	> 1440

*consists of 4.4 wt.-%$_{db}$ initial ash and 6.6 wt.-%$_{db}$ pre-mixed $CaCO_3$

Results and Discussion

The gasification temperature of the EOP had to be decreased significantly due to the low ash deformation temperature, which is an indicator for the risk of agglomeration and sintering effects with ash and bed material particles in the fluidized bed system. Figure 1 shows the time averaged temperature profile over the height of the GR and CR and Figure 2 presents the temperature trend of selected measurement points of the GR for the steady-state operation phases of the test plant. For EOP a gasification temperature of 870 °C in the hottest part of the GR, which is the upper countercurrent GR, was not exceeded. While for SCB a temperature higher than 940 °C was reached. The gasification temperature GR6, near the fuel input in the lower bubbling bed GR, was around 758 °C for EOP and 806 °C for SCB. Because of the higher gasification temperature for SCB and, therefore, enhanced steam reforming reactions one would expect that the H_2 content is higher for gasification of SCB than for EOP. However, according to Figure 3 we observed a different behavior during the gasification experiments. An average value of 38.3 vol.-%$_{db}$ has been measured for SCB. In contrast to EOP, were 47.5 vol.-%$_{db}$ have been measured. The bed material composition has to be investigated to understand this issue: For better tar conversion a mixture of coarse and fine olivine with calcite is used (Table 1). Calcite forms calcium oxide for temperatures above 800 °C in the CR, but is suspected to partly form calcite with carbon dioxide from the product gas again in the lower GR at lower temperatures. Hence it is likely that for the gasification of EOP a process took place, where carbon dioxide was transported from the GR to the CR via calcite in the bed material [4]. The loss of carbon dioxide in the product gas might lead to slightly higher hydrogen contents according to the water-gas-shift reaction and the principle of least constraints. Comparatively low CO_2 contents in the EOP product gas (20.2 % compared to 25.0% CO_2 for SCB) support this assumption. Especially tars are critical components of the product gas stream. They are responsible for fouling in downstream plant components and therefore highly undesirable. Tar measurement during stationary operation of the test plant showed similar gravimetric tar contents (i.e. tar components with a molecular weight

higher than toluene), but twice as much GCMS tars for SCB compared to EOP. Despite low gasification temperatures the EOP fuel shows low tar contents in the range of wood pellets [5]. On the other hand dust measurement showed a different behavior because of the higher ash content in the fuel EOP.

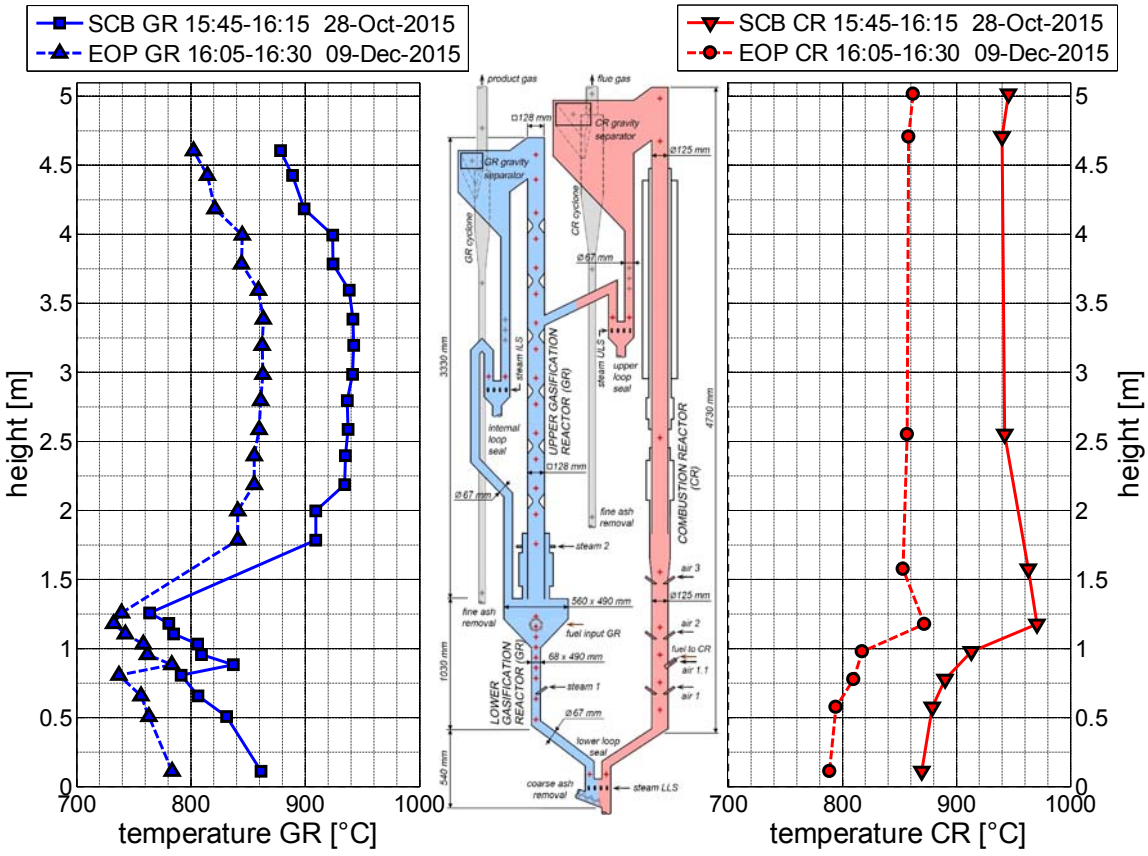

Figure 1: Temperature profile (average values) of GR and CR for fuel SCB and EOP.

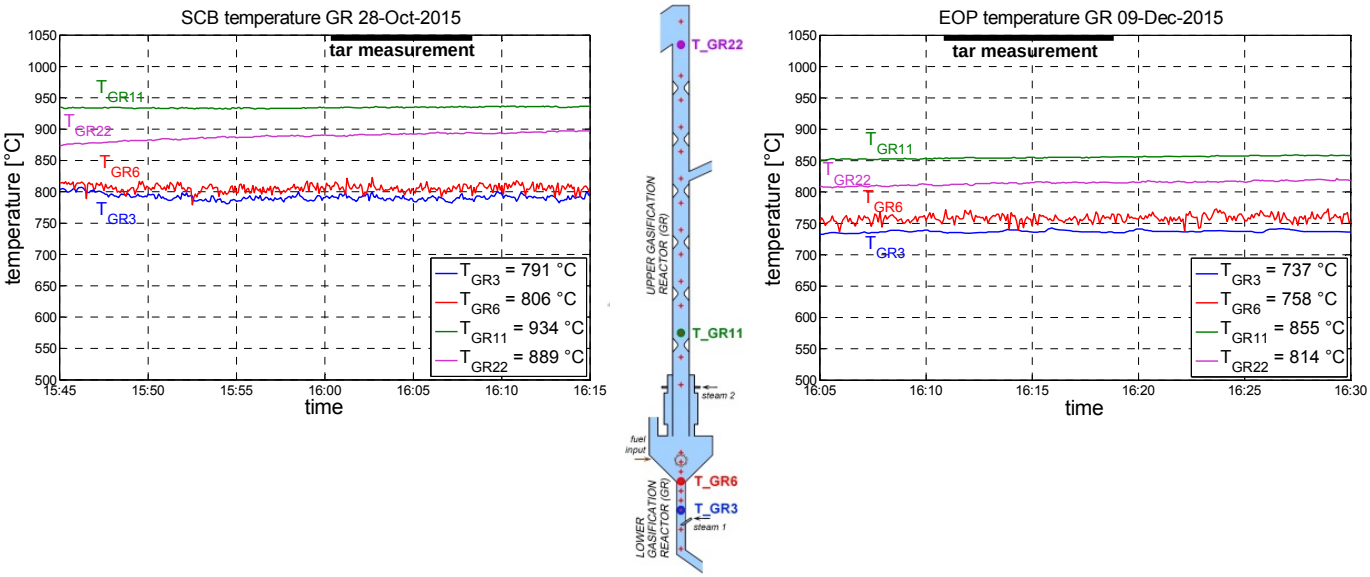

Figure 2: Temperature trend of GR for fuel SCB and EOP.

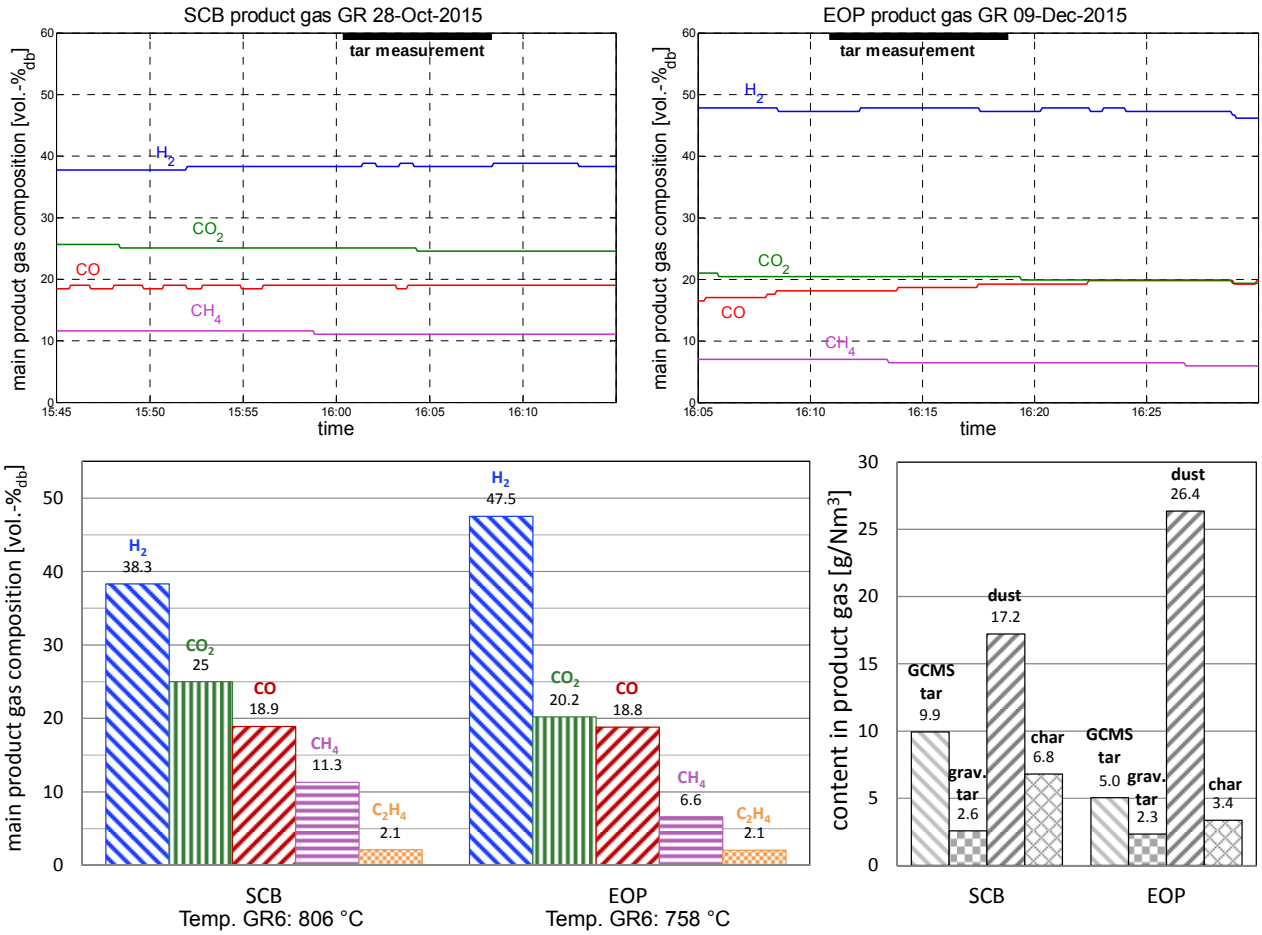

Figure 3: Main product gas composition, tar, dust, and char contents for fuel SCB and EOP.

Conclusion and Outlook

Two different biogenous alternative fuels were investigated with the novel dual fluidized bed steam gasification test plant at TU Wien. Due to a low ash deformation temperature of EOP and to prevent sintering effects in the fluidized bed, a gasification temperature in the lower GR was set in a range of 740-780 °C. Despite low gasification temperatures the EOP fuel showed low tar contents in the range of wood pellets. However, 26.4 g/Nm^3 dust in the product gas were more than 50% higher than for SCB. The reason for this circumstance was the higher ash content in the fuel. For the gasification with EOP comparatively high H_2 contents and low CO_2 contents in the product gas might indicate that a process took place, where CO_2 was transported selectively via the bed material from the GR into the CR. But also catalytically active fines from the EOP ash are able to increase the hydrogen content in the produced gas. The gasification of EOP leads to a significant dust content in the product gas due to the high ash content in the fuel. For SCB a gasification temperature in the lower GR was set in a range of 780-840 °C. However, compared to EOP the measured GCMS tar contents were clearly higher. A low gravimetrical tar content, which indicates the higher tar components, was measured for the gasification of both fuel types. Thus, the upper countercurrent gasification reactor seems to minimize the long-chained tars in the up flowing product gas stream effectively. The system flexibility with regard to the application of different fuels is a major issue of current experimental research. The successful gasification of the two alternative fuels has been proven with the novel dual fluidized bed gasification system and shows the potential of the novel reactor concept. Especially for EOP additional experimental gasification test runs are

advised, with respect to bed material agglomeration. Future work will focus on gasification experiments with other alternative fuels. Further replacement of the olivine/calcite mixture through calcite only should be investigated, because of the high catalytic activity of calcite.

Acknowledgement

The present work contains results from a research project with the company Fitroleum Biochemicals GmbH and the project PHENOLIVE which has received funding from the European Union's Seventh Framework Program managed by REA Research Executive Agency under grant agreement n° FP7-SME-2013-605357.

Literature

[1] Schmid, J.C., 2014, "Development of a novel dual fluidized bed gasification system for increased fuel flexibility", doctoral thesis, Institute of Chemical Engineering, TU Wien, ISBN 978-3-9502754-6-9

[2] Aguiari, C.J., doctoral thesis, Institute of Chemical Engineering, TU Wien, to be published

[3] CEN/TS 15439:2006 "Biomass Gasification - Tar and Particles in Product Gases - Sampling and Analysis"

[4] Müller, S., 2013, "Hydrogen from Biomass for Industry - Industrial Application of Hydrogen Production Based on Dual Fluid Gasification", doctoral thesis, Institute of Chemical Engineering, TU Wien, ISBN: 978-3-9502754-5-2

[5] Benedikt, F., 2016, "The Novel DFB-Gasifier at TU Wien, Part I: Parameter Variation with Wood Pellets", Minisymposium für Verfahrenstechnik 12

Investigation into thermal runaway of Li-ion batteries

Michael Lammer, Alexander Königseder, Viktor Hacker
Institut für Chemische Verfahrenstechnik und Umwelttechnik, NAWI Graz,
Technische Universität Graz
8010 Graz, Inffeldgasse 25/C
michael.lammer@tugraz.at

Abstract

Li-ion cells with the dimension 18650 are charged to defined states of charge and placed in a specially designed sample holder to fix them in place during the test series in the electrically heated stainless steel tubular reactor. The sample holder contains thermocouples and voltage sensing connectors to monitor the cell during the heat ramp experiment. During the thermal runaway several characteristic phases are observed like melting of the separator, evaporation of the electrolyte and cell disintegration. The characterisations of the cells are performed by online monitoring of cell temperature and voltage as well as gas sampling during the test.

Introduction

Lithium ion batteries feature high energy density as well as reliability even after numerous discharge/charge cycles. They have taken a dominant position in application for battery electric vehicles and also portable electronic devices. However failure of the cell resulting from thermal runaway is possible because of critical operating conditions like short circuiting or high heat influx from external sources. Thermal runaway is characterised by several chemical reactions as well as phase transitions leading to enormous heat evolution and emission of gas and particles [1].

This type of battery failure proposes a serious threat for human operators, machines and the environment. Single catastrophic failing cells can set in motion a chain of events as neighbouring cells in the battery pack are heated up to critical temperature as well, possibly leading to catastrophic damage to the system, e.g. an electric vehicle. The fumes emitted from the cells contain carbon monoxide as well as hydrogen fluoride, thus being highly toxic [2]. Burning battery systems also pose a serious challenge to fire fighters, as high currents and voltages are present in these devices.

Investigating the behaviour of Li-ion cells under damaging conditions allows the assessment of risks and potential dangers arising from different kinds of cell components, e.g. the battery's electrode materials. Measuring the cell temperature and voltage serve as basic methods of characterisation. These are complemented by taking gas samples for chromatographic analysis at critical points of operation as well as ex-situ cell characterisation by opening and determining cell component dimensions and mass.

Methods and Procedures

The main component of the test rig is a tubular reactor containing the sample and heated by an electric resistance furnace. Nitrogen is used as carrier gas and by its defined flow it also acts as internal standard for the gas chromatographic analysis. The reaction off gas is led through a particle filter before leaving the system. The system is shown schematically in Fig. 1.

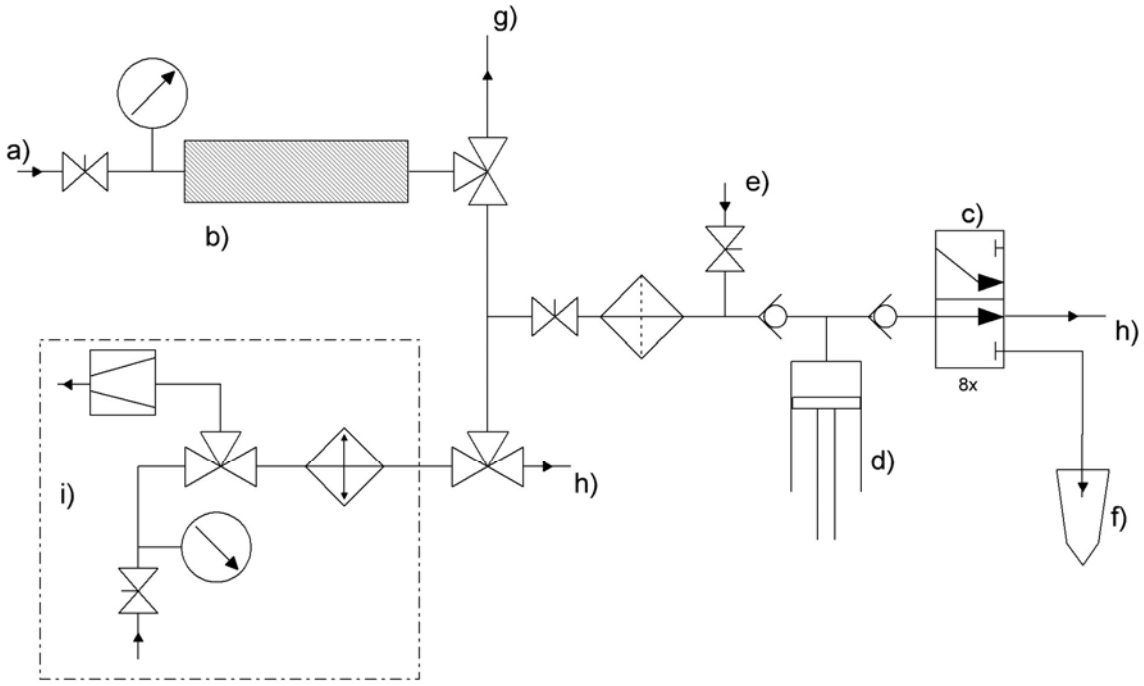

Fig. 1: Thermal runaway test rig consisting of a) carrier gas inlet (N_2), b) tubular reactor with sample, c) multi-port valve, d) syringe pump, e) vial purge gas (Ar), f) crimp vials, g) optional impinge system, h) off gas and i) optional multi-purpose vacuum system.

Temperature measurement during the experiment is achieved via type K thermocouples mounted onto the cell surface as well as into the sample holder and the furnace. The cell voltage is observed via connectors located within the sample holder and is measured simultaneously to the temperature. The signals of all sensors are logged at 75 Hz.

Gas sampling is performed via a custom made sampling device connected to the gas line. This system consists of an electronically controlled multi-port valve (Vici Valco) to lead the product gas stream into sampling vials. A syringe pump is used to retain the gas flow. The filling operation is initiated by switching to the appropriate vial. Then the syringe pump transports product gas into the vial. By switching to the next port, the previously filled vial is sealed and ready for ex-situ GC analysis.

Analysis of the gas samples is performed with an Inficon micro-GC. A molecular sieve column as well as a Plot U nonpolar column is used for quantifying H_2, O_2, CO, CO_2, CH_4, C2 and C3 components using the carrier gas N_2 as internal standard. Alternatively the gas stream can be directed into an impinger bottle system after leaving the reactor through a filter. This device is used to absorb soluble components into aqueous solution. Consecutive quantification of fluoride is achieved potentiometrically by using a fluoride selective electrode.

Experimental procedure

A Li-ion cell type of chosen design is charged up to a defined state of charge and put into the sample holder. Thermocouples are fixed to the cell's surface and the sample holder at defined positions. For measuring the cell voltage during the experiment the sensing wires

are connected. The closed sample holder is then placed in the centre of the tubular reactor. Flushing the reactor and connecting tubing with nitrogen establishes inert gas test conditions.
Crimp vials are sealed with septa and connected to the multi-port valve via injection needles and custom made pressure compensation to allow filling of the vials. The gas sampling station including the vials is flushed with argon to replace any gases present within. Argon is used as a carrier gas in the gas analysis and as the gas is not detected it acts as a blank background.

The experiment is started by initiating the heating using a laboratory power supply. A linear heating ramp is maintained throughout the experiment. The specimen within the sample holder experiences an increase of temperature according to the heat influx induced by the furnace. As soon as internal reactions set in, a deviation from linear behaviour is detected. After reaching a predefined cell temperature, the automatic gas sampling starts and collects samples of product gas for chromatographic analysis. Manual sampling is also possible and allows picking samples on demand.

Simultaneous testing of a charged and discharged cell experiencing the same heat influx allows characterisation of exothermic and endothermic reactions occurring. Discharged cells do not show any reactions except physical phase transitions whereas charged cells are highly reactive. This way of experimental setup is used to obtain an overview of the cell and to find characteristic behaviour of the respective battery type.

Data evaluation

Diversion from the measured temperature increase of discharged cells or comparison to the sample holder temperature indicates the occurrence of several chemical and physical processes. Endothermic melting of the polymeric separator is signified by a slight drop of cell temperature. As the temperature rises, volatile components like the organic electrolyte evaporate and decompose leading to elevated pressure within the battery can. Venting of the cell can also be observed by monitoring the temperature, as pressure release allows total evaporation which consumes heat. This is followed by a continuous rising cell temperature well above the sample holder temperature indicating exothermic reactions of the electrode materials. The final stage is the thermal runaway with sudden temperature increase and incineration of the reactive components, accompanied by violent venting and extreme temperatures, as depicted in Fig. 2.

Gas analysis by micro GC is used for identification and quantification of gaseous components at different stages of the experiment, e.g. after the first venting, shortly before thermal runaway or after final runaway and venting. The product gas stream consists of H_2, CO, CO_2, CH_4 and various C2 and C3 components with differing concentration depending on the emission event as well as heat ramp.

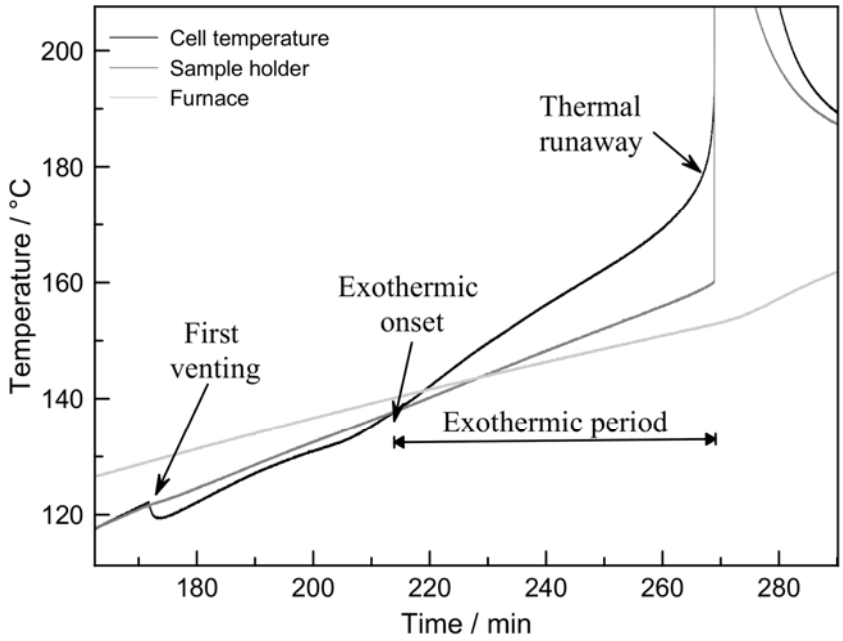

Fig. 2: Thermal schematic of the final phase of an experiment indicating the transgression into thermal runaway reaching up to 850 °C (cut off).

Summary and outlook

Li-ion cells are charged to defined states of charge. The cells are heated continuously by using a heated tubular reactor and their temperature and voltage are monitored. Endothermic and exothermic effects are evaluated and gas samples are collected. A gas chromatograph is used to analyse the gas samples to quantify the product gases.

The cell components not only react with each other but also decompose themselves. Further effort will go into the quantification of hydrogen fluoride emission deriving from conducting salt decomposition at elevated temperatures [3]. This extremely toxic compound is also highly reactive, making quantification in mixed gas streams a challenging task and main objective of future investigations.

Acknowledgement

This work is funded by the Austrian Federal Ministry of Transport, Innovation and Technology (BMVIT) and The Austrian Research Promotion Agency (FFG) through the program “Mobilität der Zukunft” (2014-2017).

Literature

[1] Larsson, F., Andersson, P., Blomqvist, P., Lorèn, A., & Mellander, B.-E. (2014). Characteristics of lithium-ion batteries during fire tests. *Journal of Power Sources*, P. 414-420.

[2] Golubkov, A., Scheikl, S., Planteu, R., Voitic, G., Stangl, C., Fauler, G., et al. (2015). Thermal runaway of commercial 18650 Li-ion batteries with LFP and NCA cathodes – impact of state of charge and overcharge. *RSC Advances*, P. 57171-57186.

[3] Wang, Q., Ping, P., Zhao, X., Chu, G., Sun, J., & Chen, C. (2012). Thermal runaway caused fire and explosion of lithium ion battery. *Journal of Power Sources*, P. 210-224.

Non-precious cathode catalysts for direct liquid fuel cells

Ilena Kaltenböck, Christoph Grimmer, Birgit Pichler, Bernd Cermenek, Alexander Schenk, Viktor Hacker
Graz University of Technology, Institute of Chemical Engineering and Environmental Technology, NAWI Graz, Inffeldgasse 25C, 8010 Graz, Austria
i.kaltenboeck@tugraz.at

Introduction

Fuel cells convert chemical energy into electrical energy with the significant benefit of water and heat being the only emissions.
In fuel cells hydrogen is usually chosen as fuel on the anode side and oxygen on the cathode side. However, despite the clean and environmental friendly usage of hydrogen as fuel in fuel cells, a significant drawback has to be considered. The storage and transportation of gaseous or liquid hydrogen is very expensive and requires a completely new fuel infrastructure. In order to overcome such challenges it would be most suitable to find liquid hydrogen storage media, which can be utilized as fuel in fuel cells.
In direct liquid fuel cells the anodes are fed by an oxidizable liquid such as methanol, ethanol or metal borohydride solutions instead of hydrogen. Safe storage and high energy densities are the main advantages of these types of fuels. Direct methanol fuel cells are the only liquid fuel cells being commercially available by now. Ethanol- and borohydride-fed fuel cells are promising candidates for future fuel cell applications. The scheme of a borohydride fuel cell is shown in figure 1. [1-3]

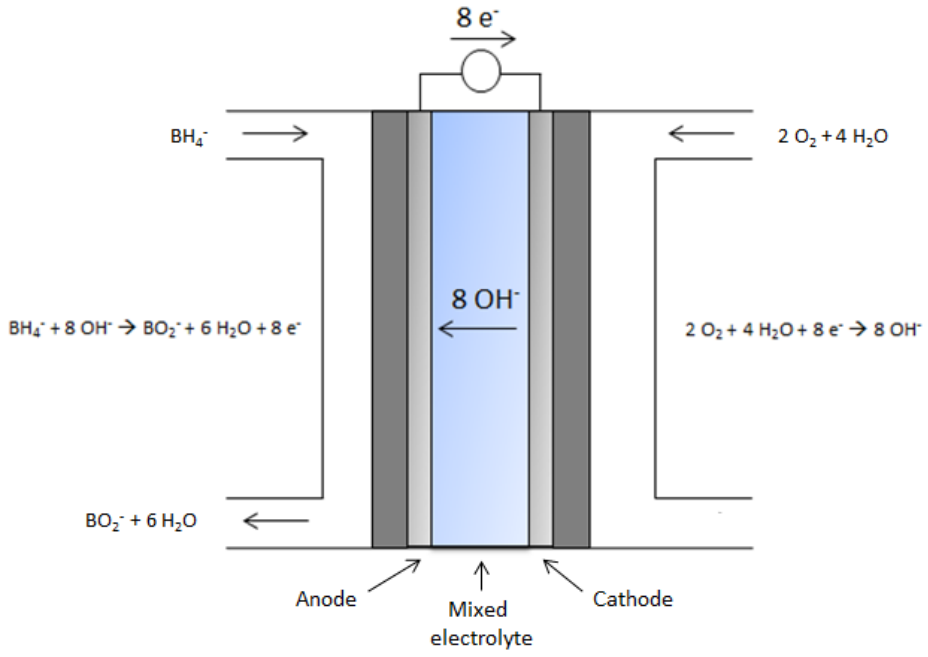

$$BH_4^- + 2\ O_2 \rightarrow BO_2^- + 4\ H_2O$$

Figure 1: Scheme of a single cell set up of a borohydride fuel cell

The possibility of storing hydrogen in liquid form e.g. the storage in metal borohydrides such as $NaBH_4$, could solve the danger problems of the oxyhydrogen reaction.

At the anode borohydride is oxidized and the cathode performs the oxygen reduction reaction comparable to conventional fuel cells. Well performing as well as resistant catalysts are required on anode and cathode sides. [1-3] In this work novel cathode catalyst materials with high activity toward oxygen reduction and high tolerance toward borohydride poisoning are investigated.

Experimental

Cathode catalyst fabrication:
For the Ag-Mn_3O_4/C catalyst $AgMnO_4$ precursor salt was prepared using $AgNO_3$ and $KMnO_4$ dissolved in water and acidified with HNO_3 at 80 °C. The solution was cooled down to 0 °C resulting in a precipitation which was filtered and washed (ice water). The respective carbon support (Vulcan XC72R or Black Pearls 2000) was dispersed in ultrapure water at 40-50 °C with an Ultrasonic Homogenizer. The precursor salt was added to the carbon suspension which was stirred at ~60 °C to evaporate the solvent. The resulting powder was ground and tempered at 400 °C (temperature ramp: 5 °C min^{-1}) for 2 h under N_2 atmosphere. [1]

The Ag-Mn_3O_4 catalyst was in-situ and ex-situ investigated. After in-situ characterization as cathode in a half cell test, it was also used in a single cell set up of a borohydride fuel cell with a platinum anode. [1]

Ex-situ ring disc electrode (RDE) measurements of Ag-Mn_3O_4 cathode catalyst: a Reference 600 potentiostat from Gamry and a RDE set-up from Pine Instruments Company (AFE5T050GC) were used for the experiments. A glassy carbon disk electrode with an area of 0.196 cm^{-2}, coated with 10 µl catalyst ink ($AgMn_3O_4$/C dispersed in water and 2-propanol (ratio 3:7)), was used as working electrode. To obtain a homogeneous film of the catalyst on the glassy carbon electrode, it was rotated at a speed of 700 rpm during evaporation of the solvent. The final Ag-Mn_3O_4 catalyst loading was 56 µg cm^{-2}. Measurements were performed with 0.1 M KOH as electrolyte (saturated with ultrapure nitrogen or oxygen) in a temperature controlled glassware at 30 °C. A glassy carbon rod was used as counter electrode and a reversible hydrogen electrode (RHE, Hydroflex, Gaskatel) as reference electrode. [1]

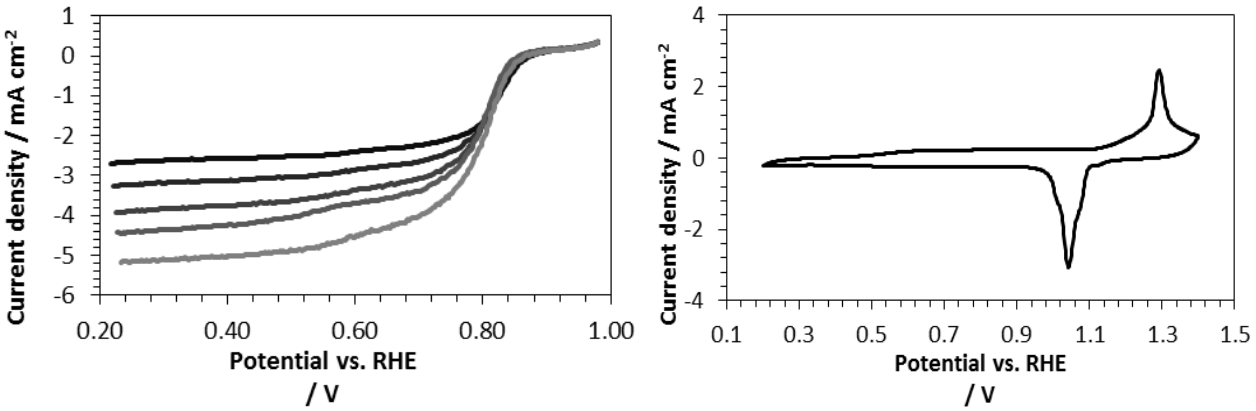

Figure 2: left: RDE measurements of Ag-Mn_3O_4/C catalyst in 0.1 M KOH, 10 mV s-1, 400-1600 rpm; right: Cyclic voltammorgram of $AgMn_3O_4$ in deaerated electrolyte (N_2 flushed)

The cyclic voltammogram (Fig. 2, right) shows the distinctive peaks for manganese and silver. The two most prominent peaks at 1.30 V and 1.04 V are assigned to the oxidation of

Ag to Ag_2O at 1.30 V vs. RHE and the reduction at 1.04 V vs. RHE back to pure Ag. [1]
Two weak oxidation peaks at 0.62 V and 0.93 V vs. RHE can be attributed to the oxidation of Mn(II) to MnOOH at 0.62 V, which is further oxidized to MnO_2 at 0.93 V vs. RHE.
Potential cycling up to 1.40 V vs. RHE led to constant degradation of the catalyst. Therefore the thin film on the RDE is renewed before ORR experiments. CVs are conducted between 0.20 and 1.00 V vs. RHE. The onset potential is ~0.880 V vs. RHE, see Fig. 2. [1]

The Ag-Mn_3O_4 catalyst was used for electrode manufacturing employing a cross rolling method with PTFE powder (3 M Dyneon, TF 2021Z) as binder. For the gas diffusion layer acetylene black and PTFE were dispersed in 2-propanol/water (1/1) and also cross rolled.
Active layer and gas diffusion layer were combined by rolling to a thickness of 1.5 mm. After dry pressing of the electrode, it was hot-pressed at 300 °C with a pressure of 120 kg cm^{-2} on a nickel mesh acting as current collector. The loading of the Ag-Mn_3O_4 catalyst was 11 mg cm^{-2} with an active area of 4 cm^2, the final thickness with the current collector was 0.8 mm. [1]

The cathode was in-situ characterized in a half cell set up, results without (black) and with (gray) correction for internal resistances are shown in figure 3.

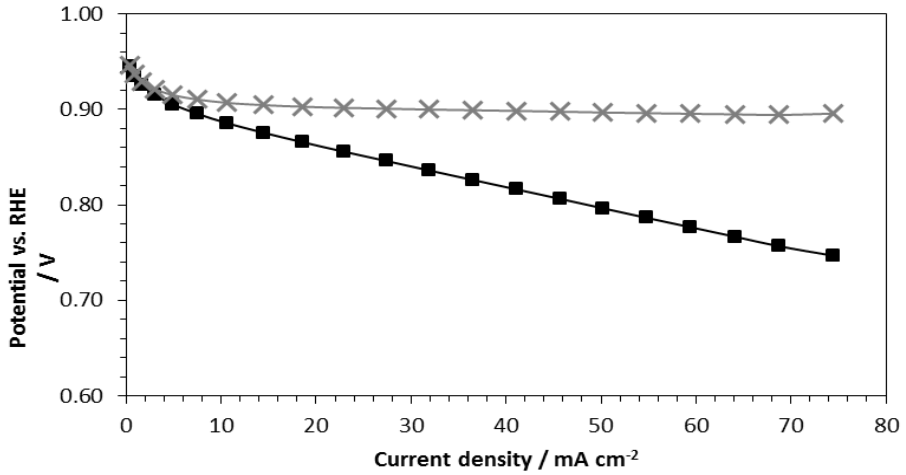

Figure 3: Polarization curve of Ag-Mn_3O_4/C cathode in a half cell set up in 6 M KOH, with (gray) and without (black) iR correction

The Ag-Mn_3O_4 cathode had an OCP of 0.945 V vs. RHE, higher than expected from ex-situ results (onset potential of ~0.880 V vs. RHE). Polarization curve of the cathode, see Fig. 3, is measured in potentiostatic mode from OCP to 0.750 V in 10 mV steps. The polarization curve was measured to 0.750 V due to the limited stability of Mn_3O_4 below ~0.700 V. According to the Pourbaix diagram Mn_3O_4 converts to the soluble $Mn(OH)_3$ at potentials lower than 0.700 v vs. RHE at pH 14. [1]

For the single cell tests, the anode was fabricated with a commercial Pt/C from Alfa Aesar (50 wt% Pt on carbon) with a Pt loading of 1.0 mg cm^{-2} and a FAA3 (FumaTech) ionomer as binder. The active layer containing Pt/C and binder (20 wt% based on Pt/C) was dispersed in 1-propanol by ultrasonification. A carbon cloth was used as substrate material and coated with the active layer by the drop-coating method. Additionally a pore former, ammonium carbonate dissolved in water, was drop-coated on the anode (15 wt%). The active area was 4 cm^{-2}. The anode was soaked 3 times in 1 M NaOH for alkalization.
The mixed liquid electrolyte used in this work for the single-cell measurement of the

borohydride fuel cell also acted as fuel consisting of 1 M $NaBH_4$, 1 M NaOH, and 5 mM thiourea. It was supplied with a flowrate of 10 ml min^{-1} and heated to 30 °C. The synthetic air flow rate was 50 ml min^{-1} at the cathode. The single cell set up is schematically shown in Fig. 1. [1]

The polarization curve of the single cell was recorded in galvanostatic mode by a Zahner IM6 potentiostat. The IR corrected VI curve is given in Fig. 4. The OCV of the mixed electrolyte BH_4^-/O_2 cell was 0.702 V. The anode potentials were followed during the characterization, starting with an OCP of -0.024 V vs. RHE. The cathode potentials were calculated from the difference of the cell voltage and the anode potential, plotted in Fig. 4. The OCP of the cathode was 0.678 V vs. RHE, which was ~0.270 V below the potential of half-cell measurements in 6 M KOH. This can be ascribed to the formation of a mixed potential in the presence of BH_4^- at the cathode. [1]

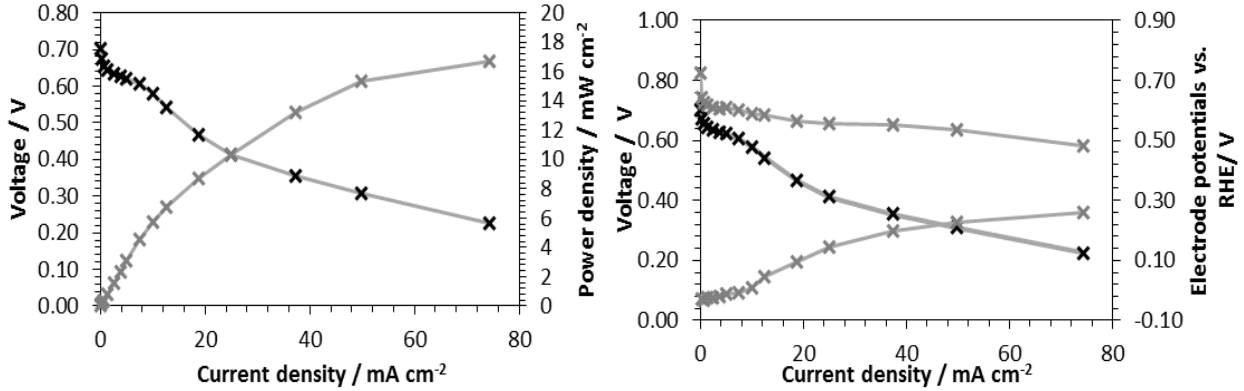

Figure 4: left: Polarization curve (black) of the single cell with the corresponding power density (gray); right: Cell voltage (black) and electrode potentials (gray)

Conclusion

The Ag-Mn_3O_4 cathode showed poor tolerance toward borohydride poisoning, having an OCP of 0.678 V, ~0.270 V lower compared to measurements without borohydride. Using a membrane could avoid borohydride crossover and consequently a mixed potential of the cathode. Nevertheless, the cathode showed excellent stability and durability during characterizations. [1]

References

[1] C. Grimmer et al., J. Electrochem. Soc., 163 (3) F278-F283 (2016)
[2] G. L. Soloveichik, Beilstein J Nanotechnol., 5 1399–1418 (2014)
[3] I. Kaltenboeck et al., 1st International Workshop on Hydrogen and Fuel Cells, 18 - 19 (2015)

Design of bifunctional air electrodes for rechargeable zinc/air redox flow systems

Birgit Pichler, Viktor Hacker
Institute of Chemical Engineering and Environmental Technology, Graz University of Technology, Inffeldgasse 25C, 8010 Graz, Austria
birgit.pichler@tugraz.at

Abstract

The environmentally friendly and safe zinc/air redox flow battery offers a possible solution to overcome irregular electricity fluctuations caused by wind and solar power systems. However, stability issues regarding Zn deposition and air electrode cyclability still limit their implementation as energy storage system into our electricity grid. In this work air electrodes catalyzed with $La_{0.6}Ca_{0.4}CoO_3$ perovskite supported on Ni foam and Ni cloth respectively were manufactured and electrochemically characterized. The electrodes show good performance with regard to the charging reaction i.e. oxygen evolution reaction, however, further experiments concerning the oxygen reduction during discharge need to be performed.

Introduction and Motivation

Due to its natural fluctuations, an increasing share of electricity produced by solar and wind power systems poses a challenge to electricity grid stability. In order to compensate for irregular current spikes and uneven load distribution, inexpensive and environmentally friendly electricity storage systems need to be developed. The Zn/air redox flow battery is a highly promising storage system due to its separate scaling of power density (increase number of cells) and energy density (increase Zn electrolyte reservoir). Furthermore, it uses inexpensive materials (zinc, potassium hydroxide) and has high energy density as only one electrolyte reservoir is required. A schematic of the energy storage system is shown in Figure 1 (left).

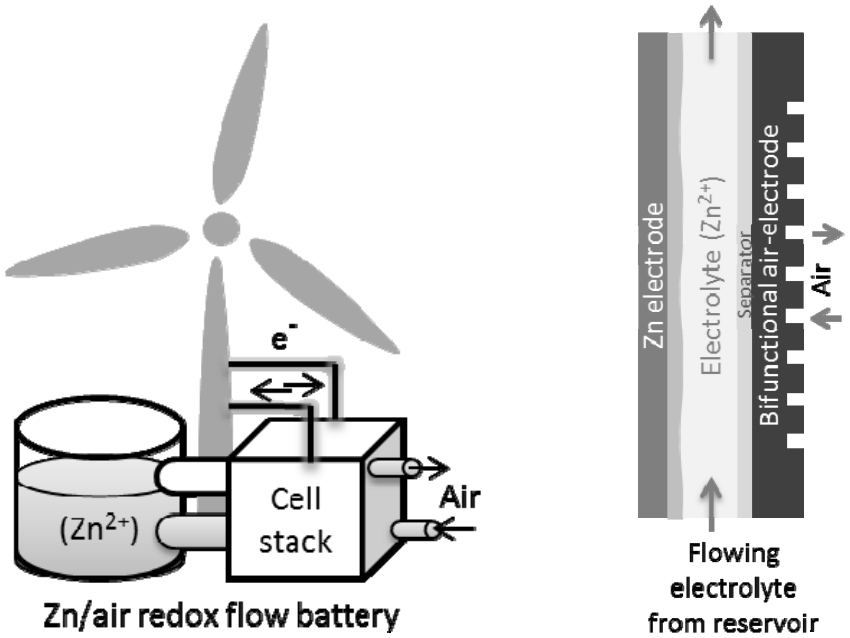

Figure 1: Schematic of the Zn/air redox flow system (left) and of one cell in detail (right)

Each rechargeable electrochemical cell consists of a Zn electrode, a highly alkaline electrolyte and an air electrode as shown in Figure 1 (right). During discharge oxygen from the ambient air is reduced to hydroxide ions (Table 1, equation (2)), which react with Zn to $Zn(OH)_4^{2-}$ (Table 1, equation (1)). During charging Zn^{2+} is electrochemically redeposited on the Zn electrode while on the air electrode O_2 is generated [1,2].

Table 1:Chemical reactions in a Zn/air battery - charging reaction from left to right

Negative electrode	$Zn(OH)_4^{2-} + 2\ e^- \rightleftarrows Zn + 4\ OH^-$	(1)
Positive electrode	$4\ OH^- \rightleftarrows O_2 + 2\ H_2O + 4\ e^-$	(2)
Overall reaction	$2\ Zn(OH)_4^{2-} \rightleftarrows 2\ Zn + 4\ OH^- + O_2 + 2\ H_2O$	(3)

Although primary Zn/air batteries have been utilized in in-ear devices for decades, wide-spread commercialization of rechargeable secondary Zn/air battery systems is still prevented due to its poor cycle life. Primary causes for degradation are the dendritic Zn deposition and the limited long term stability of the reversible air electrode.

This work focuses on designing and testing of bifunctional air electrodes. Selection of the most active and stable catalyst for the oxygen reduction reaction (ORR - discharge) as well as the oxygen evolution reaction (OER - charge) and the implementation thereof into a chemically and mechanically stable electrode architecture are the main goals. Particularly the formation of a high number of 3-phase zones between electrolyte/catalyst/air within the electrode is crucial. Hence, a fine balance between gas diffusivity and electrolyte impermeability is needed [2].

Experimental

Because the Zn/air system operates with alkaline electrolytes, e.g. 8 M KOH, it allows the use of non-noble metal catalysts. Especially oxide catalysts such as spinels and perovskites are in focus of many research activities due to their good catalytic activity and low cost of materials [3].

In this work the perovskite $La_{0.6}Ca_{0.4}CoO_3$ was synthesized via a simple sol-gel method [4] starting with the respective nitrate salts in the appropriate molar ratio. 1 M citric acid solution was added to the dissolved salts. After evaporation of the solvent the resulting gel was heated to 200 °C overnight. The product was ground to powder and finally calcined at 700 °C for 2 h obtaining the final perovskite catalyst.

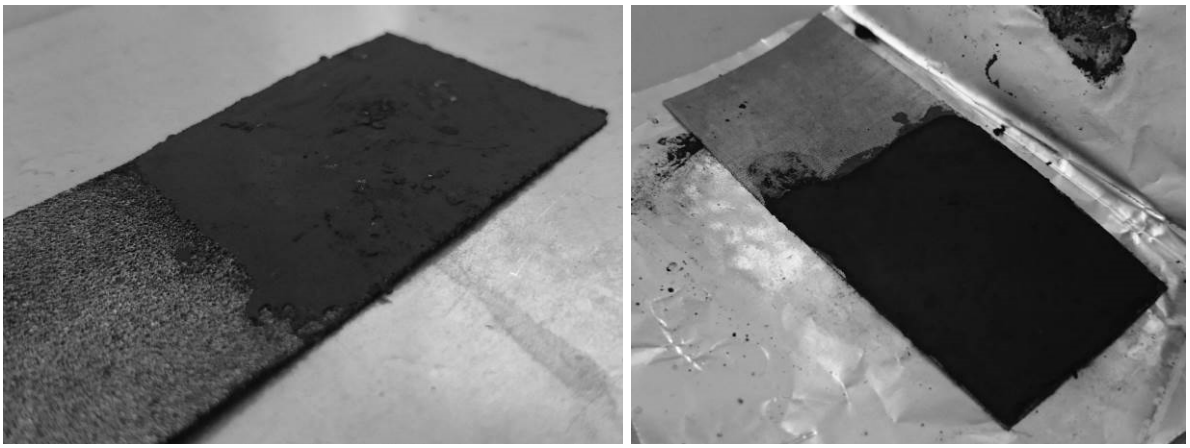

Figure 2: Pictures of electrode E1 on Ni foam (left) and electrode E2 on Ni cloth (right)

Electrodes (4 cm^2) were manufactured with Ni foam (named E1) or Ni cloth (E2) working as current collector and as mechanical backbone of the electrode. The synthesized perovskite catalyst was mixed with Ni powder and PTFE followed by dispersing and pressing the resulting dough onto the Ni support material (see Figure 2).

Electrochemical measurements were carried out at room temperature in 8 M KOH in half-cell configuration using stainless steel as counter electrode and a reversible hydrogen electrode as reference electrode. The working electrodes were supplied with synthetic air from the backside throughout the galvanostatic cycling, which was performed with a BaSyTec Cell Test System.

Results

Galvanostatic cycling (one hour per cycle) of the electrodes E1 and E2 at various applied current densities reveals similar behavior of both electrodes as shown in Figure 3 and Figure 4.

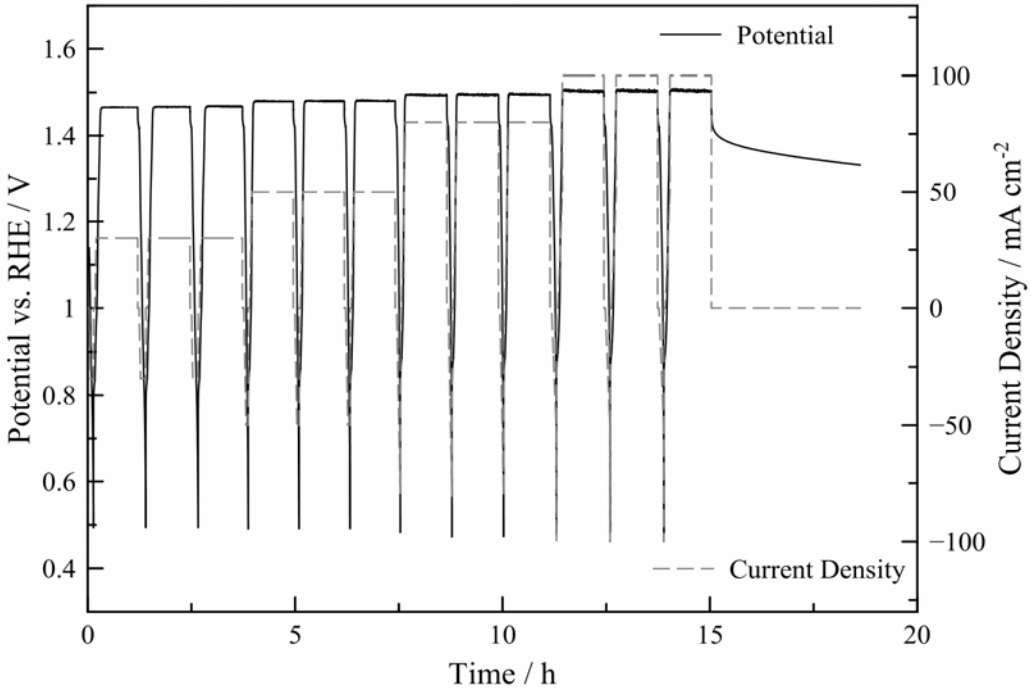

Figure 3: Galvanostatic cycling of electrode E1 at 30, 50, 80 and 100 mA cm^{-2}

During discharge the applied current density lowers the electrode potential to < 0.5 V (abort potential) within a few minutes, indicating poor gas permeability of the electrode. However, during charging both electrodes show good activity toward OER and a stable onset potential of about 1.5 V. Even at higher current densities of up to 100 mA cm^{-2} the potential of 1.51 V is not exceeded. During each cycle the OER potential remains stable and no potential drift is observed indicating good stability of the electrode. The response of the potential to the applied current density is much faster at higher current densities, as can be seen in Figure 4, when comparing the first cycles at 5 mA cm^{-2} with the cycles at 30 mA cm^{-2}.

As both electrodes show comparable behavior and by keeping the economic viability in mind, the use of Ni cloth in the electrode design is preferred over the Ni foam due to its much lower cost. The in-house synthesized perovskite shows good activity toward OER, however, its activity toward ORR has still to be determined.

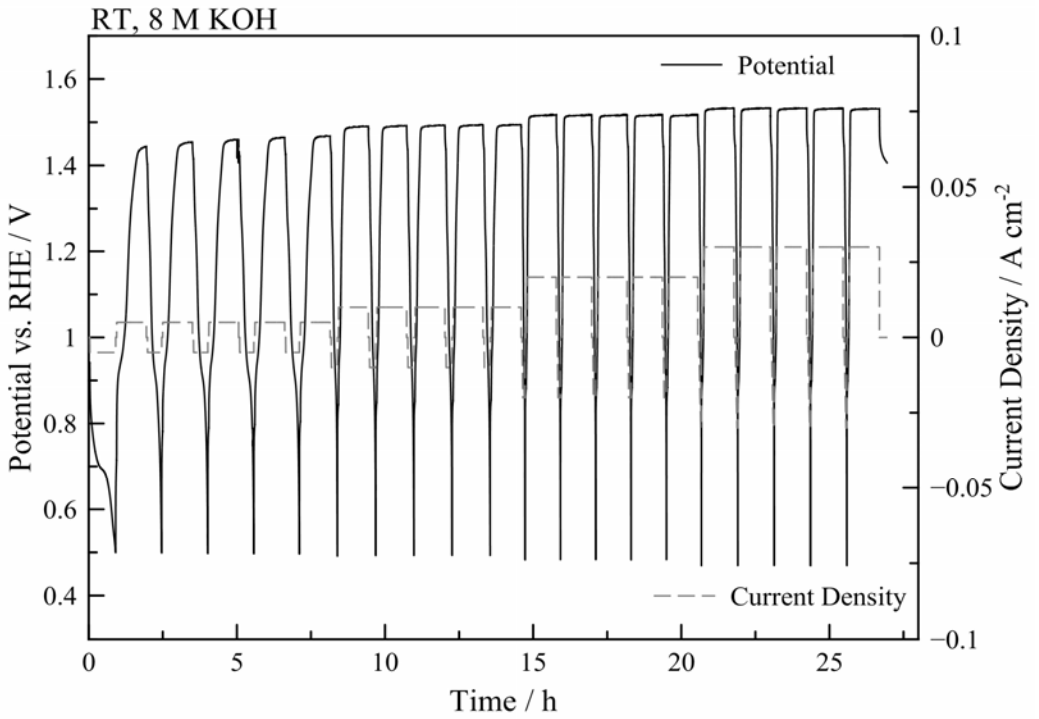

Figure 4: Galvanostatic cycling of electrode E2 at 5, 10, 20 and 30 mA cm^{-2}

Summary and Outlook

The first electrochemical measurements exhibit good performance and stability of the two electrodes E1 and E2 regarding the oxygen evolution reaction at different charging current densities. The aim of the upcoming experiments will be the improvement of ORR activity by varying the catalysts, e.g. different perovskites and spinels, and the electrode composition. In doing so Ni cloth as current collector and oxide catalysts are preferred over Ni foam and noble metal catalysts because of lower material costs. Additional characterization will be carried out by means of REM and XRD in order to gain a better insight into the composition and homogeneity of the electrodes.

Acknowledgement

Funding by the Austrian Federal Ministry of Transport, Innovation and Technology (BMVIT) and The Austrian Research Promotion Agency (FFG) through the program “e!MISSION.at Energieforschungsprogramm” (no. 848933) is gratefully acknowledged. We also want to thank our cooperation partners from the Institute of Chemistry and Technology of Materials at Graz University of Technology and our industry partner KUNKEL + Partner GmbH & Co. KG, Germany.

Literature

[1] J.-S. Lee, S. Tai Kim, R. Cao, N.-S. Choi, M. Liu, K. T. Lee, J. Cho, Advanced Energy Materials 2011, 1, 34–50.
[2] S. W. T. Price, S. J. Thompson, X. Li, S. F. Gorman, D. Pletcher, A. E. Russell, F. C. Walsh, R. G. A. Wills, Journal of Power Sources (2014), 259, 43–49.
[3] L. Jörissen, Journal of Power Sources (2006), 155, 23–32.
[4] S. Müller, K. Striebel, O. Haas, Electrochimica Acta (1994), 39, 1661–1668.

Die Herstellung von Synthesegas aus Wasserstoff und Magnesit/Dolomit

Georg Baldauf-Sommerbauer, Susanne Lux, Wolfgang Aniser, Matthäus Siebenhofer
TU Graz, Institut für Chemische Verfahrenstechnik und Umwelttechnik, NAWI Graz, 8010 Graz, Inffeldgasse 25C
baldauf-sommerbauer@tugraz.at

Kurzfassung

Bei der Erzeugung von anorganischen Oxiden, zum Beispiel Magnesia (MgO), aus karbonatischen Ausgangsmaterialien wird CO_2 frei gesetzt. Führt man die Kalzinierung reduzierend in Wasserstoffatmosphäre durch, kann Synthesegas erzeugt werden. Dadurch kann das CO_2 als Wasserstoffspeicher verwendet werden.

Einleitung

Magnesit/Dolomit wird für die Erzeugung von basischen Feuerfestmaterialien aus Magnesia verwendet [1]. Im ersten Schritt des Herstellungsverfahrens wird das karbonatische Ausgangsmaterial kalziniert.
Bei der reduzierenden Kalzinierung des Magnesitanteils von Magnesit/Dolomit wird mit Wasserstoff in einem Schritt Synthesegas (CO/H_2) erzeugt (1). Dadurch wird die CO_2-Emission der Kalzinierung deutlich erniedrigt und ein wertvolles Produktgas anstatt eines Abgases erzeugt.

$$MgCO_3 + H_2 \rightarrow MgO + (1\text{-}x)\ CO_2 + x\ CO + x\ H_2O \qquad (1)$$

Bei der Verwendung von nachhaltig produziertem Wasserstoff [2]–[4] könnte man mit diesem Prozess und einer angeschlossenen Fischer-Tropsch Synthese [5] flüssige Kohlenwasserstoffe als Nebenprodukt der Magnesiaerzeugung herstellen.

Charakterisierung der Feststoffproben

Die Zusammensetzung der Feststoffproben wurde mittels Röntgenfluoreszenzanalyse (RFA) bestimmt und auf theoretische Karbonate berechnet (siehe Abbildung 1). Das Kalzinierverhalten unter Stickstoff und 70 Vol.% Wasserstoff wurde mittels Thermogravimetrie (TG) charakterisiert. Wie in Abbildung 1 zu sehen ist, erfolgt die Kalzinierung in zwei Stufen. Der Gewichtsverlust der ersten Stufe beträgt 16,5 ± 0,7 Gew.% und entspricht dem laut RFA berechneten CO_2-Gehalt des Magnesium- und Eisenkarbonatanteil der Probe. Dabei werden Magnesiumoxid (MgO) und Eisenoxid (Fe_xO_y) gebildet. Der Gewichtsverlust der zweiten Stufe von 29,4 ± 0,2 Gew.% korreliert mit dem berechneten CO_2-Gehalt des Dolomitanteils der Probe. Der Einsatz von Wasserstoff in der Kalzinierung führt zu einer Erniedrigung der Kalziniertemperatur um ca. 60 °C.

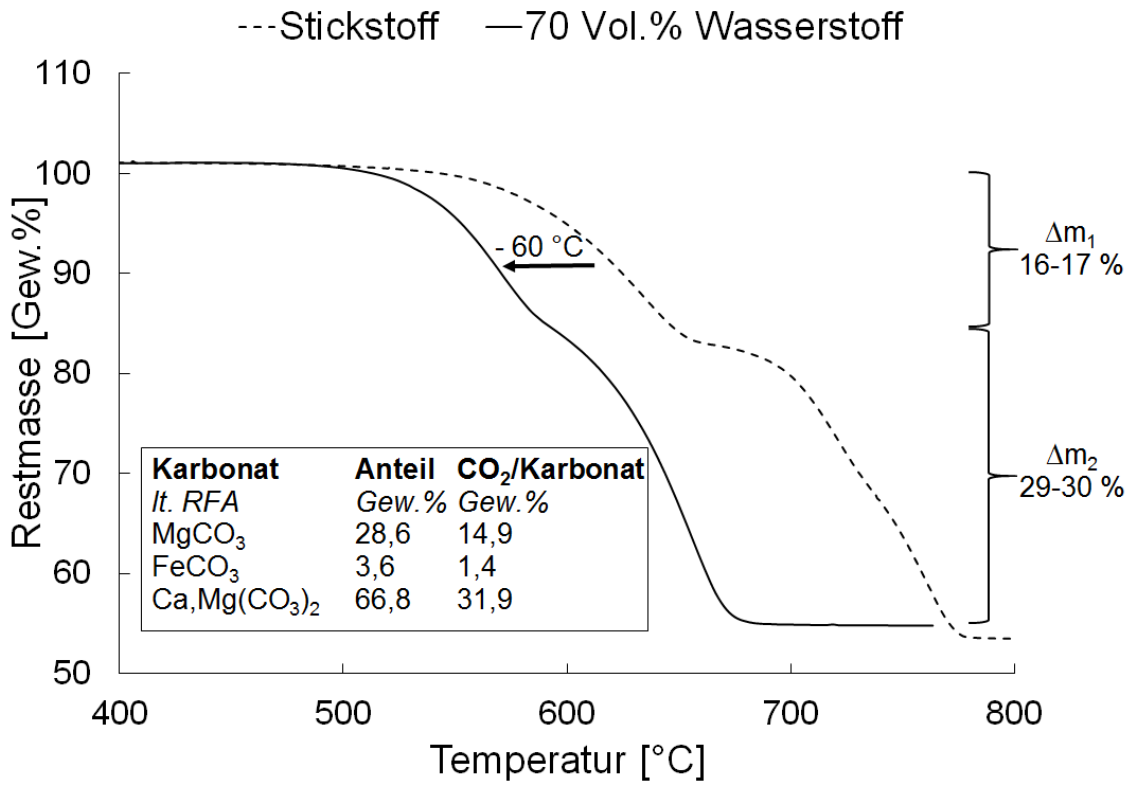

Abbildung 1: Thermogravimetrische Kurve für die inerte (N_2) und reduzierende (70 Vol.% H_2) Kalzinierung von Magnesit/Dolomit. Zusammensetzung der Probe laut RFA.

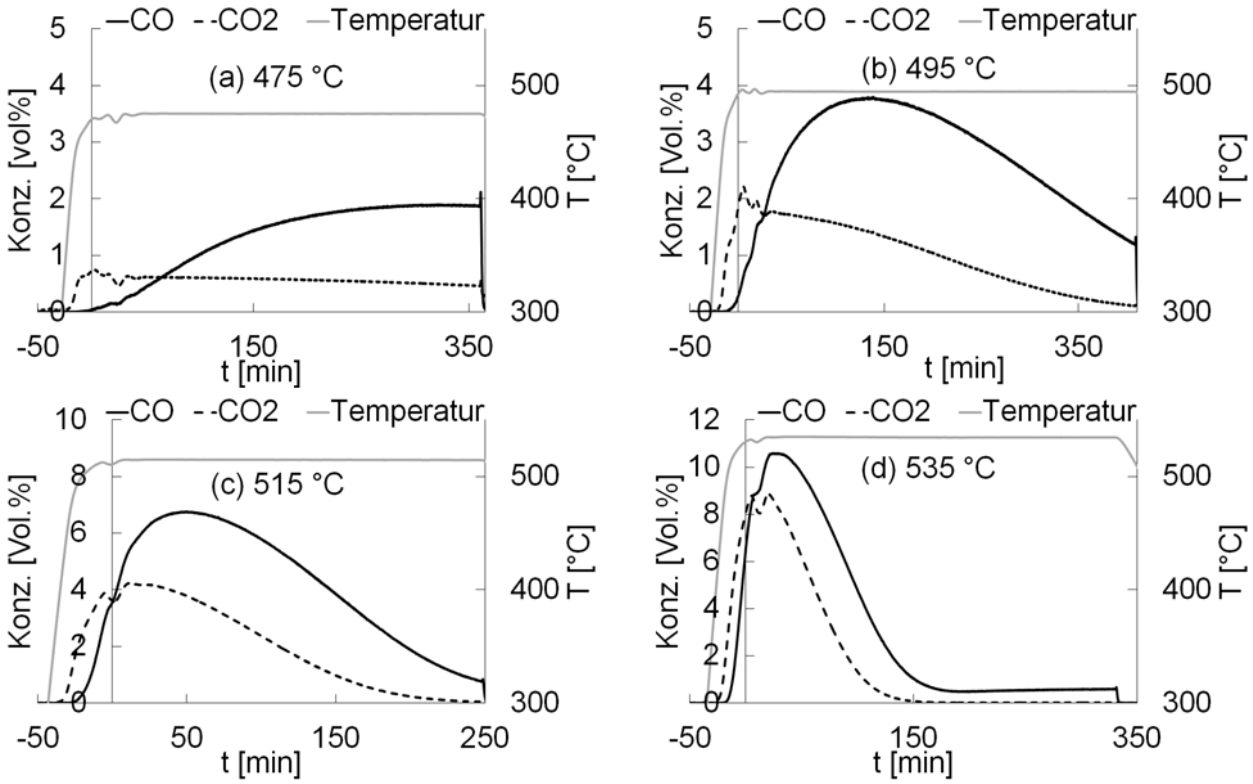

Abbildung 2: Verlauf der CO bzw. CO_2-Konzentration bei 475 °C (a), 495 °C (b), 515 °C (c) und 535 °C (d). Es wurden jeweils 121 g Magnesit/Dolomit eingesetzt und bei einer Gaszusammensetzung von 90 Vol.% H_2 und 10 Vol.% N_2 (30 NL/h)am Reaktoreingang und Umgebungsdruck gearbeitet.

Reduzierende Kalzinierung im Rohrreaktor

Die reduzierende Kalzinierung von Magnesit/Dolomit wurde bei 475-535 °C und Umgebungsdruck in einem Rohrreaktor mit online Gasanalyse (CO, CO_2, CH_4, H_2) untersucht. Für alle Versuche wurden je 121 g frisches Einsatzmaterial (Kornklasse 5-8 mm) und 90 Vol.% H_2 + 10 Vol.% N_2 im Zulauf bei 30 NL/h Fluss verwendet. Näheres zum Aufbau des Rohrreaktor-Teststandes ist im Tagungsband des Minisymposiums 2015 zu finden [6].

Interpretation und Diskussion der Ergebnisse

Die Maximaltemperatur der Versuche am Rohrreaktor lag bei 535 °C. Bei dieser Temperatur ist zu erwarten, dass der Magnesitanteil des Magnesit/Dolomit kalziniert wird und der Dolomitanteil als solcher erhalten bleibt (siehe Abbildung 1: die zweite Stufe in der TG-Kurve unter Wasserstoff beginnt bei ca. 580 °C).
Wie in Abbildung 2 zu sehen ist, kommt es bereits in der Aufheizphase (t<0) zur Produktion von CO_2. Die CO-Produktion kann zeitlich erst nach der CO_2-Produktion beobachtet werden. Dies kann als Folgereaktion interpretiert werden. Zuerst wird Kohlendioxid gebildet, welches dann, möglicherweise in einer heterogen durch Magnesit MgO oder Eisenoxid Fe_xO_y (diese Oxide werden bei der Kalzinierung der ersten Stufe laut TG-Experimenten gebildet) katalysierten Gasphasenreaktion, mit Wasserstoff nach Reaktionsgleichung (2) zu Kohlenmonoxid und Wasser umgesetzt wird.

$$CO_2 + H_2 \rightarrow CO + H_2O \qquad (2)$$

Unter der Annahme, dass bei der Kalzinierung zuerst CO_2 freigesetzt wird, welches in einer Folgereaktion zu CO umgesetzt wird, kann der relative Umsatz im Zeitverlauf über die Menge an produzierten Kohlenstoff-Komponenten $n(CO+CO_2)$ und der theoretischen CO_2-Menge, die aus dem Magnesit-Anteil der Feststoffproben freigesetzt werden kann, bestimmt werden (geschlossene Kohlenstoffbilanz). Die Berechnung des relativen Umsatzes X_{TG1} erfolgt somit mit der Einwaage an Magnesit/Dolomit EW, dem maximalen Masseverlust der ersten TG-Stufe $\Delta m_{max,TG1}$ von 16,5 ± 0,7 Gew.% und dem Molekulargewicht $MG(CO_2)$ von CO_2 (44,01 g/mol) aus der Ausbeute nach Formel (3).

$$X_{TG1} = 100\% * \frac{n(CO+CO_2)}{\frac{EW*\Delta m_{max,TG1}}{MG(CO_2)}} \qquad (3)$$

Wie in Tabelle 1 zu sehen ist, steigt der Umsatz nach 2 und 4,5 Stunden auf isothermer Temperatur mit steigender Versuchstemperatur an. Dies kann durch eine Erhöhung der Reaktionsgeschwindigkeit mit der Reaktionstemperatur erklärt werden. Die CO-Ausbeute, ausgedrückt als Verhältnis CO/CO_2, kann nur bei gleichem Magnesitumsatz verglichen werden. Der Umsatz nach 4,5 Stunden bei 495 °C entspricht dem Umsatz nach 2 Stunden bei 515 °C (jeweils 63 bzw. 64 ± 3 %). Das Verhältnis CO/CO_2 sinkt bei dieser Betrachtung von 2,16 bei 495 °C auf 1,57 bei 515 °C. Dieses Verhalten kann durch die erhöhte CO_2-Produktion in der Anfangsphase der reduzierenden Kalzinierexperimente erklärt werden.

Tabelle 1: Gasmenge und berechneter relativer Umsatz nach 2 bzw. 4,5 Stunden auf isothermer Temperatur. X_{TG1} … Relativer Umsatz berechnet nach Formel (3)

	2 Stunden isotherm		*4,5 Stunden isotherm*	
T [°C]	**CO/CO₂**	**X_{TG1} [%]**	**CO/CO₂**	**X_{TG1} [%]**
475	0,78	7 ± 1	1,81	23 ± 1
495	1,47	31 ± 1	2,16	63 ± 3
515	1,57	64 ± 3	1,94	84 ± 4
535	1,38	91 ± 4	1,51	97 ± 4

Zusammenfassung und Ausblick

Die thermogravimetrischen Untersuchungen zeigten, dass die untersuchten Erzproben aus zwei karbonatischen Bestandteilen (Magnesit und Dolomit) bestehen, da zwei eindeutig unterscheidbare Stufen in der TG-Kurve erkennbar sind. Diese zwei Stufen stimmen mit den berechneten Magnesit- und Dolomitanteilen der Erzprobe überein. Es konnte gezeigt werden, dass es möglich ist, durch die reduzierende Kalzinierung bei 475-535 °C den magnesitischen Anteil der Probe zu kalzinieren und dabei Synthesegas zu erzeugen. Die Versuchsergebnisse legen nahe, dass zuerst CO_2 freigesetzt wird, welches dann in einer Gasphasenreaktion zu CO weiterreagiert. Da die Reaktionsgeschwindigkeit der CO_2-Freisetzung eine stärkere Temperaturabhängigkeit als die Bildung von CO aus CO_2 zeigt, kann die Produktgaszusammensetzung über die Temperatur gesteuert werden. In weiteren Untersuchungen sollen die Bedingungen für eine erhöhte CO-Ausbeute experimentell gefunden und die Synthesegaserzeugung aus Magnesit/Dolomit modelliert werden.

Diese Projekt wird aus Mitteln des Klima- und Energiefonds gefördert und im Rahmen des Programms „Energy Mission Austria“ durchgeführt. Die Erzproben inkl. RFA wurden von der Firma RHI (Fr. Kaltenböck) zur Verfügung gestellt.

.

Literatur

[1] I. Szednyj und D. Brandhuber, *Stand der Technik zur Kalk-, Gips und Magnesiaherstellung: Beschreibung von Anlagen in Österreich*. 2007.

[2] T. Abbasi und S. A. Abbasi, “Renewable’ hydrogen: Prospects and challenges” *Renew. Sustain. Energy Rev.*, vol. 15, no. 6, pp. 3034–3040, 2011.

[3] O. Bičáková und P. Straka, “Production of hydrogen from renewable resources and its effectiveness”, *Int. J. Hydrogen Energy*, vol. 37, no. 16, pp. 11563–11578, 2012.

[4] R. Chaubey, S. Sahu, O. O. James und S. Maity, “A review on development of industrial processes and emerging techniques for production of hydrogen from renewable and sustainable sources”, *Renew. Sustain. Energy Rev.*, vol. 23, pp. 443–462, 2013.

[5] A. de Klerk, *Fischer-Tropsch Refining*. Weinheim: Wiley VCH, 2011.

[6] G. Sommerbauer, S. Lux, H. Schmid, A. Kogelbauer, A. Stadtschnitzer und M. Siebenhofer, “Methanisierung von Kohlendioxid und Kohlenmonoxid”, in *11. Minisymposium Verfahrenstechnik*, 2015, p. 219.

Fuel Surrogate Design and Application to Commercial European Diesel

Kathrin Kos, Thomas Wallek
Graz University of Technology, Institute of Chemical Engineering and Environmental Technology, 8010 Graz, Inffeldgasse 25/C/I
kathrin.kos@tugraz.at, thomas.wallek@tugraz.at

Abstract

In engine simulation technology, simplified substitute mixtures referred to as surrogates are required for the emulation of complex petroleum-derived fuels. In this contribution, representative surrogates for commercial diesel fuels consisting of four to eight real chemical components are presented, which accomplish the simultaneous emulation of various target properties (design criteria). The design criteria chosen were the true boiling point (TBP) curve, cetane number (CN), liquid density, C/H ratio, lower heating value (LHV) and biodiesel content (FAME). In order to identify a representative set of compounds and to calculate the optimal surrogate composition, an optimization algorithm was developed and successfully applied to various diesel fuels [1]. Based on the optimization results, one of these blends was produced, showing excellent agreement with the measured data of the real target fuel. A profound evaluation of the effect of different fuel properties on the respective processes in the engine during fuel combustion was performed. For the application of the calculated multi-component fuel surrogates in engine CFD simulations, ongoing efforts are focused on the development of a multi-component kinetic reaction mechanism of fuel combustion.

Background

Optimization of modern diesel engines is needed in order to meet new, more stringent emission limits while maintaining an efficient engine mode (low fuel consumption). Simulation technology such as computational fluid dynamics (CFD) simulations is a valuable tool for time- and cost-efficient engine development.
Conventional petroleum-derived diesel fuel is a complex, heterogeneous blend of several hundreds of individual hydrocarbon species. The composition of diesel fuel underlies significant variations depending on the respective petroleum source and the various treatment processes in the refinery. However, knowledge of the composition of the resulting diesel fuel blend is very poor.
The characterization of such complex, heterogeneous hydrocarbon mixtures is a challenging task. For simulation purposes, substitute mixtures (surrogates) consisting of few representative species, have to be defined. The method presented in this contribution is the *real component approach*, which deals with real chemical species (in contrast to the pseudo-component approach). The ultimate goal in surrogate formulation is to specify a blend that is able to mimic various selected target properties (design criteria) of the respective target fuel. Such design criteria can be (thermo-) physical properties as well as ignition and combustion relevant characteristics. These diesel surrogates with defined composition can then be produced and used for research purposes. Regarding experiments, the advantage of surrogates over diesel fuels from refinery streams is the knowledge of the exact composition which allows for a reproducibility of the used diesel mixture at any time at any place and, therefore, makes the reproducibility of test results possible.

Methods

The optimal surrogate composition is calculated by means of an algorithm [1] based on simultaneous fitting of selected physical and chemical target properties, referred to as design criteria. The corresponding values of the target properties are obtained from measured data of the respective target fuel. The applied procedure for surrogate formulation comprises three to four consecutive steps:

1) Decision upon the design criteria and the associated weighing factors
2) Choice of an appropriate set of real hydrocarbon components
3) Calculation of the optimal composition by the developed optimization algorithm in order to meet the target values
4) Additional (for a closer match): Variation of the weighing factors of the individual criteria which results in variations of composition; Automated reduction or inclusion of components depending on the desired final number of species

The objective function used within the optimization algorithm is derived from a least squares approach. The design criteria taken into account are the true boiling point (TBP) curve, cetane number (CN), liquid density at 15 °C (ρ), C/H ratio, lower heating value (LHV) and biodiesel content (FAME) (Eq. 1):

$$ObjFunc = \left(\frac{\Delta TBP}{\Delta TBP_{ref}}\right)^2 + \left(\frac{\Delta CN}{\Delta CN_{ref}}\right)^2 + \\ + \left(\frac{\Delta \rho}{\Delta \rho_{ref}}\right)^2 + \left(\frac{\Delta (C/H)}{\Delta (C/H)_{ref}}\right)^2 + \left(\frac{\Delta LHV}{\Delta LHV_{ref}}\right)^2 + \left(\frac{\Delta FAME}{\Delta FAME_{ref}}\right)^2 \rightarrow min$$

Equation 1: Objective function of the optimization algorithm

The nominator of the individual terms contains the difference between the measured value of the target fuel and the calculated value for the surrogate. In the case of the TBP curve, this difference is equal to an average deviation between the TBP curve of the target fuel and the approximation by the surrogate. To allow comparability and weighing of the different optimization criteria a so-called reference value is used in the denominator. The degree of freedom is the composition of the surrogate. The optimal composition is obtained where the objective function of the algorithm reaches the global minimum.

Potential components and the corresponding pure component property data are incorporated in a comprehensive database. The required pure component property data include Antoine parameters, critical data, acentric factor, melting point, enthalpy of fusion, liquid density at 15 °C, lower flammability limit, cetane number, viscosity at 40 °C and ideal gas heat capacity parameters. This database contains components from all hydrocarbon classes. The majority of the components belongs either to the homologous series of n-alkanes, n-alkyl-benzenes or n-alkyl-naphthenes. Additionally, further naphthenes and aromatics, as well as few poly-aromatics and iso-alkanes are available. For the emulation of pure biodiesel fuel and blends of diesel with biodiesel several saturated and unsaturated fatty acid methyl esters (FAME) are included in the data bank. The developed component selection method allows for automated reduction or inclusion of chosen compounds depending on the desired final number of surrogate species.

Applications

Surrogate Generation

The algorithm was successfully applied to the emulation of various European and North American diesel fuels (B0) [1], to pure biodiesel (B100) and to common blends (B7).
Additionally, the surrogate blend calculated for a selected commercial European diesel fuel was also produced. Both, calculated and experimental, surrogates provide an excellent representation of the target fuel (Tab. 1). The target properties as well as further physical properties such as viscosity, flash point and cloud point of the target fuel are realistically reproduced.

Commercial Europ. Diesel	Surrogate		Target Fuel
	calc.	exp.	exp.
Cetane number [-]	60,3	59,4	59,9
Liq. density at 15 °C [kg/m³]	824	825	824
C/H ratio [kg C / kg H]	6,50	6,20	6,31
Lower heating value [MJ/kg]	42,7	42,8	43,2
Kin. viscosity at 40 °C [mm²/s]	2,62	2,53	2,96
Flash point [°C]	69,2	73,5	72,5

Tab. 1: Fuel properties of surrogate (calc. and exp.) and target fuel

Evaluation of Fuel Properties

The generated surrogate allows for a comprehensive evaluation of various fuel properties significantly affecting the processes in a conventional DI diesel engine during fuel combustion: spray formation, vaporization, fuel-air mixing, ignition and combustion including pollutant formation. Among all these stages of combustion, spray formation is the most influential mechanism; all further processes depend on the atomization quality of the fuel. The higher the density and the lower surface tension and viscosity of the liquid fuel, the higher is the atomization quality. A fine dispersion allows for a quick vaporization and a good mixing of fuel vapor and air leading to a more homogeneous fuel distribution in the combustion chamber.
Target properties can be grouped into (thermo-) physical and chemical properties. Thermo-physical properties such as density, viscosity and distillation curve are crucial for spray formation and further physical processes in the engine. But when it comes down to ignition and combustion behavior, chemical properties such as cetane number, C/H ratio and lower heating value play a central role. The biggest challenge in surrogate design – which means choice of design criteria and components – is the fact that it is impossible to develop a universal surrogate satisfying physical and chemical demands at the same time. Surrogates developed by matching thermo-physical targets plus cetane number cannot be expected to show appropriate ignition and combustion behavior. Similarly, chemical surrogates are very likely to fail in emulating distillation curve and fuel viscosity.

Chemical Kinetic Combustion Mechanisms

In order to emulate ignition and combustion behavior of conventional diesel fuel, a multi-component chemical kinetic reaction mechanism is required. For the majority of potential surrogate components single-component mechanisms are available from literature. The

available mechanisms comprise detailed and reduced mechanisms including high and low temperature regime sub-mechanisms. Concerning multi-component mechanisms, few mechanisms have been published for diesel fuel so far and not all of them are freely available. The ongoing efforts of developing a novel multi-component mechanism for diesel combustion rely upon mechanisms available in the literature such as a brand new reaction mechanism [2] containing four representative components. This mechanism includes the cool flame phenomenon (two-stage ignition) traditionally observed at low ignition temperatures and allows for the calculation of realistic ignition delay times. Figure 1 shows cool flame and main ignition delay times in dependence of the ignition temperature.

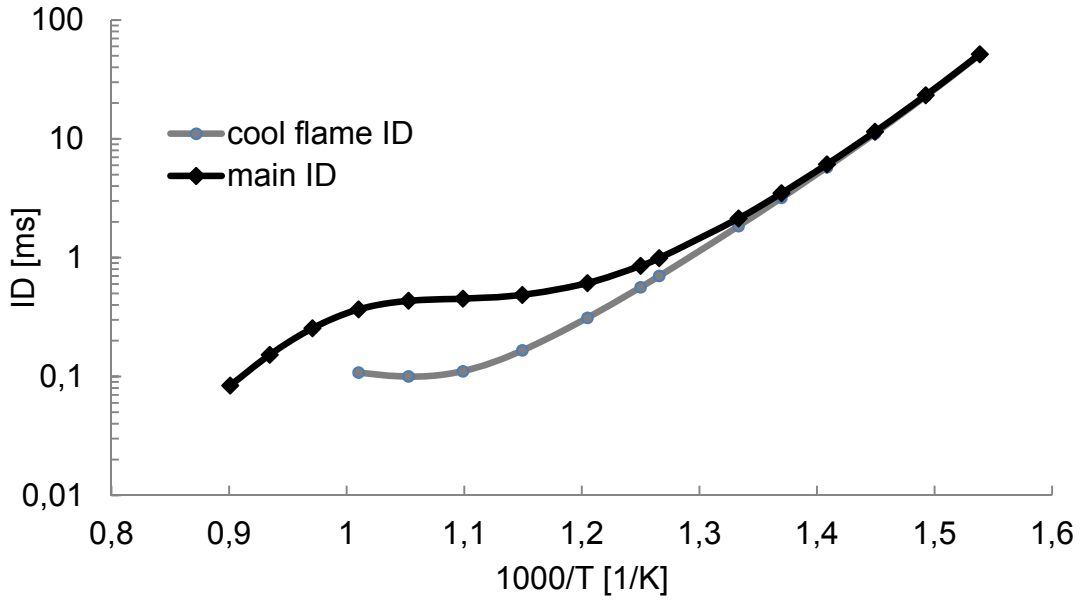

Fig. 1: Ignition delay times of a 4-component diesel surrogate as a function of ignition temperature at 40 bar and stoichiometric fuel/air ratio

Conclusion and Prospects

In this contribution, an optimization algorithm developed for fuel surrogate design is presented and the successful characterization of complex fossil and biogenic fuels by means of this algorithm is demonstrated. Representative surrogates consisting of four to eight real chemical components, which accomplish the simultaneous emulation of various target properties of commercial diesel fuels, were calculated. Crucial fuel properties were evaluated concerning their influence on specific processes in a conventional DI diesel engine.
Ongoing efforts are now focused on the development of a multi-component kinetic reaction mechanism of diesel combustion for the application in engine CFD simulations. Furthermore, the optimization algorithm will be extended for the application to further fuels such as gasoline and jet fuel as well as to diverse hydrocarbon streams within a refinery.

References

[1] Reiter, A. M., Wallek, T., Pfennig, A., & Zeymer, M. (2015). *Surrogate generation and evaluation for diesel fuel.* Energy & Fuels, 29(7), 4181-4192.

[2] Puduppakkam, K., Naik, C., Meeks, E., Krenn, C., Kroiss, R., Gelbmann, J., & Pessl, G. (2014). *Predictive Combustion and Emissions Simulations for a High Performance Diesel Engine Using a Detailed Fuel Combustion Model* (No. 2014-01-2570). SAE Technical Paper.

Bilanzierung eines mehrstufigen Prozesses zur Karbonatisierung mineralischer Rohstoffe

Iris Niesenbacher, Markus Lehner
Lehrstuhl für Verfahrenstechnik des industriellen Umweltschutzes
Montanuniversität Leoben, Franz-Josef-Straße 18, 8700 Leoben
iris.niesenbacher@unileoben.ac.at, markus.lehner@unileoben.ac.at

Kurzfassung

Die dauerhafte Speicherung von Kohlendioxid in Form von Karbonaten ist eine von mehreren Möglichkeiten, CO_2 zu nutzen. Im Research Studio Austria „Carbo Resources“ wird ein mehrstufiger Prozess entwickelt mit dem Ziel, nutzbare, mineralische Wertstofffraktionen zu erzeugen. In Laborversuchen ist es gelungen, einzelne Prozessschritte zu bilanzieren und so eine Massenbilanz für den Gesamtprozess zu erstellen.

Einleitung

Karbonatisierungsverfahren können für einige Industriezweige eine signifikante Reduktion der Kohlendioxidmenge ermöglichen, indem sie das anfallende CO_2 direkt am Entstehungsort in eine feste Matrix einbinden. Dabei reagiert Kohlendioxid mit primären bzw. sekundären Rohstoffen in einem ein- oder mehrstufigen Prozess zu festen und vor allem stabilen Mischkarbonatverbindungen. Diese Verfahren werden weltweit von verschiedenen Forscherteams seit Jahren intensiv untersucht [1]. Die Variation der Prozessparameter und vor allem die Auswahl der Ausgangsstoffe wurde u.a. von einem finnischen Team sehr genau betrachtet [2]. Zur Prozessoptimierung gibt es auch im Bereich der Karbonatisierung ausführliche Studien zur Anwendung von Ultraschall [3].
Das Research Studio Austria „Carbo Resources“ beschäftigt sich seit Juli 2014 ebenfalls mit dieser Thematik, jedoch mit dem zusätzlichen und einzigartigen Fokus auf die entstehenden Produktfraktionen. Ziel hierbei ist es nicht nur den Prozess zu verbessern, sondern auch die erzeugten Produkte so zu designen, dass sie auf dem Markt Anwendung finden können.

Methode

Das Ziel des Projektes ist es, einen Prozess zu entwickeln, der aus primären (Serpentinit) bzw. sekundären Rohstoffen (Asche, Schlacke) und Kohlendioxid ein möglichst reines Mischkarbonat aus Kalzium und Magnesium herstellt.
Bei dem Projekt „Carbo Resources“ handelt es sich um ein indirektes Karbonatisierungsverfahren und deshalb läuft der Prozess in diesem Fall dreistufig ab. Beim **Löseprozess** werden die Elemente Magnesium und Kalzium aus der Trägermatrix mithilfe von Salzsäure während eines temperierten Rührprozesses herausgelöst. Anschließend werden andere Metalle bzw. Metallverbindungen, welche aus dem Trägermaterial ebenfalls herausgelöst wurden aus der weiterzuverarbeitenden Lösung **eliminiert**, um die Reinheit des Endproduktes zu begünstigen. Dieses Eliminierungsverfahren wird durch einfache Fällungsreaktionen mit Feinserpentinit durchgeführt. Den abschließenden Prozessschritt stellt die eigentliche **Karbonatisierungsreaktion** dar, bei der in die kalzium- und magnesiumreiche Lösung, welche nach dem Eliminierungsschritt angereichert zurückbleibt, Kohlendioxid eingebracht wird, um feste Karbonatverbindungen herzustellen. Die Karbonate fallen bei einer pH-

Wert-Anhebung der Lösung aus. [4]

Erste Ergebnisse

Löseprozess

Im ersten Prozessschritt – dem Löseprozess - kann die gelöste Magnesiummenge durch Einsatz von Ultraschall nachweisbar erhöht werden. Durch die Anwendung von Ultraschall während des Löseprozesses, können die Salz- und Silikatschichten auf den Probepartikeln durch die Kavitationswirkung des Ultraschalls zerstört werden. Somit bleibt die reaktive Oberfläche erhalten. Das bedeutet weiters, dass durch gezielten Ultraschalleinsatz die Dauer des Löseprozesses signifikant verkürzt werden könnte. Eine Erhöhung der Ultraschallintensität hingegen bringt keine weitere Verbesserung. Abb. 1 ist zu entnehmen, dass bei sehr geringem Ultraschalleintrag bereits nach einer Stunde ungefähr dieselbe Menge an gelöstem Magnesium vorliegt wie bei einer Versuchsdauer von drei Stunden ohne Ultraschalleinsatz. Eine kürzere Versuchsdauer wirkt sich außerdem bei einem Scale-up positiv auf die Reaktorgröße aus, geringeren Verweilzeiten im Reaktor tragen automatisch dazu bei, dass die Gesamtkosten des Prozesses gesenkt werden. [4]

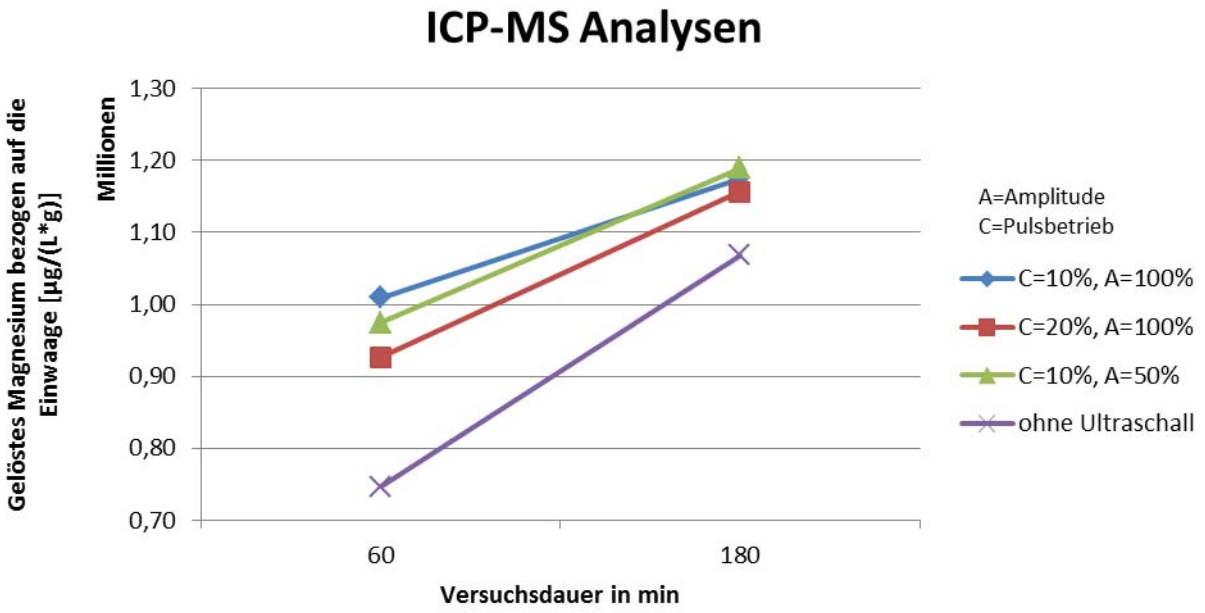

Abb.1: Gelöste Magnesiummenge mit und ohne Ultraschallanwendung

Eliminierung der Begleitelemente

Eine sehr vielversprechende Eliminierungsvariante stellt derzeit die Fällungsreaktion mit Feinserpentinit dar. Der pH-Wert der Lösung wird durch die Zugabe von Feinserpentinit deutlich angehoben, dies begünstigt die Ausfällung von Fe, Mn und Ni. Feinserpentint hat außerdem den Vorteil, dass er bei der Aufmahlung des Rohmaterials Serpentinit für den Löseprozess als Abfallprodukt anfällt. Durch diese Weiterverwendung des Materials wird kein Abfall produziert und dem Prozess wird die Zugabe einer anderen basischen Chemikalie erspart, wodurch wiederum die Prozesskosten positiv beeinflusst werden.[4]

Karbonatisierungsverfahren

Für den letzten Prozessschritt, nämlich die eigentlichen Karbonatisierung, haben bereits erste Vorversuche mit einer TGA (Themogravimetrische Analyse) stattgefunden, um das Verhalten der magnesiumreichen Lösung bei unterschiedlichen Temperaturen und

Gaszusammensetzungen einschätzen zu können. [4]

Massenbilanz

Nach der Auswertung der derzeitig vorhandenen Versuchsdaten aus dem Projekt „Carbo Resources“, konnte eine erste grobe Massenbilanz aufgestellt werden, welche im Flowsheet in Abb. 2 dargestellt ist. Die errechneten Daten beziehen sich darauf, dass beim Löseprozess Ultraschall zum Einsatz kommt und beim Karbonatisierungsprozess eine Gas-Feststoff-Reaktion angewendet wird. Das bedeutet, dass die kalzium- und/oder magnesiumhaltige Lösung nach der Fällung der Begleitelemente in einem Röstprozess zu Oxiden zersetzt wird, wobei Salzsäure abdampft und rezykliert werden kann. Die erzeugten Oxide reagieren dann in einer tiefer liegenden Reaktionszone der Brennkammer mit Kohlendioxid zu festen und vor allem stabilen Mischkarbonaten.
Die in Abb. 2 dargestellten Werte decken sich mit den von O’Connor et al. publizierten Daten. Laut seinen Angaben benötigt man, abhängig vom Prozess, zwischen 1,8 - 2,8 t Serpentinit, um eine Tonne CO_2 karbonatisieren zu können [5].
In unserem Fall wird ungefähr die 2,4-fache Menge an Grobserpentinit benötigt, um CO_2 binden zu können.

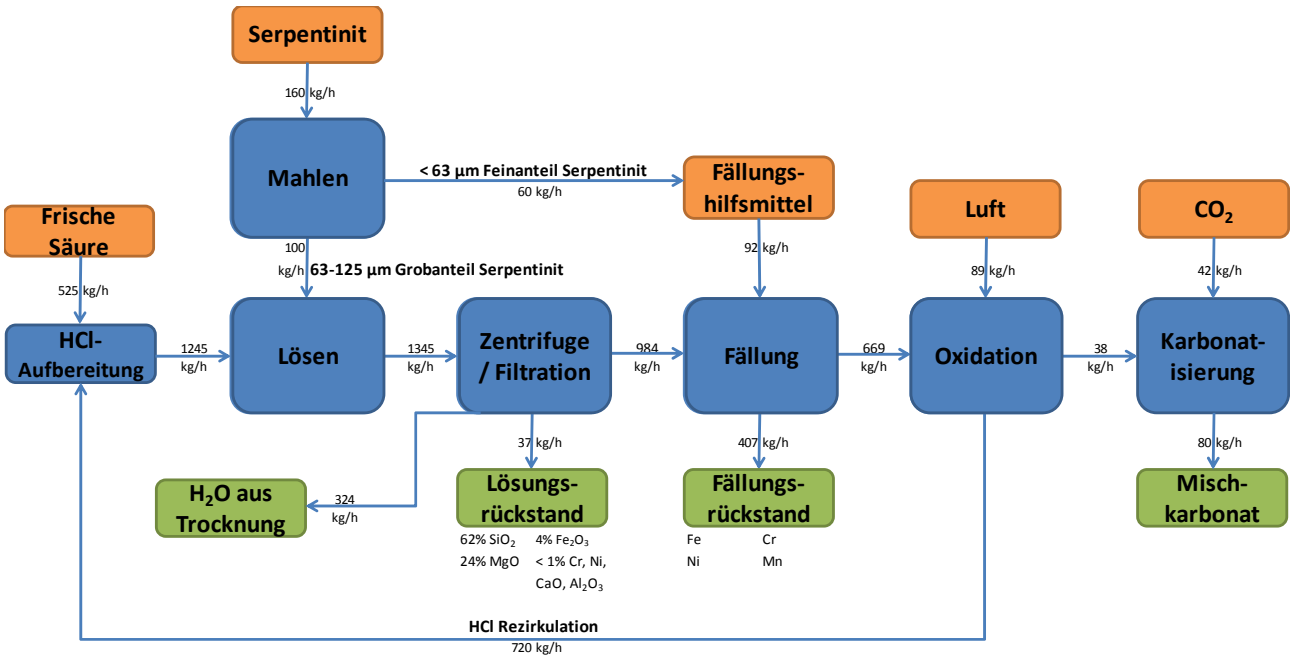

Abb. 2: Massenbilanz eines indirekten Karbonatisierungsprozesses unter Einsatz von Ultraschall

Ausblick

In den kommenden Monaten werden die Karbonatisierungsversuche intensiviert, um den Datensatz für den Projektabschluss im Sommer zu vervollständigen.
Anhand der vorliegenden Daten aus den Laborversuchen werden neben der in diesem Abstract präsentieren Massenbilanz auch eine CO_2- und eine Energiebilanz erstellt, sowie die Kosten für einen industriellen Prozess kalkuliert.

Acknowledgement

Die Forschungsarbeit am Projekt „Carbo Resources“ wird dankenswerter Weise von der Österreichischen Forschungs-Förderungsgesellschaft (FFG) durch die Förderschiene des Research Studio Austria unterstützt.

Literatur

[1] Olajire, A. (2013): A review of mineral carbonation technology in sequestration of CO2. In: *Journal of Petroleum Science and Engineering* 109, S. 364–392.

[2] Teir, S.; Revitzer, H.; Eloneva, S.; Fogelholm, C.; Zevenhoven, R. (2007): Dissolution of natural serpentinite in mineral and organic acids. In: *International Journal of Mineral Processing* 83 (1–2), S. 36–46.

[3] Santos, R.; François, D.; Mertens, G.; Elsen, J.; van Gerven, T. (2013): Ultrasound-intensified mineral carbonation. In: *Applied Thermal Engineering* 57 (1-2), S. 154–163.

[4] Lehner, M.; Niesenbacher, I.; Höllen, D. (2015): FFG Zwischenbericht Nr. 1, RSA Carbo Resources.

[5] O'Connor, W.; et al. (2005): Aqueous Mineral. Mineral Availability, Pretreatment, Reaction Parametrics, And Process Studies. Final Report.

Pressurized Hydrogen Production by Fixed-Bed Chemical Looping

Gernot Voitic[a], Stephan Nestl[a], Michael Lammer[a], Julian Wagner[b], Viktor Hacker[a]
Institut für Chemische Verfahrenstechnik und Umwelttechnik,
Technische Universität Graz, Graz, Inffeldgasse 25/C
[b]Institut für Elektronenmikroskopie und Nanoanalytik,
Technische Universität Graz, Graz Steyrergasse 17/III
gernot.voitic@tugraz.at, stephan.nestl@tugraz.at, viktor.hacker@tugraz.at

Kurzfassung

Es wurden zyklische Reduktions- und Oxidationsversuche mit einer Eisenoxid-Kontaktmasse durchgeführt. Die Reduktion erfolgte mit 25 ml·min^{-1} Wasserstoff bei 750 °C bis zur vollständigen Reduktion des Eisenoxids. Die anschließende Oxidation des Eisens mit Wasserdampf (0,03 g·min^{-1}) bei 750 °C führte zur Freisetzung von Wasserstoff. Die Oxidationsversuche wurden unter erhöhtem Systemdruck, zur Produktion von Druckwasserstoff, durchgeführt. Während der 15 Zyklenversuche konnte ein maximaler Wasserstoffdruck von 22 bar erreicht werden. Die Experimente zeigten eine lineare Abnahme des Kontaktmassenumsatzes, welche jedoch unabhängig vom erreichten Maximaldruck war. Mit Hilfe von elektronenmikroskopischen Aufnahmen wurden ein Zusammenwachsen der Granulate und eine geglättete Probenoberfläche festgestellt. Dies ist ein Hinweis für die Versinterung der Eisenpartikel, welche mit einer Verringerung der Porosität einhergeht und die die Ursache für den Rückgang des Kontaktmassenumsatzes ist.

Einleitung

Durch Wasserstoff betriebene Brennstoffzellenfahrzeuge ermöglichen eine CO_2 freie Mobilität. Eine wesentliche Voraussetzung für die erfolgreiche Marktpenetration der Brennstoffzellen-PKWs ist die flächendeckende Verfügbarkeit von günstigem Wasserstoff an Tankstellen. Aktuell wird der Wasserstoff großtechnisch in Raffinerien mittels katalytischer Dampfreformierung hauptsächlich aus Erdgas hergestellt und mit einem 2-stufigen Wasser-Gas-Shift-Reaktor sowie Druckwechseladsorption nachgereinigt. Anschließend erfolgt der Transport per LKW meist in komprimierter Form zur Tankstelle. Sowohl der Transport als auch die Wasserstoffverdichtung mit Gaskompressoren sind wesentliche Kostenfaktoren für die Produktion von Wasserstoff.

Eine interessante Alternative zur konventionellen Dampf-Reformierung ist die Wasserstoffherstellung mittels chemical-looping-water-splitting-Verfahren [1]. In diesem Verfahren wird ein fester Sauerstoffträger, beispielsweise ein Metalloxid, mit einem reduzierenden Gas zu einer niedrigeren Oxidationsstufe reduziert. Die anschließende Oxidation des Metalls mit Dampf führt zur Freisetzung von hochreinem Wasserstoff. An dem Institut für Chemische Verfahrenstechnik und Umwelttechnik der TU Graz wird an einer kompakten dezentralen Anwendung dieses chemical-looping-Verfahrens, dem Reformer Eisen Dampf Prozess, gearbeitet [2]. Dabei wird ein Kohlenwasserstoff (Erdgas, Biogas) mittels katalytischer Dampfreformierung in ein Synthesegas umgewandelt (Gl 1). Dieses Gas wird anschließend eingesetzt um eine auf Eisen basierende Kontaktmasse zu reduzieren (Gl 2 – 3). Die darauffolgende Oxidation mit Wasserdampf ermöglicht die Produktion von reinem Wasserstoff (Gl 4).

$$CH_4 + H_2O \rightarrow 3H_2 + CO \quad (1)$$

$$Fe_3O_4 + H_2/CO \rightarrow 3FeO + H_2O/CO_2 \quad (2)$$

$3FeO + 3(H_2/CO) \rightarrow 3Fe + 3(H_2O/CO_2)$ (3)

$3Fe + 4H_2O \rightarrow Fe_3O_4 + 4H_2$ (4)

Nestl et al. zeigten in ihrer Arbeit, dass dieser Prozess zur direkten Herstellung von Druckwasserstoff geeignet ist [3]. Die Reformierung und Reduktion der Kontaktmasse muss aus thermodynamischer Sicht unter atmosphärischen Bedingungen durchgeführt werden. Die Oxidation der Kontaktmasse kann jedoch unter erhöhtem Systemdruck, welcher durch die Verdampfung von Wasser im geschlossenen System aufgebaut wird, erfolgen. Der Einsatz einer solchen dezentralen Anlage an Tankstellen zur direkten Herstellung von Druckwasserstoff würde die beiden oben beschriebenen Kostentreiber der Wasserstoffherstellung (Transport und Verdichtung) deutlich reduzieren und die erfolgreiche Einführung von Wasserstoff als Energieträger für die Mobilität beschleunigen.

Zur weiterführenden Untersuchung des Verfahrens zur Produktion von Hochdruckwasserstoff wurden zyklische Reduktions- und Oxidationsversuche der Kontaktmasse unter erhöhtem Systemdruck durchgeführt. Dabei wurde der Einfluss des erhöhten Wasserstoffdrucks auf die Stabilität und die Reaktivität der Kontaktmasse analysiert. Die Ergebnisse dieser Versuche wurden in der Veröffentlichung *Pressurized hydrogen production by fixed-bed chemical looping, Appl. Energy 157, 2015, 399-407*, ausführlich behandelt. Auszüge aus dieser Arbeit werden in diesem *extended abstract* behandelt [4].

Methoden und Verfahren

Eine Kontaktmasse mit der Zusammensetzung von 90% Hämatit (325 mesh) und 10% Aluminiumoxid (20-50 µm) wurden mittels mechanischem Mischverfahren in einem geschlossenen Intensivmischer (Maschinenfabrik Gustav Eirich GmbH & Co KG) durch stufenweise Zugabe von vollentsalztem Wasser pelletiert. Die Pellets wurden anschließend fraktioniert und bei 900°C für 3 Stunden kalziniert. 3,57 g der Probe mit einem Durchmesser von 90 – 125 µm wurden für die zyklischen Experimente im Festbettreaktor eingesetzt.

Experimentelle Durchführung

Es wurden 15 zyklische Reduktions- und Oxidationsexperimente in einem umgebauten Katalysatorteststand (Microactivity-Reference, PID Eng&Tech) durchgeführt. Die Oxidationen erfolgten bei unterschiedlichem Systemdruck (1 – 22 bar), gefolgt von einer Reduktion unter atmosphärischen Bedingungen. Die Probe wurde in einen Festbett-Rohrreaktor mit einem Innendurchmesser von 0,9 cm gefüllt. Der Eingang und der Ausgang des Reaktors wurden mit einem Inertmaterial (Al_2O_3-Pellets) gefüllt, um Bewegungen im Festbett zu verhindern und um die Reaktionsgase vorzuheizen. Ein elektrischer Ofen heizte den Rohrreaktor auf die Reaktionstemperatur von 750 °C. Die Temperaturregelung erfolgte mittels Typ-N Thermoelement, welches in der Mitte des Festbetts positioniert wurde.

Ein vollständiger Zyklus beginnt mit der Reduktion der Kontaktmasse mittels Wasserstoff (25 $ml \cdot min^{-1}$) bei 750 °C unter atmosphärischen Bedingungen. Nach der vollständigen Reduktion der Kontaktmasse erfolgt die Oxidation mit Dampf bei 750 °C unter erhöhtem Druck. Hierzu werden mit einer HPLC-Pumpe 0,03 $g \cdot min^{-1}$ Wasser in das heiße System gepumpt und verdampft. Die Rohrleitungen des Systems werden mit Heizschnüren zusätzlich beheizt um eine Kondensation des Dampfs bei erhöhtem Systemdruck zu verhindern. Der Dampf oxidiert die Kontaktmasse zu Magnetit unter der Freisetzung von

Wasserstoff. Der nicht umgesetzte Dampf wird in einem Peltierkühler auskondensiert. Der Druckaufbau im System erfolgt durch das Verdampfen des Reaktionswassers. Der Ausgang der Anlage wird dabei mittels Massendurchflussregler geschlossen bzw. gedrosselt. Die produzierte Menge an Wasserstoff wird durch die Analyse des Wasserstoffflusses am Systemausgang mittels Massendurchflussmessung durchgeführt.

Auswertung

In Abbildung 1 (links) ist eine repräsentative Reduktion der Kontaktmasse mit Wasserstoff ausgehend vom Magnetit dargestellt. Die Kurve weist 2 charakteristische Stufen auf. Der Beginn der Reduktion startet mit einem Wasserstoffumsatz von ca. 50 %, welcher dem Übergang von Magnetit zu Wüstit entspricht (Gl 2). Der darauffolgende quasi-stabile Umsatz von ca. 30% entspricht dem Reduktionsschritt Wüstit zu Eisen (Gl 3).

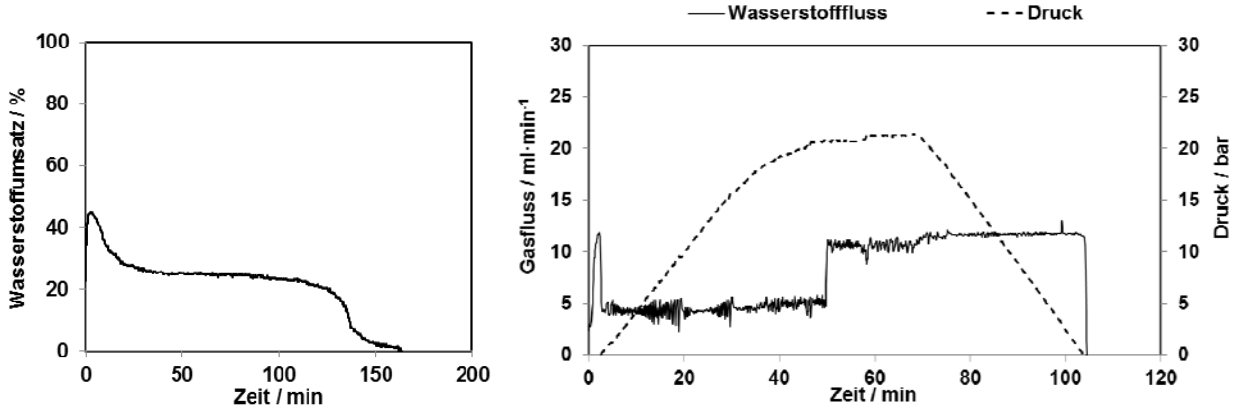

Abbildung 1: Links: repräsentative Reduktion von Magnetit zu Eisen. Die Reduktion wurde mit 25 ml·min^{-1} H_2 bei 750 °C drucklos durchgeführt. Rechts: Gasfluss des freigesetzten Wasserstoffs und Systemdruck einer repräsentativen Dampf Oxidation bei 750 °C [4].

In der darauffolgenden Oxidation mit Dampf wird das Eisen zu Magnetit oxidiert (Gl.4). Abbildung 1 (rechts) zeigt eine repräsentative Druckoxidation. Zu Beginn wird der Wasserstofffluss am Ausgang gedrosselt. Dies führt zu einem linearen Druckanstieg im System. Ab Minute 40 kommt es zu einem Abflachen des Druckanstiegs und zu einer stabilen Wasserstoffproduktion unter erhöhtem Druck. Während dieser Phase wird der Wasserstofffluss am Ausgang erhöht um die Reaktionsdauer zu verkürzen. Am Ende der Reaktion ist der Abbau des Systemdrucks auf Grund der vollständigen Oxidation der Kontaktmasse zu beobachten.

Aus den Messdaten der Flussmessung während der Reduktion bzw. Oxidation wird das Gesamtvolumen des produzierten sowie verbrauchten Wasserstoffs ermittelt.

Nach Gleichung 5 kann daraus der Umsatz der Kontaktmasse OC_{con} ermittelt werden. n_{H2} entspricht dem produzierten bzw. verbrauchten Wasserstoff in mol und n_{Fe} entspricht dem Anteil an Eisen in der Kontaktmasse in mol.

$$OC_{con} = 4/3 \cdot \Sigma n_{H2} / n_{Fe} \quad (5)$$

Der Kontaktmassenumsatz der Reduktion bzw. Oxidation betrug in den 15 durchgeführten Zyklenversuchen zwischen 80% und 70%, wobei ein linearer Rückgang über die Dauer der Versuchsserie festgestellt werden konnte. Dies deutet auf eine Verschlechterung der Reaktivität der Kontaktmasse hin.
Um einen möglichen Einfluss des erhöhten Systemdrucks auf die Stabilität und Zyklisierbarkeit der Eisenpellets zu beurteilen, wird der Kontaktmassenumsatz der

Reduktionen und Oxidationen in Abhängigkeit des Systemdrucks ausgewertet (Abbildung 2). Dabei wird für jede Reduktion der Maximaldruck der vorangegangenen Oxidation aufgetragen. In beiden Abbildungen ist die lineare Abnahme des Umsatzes klar ersichtlich. Die Umsätze der Oxidationen zeigen dabei größere Schwankungen als die Umsätze der Reduktionen. Die Ursache hierfür ist die diskontinuierliche Verdampfung des Wassers während der Oxidation. Dies führt zu Druckstößen im System, welche sich in der Analyse des Wasserstoffflusses durch den Massenflussmeter bemerkbar machen. Daraus resultiert ein größerer Fehler der Quantifizierung des produzierten Wasserstoffs während der Oxidation gegenüber der Reduktion. Die Analysedaten der Zyklenexperimente legen den Schluss nahe, dass keine Abhängigkeit zwischen dem Rückgang des Kontaktmassenumsatzes und den unterschiedlichen Systemdrücken während der Reduktion und der Oxidation besteht.

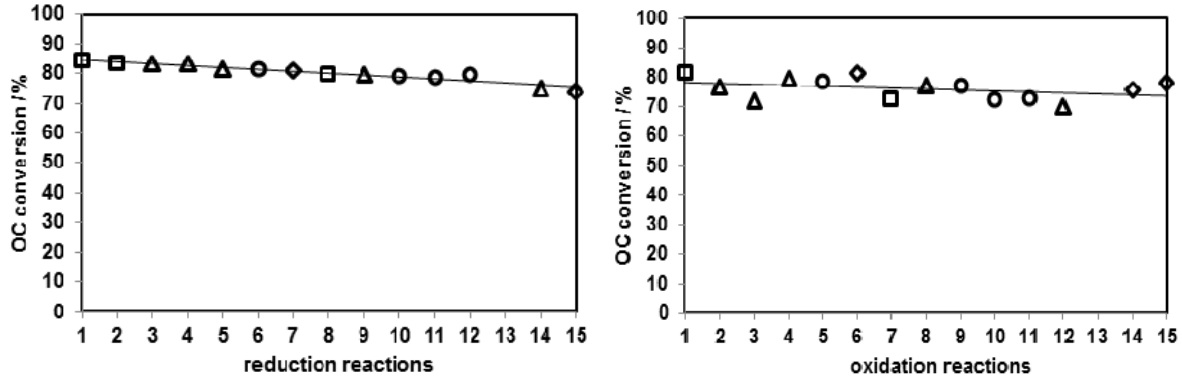

Abbildung 2: Links: Kontaktmassenumsatz der 15 Reduktionsreaktionen. Rechts: Kontaktmassenumsatz der 15 Oxidationsexperimente. Die unterschiedlichen Symbole deuten den erreichten Maximaldruck der Oxidation an (in der linken Abbildung den Maximaldruck der vorangegangenen Oxidation). Raute: < 10 bar, Quadrat: 10 – 15 bar, Dreieck: 16 – 20 bar, Kreis: > 20 bar [4].

Der Umsatzrückgang der Kontaktmasse wurde zusätzlich durch elektronenmikroskopische Aufnahmen der Eisenpellets untersucht. Abbildung 3 (links) zeigt die Eisenprobe, welche unter erhöhtem Systemdruck zyklisiert wurde. Als Vergleich zeigt Abbildung 3 (rechts) die Aufnahme einer Eisenprobe, welche unter atmosphärischen Bedingungen in einer thermogravimetrischen Waage bei 750 °C geprüft wurde. Aus den Abbildungen ist ersichtlich, dass die skelettartige Struktur der Eisenpellets unter erhöhtem Wasserstoffdruck erhalten bleibt und die Probe eine ausreichende Porosität besitzt. Eine Aufnahme der Eisenprobe mit höherer Auflösung (Abbildung 3 Mitte) zeigt geglättete Strukturen und verwachsene Partikel. Diese Strukturveränderungen sind ein Indiz für Sintereffekte, welche durch die hohen Reaktionstemperaturen von 750 °C verursacht werden. Die Versinterung der Eisenpartikel geht einher mit einer Verringerung der Porosität der Probe und ist die Ursache für den linearen Rückgang des Kontaktmassenumsatzes.

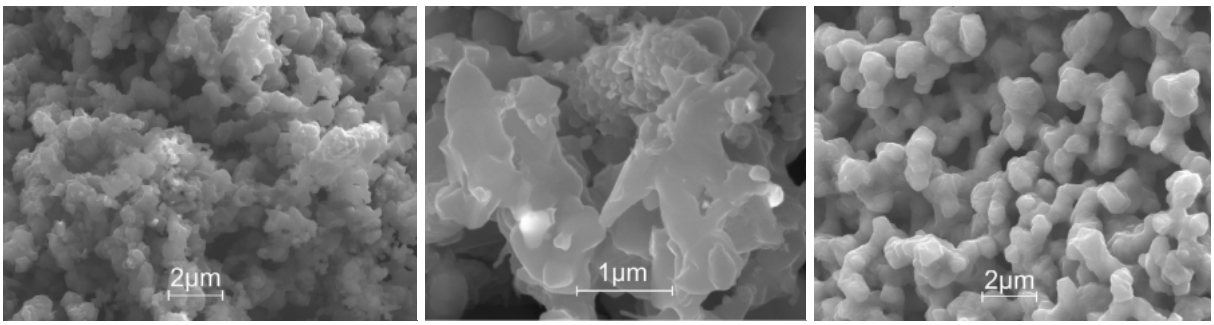

Abbildung 3: Rasterelektronenmikroskopische Aufnahmen der Kontaktmasse (90wt% Fe_2O_3, 10wt% Al_2O_3, 90-125 µm) nach den Zyklenversuchen zur Freisetzung von Druckwasserstoff (links und Mitte). Rechts: Vergleichsprobe mit der gleichen Zusammensetzung nach 8 Zyklenversuchen unter atmosphärischem Druck und 750 °C [4].

Zusammenfassung

Zyklische Reduktions- und Oxidationsexperimente basierend auf dem Eisen-Dampf Prozess zur direkten Herstellung von Druckwasserstoff wurden durchgeführt. In den Experimenten konnte ein maximaler Wasserstoffdruck von 22 bar erreicht werden. Die Analyse der Kontaktmassenumsatze über 15 Zyklen zeigten eine lineare Abnahme bei Reduktion und Oxidation. Bei genauerer Analyse des Rückgangs konnte gezeigt werden, dass der erhöhte Systemdruck während der Oxidation keinen negativen Einfluss hatte. Elektronenmikroskopische Aufnahmen der Eisenproben nach den Zyklenversuchen zeigten, dass die poröse Struktur der Pellets trotz erhöhtem Systemdruck erhalten blieb. Eine höhere Auflösung offenbarte zusammengewachsene Partikel und eine geglättete Oberflächenstruktur. Dies ist ein Hinweis auf Versinterung der Eisenpartikel, verursacht durch die hohe Reaktionstemperatur von 750 °C. Diese Sintereffekte führen zu einem Rückgang der Porosität der Pellets und sind die Erklärung für den Rückgang des Kontaktmassenumsatzes.

Literatur

[1] C. R. R. Müller, C. D. D. Bohn, Q. Song, S. a. a. Scott, and J. S. S. Dennis, “The production of separate streams of pure hydrogen and carbon dioxide from coal via an iron-oxide redox cycle,” *Chem. Eng. J.*, vol. 166, no. 3, pp. 1052–1060, 2011.

[2] V. Hacker, “A novel process for stationary hydrogen production: the reformer sponge iron cycle (RESC),” *J. Power Sources*, vol. 118, no. 1–2, pp. 311–314, 2003.

[3] S. Nestl, G. Voitic, M. Lammer, B. Marius, J. Wagner, and V. Hacker, “The production of pure pressurised hydrogen by the reformer-steam iron process in a fixed bed reactor system,” 2015.

[4] G. Voitic, S. Nestl, M. Lammer, J. Wagner, and V. Hacker, “Pressurized hydrogen production by fixed-bed chemical looping,” *Appl. Energy*, vol. 157, pp. 399–407, 2015.

Continuous hydrodeoxygenation of liquid phase pyrolysis oil

Andrea Rollett, Michael Schadler, Nikolaus Schwaiger
TU Graz, Institut für Chemische Verfahrenstechnik und Umwelttechnik,
8010 Graz, Inffeldgasse 25c/II
nikolaus.schwaiger@tugraz.at

Abstract

This work presents an alternative dual step concept for biomass liquefaction and hydrogenation, intending production of liquid energy carriers. The first step of this concept is liquid phase pyrolysis, which was performed at OMV refinery in pilot scale. During pyrolysis lignocellulose is dehydrated to form biochar and pyrolysis oil. Sufficient chemical stability of these intermediates and products is needed for further processing and achieved through product upgrading.
Hydrodeoxygenation of liquid phase pyrolysis has already been done in lab-scale batch reactors. For scale up purposes a plug flow reactor has been implemented and operated. The continuous hydrodeoxygenation experiments delivered a promising product phase with characteristic properties of a mixture of gasoline, kerosene and diesel.

Introduction

Growing global population directly leads to rising demand of liquid transportation fuels.[1] To satisfy the need of mobility, lignocellulosic biomass can contribute with considerable amounts to production of liquid transport fuels. Several thermochemical pathways are possible to convert lignocellulose into liquid fuels, gasification with subsequent Fischer-Tropsch synthesis [2], flash pyrolysis with gasification and Fischer-Tropsch synthesis [3] and flash pyrolysis in a first step [4] with subsequent hydrodeoxygenation (HDO) [5], [6]. All these biomass liquefaction methods have advantages and disadvantages. Fischer-Tropsch synthesis is very limited to the sulfur content in synthesis gas composition, because the sulfur content leads to rapid catalyst deactivation. Flash pyrolysis oil suffers from weak pyrolysis oil stability, high acidity, char and inorganics loading [7], [8].

Liquid phase pyrolysis oil for subsequent hydrodeoxygenation and biochar for following liquefaction were produced in the bioCRACK pilot plant [9], operated by BDI BioEnergy International, at OMV Refinery at Schwechat/Vienna.
Liquid phase pyrolysis (LPP) oil and biochar have been hydrodeoxygenated and respectively liquefied in batch reactors. In a next step the LPP oil has been hydroeoxygenated in a continuous lab scale plug flow reactor for scale up purposes at the Institute of Chemical Engineering and Environmental Technology.

Analytics

All liquid and solid products and the feed were characterized by elemental analysis with a Vario macro CHNO-analyzer, from Elementar Analysensysteme, in CHN mode. The heat carrier and entrained heat carrier composition for liquid phase pyrolysis were determined with a GC-SimDis[1] MXT 2887, 10m column from Restek and an Agilent 7890A GC. Water

[1] Simulated distillation with GC

was measured with GC-TCD[2] on an HP-Innovax column. The gas composition was analyzed for CH_4, O_2, CO, CO_2. While CH_4, CO, CO_2 concentrations were measured by infrared gas analysis, the O_2 concentration in the gas was determined with an electrochemical sensor. TAN[3] was measured with a Tim 900 Titra Lab Titration manager.

Experiments - Continuous HDO of liquid phase pyrolysis oil

The LPP oil for HDO was provided by BDI. Elemental composition is shown in Table 1. Viscosity of the LPP oil was 3.24 mm^2/s and density was 1.092 g/cm^3. Total acid number was 39.40 mg_{KOH}/g_{sample} and the water content was 58.9 %.

Table 1: Elemental composition of liquid phase pyrolysis oil

	C [%]	H [%]	N [%]	ND [%]
PYO	21.48	9.45	0.47	68.60

Hydrodeoxygenation was performed in a plug flow reactor (shown in Figure 1) with a liquid flow rate of 6 g/h and a gaseous flow rate of 40 mln/min H_2 at 400°C and 121 bar H_2 pressure. The reactor was filled with a CoMo oxide on alumina catalyst. The catalyst was pre-treated for eight hours with di-tert butyl disulphide in decane. The HDO experiments were carried out subsequently after pre-treatment for 24 hours.

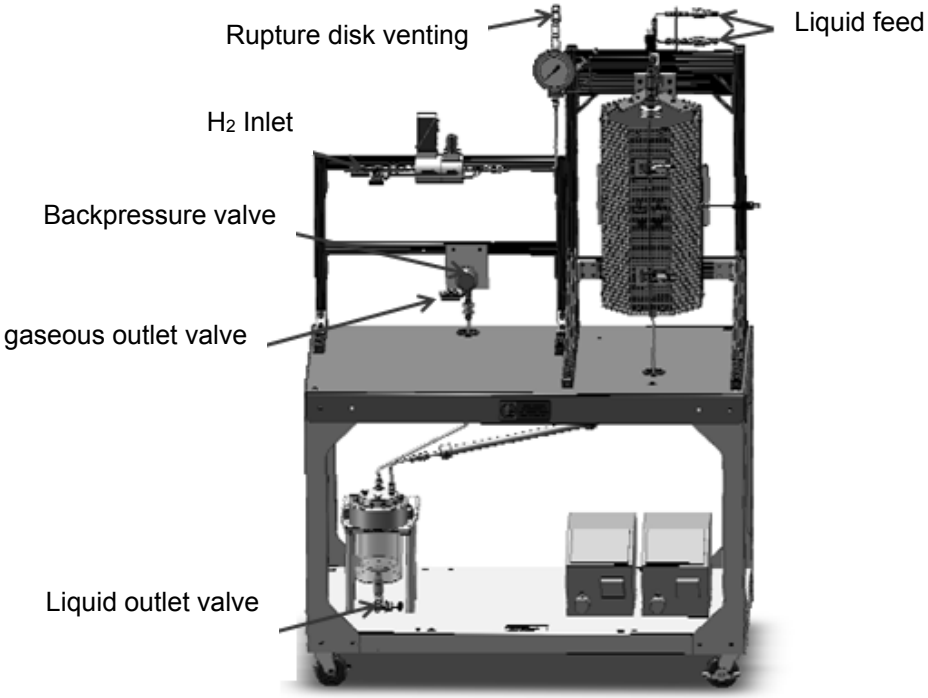

Figure 1: Continuous HDO labscale reactor.

[2] Thermal conductivity detector
[3] Total acid number mg_{KOH}/g_{sample}

The experiment parameters were monitored and controlled by SpecView, provided by Parr Instruments. The Flowsheet of the reactor is shown in Figure 2.

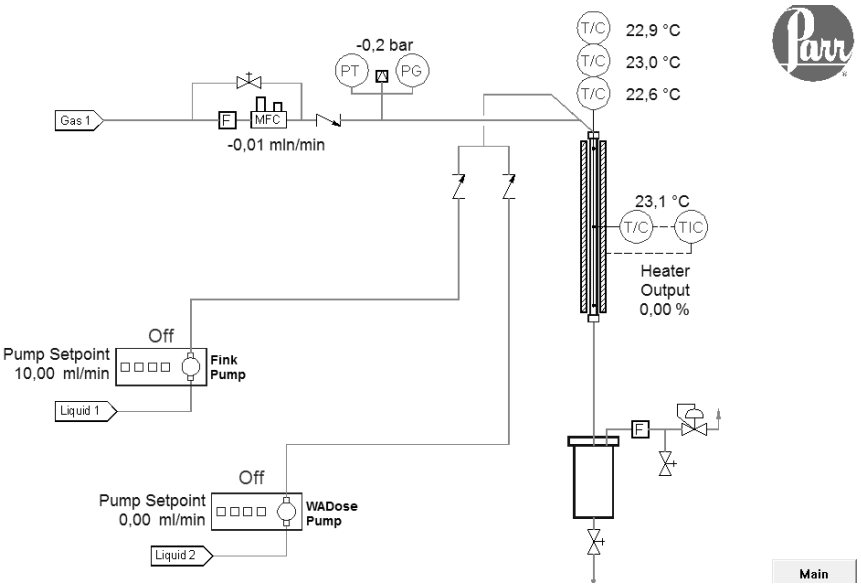

Figure 2: Flowsheet of the continuous HDO labscale reactor

After HDO of LPP oil a phase separation was observed. A water phase and an oil phase were collected. Total carbon transfer into oil phase was about 45.3 %.The carbon content of the oil phase after continuous HDO was 85.9 %, Hydrogen content was 13.4 % and water content was 0.12 %. Dynamic viscosity was 0.86 mPa s at T=20°C. Total acid number (TAN) was below detection limit. Figure 3 shows the boiling behaviour of the oil phase which has a boiling range from 100°C to 350°C and corresponds with the boiling behaviour of gasoline for the lower temperature range, kerosene for the middle temperature range and diesel for the high temperature range.

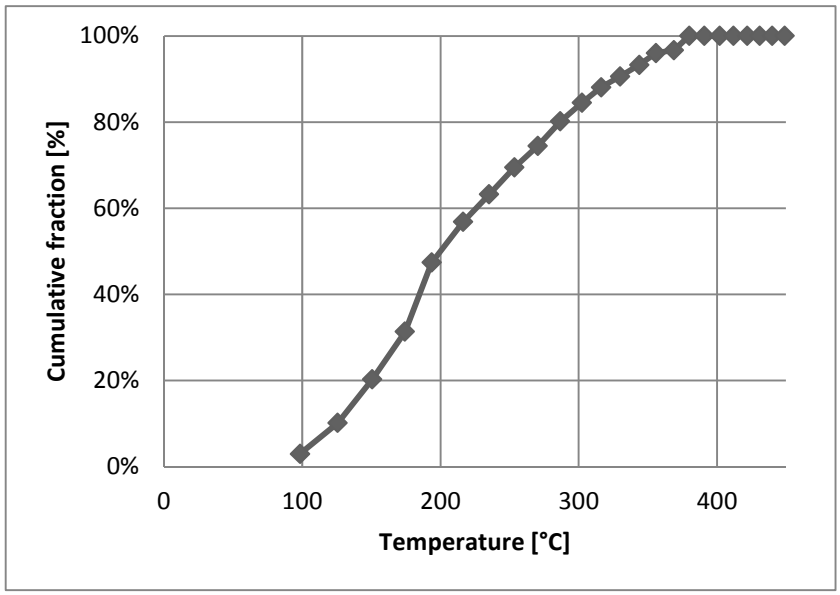

Figure 3: Boiling range of continuously hydrodeoxygenated fuel.

Summary

It was shown in labscale that continuous HDO of LPP oil is feasible. Product quality corresponds nicely to industrial standards. A parameter study in terms of Hydrogen feed, residence time and a catalyst study is under way.

Literature

[1] M. Balat, “Production of bioethanol from lignocellulosic materials via the biochemical pathway: A review,” *Energy Convers. Manag.*, vol. 52, no. 2, pp. 858–875, 2011.

[2] D. Leckel, “Diesel Production from Fischer−Tropsch: The Past, the Present, and New Concepts,” *Energy & Fuels*, vol. 23, no. 5, pp. 2342–2358, May 2009.

[3] H. Leibold, A. Hornung, and H. Seifert, “HTHP syngas cleaning concept of two stage biomass gasification for FT synthesis,” *Powder Technol.*, vol. 180, no. 1–2, pp. 265–270, Jan. 2008.

[4] D. Meier, B. van de Beld, A. V. Bridgwater, D. C. Elliott, A. Oasmaa, and F. Preto, “State-of-the-art of fast pyrolysis in IEA bioenergy member countries,” *Renew. Sustain. Energy Rev.*, vol. 20, pp. 619–641, Apr. 2013.

[5] J. Wildschut, F. H. Mahfud, R. H. Venderbosch, and H. J. Heeres, “Hydrotreatment of Fast Pyrolysis Oil Using Heterogeneous Noble-Metal Catalysts,” *Ind. Eng. Chem. Res.*, vol. 48, no. 23, pp. 10324–10334, Dec. 2009.

[6] Y. Wang, T. He, K. Liu, J. Wu, and Y. Fang, “From biomass to advanced bio-fuel by catalytic pyrolysis/hydro-processing: hydrodeoxygenation of bio-oil derived from biomass catalytic pyrolysis.,” *Bioresour. Technol.*, vol. 108, pp. 280–4, Mar. 2012.

[7] D. Mohan, C. U. Pittman, and P. H. Steele, “Pyrolysis of Wood/Biomass for Bio-oil: A Critical Review,” *Energy & Fuels*, vol. 20, no. 3, pp. 848–889, May 2006.

[8] A. Oasmaa, J. Korhonen, and E. Kuoppala, “An Approach for Stability Measurement of Wood-Based Fast Pyrolysis Bio-Oils,” *Energy & Fuels*, vol. 25, no. 7, pp. 3307–3313, Jul. 2011.

[9] J. Ritzberger, P. Pucher, N. Schwaiger, and M. Siebenhofer, “The BioCRACK Process-A Refinery Integrated Biomass-to-Liquid Concept to Produce Diesel from Biogenic Feedstock,” *Chem. Eng. Trans.*, vol. 39, pp. 1189–1194, 2014.

[10] N. Schwaiger, R. Feiner, K. Zahel, A. Pieber, V. Witek, P. Pucher, E. Ahn, P. Wilhelm, B. Chernev, H. Schröttner, and M. Siebenhofer, “Liquid and Solid Products from Liquid-Phase Pyrolysis of Softwood,” *BioEnergy Res.*, vol. 4, no. 4, pp. 294–302, Jun. 2011.

[11] N. Schwaiger, V. Witek, R. Feiner, H. Pucher, K. Zahel, A. Pieber, P. Pucher, E. Ahn, B. Chernev, H. Schroettner, P. Wilhelm, and M. Siebenhofer, “Formation of liquid and solid products from liquid phase pyrolysis.,” *Bioresour. Technol.*, vol. 124, pp. 90–4, Nov. 2012.

[12] R. Feiner, N. Schwaiger, H. Pucher, L. Ellmaier, P. Pucher, and M. Siebenhofer, “Liquefaction of pyrolysis derived biochar: a new step towards biofuel from renewable resources,” *RSC Adv.*, vol. 43, no. 0, pp. 1–6, 2013.

Modeling of fouling in Crude Oil Heat Exchangers:

Elisabeth Rammerstorfer [1], Matthäus Siebenhofer [2]
[1] Prozess Optimal Holzer Gmbh, Donaulände 11/8, 4100 Ottensheim, rammerstorfer@prozess-optimal.at
[2] Institut für Chemische Verfahrenstechnik und Umwelttechnik, Inffeldgasse 25/C/II, 8010 Graz, m.siebenhofer@tugraz.at

Abstract

Fouling is the unwanted accumulation of material on the thermal exchange surface which reduces thermal efficiency. Crude oil fouling leads to reduced energy transfer, and it causes significant additional emissions. Therefore it is a serious environmental problem. Locations of crude oil fouling and the mechanisms leading to crude oil fouling are investigated.

Introduction

Atmospheric crude oil distillation is the first step in oil refining. The whole energy input for the distillation process comes from the crude oil, which is heated in the crude preheat train and a downstream furnace. The crude preheat train usually consists of a set of heat exchangers which transfer energy from processed bottoms of the crude oil distillation column. Heat exchangers in the crude oil preheat train have a tendency to fouling.

Fouling has a substantial economic and environmental impact. The costs of crude oil fouling in the western world are estimated with 4500 million USD per year [1]. Fouling in refineries was estimated to be responsible for 2,5% of total worldwide anthropogenic CO_2-emissions in 2009 [2].

Location of crude oil fouling

Fouling is found in the whole preheat train but is severest for the last heat exchangers where high temperature levels are needed. The crude oil is usually heated up to about 200°C in the crude oil heat exchanger. Figure 1 shows the units with an indication of hot spots with distinct tendency to severe fouling.

Deposit composition for four crude oils from laboratory units were published [3]. The data shows mixed organic and inorganic deposits. The carbon content ranges between 23% to 46%, the sulphur content between 12% and 22% and the iron content between 21-49%. This clearly shows, that inorganic fouling and organic fouling occur.

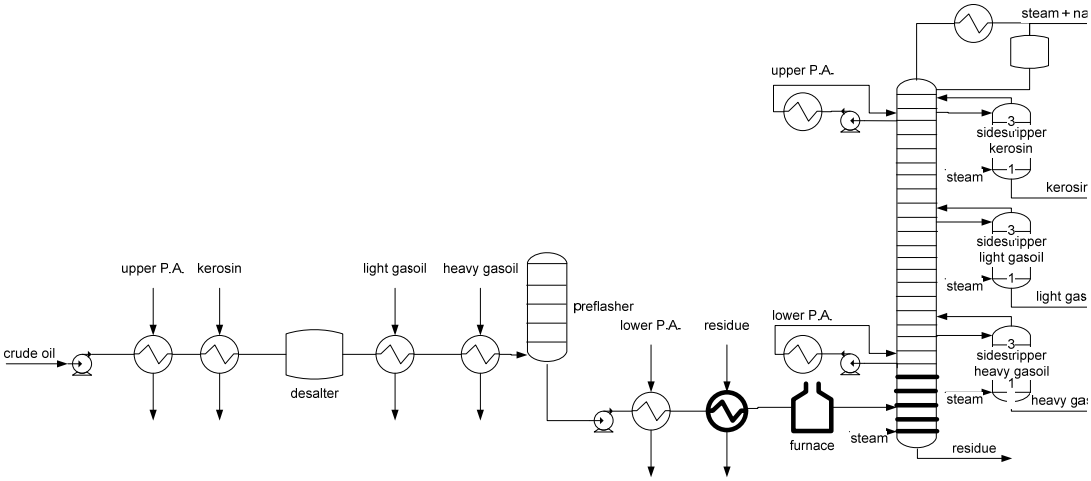

Figure 1: Preheat train and atmospheric crude oil distillation. Bold lines: hot spots with a tendency to severe fouling.

Fouling mechanisms

Several fouling mechanisms are mentioned in the literature. While biofouling and crystallisation fouling don't play an important role in crude oil fouling, asphaltene precipitation, particulate fouling, corrosion fouling and several chemical reactions are relevant mechanisms for crude oil fouling, see table 1.

	Fouling Mechanisms
Biofouling	
Fouling based on Solubility Changes	
Crystallisation Fouling	
Wax Crystallisation Fouling	
Asphaltene Precipitation	x
Particualte Fouling	x
Corrosion Fouling	x
Chemical Rection Fouling	
Autoxidation	x
Polymerization	x
Thermal Cracking	x

Table 1: Fouling mechanisms relevant for crude oil fouling

The main fouling processes are the formation of coke from asphaltenes and the formation of FeS [4]. At low temperatures inorganic fouling will be dominant, while at high temperatures organic fouling will be dominant.

Furthermore the dominant fouling mechanism seems to be a function of the processed crude oil [5]. While for low sulphur light crude oils particulate fouling and autoxidation seem

to play an important role, medium sulphur crude oils do cause corrosion fouling and asphaltene precipitation is the relevant fouling mechanism for blend heavy oils .

Outlook

Further research in the field of crude oil fouling will focus on the fouling sequence (initiation, mass transport, deposit forming, removal and aging). Variables affecting fouling like crude oil composition, temperature and shear stress (velocity) shall be identified. Based on this classification a problem definition matrix shall be developed with the goal to mitigate crude oil fouling.

Furthermore a focus will be set on heat exchanger design methodologies. Traditional design methodologies use fixed fouling factors and don't take into account that fouling is a time depended process. The consequence is the use of safety factors which lead to oversized heat transfer areas. Safety factors should in theory compensate for reduced thermal efficiency caused by fouling, however in reality worsen fouling due to smaller flow rates. In the last years a series of models have been developed, which can describe different crude oil fouling mechanisms. However, all this knowledge has so far not been fully exploited to improve design methodologies for heat exchangers. Final goal is the development of time dependent fouling coefficients in the design of heat exchangers.

Literatur

[1] ESDU (2000): "Heat exchanger fouling in the pre-heat train of a crude oil distillation unit", Data Item 00013, ESDU International plc, London.

[2] Müller-Steinhagen H., Malayeri H., Watkinson M.P. (2009): "Heat exchanger fouling: environmental impacts", Heat Transfer Engineering, 30 (10), 773-776.

[3] Wang W., Watkinson A.P. (2011): "Iron sulphide and coke fouling from sour oils: review and initial experiments", Proceedings of international conference on heat exchanger fouling and cleaning, published online: www.heatexchanger-fouling.com.

[4] Wang W., Watkinson A.P. (2011): "Iron sulphide and coke fouling from sour oils: review and initial experiments", Proceedings of international conference on heat exchanger fouling and cleaning, published online: www.heatexchanger-fouling.com.

[5] Watkinson A.P. (2005) : "Depositon from Crude Oils in Heat Exchangers", ECI symposium series, Volume RP2: Proceedings of 6th international conference on heat exchanger fouling and challenges and opportunities, Engineering conference international, Germany.

Study on ethanol-tolerant electrocatalysts for oxygen reduction reaction in alkaline media

Chakkrapong Chaiburi, Bernd Cermenek, Birgit Elvira Pichler, Christoph Grimmer, Viktor Hacker
Institute of Chemical Engineering and Environmental Technology, Fuel Cell Systems Group, Graz University of Technology, NAWI Graz, Inffeldgasse 25C, 8010 Graz, Austria
chakkrapong.chaiburi@student.tugraz.at

Abstract

Ag/C, Mn_3O_4/C and $AgMn_3O_4$/C electrocatalysts were synthesized by means of colloid method and their ethanol tolerance was investigated by cyclic voltammetry using a rotating disc electrode. Further, the morphology, structure and element composition of electrocatalysts were characterized by transmission electron microscopy and energy dispersive X-ray spectroscopy, respectively. The electrocatalysts showed ethanol-tolerance for oxygen reduction reaction in KOH electrolyte. As a result all of the electrocatalysts prevented ethanol oxidation reaction. The most recent result confirmed that the $AgMn_3O_4$/C electrocatalyst improved the catalytic activity significantly.

Introduction

There are varying reasons for performance loss during lifetime of an alkaline direct ethanol fuel cells (ADEFCs), including exposure to crossover compounds like ethanol. The fuel is ethanol containing KOH. At the cathode compartment, the oxidant is air. However, the ADEFCs efficiency is influenced by ethanol crossover via a membrane from the anode to cathode side. The ethanol are adsorbed on the active surface of the electrocatalyst, thereby blocking and preventing the adsorption of oxygen molecules. Therefore, the development of ethanol-tolerant cathode catalysts for ADEFCs is necessary. In this research, the activities of Ag/C, Mn_3O_4/C and $AgMn_3O_4$/C electrocatalysts towards oxygen reduction reaction (ORR) were investigated in a KOH/EtOH electrolyte by cyclic voltammetry using a rotating disk electrode (RDE).

Experimetal investigation

Synthesis of cathode electrocatalysts

The Ag/C electrocatalyst was synthesized by colloid method [1]. The 20 wt. % Ag/C catalyst was prepared using mixture of trisodium citrate dihydrate and $AgNO_3$, which were dissolved in ultrapure water (~18 MΩ-cm). The solution was stirred until it clearified completely. After some minutes of stirring a drop of $NaBH_4$ solution was added to the Ag solution. The colloid solution exhibited a yellowish-brown colour. Over a period of 15-20 min the whole $NaBH_4$ solution was dropped slowly to the fast stirred Ag solution. The solution became dark brown. The Ag nanomaterial was stirred for 15-30 min. Afterwards, Vulcan XC-72R carbon black as support material was dispersed in ultrapure water with an ultrasonic probe approximately 10 min and added slowly to fast stirred Ag solution. The Ag was precipitated on the carbon back. The mixture was stirred approximately 3 h. The suspension was centrifuged at 11400 rpm for 10 min. The Ag nanoparticles were filtrated and washed twice with ultrapure water. After that, the Ag/C catalyst was dried over night at 90 °C. The yield exhibited between 88% and 93%. The Mn_3O_4/C electrocatalyst [1] was

prepared by blending Vulcan XC-72R dispersed in ethanol-water mixed solution (8:2 v/v). Afterwards, $Mn(NO_3)_2{\cdot}4H_2O$ was added and the solvent of the slurry was removed by stirring over night at 60 °C. Finally, the Mn_3O_4/C was calcined in a furnace at 400 °C for 2 h under N_2 atmosphere (heating rate 5 °C min^{-1}). The $AgMn_xO_y$ electrocatalyst [1, 2, 3] was obtained by two-step synthesis. In the first step $AgNO_3$ and $KMnO_4$ (molar ratio 1:1) were dissolved in ultrapure water at 80 °C, which was acidified with a drop of 65% HNO_3. The solution was slowly cooled to 0 °C. The suspension came dark-blue needles and precipitated. The $AgMnO_4$ was filtrated, washed with ice ultrapure water and dried. In the next step, the $AgMn_3O_4$/C catalyst was synthesized dissolving of $AgMnO_4$ in ultrapure water at ca. 40-50 °C. An approximate amount of Vulcan XC-72R carbon black was added. The black slurry was dispersed with ultrasonic for 15 min. After that, the water in black slurry was slowly evaporated at constant 60 °C. Finally, the dry powder was calcined in a tubular furnace for 2 h at 400 °C under N_2 atmosphere with a heating rate 5 °C min^{-1} and $AgMn_3O_4$/C electrocatalyst obtained.

Characterisation of cathode electrocatalysts

The morphology of Ag/C, Mn_3O_4/C and $AgMn_3O_4$/C electrocatalysts were determined by transmission electron microscopy (TEM), which is a type of electron microscope that can transmit via an ultra-thin specimen and present high resolution images of the sample surface. The element compositions of Ag/C, Mn_3O_4/C and $AgMn_3O_4$/C electrocatalysts were measured by energy dispersive X-ray spectroscopy (EDX).
The activities of all electrocatalysts were determined by cyclic voltammetry using a rotating disk electrode (RDE). All electrochemical measurements were carried out with a standard three-electrode configuration in a 0.1 M KOH electrolyte at 30˚C. For the experimental setup, a reversible hydrogen electrode (RHE) as reference electrode , a platinum electrode as counter electrode and a rotating disk electrode (RDE) as working electrode were used. The electrocatalyst loading on the RDE was 56 μg cm^{-2}. A commercial Pt/C electrocatalyst was used as reference.

Physical characterisation of $AgMn_3O_4$/C catalysts

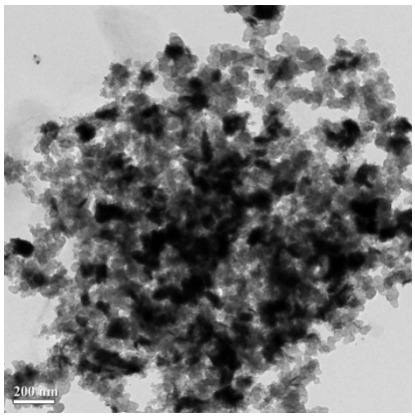

Fig. 1. *Transmission electron microscopy (TEM) of the $AgMn_3O_4$/C electrocatalyst.*

The TEM image shows three morphologies, including (1) dark spherical particles, (2) gray spherical particles and (3) branch-like particles. The dark spherical particles are attributed to Ag or Mn and the gray spherical particles as activated carbon. The branch-like particles are likely manganese oxides [4].

Electrochemical measurements

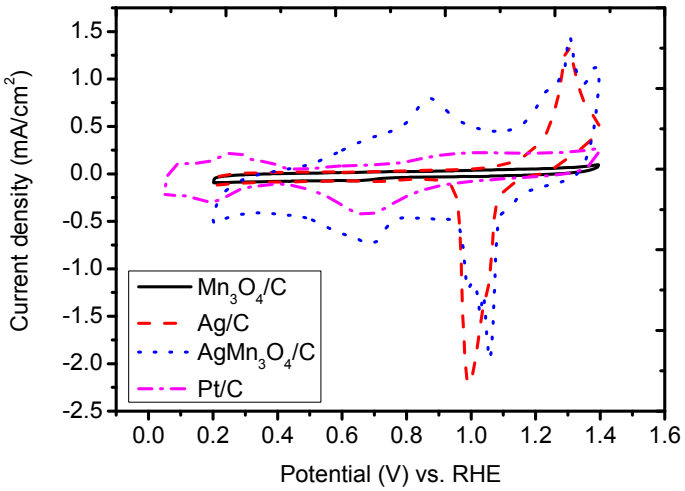

***Fig. 2**. Base cyclic voltammograms of Ag/C, Mn_3O_4/C and $AgMn_3O_4$/C electrocatalysts in a deaerated 0.1 M KOH at 30 ℃, with sweep rate of 10 mV s^{-1}.*

The $AgMn_3O_4$/C electrocatalysts exhibits overlapping of the oxidation peaks of Ag and Mn_3O_4 (at a potential of 1.2-1.4 V). However, the reduction peak of $AgMn_3O_4$ (at a potential of 0.9-1.1 V) is higher than the reduction peak of Ag (Fig. 2). The $AgMn_3O_4$/C electrocatalysts are believed to be advantageous for improving ORR activity [5].

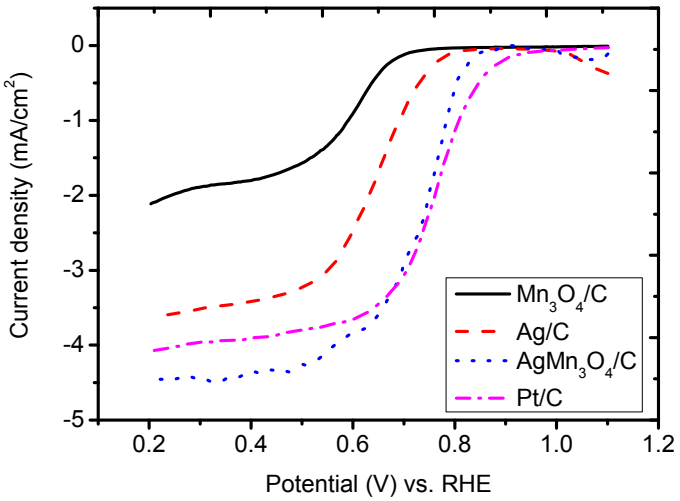

***Fig. 3**. Linear potential scan curves of Pt/C, Ag/C, Mn_3O_4/C and $AgMn_3O_4$/C electrocatalysts on a rotating disk electrode in an O_2 saturated 0.1 M KOH at 30 ℃, with a sweep rate of 10 mV s^{-1} and a rotation rate of 1600 rpm.*

ORR polarisation curves of Ag/C, Mn_3O_4/C and $AgMn_3O_4$/C electrocatalysts under an O_2 atmosphere 0.1 M KOH electrolyte at 30 °C with a scan rate of 10 mV s^{-1} and a rotating rate of 1600 rpm are shown in Figure 3. The initial ORR polarisation curves of the electrocatalysts possess a well defined diffusion-limiting current at a potential between 0.20 and 0.70 V, followed by a region under mixed kinetic-diffusion control at 0.70 < E < 0.90 V (Fig. 3). The performance of the $AgMn_3O_4$/C electrocatalyst was compared to Pt/C electrocatalyst and found to be nearly the same in 0.1 M KOH at 30 °C.
Electrocatalytic activities towards oxygen reduction of Pt/C, Ag/C, Mn_3O_4/C and

$AgMn_3O_4/C$ electrocatalysts in a 0.1 M KOH with different ethanol concentrations are shown in Figure 4.

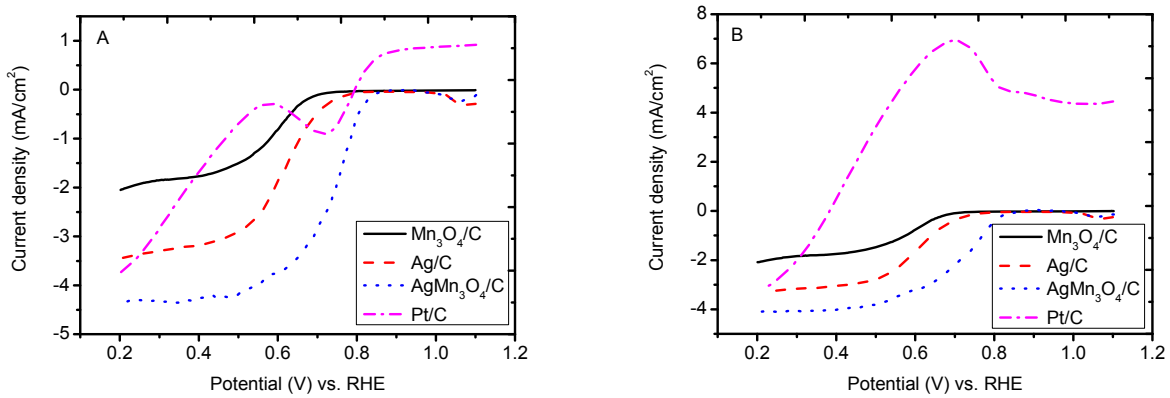

Fig. 4. *(A) Linear potential scan curves of Pt/C, Ag/C, Mn_3O_4/C and $AgMn_3O_4/C$ on a rotating disk electrode in an O_2 saturated 0.1 M KOH with 0.1 M ethanol at 30 ℃, a sweep rate of 10 mV s^{-1} and a rotation rate of 1600 rpm. (B) Linear potential scan curves of Pt/C, Ag/C, Mn_3O_4/C and $AgMn_3O_4/C$ on a rotating disk electrode in an O_2 saturated 0.1 M KOH with 1.0 M ethanol at 30 ℃, a sweep rate of 10 mV s^{-1} and a rotation rate of 1600 rpm.*

The effect of various ethanol concentrations in alkaline electrolyte on the performance of oxygen reduction of Pt/C working electrode is shown in Figure 4. The results of linear potential scan curves of Pt/C electrocatalyst exhibits ethanol oxidation (at a potential of 0.4-0.75 V) in the presence of ethanol. The opposite way, Ag/C, Mn_3O_4/C and $AgMn_3O_4/C$ electrocatalysts are tolerant towards ethanol for oxygen reduction reaction. This confirms the result of $AgMn_3O_4/C$ electrocatalyst showing significantly enhancement of its ORR activity (Fig.4) towards oxygen reduction.

Conclusion

Ag/C, Mn_3O_4/C and $AgMn_3O_4/C$ electrocatalysts were investigated for oxygen reduction reaction for cathodes of alkaline fuel cells in the presence of different ethanol-concentrations with KOH electrolyte. The electrocatalysts did not oxidise ethanol oxidation and therefore are suitable as cathode catalysts in alkaline direct ethanol fuel cells. $AgMn_3O_4/C$ electrocatalysts showed the best performance for oxygen reduction reaction in presence of ethanol.

References

[1] Q. Tang, L. Jiang, J. Qi, Q. Jiang, S. Wang, G. Sun, Applied Catalysis B: Environmental 104 (2011) 337-345.
[2] Q. Wu, L. Jiang, L. Qi, L. Yuan, E. Wang, G. Sun, Electrochimica Acta 123 (2014) 167-175.
[3] C. Grimmer, R. Zacharias, M. Grandi, B. E. Pichler, I. Kaltenböck, F. Gebetsroither, J. Wagner, B. Cermenek, S. Weinberger, S. Schenk, V. Hacker, Journal of the Electrochemical Society 163 (2016) 278-283.
[4] W. Sun, A. Hsu, R. Chen, J. Power Sources 196 (2011) 627-635.
[5] S. Park, H. Lim, Y. Kim, ACS Catal. 5 (2015) 3993-4002.

bioCH4.0
Biogas Upgrading zu Biomethan im kontinuierlichen Temperaturwechsel Adsorptionsprozess

Julius Pirklbauer[1], Gerhard Schöny[2], Hermann Hofbauer[3]

[1,2,3] Institute of Process Engineering, Vienna University of Technology, Getreidemarkt 9/166, 1060 Vienna, Austria.
[1]julius.pirklbauer@tuwien.ac.at, [2]gerhard.schoeny@tuwien.ac.at,
[3]hermann.hofbauer@tuwien.ac.at

Kurzfassung

Eine an der TU Wien entwickelte Technologie zur effizienten CO_2 Abscheidung aus Rauchgasströmen wird im Rahmen des FFG-Projekts bioCH4.0 auf ihre Eignung zur Biogasaufbereitung untersucht. Die Technologie basiert auf einem kontinuierlich betriebenen Adsorptionsprozess, bei dem selektive CO_2 Adsorbens innerhalb eines mehrstufigen Wirbelschichtreaktorsystems zum Einsatz kommen. Die Technologie verspricht wesentliche Effizienzsteigerungen und Kostenreduktionen gegenüber bestehenden Aufbereitungstechnologien im Bereich der Rauchgasreinigung und soll nun für den Einsatz im Bereich Biogasaufbereitung adaptiert werden. Hierzu müssen geeignete Adsorptionsmittel identifiziert und das bestehende Reaktorsystem entsprechend adaptiert werden. Weiter werden innovative Wärmeintegrationsmaßnahmen untersucht die einen noch effizienteren Betrieb des Adsorptionsprozesses ermöglichen sollen. Abschließend soll eine bestehende Laboranlage der TU Wien adaptiert werden um die Aufbereitung von realem Biogas im kontinuierlichen Adsorptionsprozess im kleinen Maßstab zu demonstrieren. Die praktischen Ergebnisse des Projekts dienen schließlich als Inputs bei einer techno-ökonomischen Bewertung der Technologie und beim Vergleich mit bestehenden Technologien zur Biogasaufbereitung.

Einleitung

Biogas wird derzeit primär zur Strom- und Wärmeerzeugung direkt am Erzeugungsort eingesetzt da das erzeugte Gas einen zu geringen Reinheitsgrad aufweist um als Erdgasersatz in das Gasnetz eingespeist werden zu können. Aufgrund der zunehmenden erneuerbaren Erzeugungskapazitäten am Strommarkt ist eine alternative Nutzung des Biogases in Form einer Aufbereitung zu Bio-Methan mit einem Methangehalt von >95% sinnvoll. Bei der Aufbereitung von Biogas zu Bio-Methan hat der Schritt der CO2-Abtrennung maßgeblichen Einfluss auf die Gesamt-Effizienz bzw. die Gesamt-Kosten der Biogasanlage. Als derzeitiger Stand der Technik für die CO2-Abtrennung von Biogas zu Biomethan werden derzeit hauptsächlich Verfahren wie Druckwasser- und Aminwäsche, Druckwechseladsorption und Membrantrennverfahren eingesetzt. Diese drei Technologien sind in dem derzeit noch sehr kleinen Markt an Methanaufbereitungen gleichmäßig aufgeteilt. [1]

Methode

Von den angeführten Verfahren erscheint vom technischen Standpunkt aus die Aminwäsche (AW) am vergleichbarsten, sodass im Rahmen des Projektes bioCH4.0 versucht wird, die Vorteile des AW-Verfahrens möglichst beizubehalten und gleichzeitig die

wesentlichen Nachteile weitgehend zu beseitigen. Auf Basis von vielversprechenden Vorversuchen wird ein Temperaturwechseladsorptionsprozess (TSA) mit mehrstufigem Wirbelschichtdesign auf Basis eines festen Aminadsorbens eingesetzt. Durch den Einsatz von Feststoffen anstelle von Wasser fällt der Energieverbrauch im Vergleich zur konventionellen AW signifikant geringer aus. In Kombination mit einer neuartigen in den Prozess integrierten Wärmeverschaltung unter Nutzung eines innovativen Wärmetauscherdesigns und einer Wärmepumpe werden die Energieeinsparungen weiter unterstützt.

In erster Linie werden Adsorptionstest in kleinen Testapparaturen durchgeführt um das Adsorptionsverhalten von CO_2 und CH_4 der einzelnen Materialien zu bestimmen. Auf Basis dieser Ergebnisse wird ein mathematisches Modell entwickelt um die theoretischen Abscheideleistungen zu berechnen. Durch die Nachbildung dieses Prozesses können erste Abschätzungen zu Materialbedarf und Energieverbrauch des Prozesses für größere Anlagen getroffen werden um einen Vergleich mit bestehenden Verfahren zu ermöglichen.

Im Jahr 2011 hat die TU Wien die Entwicklung eines TSA Verfahrens mit Feststoffen zur Abscheidung von CO_2 aus Abgasströmen begonnen und über die letzten Jahre weiter optimiert. Mittlerweile verfügt sie über eine voll funktionsfähige kontinuierliche mobile mehrstufige Wirbelschicht Adsorptionsanlage (siehe Abbildung 1) welche zu unterschiedlichsten Abscheideexperimenten eingesetzt werden kann.

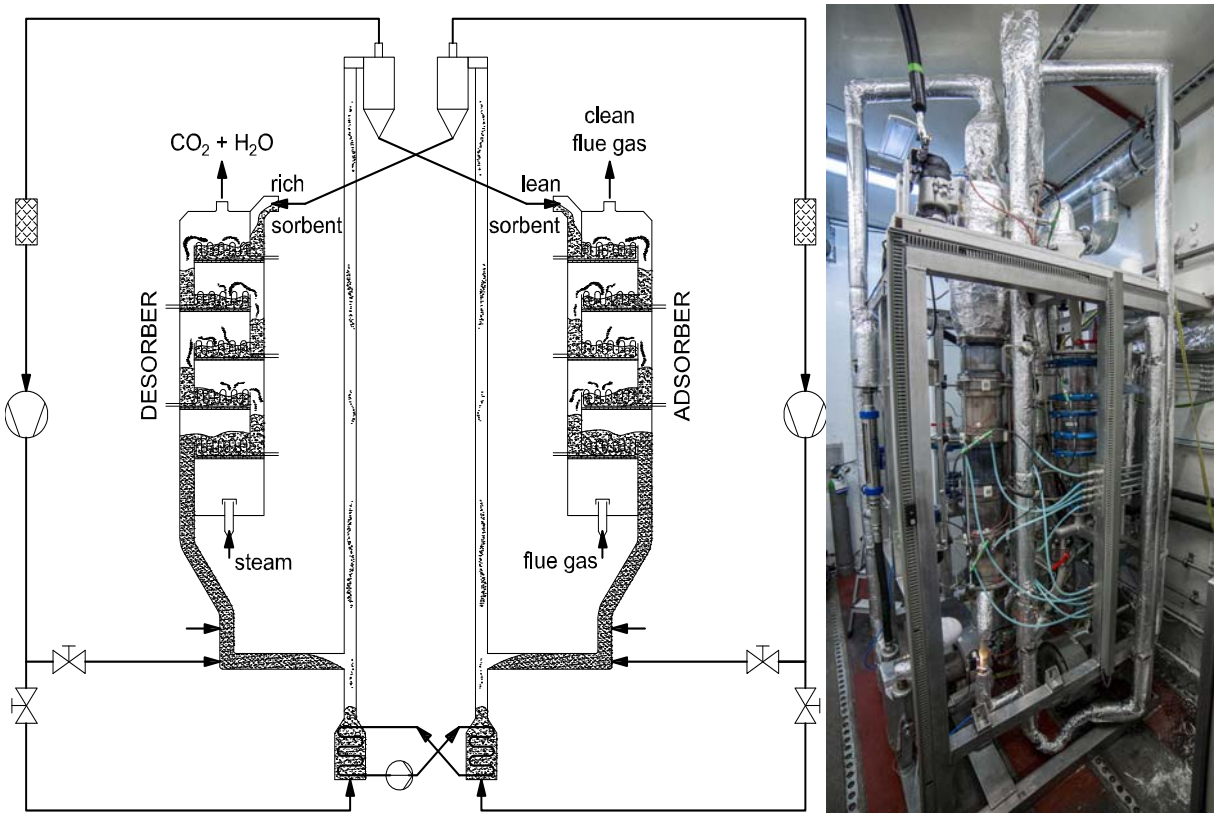

Abbildung 1: Mehrstufige zirkulierende Wirbelschichtanlage auf Prinzip der Temperaturwechseladsorption [2], [3]

Im Rahmen des Projekts soll die Testanlage für die zusätzlichen Anforderungen der Experimente zur Abscheidung von CO_2 aus Biogas vorbereitet und ausgebaut werden.

Experimente

Nach Vorbereitung der Testanlage wird sie zu einer in Betrieb befindlichen Biogasanlage transportiert um den Abscheideprozess mit realem Biogas zu testen und die Reinigungsleistung von Methan zu validieren.

Abbildung 2: mobile TSA Anlage [4]

Ergebnisse und Zusammenfassung

Übergeordnetes Ziel ist es, am Ende des Projektes ein effizienteres und deutlich kostengünstigeres Verfahren als die bisher eingesetzten Technologien zur Erzeugung von Bio-Methan aufgezeigt zu haben. Durch einen techno-ökonomischen Vergleich mit den derzeit bestehenden Technologien besteht die Chance den Prozess in Form von größeren Demonstrationsanlagen zu bauen und in weiterer Zukunft als konkurrenzfähige Technologie im Bereich der Biomethananlagen anbieten zu können.

Literatur

[1] Fachagentur Nachwachsende Rohstoffe e.V (FNR), 2015. http://www.fnr.de/nachwachsende-rohstoffe/bioenergie/biogas/)

[2] Pröll, T., Schöny, G., Sprachmann, G., Hofbauer, H., 2016. Introduction and evaluation of a double loop staged fluidized bed system for post-combustion CO_2 capture using solid sorbents in a continuous temperature swing adsorption process. Chem. Enc. Sci. 141, 166-174.

[3] Schöny, G., Zehetner, E., Fuchs, J., Pröll, T., Sprachmann, G., Hofbauer, H., 2016. Design of a bench scale unit for continuous CO2 capture via temperature swing adsorption – Fluid-dynamic feasibility study. Chem. Eng. Res. Des. 106, 155-167.

[4] Schöny, G., Fuchs, J., Pröll, T., Sprachmann, G., van Mossel, G., Moene, R., Hofbauer, H., 2015. A novel stacked fluidized bed system for continuous CO_2 capture via TSA. Presented at the COSIA Innovation Summit, Mar 31-Apr 2, Banff, Alberta, Canada.

Thermo Chemical Recuperation of diesel exhaust gas

Michael Derntl, Martin Schüßler
AVL List GmbH, Hans-List Platz 1, 8020 Graz
Michael.Derntl@avl.com, Martin.Schuessler@avl.com

Abstract

Thermo Chemical Recuperation (TCR) through reforming reactions is a promising way to raise the efficiency of an internal combustion engine [1]. The feasibility of the low temperature reforming (300-500°C) of Ethanol is investigated at various O/C and S/C ratios. It can be shown, that the reforming of Ethanol is favored with high temperatures and that the O/C ratio determines the heat of reaction primarily. It was possible to reform Ethanol in the presence of oxygen and water to a combustible syngas, which has a 4% higher heating value than the original feedstock.

Introduction

Currently internal combustion engines (ICE) are the mayor consumer of fossil fuels in matters of mobility. Since in the short to medium term future fossil fuels will still be in use, there is a lot of interest in the development of cleaner and more efficient vehicle powertrains [1], [2]. Actually only 30-40% of the fuel's energy can be converted to mechanical work in a vehicle [4]. That means 60-70% of the fuel's energy is still lost as waste heat through the coolant, friction or the exhaust gas. This loss of energy brings a big potential to systems that are able to convert waste heat to usable energy. If the waste heat can be recovered, the efficiency of an ICE can be significantly improved. Several technologies for efficiency improvement have been investigated in the last few decades [5]. Typical systems for waste heat recovery are the Rankine Cycle (RC), Thermoelectric Generation (TEG), Turbocharging systems and Thermo Chemical Recuperation (TCR) [6], [7], [8]. Also Piezoelectric Generation through devices, that convert vibrations to electric energy, have been mentioned in literature [9].
The main focus of research is a TCR system, where the waste heat of an automotive exhaust gas is used to run additional reforming reactions in a separate reactor. As a feedstock for the reforming process any hydrocarbons are suitable. The main purpose of the reforming process is to produce a combustible gaseous mixture (syngas) consisting of H_2, CO, CH_4 and also CO_2, H_2O. The reforming reactions may take place directly in the hot exhaust gas recirculation pipe (EGR), where the reactants for reforming reactions are provided e.g. H_2O, CO_2 and O_2. In addition to EGR, a separate heat exchanger can provide even more heat for the reformer. The basic flow sheet of the investigated TCR system is shown in *Illustration 1.*

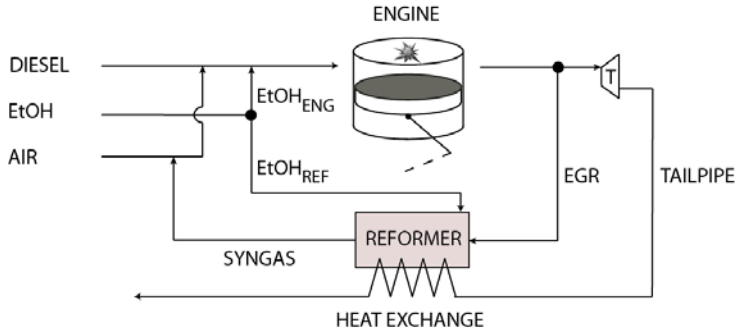

Illustration 1: TCR System

The TCR system works with diesel as a primary fuel and also with a second fuel, in this case with Ethanol (EtOH) as a renewable fuel. EtOH is fed to the reformer but can also be used for combustion. When the system is running in the loop with opened EGR valve, the engine will be fed with additional syngas. If the overall reaction in the reformer is endothermic, waste heat will be converted to chemical energy and the lower heating value (LHV) of the syngas will be increased in comparison to the LHV of the original biofuel [10]. The increase of LHV and the addition of syngas to the engine may have positive effects on the overall systems efficiency and emissions [11].

Methodic

The simulation of the TCR system shows the dependencies between EGR flow, air to fuel ratio (λ) and the EtOH/Diesel ratio. As an important output information, the theoretical gain in efficiency (Δη) of the system can be forecasted. The simulation assumes ideal combustion in the engine and 100% conversion in the adiabatic reformer. The assumed overall reforming mechanism (*Table 1*) consists of (1), the combustion of ethanol with excess oxygen from EGR and (2), a combination of thermal decomposition and steam reforming reactions [10], [12], [13]. The x value in reaction (2) defines the ratio between decomposition and steam reforming and is assumed to 0.7 as a constant. The reforming mechanism ends by reaching water gas shift equilibrium. The formation of coke and other byproducts is neglected in this simulation.

	Reactions	$\Delta H_R^0\ [kJ/mol]$
(1)	$C_2H_5OH + 3O_2 \longrightarrow 2CO_2 + 3H_2O\ (g)$	-1278
(2)	$C_2H_5OH + x\ H2O\ (g) \longrightarrow (2x + 1 - x)\ CO + (4x + 1 - x)\ H_2 + (1 - x)\ CH_4$	$49\ (1 - x) + 254\ x$
(3)	$CO + H_2O\ (g) \longrightarrow CO_2 + H_2$	-41

Table 1: EtOH reforming reactions, heat of reaction ΔH_R°

To examine the quality of the reforming process, the gain of the LHV (ΔLHV) can be calculated as a representative percentage number. In a next step ΔLHV enables the calculation of the increase in efficiency (Δη) of the whole TCR system. The calculation is done with *equations 1* and *2*.

$$\Delta LHV\ [\%] = \frac{LHV_{SYNGAS}}{LHV_{EtOH,REF}} - 1$$

Equation 1: gain of Heating Value ΔLHV [%]

$$\Delta\eta\ [\%] = \frac{\Delta LHV * LHV_{EtOH,REF} + LHV_{Diesel} + LHV_{EtOH}}{LHV_{EtOH} + LHV_{Diesel}} - 1$$

Equation 2: gain in efficiency Δη [%]

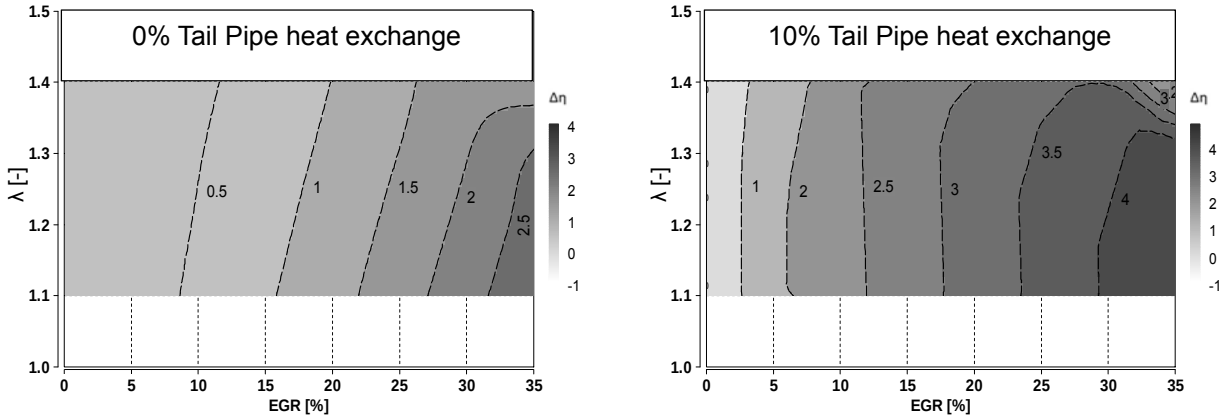

Illustration 2: Δη= f (EGR,λ)

Illustration 2 shows the influence of the EGR rate and the λ value on Δη. A positive Δη value implies, that the overall reforming reaction is endothermic and it can be seen, that Δη is theoretically positive in the observed field of parameters. With a higher EGR rate, more heat can be provided for the reforming reactions, but also more O_2 is provided forcing exothermic reactions. The amount of oxygen can either be controlled by the EGR rate or the λ value. In this field Δη reaches values around 2.5-3% (*Illustration 2*, left side). If heat can be transferred from Tail Pipe through additional exchange, even more heat can be provided for the reforming process. It can be seen, that additional heat exchange transforms the dependencies of EGR and λ extensively and Δη changes also. Theoretically at high λ values and EGR rates it is possible to feed all available EtOH to the reformer. Hence the combustion engine will run with only Diesel and Syngas. In this case the highest Δη values around 4-5% can be achieved (*Illustration 2*, right side).

Experiments

The aim of the experiments is investigating the feasibility of the reforming of EtOH in the presence of oxygen and water. The maximum amount of oxygen for endothermic reforming reactions is especially of interest.
The experiments are done on a synthesis-gas test bed, where any exhaust gas can be simulated physically in its composition, temperature and volumetric flow. The EtOH is injected directly in the hot gas stream for evaporation and is transported through a mixing section to the reformer catalyst. The reformer itself consists of a monolithic PGM catalyst sample (d=38mm, L=80mm, 600 cpsi, 90 g/in³ PGM load), which is built in a steel pipe. On the steel pipe there are different positions to measure the temperature profile and also the inlet and outlet concentration of the gaseous species. The analysis of the gaseous species is done with the *Agilent Micro GC 490*. *Illustration 3* shows a picture of the reformer and the test bed. The whole system is insulated additionally to minimize the heat loss of the reformer.

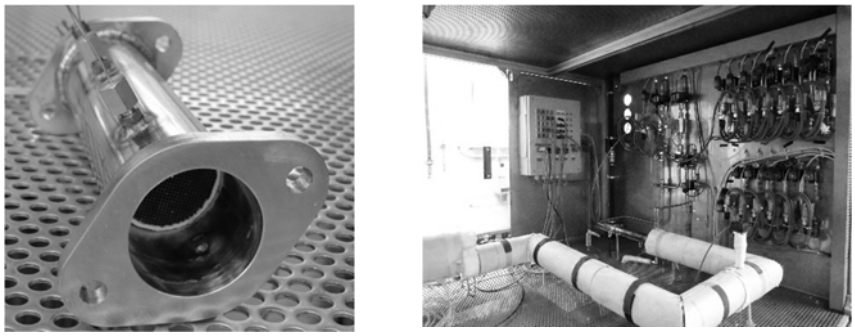

Illustration 3: Reformer (left); test bed (right)

Results

The reforming of EtOH gives a syngas with the main products H_2, CO, CH_4 and CO_2 and also H_2O. *Illustration 4* shows the dry product distribution as a function of temperature at O/C=0 and S/C=4. It can be seen, that the moles of formed products follow the scale H_2>CO>CH>CO_2 and change with temperature. Without the presence of oxygen it is easy to run endothermic steam reforming reactions in a temperature range between 300°C and 450°C. In reality diesel exhaust gas often includes also reactive oxygen, so that O/C=0 is very unlikely. Experiments at various O/C ratios and constant S/C=3 (*Illustration 5*) show, that the addition of oxygen has a huge influence on the heat of reaction (ΔH_R). A small O/C ratio of 0.05 can even support endothermic reactions through additional heat. On the one hand the conversion of EtOH increases with increasing O/C ratio up to **70%** but also ΔH_R is shifted towards smaller values and will get negative (exothermic). It can be seen, that the temperature and the O/C ratio are the key parameters for endothermic reforming.

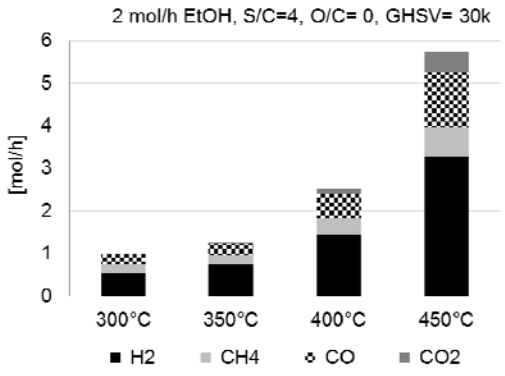

Illustration 4: Product distribution vs. T [°C]

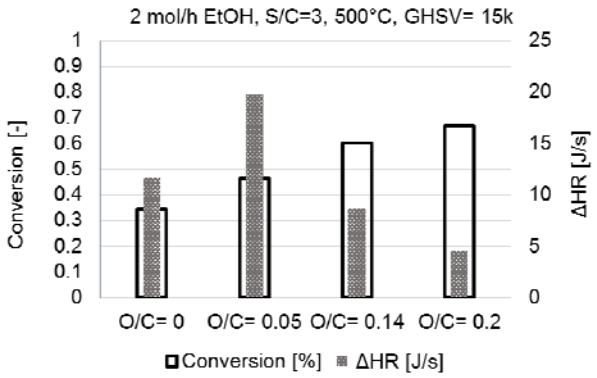

Illustration 5: Conversion and ΔHR vs. O/C

As exhaust gas also contains CO_2, experiments with a real exhaust gas were conducted on the reforming test bed as well. The gas composition and the amount of injected $EtOH_{REF}$ were chosen according to simulation results as factor scale. In this operating point the engine was running solely with diesel and syngas, 0% additional heat exchange was assumed. *Table 2* shows the simulated TCR operating point and the settings for the experiment.

TCR Simulation							
Engine				Exhaust gas composition			
λ	EGR	Diesel	$EtOH_{REF}$	O_2	N_2	CO_2	H_2O
1.2	35%	1.2 kg/h	4 kg/h	1.7%	69.2%	11%	18%
Experiment							
GHSV= 18k		T_{IN}= 500°C	0.28 kg/h EtOH		O/C=0.2		S/C=1

Table 2 : simulated TCR, Settings experiment

At this set of parameter the reforming of EtOH results the best composition of syngas and also the highest conversion is obtained. The overall reforming reaction is endothermic and waste heat can be converted to chemical energy. The calculated ΔLHV value from the experiment is **4%** and yields a Δη value of **1.5%**. The conversion of EtOH was **75%**. If there was additional heat exchange e.g. through Tail Pipe, the Δη value and the conversion would even be higher. This would make the reforming more profitable.
Illustration 6 shows the complete composition of syngas from the experiment and the simulation. Although the EtOH conversion was not 100% in the experiment, the syngas composition comes quite close to the simulative composition. Within this experiment, the limit for endothermic reforming (O/C=0.2, S/C=1) has been reached. With a higher O/C value it was not possible to run endothermic reforming, even when the S/C ratio was 4.

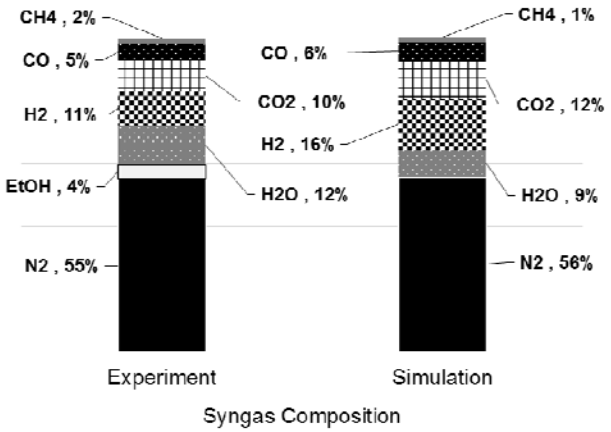

Illustration 6: Experiment vs.Simulation

Typically the exhaust gas of a diesel engine provides even higher oxygen levels than 1.7%, which restricts the reformer system to only a few engine operating points at the moment.

Summary

The reforming of EtOH was investigated as part of a TCR system. Theoretically high Δη values up to 4-5% can be achieved, depending on λ values, EGR rates and additional heat exchange. In reforming experiments it was found, that endothermic steam reforming is possible at temperatures from 300-500°C. At the presence of oxygen, the O/C ratio in the reformer determines the heat of reaction, whereas the S/C plays a subordinated role to suppress exothermic reactions. The maximum O/C ratio was 0.2, which resulted in a Δη value of 1.5% at 75% EtOH conversion. In conditions with low oxygen content in the exhaust gas, the reforming process will be endothermic and increase the systems efficiency.

Acknowledgement

Michael Derntl and Martin Schüßler give special thanks to CEET (Graz University of Technology), Institute for Powertrains and Automotive Technologies (Vienna University of Technology) and OMV Refining & Marketing GmbH for the cooperation and the support. This work was funded by the Austrian Research Promotion Agency (FFG).

Literature

[1] V. K. Chakravarthy, C. S. Daw, J. a. Pihl, and J. C. Conklin, “Study of the theoretical potential of thermochemical exhaust heat recuperation for internal combustion engines,” *Energy and Fuels*, vol. 24, no. 3, pp. 1529–1537, 2010.

[2] R. Horng and M. Lai, “Waste Heat Recycling for Fuel Reforming,” *Mech. Eng.*, pp. 355 – 380, 2012.

[3] R. Saidur, M. Rezaei, W. K. Muzammil, M. H. Hassan, S. Paria, and M. Hasanuzzaman, “Technologies to recover exhaust heat from internal combustion engines,” *Renew. Sustain. Energy Rev.*, vol. 16, no. 8, pp. 5649–5659, 2012.

[4] C. Yu and K. T. Chau, “Thermoelectric automotive waste heat energy recovery using maximum power point tracking,” *Energy Convers. Manag.*, vol. 50, no. 6, pp. 1506–1512, 2009.

[5] G. S. Xingyu Liang, Xiangxiang Wang, “A review and selection of engine waste heat recovery technologies using analytic hierarchy process and grey relational analysis,” *Int. J. energy Res.*, vol. 31, no. August 2007, pp. 135–147, 2007.

[6] A. Domingues, H. Santos, and M. Costa, “Analysis of vehicle exhaust waste heat recovery potential using a Rankine cycle,” *Energy*, vol. 49, no. 1, pp. 71–85, 2013.

[7] R. Kumar, A. Sonthalia, and R. Goel, “Experimental study on waste heat recovery from an IC engine using thermoelectric technology,” *Therm. Sci.*, vol. 15, no. 4, pp. 1011–1022, 2011.

[8] L. Tartakovsky, V. Baibikov, M. Gutman, A. Poran, and M. Veinblat, “Thermo-Chemical Recuperation as an Efficient Way of Engine’s Waste Heat Recovery,” *Appl. Mech. Mater.*, vol. 659, pp. 256–261, Oct. 2014.

[9] J. S. Jadhao and D. G. Thombare, “Review on Exhaust Gas Heat Recovery for I . C . Engine,” *Int. J. Eng. Innov. Technol.*, vol. 2, no. 12, pp. 93–100, 2013.

[10] P. Leung, A. Tsolakis, J. Rodríguez-Fernández, and S. Golunski, “Raising the fuel heating value and recovering exhaust heat by on-board oxidative reforming of bioethanol,” *Energy Environ. Sci.*, vol. 3, no. 6, p. 780, 2010.

[11] a. Abu-Jrai, J. Rodríguez-Fernández, a. Tsolakis, a. Megaritis, K. Theinnoi, R. F. Cracknell, and R. H. Clark, “Performance, combustion and emissions of a diesel engine operated with reformed EGR. Comparison of diesel and GTL fuelling,” *Fuel*, vol. 88, no. 6, pp. 1031–1041, 2009.

[12] E. D. Sall, D. A. Morgenstern, J. P. Fornango, J. W. Taylor, N. Chomic, and J. Wheeler, “Reforming of Ethanol with Exhaust Heat at Automotive Scale,” 2013.

[13] D. A. Morgenstern and J. P. Fornango, “Low-Temperature Reforming of Ethanol over Copper-Plated Raney Nickel : A New Route to Sustainable Hydrogen for Transportation,” no. 16, pp. 1708–1716, 2005.

Methanation of CO_2 from biogas for Power-to-Gas application

Ana Roza Medved, Philipp Biegger, Markus Lehner
MU Leoben, Lehrstuhl für Verfahrenstechnik des industriellen Umweltschutzes,
Franz-Josef-Straße 18, 8700 Leoben
ana.medved@unileoben.ac.at, philipp.biegger@unileoben.ac.at,
markus.lehner@unileoben.ac.at

Abstract

Power-to-Gas technology is a storage option for renewable energies, allowing the storage of surplus electrical energy. It links the power grid with the gas grid, by converting surplus power into a compatible gas via methanation, wherein hydrogen produced by water electrolysis is reacted with carbon dioxide source to produce synthetic methane (SNG) [1].

In the frame work of the two research projects “EE-Methan aus CO_2” and “OptFuel” an experimental methanation plant was constructed, where also the “OptFuel” project contents were examined. The overall process concept was later proved in a pilot plant with other project partners.

Introduction

The overall aim of the RSA project “OptFuel” is the development of an optimized process for production of energy, from biogenic wastes with recovery of surplus electrical energy from renewable energy sources. It is a combination of biotechnological processes carried out with chemical methanation and gas treatment with membrane technology (see Fig. 1). Biogas with CH_4, H_2 and CO_2 composition is produced by fermentation of biogenic wastes. Hydrogen from water electrolysis is added to the biogas, and methanation takes place in a catalytic reactor, producing high concentrations of CH_4. In the final step produced gas goes through gas treatment, where the unreacted gases CO_2 and H_2 are return to the process and generated CH_4 can be stored in the natural gas grid [2].

Methanation

Methanation is a strong exothermic reaction where the hydrogenation of CO_2 or CO occurs, utilising group VIII metal based catalysts (Fe-, Co- and Ni-) with the overall reaction:

CO_2 (g) + $4H_2$ (g) ↔ CH_4 (g) + $2H_2O$ (g) ΔH_R^0 = -165 kJ/mol [3]

Equation 1: Synthesis of methane from carbon dioxide and hydrogen.

Proof of concept

Project “OptFuel” started in the year 2013 with duration of 3 years, where the final stage of the project took place at the sewage-treatment facility in Asten with cooperation between *Lehrstuhl für Verfahrenstechnik des industriellen Umweltschutzes, MU Leoben, Energieinstitut an der JKU Linz, Institut für Verfahrenstechnik, Umwelttechnik und Technische Biowissenschaften, TU Wien* and *Christof Industries GmbH.*

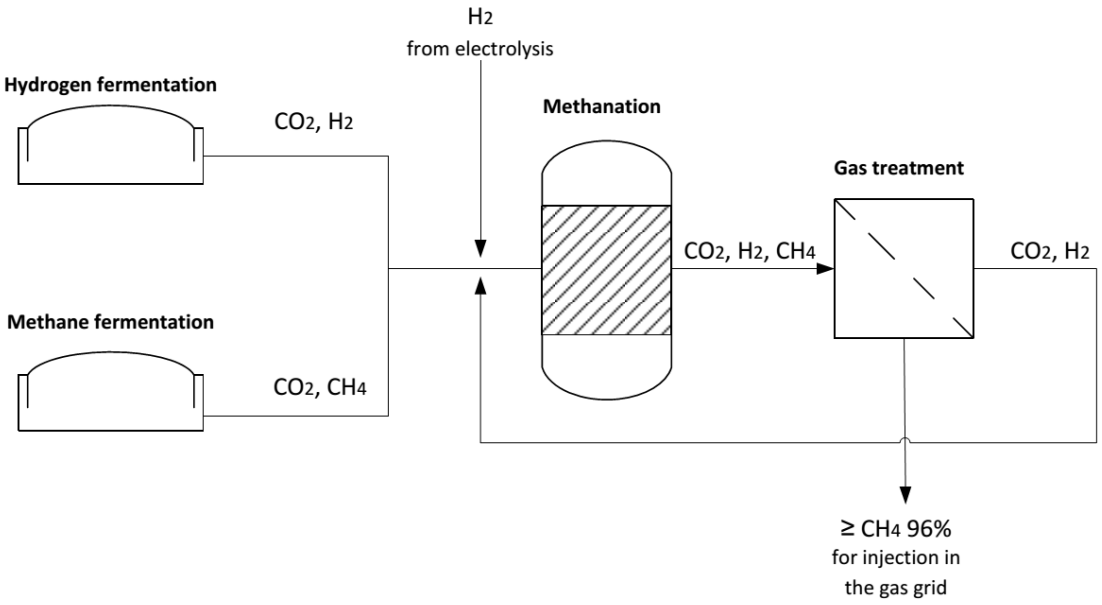

Figure 1: The process concept of fermentation coupled with chemical methanation

The overall process was realized in a continuously operated pilot plant. Biogas was produced using hydrogen and methane fermentation, leading to the chemical methanation of biogas and, in the end, gas treatment of the produced gas. This provided a basis for a possible first demonstration plant [2].

Experimental

A series of Methanation experiments were carried out on commercially used nickel bulk catalyst of 0,25 L volume on the lab scale, where one fixed bed system reactor was used. A gas mixture of H_2, CO_2 and CH_4 has been converted at different GHSVs (Gas Hourly Space Velocity) between 2000/h and 6000/h; flow rates (8,5; 12,5; 16,7;

21,0 and 25,0) NL/min, pressures (1, 5, 7,5 and 10 bar) and H_2/CO_2 ratios. Temperature in the reactor was kept constant, between 350-400 °C.

Results

In the diagram 1, the achieved methane concentrations (dry), CO_2 conversion, yield and selectivity of CH_4 are presented.

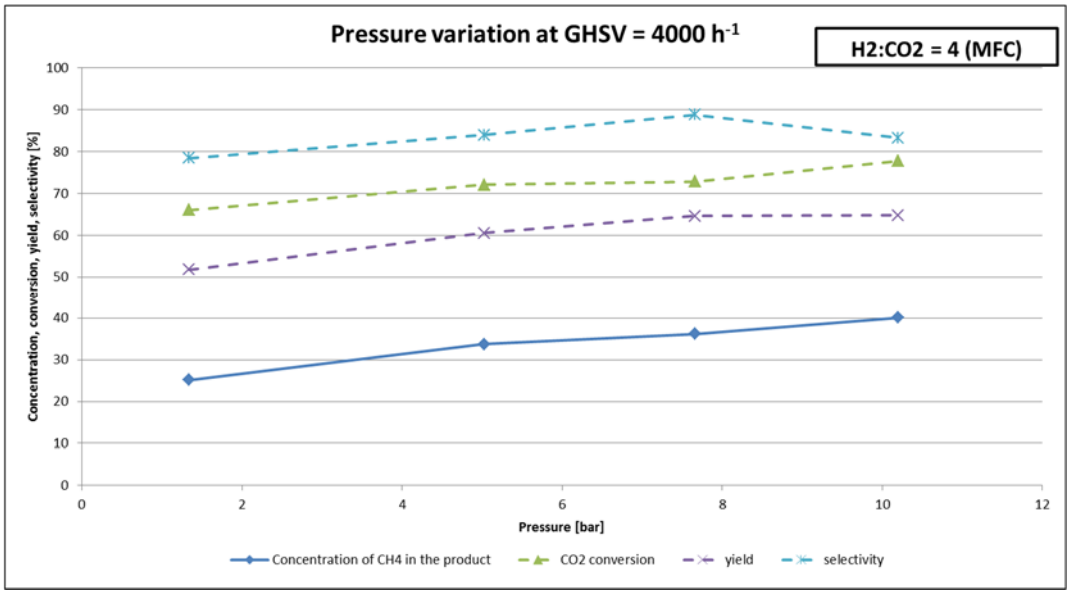

Diagram 1: Methanation results for different operating pressures

The 4:1 ratio of H_2 and CO_2, as the stoichiometric feed gas composition was set via the mass flow controller, at the constant 4000 h^{-1} GHSV. As expected, better performance of CH_4 production can be seen with pressure increasing, due to the higher number of moles of reactant as that of product, shifting the equilibrium composition on the product side [4][5].

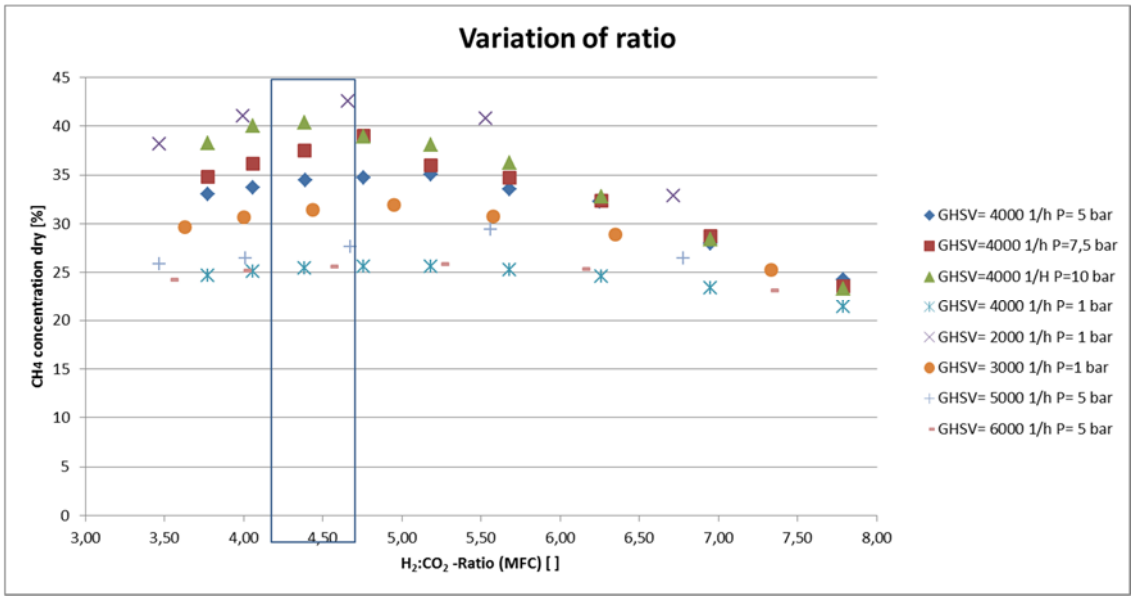

Diagram 2: Methanation results for different H_2:CO_2 ratios

As seen in the diagram 2. the best results for the product gas were observed at a slightly over the stoichiometric feed gas ratio of H_2 and CO_2. Additional positive results were noted in experiments with low GHSV which can be explained by longer residence time [4] [5].

Conclusion

An overall methanation was proposed, leading to result of a high yield at low GHSV and high pressures and ratios slightly over the stoichiometric feed gas composition. The results set a good basis for further planned experiments on the pilot plant and proof the functional capability of the process setup.

This project is funded by Christof Industries GmbH, industry partners OMV and EVN and the BMWFJ as Research Studios Austria special tender in „Energieforschungsinitiative“.

References:

[1] M. Götz et al, ´´Renewable Power-to-Gas: A technological and economic review´´, Renewable Energy 2016, pp. 1371-1390.

[2] http://www.energieinstitut-linz.at/index.php?menuid=1&reporeid=284

[3] M. Lehner, R. Tichler, H. Steinmüller, M. Koppe, ´´Power-to-Gas: Technology and Business Models´´, Leoben 2014.

[4] P. Biegger, A. Felder, M. Lehner, ‘‘ EE-Methan aus CO_2: Entwicklung eines katalytischen Prozesses zur Methanisierung von CO_2 aus industriellen Quellen‘‘ Book of Abstracts zum 9. Minisymposium der Verfahrenstechnik, Leoben 2013 pp. 105-107

[5] P. Biegger, A. R. Medved, M. Lehner, H. M. Ebner, A. Friedacher, ´´Methanisierung im Umfeld von „Power to Gas“´´, 14. Symposium Energieinnovation, Graz 2016

Hydrogen extraction facilities for utilization in a *Power to Gas* framework

Markus Groß[1], Werner Liemberger[1], Martin Miltner[1], Helga Prazak-Reisinger[2], Michael Harasek[1]
[1] Vienna University of Technology Institute of Chemical Engineering, A-1060 Vienna, Getreidemarkt 9/166, e-mail: markus.gross@tuwien.ac.at
[2] OMV Refinery & Marketing GmbH, A-1020 Vienna, Trabrennstraße 6-8

Abstract

Nowadays, excess electric energy can be used to produce storable green hydrogen with alkaline or PEM electrolysis. Hydrogen can be further converted to methane or directly stored in the natural gas grid. The well-developed existing natural gas grid can then act as storage or as transportation device for the renewable hydrogen. In a further step this hydrogen could be extracted at arbitrary locations along the whole gas grid for decentralized utilization. The current work presents an analysis of such hydrogen extracting facilities. The target of such a facility is the extraction and purification of hydrogen from mixtures with natural gas (1-10 % v/v hydrogen) and providing this hydrogen in high quality for further utilization, for instance to supply hydrogen fueling stations for use in automotive purposes. Therefore, a decent separation process is developed at the Vienna University of Technology in cooperation with OMV Gas & Power.

Introduction

The storage of fluctuating electrical excess energy from renewable sources (e.g. wind, solar power) is a key challenge of our energy transition and has gained significant importance during the last few years. Various Power to Gas concepts (one is shown in Figure 1**Fehler! Verweisquelle konnte nicht gefunden werden.**) offer a promising approach in this context. [1]

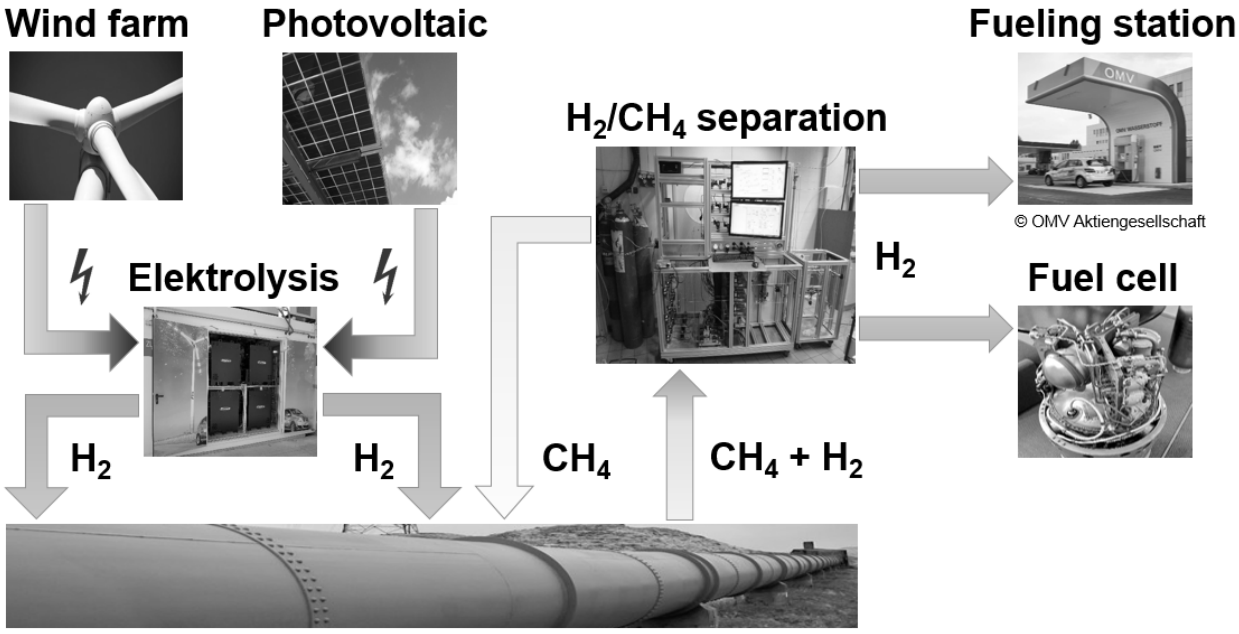

Figure 1: Power to Gas concept

Hydrogen, produced by water electrolysis, can be directly fed to the natural gas grid up to certain limits (in Austria currently 4 % v/v, [2]). The well-developed existing natural gas grid can act as storage or as transportation device for the renewable hydrogen. In a further step, hydrogen could be extracted at arbitrary locations along the gas grid for decentralized utilization. Therefore, it would be possible to supply fueling stations or other applications with delocalized renewable hydrogen. Due to the flexibility of the Power to Gas system, numerous specific applications for different targets within the energy sector have been investigated [3]. To meet the challenges of the different applications, also the process concept of extraction facilities must be highly flexible.

Methodology

The process to be developed incorporates a first pre-concentration step applying membrane-based gas permeation for an energy-efficient enrichment to approx. 35-40 % v/v hydrogen and a drastic mass flow reduction. A membrane-based gas permeation is a cost efficient process especially (but not only) for small to medium sized applications [4] Hydrogen can then be purified to the desired fuel cell quality (purity of 99.97 % v/v according to ISO 14678-2:2012, [5]) using pressure swing adsorption (PSA) as a second process step. The gas quality can be thoroughly analyzed to verify the compliance for the desired application. Both process steps, gaspermeation and PSA, provide enough degrees of freedom to allow a proper and efficient control of the product gas quality.
After an extensive experimental analysis rigorous and experimentally validated process simulation will be used to characterize and to further optimize the developed hydrogen extraction concept towards maximum energy efficiency. Furthermore, the power consumption, the efficiency, and the flexibility of the extraction facility will be investigated with different process scenarios to determine the total costs and an optimized operating point for the separation process. In a last step, possible economic locations, depending on transportation paths, gas flow and composition of the natural gas mixture, will be considered.

Experimental investigations

For demonstrating the concept, optimizing the processes and also for model validation, a lab-scale gas separation plant was built at the Vienna University of Technology (shown in Figure 2**Fehler! Verweisquelle konnte nicht gefunden werden.**). It incorporates a gas mixing station, a membrane test station, an adsorption test station and includes a possibility to analyze the gas content after each extraction step with a number of analytics devices.

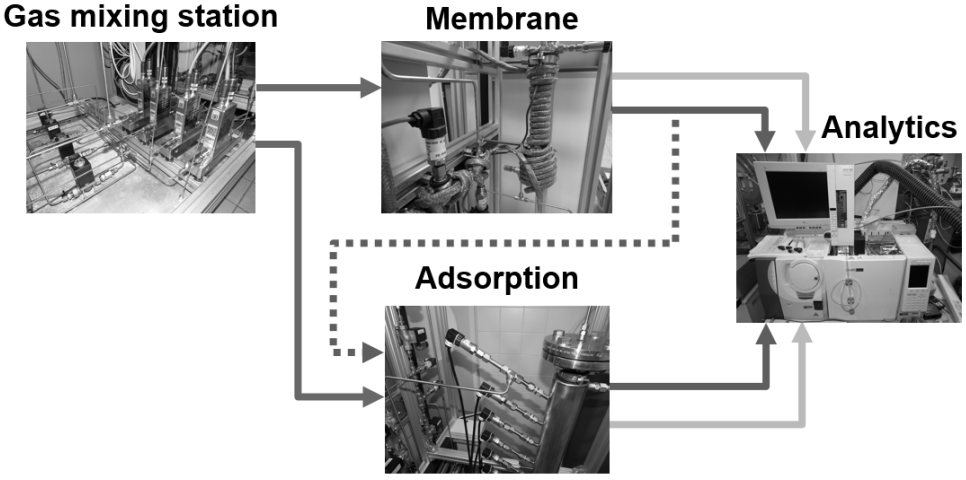

Figure 2: Lab-scale gas separation plant

The process framework conditions for the plant are shown in Table 1. Due to safety and practical aspects, the maximum volumetric feed flow is restricted to 0.5 m³/h. Nevertheless, the technological feasibility can be well investigated already with these low flows.

Table 1: Process framework conditions

Flows	Description	Value	Unit	Comment
Feed	Max. pressure	100	bar	Pressure in natural gas pipe max 70 bar
	Volumetric flow	Max. 0.5	m^3/h	
	H_2 content	1-10 %	% v/v	Max. content in natural gas 4 %, ÖVGW, G31, [2]
Product	Min. H_2 content	99.97	% v/v	ISO 14687-2:2012, [5]
Residual	Pressure	50	bar	

The gas mixing station includes four high pressure gas cylinder connections and four Coriolis mass flow controllers to provide various gas mixtures with adjustable volumetric flows.
The membrane test station (Figure 3) allows for a characterization of the used membrane module at different temperatures, pressures, feed compositions and stage cuts.
The adsorption test station (Figure 4) allows investigations of transient adsorption and desorption processes at isothermal or adiabatic conditions at different pressures. It is also practicable to determine the velocity and location of the reaction front by using temperature sensors and to measure the pressure drop over the adsorption column. The hydrogen purity after the adsorption process heavily depends on the adsorption material, the space velocity, the pressure, and the temperature. All these parameters will be investigated in the current research.
Likewise, the analytics has to meet the requirements of the lab-scale extraction plant. The measurement of various components of a natural gas mixture with high content of hydrogen is not state of the art. To satisfy the given requirements different measurement instruments are implemented into the process, including a mass spectrometer (Figure 5), a multi-component gas analyzer and a gas chromatography-mass spectrometer.

Figure 3: Membrane test station

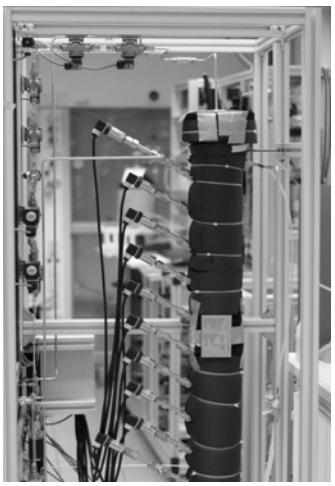

Figure 4: Adsorption test station

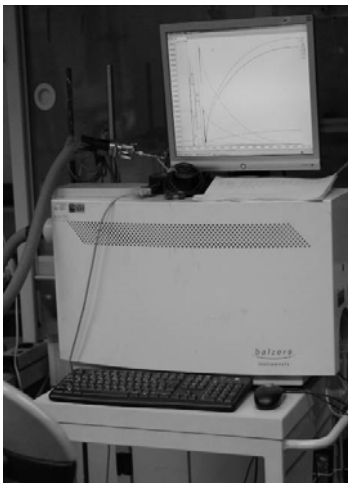

Figure 5: Mass spectrometer

The extraction plant is almost fully automated and controlled by an industrial programmable logic controller (PLC) for fast and individual operation modes.
The developed process must be highly flexible regarding pressure due to different levels in the Austrian gas grid (lowest level 6 bar, highest level up to 70 bar [6]) and hydrogen

content in the natural gas. Therefore, extensive experimental analysis will be performed in order to design an adequate process layout.
Experimental investigation of the separation process and the individual steps will be performed with pure gases, synthetic gas mixtures and finally with real gases obtained from a real-world hydrogen injection facility (wind2hydrogen project in Auersthal, [7]).

The first experimental investigations of the membrane process with H_2/CH_4 gas mixtures and different pressure levels are already done. In Figure 6 the results of the gas permeation process with a feed gas composition of 96 % v/v methane and 4 % v/v hydrogen is shown. The H_2 content in the permeate (gas that easily passes through the membrane) is in function with the stage-cut (permeate flow divided by feed flow). The fraction which does not pass through the membrane is called retentate and during the experimental investigation its pressure was 51 bar(a) and kept constant. In this application the hydrogen-rich permeate is the product of the first separation step and the retentate is not further used. This methane-rich gas is directly fed back to the natural gas line. Different permeate pressures are shown in red, orange, yellow, and green in Figure 6. As shown in the figure the membrane is able to concentrate the hydrogen from 4 % v/v (content in the feed flow) up to 30 % v/v in the permeate. It is plain to see that lower permeate pressures lead to higher H_2 content in the permeate. The difficult part is to find the optimum between stage cut and H_2 content in the permeate. On the one hand, a high permeate flow is desirable for high H_2 transfer through the membrane. On the other hand, this would lead to a lower hydrogen content in the permeate (shown in figure 6). It needs to be investigated in more detail, whether stage-cuts less than 0.1 lead to hydrogen contents exceeding 35 % v/v.

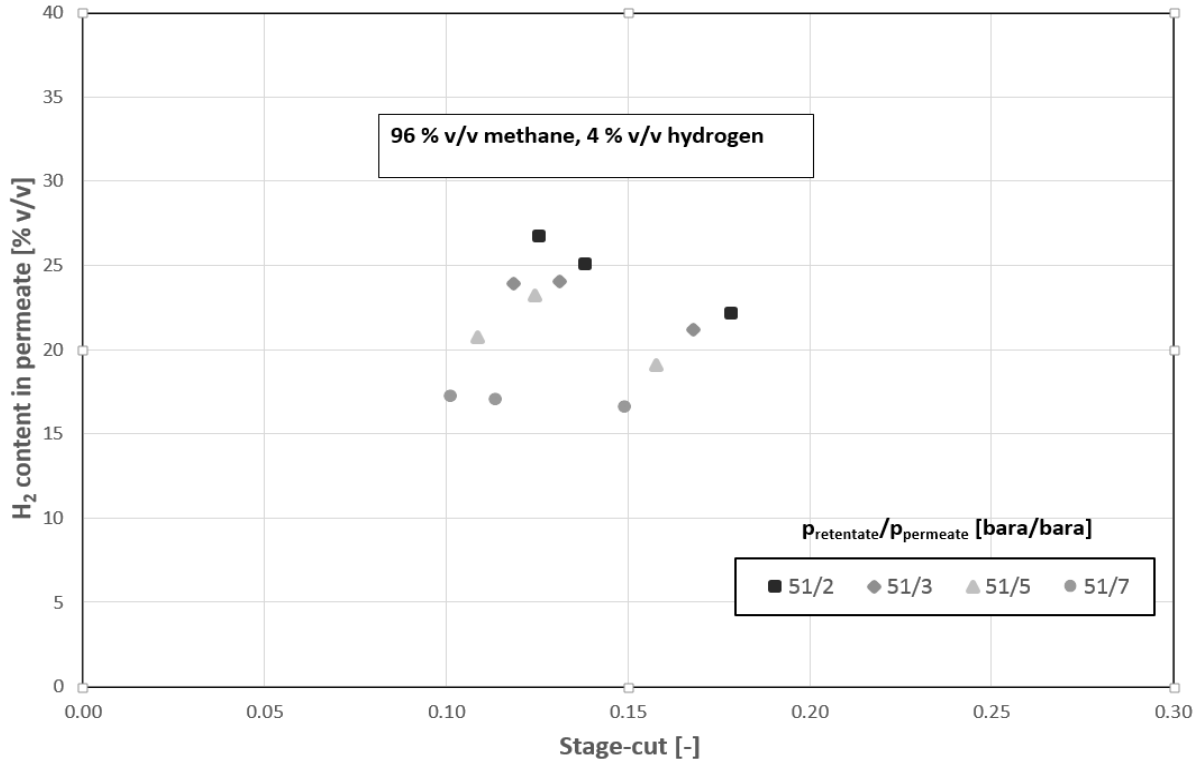

Figure 6: Permeation with 96 % v/v CH_4 and 4 % v/v H_2

Additionally, further experimental investigation of the whole separation process and the individual steps (membrane permeation and adsorption) will be performed with $CO_2/CH_4/H_2$ gas mixtures as well as real gas mixtures obtained from the hydrogen injection facility in Auersthal.

Conclusion

The current research work investigates the technical feasibility of extracting hydrogen from natural gas/hydrogen gas mixtures in the range of 1-10 % v/v with the objective to obtain hydrogen in fuel cell quality (purity of more than 99.97 % v/v hydrogen). Therefore, a specialized hybrid separation process is developed at the Vienna University of Technology. Simulation will be used to optimize the whole concept towards maximum efficiency. Also the power consumption, the efficiency and the flexibility of such an extraction facility will be investigated with different process scenarios to determine the total costs and an optimal operating point.

Acknowledgements

This work is funded by the Climate and Energy Fund in the framework of the program Energy Mission Austria. The research team is grateful to the project partner OMV Gas & Power for supporting the work.

References

[1] Jentsch, Mareike; Trost, Tobias; Sterner, Michael (2014): Optimal Use of Power-to-Gas Energy Storage Systems in an 85% Renewable Energy Scenario. In: *Energy Procedia*, p. 254–261. DOI: 10.1016/j.egypro.2014.01.180.

[2] Regeln der ÖVGW; Richtlinie G 31-Erdgas in Österreich-Gasbeschaffenheit. Österreichische Vereinigung für das Gas- und Wasserfach; Wien; (2001)

[3] Lehner, Markus; Tichler, Robert; Steinmüller, Horst (2014): Power-to-Gas: Technology and Business Models. Cham: Springer International Publishing (SpringerBriefs in Energy). Online available under http://dx.doi.org/10.1007/978-3-319-03995-4.

[4] Shao, Lu; Low, Bee Ting; Chung, Tai Shung; Greenberg, Alan R. (2009): Polymeric membranes for the hydrogen economy: Contemporary approaches and prospects for the future. In: Journal of Membrane Science 327 (1-2), p. 18–31. DOI: 10.1016/j.memsci.2008.11.019.

[5] ISO 14687-2:2012: Hydrogen fuel - Product specification - Part 2: Proton exchange membrane (PEM) fuel cell applications for road vehicles

[6] Gasnetz. Online available under http://www.e-control.at/industrie/gas/gasnetz, last checked on 01/31/2016

[7] OMV Refinery & Marketing GmbH: Factsheet-wind2hydrogen. Online available under https://www.klimafonds.gv.at/assets/Uploads/Presseaussendungen/2015/Erffnung-Wind2Hydrogen/150817Factsheet-Wind2HydrogenEN-FINAL.pdf, last checked on 01/31/2016

GUFO Lastprofile

Thomas Märzinger[1], David Wöß[1], Adolf Penthor[2], and Tobias Pröll[1]
[1]Universität für Bodenkultur, Institut für Verfahrens- und Energietechnik, Peter-Jordan-Straße 82, 1190 Wien
[2]Wien Energie GmbH, Spittelauer Lände 45, 1090 Wien
thomas.maerzinger@boku.ac.at

Kurzfassung

Die vorliegende Arbeit ist eine Zusammenstellung der Arbeiten zum Forschungsprojekt GUFO IIa, eine Kooperation der Wien Energie GmbH und dem Institut für Verfahrens- und Energietechnik an der Universität für Bodenkultur. Die Wien Energie GmbH betreibt Fernwärme Gebietsumformerstationen (GUFO) in denen Wärme vom Mitteldruck-Primärwärmenetz auf Niederdruck-Niedertemperaturnetze mit bis zu 90◦C Vorlauftemperatur übertragen wird. In diesen GUFO Stationen werden auch die Netzpumpen der Sekundärnetze betrieben. Bisher wurden die GUFO auf die Versorgungssicherheit als höchste Priorität ausgelegt. Mit der zunehmenden Bewusstseinsbildung in Richtung effizienten Energieeinsatz (Energieeffizienz-Richtlinie) und durch die spezielle Situation am Strommarkt, die die Wärmeproduktion in KWK Anlagen unattraktiv macht, entsteht der Wunsch nach einem möglichst geringen Strombedarf der Wärmeverteileinrichtungen (Netzpumpen) und nach einem möglichst geringen Wärmenetzverlust. Um dies zu erreichen sollen abgestimmte Auslegungsszenarien für die Pumpendimensionierung auf Basis der derzeitigen Messwerte generiert werden. Daher werden in diesem Projekt Lastprofile für bestehende GUFOs ausgewertet und Messungen an ausgewählten GUFOs durchgeführt.

Einleitung

Das Fernwärmesystem in Wien ist in mehrere Netzebenen unterteilt, welche für unterschiedliche Drücke und Temperaturen ausgelegt sind. Diese sind in das Primärnetz, das Sekundärnetz und tertiäre Kundennetz. Das Primärnetz verbindet Erzeugungsanlagen mit Abnehmeranlagen und dem Sekundärnetz. Die Sekundärnetze sind hydraulisch von den Primärnetzen und voneinander getrennt. Ihre Wärme beziehen die Sekundärnetze über die Gebietsumformerstationen aus dem Primärnetz. Im Fernwärmenetz werden 502 Sekundärnetze über GUFOs Versorgt. Die Kundennetze befinden sich in den Abnehmeranlagen und beziehen ihre Wärme aus dem Sekundärnetz oder über Umformerstationen aus dem Primärnetz. Ein Kundennetz ist immer hydraulisch vom Primärnetz getrennt. Wird ein Abnehmer aus dem Sekundärnetz versorgt geschieht dies meist direkt. Sowohl das Sekundär- als auch das Primärnetz werden im Allgemeinen gleitend betrieben. Das bedeutet, dass die Temperatur des Netzes möglichst niedrig gehalten wird, um Netzverluste zu verringern und Erzeugungsanlagen energiewirtschaftlicher betreiben zu können. Dabei wird die Vorlauftemperatur in Abhängigkeit von der Außentemperatur geregelt. Die allgemeinen Betriebsbedingungen des Sekundärnetzes sind den technischen Richtlinien zu entnehmen. [3]. Die Fernwärme-Gebietsumformerstationen in denen Wärme vom Mitteldruck-Primärwärmenetz auf Niederdruck- Niedertemperaturnetze mit bis zu 90◦C Vorlauftemperatur übertragen wird. In diesen Stationen werden auch Netzpumpen der Sekundärnetze betrieben. Bisher werden die Gebietsumformerstationen hauptsächlich auf Versorgungssicherheit ausgelegt. Aus dem Vorprojekt sind folgende Ergebnisse bekannt [4]:

- Derzeit arbeiten die in den GUFOs eingesetzten Pumpen im Schwachlastfall bei teilweise sehr geringen Drehzahlen. Dies führt zu geringen Pumpenwirkungsgraden und daher auch zu elektrischen Mehraufwand.

- Des Weiteren kann dauerhafter Betrieb bei niedrigen Drehzahlen zu Lebensdauereinbußen bis hin zu thermischen Versagen der Pumpen führen.

Im gegenständlichen Projekt werden Lastprofile für bestehende GUFOs ausgewertet. Zusätzlich gibt es Messungen an ausgewählten GUFOs, welche als Grundlage zur Unterteilung in verschiedene Lastprofiltypen dienen sollen. In Abbildung 1 sind Pumpen mit unterschiedlicher Leistung, gemessen in derselben GUFO, zu sehen. Dargestellt sind die Wirkleistungen bezüglich dem Produkt von Volumenstrom und Druck. Wobei die Messpunkte über ein Regressionspolynom geglättet wurden. Für diese Lastkategorien sollen dann entsprechende Pumpencluster für einen optimierten Betrieb ausgelegt werden. Das gegenständliche Projekt zielt daher auf folgende zentrale Fragestellungen ab:

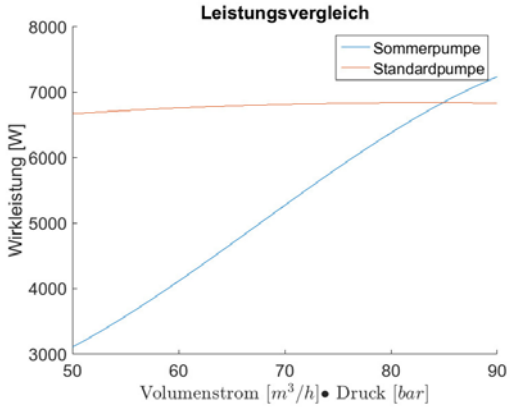

Abbildung 1: Pumpenvergleich

- Ist es möglich die Gebietsumformerstationen auf Basis der Kenntnis der Verbrauchertypen (Wohnungen, Bürogebäude, ...) in Lastprofiltypen einzuteilen.
- Welche Kategorien von Lastprofiltypen können daraus abgebildet werden.
- Können wirtschaftlich signifikante Einsparungen durch ein angepasstes Pumpenclusterdesign erzielt werden.

Methoden und Verfahren

Im ersten Projektschritt liegt das Hauptaugenmerk auf der automatischen Erkennung und Einteilung der einzelnen Lastprofile, zu den einzelnen Klassen von Verbrauchertypen. Um diese Fragestellung zu beantworten werden folgende Methoden eingesetzt.

- Zusammenstellung der relevanten Messdaten aus dem Leitsystem der Wien Energie.
- Abbildung einer GUFO Station in einem dynamischen Simulationsprogramm zur Überprüfung der Massen- und Energiebilanz auf Basis vorhandener bzw. erhobener Messdaten.
- Erstellung von Lastprofilen aus dem Leitsystem der Wien Energie.
- Einteilung und Analyse der Lastprofile.

In diesem Projekt stehen zur Einteilung und Analyse die Messwerte der GUFO Stationen aus dem Leitsystem der Wien Energie zur Verfügung. Es fliesen die statischen Werte über

die Anzahl und installierte thermischen Leistung der Wärmetauscher ein. Des Weiteren

Jahr	Frühling	Sommer	Herbst	Winter
2013	20.März	21.Juni	22.September	21.Dezember
2014	20.März	21.Juni	23.September	22.Dezember
2015	20.März	21.Juni	23.September	22.Dezember

Tabelle 1: Beginn der astronomischen Jahreszeiten.

werden auch die Viertelstunden Werte der thermischen Leistungen und Volumenströme über einen Zeitspanne von 3 Jahren (2013, 2014, 2015) und einer gesamten Aufzeichnung von 2 Jahren (September 2013 bis August 2015) betrachtet. Hierzu werden die ausgelesenen Datensätze in Bezug zur installierten Leistung auf ihre Plausibilität überprüft und vorhandene Messfehler weitest möglich ausgeschlossen. Die einzelnen Jahreszyklen wurden in die astronomischen Jahreszeiten unterteilt. In Tabelle 1 sind die Beginn Zeiten der Jahreszeiten der entsprechenden Jahre zu sehen. Für die Zuordnung zu den einzelnen Verbrauchertypen werden Korrelationen betrachtet. Bei Wohngebäude existiert eine erhöhte Korrelation bezüglich der Außentemperatur. Dies spiegelt sich in einem höheren Verbrauch während sogenannter Heiztage wieder [2]. Bei einem Heiztag handelt es sich um einen Tag mit einer mittleren Temperatur von unter 12°C. Hieraus ermitteln sich die Heizgradtage z. Diese ergeben sich aus der Differenz zwischen der angenommenen Innentemperatur θi und der mittleren Außentemperatur θa des gesamten Tages. Somit folgt die Berechnung der Heizgradtage $HGT_{20/12} = P_{z1}(20 - \theta a)$. Bei gewerblichen Abnehmern ist eine Korrelation bezüglich Werktagen und Außentemperatur zu erwarten. Bei industriellen Abnehmern hingegen ist keine besondere Korrelation bezüglich der Außentemperatur zu erwarten. Um Änderungen der Lastprofile im Laufe der Jahreszeiten zu beschreiben wurden die mittleren Temperaturen aus den Messdaten der ZAMG (Station ...) herangezogen. Hierzu wurde mittels eines erwartungstreuen Schätzers [1] der Erwartungswert der mittleren Tagestemperatur bezüglich der Jahreszeiten berechnet. Im nächsten Schritt wurde ein Temperaturband um die entsprechenden Erwartungswerte ermittelt, in dem eine beherrschbare Anzahl von Tagen liegt. Für diese Tage wurden die Lastprofile und die Heizgradstunden statistisch ausgewertet. Dabei werden Heizgradstunden als eine vereinfachte Methode zur Bestimmung der Wärmeverluste von Gebäuden verwendet. Zur Ermittlung der Wärmeverluste für den Zeitraum (t1, t2) über die Temperaturdifferenz θi − θa mit Q = L(θi − θa) werden folgende Annahmen getroffen. Der Leitwerte L sei konstant. Sei die Innentemperatur θi = 20°C. Wir berechnen das Integral nur für Tage mit einer Außentemperatur θa ≤ 12°C. Diese Tage werden als Heizgradtage bezeichnet [2]. Da wir nur die Korrelation zwischen Heizgradstunden und Lastprofiel berechnen sei L = 1. Auf dieser Grundlage lassen sich nun mit Hilfe von stochastischen Optimierungsalgorithmen Pumpencluster auslegen und wirtschaftlich bewerten.

Experimentelle Durchführung

Es wurden die Daten von 127 ausgewählte GUFOs Ausgewertet. Die mittleren Temperaturen für Wien wurden von der Zentralanstalt für Metrologie und Geodynamik (ZAMG) bezogen. In Abbildung 2 dargestellt sind die mittleren Tagestemperaturen mit den saisonabhängigen Mittelwerten. Bei den Messwerten, aus dem Leitsystem der Wien Energie GmbH, wurden jene Werte entfernt welche die installierte Leistung in den GUFOs um den Faktor 2 übertrafen. Anschließend wurden mit Hilfe von Matlab aus den Datensätzen Jahres-, Saisonale- und Tageslastprofile generiert. Bei diese wurden Minima, Maxima, Erwartungswerte und Quantile ausgewertet.

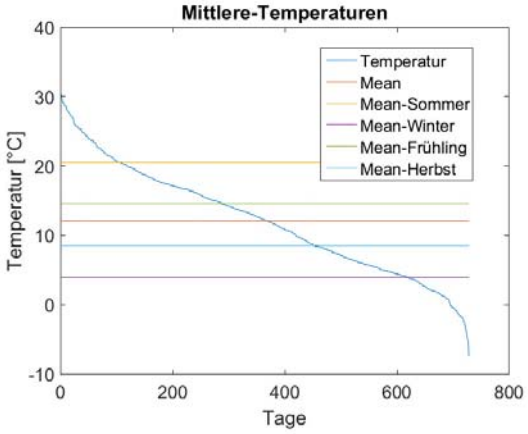

Abbildung 2: Mittlere-Temperaturen

Auswertung

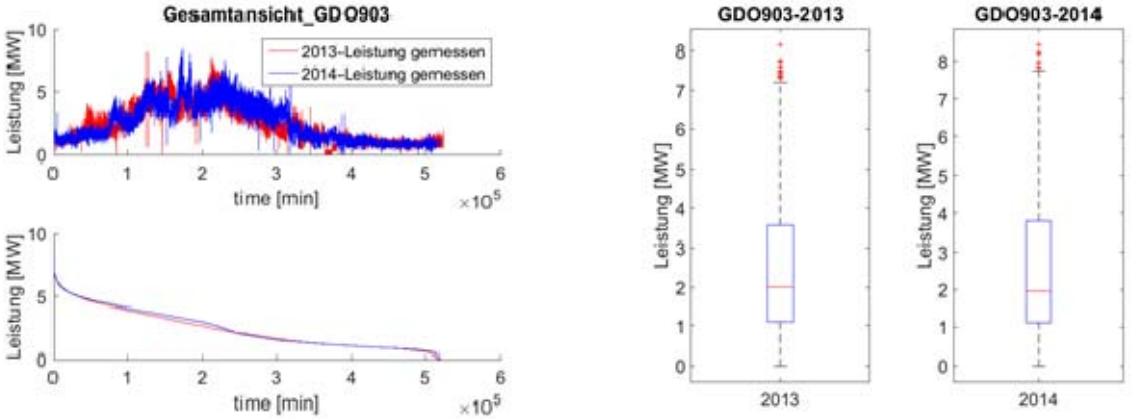

(a) Lastprofile (b) Box Plots

Abbildung 3:Jahres Profile

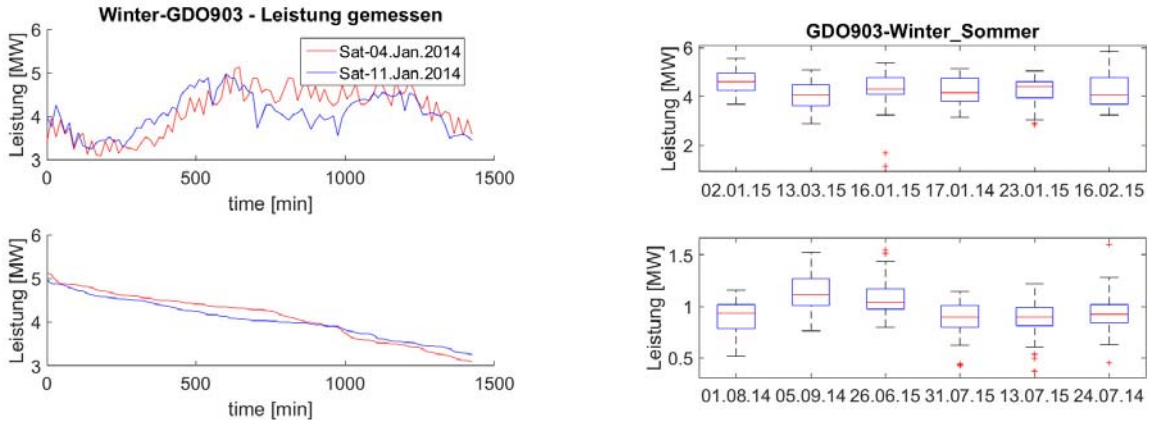

(a) Lastprofile (b) Box Plots

Abbildung 4: Saisonale Profile

Die Herausforderung für die Auswertung war die große Datenmenge. Im Folgenden kann

leider nur ein kleiner Ausschnitt der gewonnenen Ergebnisse dargestellt werden. Bei den verschiedenen Auswertungen hat sich gezeigt dass eine Unterteilung in Wärme-, Kälte- und Übergangszeit unbrauchbar ist. Da sich Frühling und Herbst zu sehr unterscheiden. Dieser Umstand ist in Abbildung 2 zu erkennen. Die Erwartungswerte der Temperatur weichen für Frühling und Herbst stark voneinander ab. Würde man sie geschlossen als Übergangszeit betrachten ergibt sich als erwartete Temperatur die in Abbildung 2 mit Mean bezeichnete Außentemperatur. Nun folgend in Abbildung 3 die Daten für die Jahres basierende Betrachtung. Wie im Boxplot aus Abbildung 3 gut zu erkennen ist befinden sich 75% der Betriebspunkte in der unteren Lasthälfte. Aus dem Lastprofil ist zu entnehmen das sich die Betriebspunkte in einem relativ engen Band, abhängig vom Jahresverlauf, bewegen. Betrachten wir noch die beiden Grenzfälle Sommer und Winter. In Abbildung 4 sehen wir exemplarisch links die Lastprofile von zwei durchschnittlichen Tagen am Wochenende im Winter und rechts Box Plots von typischen Wochentagen im Sommer und Winter. Schön zu sehen ist das die Abhängigkeit zur Außentemperatur die Betriebspunkte im Winter in einem relativ konstanten Bereich hält, wobei im Sommer die Schwankungen bei gleicher Außentemperatur größer sind. Aber gesamt ist zuerkennen, das sich die Betriebspunkte wieder in einem Saisonal und Außentemperatur abhängigen Band konzentrieren.

Zusammenfassung

Um Wärme über die Gebietsumformerstationen und zu den Verbrauchern zu transferieren, muss Pumparbeit im Bereich der GUFOs geleistet werden. Dies stellt den größten Energieverlust dar. Bisher wurden die GUFOs auf extreme Bedingungen im Winter ausgelegt. Diese Auslegungskriterien führen dazu, dass die Stationen meistens im Teillastbereich betrieben werden. Im Vorläuferprojekt wurden Kennzahlen zur Bewertung der Energieeffizienz von GUFOs entwickelt. In diesem Projekt werden die Lastprofile der GUFOs stochastisch ausgewertet. Wie also aus den Auswertungen zu entnehmen ist konzentrieren sich die Betriebspunkte global gesehen im unteren Lastbereich. Bei Berücksichtigung der Korrelationen der Betriebspunkte mit dem Jahresverlauf ergeben sich unterschiedliche, aber definierte, Bereiche in denen sich der Großteil der Betriebspunkte befindet. Somit erhalten wir die Grundlage für eine möglichst optimale Auslegung von Pumpenclustern. Aus den bereits durchgeführten Messungen geht hervor, dass eine Einsparung durch ein optimiertes Pumpenclusterdesign von bis zu 30% des Stromeinsatzes möglich ist.

Literatur

[1] Claudia Czado and Thorsten Schmidt. Mathematische Statistik. Springer Heidelberg Dordrecht London New York, 2011.

[2] E. Tshegg, W. Heindl, and A. Sigmund. Grundzüge der Bauphysik. Springer Verlag Wien New York, 1984.

[3] Energie GmbH Wien. Wien energie | technische richtlinien | technische richtlinien | planung und errichtung fernwärme | fernwärme-partner-plattform | unternehmen:. http://www.wienenergie.at/media/files/2013/tr-technische.

[4] David Wöß, Angelika Schiebel, Adolf Penthor, and Tobias Pröll. Gufo effizienzkennzahlen. 11. Minisymposium Vervahrenstechnik, 2015.

Charakterisierung natürlicher Zeolithe für die Ammoniumentfernung aus Trübwässern

Markus Ellersdorfer[1], Jan Lubensky[1], Kristina Stocker[2]
[1] Montanuniversität Leoben, Lehrstuhl für Verfahrenstechnik des industriellen Umweltschutzes, 8700 Leoben, Franz-Josef-Straße 18
markus.ellersdorfer@unileoben.ac.at, jan.lubensky@unileoben.ac.at
[2] Montanuniversität Leoben, Lehrstuhl für Rohstoffmineralogie, 8700 Leoben, Peter-Tunner Straße 5
kristina.stocker@unileoben.ac.at

Kurzfassung
Im vorliegenden Beitrag werden Möglichkeiten zur Charakterisierung von Zeolithen für den Einsatz als Festbett-Ionentauscher beschrieben. Diese natürlichen, mineralischen Rohstoffe sollen in einem neu entwickelten Verfahren zur Rückgewinnung von Ammonium aus Gärresten von Biogasanlagen und Trübwässern kommunaler Kläranlagen eingesetzt werden. In Zusammenarbeit zwischen Verfahrenstechnikern und Mineralogen konnte ein für die Anforderungen des Verfahrens optimal geeigneter Zeolith ausgewählt und die Packungsgrößen einer sich aktuell im Bau befindlichen Pilotanlage dimensioniert werden.

Einleitung
Im Forschungsprojekt „ReNOx“ wird die Kopplung von Biogasanlagen mit Zementwerken untersucht. Durch wechselseitige Nutzung von Stoff- und Energieströmen ergeben sich bei einer Kopplung diverse Synergieeffekte, die eine im Vergleich zur konventionellen Biogaserzeugung wirtschaftlichere und ökologischere Betriebsweise ermöglichen können. Unter anderem stellt die Rückgewinnung von Ammonium (NH_4^+) aus Gärresten zur Produktion eines industriellen Entstickungsmittels ein zentrales Thema dar. Für diese Aufgabe wurde ein neuartiges Verfahren, das „Ionentauscher-Loop-Stripping“, entwickelt [1], welches einen Festbett-Ionentauscher-Prozess mit einer simultanen Luftstrippung kombiniert. Dabei kann ein industriell einsetzbares Entstickungsmittel mit dem Vorteil eines ganzjährigen Bedarfs und einer Entlastung des Stickstoffkreislaufs in landwirtschaftlich intensiv genutzten Regionen produziert und der entfrachtete Gärrest als Prozesswasser rückgeführt werden. Im Vergleich zu konventionellen Strippverfahren zeichnet sich das Ionentauscher-Loop-Stripping durch eine kompaktere Bauweise und einen geringeren Chemikalienverbrauch aus. Das Verfahren kann auch an kommunalen Kläranlagen zur NH_4^+-Rückgewinnung aus Trübwässern eingesetzt werden, wodurch die Stickstoffrückbelastung an der Kläranlage verringert wird. Im Vergleich zu anderen Verfahren (z.B. SBR, Anammox) wird NH_4^+ dabei nicht in gasförmigen N_2 umgewandelt, sondern als konzentriertes, marktfähiges Produkt rückgewonnen und stofflich genutzt.
Im Ionentauscher-Loop-Stripping werden natürliche, aus entsprechenden Lagerstätten gewonnene, Zeolithe als Festbett-Ionentauscher verwendet, da diese aufgrund ihrer großen Oberfläche und die nanoporöse Struktur sowie ihrer Gittereigenschaften eine hohe Selektivität für NH_4^+ bei gleichzeitig niedrigen Kosten aufweisen. Um eine möglichst hohe Abtrennleistung des Gesamtverfahrens zu erreichen, sind die Ionenaustauschvorgänge an der Zeolithpackung entscheidend. Neben der Auswahl eines ammoniumselektiven Zeoliths, des Zeolith- zu Trübwasser-/Gärrestverhältnisses und einer optimalen Korngröße durch Abwägung zwischen Druckverlust und Austauschfläche sind die Austauschkapazitäten und Standzeiten entscheidend. Natürliche Zeolithe sind ein Gemisch aus den eigentlichen Zeolithmineralen und „Fremdmineralen“, welche nicht am Ionenaustausch teilnehmen. Im Hinblick auf die Dimensionierung der Packungsgrößen kommt der Bestimmung dieses Fremdmineralgehalts große Bedeutung zu.

Methoden und Verfahren
In Zusammenarbeit mit dem Lehrstuhl für Rohstoffmineralogie wurden unter Einsatz mineralogischer Analysemethoden (Röntgendiffraktometrie, Elektronenstrahlmikrosonde, Elektronenmikroskopie) Zeolithe unterschiedlicher Lieferanten charakterisiert und deren Zeolith- und Fremdmineralgehalte bestimmt. Weiters wurden die Adsorptionsisothermen für Ammonium an den unterschiedlichen Proben bestimmt und verglichen.

Experimentelle Durchführung
Ein Teil der Zeolithproben (Körnung 1-3 mm) wurde mit einem Mörser zerkleinert (<100 µm) und in Pulverform mittels Röntgendiffraktometrie untersucht. Die Beugungs- und Rückstreuungsmuster der Röntgenstrahlung an den einzelnen Netzebenen der in der Probe enthaltenen Minerale erlauben Rückschlüsse auf die Art der enthaltenen Minerale, da sich für bestimmte Mineralphasen typische Refelxionsmuster ergeben, die in Form von Peaks im Röntgendiffraktogramm identifiziert werden können.
Eine weitere Teilprobe wurde in der Ursprungskörnung in Kunstharz eingebettet und für eine Untersuchung an der Elektronenstrahlmikrosonde (EMPA) poliert. Mittels EMPA ist es möglich, hochauflösende, zerstörungsfreie in-situ Untersuchungen von Element-konzentrationen in Festkörpern durchzuführen, indem diese mittels eines hochenergetischen Elektronenstrahls angeregt werden. Neben einer qualitativen Information konnten damit Verhältnisse von für Zeolithe charakteristischen Elementen (Si/Al) sowie der natürliche Kationengehalt semiquantitativ abgeschätzt werden. Zusätzlich liefern Sekundärelektronen und rückgestreute Elektronen (BSE) Bildinformationen.
Die Bestimmung der Adsorptionsisothermen der Zeolithproben erfolgte durch Einwiegen bestimmter Zeolithmengen (je ca. 10 g) in 250 ml Glasgefäße und Zugabe von Ammoniumsulfat-Lösungen mit definierten Ammoniumkonzentrationen (500, 1000, 1500, 2000, 2500 und 5000 mg NH_4^+/l). Die Glasgefäße wurden in einem Überkopfschüttler eingespannt und zur Gleichgewichtseinstellung bei Raumtemperatur für 24 h geschüttelt. Danach wurden Proben aus der überstehenden Flüssigphase entnommen, filtriert und der Restammoniumgehalt mittel Trägerdampfdestillation (Kjeldahl) bestimmt. Die Ergebnisse wurden in Form der Gleichgewichtskonzentration in der Lösung gegen die Gleichgewichtsbeladung des Zeolith für die jeweiligen Proben dargestellt und mit Literaturmodellen (Langmuir, Freundlich usw.) verglichen, um das für die Ammoniumadsorption an den untersuchten Zeolithen passendste Modell zu finden.

Auswertung
In Abbildung 1 sind beispielhaft die Röntgendiffraktogramme zweier Zeolithproben (Z-01 und Z-08) angeführt.

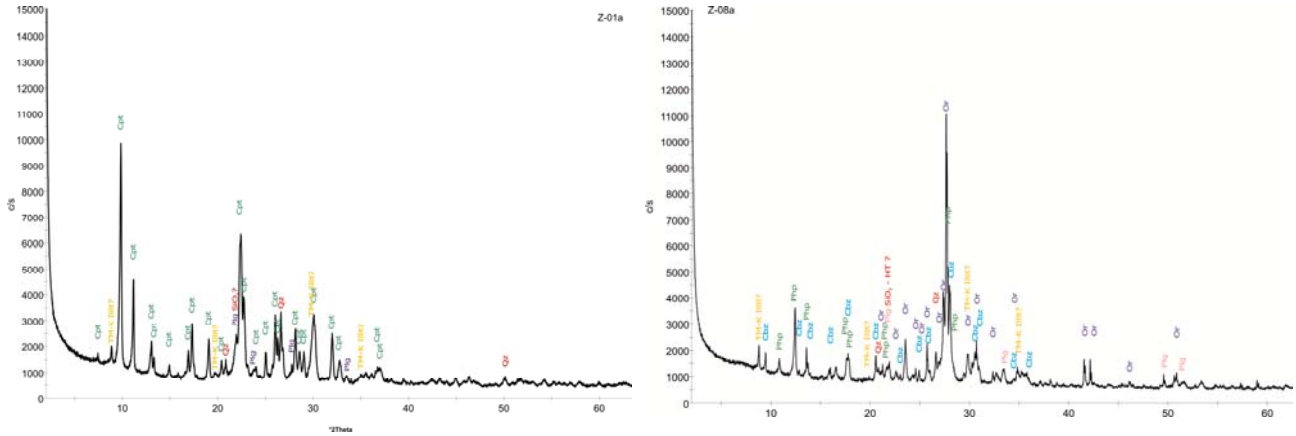

Abbildung 1 – Röntgendiffraktogramme zweier ausgewählter Zeolithproben (Z-01 links, Z-08 rechts); Minerale: Cpt...Klinoptilolith; Cbz...Chabazit; Php...Phillipsit; Qz...Quarz; Plg...Plagioklas; Or...Orthoklas; TM-K...K-reiche Tonminerale; SiO_2-HT?...Cristobalit

Bei der Probe Z-01 handelt es sich um natürlichen Zeolith mit dem Hauptmineral Klinoptilolith. Die zusätzlich identifizierten Nebengemengteile entsprechen den natürlichen, geologischen Vergesellschaftungen. Es handelt sich zum Großteil um Feldspäte der Plagioklas-Reihe sowie verschiedenen SiO_2-Phasen (Quarz und Cristobalit). Akzessorisch finden sich K-reiche Phyllosilikate sowie Apatit, Titanoxid, Ilmenit, Zirkon und sehr untergeordnet Pyrit. Die semiquantitative, chemische Analyse des Klinoptilolith mittels Elektronenstrahlmikrosonde zeigte, dass in diesem hauptsächlich Na und K sowie untergeordnet auch Ca als austauschbare Kationen vorhanden sind (Abbildung 2).
Bei der Probe Z-08 handelt es sich vermutlich um ein künstliches Gemisch natürlicher Ausgangsstoffe, wobei der Gehalt an Zeolithmineralen im Vergleich zu Probe Z-01 deutlich geringer ist. Den Hauptgemengteil bildet Orthoklas, ein kaliumreiches Silikat der Feldspatgruppe, welches aufgrund seiner Gitterstruktur als Ionentauscher nicht wirksam ist. Als Zeolithminerale wurden Phillipsit und Chabazit identifiziert.

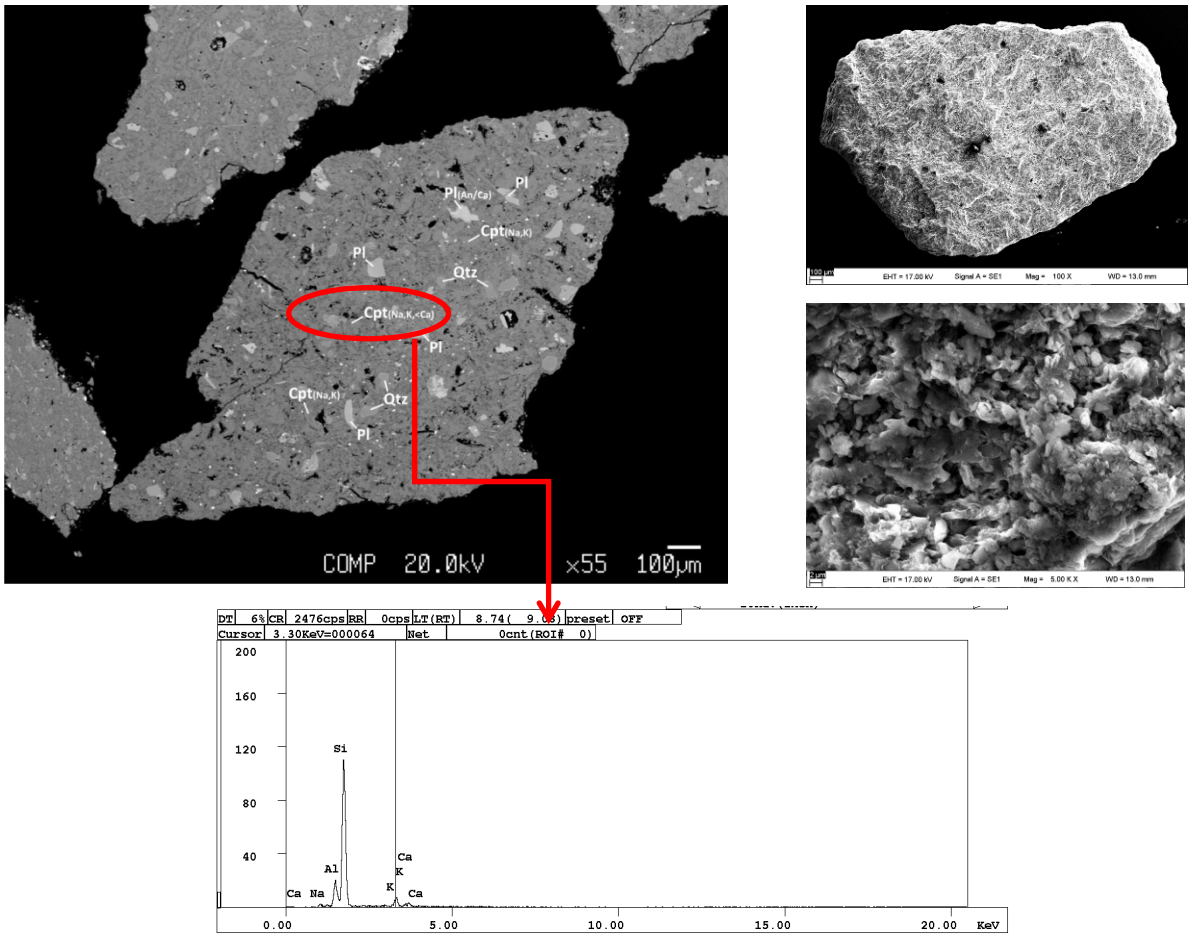

Abbildung 2 - BSE-Aufnahme eines Zeolithkorns in der Elektronenstrahlmikrosonde, poliertes Kornpräparat (links oben) inklusive Mineralphasenbezeichnungen (Cpt … Klinoptilolith; Qtz … Quarz; Pl … Plagioklas); REM-Aufnahmen der Oberflächenstruktur eines Korns derselben Probe (rechts oben); EDS-Spektrum zur semiquantitativen Bestimmung des Elementgehaltes des markierten Zeolithminerals (unten)

In Abbildung 3 sind die für die beiden Proben Z-01 und Z-08 bestimmten Adsorptions-isothermen angeführt.

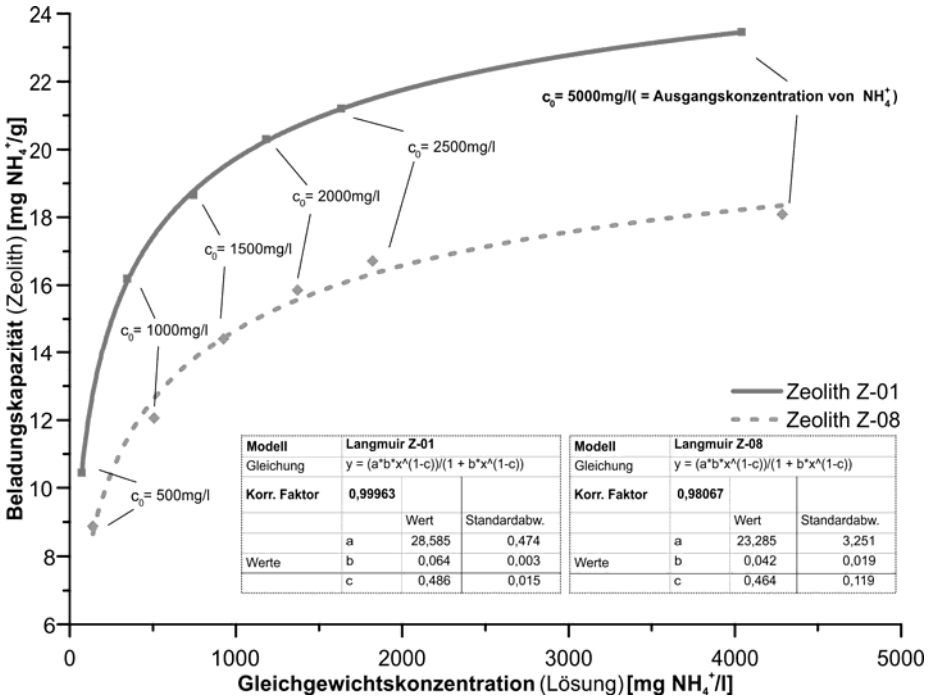

Abbildung 3 – Adsorptionsisothermen für NH_4^+ an ausgewählten Zeolithproben

Es zeigt sich, dass die Probe Z-01 im Vergleich zu Z-08 wesentlich höhere Aufnahmekapazitäten für NH_4^+ besitzt. Reiner Klinoptilolith besitzt Aufnahmekapazitäten zwischen 24 und 28 [mg NH_4^+/g] [2], weshalb der Anteil an Klinoptilolith in dieser Probe relativ hoch sein dürfte. Im Vergleich dazu ist die Aufnahmekapazität der Probe Z-08 deutlich geringer, was auf einen niedrigeren Anteil an Zeolithmineralen, in diese Fall Phillipsit und Chabazit, hinweist. Diese Beobachtungen decken sich mit den Ergebnissen der mineralogischen Untersuchungen. Von allen getesteten Adsorptionsmodellen (Freundlich, Langmuir, BET) zeigt das Modell nach Langmuir die beste Übereinstimmung mit den Ergebnissen der Adsorptionsmessungen. Während bei Probe Z-01 eine nahezu vollständige Übereinstimmung des Modells mit den Ergebnissen erreicht wird, ist der Korrelationsfaktor bei Probe Z-08 etwas geringer. Dennoch beschreibt dieses Modell die Ionenaustauschvorgänge für Ammonium an natürlichen Zeolithen in den vorliegenden Fällen am besten. Aufgrund der erzielten Ergebnisse wird für künftige Versuche an einer Pilotanlage vorrangig Zeolith Z-01 eingesetzt.

Zusammenfassung

Die Charakterisierung natürlicher Zeolithe in mineralogischer wie auch in chemisch/ physikalischer Sicht ist entscheidend für deren Einsatz im Bereich der Ammoniumentfernung aus Trübwässern. Unter Zuhilfenahme von Untersuchungsmethoden beider Fachbereiche können optimal passende Zeolithe ausgewählt und eine Grobauslegung einer Ionentauscherpackung durchgeführt werden. Für den technischen Einsatz sind aber nicht allein die Beladungskapazitäten entscheidend, es müssen auch die Kinetik des Ionenaustauschs sowie die erreichbaren Standzeiten (Zahl an Beladungs-/Regenerationszyklen) berücksichtigt werden, um eine optimale Prozessgestaltung zu ermöglichen. Weiterführende Untersuchungen dazu sind geplant.

Literatur

[1] Ellersdorfer, M.: Integrierte Produktion und Verwertung von Biogas in Zementwerken, Dissertation (2012), Montanuniversität Leoben.

[2] Wang, S., Peng, Y.: Natural zeolites as effective adsorbents in water and wastewater treatment. J. Chem. Eng. (2010), 156, 11 – 24.

Optimierung der Betriebsparameter einer Versuchsanlage am Beispiel Plastic Reborn

Daniel Schwabl[1], Helmut Flachberger[1], Lukas Himler[2], Markus Bauer[2], Markus Lehner[2], Lukas Kranzinger[3], Roland Pomberger[3]

Montanuniversität Leoben
[1] Lehrstuhl für Aufbereitung und Veredlung
[2] Lehrstuhl für Verfahrenstechnik des industriellen Umweltschutzes
[3] Lehrstuhl für Abfallverwertungstechnik und Abfallwirtschaft
Franz-Josef-Straße 18; 8700 Leoben

daniel.schwabl@unileoben.ac.at; markus.bauer@unileoben.ac.at;
lukas.kranzinger@unileoben.ac.at

Kurzfassung

Das Research Studio Austria „Plastic Reborn“ hat es sich zum Ziel gesetzt, die (werk-) stoffliche Verwertung polyolefinreicher Altkunststofffraktionen durch Erforschung eines neuartigen nass-mechanischen Aufbereitungsverfahrens zu untersuchen. Zu diesem Zweck wurde eine Versuchsanlage im Technikumsmaßstab ausgelegt, konstruiert, errichtet und in Betrieb genommen. Auf Basis einer systematischen Parameterstudie wurden drei Hauptanlagenparameter des im Zentrum stehenden Zentrifugalkraftscheiders – Neigung, Länge und Leistung der Versorgerpumpe - untersucht, um das Trennergebnis zu optimieren.

Einleitung

Altkunststoffe werden aktuell überwiegend thermisch verwertet, also in Zementwerken oder Verbrennungsanlagen als Ersatzbrennstoff eingesetzt. Eine (werk-)stoffliche Verwertung wird hauptsächlich dadurch limitiert, dass die in Frage kommenden Altkunststoffe nicht sortenrein genug anfallen. Kritische werkstoffliche Eigenschaften von Kunststoffen wie etwa das Verhalten bei mechanischer Belastung oder hohen Temperaturen können sich aber bereits durch geringe Verunreinigungen erheblich ändern [1]. Es ergibt sich daher der Bedarf nach einem sehr trennscharfen Aufbereitungsverfahren, um aus den verfügbaren Altkunststoffen entsprechend hochqualitative Sekundärrohstoffe aufzukonzentrieren.

Methoden und Verfahren

In einer dem RSA „Plastic Reborn“ vorangegangen Arbeit wurde erkannt, dass sich vor allem Polyolefine für ein (werk-)stoffliches Recycling eignen. Da Polyolefine im Gegensatz zu den meisten anderen Kunststoffen eine geringere Dichte als Wasser aufweisen, wird in dieser Arbeit ein nass-mechanischer Prozess unter Verwendung eines Zentrifugalkraftscheiders empfohlen [2].
Das Trennmedium des Zentrifugalkraftscheiders (siehe Abbildung 1) wird dabei am unteren Ende des leicht geneigten Scheiders tangential eingebracht, wodurch sich im Scheider ein Fluidwirbel mit Luftkern ausbildet. Direkt in diesen Wirbel wird das zu trennende Gut am oberen Ende des Scheiders aufgegeben. Jene Anteile, die spezifisch schwerer als das Trennmedium sind, wandern durch die wirkenden Zentrifugalkräfte nach außen in Richtung Scheiderwandung und werden als Schwergutfraktion mit dem

Trennmedium am oberen Ende des Zentrifugalkraftscheiders tangential ausgeschleust. Die spezifisch leichteren Anteile verbleiben eher im Nahbereich der Grenzschicht Trennmedium/Luftkern und werden als Leichtgutfraktion mit einer geringen Menge an Trennmedium am unteren Ende des Zentrifugalkraftscheiders ausgebracht.

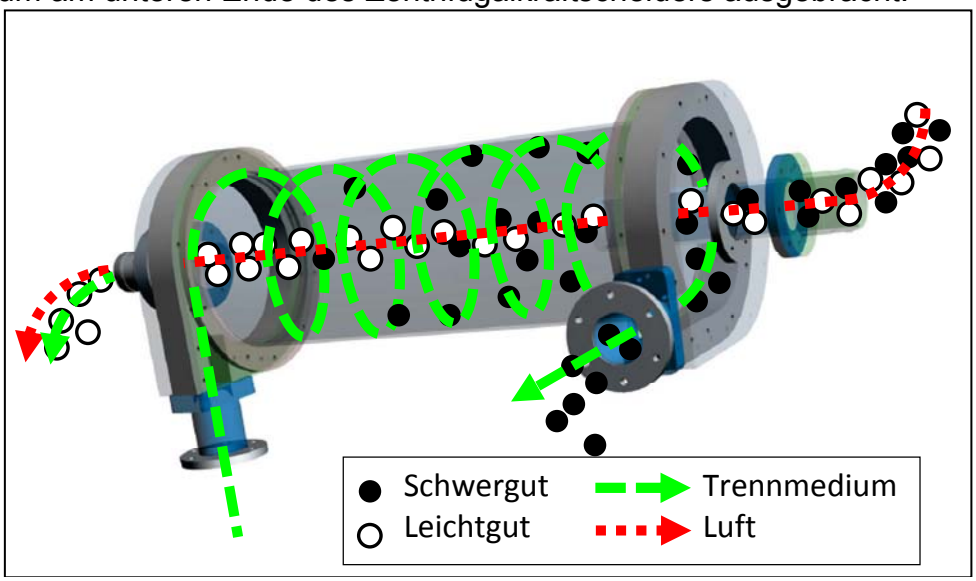

Abbildung 1: Funktionsweise des Zentrifugalkraftscheiders

Ziel der ersten Versuchsreihe auf dem Zentrifugalkraftscheider war es, die Auswirkung der Veränderung von spezifischen Betriebsparametern auf dessen Trennschärfe zu bestimmen und optimale Betriebspunkte auszuloten. Zu diesem Zweck wurde ein 2^k-faktoriellen Test gewählt, da so eine beliebige Anzahl an (Einfluss-)Faktoren überprüft, jedoch durch die Wahl von nur 2 Niveaus, die Anzahl der durchzuführenden Versuche niedrig gehalten werden kann. Zudem liefert dieser Test nicht nur eine Aussage über die direkte Auswirkung eines Faktors, sondern bewertet auch deren wechselweise Beeinflussung (vgl. Abbildung 2), stellt sie in ihrer Bedeutung gegenüber und prüft, ob diese statistisch signifikant sind.

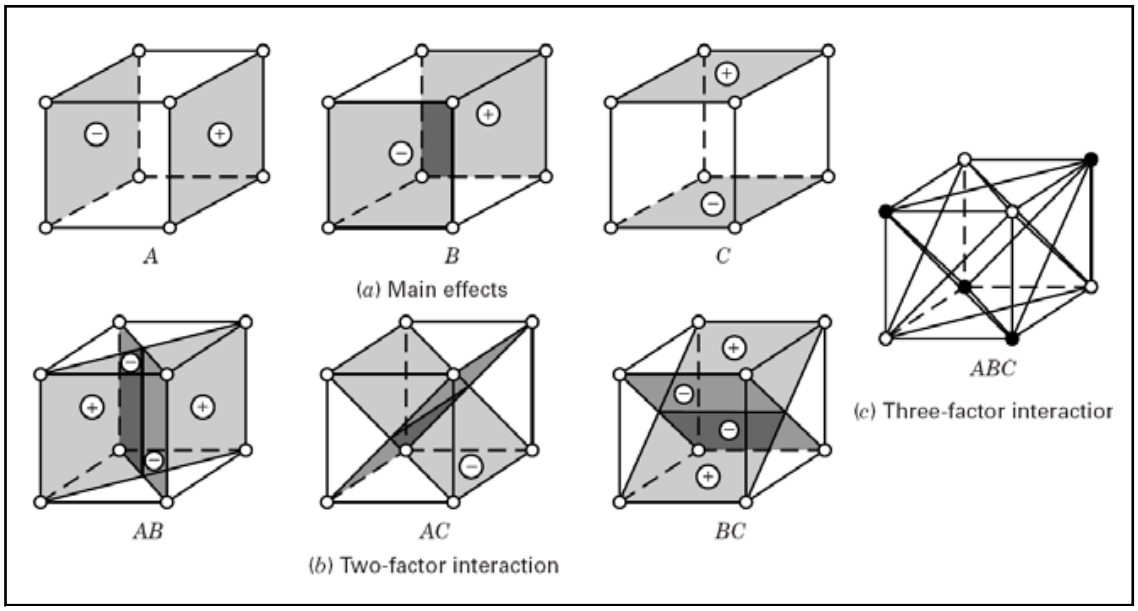

Abbildung 2: Faktorbewertung im 2^k-faktoriellen Test mit 3 Faktoren [3]

Auf ein Partikel im Zentrifugalkraftscheider wirken neben dem Auftrieb, der sich durch den Dichteunterschied des Partikels und dem umgebenden Trennmedium ergibt, die Gravitationskraft sowie strömungsbedingte Kräfte (Zentrifugalkraft, Widerstands- und

Schleppkräfte). Da der Einfluss von Gravitations- und Auftriebskraft über die Neigung des Zentrifugalkraftscheiders und jene der strömungsbedingten Kräfte über die Pumpleistung variiert werden können, wurden diese beiden Faktoren für den Test ausgewählt. Zusätzlich wurde noch die Länge des Zentrifugalkraftscheiders als dritter Faktor miteinbezogen, da über diese der trennaktive Bereich, also der Grenzbereich zwischen Luftkern und Trennmedium, vergrößert und damit die Verweilzeit verlängert werden kann.

Experimentelle Durchführung

Als Probenmaterial wurden aus reinem Polypropylen (ρ ~ 0,9 [g/cm³]) und Polyethylenterephthalat (ρ ~ 1,3 [g/cm³]) hergestellte und auf eine Korngröße kleiner 20 mm geschredderte Folien mit einer Dicke von 100 µm eingesetzt. Um Auswertungsfehler zu vermeiden, wurden die PP-Folien lila und die PET-Folien türkis eingefärbt.

Für die Versuchsreihe wurden 3 (Einfluss-)Faktoren auf je 2 Niveaus gewählt:

A. Die Pumpleistung bei 65 und 75 % (entspricht etwa 21,5 und 25,5 m³/h).
B. Die Neigung des Zentrifugalkraftscheiders bei 20 und 40°.
C. Die Länge des Zentrifugalkraftscheiders bei 750 und 1.250 mm.

Da der Umbau des Zentrifugalkraftscheiders von 750 auf 1.250 mm Länge sehr aufwändig ist und ein systematischer Fehler hier ausgeschlossen werden kann, wurden zwei separate Versuchsreihen mit diesen Längen durchgeführt. In jeder dieser Versuchsreihen wurden die 4 möglichen Kombinationen der Niveaus je dreimal eingestellt und Trennprodukte erzeugt. Die Reihenfolge der Versuche wurde durch Auslosen festgelegt, um einem systematischen Fehler vorzubeugen. Um Probenahmefehler zu vermeiden, wurden die gesamten aufgegebenen 500 g Probenmaterial (~200 g PP und ~300 g PET) als Trennprodukte entnommen und ausgewertet.
Die Trennprodukte wurden im Anschluss über eine Schwimm-/Sink-Analyse in Wasser in eine Schwimm- und Sinkgutfraktion getrennt. Diese Fraktionen wurden anschließend bei 80°C für 24 Stunden getrocknet und für die Auswertung ausgewogen.

Auswertung

Als Bezugswert für die statistische Auswertung der Ergebnisse laut 2^k-Test wurde der erzielte Gehalt an Polypropylen im Leichtgut gewählt, da dieser ein Maß für die Trenngüte des Prozesses darstellt.

Variante	Faktoren*			$g_{PP,LG}$ [%]			Summe
	A	B	C	I	II	III	
(1)	-	-	-	98,82	98,35	98,01	295,19
a	+	-	-	99,50	97,92	98,35	295,77
b	-	+	-	96,84	96,10	96,30	289,24
c	-	-	+	99,01	98,48	98,97	296,47
ab	+	+	-	97,99	97,80	97,50	293,29
ac	+	-	+	99,48	99,50	99,50	298,48
bc	-	+	+	97,81	98,01	98,51	294,34
abc	+	+	+	99,50	99,50	99,48	298,48

** A – Pumpleistung 65 (-) und 75% (+); B – Neigung 20 (-) und 40° (+); C – Länge 750 (-) und 1.250 mm (+)*

Tabelle 1: Versuchsergebnisse des 2^k-faktoriellen Tests

Die erste wichtige Erkenntnis wird aus den Werten der mittleren Effekte gezogen (siehe Tabelle 2, Spalte 2). Die Werte der Faktoren A und C sind positiv, daher kann

geschlussfolgert werden, dass eine hohe Pumpleistung und ein langer Zentrifugalkraftscheider die Aufkonzentrierung einer qualitativ hochwertigen Leichtgutfraktion begünstigen. Der mittlere Effekt von B ist negativ, daher führt eine starke Neigung des Zentrifugalkraftscheiders zu einer stärkeren Verunreinigung der Leichtgutfraktion. Weiters kann der Einfluss der mittleren Effekte gereiht werden, indem ihre Absolutwerte einander vergleichend gegenübergestellt werden. Somit ist die Länge des Zentrifugalkraftscheiders für die Erzielung höherer Trenngüten von etwas größerer Bedeutung, als es dessen Neigung und die Pumpleistung sind. Bei dieser Betrachtung wird ebenso ersichtlich, dass der Einfluss von Faktorinteraktionen (AB, BC, AC, ABC) im Vergleich zu jenem der Faktoren selbst von untergeordneter Bedeutung ist.
Mit Hilfe einer Signifikanzanalyse (siehe Tabelle 2, Spalten 6 - 8) wurde im Anschluss überprüft, ob die aus den mittleren Effekten gewonnenen Schlussfolgerungen über den Einfluss der Faktoren statistisch signifikant sind. Hier ergibt sich das klare Bild, dass die drei Hauptfaktoren einen signifikanten Einfluss besitzen, die Querbeeinflussungen bis auf das Zusammenspiel von Länge und Neigung des Zentrifugalkraftscheider hingegen nicht.

Faktor**	Mittlerer Effekt*	Quadrat-summen*	Freiheits-grade	Mittlere Quadrate*	Test der Signifikanz (α=0,01)		
					Variable	Ablehnung	Signifikanz
i	-	SS_i	-	MS_i	F_i	F_0	-
A	9,00	485,80	1	485,80	30,66	8,53	Ja
B	-8,80	464,86	1	464,86	29,34	8,53	Ja
C	11,90	849,95	1	849,95	53,65	8,53	Ja
AB	4,66	130,45	1	130,45	8,23	8,53	Nein
AC	1,26	9,49	1	9,49	0,60	8,53	Nein
BC	5,25	165,28	1	165,28	10,43	8,53	Ja
ABC	-1,12	7,49	1	7,49	0,47	8,53	Nein
Fehler	-	253,48	16	15,84	-	-	-
Gesamt	-	2366,79	23	-	-	-	-

**Zur besseren Darstellbarkeit wurden in der Berechnung die Summen aus Tabelle 1 mit 10 multipliziert.*
***A – Pumpleistung; B – Neigung; C – Länge; AB, AC, BC, ABC – wechselweise Beeinflussung*

Tabelle 2: Versuchsauswertung mittels ANOVA-Tabelle

Zusammenfassung

Die Versuchsreihe zur Bewertung der Einflussfaktoren „Neigung und Länge des Zentrifugalkraftscheiders“ sowie „Pumpleistung“ auf die Reinheit der aufkonzentrierten Leichtgutfraktion kam zu dem Ergebnis, dass ein wenig geneigter, langer Zentrifugalkraftscheider bei hoher Pumpleistung optimale Trennergebnisse liefert. Die wechselweise Beeinflussung dieser Parameter ist von untergeordneter Bedeutung. Zudem konnte mit Ausnahme des Zusammenspiels von Neigung und Länge des Zentrifugalkraftscheiders ein signifikanter Einfluss auf die Reinheit des Leichtgutes nicht nachgewiesen werden.

Literatur

[1] W. Michaeli, M. Bittner, L. Wolters; (1992): Stoffliches Kunststoff Recycling
[2] M. Bauer; (2014): Mechanical processing of post-consumer plastics for chemical recycling, Dissertation am Lehrstuhl für Verfahrenstechnik des industriellen Umweltschutzes, Montanuniversität Leoben
[3] T. Kiesling; (2011) Faktorielle Versuchspläne, Vorlesungsunterlagen vom 18.11.2011, Institut für Statistik, Ludwig-Maximilians-Universität München

Wetting control of Multiscale-Layer Membranes for Membrane Distillation

Mohammad Rezaei, Wolfgang M. Samhaber
Johannes Kepler University Linz, Institute of Process Engineering, 4060 Leonding, Welser Straße 42
mohammad.rezaei@jku.at, wolfgang.samhaber@jku.at

Abstract

Membranes used in membrane distillation still suffer from the lack of hydrophobicity robustness when treating low surface tension solutions. In this work, the multiscale-layer superhydrophobic membrane is prepared by casting polyvinylidene fluoride solution on hydrophilic-hydrophobic non-woven supports using dry-wet phase inversion technique to modulate membrane wettability toward extremes. The membrane surface chemistry at the microscopic level is altered through self-assembly of a monolayer organosilane while the surface geometrical structure is modified by coating SiO_2/TiO_2 nanoparticles. Direct contact membrane distillation experiments show that the persistence high salt rejection in the presence of a wetting agent is achieved while similar flux to other MD membranes is attainable.

Introduction

Since 1963 [1], membrane distillation (MD) has been studied increasingly as a promising alternative to conventional separation techniques such as ordinary distillation or evaporation [2]. In membrane distillation where a hydrophobic macroporous membrane acts as a physical barrier between feed and permeate, only vapors of volatile components with trans-membrane vapor pressure difference can pass through the membrane pores and the remaining constituents stay in the brine side of the membrane. Simultaneous heat transfer occurs through the membrane matrix and its pores. The heat flux comprises the vapor latent heat convection in membrane pores and conduction across the membrane material and gas-filled pores. MD offers following advantages compared to conventional separation processes such as distillation and other membrane processes:

1. operating at lower temperatures than the boiling point of the feed solutions which makes it desirable for heat sensitive products
2. unrestrained by high osmotic pressure compare to pressure-driven membrane processes which make it attractive in desalinating high salinity brines
3. lower capital cost compares to reverse osmosis or nanofiltration due to the absence of expensive equipment, such as high-pressure pumps and vessels
4. capable of using available low-grade waste heat and renewable energy sources
5. high rejection factor of non-volatile solutes leading to high product quality
6. requiring lower vapor space leading to plant compactness compared to distillation
7. ability to integrate with other pressure-driven membrane processes
8. can be used for small-scale desalination in remote regions

Although membrane distillation offers several advantages, the possibility of membrane pores wetting by liquid feed is one of the main reasons that hinders its application in large scales [3]. Membrane wetting occurs if the trans-membrane pressure exceeds the breakthrough pressure of the membrane, known as liquid entry pressure (LEP). The LEP of a surface is directly proportional to the surface roughness (SR) and the surface free energy (SFE) [4]. The surface roughness of a porous membrane has been proved to be

increased by the addition of hydrophobic layer or coating nanoparticle materials on the surface of a porous membrane [5] while reducing surface free energy is realized by functionalization of low surface energy materials particularly fluorosilane [6]. A variety of methods has been employed to create or change surfaces of many substrate materials to control surface wettability. Novel MD membranes such as composite hydrophilic-hydrophobic membranes [7], superhydrophobic membranes [8] and omniphobic membranes [9] using biomimetic approaches have been developed.
This study aims to investigate wetting control in MD by making a robust anti-wetting multiscale-layer membrane (MSLM) through a combination of fabricating macroporous hydrophilic/hydrophobic composite membranes, SiO_2/TiO_2 nanoparticle coating onto the composite membrane and surface silanization (figure 1). Embedding nanoparticles on extra macroscale surface roughness caused by hydrophobic NWS and reduction of surface free energy by surface silanization will increase membrane robustness against wetting. The fabricated membranes are characterized by atomic force microscopy (AFM), contact angle goniometry and LEP measurement. Wetting behavior of the membranes is assessed by examination of membrane performance in a direct contact membrane distillation set-up in the presence of a wetting agent (sodium dodecyl sulfate).

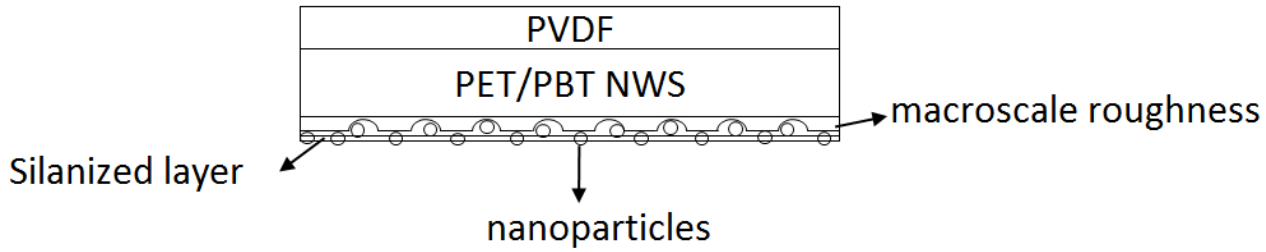

Figure 1: Schematic illustration of multiscale-layer membrane

Materials

Polyvinylidene fluoride (PVDF, Kynar 761, 370 kg/mol) as polymer powder was purchased from Arkema. Tetraethyl orthosilicate (reagent grade) and titanium(iv) isopropoxide (97%) as SiO_2 / TiO_2 precursors, 1H, 1H, 2H, 2H-perfluorododecyltrichlorosilane (FTCS) as surface energy reducing agent, absolute isopropanol and ethanol as solvents, sodium dodecyl sulphate as surfactant, hydrochloric acid (33%), sodium chloride (NaCl) were purchased from Sigma–Aldrich. Toluene and N,N-Dimethylacetamide as solvents were supplied by VWR and J. T. Baker.

Experiments

Membrane Preparation

Fabricating hydrophilic/hydrophobic composite membrane

Composite membrane is fabricated based on Bilad et al.´s work [3] by casting the polymer solution (PVDF dissolved at 15% w/w in Dimethylacetamide) on the hydrophilic non-woven support (NWS, Novatexx 2481) which is on top of the pre-wetted hydrophobic NWS (Novatexx 2473) with ethanol at room temperature. The wet-casting thickness is adjusted to 500 µm using a doctor blade. After casting, the polymer film is exposed to air for film penetration in NWSs for 5 min and dipped in a coagulation bath containing deionized (DI) water and SiO_2/TiO_2 nanoparticles. Upon concluding the fast phase inversion process, the membrane is peeled off by hand from the hydrophobic NWS. The aim of introducing a

hydrophobic NWS and embedding nanoparticle in membrane matrix is to induce multi-scale structure on the surface of the bottom layer which results in added macro-scale roughness.

Coating of SiO_2/TiO_2 nanoparticles onto the composite membrane

To increase the surface roughness of the membranes, SiO_2/TiO_2 nanoparticles is coated on the surface of composite membranes. The membranes are dip-coated in the coating solution (prepared based on our earlier work [10]). The coated membranes are dried at room temperature and in the oven at 120 °C each for 1 h. At the end of the 2 h, the membranes are gently rinsed with DI water and are irradiated with UV light for 5 h.

Surface silanization of the multiscale-layer membrane

The coated composite membranes are filtered with a solution of FTCS dissolved in toluene (5 wt%) at a slight vacuum. After filtration, the membranes are rinsed with fresh toluene to remove any residuals. The silanized membranes are then placed in the oven at 120 °C for 2 h.

Membrane Characterization

The membranes on each step of fabrication and modification are characterized in terms of surface roughness by atomic force microscopy, wettability by liquid entry pressure experiment [11], contact angle by a goniometer.

Membrane performance

Fabricated membranes are tested in a direct contact membrane distillation (DCMD) configuration. Figure 3 illustrates the schematic diagram for a laboratory-scale system composing of a feed reservoir, a permeate container, and the membrane distillation cell. The hot solution (1 molar NaCl) in presence of sodium dodecyl sulfate is supplied to

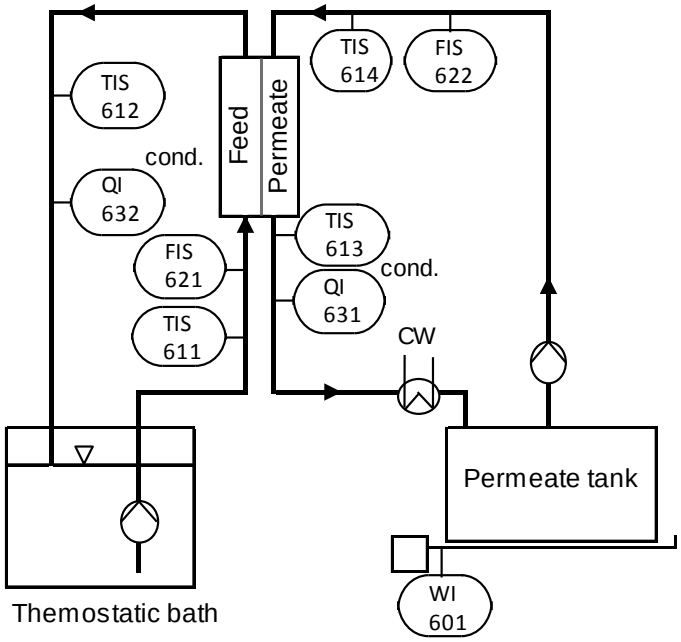

Figure 3: Schematic diagram for the laboratory-scale DCMD system

contact directly with the hot membrane side surface using a thermostatic bath. A balance is used to measure permeate flux through the membrane. Pore wetting is analyzed through permeate quality by measuring permeate electrical conductivity.

Conclusion

The multiscale –layer flat-sheet membranes are prepared using a combination of the dry-wet phase inversion membrane fabrication technique and physical/chemical surface modifications. This is achieved by casting a PVDF solution on a hydrophilic NWS on top of pre-wetted hydrophobic NWS. The surface free energy is reduced by self-assembly of perfluorodecyltrichlorosilane through van der Waals interactions between alkylchains, while surface roughness is increased by coating of the surface with the SiO_2/TiO_2 nanoparticle. It is observed that anti-wettability of MSL membranes is strongly dependent on the membrane surface free energy and membrane roughness. Direct contact membrane distillation experiments show that obtained permeate flux of MSL membranes is similar to other MD membranes and a persistence high salt rejection in the presence of a wetting agent is obtainable.

Reference

[1] B. R. Bodell, “Silicone rubber vapor diffusion in saline water distillation,” *United States Pat. Ser. No. 285,032*, 1963.

[2] M. Khayet and T. Matsuura, *Membrane Distillation Principles and Applications*. 2011.

[3] M. S. El-Bourawi, Z. Ding, R. Ma, and M. Khayet, “A framework for better understanding membrane distillation separation process,” *J. Memb. Sci.*, vol. 285, no. 1–2, pp. 4–29, Nov. 2006.

[4] J. D. Miller, S. Veeramasuneni, J. Drelich, M. R. Yalamanchili, and G. Yamauchi, “Effect of roughness as determined by atomic force microscopy on the wetting properties of PTFE thin films,” *Polym. Eng. Sci.*, vol. 36, no. 14, pp. 1849–1855, 1996.

[5] J. Zhang, Z. Song, B. Li, Q. Wang, and S. Wang, “Fabrication and characterization of superhydrophobic poly (vinylidene fluoride) membrane for direct contact membrane distillation,” *Desalination*, vol. 324, pp. 1–9, 2013.

[6] E. Erasmus and F. a. Barkhuysen, “Superhydrophobic cotton by fluorosilane modification,” *Indian J. Fibre Text. Res.*, vol. 34, no. 4, pp. 377–379, 2009.

[7] F. A. A. M. and H. A. A. Muhammad R. Bilad, “New Concept for Dual-Layer Hydrophilic/Hydrophobic Composite Membrane for Membrane Distillation,” pp. 122–129, 2015.

[8] A. Razmjou, E. Arifin, G. Dong, J. Mansouri, and V. Chen, “Superhydrophobic modification of TiO2 nanocomposite PVDF membranes for applications in membrane distillation,” *J. Memb. Sci.*, vol. 415–416, no. July, pp. 850–863, Oct. 2012.

[9] S. Lin, S. Nejati, C. Boo, Y. Hu, C. O. Osuji, and M. Elimelech, “Omniphobic Membrane for Robust Membrane Distillation,” *Environ. Sci. Technol. Lett.*, vol. 1, no. 11, pp. 443–447, Nov. 2014.

[10] M. Rezaei and W. Samhaber, “Wetting Behaviour of Superhydrophobic Membranes Coated with Nanoparticles in Membrane Distillation,” *Chem. Eng. Trans.*, vol. 47, 2016.

[11] M. Rezaei and W. M. Samhaber, “Wetting phenomenon in membrane distillation processes,” in *Minisymposium der Verfahrenstechnik in Österreich*, 2014, no. 10, pp. 56–58.

Experimental study of separation performance of nanofiltration process for complex mono and multivalent salts during sugar concentration

Muhammad Ali Samee *, Amal Ahmed, Michael Harasek, Anton Friedl
Vienna University of Technology, Institute of Chemical Engineering
Getreidemarkt 9/166, A-1060 Vienna
*muhammad.ali.samee@tuwien.ac.at

Abstract

The energy consumption of the sugar industry is quite high due to the thermal energy required for multistage evaporation. Alternative processes have been studied to reduce this energy demand. Membrane technology is a well-established process for water treatment. Reverse osmosis (RO) and nanofiltration (NF) have also been examined for the pre-concentration of clarified thin sugar juice to reduce the role of evaporation [1]. The clarified thin sugar juice contains 15 °Brix (15 w%) of sugar and about 0.25 - 0.40 w% ionic compounds [2,3]. In this paper the effect of the presence of monovalent and multivalent salts on the separation performance of a nanofiltration membrane during sugar concentration has been studied experimentally. The sugar rejection was not affected much by the salt concentration but the salt rejection was highly dependent on the sugar concentration.

Introduction

Membrane technology is a novel process. Membrane processes can be applied without any addition of solvent and heat. Many researchers have investigated the potential application of membranes in the sugar industry for the purification of raw sugar juice in order to reduce the use of lime and multiple purification steps [4, 5]. RO/NF has the advantage of removing water from the aqueous solution of sugar below its boiling point avoiding degradation [6]. In the present experimental work, the separation behavior of the NF membrane for different ionic compounds (monovalent and multivalent) and sugar mixtures have been explored.

Experimental setup

The experiments were conducted on a lab-scale cross-flow membrane unit OS-MC-01 from Osmota with an effective membrane area of 0.008 m^2. Sugar concentration was measured by a digital refractometer DR301-95 from Krüss. The concentrations of dissolved anions and cations in the feed and permeate samples, collected during the experiments, were analysed on a Dionex ICS 5000+ DC ion chromatography equipment [6]. In this work, a negatively charged NF membrane (MPF-34) from Koch Membrane was used [7]. It has a maximum operating temperature limit of 70 °C, a pressure range of 5 - 35 bar, and a pH range 0 - 14. All the experiments were performed at the same process conditions of 32 bar, 60 °C, feed flowrate of 2.5 L/min, starting with a feed sugar concentration of 15 °Brix and 0.25 w% of each electrolyte. The temperature was maintained constant by using a thermostat. The permeate weight was measured gravimetrically with an electric balance in specified intervals to calculate the flux. Pure water permeability was tested before and after each experiment at 32 bar, 2.5 L/min and 30 °C.

Results and Discussion

The flux of the model sugar solution decreases with the sugar concentration from 65 kg/m^2h at 13 °Brix to less than 10 kg/m^2h at 24 °Brix. This is due to the increase in osmotic pressure

with the increasing sugar concentration and as a result the net driving force is decreased. The addition of a single monovalent/divalent salt or a complex mixture of both, in the sugar solution, contributes to increase the osmotic pressure resulting in less permeate flux than the flux value of model sugar solution. This addition does not affect the flux considerably but it gives the same decreasing trend as shown in figure 1.

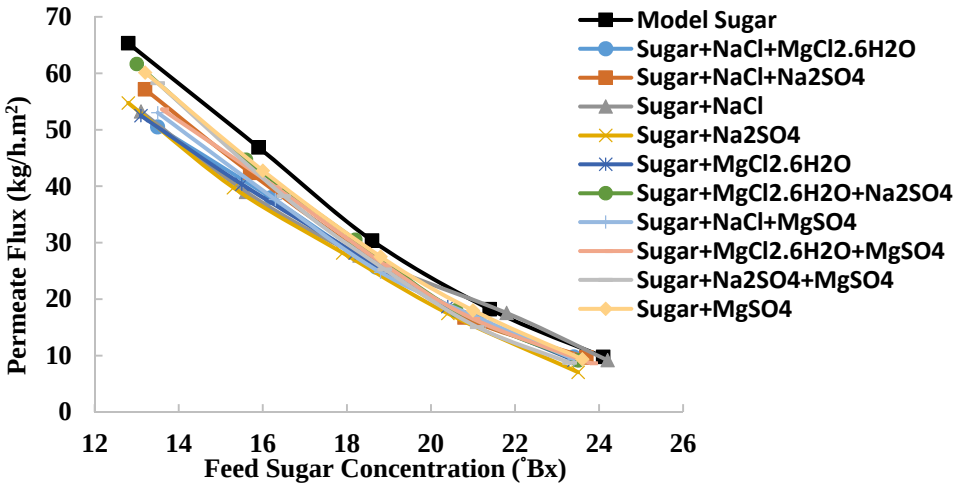

Fig 1. Influence of the sugar concentration on the permeate flux

The sugar rejection of the model sugar solution is very high (98 - 97%) as shown in figure 2. The sugar concentration has no significant influence on the sugar rejection. Similarly, the addition of a single monovalent/divalent salt or a complex mixture of both in the sugar solution does not show a pronounced decrease in the sugar rejection (98 - 94%).

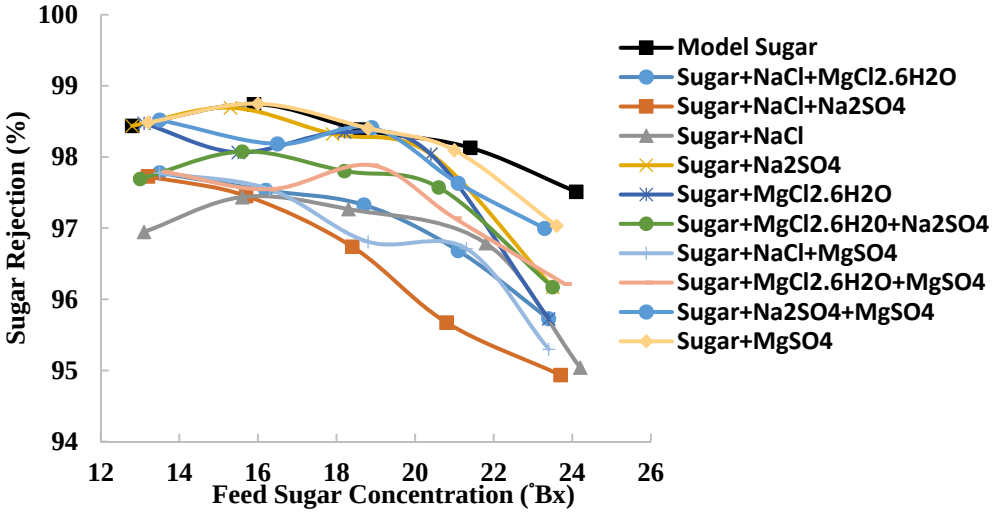

Fig 2. Effect of the sugar concentration on the sugar retention

The rejection of monovalent cations e.g Na^{1+} has been investigated as a function of sugar concentration as presented in figure 3. The rejection of Na^{1+} decreases with increasing sugar concentration. It demonstrates a varying degree of rejection 94 to (-21%) in a mixture of sugar, monovalent and/or multivalent cations and anions.

Figure 4 describes the rejection of divalent cations e.g. Mg^{2+} as a function of sugar concentration. Mg^{2+} shows a higher rejection (> 88 %) in sugar, monovalent and/or divalent ionic mixtures.

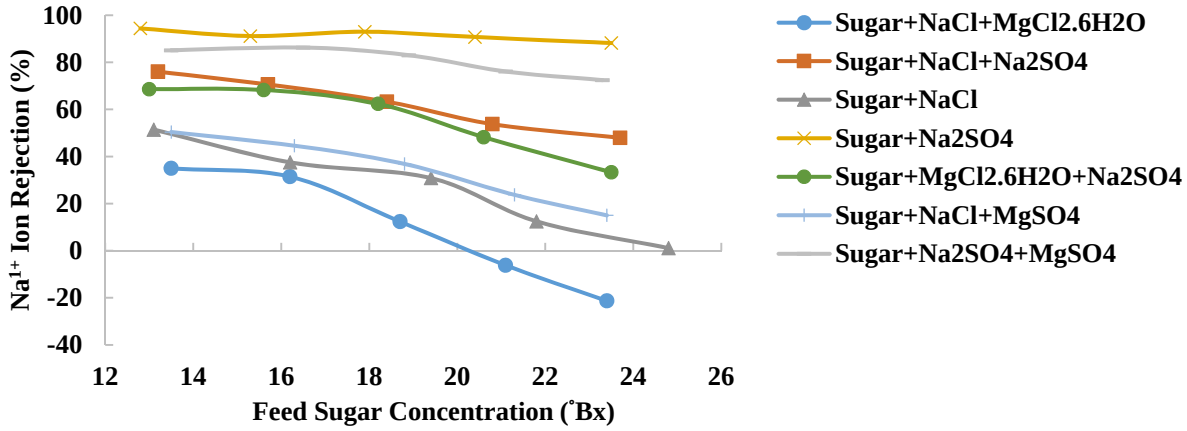

Fig 3. Rejection of Na^{1+} ion as a function of feed sugar concentration

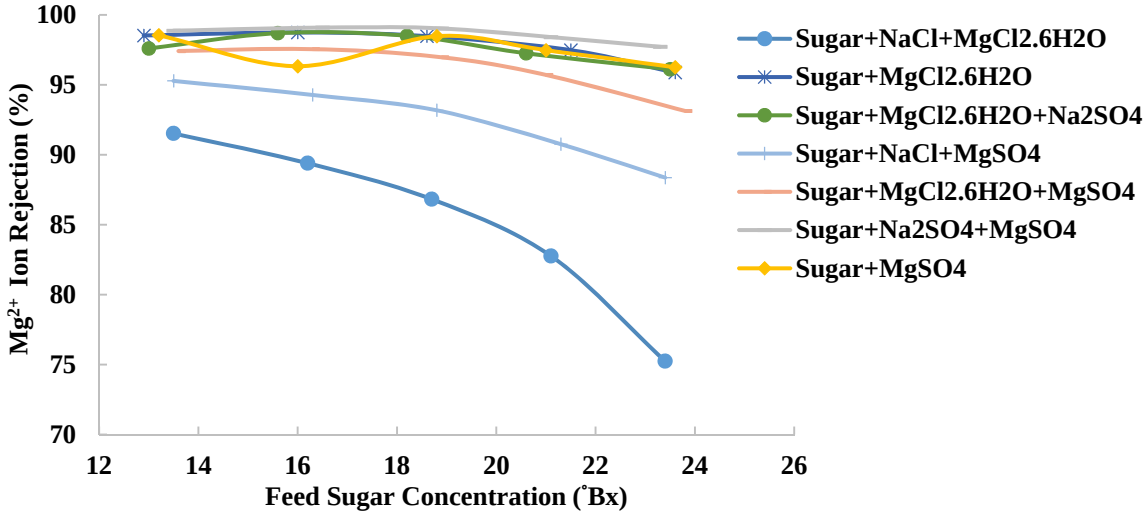

Fig 4. Rejection of Mg^{2+} ion as a function of feed sugar concentration

The rejection of monovalent anions e.g. Cl^{1-} has been investigated as a function of sugar concentration as shown in figure 5. The rejection of Cl^{1-} decreases with the increasing sugar concentration. It gives a varying degree of rejection 98 to (-46%) in a mixture of sugar, monovalent and/or multivalent cations and anions.

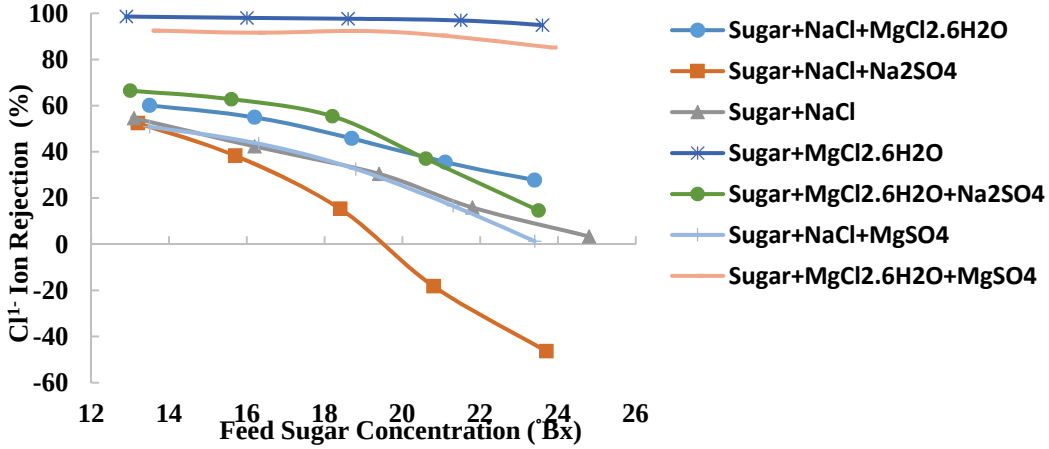

Fig 5. Rejection of Cl^{1-} ion as a function of feed sugar concentration

Figure 6 depicts the rejection of divalent anions e.g. SO_4^{2-} as a function of sugar concentration. SO_4^{2-} presents a higher rejection (> 88 %) in the sugar, monovalent and/or divalent ionic mixtures.

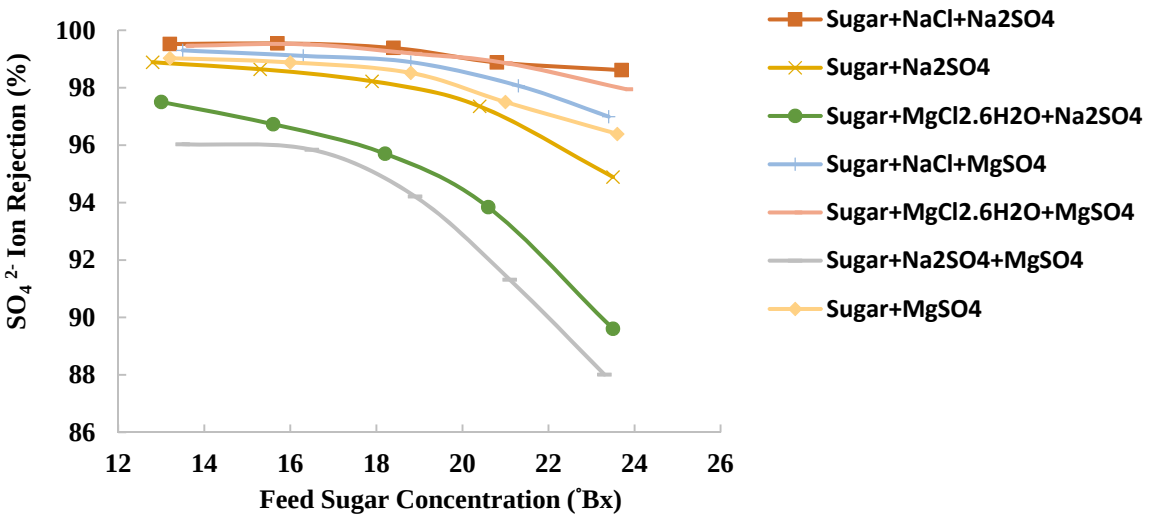

Fig 6. Rejection of SO_4^{2-} ion as a function of feed sugar concentration

Conclusions

The permeate flux for aqueous solution of sugar and monovalent/divalent salt (single or mixture) decreases with the sugar concentration. In addition, it is dependent on osmotic pressure of the solution and pure water permeability of the membrane. Sugar rejection in all cases is always higher than 95% and is not effected much by the sugar concentration and the salt concentration in the range studied. Na^{1+} gives negative rejection in the presence of sugar, monovalent anion and divalent cation and shows almost zero rejection in the presence of sugar and only one monovalent anion. Similarly, Cl^{1-} exhibits a negative rejection in the presence of sugar, monovalent cation and divalent anion and shows almost zero rejection in the presence of sugar and only one monovalent cation. It can be generalized that by adding sugar to different ionic mixtures with one ion with a maximum valence of 2 will govern the negative retention of corresponding monovalent ion as observed in case of Na^{1+} and Cl^{1-}. Mg^{2+} and SO_4^{2-} show a rejection greater than 90% in most of the solutions containing sugar, monovalent and multivalent ions.

References

[1] S. Gul, M. Harasek, Energy saving in sugar manufacturing through the integration of environmental friendly new membrane processes for thin juice pre-concentration, Applied Thermal Engineering 43 (2012) 128-133.
[2] P. Pinacci, M. Radaelli and M.C. Benedetto, Demineralization of thin juice by electrodialysis in the beet sugar manufacturing industry, Process engineering with membranes, Granada, Spain, June3 - 6, 2001.
[3] Data received from AGRANA Zucker GmbH Austria.
[4] V. Hakimzadeh, S.M.A. Razavi, M.K. Piroozifard, and M. Shahidi, The potential of microfiltration and ultrafiltration process in purification of raw sugar beet juice, Desalination, 200(1-3) (2006) 520–522.
[5] A. Hinkova, Z. Bubnik, P. Kadlec, and J. Pridal, Potentials of separation membranes in the sugar industry, Separation and Purification Technology, 26(1) (2002)101–110.
[6] http://www.dionex.com/en-us/products/ion-chromatography/ic-rfic-systems/ics-5000/lp-72594.html (Accessed on: 05-02-2016)
[7] Koch membrane. http://www.kochmembrane.com/

Regenerierung von staubbeladenen Filtermedien mittels Absaugung

Thomas Laminger*, Elisabeth Salajka
TU Wien, Institut für Verfahrenstechnik, Umwelttechnik und Technische Biowissenschaften, Getreidemarkt 9/166, 1060 Wien
thomas.laminger@tuwien.ac.at

Kurzfassung

Eine häufig angewendete Methode zum Regenerieren eines mit Staub beladenen Filtermittels stellt das Pulse-Jet-Verfahren dar. Dabei kann es aber bei der Abscheidung von nanoskaligen Stäuben dazu kommen, dass sich der abgeschiedene Filterkuchen nicht erfolgreich vom Filtermittel wiederabreinigen lässt. Daher wurde in dieser Arbeit die Filterregeneration durch Absaugen mittels flacher und rotierender Absaugdüsen untersucht.
An einem Filterprüfstand wurde mit verschiedenen Filtermitteln, Teststäuben und Absaugdüsen die Effizienz der Regeneration durch das Absaugen ermittelt. Dabei wurde ein Filtermittel mit Staub beladen und anschließend mit einer Absaugdüse gereinigt. Dieser Vorgang wurde zehn Mal (zehn Filtrations- gefolgt von zehn Regenerationszyklen) wiederholt. Besonderes Augenmerk wurde auf den Verlauf des Restdruckverlusts mit steigender Zykluszahl und die bildoptische Analyse der Filtermitteloberfläche nach Versuchsende gelegt.
Die bildoptische Analyse der bestaubten Filtermittel mit einem Mikroskop zeigte, dass die rotierenden Borsten im Falle von Membranfiltermedien eine Schädigung der Filtermitteloberfläche bewirken. Die Filtermittel Nadelfilz und Gewebe zeigten jedoch keine nennenswerten Oberflächenbeschädigungen. Die flache Düse bewirkte keine erkennbare Beschädigung bei allen drei Filtermitteln. Anhand der Verläufe des Restdruckverlusts nach einer Filtermittelregeneration zeigte sich, dass die Absaugdüse mit rotierenden Borsten, bei der es zwar zur Saugkraftverlust durch das Antreiben einer mit Borsten versehenen Rolle kommt, ähnlich effizient wie die flache Düse den Staubkuchen entfernt. Weitere Untersuchungen mit elektrisch angetriebenen rotierenden Bürsten, bei denen die Intensität der mechanischen Einwirkung über die Bürstendrehzahl variiert werden kann, sollen weiteren Aufschluss über die Mechanismen der Abreinigung durch Absaugen bringen.

Einleitung

Es stehen mehrere Möglichkeiten der Filtermittelregeneration bei der Entstaubung zur Verfügung [1, 2]. Sehr häufig wird dabei das Pulse-Jet-Verfahren angewendet, bei denen ein Druckluftimpuls von der Reingasseite den aufgebauten Filterkuchen auf einem Filterschlauch abwirft. Je kleiner die Partikel sind, aus denen der Filterkuchen aufgebaut ist, desto größer sind die Anziehungskräfte. Dies kann so weit führen, dass die Adhäsionskräfte zwischen Filtermedium und Staub beim Aufblähen des Schlauches nicht überwunden werden können. Auch die Anziehungskräfte zwischen den einzelnen Partikel können durch den Druckstoß überwunden werden und dazu führen, dass der Staubkuchen reißt. Die Druckluft entweicht durch die entstandenen Risse und löst den Kuchen nicht vom Filtermittel ab, was zu einer zunehmenden Verstopfung und schlussendlich zum Austausch des Filtermittels führt [3].
Eine Alternative für die Filtermittelregeneration beim Vorhandensein von Stäuben, die

keinen geschlossenen homogenen Staubkuchen bilden (unter anderem auch faserige Stäube), ist die Verwendung von Absaugdüsen. Vor allem in der Entstaubung in der Textilindustrie ist dies ein häufig angewendetes Verfahren. Die relative Bewegung zwischen Absaugdüse und dem Filtermittel kann auf verschiedene Arten erfolgen. Das Filtermittel kann unbeweglich und die Absaugdüse sich bewegen (zB. flacher Panelfilter) oder das Filtermittel kann sich bewegen und die Absaugdüse fixiert bleiben (zB. ein rotierender Trommelfilter) [2].

Im Zuge einer vorangegangenen Arbeit [4] wurde ein Filtermittelprüfstand im Labormaßstab aufgebaut, der von oben nach unten durchströmt wird. Ein flaches Filtermittel wird dabei von einer bewegten Absaugdüse in horizontaler Ebene von Staub befreit. Mit diesem Filtermittelprüfstand wurden bereits Untersuchungen zur Absauggeschwindigkeit, Absaugluftvolumenstrom, Düsenabstand und Verschubgeschwindigkeit der Absaugdüse vorgenommen, um ein möglichst effizientes Regenerieren des Filtermittels zu erreichen [5, 6]. Es fehlen allerdings Analysen der Auswirkungen von verschiedenartigen Düsenaufsätzen auf das Regenerationsverhalten von unterschiedlichen mit Staub beladenen Filtermitteln, welche Gegenstand dieser Arbeit sind.

Versuchsdurchführung und Auswertung

Absaugdüsen

Zur Absaugung der bestaubten Filtermittelproben (effektive Filterfläche 10x30cm) wurden handelsübliche Staubsaugerdüsen verwendet. Zwei Absaugdüsen, eine rotierende Bürste und eine herkömmliche unten abgeflachte Düse (Abb. 1) wurden eingesetzt. Der effektive Einsaugbereich beider Düsen war ca. 13cm×3cm gleich groß. Der Absaugvolumenstrom von 40m³/h war bei beiden Düsen gleich groß. Bei der rotierenden Bürste wird der Absaugvolumenstrom auch dazu genützt, um über ein Schaufelrad die Bürste in Rotation zu versetzen. Daher wirkt zum Ablösen der Staubschicht zusätzlich zum Luftstrom durch das Filtermittel auch die mechanische Bewegung der Borsten.

Abbildung 1: Verwendete Absaugdüsen; rotierende Bürste (links), flache Düse (rechts)

Filtermittel und Teststäube

Es wurden drei verschiedene Filtermittel mit variierenden Oberflächen verwendet. Gewählt wurden ein mit einer Teflonmembran beschichtetes Glasfasergewebe, ein Polyamid–Nadelfilz mit einer kalandrierten Oberfläche und ein Glasfasergewebe ohne Oberflächenbeschichtung.

Versuchsdurchführung

Das zu untersuchende neuwertige Filtermittel wurde mit Teststaub beladen, bis der Druckabfall über das Filtermittel ein Maximum erreicht. Beim Membran-Filtermittel sowie Gewebefilter betrug dieser Wert 1000Pa und beim Nadelfilz 500Pa. Beim Erreichen dieses

Maximums wurde das Filtermittel mit einer Absaugdüse abgesaugt und nach der Reinigung erneut beladen (in Summe 10 Filtrations- und Regenerationszyklen). Analog wurde mit allen Stäuben, Filtermitteln und Absaugdüsen verfahren.
Durch die Aufzeichnung des Druckverlaufes bei voranschreitender Versuchszeit konnten der Restdruckverlust nach jeder Regeneration und die Zyklusdauer bestimmt werden. Die gebrauchten Filtermittel wurden zusätzlich unter dem Lichtmikroskop (Olympus BX 62) betrachtet um eventuell aufgetretene Schäden der Filtermitteloberfläche durch die sich wiederholende Belastung der Düsen während des Absaugens feststellen zu können.

Vergleich der Absaugdüsen anhand des Restdruckverlusts nach einer Regeneration

Der Restdruckverlust nach einer Abreinigung des bestauben Filtermittels erlaub eine Beurteilung des verbliebenen Staubes in der Tiefe oder an der Oberfläche des Filtermittels und somit auch über die Effektivität über die Regeneration an sich. In Folge wurde von zehn Filtrationszyklen der mittlere Restdruckverlust als Maß zur Beurteilung der Regenerationseffizienz der untersuchten Absaugdüse gewählt.

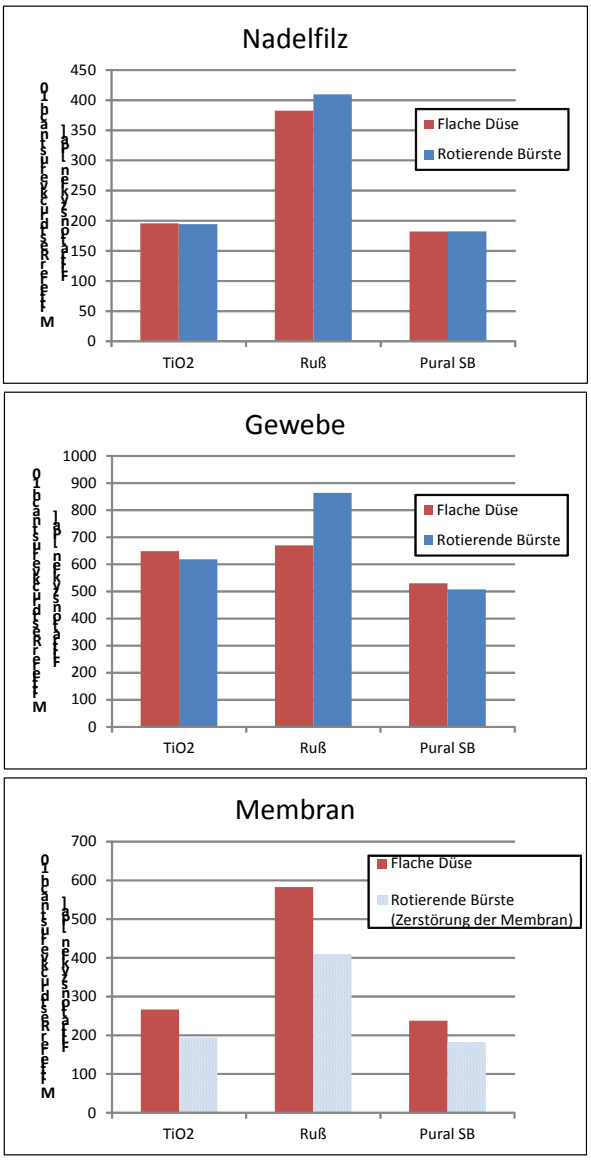

Abbildung 2: Mittlerer Restdruckverlust nach 10 Filtrationszyklen von drei Filtermitteln und je drei Staubarten

Wie man in Abbildung 2 erkennen kann, zeigen die mittleren Restdruckverlustwerte nach 10 Filtrationszyklen bei den Filtermitteln Nadelfilz und Gewebe für alle drei Teststäube keine nennenswerten Unterschiede. Dieses Ergebnis ist dahingehend interessant, weil die rotierende Bürste trotz geringerem Absaugvolumenstrom (ein Teil geht durch den Antrieb der rotierenden Bürste verloren) die Stäube genauso gut entfernt wie die flache Düse.

Große Unterschiede zeigen sich jedoch beim Filtermittel Membran. Der geringere mittlere Restdruckverlust bei der rotierenden Bürste lässt zunächst ein besseres Entfernen des abgelagerten Staubes vermuten. Eine Analyse des Kurvenverlaufs des Restdruckverlusts über die Anzahl der Filtrationszyklen (Abb. 3 – exemplarisch für die Kombination Membran-TiO_2) zeigt jedoch den dahinterliegenden Grund dafür: Man kann erkennen, dass bereits nach der zweiten Regeneration ein starker Abfall des Restdruckverlusts erfolgt und dieser sogar unter den Druckverlust des neuwertigen Filtermittels (210Pa) fällt. Dies kann nur durch eine entsprechende Veränderung der Filtermittelstruktur erklärt werden.

Ergebnisse der bildoptischen Untersuchung der Filtermitteloberflächen

Anhand von bildoptischen Untersuchungen der bestauben Filtermittel nach den zehn Filtrationszyklen sollte zunächst die verbleibende Staubmasse quantitativ vermessen werden, um eventuell Inhomogenitäten der Filtermittel-oberfläche oder der Luftströme beim Absaugen zu erkennen. Aufgrund der Kurvenverläufe (Abb. 3) des Restdruckverlusts wurde jedoch eine qualitative Analyse der Oberfläche der Filtermittel vorgenommen.

Für die Kombination Membran-Filtermittel und TiO_2 als Teststaub zeigt Abbildung 4 exemplarisch die mikroskopischen Aufnahmen der Filtermittel-oberfläche. Im neuwertigen Zustand ist die geschlossene Membran zu erkennen. Die Aufnahme nach der Absaugung mit rotierender Bürste zeigt, wie die Membran aufgerissen wurde und dass das Stützgewebe bereits frei liegt.

Für die anderen zwei Filtermittel (Gewebe und Nadelfilz) konnten zwar einige Spuren des Verfahrens der Absaugdüsen auf den Oberflächen im Mikroskop identifiziert werden. Eine nennenswerte Beschädigung oder Zerstörung war jedoch nicht erkennbar.

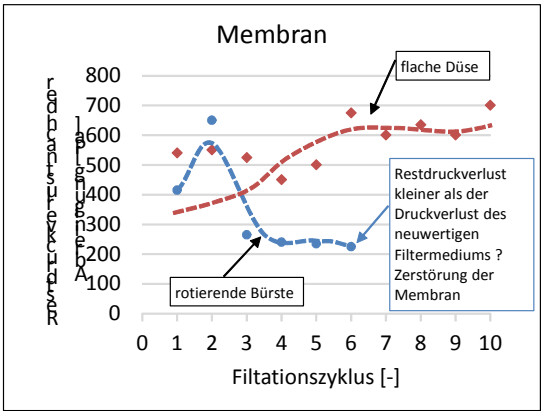

Abbildung 3: Restdruckverlust als Funktion des Filtrationszyklus für das Membran-Filtermittel mit Teststaub TiO_2

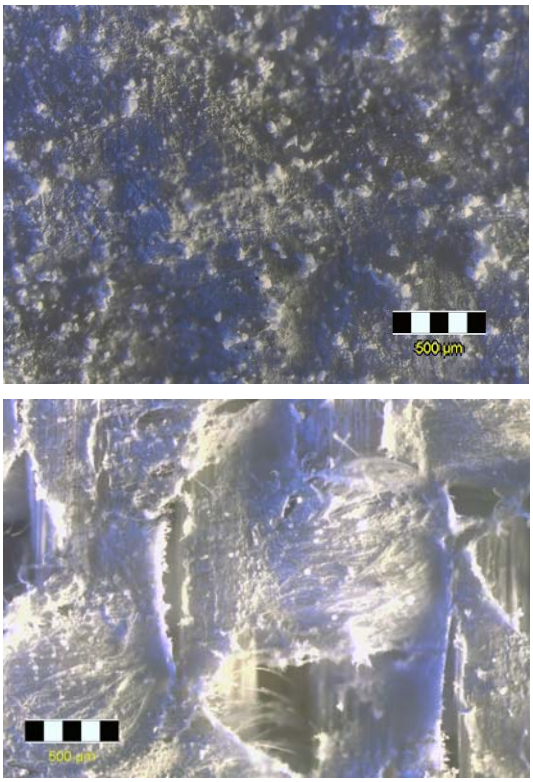

Abbildung 4: Mikroskopische Aufnahme der Oberfläche des Membran-Filtermittels; neuwertiges Filter (oben); nach Absaugung mittels rotierender Bürste (unten)

Schlussfolgerung und Ausblick

Der Einsatz der rotierenden Bürste zur Entfernung von abgeschiedenen Staub von der Filtermittel-oberfläche ist bei den Filtermitteln Gewebe und Nadelfilz mit gleich gutem Erfolg zu beurteilen. Bei der rotierenden Bürste konnte durch die zusätzliche mechanische Bewegung eine Kompensation des Saugkraftverlusts durch den Antrieb der Bürstenschaufeln erzielt werden.

Da dieser Effekt sowohl für die mikroskaligen (PuralSB) als auch für die nanoskaligen Teststäube (TiO_2 und Ruß) erkennbar ist, könnte diese Art der Filtermittelregeneration für besonders haftfähige Staubarten interessant werden. Es ist angedacht, die Versuche mit einer rotierenden Bürste mit unabhängiger Bürstendrehzahleinstellung (zB. durch einen Elektromotor) zu wiederholen. Damit könnte der Einfluss der zusätzlichen mechanischen Bewegung (Abbürsten des Staubes) untersucht werden.

Literatur

[1] Löffler, F.; Dietrich, H.; Flatt, W.: „Staubabscheidung mit Schlauchfiltern und Taschenfiltern“; Braunschweig/Wiesbaden: Friedr. Vieweg & Sohn; 1984.

[2] MikroPul GmbH & Co. KG und W.L. Gore & Associates GmbH: „Moderne Entstaubungstechnik mit Oberflächenfiltern“; Online-PDF-Dokument, letzter Zugriff: 25.1.2016. http://www.mikropul.de/downloads/MikroPul-Entstaubungstechnik-Oberflaechenfilter.pdf

[3] Stecher, M.: „Analyse der künstlichen Filtermittelalterung bei der Abreinigungsfiltration und Modellierung der damit verbundenen Verstopfungsvorgänge“; Dissertation, Technische Universität, Wien 2014.

[4] Wolfslehner, J.: „Regeneration von textilen Filtermitteln durch Absaugung“. Dissertation, Technische Universität, Wien 2014.

[5] Höflinger, W.; Laminger, T.; Wolfslehner, J.: "Operation Parameters of Vacuum Cleaned Filters"; World Academy of Science, Engineering and Technology, 8 (2014), 2; S. 935 - 941.

[6] Laminger, T.; Wolfslehner, J.; Höflinger, W.: “Design of vacuum cleaned dust filter with modular filter units”; Chem. Eng. Technol. 10.1002/ceat.201500351 (online verfügbar); 2015.

Einflussgrößen des Druckverlustes bei der Durchströmung von Sinterbetten

N. Tsioutsios[1*]; J. Rieger[2], C. Weiss[1]

1 Chair of Process Technology and Industrial Environmental Protection (VTIU), Montanuniversität Leoben, Austria
2 K1-MET GmbH, Leoben, Austria

* Corresponding author

Kurzfassung

Sinteranlagen in der stahlerzeugenden Industrie stellen ressourcenintensive Anlagen dar. Durch eine Kreislaufführung von Feinmaterial wird eine Erhöhung der Einsatzmaterialeffizienz erreicht. Negative Effekte, wie z.B. eine Erhöhung des Druckverlustes bei der Gasdurchströmung der Sinterschüttung können dabei beobachtet werden. Die aktuellen Forschungsarbeiten sollen Grundlagen erarbeiten, um optimierte Prozessgestaltungen dieser und analoger Bettdurchströmungen mit und ohne teilweiser Aufschmelzung des Einsatzmaterials zu ermöglichen.

Einleitung

Unter Sintern wird das Zusammenbacken von Schüttungen mit unterschiedlichen Korngrößen verstanden. Dazu wird das auf einem umlaufenden Band aufgebrachte Einsatzmaterial von einem heißen Luftstrom durchströmt. Dies führt zu einem Auf- und Zusammenschmelzen wobei flüchtige Bestandteile ausgetrieben werden. Das Material erfährt so eine Verfestigung. Der für die Sinterung benötige Luftstrom wird durch eine Verbrennung von feinem Kohlenstoff (auch als Koksgrus bezeichnet) aufgeheizt (= oxidierendes Sintern). Durch das Sinterbett erfährt die Strömung einen Widerstand, welcher sich als Druckverlust äußert. Die rechnerische Analyse dieses Druckverlustes ist Bestand der aktuellen Untersuchungen. Abbildung 1 zeigt eine schematische Darstellung des großtechnischen Sinterprozesses mit Bezeichnung der Anlagenteile.

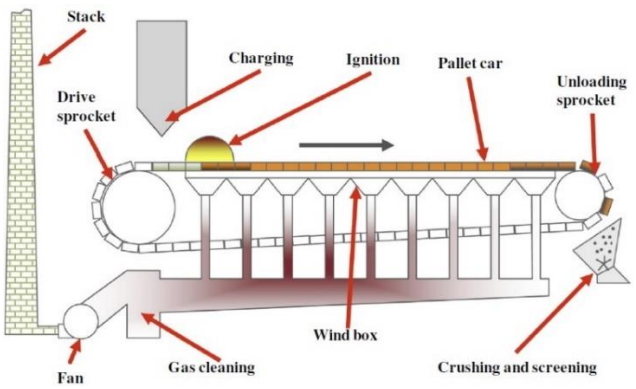

Abbildung 1: Schematische Darstellung eines Sinterprozesses zur Aufbereitung eisenhaltiger Einsatzstoffe für Roheisenerzeugung mittels Hochofenroute [1].

Vor der Aufgabe auf den Wanderrost wird das Ausgangsmaterial befeuchtet, um eine Agglomeration von Fein- und Grobkornanteil zu unterstützen.
Anschließend erfolgt die Zündung des Koksgruses in der Sintermischung. Bis zum Materialabwurf des Fertigsinters durchläuft der heiße Luftstrom, beginnend von der Zündstelle an der Bettoberfläche (= Zündhaube mit Gasbrenner am Beginn des Sinterbandes), das gesamte Bett vertikal abwärts gerichtet. Durch ein Ansaugen der an den Windboxen angeschlossenen Saugzüge (die Windboxen werden auch Saugkästen genannt, befinden sich unterhalb des Sinterbandes), wird das Voranschreiten der Brennfront durch das Sintermaterial gewährleistet. Eine Sammelleitung zum Abtransport der Abgase verbindet die Saugkästen miteinander. An der Sinterabwurfstelle am Ende des Sinterbettes bricht eine Zerkleinerungseinheit (z.B. Stachelbrecher) das agglomerierte Sintermaterial auf die gewünschte Größe. Nach einer Siebung wird der Feinanteil wieder dem Aufgabegut zugeführt [2].

Das Sintern des Eisenerzes bewirkt neben einer Feinanteil- bzw. Kreislaufstoffverhüttung auch einen geringeren Glühverlustwert sowie eine Vorreduzierung des Eisenoxids im Fertigsinter. Dadurch können beim anschließenden Hochofenprozess die Effizienz gesteigert und die entstehende Gichtgasmenge reduziert werden.

Berechnungsgrundlagen

Druckverlust entsteht durch Fluidreibung an Rohrwänden oder durch das Fluid selbst, wenn zwischen dem Ein- und Austritt an verfahrenstechnischen Bauteilen oder Armaturen ein Strömungswiderstand verursacht wird [3]. Bei der Durchströmung von Schüttgutpackungen können folgende sechs Größen einen Einfluss auf das Durchströmungsverhalten ausüben [4]:

- Druckgradient Δp/H [Pa/m]
- Partikelgrößen- und Formverteilung
- Fluiddichte ρ_f [kg m^{-3}]
- Viskosität η_f [kg $m^{-1}s^{-1}$]
- Zwischenraumfluidgeschwindigkeit w/ε [m s^{-1}]
- Porosität ε [-] und andere Packungsstrukturparameter, wie etwa die Tortuosität

Eine erste vereinfachte Berechnungsgrundlage stellt hier die Ergun-Gleichung zur Berechnung des Druckgradienten dar, welche 1957 durch Kombination der Euler- und Reynoldszahl definiert wurde [5].

$$\frac{\Delta p}{\Delta H} = 150 * \frac{(1-\varepsilon)^2}{\varepsilon^3} * \frac{\eta_f * w}{d^2} + 1{,}75 * \frac{(1-\varepsilon)}{\varepsilon^3} * \frac{\rho_f * w^2}{d}$$

Dabei ist jedoch zu berücksichtigen dass diese Formel von einer gemittelten Korngröße und einer idealisierten Kugelform der Partikel ausgeht.

Da sich während des Sinterprozesses, bei konstant gehaltener Bettdurchströmung, Gasdichte, Viskosität und die Geschwindigkeit infolge einer Temperaturerhöhung lokal ändern, beeinflusst das auch den Druck, welcher aufgebracht werden muss, um

die Ansaugluft durch das Sintermaterial zu befördern. Daher kann bei einer Geschwindigkeitserhöhung auch auf eine gesteigerte Druckdifferenz geschlossen werden.

Einflussgrößen

Partikelgröße und Formverteilung:

Das Sintermaterial des Grünbettes (= Ausgangsmischung) besteht aus Partikeln unterschiedlicher Korngrößen. Allgemein kann davon ausgegangen werden, dass ein größerer Feinkornanteil im Sinterbett zu einem steigenden Druckverlust führt. Durch Messungen an Modellschüttungen, bestehend aus großen Keramikkugeln (Ø ~9,5 mm) und feinem Glasgranulat (Ø 1,25-1,65 mm) im laminaren Strömungsbereich, kann dies weitgehend bestätigt werden (siehe folgende Abbildung 2). Der massenbezogene Anteil wg der Feinfraktion (Glasgranulat-Anteil) in der Packung ist in Abbildung 2 als Parameter der untersuchten Modellschüttungen in Abhängigkeit des Druckverlustes der Sintergrünbett-Mischung dargestellt.

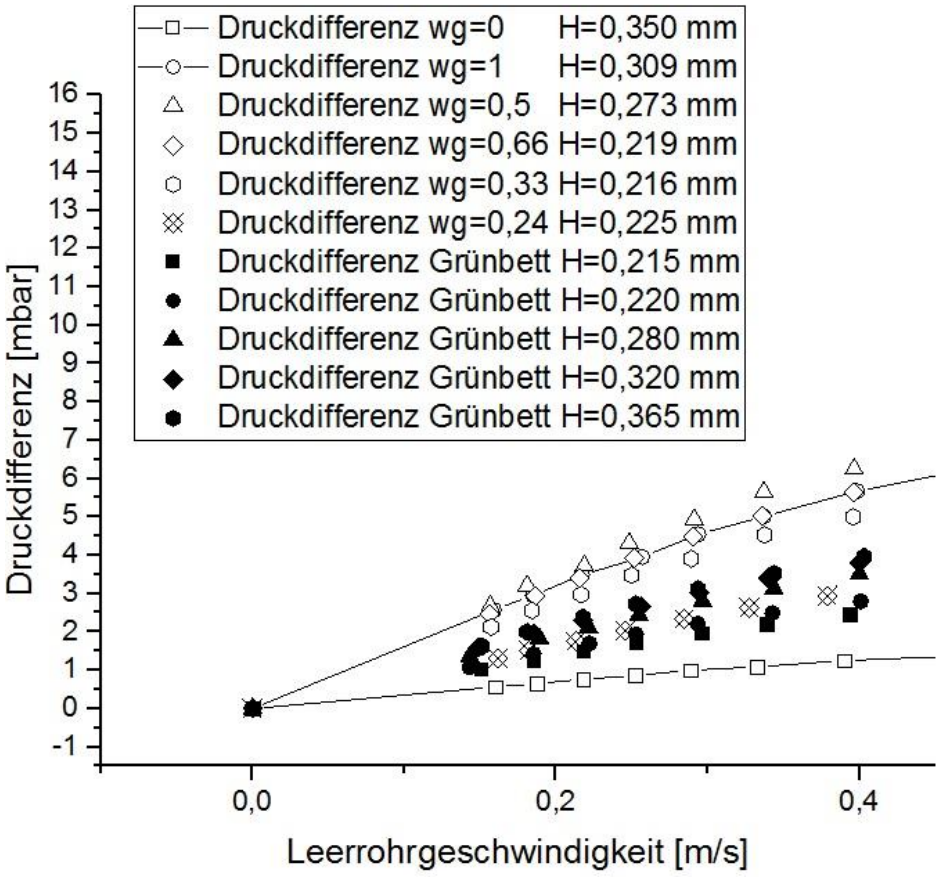

Abbildung 2: Druckverlust bei der Durchströmung verschiedener Modellschüttungen mit Luft bei annähernd konstant gehaltener Porosität (ε = 0,42) bei Raumtemperatur; die Schüttung besteht aus feinem Glasgranulat und Keramikkugeln mit Massenanteil der Feinfraktion wg im Vergleich zu realen Sintergrünbett-Mischungen; durchgezogene Linien entsprechen der Druckverlust-Korrelation nach der Ergun-Gleichung für Schüttungsmischungen aus reinem Fein- bzw. Grobanteil.

Ein Vergleich zeigt, dass die Charakteristik des Durchströmungsdruckes für das reale Sintermaterial im Grünbettzustand vom Durchströmungsverhalten der Modell-schüttungen prinzipiell gut abgebildet werden kann.

Feuchtigkeit:

Eine Befeuchtung des Sintermaterials sorgt für eine Agglomeration des vom Sinterband rückgeführten Feinmaterials mit dem neu eingesetzten Eisenfeinerz. Dies wirkt sich positiv auf die erzielbare Permeabilität aus. Der Wassergehalt muss in einem Bereich liegen, damit es bevorzugt zu einer Anhaftung des Feinanteils auf dem Grobanteil und gleichzeitig zu keinem Abfließen des feinen Materials vom groben Strukturanteil kommt. In Abbildung 3 ist das Anbacken mit steigendem Feuchtigkeitsgehalt schematisch dargestellt.

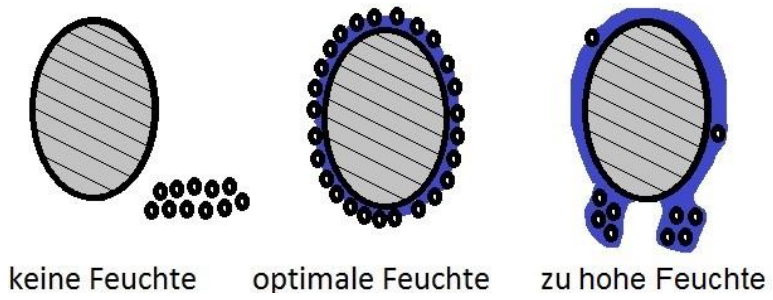

Abbildung 3: Einfluss des Feuchtegehaltes im Sinterrohmix bezüglich einer Aufbauagglomeration des Feinanteils auf groben Trägerpartikeln; dieser Vorgang stellt die Basis einer stabilen Packungsstruktur und ausreichenden Permeabilität des Sintergrünbettes dar.

Temperatur:

Das Sintermaterial erfährt bei der großtechnischen Herstellung (siehe Abbildung 1) eine Temperaturveränderung, ausgehend von der Zünd-Zone am Bettbeginn. Über den Weg am Wanderrost wandert die Brennfront, infolge der Ansaugluft, vertikal abwärts gerichtet durch die Schüttung. Schematisch ist die Verschiebung der Heißtemperaturzone in folgender Abbildung 4 zu sehen.

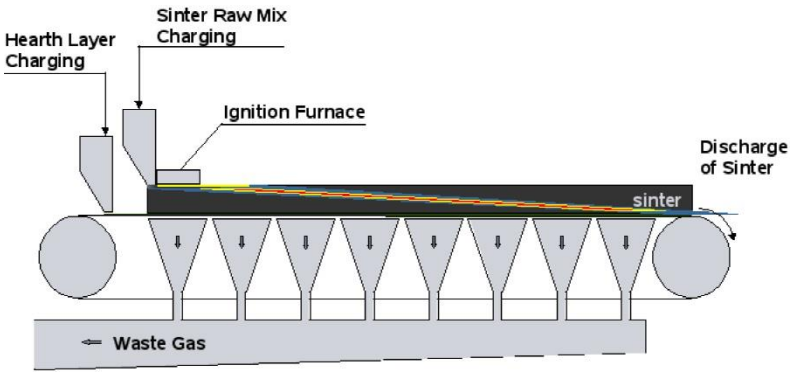

Abbildung 4: Wanderung der Heißtemperaturzone (= Brennfront) durch das Sinterbett entlang der Fortbewegungsrichtung des Wanderrostes [6].

Auch bei der Untersuchung von Sintervorgängen im Labor z.B. im Zuge von Sintertopfversuchen durchläuft das Material, je nach Brennfrontfortschritt, unterschiedliche Temperaturzonen (siehe folgende Abbildung 5).

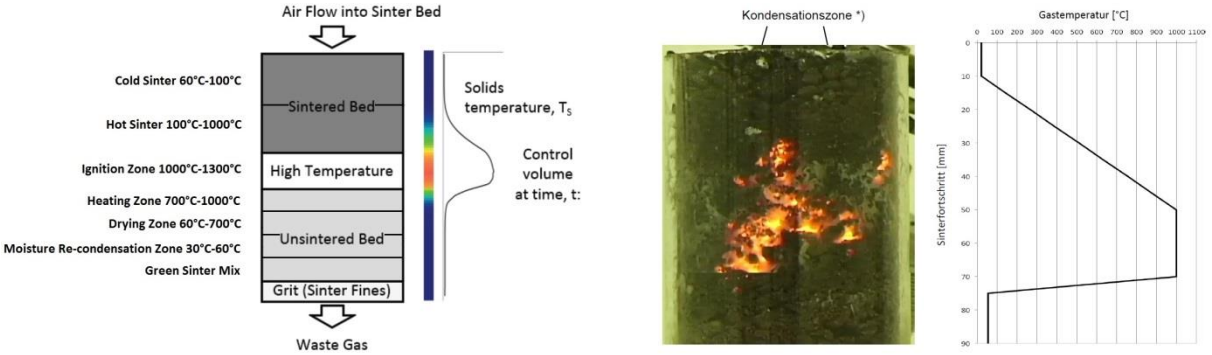

Abbildung 5: Vergleich der Zonenbildung eines Sintertopversuches mit experimentellen Messergebnissen;
Links: Schematische Darstellung der Temperaturzonen im Sinterband;
Rechts: Brennfrontfortschritt bei einem Laborsinterversuch in einer Quarzglasröhre (eine Kondensatbildung in Stromabwärtsrichtung kann beobachtet werden) [2, 7, 8].

In der Trockenzone wird dem Material durch die herannahende Heißgasfront infolge einer Energiefreisetzung Feuchte entzogen. Die Rekondensationszone enthält neben der vor dem Prozess beigemengten Feuchtigkeit auch jene der Trockenzone. Diese Feuchtemenge kann unter Umständen die Porosität und die Permeabilität in diesem Schüttungsabschnitt verschlechtern. Gemäß Abbildung 5 sowie in Übereinstimmung mit bekannten Erfahrungen aus Literatur [8] hat der bei der Herstellung der Sinterausgangsmischung realisierte Wassergehalt letztlich einen entscheidenden Einfluss auf die generelle Effizienz des Sinterprozesses.
Messungen im VTIU-Technikum bestätigen die bekannte Theorie, dass eine Rekondensation in noch nicht gesinterten Zonen tatsächlich auftritt. Wiederbefeuchtetes Sintermaterial, welches eine schwammähnliche Struktur besitzt, kann darüber hinaus ebenfalls zur Druckverlusterhöhung bei einem erhöhten Feuchtegehalt der Ansaugluft führen. Der Feuchtegehalt besitzt demnach einen bedeutenden Einfluss für die Durchströmungscharakteristik des Sintermaterials ist.

Zusammenfassung

Die umfassende Aufklärung der Einflussfaktoren, insbesondere der Feuchtigkeit, im Hinblick auf den Durchströmungsdruckverlust durch das Schüttbett, kann den Energieverbrauch einer Sinteranlage beträchtlich senken.
Die weiteren Untersuchungen zielen auf ein verbessertes Verständnis des Verhaltens der während der Sinterung entstehenden gasförmigen, flüssigen und festen Reaktionsprodukte ab. Die physiko-chemischen und kinetischen Gas-Flüssig-Fest Wechselwirkungen beeinflussen letztendlich die nachfolgenden aufbereitungstechnischen Aufwendungen des Fertigsinters sowie die Bildung und Freisetzung von Schadstoffen während des Sinterprozesses.

Literatur

References

[1] N.-Y. Ma, “A case study on the fracture of sinter machine pallet axles,” *Engineering Failure Analysis*, vol. 42, pp. 345–352, 2014.

[2] Haider,A,F, “Untersuchung des Druckverlusts in der Sinterschicht,” Bachelorarbeit, Verfahrenstechnik, Montanuniversität, Leoben, 2015.

[3] Menapace H, “Untersuchungen zum Agglomerations- und Rollierverhalten des Intensivmischers der voestalpine Stahl Donawitz,” Masterarbeit, Verfahrenstechnik, Montanuniversität, Leoben, 2004.

[4] M. Bohnet, Ed, *Mechanische Verfahrenstechnik,* 1st ed. Weinheim: Wiley-VCH, 2012.

[5] S. Ergun, “Fluid Flow through packed columns,” *Chemical Engineering Progress*, no. 48, pp. 89–94, 1952.

[6] J. Reidetschlaeger, Ed, *Numerical simulation of the sintering and the pelletizing processes*. Düsseldorf, 2015.

[7] J. Muller, de Vries,T,L, Dippenaar,B,A, and J. C. Vreugdenburg, “Development of an iron ore sinter process model to predict sinter strand operating parameters using the finite difference method: Pyrometallugical Modelling,” The South Africa Institute of Mining and Metallury, South Africa.

[8] A. Mallick, S. Dhara, S. Kumar, and Sahu,A,K, Eds, *Optimisation of Sintering Operation through Permeability Control at Bokaro Steel Plant, India*. Düsseldorf, 2015.

Development of a dust dispersion system for investigations on reduced pressure conditions in the 20 liter SIWEK apparatus using OpenFOAM

Werner Pollhammer [a,b], Christoph Spijker [a], Hannes Kern [a] & Harald Raupenstrauch [a]
[a] Montanuniversitaet Leoben, Department of Thermal Process Engineering
8700 Leoben, Franz-Josef-Straße 18
[b] K1-Met GmbH
4020 Linz, Stahlstraße 14
werner.pollhammer@k1-met.com

Abstract

To improve laboratory tests in the 20 liter SIWEK apparatus for non-atmospheric conditions a simulation toolkit was developed in OpenFOAM, to simulate the dust dispersion process in the vessel. The aim of the work is to study the injection process of the standard apparatus and to develop a new dispersion system which enables lab tests under reduced pressure conditions. The Lagrangain model was used for the calculation of the injection process for the standard apparatus with the rebound nozzle. This study was repeated for reduced pressure conditions. In this case the apparatus was evacuated to 0.1 bar instead of 0.4 bar. The outcome shows that this leads to very inhomogeneous dust concentrations. Because of the high pressure difference the velocities are high enough to cause particle agglomeration in the outer region of the vessel. To avoid separation a new dispersion system using a rotating disk was developed. The dust was injected before the evacuation to the specified pressure condition. The rotating disk generates a flow which disperses the particles in a way which is more homogeneous than the standard injection system using a differential pressure. To conclude the work a CFD simulation was used to model the dispersion of lycopodium dust in air under reduced pressure conditions. The standard test was described in detail using the simulation to generate a location dependent dust concentration plot. By modifying the simulation a new dispersion system was developed step by step and characterized in detail. Both systems and results were compared and the pros and cons were discussed. A lab test was reproduced by simulation using a dust explosion model developed in a previous work. Furthermore, a detailed study of the processes during the dust combustion is possible.

Introduction

The aim of this work is to develop and simulate a new dust dispersion system for the 20 liter Siwek apparatus. For further investigation on the ignition process of a dust explosion it was necessary to describe the internal dust decomposition of the standard Siwek test. Simulation for the reduced pressure condition showed the necessity to develop an alternative dispersion system for the dust in the vessel to reach an ambient pressure of about 0.2 bar. The idea was to disperse the dust by a rotating disc and to develop this system using CFD simulation which models the process of dispersion of Lagrangian particles in a flow field. For the rotating disc, a multi reference frame was used to avoid the need for a dynamic mesh implementation. The case was set up in OpenFOAM and the simulation was used to design and optimize the geometry of the disc.

Simulation of the dust dispersion system

Simulation set up was defined to model the injection of dust into the 20 liter vessel. For this purpose a mesh was generated using “snappyHexMesh”. For the material properties of dust, values from lycopodium were used, with a diameter of 30 µm and 800 kg/m³ density [1]. For the calculation with an initial concentration of 200 g/m³, approximately 353.677.700 particles would be needed. Such a high number of lagrangian particles would demand very high computing power, so that particle clustering defined in OpenFOAM was implemented as a solution to this problem. Within this option the balance equation are calculated for only a part of particles so called parcels and then be transferred to the whole cloud. This reduced the number of particles for calculation to 3.536.777 representative parcels. Using this reduction the calculation time was 6 weeks on a 6 x 3.4 GHz i7-4930K machine. Following simulations are all calculated with an initial dust concentration of 200 g/m³. This was the standard for all simulation experiments when the concentration is not explicitly named.
To set up the parcel’s initial position in the simulation, a short Matlab program was developed to generate the coordinates of the parcel cloud. The whole cloud was injected within first time step, in the tube between the pressure vessel and the magnetic nozzle. The detailed geometry from the meshing tool and initialized particle cloud for the first time step are shown in Fig. 1.

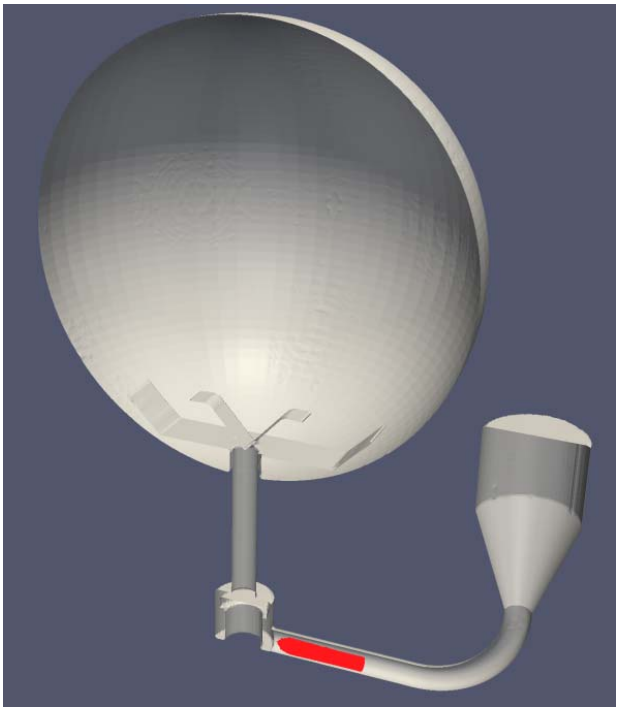

Fig. 1: Initial position of the particle cloud (red) in the first time step [2]

Using the setFields option the pressure field was initialized and the starting condition for the experiment specified. The simulation results have been used for detailed investigations on dust dispersion as well as the characterization of turbulent conditions. Using the simulation data it was possible to investigate the internal flow conditions more in detail as it is the case in laboratory tests.

Development of the dust dispersion system using rotating disc

The results from previous simulation have been used to define requirements for possible improvements. This chapter describes the most important steps in development and design of the rotating disc disperser.
In the development of the new disperser, following demands have been considered:

- Even dust concentration in the whole sphere at lower ambient pressure
- Avoidance of regions with extreme high or low turbulence to achieve uniform conditions in the whole vessel
- Possibility to vary flow conditions to investigate the impact of turbulence and ambient pressure on flame propagation
- Expandability of existing geometry

The idea was to run the dispersion system using a rotating disc for dust distribution. The disc causes a flow field which keeps the particles in the flow. It is very important to avoid regions with low fluid velocity to prevent particle separation on the wall. The particles were injected before the disc was set in motion. In a first step, only a rotating disc was used. But without any baffle only the rotating flow will occur, which causes very inhomogeneous dust dispersion. To overcome identified problems, more complex geometry was generated using static walls as guide vane and for efficiency improvement of the rotator, as well as for the reduction of motor revolutions. Fig. 2 shows the comparison between investigated dispersion systems as well as the initial concentration. The rebound nozzle is the existing system and the disc disperser is the new developed one.

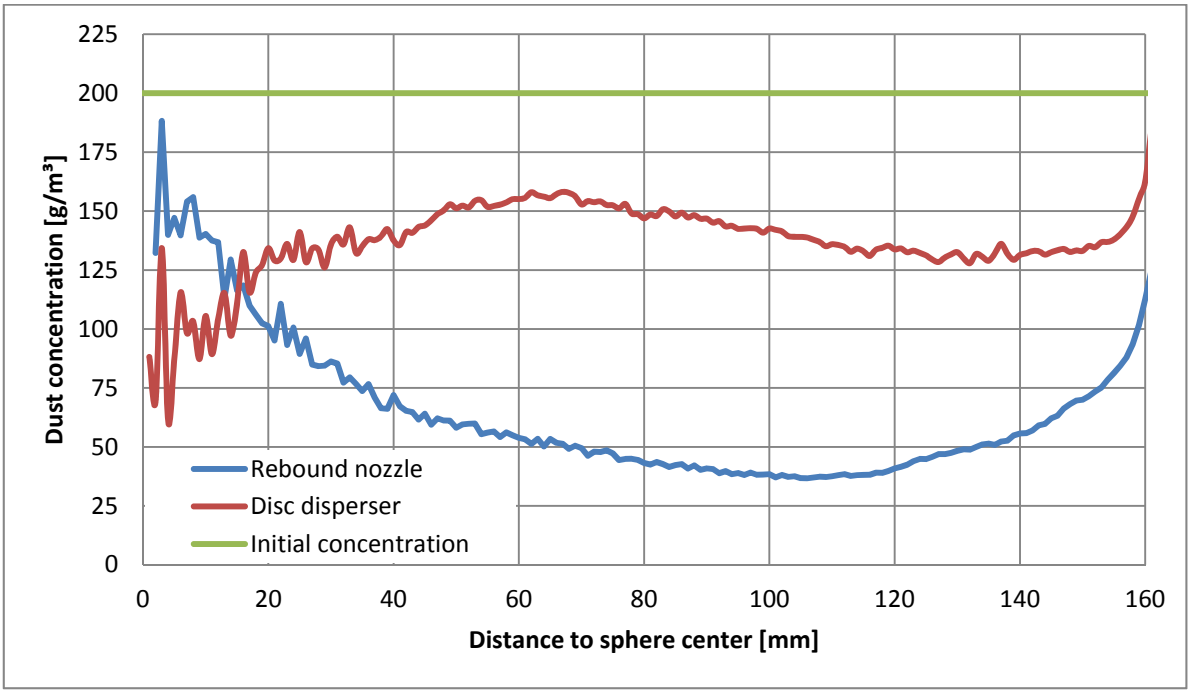

Fig. 2: Comparison of local dust concentration using different dispersion systems [2]

The new system shows much better dispersion then the rebound nozzle. The higher difference to the intended concentration occurs only in a very small inner region. In the rest of geometry the gap between the particle concentrations to the intended one is much lower.

As can be seen in Fig. 3, particle cloud shows also much more homogenous distribution. Using rebound nozzle, there are four particle stripes generated by cycling flow at injection. The distribution of the particles using the disc disperser is much more uniform. The particles are colored by the distance to the ignition zone, whereas the blue particles are near the center and the red ones are located on the wall.

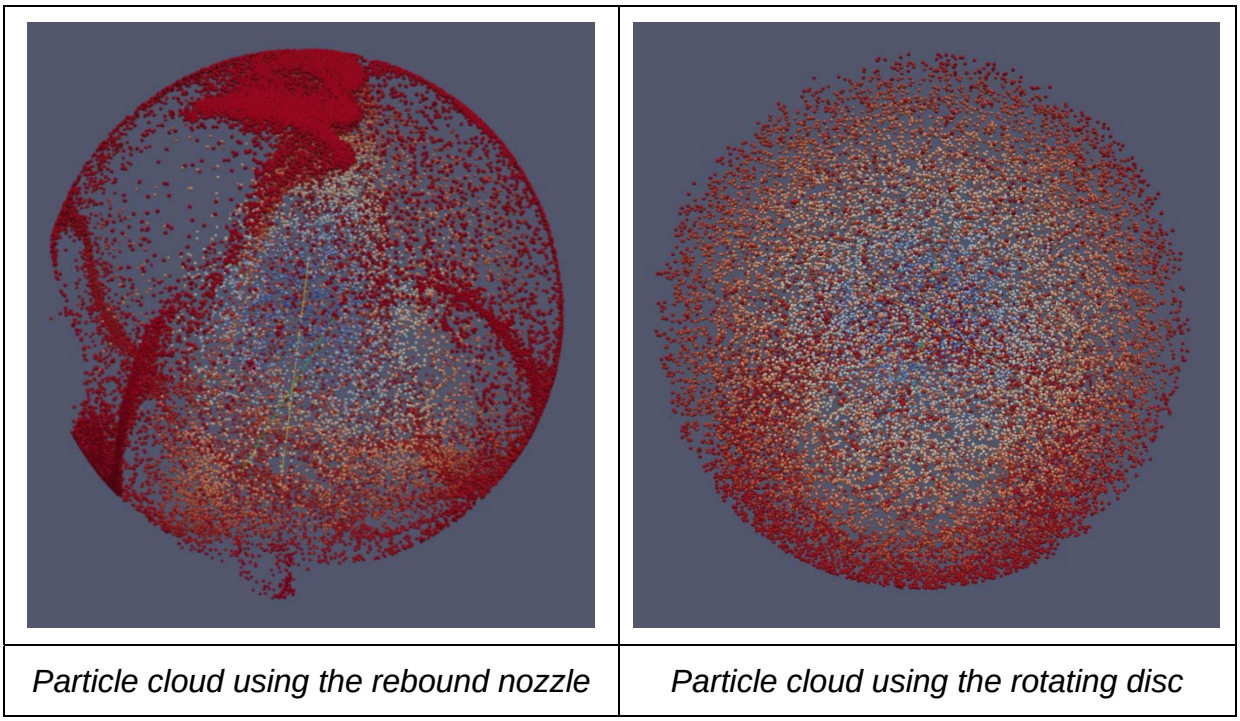

Particle cloud using the rebound nozzle	*Particle cloud using the rotating disc*

Fig. 3: Comparison of the particle clouds using rebound nozzle and disc disperser [2]

Conclusions

A detailed study of lycopodium injection into the 20 liter sphere vessel was done. The aim of this simulation using CFD methods was to find out if it is possible to run the lab test at reduced ambient pressure and to generate data which cannot be measured in laboratory. Simulation showed that ambient pressure condition and the rebound nozzle dispersion system are inducing very inhomogeneous dust concentrations. To overcome this problem a new dispersion system using a rotating disc was designed. Simulation was used to develop the geometry of the system by designing the geometry variation in a CAD program and subsequently validating it using OpenFOAM. Step by step, the final geometry was generated. From the steady state conditions of the rotating system and the flow conditions and dust concentration of the injecting system, a particle combustion simulation was set up. Based on these two simulations further studies of the impact on flame propagation were possible

Literature

[1] Werner Rudolf Pollhammer, Numerische Untersuchung der Mindestzündenergie sowie der Flammenfortpflanzung in Staub/Luft – Gemischen mittels eines Euler – Lagrange – Modells in OpenFOAM, Master Thesis, Montanuniversitaet Leoben, Leoben, 2014.

[2] Werner Rudolf Pollhammer, Entwicklung eines alternativen Staubverteilungssystems für die 20 Liter SIWEK – Apparatur mittels CFD – Methoden, Master Thesis, Montanuniversitaet Leoben, Leoben, 2015.

Thermogravimetric analysis of pure and additive-commingled polypropylene

Teresa Schubert[a], Markus Lehner[a], Wolfgang Hofer[b]
[a]*Montanuniversitaet Leoben, Chair of Process Technology and Industrial Environmental Protection, A-8700 Leoben, Franz-Josef-Str. 18*
[b]*OMV Refining & Marketing GmbH, Mannswörther Straße 28, 2320 Schwechat, Austria*
teresa.schubert@unileoben.ac.at

Abstract

Pyrolytic conversion of post-consumer plastics represents an attractive way of recycling valuable organic matter. Thermal or thermo-catalytic cracking can be used to produce gaseous or liquid hydrocarbon fractions for further usage as petrochemical raw materials or energy carrier. To engineer an economical and technical mature concept of this procedure, detailed knowledge of the intrinsic chemical processes is necessary, for the sole virgin polymer as well as for artificial mixtures. For this purpose, thermogravimetric analysis offers a simple and effective method, illustrating the weight loss in dependence of temperature.

In this research, dynamic TGA runs with virgin pure polypropylene and polypropylene mixed with $CaCO_3$, Fe_2O_3, Al_2O_3, TiO_2 and carbon black were carried out at different heating rates under inert N_2 atmosphere. With increasing heating rate, a shift of degradation to higher temperatures was observable. Furthermore, mixtures with Fe_2O_3, carbon black and TiO_2 showed a higher thermal stability compared to polypropylene without additives. Adding $CaCO_3$ and Al_2O_3 did not affect the pyrolysis of the polymer significantly. Based on these results, it is necessary to consider the influence of additive materials and to examine the underlying mechanisms more closely.

Introduction

In 2012, more than 350.000 t of plastic waste was produced in Austria [1]. Recycling of these waste materials efficiently will be of growing interest in the future, especially to regain valuable substances. This can be achieved by pyrolytic conversion of post-consumer plastics to produce processable hydrocarbons. Pyrolysis is capable to recover liquid and gaseous products by thermal and catalytic cracking, respectively, of polymer chains for petrochemical usage and as fuels.

It is essential to understand the reaction mechanisms and kinetics of degradation under oxygen-free conditions to develop efficient processes and engineer suitable plants. For this purpose, one main focus of research in the past decades in this field takes advantage of the application of thermogravimetric analysis (TGA). Heating a small amount of any sample of interest with an adequate heating program under pyrolytic atmosphere while recording the resulting mass loss simultaneously gives information about the reaction temperature and reaction rates. Furthermore, kinetic parameters (activation energy, frequency factor, order of reaction) can be obtained by different calculation methods. [2, 3, 4]

Plastics for consumer products do not consist exclusively of pure polymers, different organic and anorganic substances are added to modify the properties and to reduce costs.

These additives can influence the behavior and reactions of polymeric materials and have to be considered regarding pyrolysis processes. In literature, research of the impact of anorganic fillers and colorants is sparse and inconsistent. For example, Murty et al. [5] observed via TGA an increase in degradation temperature of high-density polyethylene in the presence of Al_2O_3 and a decrease in the presence of $CaCO_3$, whereas Fe_2O_3 did not affect the degradation process despite catalytic activity of Fe compounds. On the other hand, other research did not show any significant effect of $CaCO_3$ on the thermal stability of a mixture of PP/HDPE/ERP [6], and present results with improved thermal stability under oxidative conditions of PMMA in mixtures with Fe_2O_3 and TiO_2. [7] Admixing carbon black to polyolefins was observed to be able to promote or to impede thermal degradation of the polymers, depending on the volatile content of the used carbon black, whereas low volatile content increased thermal stability of polymers. [8]

Therefore, the aim of this work is to gain information about the degradation reaction of polypropylene, which represents a major component of post-consumer plastics, as virgin material and in combination with five different filler and colorant materials, $CaCO_3$, Fe_2O_3, Al_2O_3, TiO_2 and carbon black.

Experimental

To investigate degradation temperature and kinetics, thermogravimetric analysis was used. A grinded sample (mass between 2 and 6 mg, depending on the density, < 0.5 mm) was inserted into a sample pan and heated with a fixed heating rate in a Perkin Elmer Pyris 1 Thermogravimetric Analyzer. 20 ml/min nitrogen purge gas was fed into the system to provide inert reaction conditions. During heating from room temperature up to 900°C, the sample mass was recorded to obtain the temperature-depending mass loss curve.

The used polypropylene type BC142MO, a controlled rheology heterophasic copolymer, obtained from Borealis was grinded to a particle size below 0.5 mm. For blending, aluminum(IV) oxide, carbon black (acetylene), iron(III) oxide and titanium(IV) oxide (rutile) from Alfa Aesar and calcium carbonate precipitated from Merck in powder form (particle size between 1 and 50µm) were mixed manually with virgin polypropylene. Therefor, 50 wt.% of $CaCO_3$, Fe_2O_3 and Al_2O_3 or 30 wt.% of TiO_2 or 3 wt.% of carbon black were mixed with the polymer to produce a dry blend.

To investigate the influence of the heating rate, pure polypropylene was pyrolysed at 5, 15, 25 and 40°C/min. Thermogravimetric analyses with blends were performed at 5 and 25°C/min.

Results

The calculated results of all TGA runs are summarized in Table 1, where the starting temperature T_{start}, temperature of maximum weight loss (T_{max}) and ending temperature (T_{end}) are recorded. The starting and ending temperature were obtained by the intersection of the inflexional tangent and the tangent of the stable mass area before and after degradation, respectively. The temperature of maximum weight loss is represented by the inflexion point.

The degradation curves (Figure 1) obtained from virgin pure polypropylene show a depolymerization window between 400 and 530°C, depending on the heating rate. Temperatures, where degradation begins, lie between 434 and 463°C, giving the minimum temperatures for technical processes. At temperatures between 456 and 491°C, the weight

loss reaches its maximum in accordance with literature values from 434 to 472°C for heating rates of 5 and 20°C/min, respectively. [2]

	Heating rate	T_{start}	T_{max}	T_{end}
PP	5	434,0	456,1	467,5
	15	452,9	476,2	493,0
	25	459,1	483,2	508,9
	40	462,3	490,7	530,6
PP + Al_2O_3	5	436,6	458,5	471,3
	25	456,4	483,8	507,0
PP + $CaCO_3$	5	432,3	457,6	479,5
	25	460,2	488,4	536,2
PP + CB	5	440,0	462,6	474,6
	25	467,1	493,3	516,5
PP + Fe_2O_3	5	457,2	477,8	491,9
	25	478,0	505,2	528,8
PP + TiO_2	5	441,7	463,8	478,3
	25	464,9	493,5	517,1

Table 1: Characteristic temperatures of pure polypropylene and polypropylene mixed with filler materials obtained from TGA data.

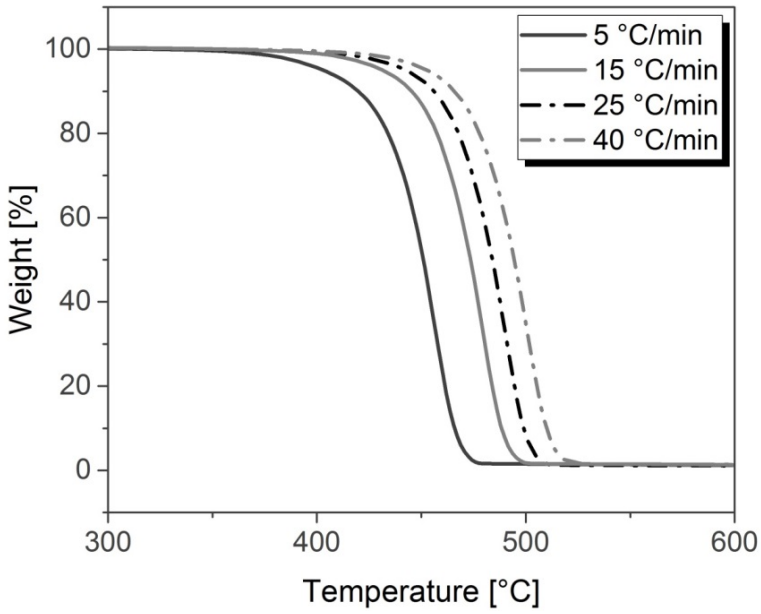

Figure 1: Thermogravimetric curves of polypropylene at four different heating rates.

The displacement of thermogravimetric curves has been discussed in the literature several times. Different explanations of the influence of the heating rate exist, for example a shift in mechanism, inefficient heat transfer and the mathematical form of kinetic laws, which may lead to displacements of the weight loss curves at increasing heating rates. [3]

Figure 2 and Table 1 show the results of the TGA of polypropylene-additive mixtures at two different heating rates in the corrected form, in which the sample mass was reduced by the additives mass proportionately. Admixing of aluminum(IV) oxide and calcium carbonate did not affect the degradation of the polymer significantly. In contrast to [5], most notably the presence of iron(III) oxide increased the thermal stability by 20°C. Also enhanced thermal stability was observed in mixtures with carbon black and titanium(IV) oxide as well, especially considering the low weight fraction of 3 and 30% respectively. These results conform to data from literature for TiO_2 and carbon black [7, 8], given that the used carbon black type is of low volatile content (according to TGA curves of pure carbon black).

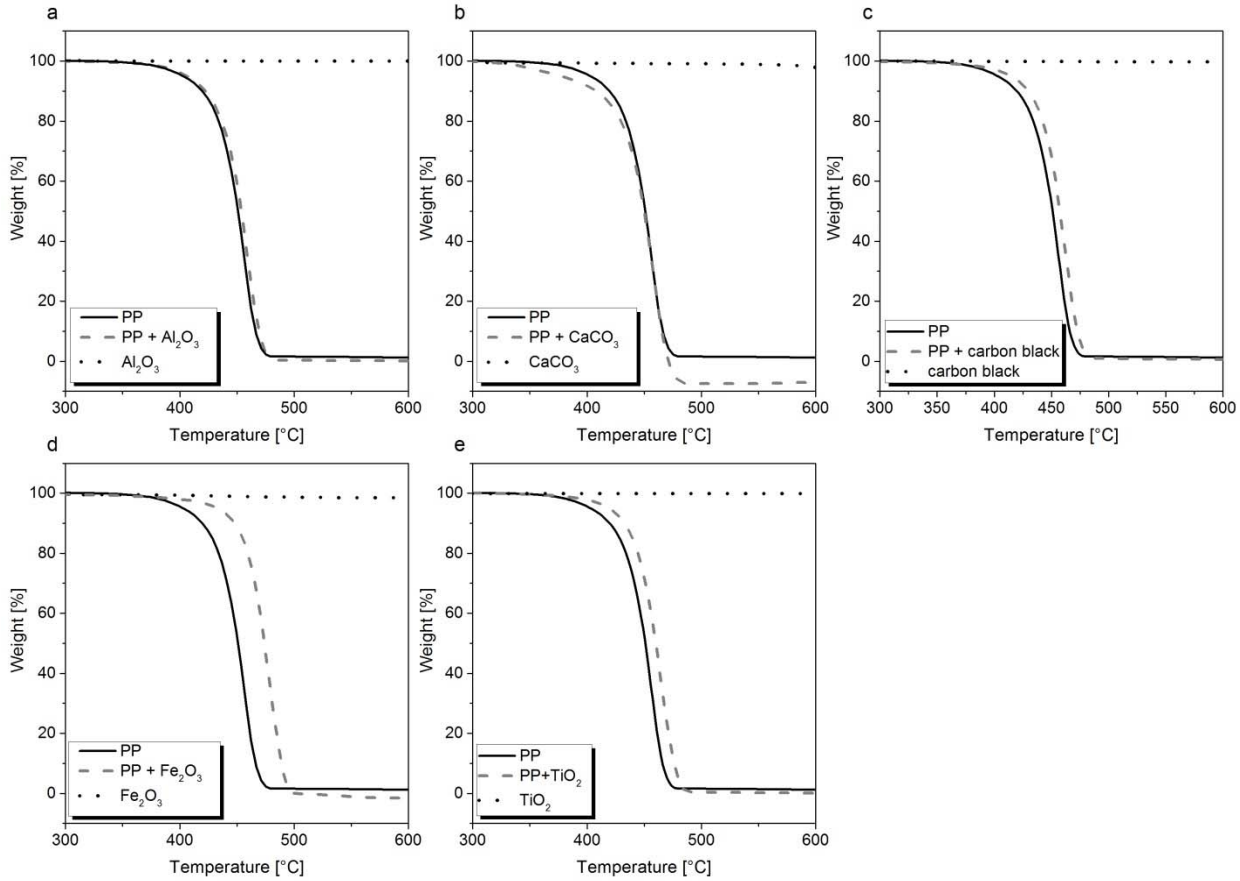

Figure 2: Thermogravimetric curves of polypropylene with Al_2O_3, $CaCO_3$, carbon black, Fe_2O_3 and TiO_2 at 5°C/min. [9]

Conclusion

Thermogravimetric analyses of pure polypropylene were performed at four different heating rates, 5, 15, 25 and 40°C/min, to gain information about the temperature range of pyrolytic degradation. Degradation starts at 434°C at 5°C/min and increased heating rates lead to higher weight loss temperatures.

Polypropylene commingled with various additive materials (Al_2O_3, $CaCO_3$, carbon black, Fe_2O_3 and TiO_2) was also pyrolysed using TGA to be able to estimate the influence of these filler materials on the depolymerization mechanism. Depending on the substance an increase in thermal stability was observable in the presence of carbon black, Fe_2O_3 and TiO_2, resulting in a delay of degradation. The requirement of higher degradation temperatures and energy input has to be considered in technical implementations of this method.

In further research, the underlying mechanism and cause for degradation delays will be investigated in more detail. Furthermore, kinetic analysis of the generated TGA data is under progress and can quantify the observed phenomena more accurately. Kinetic parameters are necessary for modelling and simulation as well.

References

[1] [Online]. Available: http://ec.europa.eu/eurostat/de/data/database. [Accessed 11 01 2015].

[2] J. H. Chan and S. T. Balke, “The thermal degradation kinetics of polypropylene: Part III. Thermogravimetric analyses,” *Polymer Degradation and Stability,* no. 57, pp. 135-149, 1997.

[3] J. A. Conesa, A. Marcilla, R. Font and J. A. Caballero, “Thermogravimetric studies on the thermal decomposition of polyethylene,” *Journal of Analytical and Applied Pyrolysis,* no. 36, pp. 1-15, 1996.

[4] A. Aboulkas, E. El harfi and A. El Bouadili, “Thermal degradation behaviors of polyethylene and polypropylene. Part I: Pyrolysis kinteics and mechanisms,” *Energy Conversion and Management,* no. 51, pp. 1363-1369, 2001.

[5] M. V. S. Murty, E. A. Grulke and D. Bhattacharyya, “Influence of metallic on the thermal degradation and liquefaction of high density polyethylene (HDPE),” *Polymer Degradation and Stability,* no. 61, pp. 421-430, 1998.

[6] J. González, C. Albano, M. Ichazo, M. Hernández and R. Sciamanna, "Analysis of thermogravimetric data of blends of polyolefins with calcium carbonate treated with Lica 12," *Polymer Degradation and Stability,* no. 73, pp. 211-224, 2001.

[7] A. Laachachia, M. Concheza, M. Ferriola, J. M. Lopez-Cuestab and E. Leroyb, “Influence of TiO2 and Fe2O3 fillers on the thermal properties of poly(methyl methacrylate) (PMMA),” *Materials Letters,* no. 59, pp. 36-39, 2005.

[8] E. Jakab and M. Omastová, “Thermal decomposition of polyolefin/carbon black composites,” *Journal of Analytical and Applied Pyrolysis,* no. 74, pp. 204-214, 2005.

[9] T. Schubert, M. Lehner and W. Hofer, “Influences of impurities on thermal cracking of polyolefin-rich post-consumer plastics,” in *8th International Symposium on Feedstock Recycling of Polymeric Materials (8th ISFR 2015)*, Leoben, 2015.

Energy optimization of cross-linked plants using the example of a refinery

[1]Florian Pöllabauer, [2]Gerald Bachmann, [1]Thomas Wallek
[1]Graz University of Technology, NAWI Graz, Institute of Chemical Engineering and Environmental Technology, 8010 Graz, Inffeldgasse 25/C,
florian.poellabauer@tugraz.at, thomas.wallek@tugraz.at;
[2]OMV Refining & Marketing GmbH, 1020 Wien, Trabrennstraße 6-8,
gerald.bachmann@omv.com

Abstract

An oil refinery is a typical example of a complex compound system consisting of several cross-linked plants, which are supplied with energy by power plants.

In order to optimize product streams and energy consumption a simplified model of the compound system is developed. Reduction of the modeling-depth is achieved by breaking down the real system into an aggregation of appropriate sub-systems (plants). Based on measured data from the plants each plant is simplified to a deterministic black box by a fit of linear functions for which the fulfilment of mass balances is a crucial aspect of the model. The resulting set of functions describes the main product streams and their specific energy consumption. The static model of the refinery consists of mixers, splitters and the fitted functions. The overall steam consumption is calculated by summation of the individual steam consumptions of all plants.

The modular structure of the model provides possibilities for further detailing. The methodology presented in this work can smoothly be transferred to other compound systems of plants in chemical industry.

Introduction

In an oil refinery several plants are interconnected in order to produce numerous product streams such as fuels and petrochemicals from crude oil. Residue-fired power plants provide the production plants with steam and electrical power. Each of these plants as well the whole refinery can be optimized to meet different target criteria.

For single plants, the use of commercial process simulation tools is state of the art as a basis for tuning of operating points, conducting energetic optimization on column-level, trouble management, case studies and even dynamic simulations for emulation of step-tests to determine control-parameters. While for these applications a modeling-depth down to each single equilibrium stage is desirable, the usually huge number of streams, recycles, apparatuses and chemical compounds makes it difficult to combine such models for simultaneous optimization of several plants, and maintain model stability while pending reasonable amounts of simulation time. In contrast, this paper suggests a comprehensible methodology to reduce the modeling-depth of a compound system in such a way that the resulting model is reduced to the main product streams while providing links with the steam network. Notably in view of using the model for cross-plant energetic optimization tasks, the implementation of an integrated static model covering plants and utilities is required. Reduction of the modeling-depth is achieved by decomposing the real system into an aggregation of appropriate sub-systems [1].

The model equations for each sub-system are fitted to real measured data of mass flows from representative stable runs of each unit.

Model concept

Each plant (sub-system) is regarded as a deterministic black box, which processes n feed streams F_i to produce m product streams P_j. In the general model concept each plant can import and export steam from each of the three steam networks.

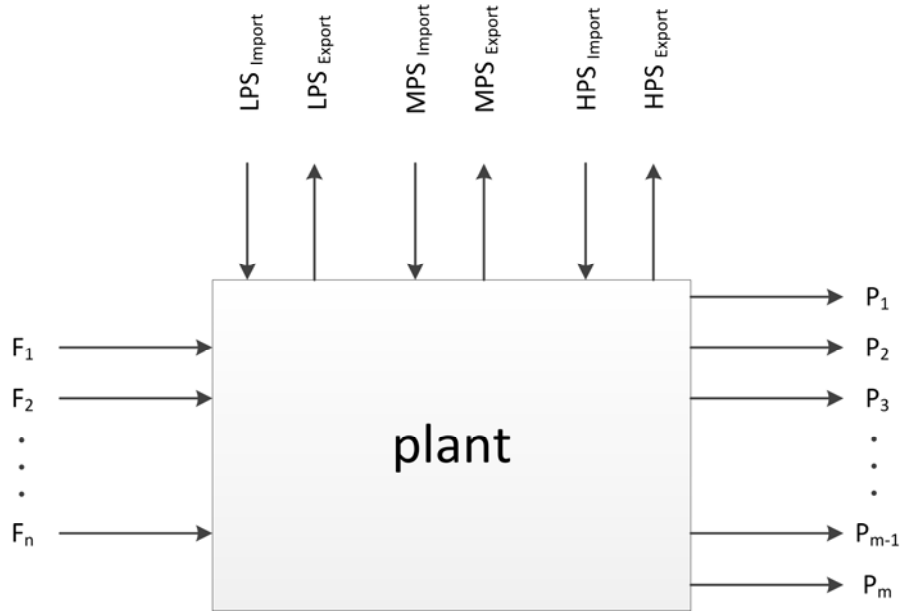

Figure 1: model concept of a plant; F…feed, P…product, LPS…low pressure steam, MPS…medium pressure steam, HPS…high pressure steam

Product streams (P_j) and steam streams (S_k) are described as a linear function of the feeds.

$$P_j = b_{0,j} + b_{1,j}F_1 + b_{2,j}F_2 + ... + b_{n,j}F_n$$
$$S_k = \tilde{b}_{0,k} + \tilde{b}_{1,k}F_1 + \tilde{b}_{2,k}F_2 + ... + \tilde{b}_{n,k}F_n$$

The intercept parameter $b_{0,j}$ and the slope parameters $b_{i,j}$ for each feed i, respectively $\tilde{b}_{0,k}$ and $\tilde{b}_{i,k}$ for steam streams, are obtained by regression.

The mass balance must be fulfilled for every plant, which yields the constraints for the model parameters.

$$\sum_{i=1}^{n} F_i = \sum_{j=1}^{m} P_j$$

The parameter $b_{i,j}$ represents the proportion of the feed i in the product stream j.

$$b_{0,j} = 0 \qquad \forall j \in N \,|\, 1 \le j \le m$$

$$\sum_{j=1}^{m} b_{i,j} = 0 \qquad \forall i \in N \,|\, 1 \le i \le n$$

This work only reports on results obtained with these constraints, whereas one can also use alternative formulations.

Methods

The model equations are fitted to measured mass flow data of the real plants using *Wolfram Mathematica*. The constrained regression for the product streams is performed using the function *NonlinearModelFit* (NLM-Fit). This function minimizes the sum of the deviations of all product streams. Additionally, the slope parameters are bounded by the interval [0,1]. The steam streams are fitted via linear regression using the function *LinearModelFit*. Figure 2 depicts two examples of results of the constrained regression compared to the normal unconstrained linear regression (dotted line), which has the lowest possible deviation from the measured data, but does not fulfil the mass balance.

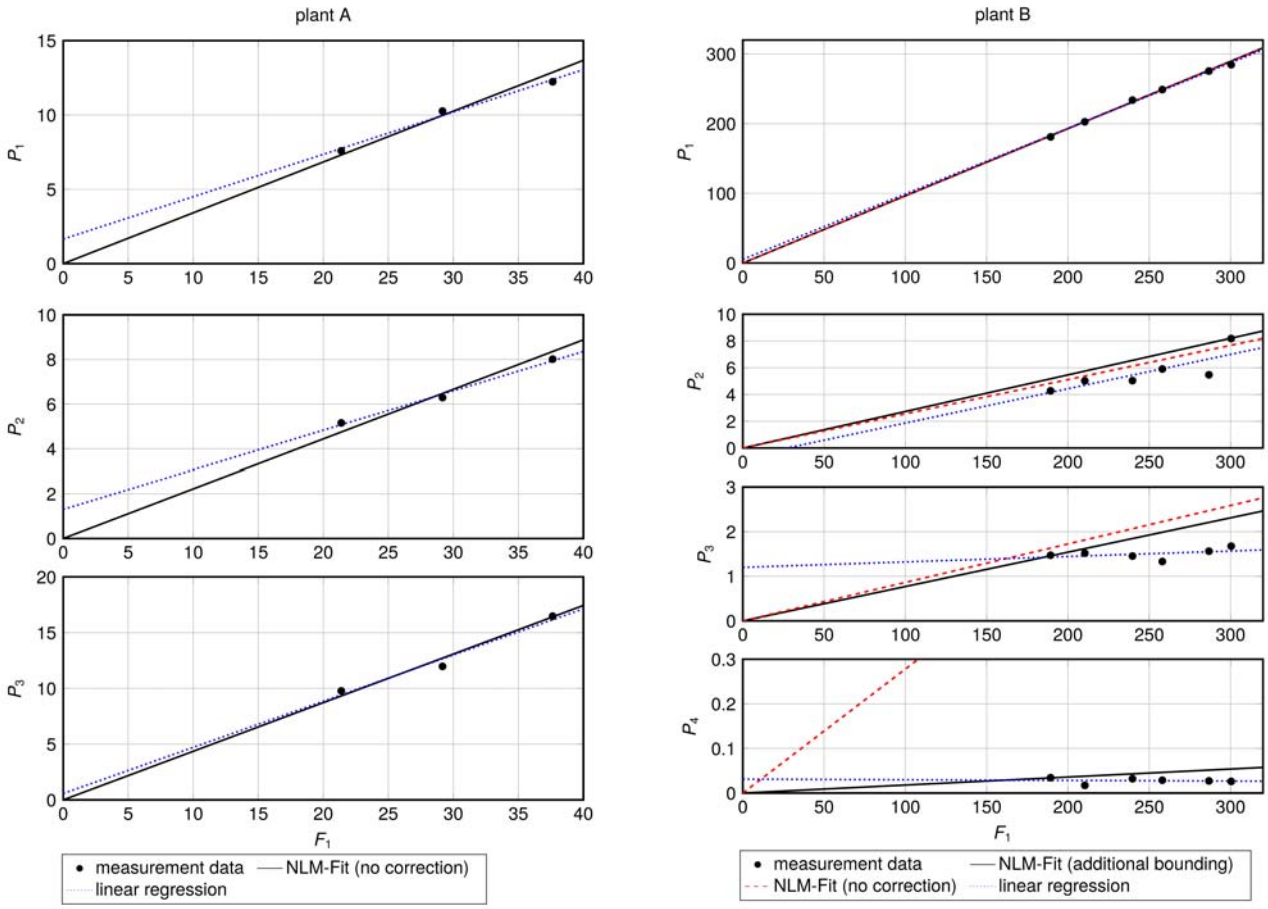

Figure 2: comparison of different regression methods for product streams

For plant A, where all three product streams appear in similar orders of magnitude, both regression methods show roughly the same result. In contrast, for plant B one product stream accounts for more than 95 % of the feed and is well represented by all regression methods. The data of the other product streams, especially of the smallest, cannot be described by the constrained regression (dashed line). Bounding the parameters for the streams P_3 and P_4 to a smaller interval improves the results for these streams, but the results for P_2 get worse (solid line).

These fitted functions are combined to form the overall model of the refinery using mixers and splitters. The feeds of downstream plants are defined from the products of the upstream plants. This procedure results in a set of functions in which all product streams and steam streams are only dependent on the crude oil mass flow and several split factors. The steam demand from the power plants is modelled as the sum of all steam demands of each plant.

$$LPS_{demand} = \sum_{plants} LPS_{import} - \sum_{plants} LPS_{export}$$
$$MPS_{demand} = \sum_{plants} MPS_{import} - \sum_{plants} MPS_{export}$$
$$HPS_{demand} = \sum_{plants} HPS_{import} - \sum_{plants} HPS_{export}$$

The treatment of recycle streams is posing a challenge as during function definition in *Wolfram Mathematica* the defined functions call themselves, causing an infinite loop. In order to overcome this problem the model concept is rearranged. This can be done by modifying the interconnection of the plants, by narrowing or broadening the balance boundaries of the sub-systems (plants) or by explicitly solving the model equations for the recycle streams.

Application and results

The resulting set of functions describing the main characteristics of each process step in terms of product yield and energy consumption can be used to formulate one target criterion or a weighted sum of several target criteria that can be influenced by both production and utilities. Maximum and minimum feeds of every plant are used as contraints for the optimization. This methodology is applied to build a simplified model of the refinery Schwechat in Austria. It covers 21 main plants, 14 splitters, 2 crude oil feeds and 25 product streams.

Conclusion and outlook

The presented model is capable of optimizing both product yield and energy demand and can easily be extended and further detailed. The constraints for the fit are considerably restrictive and do not represent the measurement data as good as the linear regression without constraints. But on the other hand the inherent fulfilment of the mass balance is a major advantage of the presented modeling approach. The description of the measurement data can be improved by reformulating the constraints using relative deviations and a non-zero intercept parameter. A model of the power plants is to be incorporated as the interaction between production and utilities is strongly influenced by the fact that the power plants are fired by residues from the production plants.

References

[1] Klatt, K.U., Marquardt, W., 2009: Perspectives for process systems engineering - Personal views from academia and industry, Computers and Chemical Engineering, 33(3), 536–550, selected Papers from the 17th European Symposium on Computer Aided Process Engineering held in Bucharest, Romania, May 2007.

ABSORPTION OF OXYGEN BY SODIUM SULFITE DROPLETS

Anda Lucia[1,2], Markus Lehner[1], Johannes Rieger[1], Christian Weiß[1]

[1] Chair of Process Technology and Industrial Environmental Protection, Montanuniversität, Franz-Josef-Straβe 18, Leoben, Styria, 8700, Austria.
[2] Research and Development Center for Oil and Gas Technology "Lemigas", Jl. Ciledug Raya Kav. 109 Cipulir, Jakarta, 12230, Indonesia

ABSTRACT

Gas absorption by liquid droplets in a spray column is one common method for gas cleaning. The simple design, low pressure drop, and the possibility of its application in liquid systems containing solids are benefits of this method. The mass transfer coefficient of gas-liquid absorption depends on droplet size, concentration of liquid or gas and the physic-chemical system. Experiments to study the mass transfer using the air-oxygen/sulfite system have been performed.

The dispersed droplets were generated by pumping the liquid through a needle with certain flowrate. A High Speed Camera with shadowgraph method and image processing was used for measurement of droplet size and velocity accurately. The shapes of the droplets were relatively not spherical because of oscillating movement. The droplets are slightly accelerated after detach from the needle. The oxygen concentrations were determined by means of spectrophotometric method. The mass transfer coefficient of the experiment is calculated from the experimental data, and compared with the model equations from the literature.[1]

INTRODUCTION

Mass transfer from and to droplets is a phenomenon that often occurs in the chemical industry e.g., gas absorption. Liquid dispersed as droplets in a gas e.g. in stripper or scrubbers are important applications of mass transfer between gas and liquid phases. Gas absorption in a spray column is widely used particularly due to a simple design, low pressure drop, and the possibility of its application in liquid systems containing solids. A better understanding of the factors influencing the transfer between the dispersed phases with the continuous phase is needed for the design of spray tower as well as predictions of individual phase mass transfer, taking into account the spray formation process.

Some researchers have studied mass transfer from CO_2-water system in form of water droplets [1,2,3,4,5,6], laminar flow jet [7] and turbulent flow jet [8]. Other investigations for the oxygen-sulphite system have also been done in stirred tank [9,10,11] and in packed column [12]. In the cases where the internal resistance is important, some researchers have investigated a single droplet [13], whereas for a droplet stream only Srinivasan [1] reports for CO_2 absorption system with a stream of water droplets.

Until now the oxygen mass transfer in sulphite solution particularly in the form of droplets or a stream of droplets has not been investigated, which is the primary motivation in this study. Since the characterization of droplet size and droplet velocity are very important

parameters for calculating the mass transfer coefficient, a highly precise measurement of that parameter is one basis for deriving exact mass transfer coefficients.

In this study, an apparatus for measuring the droplet size and the droplet velocity was established with shadowgraph method and image processing. The mass transfer coefficient of the experiment is determined from the experimental data, and compared with the model equations from the literature [1]

EXPERIMENTAL

A single droplet is produced by pumping the solution through a needle with certain flowrate, i.e. 1.0, 1.5 and 2.0 ml/minute. For measuring the exact diameter of droplet and the droplet velocity an image processing system with long distance microscope and high speed camera was used (Figure 1.).

The droplets fall free in air with a falling height 10, 15 and 20 cm, respectively, and are finally deposited under kerosene. The concentration of sodium sulphite solution before and after the droplet contacted the air, is analysed by spectrophotometer. The data obtained is used for the calculation of the rate of absorption.

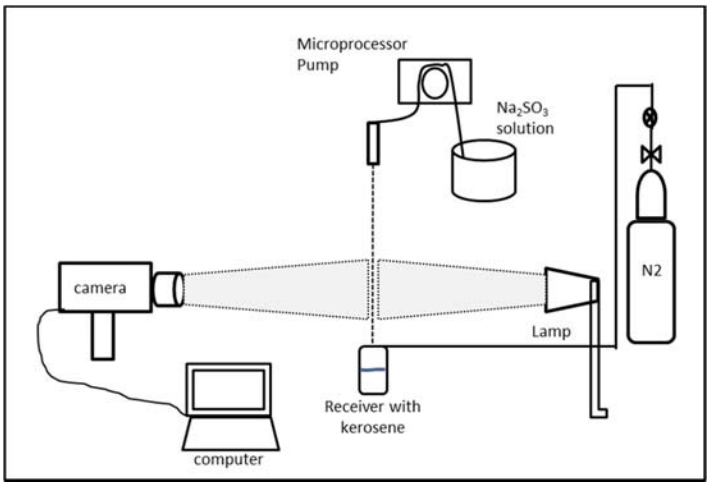

Figure 1. Scheme of experimental set-up

Sodium sulphite solution (100 mmol/l) was used as dispersed liquid. After absorption or after the droplets discharged from needle, the samples were taken on the receiver about 5 μl and added with 4 ml acetate buffer (pH 6) and 2 ml DTNB (5,5'-dithiobis 2-nitrobenzoic acid, 1 mmol/l). After that the solution is analysed by means of a calibrated spectrophotometer in order to determine the concentration of sulphite.

The reaction of sodium sulphite and oxygen proceed according to Eq (1), while reaction DTNB and sodium sulphite follow reaction Eq (2). Quantification of O_2 absorption rate is possible by measuring either the reactants or the products. Oxygen absorbed during a run was calculated from the change in sulphite concentration of the absorbing solution at the initial and the certain experimental condition (at different position). Sulphite concentrations were determined by spectrophotometric method.

$$2Na_2SO_3 + O_2 \rightarrow 2Na_2SO_4 \quad (1)$$

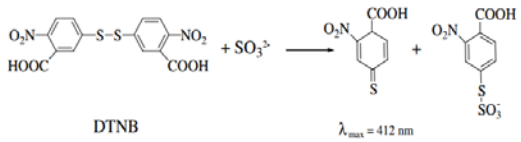

(2)

Mass Transfer Coefficient Calculation

As the gas phase mass transfer coefficient is much greater than the liquid mass transfer coefficient in this case, the absorption process is controlled by the liquid phase resistance [1].

An model equation for liquid mass transfer coefficient was expressed by Srinivasan and Aiken:

$$k_L = 0.16\left(\frac{\mu^3 D}{\rho^2 d^3 \sigma}\right)^{1/2} Re^{1.313} \quad (3)$$

where k_L represent mass transfer coeficient (m/s), μ is absolute viscosity (N.s/m^2), D is diffusivity (m^2/s), ρ is density (kg/m^3), d is droplet diameter (m), σ is surface tension (N/m) and Re is Reynold number.

Hereafter the liquid mass transfer coefficient obtained from Eq. (3) have been compared with the measurement, calculated with Eq. (4). The physical data used for the equations above are summarized in Table 1.

$$V_d \frac{dC}{dt} = k_L A_d (C^* - C) \quad (4)$$

Which, V_d represent droplet volume (m^3), C is concentration of oxygen (mol/L), C* is concentration of oxygen at equilibrium with respect to partial pressure in gas (mol/L), A_d is droplet surface area (m^2), t is contact time (s) and k_L represents the mass transfer coeficient (m/s).

Table 1. Physical data properties

Data	Value and Unit	Ref.
Diffusivity of O_2[a], D_o	2.16 x 10^{-9} m^2/s	[14]
Surface tension[b], σ	72.58 x 10^{-3} N/m	[15]
Density of Na_2SO_3[b], ρ	1007.2 kg/m^3	[15]
Absolute viscosity[b], μ	93.96 x 10^{-4} N.s/m^2	[15]

[a] in sodium sulphite concentration of 0.25mol/L
[b] sodium sulphite concentration of 0.1mol/L

RESULTS AND DISCUSSION

Droplet size and velocity of droplet

The droplet sizes are independent of the position, but slightly different for changing flowrates, due to the effect of pushing force caused by flowrate and the constant surface tension of the solution (Table 2). The droplet velocities are not the same at different positions due to gravitation force.

Mass transfer coefficient

The absorption process is controlled by the liquid phase resistance because of the molecular diffusion coefficient of solutes are several order of magnitude greater in gases than in liquids. The liquid phase mass transfer coefficient between liquid droplets and gas was derived based on the following assumption:

- The droplets are spherical during experiment.
- The droplet diameter and droplet formation time are constant during each experiment.

The experimental results are summarized in Figure 2.

Table 2. Experimental data for different flowrates and droplet positions

Flowrate, [ml/min]	1			1.5			2		
Position, [cm]	10cm	15cm	20cm	10cm	15cm	20cm	10cm	15cm	20cm
Droplet Diameter,[m]	0.00352	0.00352	0.00352	0.00362	0.00362	0.00362	0.00368	0.00368	0.00368
Droplet Volume, [L]	2.28E-05	2.28E-05	2.28E-05	2.48E-05	2.48E-05	2.48E-05	2.61E-05	2.61E-05	2.61E-05
velocity, [m/s]	1.312	1.6369	1.879	1.312	1.6369	1.879	1.312	1.6369	1.879
Formation time, [s]	2.36	2.36	2.36	1.49	1.49	1.49	1.14	1.14	1.14
Falling time, [s]	0.142	0.174	0.201	0.142	0.174	0.201	0.142	0.174	0.201
Reynold	4951	6176	7090	5091	6352	7291	5176	6457	7412
Weber number	84	131	172	86	135	177	88	137	180
Schmidt number	431.89								
Ohnesorge number	0.0019	0.0019	0.0019	0.0018	0.0018	0.0018	0.0018	0.0018	0.0018
C* [mol/L]	0.000268								

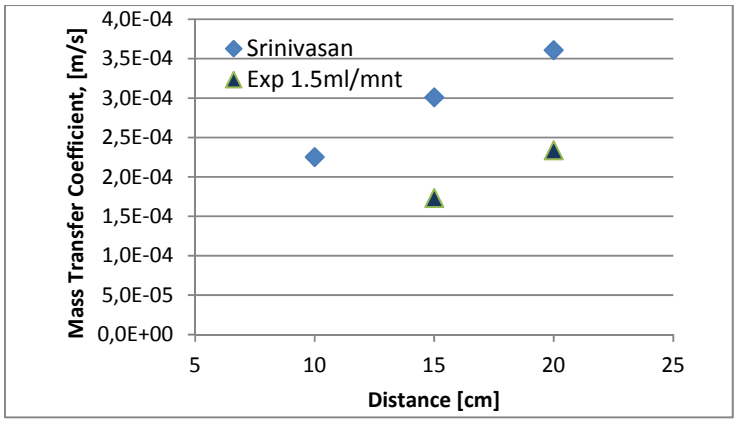

Fiqure 2. Comparison between mass transfer coefficient model and experiment

The experimental liquid mass transfer coefficients are 2 times lower than the model. It is assumed that reaction between oxygen and sulfite is low, and the total mass transfer is strongly influenced by the droplet formation. Experimental procedure and set-up has to be further improved to gain results that comply with the theory, like adding a catalyst for enhancing the reaction, and like separately investigating the mass transfer during droplet formation and falling.

REFERENCES

[1] Srinivasan, V. and Aiken, R.C. (1988): “Mass Transfer to Droplets Formed by The Controlled Breakup of Cylindrical Jet-Physical Absorption”. *Chem. Eng. Sci,* 43(12), pp.3141-3150.
[2] Whitman, G.W., Long, L.,Wang, H.W, (1926): Absorption of gases by liquid drop. *Industrial and Engineering Chemistry.* 18/4, pp.363 – 367.
[3] Dixon, B.E., and Russel, A.W. (1955). “The absorption of carbon dioxide by liquid drops”. *J.S.C.I.,* 69, 1950, pp.284-288.
[4] Adewuyi, Y.G. (1982): “A theoretical investigation of gaseous absorption by water droplets from SO_2-HNO_3-NH_3_CO_2-HCl mixture”. *Atmospheric Environment*, Volume 16, 4, pp. 719-729.
[5] Altwicker, E.R. and Lindhjem, C.E. (1988): “Absorption of Gases into Drop”. *AIChE J.* 34(2), pp.329-332.
[6] Han, J., Eimer, D.A. and Melaaen, M.C. (2013): “Liquid Phase Mass Transfer Coeficient of Carbon Dioxide Absorption by Water Droplet”. *Energy Procedia*, 37, pp.1728-1735.
[7] Scriven, L.E., and Pigford, R.L.. (1958): “On Phase Equilibrium at the Gas-Liquid Interface During Absorption”. *AIChe Journal* 4 (4), pp.439-444.
[8] Davies, J.T., and Ting, S.T. (1967): “Mass Transfer into Turbulet Jets”. *Chem. Eng. Sci,* 22, pp.1539-1548.
[9] Yagi, S., and Inoue, H. (1962): “The absorption of Oxygen into Sodium Sulphite Solution”. *Chem. Eng. Sci,* 17, pp.411-421.
[10] Linek, V., Mayrhoferova, J. (1970): “The Kinetic of Oxidation of Aqueous Sodium Sulphite Solution”. *Chem. Eng. Sci.,* 25, pp 787-800.
[11] Linek, V. (1972): “Interfacial Turbulence Accompanying Oxygen Absorption in Sulphite Solution”. *Chem. Eng. Sci.,* 27, pp 627-637.
[12] Onda, K., Takeuchi, H., and Maeda, Y. (1972): “The absorption of Oxygen into Sodium Sulphite Solution in Packed Column”. *Chem. Eng. Sci,* 27, pp.449-451.
[13] Kronig, R., and Brink, J.C., (1950). “On the theory of extraction from falling droplets”. *Applied Science Research*, volume A2, pp.142-154.
[14] Green. D.W and Perry, R.H. (2008): “Perry’s Chemical Engineers Handbook”.8th edition, McGraw Hill, New York City, pp. 5-73.
[15] Vasquez, G., Alvarez. E., Cancela, A. and Navaza, J.M. (1995): “Density, Viscosity, and Surface Tension of Aqueous Solution of Sulfite and Sodium Sulfite + Sucrose from 25 to 40^{o}C”. *J.Chem. Eng*. *Data*, 40, pp.1101-1105.

NIR-BASED REAL TIME RELEASE TESTING OF PRINTED ORODISPERSIBLE FILMS

Miriam Wimmer-Teubenbacher, RCPE, Inffeldgasse 13, 8010 Graz, Austria, m.wimmer-teubenbacher@rcpe.at, Heinz Pichler, RCPE, Inffeldgasse 13, 8010 Graz, Austria, heinz.pichler@rcpe.at, Matthias Kerschhaggl, EVK DI Kerschhaggl GmbH, Josef-Krainer-Str. 35, 8074 Raaba, Austria, matthias.kerschhaggl@evk.biz, Carole Planchette, University of Technology Graz, Institute of Fluid Mechanics and Heat Transfer, Inffeldgasse 25/F, 8010 Graz, carole.planchette@tugraz.at, Heidrun Gruber-Wölfler, RCPE, Inffeldgasse 13, 8010 Graz, Austria, 8010 Graz, woelfler@tugraz.at, Wen Kai Hsiao, RCPE, Inffeldgasse 13, 8010 Graz, Austria, hsiao@rcpe.at,Amrit Paudel, RCPE, Inffeldgasse 13, 8010 Graz, Austria, amrit.paudel@rcpe.at, Johannes Khinast, RCPE, Inffeldgasse 13, 8010 Graz, Austria, khinast@rcpe.at, Sven Stegemann, University of Technology Graz, Institute of Process and Particle Technology, Inffeldgasse 13, 8010 Graz, sven.stegemann@tugraz.at

Abstract

Printing medicine on orodispersible films is a promising way to manufacture individualized dosage forms for personalized medicine. Since each patient needs an individual dosage, we have developed a real-time release testing (RTRT) concept based on near-infrared (NIR) spectroscopy which allows to determine the amount of printed active pharmaceutical ingredients (API) on every single printed dose. We have used a non-contact, piezoelectric inkjet printing system to deliver sodium picosulfate and sodium saccharin onto orodispersible films and inspected the printed films using a NIR camera. Our preliminary results verified good signal contrast between the printed and unprinted areas and that sodium saccharin improves the NIR signal strength per printed amount.

Introduction

Personalized medicine is one of the “megatrends” stated by the FDA [1, 2]. Printing medicine has several advantages compared to other processes for individualized manufacturing of personalized medicine [3, 4]. Specifically, the API dose can be adjusted easily and precisely to meet the needs of individual patients. Additionally, printing onto orodispersible films can improve patient`s compliance since patient groups such as geriatric, pediatric and about a third of the “normal” patient group are suffering from dysphagia [5, 6]. Printing medicine can additionally be considered as continuous manufacturing process. To ensure the quality of each individualized dosage, an integrated in-line monitoring system to allow real time release testing (RTRT) is required [7, 8]. For this study, we have chosen near-infrared (NIR) spectroscopy as the preferred method since it has been successfully applied in tableting and other pharmaceutical production processes [9].

Materials and Methods

Ink Formulation Two different inks were used in this study. An aqueous solution containing 200 mg/ml sodium picosulfate (Chemos Gmbh, Rgenstauf, Germany) was prepared by dissolving the API in purified water (MilliQ, Millipore, Darmstadt, Germany). The ink was filtered with 0.45 µm Nylon syringe filters (Roth GmbH, Karlsruhe, Germany). A combined ink containing both 200 mg/ml sodium picosulfate and 50 mg/ml sodium saccharin (Roth GmbH, Karlsruhe, Germany) was prepared by adding sodium saccharin before dissolution in water. Density, surface tension and viscosity (const. shear rate 100

1/s) are listed in Table 1.

Table 1. Liquid properties of ink formulations

property	sodium picosulfate ink	combined ink
density [g/cm^3]	1.078	1.0995
surface tension [Nm/m]	63.9±0.5	80.3±0.6
viscosity [mPa.s]	1.86±0.03	2.02±0.04

Sodium picosulfate ink was printed with the following parameters: excitation voltage: 83 – 86 V, pulse duration: 47-50 µs, print frequency: 300 Hz. Average volume of drops was 427 pl with a standard deviation of 1.5 %. The combined ink was printed with an excitation voltage of 89V, pulse duration of 48 µs, a print frequency of 300 Hz. Average drop volume was 391 pl with 1.7% standard deviation.

Printing For printing a piezoelectric system (SciDrop Pico from Scienion, Berlin, Germany) was used. A standard non-coated borosilicate glass nozzle with 80 µm diameter (PDC 80) was used to print both inks. The printer has an integrated drop watcher, located beside the printing stage, which measures the volume of the jetted drops. Printability of inks was determined by printing 10,000 drops and measuring the volume once every 500 drops. The standard deviation in drop volume should not exceed 3%. Samples with different API amounts were printed onto two types of orodispersible films: Rapidfilm®, a hydrophilic, fast dissolving film (Tesa Labtec GmbH, Langenfeld, Germany) and a hydrophobic, non-porous and medical-grade oral film (Cure Pharmaceutical Crop., Oxnard, USA). Squares of 5x5 mm and different distances (x and y direction) between spots were printed onto the substrates (1000, 500, 300 and 200 µm distance with an increasing amount of 25, 100, 289 and 625 spots, respectively).

NIR measurements A NIR camera (Helios, EVK GmbH, Raaba, Austria) was used to obtain spectroscopic images of printed samples. RefSpecManager and Helios Viewer software were used to create reference spectra and chemical images. For the chemical images, reference spectra for bare substrate and API were compared and spectral regions showing best contrast were chosen for further measurements. All samples were measured in reflection mode and the first derivation of the spectra was created.

Results

The results of NIR chemical imaging are shown in Fig. 1 and 2. Combined ink was printed with 200 µm distance between spots on Rapidfilm® with 5 drops per spot. The sample was measured with reference spectra for sodium picosulfate and sodium saccharin. Even though the concentration of sodium saccharin was lower than the one of sodium picosulfate, the signal strength was much better. We have also compared visibility of sodium saccharin on two different substrates. Distance between spots ranging from 1000 to 200 µm, 5 drops per spot, were printed on Rapidfilm® and Cure Pharmaceutical substrate. The signal was shown to be stronger on Rapidfilm®.

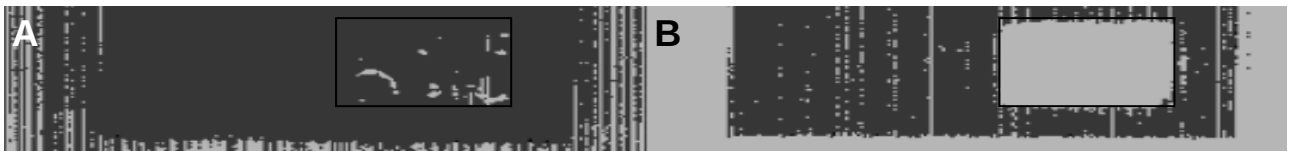

Fig. 1 NIR chemical imaging; substrate is colored dark gray and API light gray; A: sodium picosulfate on tesa 5 drops per spot, 200 µm distance, 10.8 µg/mm^2; B: sodium saccharin on tesa 5 drops per spot, 200 µm distance, 2.7 µg/mm^2;

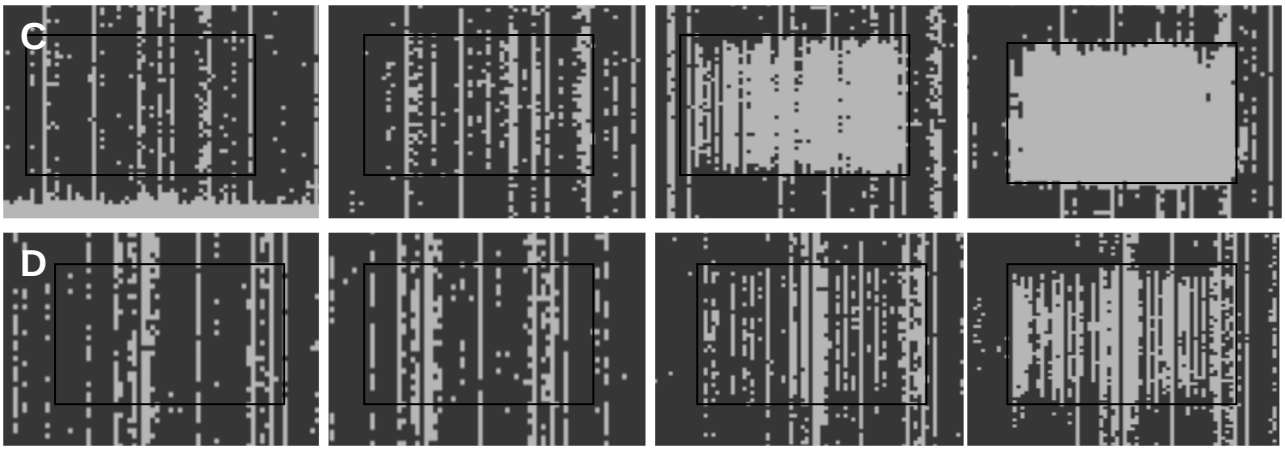

Fig. 2 NIR chemical imaging; C and D l. to r.: 1000 µm to 200 µm distance between spots, 5 drops per spot sodium saccharin ink, 0.1, 0.4, 1.2 and 2.7 µg/mm^2; C represents Rapidfilm® and D the film of Cure Pharmaceutical.

Discussion

Both inks showed very good printability and the standard deviation in drop volume was clearly below the targeted value of 3%. Adding sodium saccharin to the sodium picosulfate ink increased the NIR signal dramatically. Sodium saccharin has a carbonyl-group which responses strongly in NIR spectrum [10] and likely explains the increased visibility. Printed onto Rapidfilm®, sodium saccharin showed a better visibility than printed onto the Cure Pharmaceutical film. Sine Rapidfilm® and Cure Pharmaceutical film exhibit different NIR spectra, different spectral domains of the sodium saccharin reference spectra were chosen for chemical imaging, which might influence the intensity. More precisely, chemical imaging pictures for sodium saccharin on Rapidfilm® were acquired at 40-48, 80-103 and 145-170 nm while pictures for ink on Cure film were measured at 80-94, 128-133 and 167-178 nm. These spectral domains were chosen to maximize the spectral contrast between the sodium saccharin and substrate reference spectra. Additionally, signal intensity increases with increasing sodium saccharin concentration on both substrates, which brings us one step closer to quantification based on NIR information. Yet, we observed some spectral changes due to drying of sodium saccharin ink. Further study will be performed to evaluate the effect of drying on the quantitative NIR measurement.

Conclusion

We succeeded in printing of sodium picosulfate and the combined ink with less than 3% standard deviation in drop volume. Adding sodium saccharin to the ink formulations increases NIR visibility significantly. Additionally, NIR signal intensity is shown to increase with sodium saccharin concentrations. The effect of drying has to be better characterized to enable quantification with NIR measurements.

Acknowledgement

We would like to thank Scienion and EVK for the technical support they kindly provided; Tesa Labtec and Cure Pharmaceutical for providing the orodispersible films. We are grateful to the Austrian Research Promotion Agency (FFG) for the financial support of this work.

Literature

[1] FDA, 2013, U.S. Food and Drug Administration, Paving the Way for Personalized Medicine - FDA's Role in a New Era of Medical Product Development. Available at: http://www.fda.gov/downloads/scienceresearch/%20specialtopics/personalizedmedicine/ucm372421.pdf%202013, accessed July 9 2015.

[2] Voura et al., 2013, Printable medicines: a microdosing device for producing personalised medicines. Pharm. Technol. Eur., Vol. 23, 32-36.

[3] Planchette et al., 2015, Printing Medicines as Orodispersible Dosage Forms: Effect of Substrate on the Printed Micro-Structure, Int. J. Phram., accepted manuscript.

[4] Hoffmann et al., 2013, Advances in orodispersible films for drug delivery. Expert Opin. Drug Del., Vol. 8, 299-316

[5] Roden et al., 2013, Causes of dysphagia among different age groups: A systematic review of the literature. Otolaryngol Clin N Am, Vol. 46, 965-987.

[6] Stegemann et al., 2012, Swallowing dysfunction and dysphagia is an unrecognized challenge for oral drug therapy. Int. J. Pharm., Vol. 430, 197-206.

[7] FDA, 2009, U.S. Food and Drug Administration, Guidance for Industry - Q8(R2) Pharmaceutical Development. Available at: http://www.fda.gov/downloads/Drugs/Guidances/ucm073507.pdf, accessed May, 2015.

[8] FDA, 2004, U.S. Food and Drug Administration, Guidance for Industry - PAT - A Framework for Innovative Pharmaceutical Development, Manufacturing, and Quality Assurance. Available at: http://www.fda.gov/downloads/Drugs/Guidances/ucm070305.pdf, accessed June, 2015.

[9] Wahl et al., 2014, PAT for tableting: Inline monitoring of API and excipients via NIR spectroscopy, Eur. J. Pharm. Biopharm.

[10] Hesse et al., 2005, Spektroskopische Methoden in der organischen Chemie, Thieme; Auflage: 7.

NIR-Hyperspectral Imaging and Raman Chemical Mapping of Multilayer-Tablets

Johannes Poms[1], Otto Scheibelhofer[2], Stephan Sacher[1], Johannes G. Khinast[2]
[1]Research Center Pharmaceutical Engineering GmbH, 8010 Graz, Inffeldgasse 13
[2]Graz University of Technology, Institute for Process and Particle Engineering, 8010 Graz, Inffeldgasse 13
Johannes.Poms@rcpe.at, Otto.Scheibelhofer@tugraz.at, Stephan.Sacher@rcpe.at, Khinast@tugraz.at

Abstract

Innovative dosage forms in the pharmaceutical industry need enhanced process analytical technology tools for the control of critical quality attributes. The performance of Near-Infrared (NIR) Hyperspectral Imaging (HSI) in combination with a Principal Component Analysis (PCA) chemometric model was evaluated on multilayer-tablets. Raman mapping was used as baseline reference method.

Introduction

Multilayer–tablets are of special interest for the pharmaceutical industry for the application of novel fixed-dose combinations [1]. In an innovative approach, individually compressed layers are glued together with separation layer between individual layers [2]. This necessary barrier also prevents possible degradation reactions and incompatibilities between different excipients and the active pharmaceutical ingredients (APIs) by avoiding cross contamination. Potential critical quality attributes (pCQAs) of the bonding layer are layer thickness, defect-free layer quality over the whole tablet diameter, adhesion of the layer preventing delamination and flatness of layer surface.

This study aims to characterize the homogeneity of the bonding layer with different spectroscopic methods. Hyperspectral NIR imaging and Raman spectroscopy were selected for their non-invasive nature. Both methods give chemical information of the sample in combination with spatial resolution. By comparing the same tablets before and after application of the bonding layer, this layer is further investigated in differences of spectroscopic data. Differences and their connections with pCQAs are established.

Materials

Tablets with Ibuprofen (BASF, Ludwigshafen, Germany) as API and Tablettose 70 (Meggle Pharma, Wasserburg, Germany) as excipient were prepared via a Stylcam 200R compaction simulator (Medelpharm, Beynost, France) with a 12 mm diameter punch. An aqueous solution of 40% (w/w) PVP K25 (BASF) was prepared for the gluing component and applied to the amount of 15 mg to the tablet surface. This led to a 44 µm nominal thickness of the layer after drying.

Methods

Hyperspectral Imaging combines NIR spectroscopy with spatial information in a single image. This versatile method gives chemical information on a per-pixel basis and has lot of applications in the pharmaceutical industry as novel process analytical technology, e.g., monitoring homogeneity of powder samples, particle size determinations and content uniformity analysis [3,4,5]. Near-infrared spectroscopy relates on the overtones or combination bands of vibrational transitions of chemical bonds between light atoms. As the

neighbouring atoms have an influence on the NIR active transition (e.g. C-H, N-H, S-H or O-H bonds) each molecule has got an individual fingerprint [6,7].

The Helios Core SWNIR (EVK DI Kerschhaggl GmbH, Raaba, Austria) is a push-broom-based HSI system and was used in this study. Up to 312 spectra in a line are collected simultaneously on the detector chip. The fixed frame rate is 134 lines per second with an imaging depth of 12 bits. The sample is moved beneath the detector on a stage with a constant velocity of 0.1 mm/s, thus creating a 2-dimensional image. By using a reference grid, the spatial resolution in one direction was determined to be 90 µm per pixel, in the second, moving, direction the resolution is 7.5 µm per pixel. Scanning time was approximately 15 s per tablet.

The Raman effect is the inelastic scattering of light photons. Utilizing the interactions of the vibrational modes of the sample molecules with the incident photons, a small fraction of scattered photons differ from their initial energy. The loss of energy, or Stokes shift, is therefore characteristic of specific chemical bonds in the sample [8]. Raman and infrared spectroscopy are complementary techniques, although they probe the same range of energy, the selection rules for Raman transitions differ from the latter. Because of the weak intensities, especially for low concentrations of analyte, Raman spectra need high acquisition times.

Raman Mapping was carried out on a Raman Station 400 (PerkinElmer, Waltham, United States) equipped with a 785 nm wavelength laser with a 100 µm excitation spot size and 100 mW power. The Raman spectra were collected in a range of 200 – 3278 cm^{-1} with a spectral resolution of 2 cm^{-1}. The stage scanned 63×63 points with a spacing of 200 µm in rectangular grid, summing up to a total scan area of 12.4×12.4 mm. At every point two individual spectra of 10 seconds were accumulated. To obtain an image of the tablet the data is interpolated between the measured excitation spots.

Data pre-treatment: All calculations were performed with the help of Matlab 2013b (The MathWorks Inc., Natick, United States) and SIMCA 13.0.3 (Umetrics, Umeå, Sweden). The recorded NIR spectra form a hypercube of the reflected intensity with the dimensions of position, time and wavelength. Savitzky-Golay filtering smoothed the hypercube on the time axis. Conversion to pseudo-absorbance of the data reflects Beer's law, stating that absorbance is linearly related to chemical concentrations. 175 channels selected on best

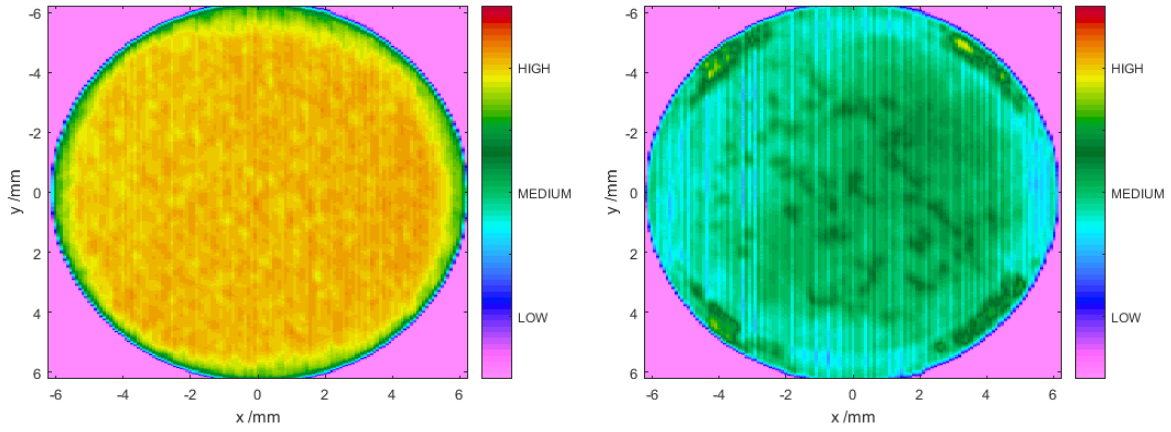

Figure 1: Roughness of the surface. Left panel: High variations in the absorbance of the tablet surface with granular like structure. Right panel: The surface of the coated tablets does not show this behaviour.

signal to noise ratio basis were normalized via the standard normal variate (SNV) filter. Raman spectra were background corrected by subtraction of a dark frame.
PCA is a multivariate data analysis method. Linear combinations of the measured wavelengths are projected onto latent variables in such a way, that variation is maximized. The first component covers most of the variation of the dataset, the second orthogonal one covers the majority of the still remaining variation, and so on. Considering only a few iterations of the algorithm, most of the dataset is approximated within the first few principal components. This leads to an enormous data reduction and extracts important factors [4,7]. By studying the latent variables, insights to uncover the underlying mechanism are provoked. The PCA-scores are the coordinates of each spectrum, with respect to the principal components spanning an orthonormal basis.

Results

Figure 1 shows the total pseudo absorbance of the tablet surface, measured by reflectance. On the left side a granular structure is visible on the pure, uncoated tablet. This corresponds to the visible roughness of the surface. The same tablet inspected after coating showed a much flatter surface (right side). To quantify coating homogeneity a PCA model was built in SIMCA using a subset of 26 642 pre-treated NIR spectra. Five principal components covered R^2=96.8% of variation in the spectra. The first component includes 82.2% variation of the data and showed highest distances between raw and PVP covered tablet spectra, thus allowing identification of the bonding layer and patches of uncoated tablets respectively. Using the score values for the first component, the whole tablet can be depicted as in figure 2. In the left panel the uncoated tablet gives negative scores. In the right panel scores for the same tablet, covered with the binding layer, are shown. Here the model predicted positive scores, with a homogeneous area in the centre and a ring of high score values near the bevelled tablet edge, corresponding with a thicker layer.

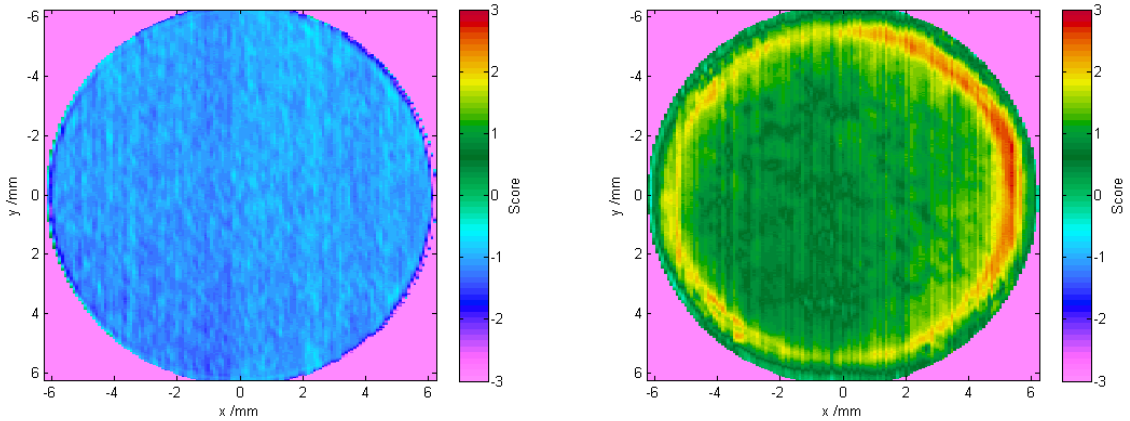

Figure 2: PCA score plots. Left panel: The raw uncoated tablet has got only negative scores. Right panel: Scores of the coated tablet are positive with higher values towards the edge.

To validate PCA results Raman mapping was performed. First Raman spectra of PVP solution on a microscope slide were collected, see figure 3, left side. The Raman peak from 932 to 936 cm^{-1} was identified to be specific for PVP and is not present in API or excipient. Raman mapping for the whole tablet revealed the same pattern of PVP distribution on the tablet, as shown with HSI. The total collection of the Raman spectra took 22 hours.

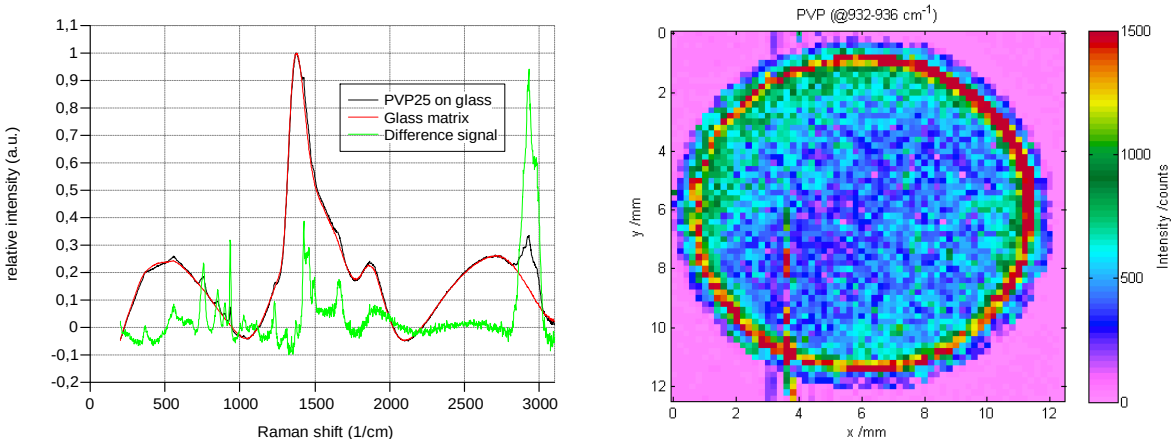

Figure 3: Left panel: Raman spectra of PVP solution on glass substrate. Right panel: Raman map of a PVP coated tablet. Specific-selected intensity plot in the wave number range of 932 to 936 cm^{-1} depicts the distribution of key component PVP.

Summary

The performance of HSI for the application of multilayered tablets was evaluated. Besides chemical content analysis HSI showed potential in the CQA monitoring of otherwise hard to analyze bonding layers. The PCA model showed high discriminative power.
Raman mapping validated the HSI results, but is clearly outperformed from the latter in terms of achievable resolution, versatility and measurement time.

This work was funded through the FFG as part of the “Gluing Pills”-Project project within the “Production of the future” program #848 582.

Literature

[1] A. Abebe, I. Akseli, O. Sprockel, N. Kottala, A.M. Cuitino, „Review of bilayer tablet technology“, *Intern J Pharmaceutics*, Vol 461, 2014, pp549-558.
[2] V. Wahl, S.Salar-Behzadi, S. Stranzinger, S. Sacher, J.G. Khinast, „Gluing Pills: An Innovation in Multiplayer Tableting“, 10th PBP World Meeting (accepted).
[3] J. Cruz, M.J. Blanco, “Content uniformity studies in tablets by NIR-CI”, *J. Pharm Biomed Anal,* Vol 56(2), 2011, pp 408-412.
[4] O. Scheibelhofer, D.M. Koller, P. Kerschhaggl, J.G. Khinast, “Continuous Powder Flow Monitoring via Near-Infrared Hyperspectral Imaging”, IEEE Instrumentation and Measurement Technology Conference Proceedings, 2012.
[5] F. Franch-Lage, JM Amigo, E. Skibsted, S. Maspoch, J. Coello, “Fast assessment of the surface distribution of API and excipients in tablets using NIR-hyperspectral imaging”, Int J Pharm, Vol 411(1-2), 2011, pp 27-35.
[6] J. Luypaert, D.L. Massart, Y.V. Heyden, “Near-infrared spectroscopy applications in pharmaceutical analysis”, *Talanta*, Vol 72(3), 2007, pp865-883.
[7] G. Reich, “Near-infrared spectroscopy and imaging: basic principles and pharmaceutical applications”, *Adv Drug Deliv Rev*., Vol 57(8), 2005, pp 1109-1143.
[8] K.C. Gordon, CM McGoverin, “Raman mapping of pharmaceuticals”, *Int J Pharm., Vol* 417(1-2), 2011, pp 151-162.

Prozessintensivierung von Batch-Destillationsverfahren zur Herstellung von Spirituosen

Peter Scherübel, Helmut Löffler, Matthäus Siebenhofer
TU Graz, Institut für Chemische Verfahrenstechnik und Umwelttechnik, 8010 Graz, Inffeldgasse 25 C/II
scheruebel@tugraz.at, m.siebenhofer@tugraz.at

Kurzfassung

Methanol entsteht insbesondere bei der Erzeugung von Kernobstbränden während der alkoholischen Gärung von Maische. Dieses bietet erhebliche Gesundheitsrisiken, und ist daher in Destillaten ein unerwünschter Begleitstoff. Am CEET werden sowohl Simulationen als auch experimentelle Untersuchungen durchgeführt, um neben Methanol die effizientere Abtrennung der Vorlaufkomponenten Ethylacetat und Acetaldehyd sowie der höheren Fuselalkohole zu untersuchen und zu modellieren, mit dem Ziel qualitativ hochwertige „schadstoffärmere“ Obstbrände zu erzeugen. Erste Ergebnisse zeigen, dass die destillative Abtrennung von Methanol im Vorlauf unter Verwendung geeigneter Destillationsanlagen grundsätzlich möglich ist.

Einleitung

Bei der Erzeugung von Destillaten, insbesondere bei der Herstellung von Kernobstbränden besteht die Gefahr der Methanolbildung in der Maische. Als Vertreter dieser Kategorie sind vor allem die Fruchtsorten Apfel, Birne, Mispeln und Quitten zu nennen, beispielsweise muss jedoch auch Beeren besondere Beachtung geschenkt werden. Der Grund hierfür liegt in wesentlichen Bestandteilen dieser Früchte – den Pektinen (siehe Abb. 1). Pektine sind Polysaccharide aus D-Galacturonsäure-Molekülen, deren Carboxylgruppen mit Methanol verestert sind – und genau hierin besteht die Gefahr. Pektine fungieren vereinfacht dargestellt als „Kittsubstanz“ zwischen den Zellen. Bei der alkoholischen Gärung, welche das gewünschte Ethanol liefern soll, werden Pektine durch fruchteigene Enzyme abgebaut, wobei dieser Vorgang im Sinne einer effizienteren Gärung durch gezielte Zugabe von Pektinesterasen forciert wird [1,2,3]. Dabei wird jedoch Methanol freigesetzt und gelangt somit in die Maische. Zwar hat Methanol an sich keine toxische Wirkung auf den menschlichen Organismus, wohl haben das aber die Stoffwechselprodukte Formaldehyd und Ameisensäure, die bis zum Tode führen können.

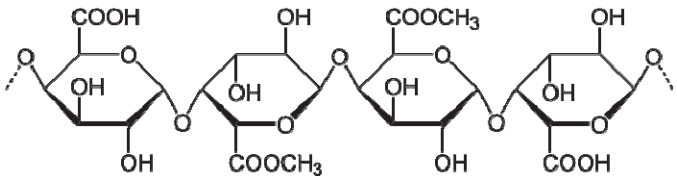

Abbildung 1: Aufbau von Pektinen (teilveresterte Polygalacturonsäure)

Entgegen der vom österreichischen Bundesministerium für Gesundheit [4] oder der pharmazeutischen Zeitung „PZ“ [5] verbreiteten Meinung kann Methanol trotz des deutlich niedrigeren Siedepunkts (64,7°C), verglichen mit Ethanol (78,4°C) unter der Verwendung herkömmlicher, in der Spirituosenerzeugung eingesetzten Destillen nicht ausreichend abgetrennt werden [6], obwohl Methanol von Ethanol im ternären System Methanol/Ethanol/Wasser vollständig abgetrennt werden kann [7]. Gleichgültig ob einfache

Vorrichtungen in Form von Brennblasen, oder mehrstufige Bodenkolonnen eingesetzt werden.

Simulation und experimentelle Untersuchung der Methanolabtrennung

Um die destillative Trennung des ternären Gemisches Methanol, Ethanol und Wasser im Batchbetrieb zu untersuchen, wurde einerseits eine dynamische Simulation einer einstufigen Batchdestillation mit Aspen Hysys, andererseits die experimentelle Untersuchung im Labormaßstab durchgeführt. Die Ergebnisse der Simulation sind in Abb. 2 dargestellt. Darin sind der Molanteil von Methanol resp. Ethanol sowie die Kopftemperatur und der Blasenfüllstand gegen die Batch-Destillationszeit aufgetragen. Betrachtet man in Abbildung 2 das Verhältnis von Methanol zu Ethanol im Destillat, welches im Laufe der Destillation stetig zunimmt wird verdeutlicht, dass Methanol unter diesen Bedingungen nicht im Vorlauf abgetrennt werden kann [8].

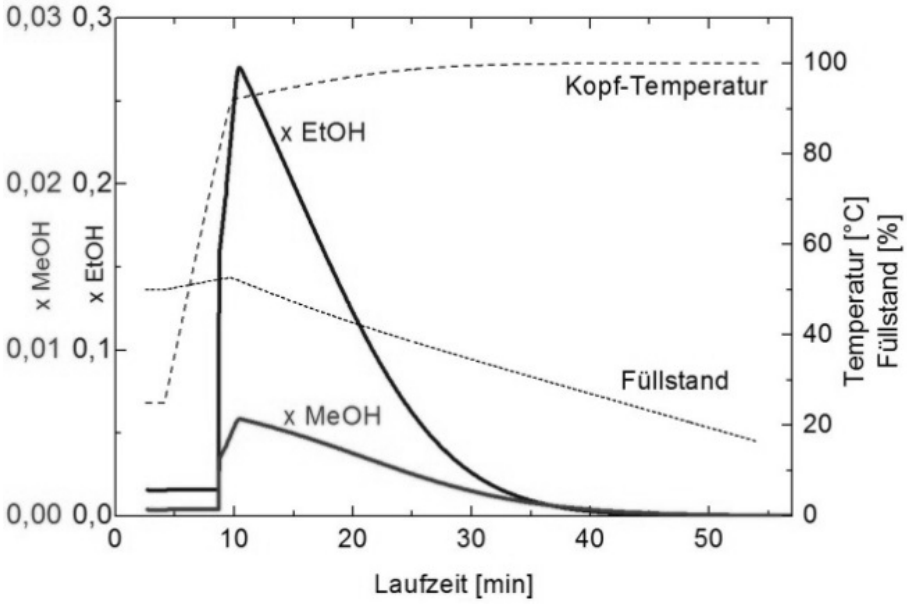

Abb. 2: Verlauf von Methanol und Ethanol im Destillat vs. Batch-Zeit – Aspen Hysys

Die Simulationsergebnisse wurden durch Laborexperimente in einer Batch-Destillationskolonne validiert. Wie in Abb. 3 ersichtlich ist, nimmt das Verhältnis von Methanol zu Ethanol im Laufe der Destillationsdauer (= äquivalent zur Kopftemperatur) praktisch bei einstufiger Destillation unabhängig vom untersuchten Rücklaufverhältnis stetig zu. Um Methanol, wie gewünscht, im Vorlauf abtrennen zu können, ist es naheliegend, die Trennleistung der Kolonne zu erhöhen. Zu diesem Zwecke wurde die Kolonne mit Raschig-Ringen gepackt und die Abtrennung analog unter Variation des Rücklaufverhältnisses untersucht. In Abb. 4 ist zu sehen, dass das Verhältnis von Methanol zu Ethanol durch die erhöhte Trennleistung der Raschigringe im Verlauf der Destillationsdauer abnimmt. Methanol ist somit durch den Einsatz geeigneter Destillationsanlagen prinzipiell größtenteils im Vorlauf abtrennbar.

Optimierung der Abtrennung

Am CEET wurde in Kooperation mit OSR Löffler ein Konzept erstellt, um herkömmliche, einfache Destillationsanlagen, wie sie bei der traditionellen Schnapserzeugung eingesetzt werden, zu optimieren. Dieses sieht vor, dass das bestehende Geistrohr, welches für gewöhnlich auf den Destillationshelm einfacher einstufiger Destillen aufgesetzt wird, wie in

Abb. 5 zu sehen ist, durch einen Bypass, die so genannte Löffler-Gabel, erweitert wird. Die Besonderheit dieser Schaltung liegt darin, dass der Bypass einer schräggestellten Kolonne mit Packung entspricht, um die Trennleistung zu erhöhen. Zusätzlich kann dieser Bypass bei Bedarf gekühlt und als Dephlegmator eingesetzt werden, um die Trennleistung über den internen Rücklauf weiter zu erhöhen. Zu Beginn der Destillation wird anstelle des herkömmlichen Geistrohres, die Bypass-Schaltung gewählt, und Methanol im Vorlauf abgetrennt. Das eigentliche Zielprodukt, der Mittellauf, wird anschließend über das herkömmliche Geistrohr gewonnen, da die erhöhte Trennleistung der Bypasskolonne zwar eine höhere Ethanolkonzentration liefert, jedoch weniger Aromastoffe ins Destillat gelangen.

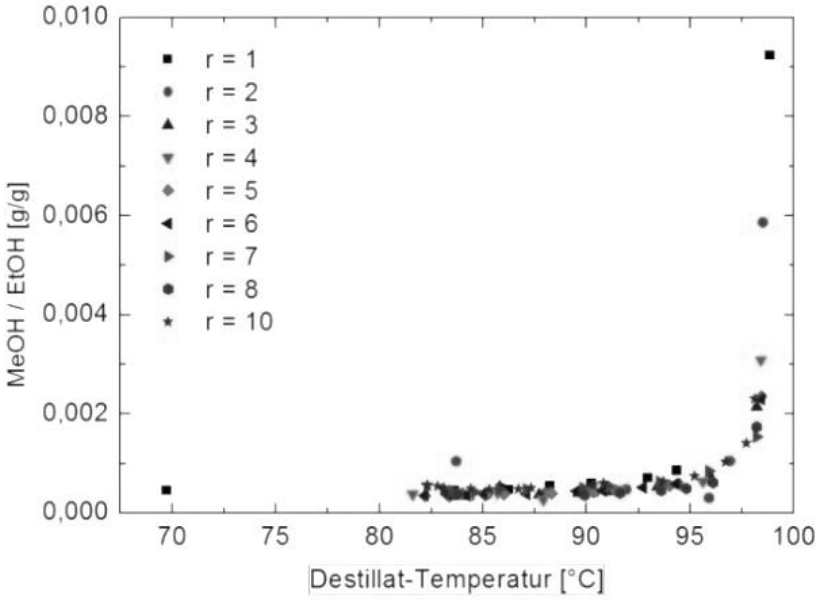

Abb.3: Verhältnis von Methanol zu Ethanol vs. Destillattemperatur –Labor-Batchdestillationskolonne ohne Einbauten

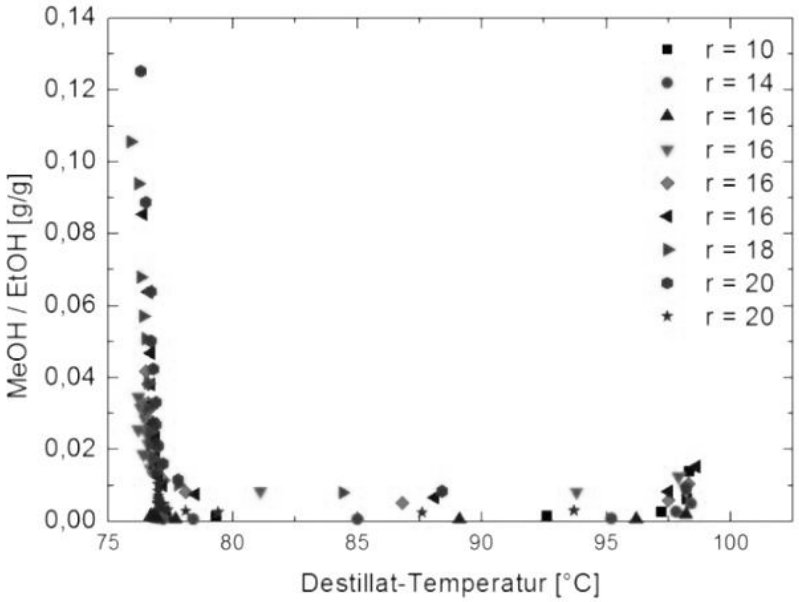

Abb.4.: Verhältnis von Methanol zu Ethanol vs. Destillattemperatur –Labor-Batchrektifikationskolonne mit Raschig-Ringen

Abb. 5: Die Löffler-Gabel: Optionaler Wechsel von herkömmlichem Geistrohr zu trenneffizienterer Kupferpackungskolonne zur Methanolabtrennung im Vorlauf

Ausblick

Neben Methanol können bei der alkoholischen Gärung von Obstmaischen weitere gesundheitsschädliche Substanzen, beispielsweise Acetaldehyd als Intermediat der alkoholischen Hauptgärung [9,10] und Ethylacetat durch Veresterung unerwünschter, bakteriell gebildeter Essigsäure entstehen [3,9]. Ebenso werden durch Aminosäuregärung von Hefestämmen höhere Alkohole, die sogenannten Fuselalkohole gebildet [3]. Eine wirkungsvolle Abtrennung dieser Komponenten vom Zielprodukt soll ebenfalls an synthetischen Systemen experimentell und mit gängigen CAE-Softwarepaketen untersucht werden. In weiterer Folge soll speziell für das Anwendungsfeld der Abfindungs- und Kleinbrennereien durch konstruktive Modifikationen der Destillationsausrüstung eine ebenso einfache wie effiziente Optimierung bestehender Destillationsanlagen ermöglicht werden.

Literatur

[1] Andraous, J.I. et al, Effect of Liquefaction Enzymes on Methanol Concentration of Distilled Fruit Spirits, Am. J. Enol. Vitic, Vol. 55, No. 2 (2004):199-201

[2] Bindler, F.; Voges E.; Laugel, P., The problem of methanol concentration admissible in distilled fruit spirits, Food Addit Contam., Vol 5, No. 3 (1988):343-51.

[3] Bonte, W., Begleitstoffe alkoholischer Getränke, Verlag Max Schmidt-Römhild, Lübeck, (1987)

[4] Uhl, A. et al, Handbuch Alkohol – Österreich, Zahlen. Fakten. Daten. Trends. Bundesministerium für Gesundheit (2009)

[5] Gensthaler, B.M., Methanol - Tödlicher Bruder des Ethanols, Pharmazeutische Zeitung, Govi-Verlag Pharmazeutischer Verlag GmbH, Eschborn, Vol. 8 (2012)

[6] Schmickl, H., Malle, B., Schnapsbrennen als Hobby, Verlag Die Werkstatt GmbH, Göttigen, (2003)

[7] Onken U., Arlt W., Monograph, The Institution of Chemical Engineers/Rugby, Warwickshire, 2 Ed., 1-61, (1990)

[8] Scherübel P., Siebenhofer, M., Das Dreistoffsystem Ethanol-Methanol-Wasser, TTTK 2015 (2015), Canazei

[9] Lachenmeier, D.W., Musshoff, F., Begleitsoffe alkoholischer Getränke – Verlaufskontrollen, Chargenvergleich und aktuelle Konzentrationsbereiche, Rechtsmedizin Vol. 104 (2004), 454-462

[10] Lachenmeier, D. W. et al., Carcinogenicity of acetaldehyde in alcoholic beverages: risk assessment outside ethanol metabolism, Addiction, Vol. 14, No.6 (2009):533-55

A rheological method to predict mucoadhesion between dosage form excipients and human saliva

Nélio Drumond, Sven Stegemann
Institute of Process and Particle Engineering, Graz University of Technology
Inffeldgasse 13/III, 8010 Graz
nelio.drumondfreitas@tugraz.at, sven.stegemann@tugraz.at

Abstract

The adhesion of a surface to a biological membrane is defined as bioadhesion. Mucoadhesion can be considered a subtype of bioadhesion, in cases where a surface is in contact with a mucus layer that covers a mucosal tissue. Mucoadhesive polymers have been increasingly used as functional coatings to enhance, modulate and targeted drug delivery through mucosal tissue. Nevertheless, the usage of polymers with mucoadhesive properties in film-coating formulations can lead to unintended esophageal adhesion, causing discomfort after swallowing and oro-esophageal adverse reactions. With the increasing age of the population, a higher incidence of swallowing disorders has been noted, raising the attention to the development of oral solid forms that can be easily/safely swallowed. Suitable film-coating polymers are suggested to improve the ease and safety in swallowing of solid dosage forms. In this study, a rheological method was used to estimate the mucoadhesive potential between different film-coating polymers and an artificial saliva formulation based on viscoelastic profiles. Results suggest high mucoadhesion for hydroxypropyl methylcellulose compared to polyvinylpyrrolidone and polyvinyl alcohol, which have shown smaller viscosity potentials. The increase in concentration and molecular weight is predictive of mucoadhesive strength, except for PEG grades.

Introduction

Bioadhesion is defined as the adhesiveness of a surface to a biological tissue or membrane. Bioadhesion describes the interfacial force resulting from the interaction between the adhesive material and the biological tissue [1]. This complex process involves chemical interactions between mucin and polymers where the degree of mucoadhesion bonding is influenced by polymer-related factors. Such features may include: average molecular weight and chain length/flexibility (Fig. 1), polymer swelling, polymer charge and hydrogen bonding capacity [2].

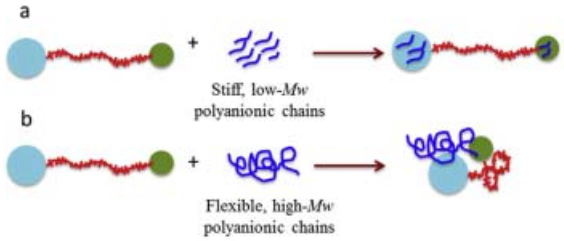

Figure 1 – Interaction between polyanions and the double globular structure of mucin [2].

In drug delivery systems, bioadhesion is usually achieved by the use of adhesive excipients (inactive ingredients, e.g. polymers) that interact with the targeted biological tissue. The term mucoadhesion can be referred to a subgroup of bioadhesion, specific to cases in which the formulation interacts with the mucus layer (e.g. in sublingual or buccal area of the mouth) that covers a mucosal tissue. Mucoadhesive polymers are important formulation tools due to their usefulness in enhancement of bioavailability, circumvent first pass metabolism, controlled and targeted drug delivery. The degree and kinetic of polymer

swelling is an important characteristic for oral solid dosage forms, since mucoadhesion reach a maximum at an optimal water content and declines with over-hydration [2,3,4]. Clear evidence for mucoadhesion properties are available in the literature regarding well-known pharmaceutical excipients. Polyacrylates, chitosan, hydroxypropyl methylcellulose (HPMC), alginates and gelatin are some examples [1,2,5].
Mucoadhesion is very predictable to occur between bioadhesive polymers and the saliva-covering layer of the oro-esophageal system [6]. Some of the mentioned polymers are not only used in tablet film-coating, providing elegance and non-powdery tablets, but also used as base polymers for capsules shells. Additionally, previous findings indicate that film-coated tablets are less adherent to the esophagus thus providing easier and safer swallowing, when compared to uncoated tablets [7]. Nevertheless, the use of film-coating polymers with mucoadhesive properties can create sticky tablets that may adhere to the esophagus after contact with saliva, inducing discomfort during swallowing, mucosal irritation and leading to cases of non-adherence to therapy.
Regarding oral solid dosage forms, the ease of swallowing has become an emerging concern in the past years due to the growing aging population and its incidence of swallowing issues. The right balance between drug delivery and safe swallowing must be taken in consideration during coating formulation, and suitable polymers must be chosen in order to achieve such requirements.
Polyvinylpyrrolidone (PVP), polyvinyl alcohol (PVA) and polyethylene glycol (PEG) are other well-known water-soluble polymers commonly used as film-coating excipients, said to exhibit poor mucoadhesive properties [2]. This experimental work evaluated the mucoadhesive potential of different pharmaceutical excipients, through the study of its interaction with human artificial saliva by means of a rheological method.

Materials and Methods

Materials

PVA grades (EG-03P, EG-05P, EG-18P, EG-30PW and EG-40P) were a kind gift from Nippon Gohsei (Düsseldorf, Germany). Plasdone grades (PVP K-15, K-25, K-29/32, K-60, K-90 and K-120) were donated by IMCD (Wien, Austria). PEG 1000, 15000 and 4000 were purchased from Alfa Aesar (Lancashire, UK). PEG 3350 and mucin from porcine stomach, type III, were purchased from Sigma-Aldrich (Munich, Germany). PEG 6000 was obtained from Research Center Pharmaceutical Engineering (Graz, Austria). Sodium phosphate monobasic (NaH_2PO_4), Sodium phosphate dibasic (Na_2HPO_4), sodium chloride (NaCl), calcium chloride ($CaCl_2$) and PEG 2000 were obtained from Capsugel (Colmar, France). HPMC was donated by Ashland. The water used was of Millipore quality.

Preparation of simulated artificial saliva

For the preparation of simulated salivary buffer, 0.021 M of Na_2HPO_4/NaH_2PO_4, 0.036 M NaCl and 0.00096 M $CaCl_2$ were dissolved in purified water. Subsequently, 5mg/ml of porcine stomach mucin was added and the mixture was allowed to stir for 120 minutes, at room temperature.

Preparation of polymer samples

For each polymer, stock solutions of 6% (w/v) were prepared in phosphate buffer, at room temperature. Remaining concentrations (1-5%) were obtained by performing dilutions of the stock solutions.

Mucoadhesion measurements

Interaction between polymer and artificial saliva was evaluated using a rheological method previously described [1,5]. One part artificial saliva solution and one part polymer solution

were mixed together at 400 rpm for 30 minutes prior to analysis. Polymer and artificial saliva solutions were also measured alone as references. All samples were measured in duplicates.
The measurements were performed with a Physica rheometer, model MCR 300 with 26.66 mm cylindrical probe (Anton Paar GmbH, Graz, Austria). The temperature was set to 37 °C and the rheometer automatically awaits equilibrium before starting a measurement. Shear rates ranged from 5 s^{-1} to 25 s^{-1}, with 10 measurements per decan.

Results and Discussion

The physical and chemical bond energies involved in mucin-polymer interactions produce mechanical energy that may lead to shape alterations or molecule arrangements. These molecular modifications produce viscosity changes and, therefore, the forces involved in a mucin-bioadhesive system can be monitored by viscosity measurements. Hereupon, the viscosity coefficient of a mucin-polymer mixture can be analyzed through the following equation:

$$\eta_t = \eta_m + \eta_p + \eta_b$$

where η_t is the viscosity coefficient of the system and η_m, η_p, are the individual viscosity coefficients of mucin and polymer, respectively. η_b is the viscosity coefficient due to the component of bioadhesion and can be obtained by rearranging the equation [1,8].
Components of adhesion were determined for PVP, PVA and PEG, at different concentrations and molecular weights (MW), and are shown in figures 2, 3 and 4, respectively. HPMC (with small/medium MW) was used as positive control, since is a well-studied mucoadhesive polymer.

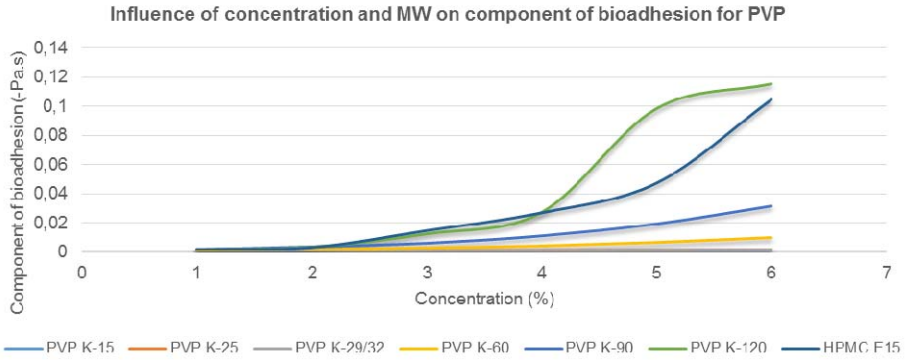

Figure 2 – Component of bioadhesion for PVP grades at different concentrations.

Considering PVP grades, increased concentration and/or MW have led to increased viscosity (Fig. 2). Maximum levels were obtained for PVP K-120, which can be correlated with high bioadhesion for concentrations within 4-6% when compared to HPMC (positive control). K-90 and K-60 species have also shown bioadhesive potential based on its viscosity profiles. For low MW grades (K-29/32, K-25, K-15), poor viscosity levels were obtained which indicate lack of bioadhesion.
PVA grades have shown similar profile, with increased viscosity with an increasing concentration and/or MW (Fig. 3). Higher levels were obtained with PVA EG-40P, which showed equal profile to the mucoadhesive polymer. Significant mucoadhesion is also predicted for EG-30PW and EG-18P grades. PVA EG-03P, EG-05P and EG-05PW showed smaller viscosities which can indicate low bioadhesive impact.

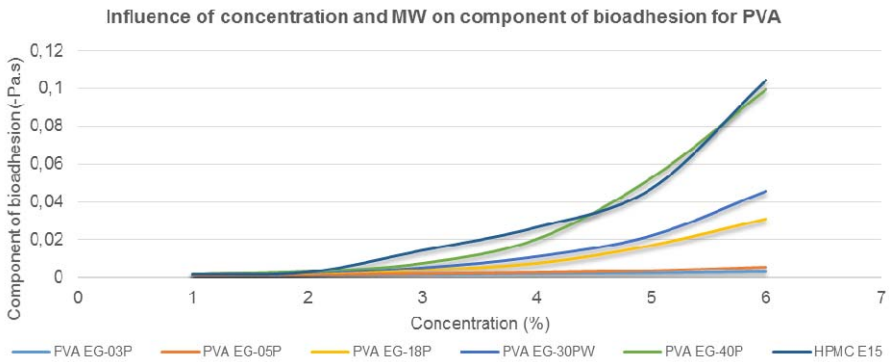

Figure 3 - Component of bioadhesion for PVA grades at different concentrations.

Regarding PEG, all grades have shown much lower viscosity when compared to HPMC indicating lack of bioadhesion. Also, concentration seems not to have impact on the profile.

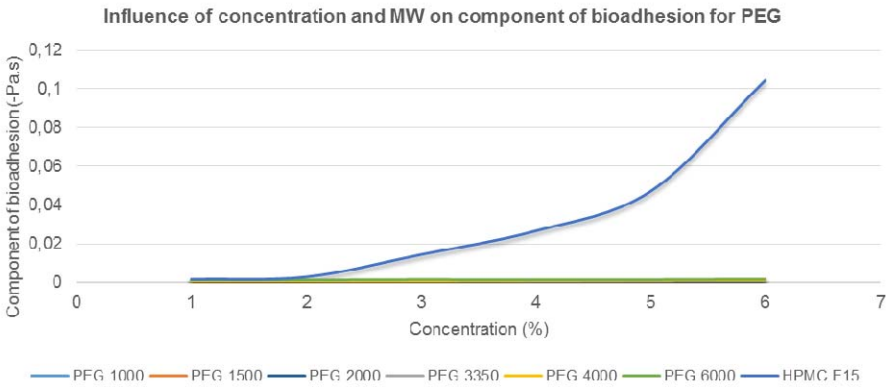

Figure 4 - Component of bioadhesion for PEG grades at different concentrations.

Conclusion

Only the highest MW for PVA and PVP have shown equivalent profile to HPMC. All other grades showed lower viscosities (lack of bioadhesion), being proportional to its MW and concentration. Concentrations of 1-3% and small molecular weights are the preferred to avoid mucoadhesive potential. In comparison to the control, PEG grades showed negligible profile suggesting that this polymer lacks in mucoadhesive properties.

References

[1] Hassan, E.E. et al. A simple rheological method for the *in vitro* assessment of mucin-polymer bioadhesive bond strength. Pharm Res. 7, 491-495 (1990).

[2] Russo, E. et al. A focus on mucoadhesive polymers and their application in buccal dosage forms. J Drug Deliv Sci Tec. 1-13 (2015).

[3] Edsman, K. et al. Pharmaceutical applications of mucoadhesion for the non-oral routes. J Pharm Pharmacol. 57, 3-22 (2005).

[4] Lee, J.W.; et al. Bioadhesive-based dosage forms: the next generation. J Pharm Sci. 89, 850-866 (2000).

[5] Ivarsson, D. et al. Comparison of *in vitro* methods of measuring mucoadhesion: ellipsometry, tensile strength and rheological measurements. Colloid Surface B. 92, 353-359 (2012).

[6] Zhang, L. et al. Strategies and therapeutic opportunities for the delivery of drugs to the esophagus. Crit Rev Ther Drug Carrier Syst. 25, 259-304 (2008).

[7] U.S. FDA. Guidance for Industry: Size, Shape and Other Physical Attributes of Generic Tablets and Capsules. Pharmaceutical Qual. 1–11 (2013).

[8] Bohdanecky, M. et al. Viscosity of polymer solutions. Polymer Science Library. 2, (1982).

Isolation of valuable components from *Acalypha indica* using solvent extraction

Surangkana Chaichoowong[1], Jan Bernd Bol[2], Pornprapa Bol[3],
Malinee Sriariyanun[1], Thomas Gamse[2]
[1]King Mongkut's University of Technology North Bangkok, The Sirindhorn International Thai-German Graduate School of Engineering, Bangkok, Thailand
[2]Graz University of Technology, Institute of Chemical Engineering and Environmental Technology, NAWI Graz, Graz, Austria
[3]Rajamangala University of Technology Thanyaburi, Faculty of Engineering, Department of Chemical Engineering, Pathum Thani, Thailand
surangkana.c-cpe2013@tggs-bangkok.org, thomas.gamse@tugraz.at

Abstract

Acalypha indica is a weed that grows in South-East Asia. It contains several valuable compounds that can be used for curing various diseases such as rheumatism, skin infection, and blood dysentery. These compounds of the plants are usually collected by extraction. In this work, the extraction of *Acalypha indica* using solid-liquid extraction was studied. The influence of parameters as types of solvents (ethanol, distilled water, hexane, and ethyl acetate), and solvent to solid ratio (416:1, 125:1, 50:1, 20:1) were observed. The results showed that ethanol provided the highest extraction efficiency and the expected yield increased when solvent to solid ratio increased. Then, the kinetic model of solid-liquid extraction based on the assumptions of the Peleg‘s law and the second-order law was compared. In this study, the second-order rate law model provided higher correlation coefficient than the Peleg’s model in all experiments.

Introduction

Acalypha indica is one of weed plants that contain important phytochemicals for human health applications. It can be found commonly in India, Pakistan, Sri Lanka and Thailand. The extracts of this plant from leaves, roots and stem parts are used as medicinal plants in various countries. Every parts of this plant is used to treat various diseases such as the skin problems, eye infections, respiratory problems, rheumatism and decreasing blood sugar level [1]. Moreover, *Acalypha indica* shows antibacterial activity [2]. There are different extraction techniques used for obtaining active components from plant materials. Soxhlet extraction has a high efficiency, but the thermal stress might degrade target components. Solid-liquid extraction is usually performed at lower temperature, but generally shows a lower extraction efficiency. Both methods can be performed by using different solvents as a selective extraction. In some cases, supercritical fluid extraction (SFE) can be of interest. This technique uses high pressure and temperature for keeping the solvent below its boiling point. There are several parameters that have effects on performance of the SFE method such as temperature, pressure, extraction time and type of solvent. CO_2 is widely used in this system because of low critical pressure and temperature. It is non-toxic and inexpensive extractant [3].

Modeling is an important part in any research including extraction. There are several mathematical models available for solid-liquid extraction. One of them is Peleg’s model. Normally, this model is applied for sorption kinetics but it is applicable for solid-liquid extraction because of a similar profile between extraction and sorption [4]. Another model is the second-order law that is the most suitable model for solid-liquid extraction. The

objective of this work is to extract active component from *Acalypha indica* by using solid-liquid extraction and to study the applicability of the Peleg's equation and the second-order law for modeling the extraction behavior of active component in *Acalypha indica*.

Materials and experimental setup

The whole plants of *acalypha indica* were collected in Thailand. They were dried under sunlight for 3 days and then sealed in plastic foils. The samples were crushed with IKA A11 basic analytical mill and then sieved with a Retsch AS200 basic sieve machine. Particles under 400 µm size were selected for all extraction experiments.
The solid-liquid extraction experiment was performed in stirred tank batch at 20°C. Four types of solvents including deionized water, ethanol, ethyl acetate and hexane were used for the extraction. These solvents cover a broad range of polarities and therefore should extract different types of plant components. The solvent to solid ratio (w/w) was varied from 416:1 to 20:1. The samples were withdrawn during the total extraction time of 90 min. After the extraction was completed, the samples were taken to determine the extracted components and their concentration by UV-VIS. The UV/VIS spectral profiles were scanned with a Shimadzu UV-1800 at 200-1000 nm wavelength. The dominant peaks were recorded for kinetic study.

Experimental results

The UV-VIS spectral profiles of samples extracted by using four types of solvents including deionized water, ethanol, hexane and ethyl acetate were depicted in Fig. 1. In ethanol, ethyl acetate and hexane, there are four peaks at wavelengths 402, 423, 459 and 653 nm. The profile of the highly polar water was different from the others. This was also optically visible due to the different color of extracts. Hexane showed a lower efficiency compared to the other solvents. The result of ethanol and ethyl acetate were comparable. Therefore, only ethanol and water were selected for the next experiments.
The amount of extracted component is heavily affected by the solid-liquid ratio. To study the kinetic, the extinctions at the peak wavelength 653 nm were plotted at different solid-liquid ratios in Fig. 2. The extraction efficiency increased when the solvent to solid ratio is increased from 416:1 to 20:1 and the similar extinction in the ratio between 416:1 and 125:1 was observed. Although 416:1 ratio showed better efficiency of extraction than 125:1, the solvent to solid ratio of 125:1 was chosen in following experiment because it requires less solvent with insignificantly difference in extinction compared to 416:1 ratio.

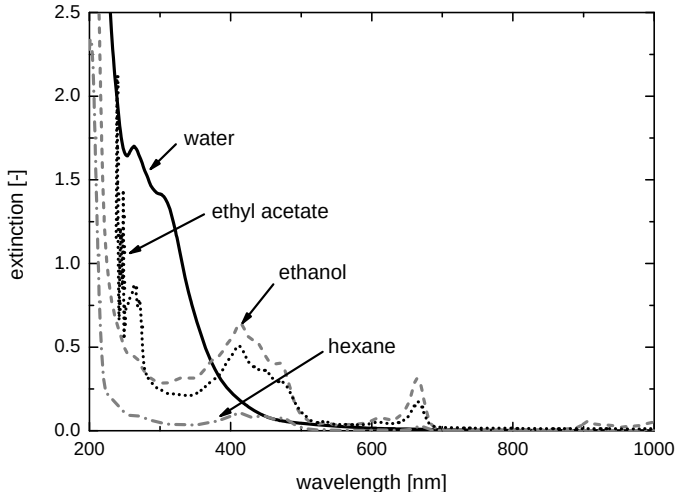

Fig. 1: Effect of solvent on extraction of *Acalypha indica* (solvent/solid ratio of 125, temperature 20°C, particle size of 300-400 µm)

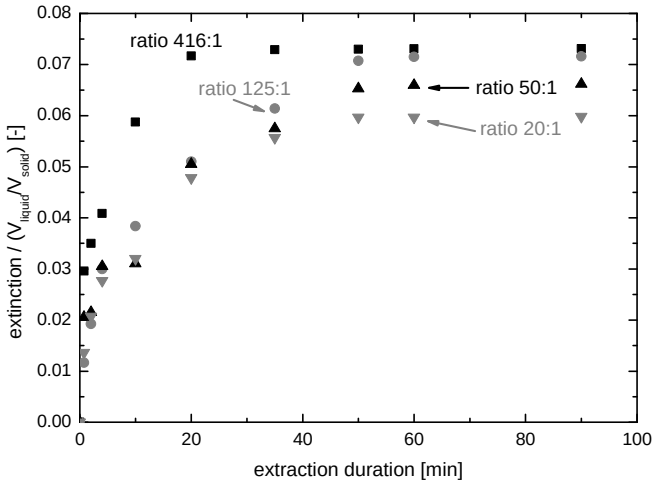

Fig. 2: Effect of solvent to solid ratio on extraction of *Acalypha indica* (ethanol, temperature 20°C, particle size of 300-400 µm)

Modeling

As an initial approach the Peleg's equation is used for modeling the extraction behavior of compounds *in Acalypha indica* because of the similarity between extraction and sorption. In the case of extraction, the Peleg's equation would be

$$c(t) = c_0 + \frac{t}{K_1 + K_2 \cdot t}, \quad (1)$$

where $c(t)$ is the concentration of extract (mol/L), t the extraction time (S), K_1 is Peleg's rate constant (min·L/mol) and K_2 is Peleg's capacity constant (L/mol). c_0, the initial concentration of extract at time $t = 0$ was zero for all experiments.

The second-order law model is usually used for clarifying the kinetics of solid-liquid extraction processes [5],[6]. This model was studied to compared with the Peleg's equation. According to the second-order rate law, the rate of extraction from *Acalypha indica* mass to solvent was performed by following equation,

$$\frac{dc_t}{dt} = k(c_s - c_t)^2, \quad (2)$$

where c_t is concentration of extracted at any time (mol/L), c_s is concentration at equilibrium (mol/L), and k is the second-order extraction rate constant ($Lmol^{-1}mim^{-1}$). The integrated form is shown below:

$$c_t = \frac{{c_s}^2 kt}{1 + c_s kt}. \quad (3)$$

Then, changing equation (3) to linear line for determining the constant values that can be obtained as:

$$\frac{t}{c_t} = \frac{1}{k{c_s}^2} + \frac{t}{c_s}, h = k{c_s}^2. \quad (4)$$

The concentration at equilibrium c_s, the initial extraction rate h and the second-order extraction rate constant k were determined by plotting t/c_t and t.

The spectral profiles of UV-VIS at 402, 423, 459 and 653 nm were selected for determining the compound contents. Both adsorption and second-order rate law model were used for studying the kinetic of solid-liquid extraction. This solid-liquid extraction (Fig. 3a) showed a similarity to the sorption process that can be well explained ($r^2 = 0.98$) by the Peleg's model.

Interestingly, the extraction specific second-order rate law model (Fig. 3b) provided a higher correlation coefficient than Peleg's mode in all experiment ($r^2 = 0.99$) and showed low RMSD (0.0166-0.0384).

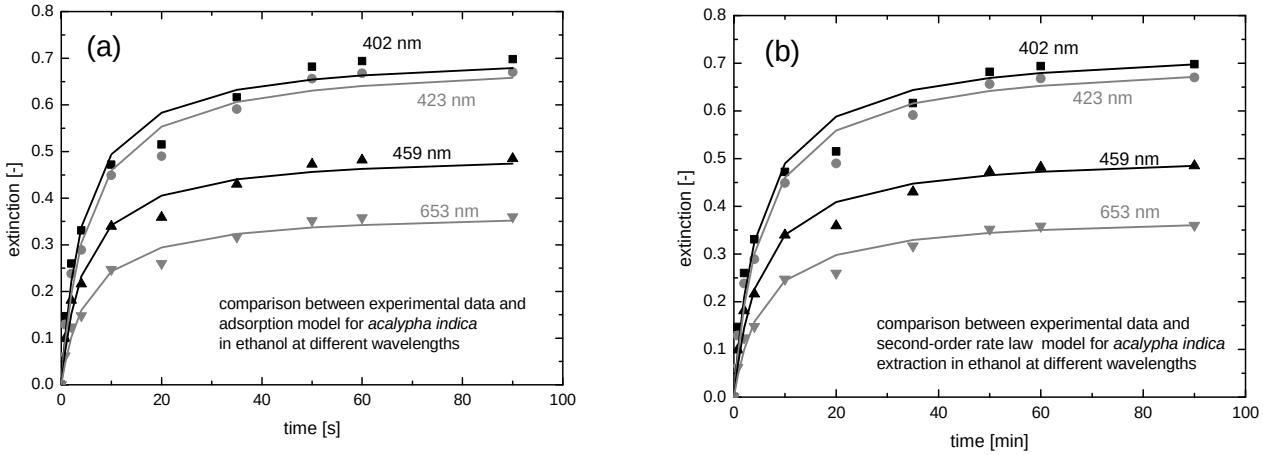

Fig. 3: Kinetic of solid-liquid by using Peleg law model (a) and second-order rate law model (b)

Conclusion

In this study, the yield and kinetic of solid-liquid extraction were influenced by solvent type and solvent to solid ratio. The second-order law model showed the best fitted model for solid-liquid extraction of *Acalypha indica*. Consequently, these results will be used for other investigations within the framework of extracted compounds from *Acalypha indica*. However, the sample should be analyzed with GC-MS to inform which groups of compounds are in extracts or used different extraction method.

Literature

[1] Seebaluck, R., Gurib-Fakim, A., Mahomoodally, F. (2015): Medicinal plants from the genus Acalypha (Euphorbiaceae) - A review of their ethnopharmacology and photochemistry. Journal of Ethnopharmacology 159, 137-157.

[2] M. govindarajan., A. jebanesan., D. reetha., R. amsath., T. pushpanathan., K. samidurai.(2008): Antibacterial activity of Acalypha indica L. European Review for Medical and Pharmacological Sciences 12, 299-302.

[3] Suwei Zhao., Dongke Zhang. (2014): Supercritical CO2 extraction of Eucalyptus leaves oil and comparison with Soxhlet extraction and hydro-distillation methods. Separation and Purification Technology 133, 443-451.

[4] Bucic-Kojic, A., Planinic, M., Tomas, S., Bilic, M., Velic, D. (2006): Study of solid-liquid extraction kinetics of total polyphenols from grape seeds. Journal of Food Engineering 81, 236-242.

[5] Lovasoa Rakotondramasy-Rabesiaka., Jean-Louis Havet., Catherine Porte., Henri Fauduet. (2006): Solid-liquid extraction of protopine from Fumaria officinalis L. - Analysis determination, kinetic reaction and model building. Separation and Purification Technology 54,253-261.

[6] Wenjuan Qu., Zhongli Pan., Haile Ma.(2010): Extraction modeling and activities of antioxidants from pomegranate marc. Journal of Food Engineering 99,16-23.

Modeling of drop sedimentation in liquid-liquid phase separation

Bhumphong Rajcharak[1], Jan Bernd Bol[2], Pornprapa Bol[3],
Tawiwan Kangsadan[1], Matthäus Siebenhofer[2]
[1]King Mongkut's University of Technology North Bangkok, The Sirindhorn International Thai-German Graduate School of Engineering, Bangkok, Thailand
[2]Graz University of Technology, Institute of Chemical Engineering and Environmental Technology, NAWI Graz, Graz, Austria
[3]Rajamangala University of Technology Thanyaburi, Faculty of Engineering, Department of Chemical Engineering, Pathum Thani, Thailand
bhumphong.r-cpe2013@tggs-bangkok.org, m.siebenhofer@tugraz.at

Abstract

In the chemical industry, liquid-liquid dispersions are often separated with settlers. During separation a sedimentation curve and a coalescence curve can be detected. Both curves show a characteristic, seemingly a sigmoidal S-shape curve. The settling curves can be fitted well with modified sigmoidal equations. Constants obtained from experimental data and target model were compared with the system's physical properties. Factors to scale the sedimentation velocity seem to be linear changing with density and viscosity of the aqueous phase, while the factor to scale the separation time is converse. Moreover, this work also proves, that sedimentation of large droplets deviates from rigid particle settling due to oscillating phenomena, while small drop behave similar to particles.

Introduction

Liquid-liquid extraction is an important separation unit in the chemical industry. With this technique target constituents can be pulled out of mixtures without heat required. By dispersing one liquid phase (overwhelmingly the light phase) in a second immiscible phase (heavy phase) by shaking or stirring, an emulsion is generated. Dispersions of liquid-liquid systems occurring in petrochemical and chemical industry are physically separated in gravity settlers. The use of gravity settlers for phase separation continues to gain importance both technically and economically. The most affecting parameters on gravitational phase separation are drop size, drop-size distribution, impurities e.g. electrolytes, as well as driving-force parameters for sedimentation and coalescence, namely density difference, viscosity and interfacial tension.
In previous works, the experimental studies of phase separation were performed with toluene + water, cyclohexanone + water [2] and methyl isobutyl ketone (MIBK) + water [3]. An ultrasonic scanner was used by Bol [4] to investigate drop dispersions in batch settling at any local hold-up and the optical cell was used to obviously detect sedimentation and coalescence preliminary. This work aims to address mathematical model describing phase separation behaviors as a function of height (h) over time (s). The constant from modeling of sedimentation in phase separation would further compile with physical properties involved as coefficients in the mathematic model.

Modeling

Performing batch settling experiments [1] leads to sedimentation and coalescence curves as depicted in Fig. 1. These lines represent states of constant hold-up. If the sedimentation

is faster than coalescence zone of dense-packed dispersed droplets forms. The sedimentation, coalescence and constant hold-up curves in the dense-packed zone show a similar trend towards a sigmoidal curve (S-shape). Hence, rate based models are modified from sigmoidal equation to address the process on a physical base according to base functions in Eq. 1 to Eq. 3 [4]. The used heights are system dependent and can be directly obtained from the measured data as seen in Fig. 1.

sedimentation curve $$h(t) = \frac{h_{heavy-phase}}{1 + b_s \cdot \exp(-c_s \cdot t)} \quad (1)$$

coalescence curve $$h(t) = h_{total} - \frac{h_{light-phase}}{1 + b_c \cdot \exp(-c_c \cdot t)} \quad (2)$$

dense-packed zone $$h(t) = h_{total} - \frac{\Delta h}{1 + b_d \cdot \exp(-c_d \cdot t)} \quad (3)$$

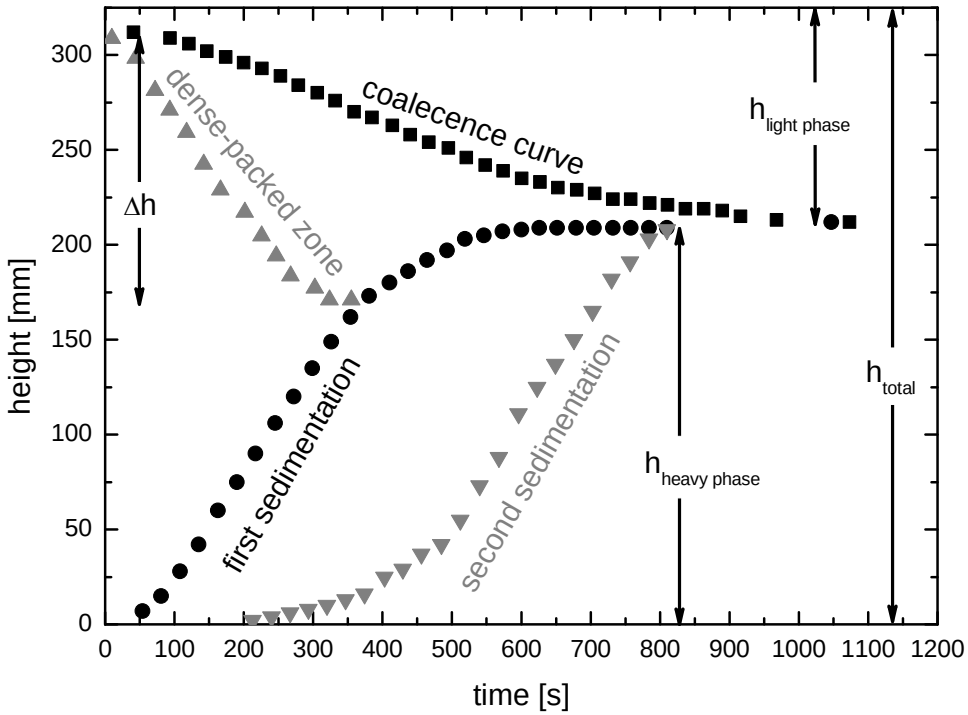

Fig. 1: Sedimentation and coalescence curves from ultrasonic experimental data of Methyl isobutyl ketone (MIBK) + water with 10%PEG content, 200 mmol/l NaCl; ambient temperature

According to equations 1 to 3 parameter *b* is a factor to scale the induction period, and parameter *c* is a factor to scale the separation time and dispersion density. To determine the value of constants *b* and *c* of sedimentation, dispersion densification and coalescence, TableCurve 2D software was applied to fit ultrasonic experimental data of settling height, coalescence height and dense-packed zone height of each curve. Constant *b* refers to drop size, dispersion density and the physical properties density and viscosity, while constant c covers the physical properties but also interphase phenomena, mainly controlled by the interfacial tension.
For demonstration Figures 2 and 3 show the effect of parameters b and c on sedimentation. In Fig. 2 parameter b was varied while parameter c was kept constant. In Fig. 3 parameter b was kept constant while parameter c was varied.

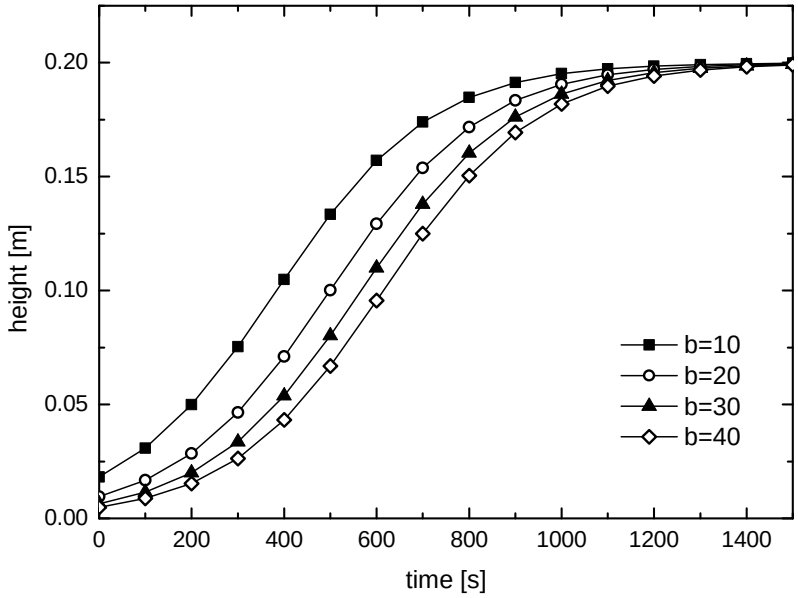

Fig. 2: Effect of parameter b (equation 1) on the induction period (h_{max} =0.2 m, c = 0.006).

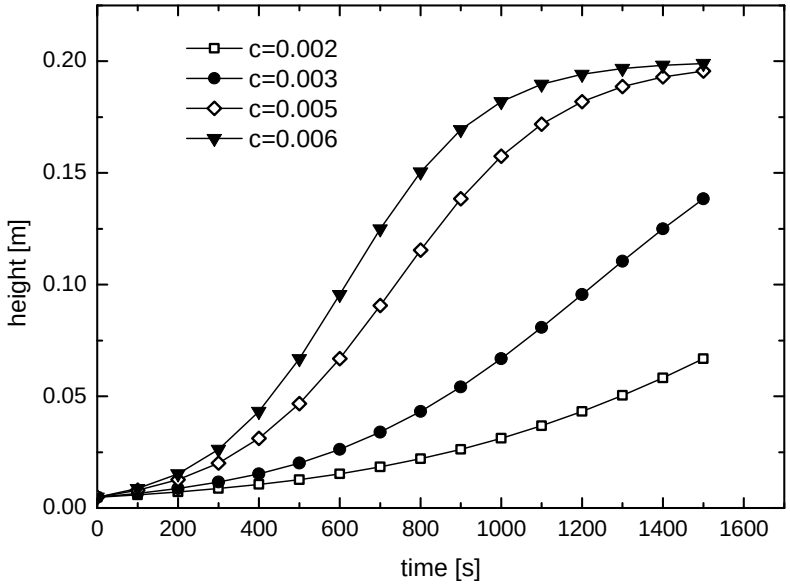

Fig. 3: Effect of parameter c (equation 1) on the rate of sedimentation (h_{max} = 0.2 m, b = 40).

Droplet size was determined from the linear section of the sedimentation curve via Henschke model [1] and then compared to rigid sphere particle sedimentation. This attempts to verify that the Henschke model is useful for droplet size calculation in liquid-liquid dispersion.

Results

The comparison of the modified sigmoidal rate based model and experimental data of cyclohexanone + water with 10%PEG content, without NaCl is depicted in Fig.4. Tab. 1 shows the constants *b* and *c* of all fitted curves. The model agrees well with the experimental data for sedimentation, coalescence and dense-packed zone.

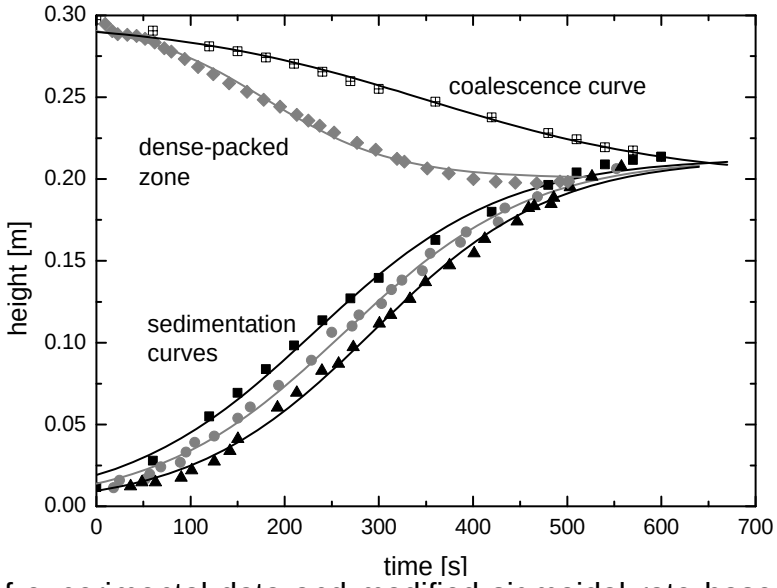

Fig. 4: Comparison of experimental data and modified sigmoidal rate based model of the system cyclohexanone + water with 15%PEG content, without NaCl; ambient temperature.

Tab. 1: Constants *b* and *c* of the modified sigmoidal rate based models in Fig. 2.

constant	1st sed.	2nd sed.	3rd sed.	coal.	d.p.z.
b	10.143	14.358	21.5369	15.0611	13.5048
c	0.010	0.0101	0.01048	0.09028	0.01447

In order to analyze the physical background for the model parameters, the parameters were plotted over different properties of the chemical system. Fig. 5 compares dependency of factor *b* and *c* with density of the aqueous phase and viscosity of aqueous phase. According to Fig. 5 Parameter *b* seems linearly direct proportional to density (actually density difference of phases) and viscosity of aqueous phase and parameter *c* inversely relates to both properties. Concluding from Eq. 1 the induction period linearly depends on the density of the continuous phase. Expectedly the rate of sedimentation is affected by the viscosity of the continuous phase as can be read from the correlation of c with the viscosity.

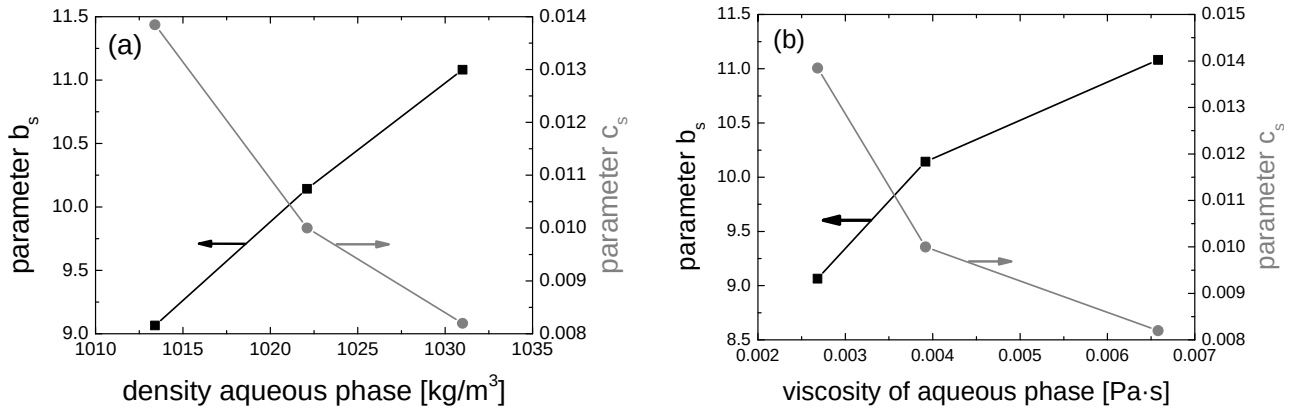

Fig. 5: Density (a) and viscosity (b) dependency of the fit parameters b_s and c_s of cyclohexanone-water system with addition of PEG4000 to the aqueous phase.

With Henschke model, drops size was calculated from the linear section of experimental sedimentation curve. Fig. 6 illustrates comparison of droplet size calculated from Henschke model and rigid sphere particle sedimentation equations using the Ljaschenko

number. The sedimentation of bigger drops deviates from rigid particle behavior due to inner circulation phenomenon (or oscillating phenomena), while small drops still behave similar to sedimenting particles.

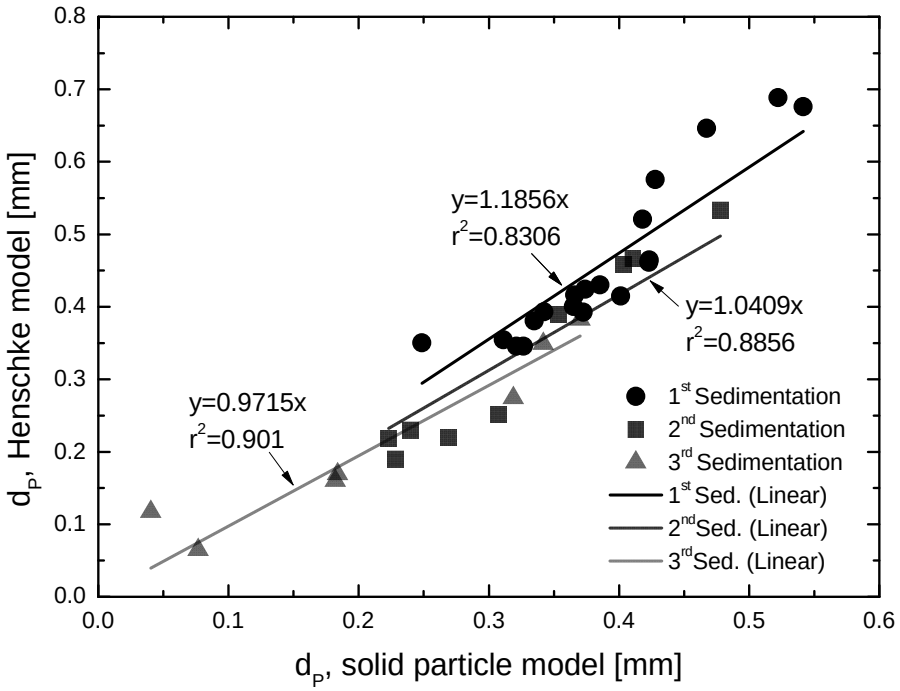

Fig. 6: Comparison of calculated droplet diameter from Henschke model and solid particle model.

Summary

The modified sigmoidal rate based model fits well with the experimental data for sedimentation, dense-packed zone depletion and coalescence of liquid-liquid dispersions. Prior to hydrodynamic analysis parameter *b* which is the factor to scale dispersion density (of hindered settling) and sedimentation velocity, has expectedly a linear trend with viscosity and density of aqueous phase. Parameter *c* seems to be indirect proportional to both properties. To verify the precision of Henschke model in droplet sedimentation, it was found that the sedimentation of bigger drop deviates from rigid particle behavior due to inner circulation phenomenon (or oscillating phenomena) while small drops still behave similar to particle settling.

Literature

[1] Henschke, M., Schlieper, L., and Pfennig, A. (2002) Determination of a coalescence parameter from batch settling experiments. Chem. Eng. J. 85:369–378

[2] Ee Pin, C. (2014) Experimental studies of the sedimentation behavior of polydisperse droplets in high viscosity systems. Student industrial project, ICVT TU Graz, Austria.

[3] Tantijamnan, C. (2014) Influence of Viscosity on Sedimentation and Coalescence Behavior. Master thesis, CEET, TU Graz, Austria.

[4] Bol, P. (2015) Investigation of drop dispersions in batch settling processes. Doctoral thesis, CEET, TU Graz, Austria.

Continuous Supercritical Fluid Extraction of Liquids Using Micro-Mixers

Candela Campos Domínguez, Andressa Karster Souza e Silva, Thomas Gamse
TU Graz, Institut für Chemische Verfahrenstechnik und Umwelttechnik,
8010 Graz, Inffeldgasse 25/C
camposdominguez@tugraz.at, thomas.gamse@tugraz.at

Abstract

The present study is focused on the utilization of micro-devices for Supercritical Fluid Extraction (SFE) purposes. Extraction experiments were carried out in a high-pressure micro-device apparatus, in which the micro-mixer is the unit where the solvent (supercritical CO_2) and the liquid feed come into contact. The extraction of ethanol from aqueous solutions by supercritical CO_2 was chosen as model system to study the feasibility of the micro-device apparatus proposed in this work. Extraction experiments were performed at 101bar, 60°C, different feed concentrations of ethanol and different solvent-to-feed ratio values. Experimental results were compared with SFE literature data. The phase behaviour of the ternary mixture CO_2-ethanol-water was modelled using ASPEN-Plus® and the Peng-Robinson EoS and it was determined that one theoretical stage could be reached in a micro-device stage. Two different micro-devices, interdigital multi-lamination and T-type lamination, were compared to study the influence of the mixing principle in the extraction process. The effects of the total flow rate, the solvent-to-feed ratio and the capillary length were investigated.

Introduction

This work is focused on the process intensification of Supercritical Fluid Extraction (SFE) of liquids by using micro-devices. It has been proved that the liquid-liquid extraction can benefit from microfluidics: the short path lengths and large interfacial area enhance the mass transfer and equilibrium can be reached within seconds [1]. However, the use of micro-mixers for SFE and Supercritical Fluid Fractionation (SFF) applications has been barely studied to date [2, 3]. Thus, the main purpose of this project is studying the efficiency and suitability of micro-mixers in SFE and SFF. For this, the continuous extraction of ethanol from aqueous solutions was chosen as the first model system to be investigated in micro-mixers in this work. The removal or extraction of ethanol by supercritical CO_2 ($scCO_2$) is a widely studied process for applications such as dealcoholisation of beverages, ethanol production or ethanol recovery from fermentation processes. Therefore, the CO_2-ethanol-water ternary mixture has been extensively investigated, as well the phase equilibrium behaviour of the system [4-6], as the extraction and the mass transfer rates.

Experimental

All experiments were performed in a high pressure micro-device extraction apparatus which mainly comprises two HPLC pumps, two separators, two regulation valves and a micro-device. The temperature and pressure in each separator are maintained constant by thermostated water baths and the two KAMMER regulation valves located just beyond each separator. Two types of micro-mixers, with different mixing principles, were utilized (Fig. 1). To test the mixing capacity of each micro-mixer and its feasibility for use in the

high-pressure extraction process, series of extraction experiments were performed, using either the Tee mixer or the multi-lamination micro-mixer.

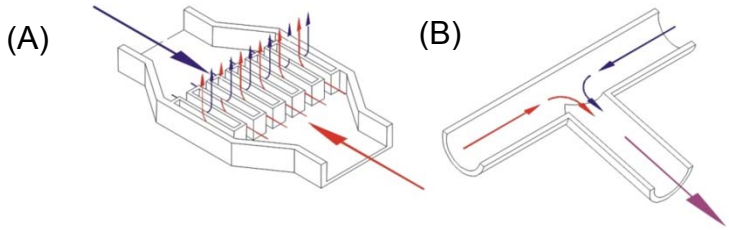

Figure 1.Description of the mixing principles studied in this work: multi-lamination (A) and T-type lamination (B).

Experimental conditions of pressure and temperature were the same in every experiment performed in this work. Mass Solvent-to-Feed ratio (S-to-F) as well as feed concentration were varied. Experimental values are presented in Table 1.

Table 1. Experimental conditions, S-to-F and feed composition values.

Feed flowrate (in the pump)	0.5 mL/min
Feed composition	10%-90% (w/w) ethanol
Mass Solvent-to-Feed ratio	5 - 25
Temperature 1st separator	60 °C
Pressure 1st separator	101 bar
Temperature 2nd separator	20 °C
Pressure 2nd separator	45 bar

Materials and methods

Distilled water and high-purity ethanol (>99.9 %) were used for the preparation of feed solutions. Technical grade carbon dioxide (>99.5%) supplied by Linde was used as the solvent.
All water-ethanol compositions were determined by density measurements using an Anton Paar DMA 45 density-meter. The ethanol mass fraction of feed, extract and raffinate was calculated from literature density tables [7].

Results and discussion

In Figs. 2-3, the experimental results obtained are compared with the phase equilibria behaviour of the ternary mixture CO_2-ethanol-water modelled in ASPEN-Plus® using the Peng Robinson equation-of-state. The relative deviation (RD) was used as an error criterion to assess the model. The values of RD of the vapour phase and the liquid phase data is 18% and 4%, respectively. Thus, we assumed that the raffinate composition (liquid phase) is more representative than the extract composition (vapour phase) for comparison of our experimental extraction results with the model.
From the results shown in Fig. 2, it is concluded that equilibrium is reached through the extraction process and one single stage is achieved. Moreover, we can state that one micro-mixer can correspond to a theoretical stage of the extraction process. By knowing this, extraction processes which require more than one single stage could simply be designed as a number of micro-devices (the same number as extraction stages are required) placed in series.

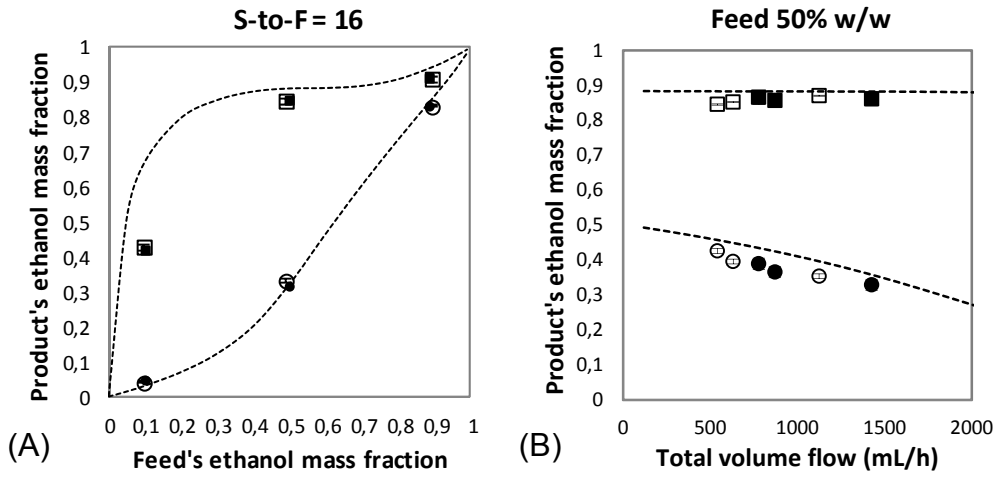

Figure 2. On the left side (A), comparison of experimental results of raffinate and extract compositions using the multi-lamination micro-mixer (●,■) and the Tee-mixer (○,□) with the model result of one single theoretical stage (S-to-F = 16). On the right side (B), product's ethanol mass fraction, raffinate (•, ○) and extract (■,□), as a function of the total volume flowrate in the micro-device (constant feed volume flowrate of 30 mL/h, variable CO_2 volume flowrate) for a feed composition of 50% w/w.

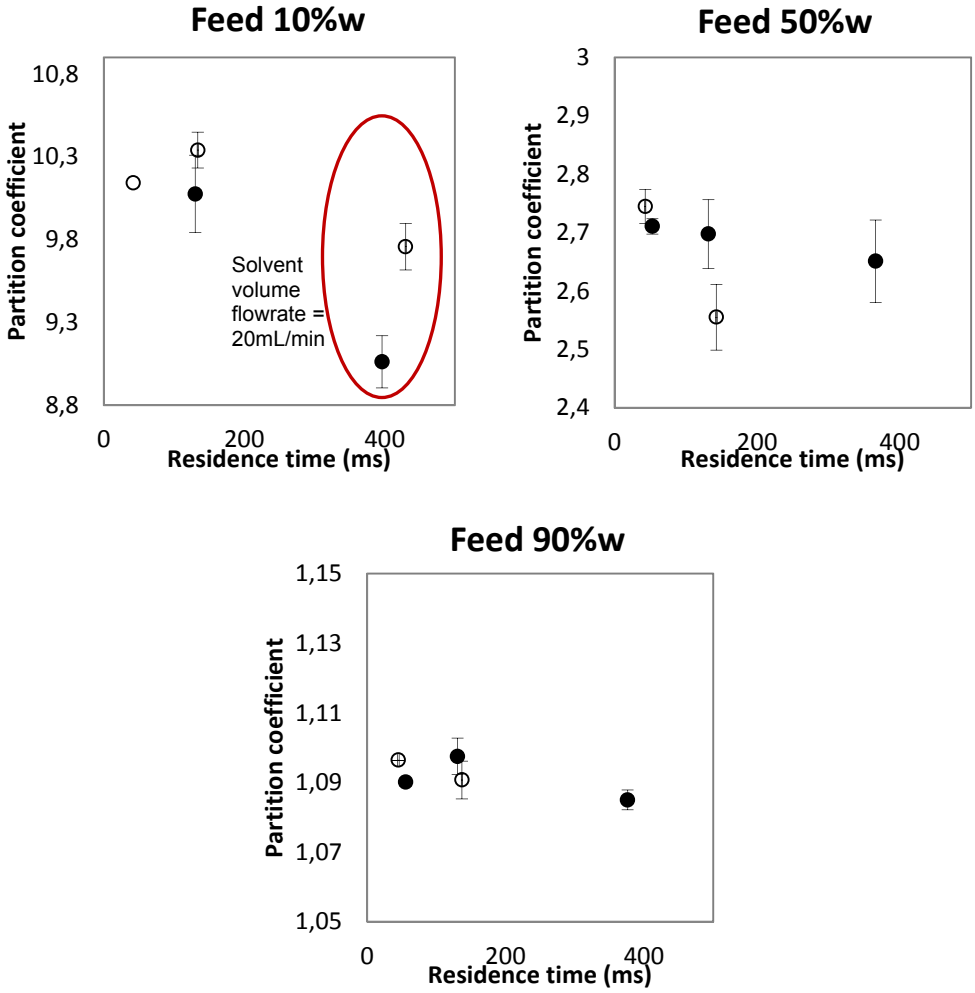

Figure 3. Partition coefficient as a function of the residence time for different feed concentration of 10%w, 50%w and 90%w of ethanol.

Regarding the influence of the capillary length in the mixing and the extraction processes, experiments with same solvent and feed flow rates (25 mL/min and 0.5 mL/min, respectively, except where otherwise noted) were performed using three different capillary lengths: 30mm, 200mm and 650mm. The capillary has an inner diameter of 0.5 mm.
As it can be expected from the small inner volume of the micro-mixers, varying the capillary length leads to remarkable changes in the residence time of the fluids in the contact area (which comprises the micro-device and the capillary). Fig. 3 shows how the partition coefficient, calculated as the quotient of the ethanol concentration in the extract and raffinate phases (CO_2-free basis), changes with the residence time. It can be observed that at different feed concentrations, the effect of the time residence in the separation process can vary.

Conclusions

The feasibility of a SFE process using micro-devices and the effects of the mixing principle in the extraction results were investigated at a lab scale. Experimental results obtained in this work concluded that separation of ethanol-water binary mixtures using $scCO_2$ as solvent in a high pressure micro-device extraction apparatus is possible and that thermodynamic equilibrium is achieved in the extraction process. Two different mixing principles are considered: multi-lamination and T-type lamination. Satisfactory results were obtained with both micro-devices, as it has been proved that equilibrium could be reached when using either one or the other one. Extraction was performed at different total volume flowrates, keeping always constant the feed volume flowrate at 30 mL/h and varying the solvent volume flowrate. It was found that in the range between 500 and 1500 mL/h, equilibrium could be reached in both micro-devices. The influence of the capillary length must be further investigated.

Literature

[1] Assmann, N., Ładosz, A., Rudolf von Rohr, P. Continuous Micro Liquid-Liquid Extraction. Chem. Eng. Technol., 2013, 36(6), 921-936.
[2] Assman N., Kaiser S., Rudolf von Rohr P. Supercritical extraction of vanillin in a microfluidic device. J Supercrit. Fluids. 2012, 67, 149-154.
[3] Assmann N., Werhan H, Ładosz A., Rudolf von Rohr P. Supercritical extraction of lignin oxidation products in a microfluidic device. Chem. Eng. Science. 2013, 99, 177-183.
[4] Furuta S., Ikawa N., Fukuzato R., Imanishi N. Extraction of ethanol from aqueous solutions using supercritical carbon dioxide. Kagaku Kogaku Ronbunshu. 1989, 15, 519-525.
[5] Budich M., Brunner G. Supercritical fluid extraction of ethanol from aqueous solutions. J. Supercrit. Fluids. 2003, 25, 45-55.
[6] Lim J.S., Lee Y.Y., Chun H.S. Phase equilibria for carbon dioxide-ethanol-water system at elevated pressures. J. Supercrit. Fluids. 1994, 7, 219-230.
[7] Perry H.R., Green D.W., 1997. Perry's Chemical Engineers Handbook (7th Edition) McGrawHill, New York, USA.

The authors want to thank the Marie Curie Initial Training Networks (ITN) for the financial support of the project "DoHip - Training Program for the Design of Resource and Energy Efficient Products by High Pressure Processes", project number PITN-GA-2012-316959).

O/W-emulsions, production and stability

Aroonrat Poonyaratanasrikhajon[1], Robert Macher-Ambrosch[2],
Tawiwan Kangsadan[1], Matthäus Siebenhofer[2]
[1]King Mongkut's University of Technology North Bangkok, The Sirindhorn International Thai-German Graduate School of Engineering, Bangkok, Thailand
[2]Graz University of Technology, Institute of Chemical Engineering and Environmental Technology, NAWI Graz, Graz, Austria
aroonrat.p-cpe2013@tggs-bangkok.org, m.siebenhofer@tugraz.at

Abstract

Turbidity control is a major issue in process engineering. By definition turbidity is the residual amount of dispersed phase in an emulsion, left in the continuous phase after primary phase separation. While turbidity is ordinarily induced unintended in industrial application, it can hardly be prepared for investigations in lab scale, especially under consideration of reproducibility. Therefore a research program on preparing turbidity with highly reproducible quality, needed for investigation of turbidity control, has been started. In a first phase emulsion formation and separation is investigated. Phase separation is recorded, but it is not the primary target of investigation. As mentioned, focus of investigation is the residual turbidity left in the continuous phase after primary phase separation. Therefore emulsion preparation and separation has to be discussed in detail.
There are many variables to get stable emulsions. The effects on the stability of emulsions are agitation rate, oil to water ratio, type of surfactant, concentration of surfactant and the chemicals used to produce the emulsions. The emulsion properties and phase separation of the dispersion are evaluated by using an ultrasonic scanner that detects the different sound speed of the mixture. In this contribution the effect of agitation rate on stability and separation properties of emulsions is investigated.

Introduction

Emulsions are known as the mixing of two immiscible liquids where one liquid forms droplets - the so called dispersed phase - which are dispersed into the second liquid the so called continuous phase. There are two types of emulsions, oil-in-water (O/W) and water-in-oil (W/O). To produce stable emulsions, the dispersed phase needs to be reduced in droplet size to reach the smallest droplet possible. Mechanical devices help to reduce the droplet size in liquid-liquid dispersions. Besides density and viscosity of constituents (actually interphase tension) are an important boundary in producing stable emulsions. Selection of surfactants accords to the HLB value estimation [1]

Liquid-liquid dispersion theory helps explain and understand the behavior of emulsions. In discussing the settling behavior of liquid-liquid dispersions one has to distinguish between sedimentation of droplets and droplets coalescence. The settling behavior of the light phase dispersed in the heavier phase in a batch settler is illustrated in Figure 1. With increasing time, droplets of the dispersed light phase move upward and interact with other drops to grow or split. Droplets continuously coalesce until they become a clear phase of former dispersed liquid. However, if the coalescence rate is less than the velocity of sedimentation of droplets, the droplets will accumulate in the dense-packed dispersion zone. [2]. To avoid confusion it has to be mentioned, that discussion of these phenomena does not address turbidity and turbidity control. This study focuses on the stability of oil-in-water (O/W) emulsions in a first phase and the discussion of turbidity control in a second step. The phase ratio of a liquid two phase system without surfactant and the agitation rate

of the stirrer are varied. As chemicals Shellsol D70 and water are used.

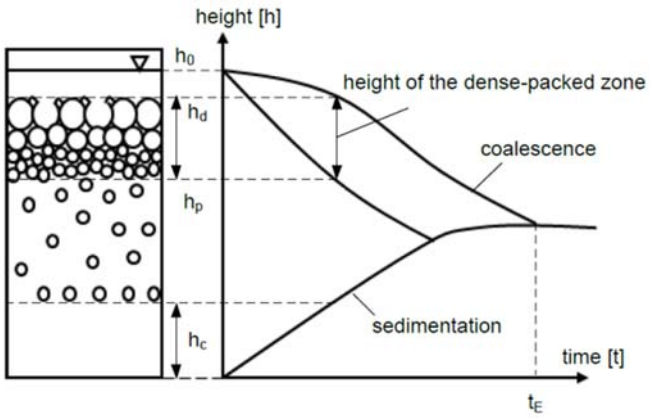

Figure 1: Schematic representation of settling behavior in batch settler according to Henschke [3].

Method and Experiment

The oil phase used in the experiments was Shellsol K (Shellsol D70) acquired from Kremer Pigments Inc. and as aqueous phase deionized water was used. To prepare emulsions with solvent and aqueous phase, the solvent and the aqueous phase were mixed and settled until both phases were mutually saturated. The saturated solvent and aqueous phase were separated in separation funnels before performing experiments.

To find the optimal agitation rate, the emulsions were produced under the following conditions unless otherwise specified: the holdup in terms of volume ratio was 0.3; the stirring intensity was 700, 900, 1100, 1300, 1500, 1700, and 1900 rpm; the mixing time was fixed with 1 min; temperature was kept constant at T = 20 °C.

The emulsions were mixed using a mixing unit consisting of two shafts with four propellers on each shaft connected to a variable speed motor. The capacity of the mixing unit was 750 ml. The propellers were rotating in opposite directions to completely mix the two immiscible liquid. The mixing unit is shown in Figure 2.

The Ultrasonic scanner Rhosonics SUSS-2008 was used to characterize the stability of the emulsions and it was operated under the following conditions unless specified otherwise: temperature 20 °C.; the speed of sound was (according to the system) 1200-1600 m/s.

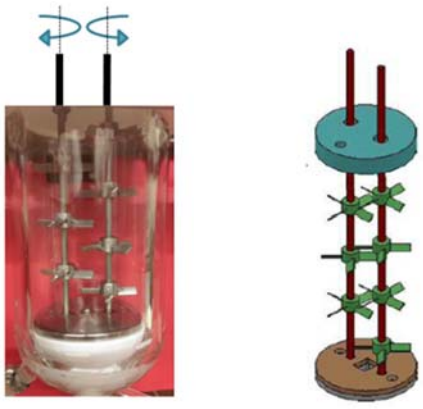

Figure 2: Mixing unit and schematic of impeller [4].

Results

The relationship between speed of sound and the hold-up (holdup in terms of volume ratio) is shown in Figure 3a. The data can be best fitted by a first order function. The dependency of the speed of sound and the hold-up can then be used to monitor the separation behavior of emulsions as shown in unterhalbFigure 4. From the difference in speed of sound the hold-up is determined.

$$\left| C_{aq} - C_{emulsions} \right| = f(\varepsilon)$$

The speed of sound as a function of hold-up is

$$\Delta c = 158.78\varepsilon$$

where the coefficient of determination r^2 is 0.999.

According to Figure 3b settling time increased with increasing agitation rate because of decreasing droplet size. Phase separation time (settling time) passes a maximum. Beyond optimum agitation for emulsification settling time again decreases.

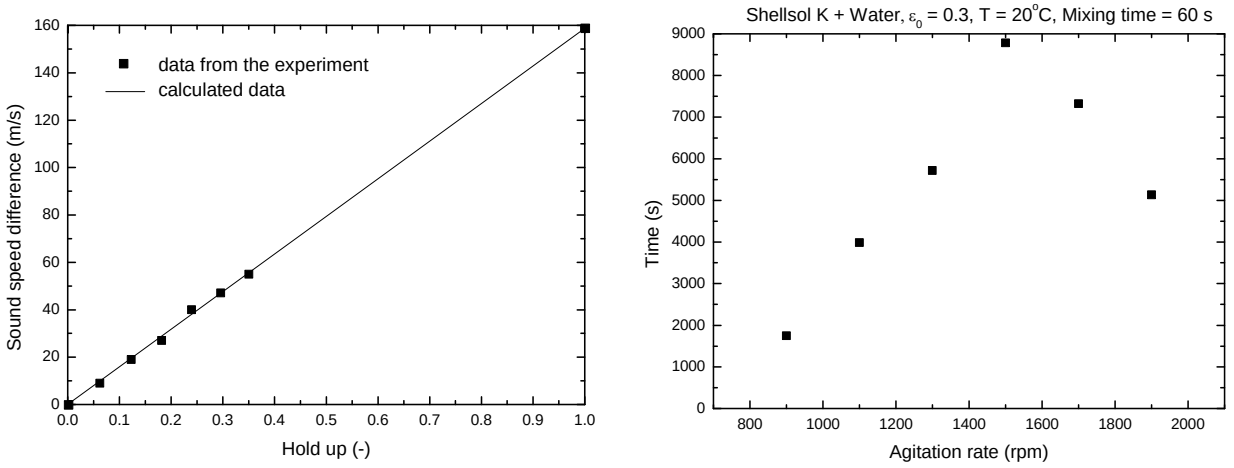

(a) *(b)*

Figure 3: (a) Relationship between sound speed and hold-up. (b) Relationship between agitation rate and settling time.

One result of phase separation, monitored in the ultrasonic scanner, is shown in Figure 4. In this case the hold-up in terms of volume ratio at the beginning was 0.3 and the agitation rate was 1500 rpm. With increasing time, the dispersed phase sediments up and forms the solvent phase through coalescence. Each shade of color shown in the figure corresponds to a specific measure of speed of sound according to the scale. The separation of the emulsion is finished when the coalescence curve and the sedimentation curve meet. In Figure 4, the rate of sedimentation is faster than the rate of coalescence, therefore a dense-packed zone occurs and has a wide area.

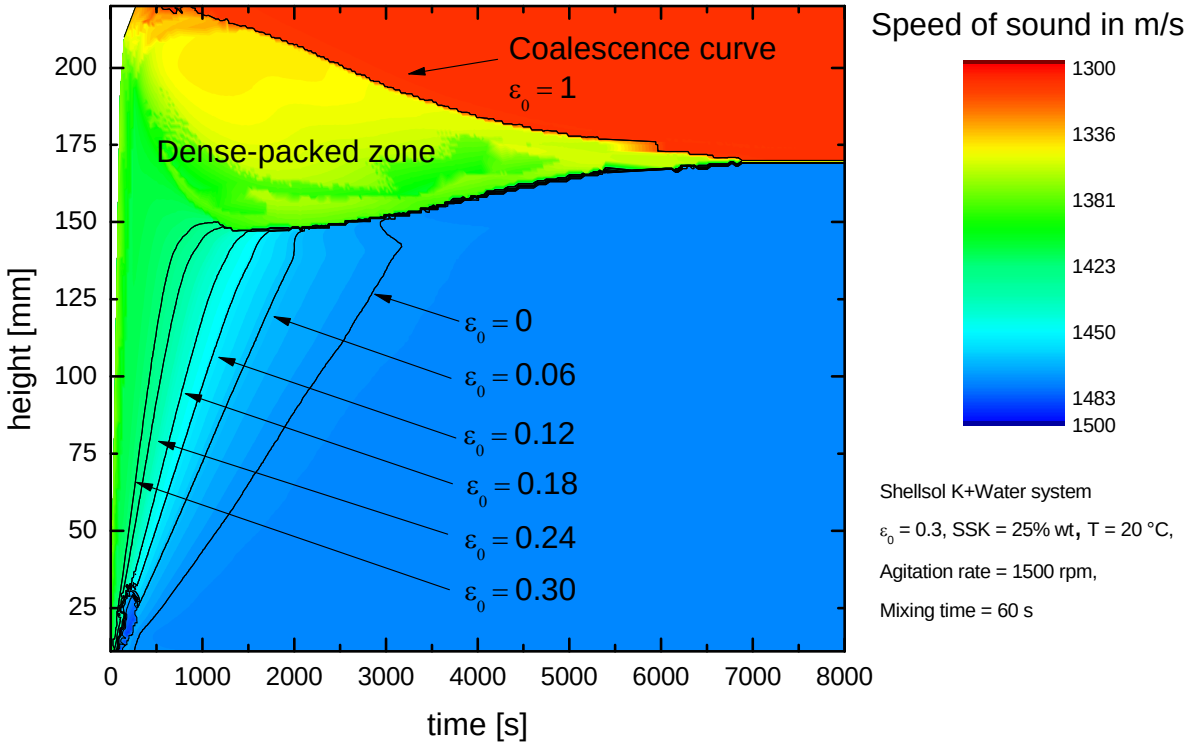

Figure 4: Ultrasonic scanner result of Shellsol K and water

Summary

In this study, the system of Shellsol K and water was selected to study the settling behavior of emulsions, prepared by stirring without surfactant, by ultrasonic scanning. The holdup was 0.3 in terms of volume ratio, the mixing time was 1 min and the temperature was kept constant at 20 °C. At constant phase ratio the influence of agitation speed on phase separation was studied. In preliminary experiments the results from the optical cell indicated an influence of the agitation rate on the settling time. As the agitation rate increases, the settling rate of the droplet will be significantly deplete because of smaller droplets. The optimum point to get an emulsion as stable as possible is 1500 rpm. Beyond optimum agitation for emulsification the settling characteristic indicates drop size enlargement by droplet-droplet interaction (coalescence).

Literature

[1] W. C. Griffin and W. C. Griffin, "Classification of surface-active agents by HLB," *Journal of the society of cosmetic chemists,* 1954.

[2] M. Henschke, Dimensionierung liegender Flüssig-Flüssig Abscheider anhand diskontinuierlicher Absetzversuche, Aachen, RWTH Aachen, 1994.

[3] C. Tantichumnan, "Influence of Viscosity on Sedimentation and Coalescence Behavior," Technische Universität Graz, 2014.

[4] P. Bol, "Investigation of drop dispersions in batch settling processes," Graz University of Technology, Graz, 2014.

Anthocyangewinnung aus der schwarzen Holunderbeere

G. Holzer, J. B. Pol, Th. Gamse, M. Siebenhofer
TU Graz, Institut für Chemische Verfahrenstechnik und Umwelttechnik, 8010 Graz, Inffeldgasse 25
guenther.holzer@student.tugraz.at,

Kurzfassung

Schwarzer Holunder (Sambucus Nigra) hat als Naturprodukt wahrscheinlich die höchste Konzentration an Anthocyanen, insbesondere die Komponenten Cyanidin 3-O-glucoside, Cyanidin-3-O-sambubioside, Cyanidin 3-O-sambubioside 5-O-glucoside sowie Cyanidin 3,5-O-diglucoside sind reichlich enthalten.
Bisher erfolgte die wirtschaftliche Verwertung in erster Linie in Form von Gesamtauszügen (Pressprodukten). Die steigende medizinische Bedeutung der Anthocyane auf Grund ihrer starken antioxidativen Kapazität steigert das Interesse an der Gewinnung der Einzelkomponenten.
Die Extraktion von Anthocyanen erfolgt mit Hilfe angesäuerter Ethanol-Wasser Gemische als Lösemittel. Hinsichtlich der Vorbehandlung der Beeren für die Extraktion bewirkt für kurze Extraktionszeiten (<2500s) die Zerkleinerung eine höhere normierte Konzentration. Auf eine längere Extraktionszeit hinweg wirkt sich das Zerkleinern jedoch negativ auf die Selektivität aus, da mit steigender Extraktionszeit immer weniger Anthocyane gelöst werden. Das Einfrieren bzw. die Lagerung über einen längeren Zeitraum scheint einen negativen Effekt auf die in den Beeren enthaltene Menge an Anthocyanen zu haben.
Für den Extrakt aus gefrorenen Beeren konnte eine normierte Konzentration von 4465mg/l nach 4800 Sekunden Extraktionszeit nachgewiesen werden. Die höchste normierte Konzentration an Anthocyanen wurde hingegen bei der Extraktion mit frischen ganzen Beeren ohne jegliche Vorbehandlung mit Ethanol erreicht. Es konnte ein normierter Wert von 6687 mg/l nach 4800 Sekunden nachgewiesen werden.
Hinsichtlich der weiteren Aufreinigung des Extraktes bieten sich Methoden der präparativen Chromatographie an. Ein wenig erforschtes, jedoch vielversprechendes Verfahren für die Purifizierung der Extraktkomponenten stellt die Zentrifugalchromatographie dar.

.

Anthocyangehalt in natürlichen Quellen	mg/100g FW
Kohlpalme	800–1000
Apfelbeere (Aronia)	200–1000 als Cyanidin
Apfel (Schale)	10-100
Aubergine (Schale)	750 als Delphinidin
Erdbeere	7–50 als Pelargonidin
Preiselbeere	25-65 als Cyanidin
Hibiskus	500-1500 Delphinidin und Cyanidin (2:1)
Holunderbeere	200–1000 als Cyanidin
Holundersaft	1900–6600 mg/100 ml als Cyanidin
Blutorange (Fruchtfleisch)	200 als Cyanidin
Brombeere	50–350 als Cyanidin
Heidelbeere (Blaubeere)	10–515 als Cyanidin
Himbeere (rot)	20–230 als Cyanidin
Himbeere (schwarz)	180–700
Kirsche	2–450 als Cyanidin
Sauerkirsche	35 als Cyanidin
Johannisbeere (rot)	10–20
Johannisbeere (schwarz)	130–420 Delphinidin und Peonidin (2:1)
Johannisbeersaft (schwarz)	1300–4000 mg/100 ml
Rotkohl	12–40 als Cyanidin
Traube (rot)	5–750 (stark sortenabhängig)
Rotwein	2–1000 mg/100 ml als Malvidin

Abbildung 1: Natürliche Vorkommen von Anthocyanen [2,11,12,13]

Einleitung

Die steigende medizinische Bedeutung von Antioxidantien aus Naturstoffen, wie sie Anthocyane darstellen, führt auch zu neuen technischen Fragestellungen hinsichtlich deren Gewinnung. Es gibt verstärkt Hinweise, dass im Bereich polyphenolischer Wirkstoffe pflanzlichen Ursprungs eine Wechselwirkung der Einzelkomponenten für die beobachtete medizinische Wirksamkeit Relevanz hat. Zum Beispiel wird die antioxidative Wirkung von Anthocyanen dem Cyanidin-Ion zugeschrieben, wobei es Untersuchungen gibt, dass die Bioverfügbarkeit im Humanstoffwechsel von den gebundenen Glucosidverbindungen abhängt. Ein wichtiges Maß zur Beurteilung von Antioxidantien stellt damit die Bioverfügbarkeit der Substanzen in Verbindung mit ihrer antioxidativen Kapazität dar, welche in Trolox Äquivalenten[1] angegeben werden kann.[2]

Anthocyangehalt Sambucus Nigra		
Cyanidin 3,5-O-diglucoside	17,46 mg /g FW	1,3%
Cyanidin 3-O-glucoside	794,13 mg /g FW	58,4%
Cyanidin 3-O-rutinoside	5,83 mg /g FW	0,4%
Cyanidin 3-O-sambubioside	462,96 mg /g FW	34,1%
Cyanidin 3-O-sambubioside 5-O-glucoside	34,48 mg /g FW	2,5%

[1] RICE-EVANS et al. (1995)
[2] WATZL und LEITZMANN 2005

Pelargonidin 3-O-glucoside	1,8 mg /g FW	0,1%
Flavonols	42 mg /g FW	3,1%
	1358,66 mg /g FW	100%

Tabelle 1: Durchschnittlicher Anthocyangehalt in der schwarzen Holunderbeere[3]

Anthocyane (Synonym: Anthocyanine) sind eine Gruppe von über 400 Verbindungen, die sich im phenolischen Kernaglykon und im Glycosylierungsmuster der konjugierenden Zucker unterscheiden[4]. In verschiedenen Beerenobstsorten findet man oft mehrere Duzend Einzelkomponenten in signifikanter Konzentration (z.B. Heidelbeeren). Die Beeren des schwarzen Holunders (Sambucus nigra) haben eine Sonderstellung, da drei Einzelkomponenten mehr als 95% des gesamten Anthocyan-Gehalts darstellen. Dadurch sind sie ein interessantes Edukt für die technische Gewinnung der Reinsubstanzen.
Die Verfügbarkeit hochreiner Wirkstoffkomponenten aus der Kategorie der sekundären Pflanzenwirkstoffe ermöglicht eine herausfordernde Basis für die Entwicklung neuer Rezepturen in der Pharmazie.

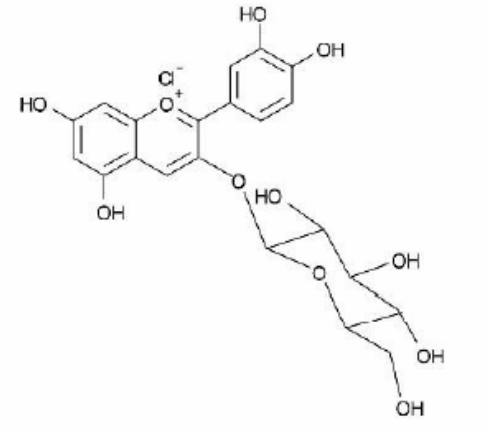

Abbildung 2: Cyanidin-3-o-glucoside

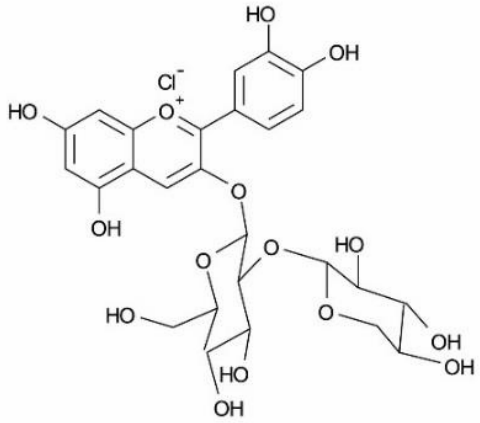

Abbildung 3: Cyanidin-3-sambubioside

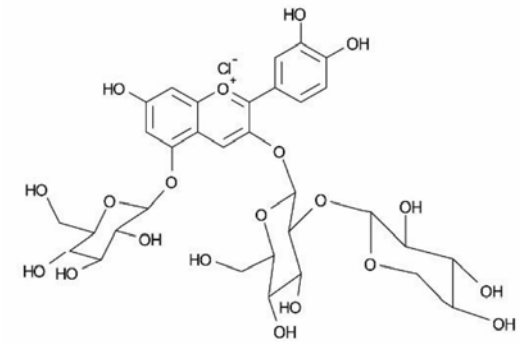

Abbildung 4: Cyanidin-3-sambubioside-5-o-glucoside

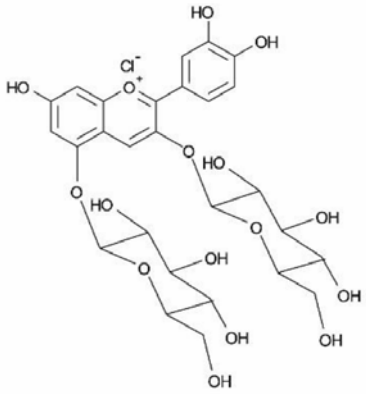

Abbildung 5: Cyanidin-3,5-o-diglucoside

Anthocyanextraktion aus der schwarzen Holunderbeere

Fest-Flüssig Extraktion

[3] http://phenol-explorer.eu/contents/food/124
[4] Fleshut 2004, Untersuchungen zum Metabolismus, zur Bioverfügbarkeit und zur antioxidativen Wirkung von Anthocyanen

Vorbehandlung[5]

Durch die hohen Trocknungstemperaturen und die lange Lagerzeit der getrockneten Beeren bauen sich so gut wie alle Anthocyane im Laufe der Zeit ab und eine Extraktion ist somit nicht mehr sinnvoll. Obwohl das Zerkleinern der Beeren für eine größere spezifische Oberfläche und somit einem besseren Stofftransport sorgen sollte, wirkt sich diese Vorbehandlungsart nur bedingt positiv aus. Für kurze Extraktionszeiten (<2500s) ergibt sich durch die Zerkleinerung eine höhere normierte Konzentration. Auf eine längere Extraktionszeit hinweg wirkt sich das Zerkleinern jedoch negativ aus, da mit steigender Extraktionszeit immer weniger Anthocyane gelöst werden. Auch eine Erwärmung von gefrorenen Beeren in der Mikrowelle wirkt sich durch die direkte Wärmeenergie negativ auf den Extraktionsprozess aus. Je länger die Beeren in der Mikrowelle erwärmt werden, desto niedriger ist auch die normierte Konzentration. Vergleicht man die Versuche, bei denen die Temperaturabhängigkeit der Anthocyane überprüft wurde, so kommt man zum Schluss, dass eine Extraktion bei 25°C am sinnvollsten ist. Eine Erhöhung der Temperatur sowie eine Verringerung der Extraktionstemperatur wirken sich negativ aus. Vor allem bei 15°C können im Vergleich nur sehr wenige Anthocyane gelöst werden. Bei frischen Beeren ist eine Extraktion mit 5%iger Essigsäure nicht sinnvoll, da die Säure nicht ins Innere der Beeren dringt und somit nur eine Konzentration von 600 mg/l erreicht werden kann. Im Gegensatz zu einer Extraktion mit Ethanol, bei der das Rührorgan aufgrund der Dichteunterschiede die Beeren mechanisch zerkleinert und somit die höchste Konzentration aller Versuche bewirkte. Die sinnvollste Art der Eduktbereitstellung ist in Form von frischem Pressrückstand der Holunderbeeren. Obwohl dieser als Nebenprodukt beim Pressen des Holundersaftes anfällt, beinhaltet er immer noch eine hohe Konzentration an Anthocyanen.

Extraktion[6]

Vorversuche ergaben, dass sich Ethanol mit 0.1% Salzsäure eignet, um die im Pflanzenstoff enthaltenen Anthocyane zu lösen. Für den Extrakt aus gefrorenen Beeren konnte eine normierte Konzentration von 4465mg/l nach 4800 Sekunden Extraktionszeit nachgewiesen werden. Die höchste normierte Konzentration an Anthocyanen wurde hingegen bei der Extraktion mit frischen ganzen Beeren ohne jegliche Vorbehandlung mit Ethanol erreicht. Es konnte ein normierter Wert von 6687 mg/l nach 4800 Sekunden nachgewiesen werden. Somit scheinen das Einfrieren bzw. die Lagerung über einen längeren Zeitraum einen negativen Effekt auf die in den Beeren enthaltene Menge an Anthocyanen zu haben. Bei den Holunderpressrückständen konnte mithilfe von 5%iger Essigsäure eine normierte Konzentration von 2375mg/l erreicht werden. Dadurch konnte gezeigt werden, dass selbst nach Abtrennung des Fruchtsaftes noch eine erhebliche Menge der Anthocyane in dem als Abfallprodukt gehandelten Pressrückstand enthalten ist. Zudem wurde bestimmt, dass die ideale Extraktionstemperatur bei 25°C liegt.

Nachweis des Anthocyangehaltes im Extrakt[7]

Die Färbung der Anthocyane ist stark vom pH-Wert des Lösungsmittels abhängig. Die rotblaue Färbung kann durch starke Basen in den grüngelben Bereich verschoben

[5] Daniel Habenbacher (2015), Einfluss verschiedener Vorbehandlungsmethoden auf die extraktive Gewinnung von Holunderpressrückständen
[6] Stephan Weixler (2015) Untersuchung des Einflusses verschiedener Lösungsmittel auf die Extraktion von Anthocyanen aus Holunderbeeren
[7] Jan Bernd Bol, Günther Holzer (2015) Extraktive Gewinnung von Anthocyanen aus Holunder Pressrückständen, CEET Konkret 2015

werden. Giusti und Wrolstad (2001) haben eine Methode vorgestellt, mit der die pH-Abhängigkeit zur Bestimmung des Anthocyangehaltes im Lösungsmittel genutzt werden kann. Dabei wird der Extrakt mit Pufferlösungen auf die pH-Werte 1.0 und 4.5 eingestellt und dann mittels UV/Vis-Photospektrometrie untersucht. Aus der Extinktionsdifferenz kann die Gesamtanthocyankonzentration berechnet werden.

In Abb. 5 ist bei pH 1.0 bei 511 nm ein deutlicher Peak im UV/Vis-Spektrum zu erkennen, der bei pH 4.5 deutlich verringert ist. Dieser Peak wird durch das Cyanidin verursacht. Interessant ist, dass der Extrakt aus getrockneten Beeren keinen solchen Peak aufweist. Es hat sich gezeigt, dass die Anthocyane temperaturempfindlich sind. Durch einstündige Trocknung bei 70°C und die anschließende Lagerung bei Raumtemperatur wurde der Anthocyangehalt vollständig abgebaut. Dies deckt sich mit den Beschreibungen in Markakis (1982), der auch angibt, dass die Stabilität der Anthocyane in sauren Medien verbessert werden kann.

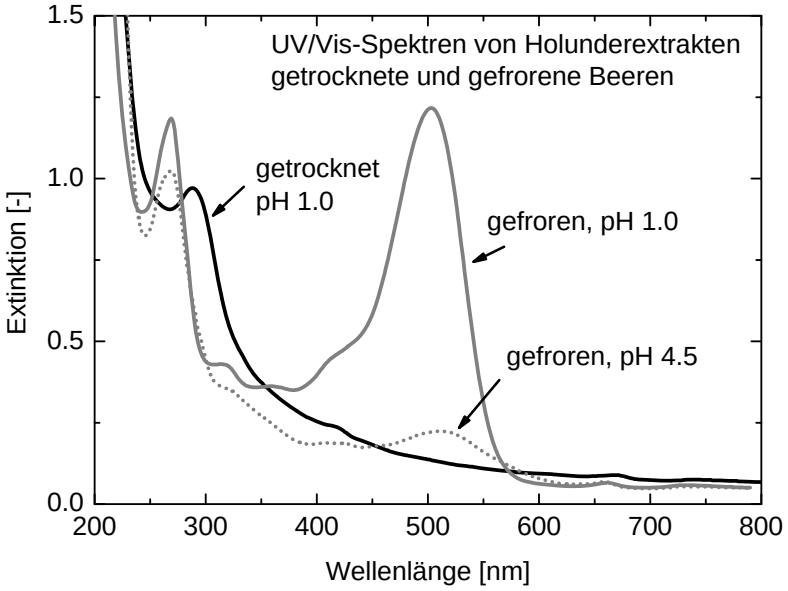

Abbildung 6: UV/Vis-Spektren ethanolischer Extrakte gefrorener und getrockneter Holunderbeeren

Aufreinigung der Extrakte

Im mg bis g-Maßstab werden Polyphenole (und auch andere sekundäre Pflanzenstoffe) mit konventionellen semi-präparativen Säulenchromatograhie-Verfahren gewonnen.
Derzeit nicht erforscht ist die Anwendung von CPC (Centrifugal Partition Chromatography) zur Gewinnung von Anthocyanen aus Sambucus Nigra. Dieses Verfahren ist hinsichtlich der Gewinnung bzw. der Aufkonzentration für eine darauffolgende präparative Chromatographie jedoch vielversprechend.
In der Praxis wird der Rotor der Zentralchromatographie an der HPLC anstatt der HPLC Säule mit festem Träger verwendet, quasi als rotierende Säule. Aber auch die Kombination von beidem ist für die Aufreinigungen von komplexen Substanzgemischen geeignet. So dient als Vorstufe der Aufreinigung die Zentralchromatographie und danach im gleichen Lauf die vorgereinigte Substanz über die HPLC Festphasen-Säule zur Feinreinigung. Diese Methode hat den Vorteil, dass die Festphasen-Säule nicht so schnell verschmutzt und ersetzt werden muss. Die Einsparung an Lösungsmittel ist ein weiterer Grund für den Einsatz dieser Technologie.

Zusammenfassung

Schwarzer Holunder (Sambucus Nigra) hat eine Sonderstellung als Rohstoff für die Gewinnung von Rein-Anthocyanen, insbesondere der Komponenten Cyanidin 3-O-glucoside und Cyanidin 3-O-sambubioside. Für die Extraktion der Anthocyane aus den Beeren bzw. aus Beerentrestern eignen sich besonders angesäuerte Ethanol-Wasser Gemische. Für eine qualitative Verfolgung der Versuchsergebnisse hinsichtlich des Gesamtanthocyangehalt des Extraktes eignet sich die Methode von Giusti und Wrolstad (2001) besonders, da sie schnell und kostengünstig durchführbar ist. Der exakte Nachweis der Einzelkomponenten benötigt eine HPLC Methode. Anthocyane sind thermisch instabil, weshalb sich eine thermische Trocknung bei Umgebungsdruck als kontraproduktiv herausstellt. Für die Konservierung der Frisch-Edukte bietet sich aufgrund der thermischen Instabilität der Zielsubstanzen eine Gefriertrocknung an.

Literatur

[1] https://www.dge.de/wissenschaft/weitere-publikationen/fachinformationen/sekundaere-pflanzenstoffe-und-ihre-wirkung/
[2] Jens Fleschhut,2004, Untersuchungen zum Metabolismus, zur Bioverfügbarkeit und zur antioxidativen Wirkung von Anthocyanen
[3] Tatsurou Koide, Yoko Hashimoto, Hideo Kamei, Takashi Kojima, Makoto Hasegawa, and Keisuke Terabe. Cancer Biotherapy and Radiopharmaceuticals. January 2009, 12(4): 277-280. doi:10.1089/cbr.1997.12.277
[4] RICE-EVANS et al. (1995)
[5] WATZL und LEITZMANN 2005
[6] http://phenol-explorer.eu/contents/food/124
[7] RICE-EVANS et al. (1995)
[8] Daniel Habenbacher (2015), Einfluss verschiedener Vorbehandlungsmethoden auf die extraktive Gewinnung von Holunderpressrückständen
[9] Stephan Weixler (2015) Untersuchung des Einflusses verschiedener Lösungsmittel auf die Extraktion von Anthocyanen aus Holunderbeeren
[10] Jan Bernd Bol, Günther Holzer (2015) Extraktive Gewinnung von Anthocyanen aus Holunder Pressrückständen, CEET Konkret 2015
[11] Lidija Jakobek, Marijan Seruga, Martina Medvidovic-Kosanovic, Ivana Novac: Anthocyanin content and antioxidant activity of various red fruit juice; In: Deutsche Lebensmittel-Rundschau. 103. Jahrgang, Heft 2, 2007.
[12] BUCHWEITZ, M., KAMMERER, D.R., CARLE, R.: Signifikante Verbesserung: Stabilisierung von Anthocyanen mit Hydrokolloiden (PDF; 2,1 MB); In: Lebensmitteltechnik, 2012, S. 42-43.
[13] Lehrbuch der Lebensmittelchemie, Tab. 18.22

Mass transfer measurements in extraction under column conditions

Eva Kalvoda[1], Andreas Pfennig[2]
[1] TU Graz, NAWI Graz, Institut für chemische Verfahrenstechnik und Umwelttechnik, 8010 Graz, Inffeldgasse 25C, eva.kalvoda@tugraz.at
[2] Université de Liège, Department of Chemical Engineering, PEPs - Products, Environment, and Processes, 4000 Liège (BE), Allée du six Aout 11, andreas.pfennig@ulg.ac.be

Abstract

Modern design methods for liquid-liquid extraction use a combination of single-drop experiments and simulation tools. In this work a new measurement cell has been developed, which allows to investigate mass-transfer at single drops under column conditions. The droplets were contacted with different concentration profiles in the continuous phase, which allows to investigate the influence of the concentration gradient in the continuous phase. The experimental design as well as first results are presented.

Introduction

The conventional approach to design liquid-liquid extraction columns is to perform pilot-plant experiments and using the data obtained for scaling up to industrial scale. Newer design methods use laboratory experiments with individual drops in combination with column simulations. In this work the population-balance tool ReDrop is used. ReDrop stands for representative drops and uses the Monte-Carlo Method to model the droplet behaviour in extraction columns. Laboratory experiments are needed to characterize the specific material system including the measurement of single-drop sedimentation and mass transfer.
Mass transfer is measured in standardized cells to understand the single-drop behaviour and to calibrate the models for the column simulation to the real material system. This is done by fitting the parameters of the single-drop models to the experimental results.

Mass-transfer models

In this work the standard test system butyl acetate + acetone + water is used, where water is the continuous phase, butyl acetate the disperse phase and acetone the transfer component. Figure 1 shows mass-transfer data with this material system for the initial concentration of 5 weight-% of acetone. The dimensionless concentration difference y^+ is plotted against the drop diameter and the residence time, where y^+ is defined as

$$y^+ = \frac{y^* - y(t)}{y^* - y_0} = f\left(d_{drop}, t\right) \quad (1)$$

with the equilibrium concentration y^*, the momentary concentration $y(t)$ and the initial concentration y_0.

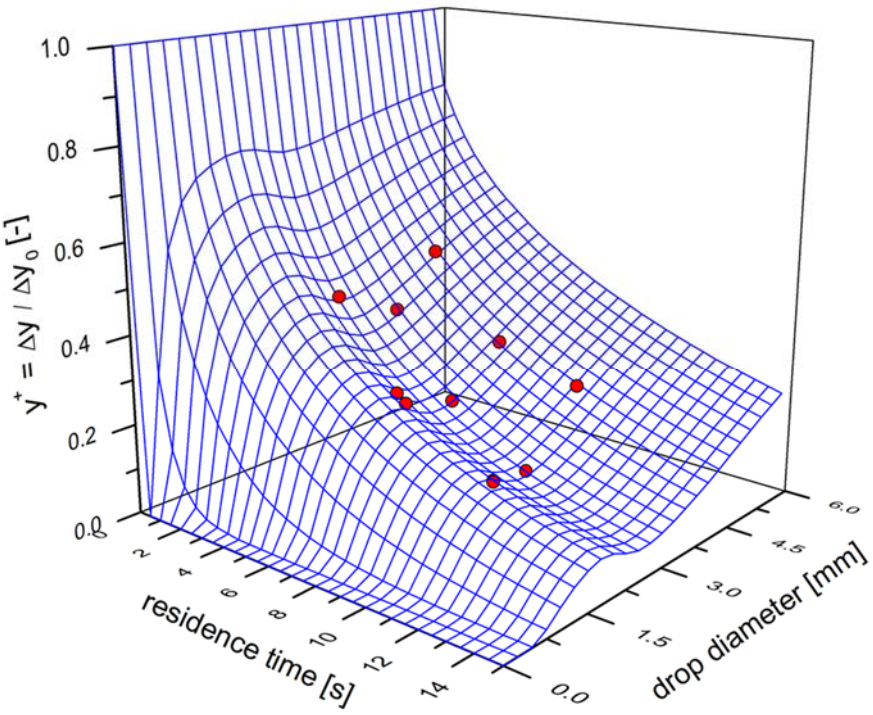

Fig. 1: Dimensionless concentration difference vs. residence time and drop diameter for butyl acetate droplets in water – x_0 = 5 wt% acetone [3], model after Henschke [1]

The experimental data in figure 1 were modelled with a model proposed by Henschke [1]. He used the analytical solution of the diffusion equation by Newman [2] which is written in spherical coordinates, assuming rotational symmetry:

$$y^+ = \frac{6}{\pi^2}\sum_{n=1}^{\infty}\frac{1}{n^2}\exp(-(n\pi)^2 Fo_d) \tag{2}$$

with the Fourier-Number $Fo_d = 4Dt/d^2$. For the diffusion coefficient, however, he used an effective diffusion coefficient ($D_{d,eff}$), which also accounts for turbulent transfer:

$$D_{d,eff} = D_d + \frac{v_\infty d}{C_{IP}\left(1+\frac{\eta_d}{\eta_c}\right)} \tag{3}$$

where D_d is the physical diffusion coefficient of the disperse phase, v_∞ is the single-drop sedimentation velocity, d is the droplet diameter and η_d and η_c are the dynamic viscosities of disperse and continuous phase respectively. The parameter C_{IP} can be adjusted for the measured material system.

Concentration Profile

The driving concentration difference in mass-transfer cells, however, differs significantly from the concentration difference in extraction columns. During the mass-transfer experiments the concentration in the continuous phase remains constant over time, leading to a large driving concentration difference at the beginning, which is reduced during the experiment. Thus, mass transfer is fast at the beginning and slows down as the concentration in the droplet approaches the equilibrium concentration with respect to the

continuous phase. In extraction columns on the other hand a concentration gradient can be found in both phases over the entire equipment height, i.e. also during the entire life-time of a drop.

The transfer from the experimental conditions to the column conditions is currently done by theoretical assumptions, which are based on calculations of the concentration profile inside the droplet. In order to validate these assumptions and quantitatively understand the influence of the concentration profile on mass-transfer kinetics, a new mass-transfer cell has been constructed, which allows to set up a concentration profile in the continuous phase and to contact the droplets with this profile. This way the concentration profiles formed in extraction columns can be mimicked in order to investigate mass transfer under more realistic conditions. Also mass transfer and sedimentation can be investigated simultaneously to understand their mutual influence.

Measurement cell with concentration profile

The measurement cell consists of a tube with 80 mm inner diameter and 1 m height and has four inlets at 125, 375, 625 and 875 mm from the bottom and four outlets on the opposite side (figure 2). Up to four layers of aqueous phase with different concentrations of acetone can be filled into the cell via two hose pumps with two pump heads each. A syringe pump is used to produce droplets of a defined size at the bottom of the cell, which are recorded by a video camera. The trajectories of the rising droplets are evaluated to be able to analyse the velocities over the height of the column in order to link sedimentation and mass transfer. Mass transfer is measured by collecting the droplets with a funnel connected to a second syringe pump and measuring the amount of acetone in the droplets after their rise. The residence time of the droplets can be varied by adjusting the height of the funnel used to collect the droplets.

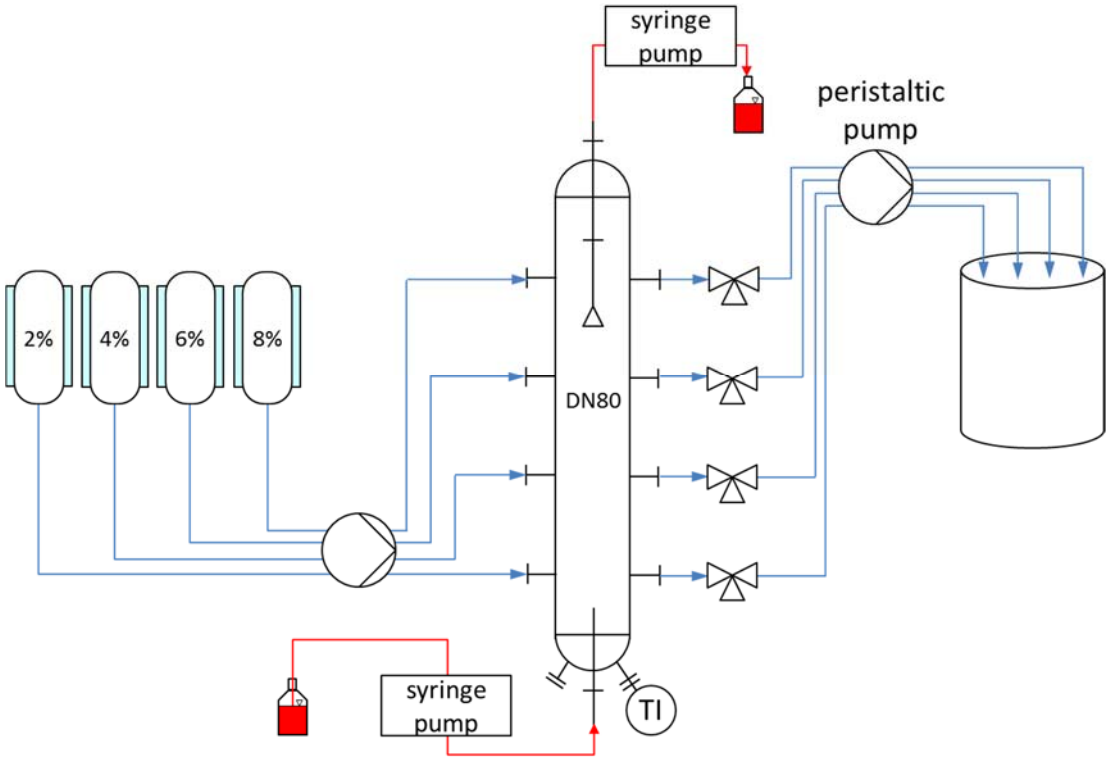

Fig. 2 Experimental setup of the mass transfer cell with concentration profile

Results

Different concentration profiles at different concentration levels have been investigated. Figure 3 shows two concentration profiles in the continuous phase. Profile 1 starts at 0 wt% acetone, profile 2 has a concentration jump at the beginning and starts at 2 wt% acetone, resulting in different concentration gradients at the bottom of the column for the two cases. The evaluation with currently used models showed that they were either able to model profile 1 or profile 2, but not both. Therefore, a new model is required that can model all different concentration gradients. To do so, mass transfer was evaluated for parameters, such as drop diameter, sedimentation velocity or concentration level. From this sensitivity analysis a model was derived, that can compute mass transfer correctly under different conditions and for various parameters.

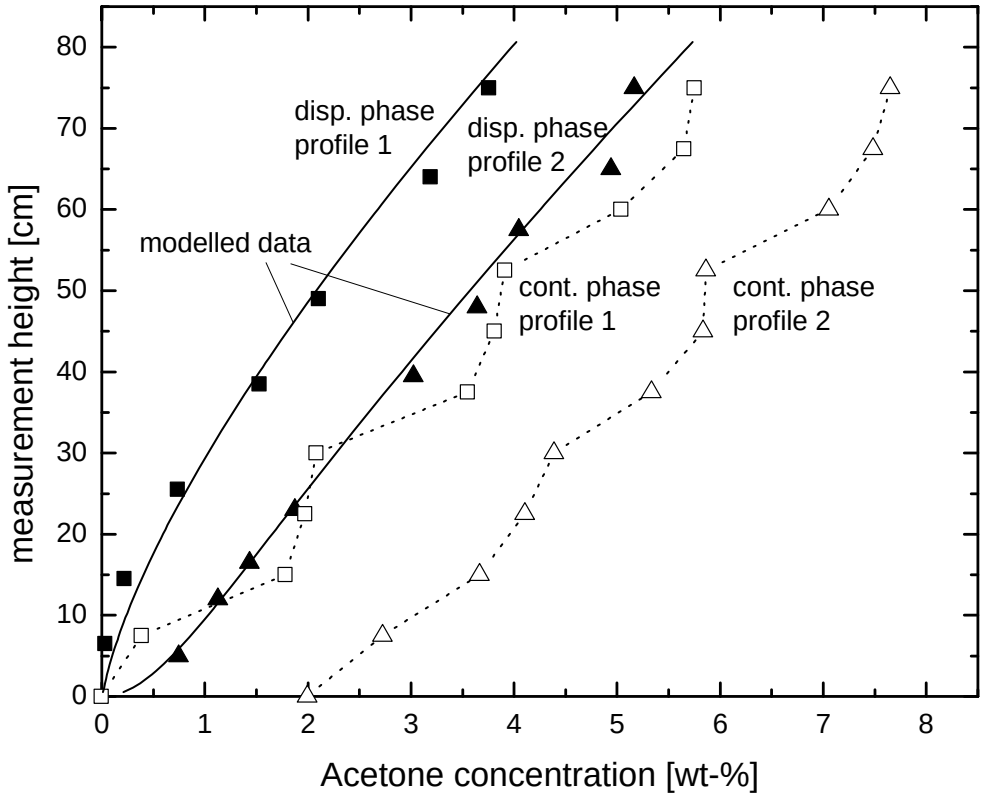

Fig. 3 Concentration profiles with different starting conditions, butyl acetate drops in water (c→d). Profile 1: no mass transfer at begin, Profile 2: concentration jump at beginning.

Literatur

[1] Henschke, M.: Auslegung pulsierter Siebboden Extraktionskolonnen. Aachen, Shaker-Verlag, (2004), ISBN 3-8322-3511-6

[2] Newman, A.B.: The drying of porous solids: Diffusion and surface emission equations, Trans. AIChE, Vol. 27 (1931) 203-220

[3] Leeheng, K.: Simultaneous measurement of sedimentation and mass transfer of single drops. Master Thesis (2014)

TCDC, design and validation

Annika Grafschafter, Enes Aksamija, Matthäus Siebenhofer
TU Graz, Institut für chemische Verfahrenstechnik und Umwelttechnik, NAWI Graz
8010 Graz, Inffeldgasse 25c
a.grafschafter@tugraz.at

Abstract

Two-phase flow is frequently needed in chemical process applications. Phase transfer catalysis has to be mentioned as an example, whereby the reactor design in liquid-liquid reaction systems inevitably leads to discussions. Liquid-liquid two-phase reactors are preferably stirred tank reactors. Taylor-Couette reactors are also recommended for phase transfer catalysis. Banded two phase flow results in small droplet size, providing large mass transfer area and narrow residence time distribution. Since banded two phase flow in Taylor-Couette reactors is a gap phenomenon a big disadvantage is the limited hydraulic capacity. By reducing the diameter of the rotating shaft and by placing rotor rings along the shaft in appropriate distance, a new two phase contactor design was developed. A similar flow pattern compared to the banded two phase flow with enhanced hydraulic capacity is obtained. The improved contactor design is similar to the most common type of liquid-liquid extractor, the Rotating Disc Contactors (RDC).
Mass transfer reactors with continuous phase contact, like liquid-liquid extraction columns, are generally designed as ideal plug flow reactors (PFR). In extraction columns pronounced axial back mixing affects reactor performance, demanding correction estimates during design. According to the mode of operation an alternative design approach has been investigated.

Introduction

The Taylor-Couette reactor is recommended for application in phase transfer catalysis. A Taylor-Couette reactor consists of two concentrically rotating cylinders. Because of a minimum ratio of the diameter of the rotating cylinder D_I to the diameter of the shell of $D_I/D_S>0.75$ the hydraulic capacity of a Taylor-Couette reactor is limited [1]. Since the Taylor-Couette vortices are a gap phenomenon, vortex instability of two phase flow at high axial flow rate and high angular velocity difference do not encourage application of Taylor-Couette reactor.
Dating back to a patent from 1952 the Rotating Disc Contactor (RDC) has established in liquid-liquid extraction [2]. The continuous phase in a RDC forms two toroidal vortices in each compartment similar to banded two-phase flow in Taylor-Couette reactors. Stator rings, subdividing the column into compartments, stabilize these toroidal vortices. RDC design is well established in industrial scale, nevertheless the design suffers from some uncertainties regarding the optimum ratio of the shaft to the shell [3]. The shaft diameter is sized very small because of fearing loss of active cross section area [4]. As a consequence of this design weakness the disperse phase tends to form stable coalesced layers at the shaft since limited vortex strength cannot keep the solvent phase dispersed in the toroidal vortex [5]. Targeting improved hydraulic capacity for banded two phase flow the basic RDC design was therefore investigated, improved and optimized. As a result a hydrodynamic hybrid of the RDC and the Taylor-Couette reactor, the Taylor-Couette Disc Contactor (TCDC) was developed [5]. The TCDC is a simplified RDC design without stator rings and increased shaft diameter. The flow pattern stabilizing effect of the stator rings is compensated by increased rotor discs and banded two-phase flow. Rejection of stator rings does help avoid crud accumulation along the tower.

Reactor modelling

Reactor modelling plays an essential role in chemical and process engineering. For continuous operation two basic “ideal reactor concepts”, the ideal plug flow reactor (PFR) and the ideal stirred tank reactor (or continuously stirred tank reactor, CSTR) are applied.
Mass transfer reactors with continuous phase contact, like stirred liquid-liquid extraction columns, are generally designed as ideal PFR, according to equations 1 through 3.

$$mass\ balance: F_A = F_A + dF_A + (-r_A'')dV\ and\ dV = A_R * dh \tag{1}$$

$$r_a = -\frac{dc}{dt} = \dot{n}\ \ and\ \dot{n} = -k'' * (c_A - c_A^*) \tag{2}$$

$$H_{column} = HTU * NTU = \frac{\dot{F}_v}{A_R * k'' * a} * \int_{c_{A0}}^{c_{A1}} \frac{dc_A}{c_A - {c_A}^*} \tag{3}$$

Modeling of ideal plug flow assumes an axial flow pattern without axial dispersion. Liquid-liquid extraction columns with rotating internals may show distinct axial back mixing. Axial dispersion is a big issue in column design and scale-up. In practical application, the HTU-NTU concept is extended by the HDU value which considers axial back mixing with the aid of the axial dispersion coefficient D_{ax} [6]:

$$H_{column} = \overline{HTU} * NTU \tag{4}$$

$$\overline{HTU} = HTU + HDU \tag{5}$$

$$HDU = \frac{D_{ax,c}}{v_c} + \frac{D_{ax,d}}{v_d} \qquad if \quad \varepsilon = 1 \tag{6}$$

Experimental validation of extractor design algorithms

The experiments were performed on a TCDC100 glass column with 1 m active height and 0.1 m diameter. Figure 1 shows the sketch of the shaft with the rotor rings and the toroidal flow pattern induced by rotation of the shaft [5].
The separation efficiency of the TCDC was determined by mass transfer experiments with the test system kerosene/n-butanol/deionized water [7]. The residence time distribution was determined by rigid sphere monitoring [8].

Figure 1: TCDC; sketch of the experimental setup and flow pattern of the continuous phase induced by rotation of the shaft. Shaft diameter: 50 mm, rotor diameter: 82 mm, compartment height: 50 mm, Shell diameter: 100 mm [5]

Results

The separation efficiency of the TCDC100 was compared with the design according to equation 3. Figure 2 (a) shows the concentration profile of the solvent along the column height for the case of ideal plug flow and seemingly pronounced axial back mixing. The ideal plug flow profile along the column height does not fit the experimental results. When fitting the real concentration profile to the experimental results the mass transfer coefficient must be altered. The adaption of the mass transfer coefficient is accompanied by significant change in concentrations at the head and bottom of the column as shown in Figure 2 (b) for ideal plug flow operation with pronounced axial back mixing [9].
The difference between ideal plug flow profile and real flow profile results in the HDU value which considers the axial dispersion of the continuous and disperse phase.
Is there any space for improvements?

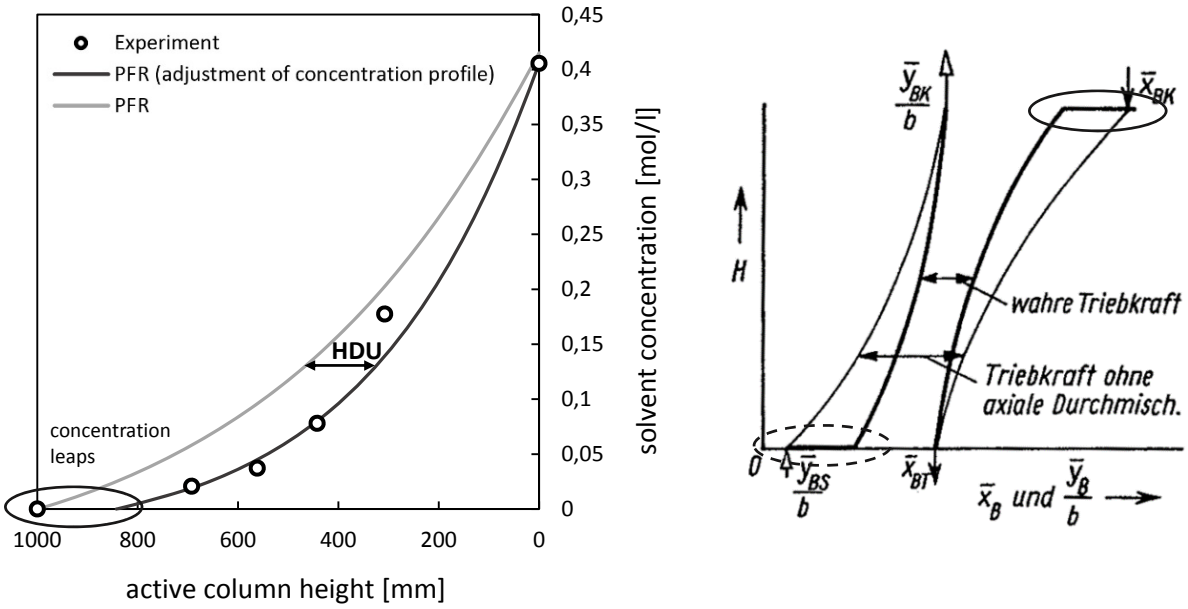

(a) (b)

Figure 2: (a) concentration profile for ideal plug flow compared with experiments; (b) effect of pronounced axial back mixing [9]

Stirred Liquid-liquid extraction columns are subdivided into compartments. Due to formation of toroidal vortices each compartment of the column actually represents two ideal stirred tank reactors with ideal mixing, suggesting CSTR design according to equations 7 through 9.

$$mass\ balance: \qquad F_{A,0} = F_A - r_A'' * V_R \tag{7}$$

$$r_a = -\frac{dc}{dt} = \dot{n} \ \ and\ \dot{n} = -k'' * (c_A - c_A^*) \tag{8}$$

$$c_{A,n} = \frac{c_{A,n-1} \pm k'' * \frac{V_r}{F_{V,0}} * a * c_A^*}{1 + k'' * \frac{V_r}{F_{V,0}} * a} \tag{9}$$

Figure 3 (a) shows the concentration profile of a CSTR cascade compared with experimental results. The concentration profile along the column as well as the mass balance calculated with CSTR design algorithm compare well with the experimental data. Figure 3 (b) shows the cumulative exit age distribution of the TCDC100 for one compartment with rigid spheres of 2 mm diameter [5] [8]. With increasing rotation of the shaft the residence time distribution approaches CSTR operation corresponding to two CSTRS per compartment.

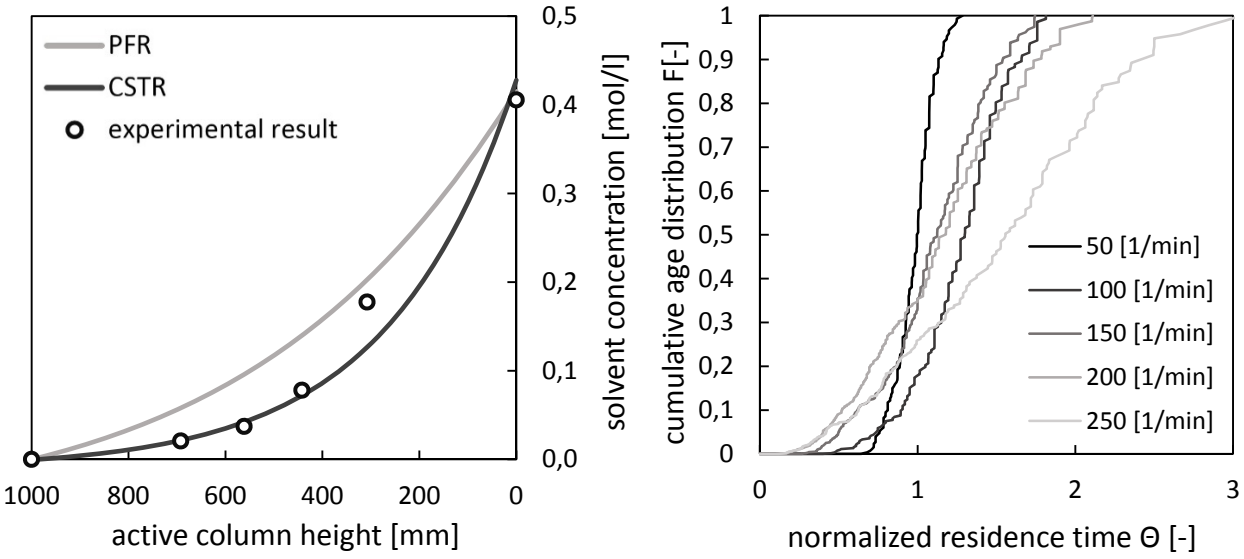

(a) (b)

Figure 3: (a) comparison of experimental and calculated concentration profile for CSTR cascade approach; (b) exit age distribution of rigid spheres in a single compartment [5] [8]

Summary

Optimization of the Rotating Disc Contactor by removing the stator rings and adjusting the diameter of the shaft to the hydraulic needs for providing banded two phase flow led to the design of a Taylor-Couette Disc Contactor. The modified design provides high hydraulic capacity. The results of mass transfer experiments and rigid sphere experiments in a pilot plant scale TCDC100 confirm the CSTR design algorithm.

Literature

[1] C. A. Jones, "Nonlinear Taylor vortices and their stability," *J. Fluid Mech. 102,* p. 249, 1981.

[2] G. H. Reman.USA Patent 2,601,674, 1952.

[3] W. C. G. Kosters, "Rotating Disc Contactor," in *Handbook of Solvent Extraction*, John Wiley & Sons, 1983, pp. 391-406.

[4] E. Müller, R. Berger, E. Blass, D. Sluyts and A. Pfennig, Liquid-Liquid Extraction, Ullmann's Encyclopedia of industrial chemistry, 2012.

[5] E. Aksamija, *Der Taylor-Couette-Disc Contactor (TCDC); ein vereinfachtes und optimiertes Design von Drehscheibenextraktoren,* Graz: Technische Universität Graz, 2014.

[6] K. Sattler and H. J. Feindt, Thermal Separation Processes - Principles and Design, Weinheim; NewYork; Basel; Cambridge; Tokyo: VCH Verlagsgesellschaft mbH, 1995.

[7] C. Weinländer, Validierung einer optimierten RDC-Kolonne mit Stoffaustauschversuchen und CFD, Graz: TU Graz, 2014.

[8] R. Sarzio, *Experimentelle Validierung der CFD-Simulation der Mehrphasenströmung in der RDC Kolonne,* Graz: TU Graz, 2015.

[9] S. Weiß, W. Berghoff, E. Grahn, G. Gruhn, M. Güsewell, W. Plötner, H. Robel and M. Schubert, "Verfahrenstechnische Berechnungsmethoden," in *Thermisches Trennen - Ausrüstungen und ihre Berechnung*, Weinheim, VCH Verlagsgesellschaft mbH, 1986.

Turbidity Control

Robert Macher-Ambrosch, Matthäus Siebenhofer
beide: TU Graz, Institut für Chemische Verfahrenstechnik und Umwelttechnik, 8010 Graz, Inffeldgasse 25/C
r.macher-ambrosch@tugraz.at, m.siebenhofer@tugraz.at

Kurzfassung

Biomasse kann in der Extraktion einen negativen Einfluss auf das Trennverhalten von wässriger und organischer Phase haben. Werden dabei Emulsionen gebildet, müssen diese in einem weiteren Trennschritt aufwändig getrennt werden. In dieser Arbeit werden Technologien zur Spaltung von O/W-Emulsionen untersucht, die zusätzlich mit Tensiden stabilisiert wurden. Der Fokus wird auf die Abtrennung von organischen Feinsttrübungen aus dem Raffinat einer Extraktionskolonne gelegt. Als Technologien kommen die thermische, die chemische, die physikalische und die elektrische Spaltung zur Anwendung. Die experimentelle Untersuchung bestätigt die Anwendbarkeit des durch Gleichstrom induzierten elektrischen Feldes auf Tensid-stabilisierte O/W-Emulsionen.

Einleitung

Die flüssig-flüssig Extraktion wird in Zukunft eine wichtige Rolle in der biobasierten Industrie spielen. Die Extraktion von Carbonsäuren aus Abwässern unter der Verwendung von Phosphanoxiden ist bereits seit Jahrzehnten Stand der Technik. Abhängig von den Bestandteilen des Abwassers und der Betriebstemperatur können in der Raffinat- und in der Extraktphase Trübungen auftreten. Dabei kann die Ursache chemischer und/oder physikalischer Natur sein. So ist es möglich, dass es aufgrund einer Temperaturänderung zu einer lokalen Übersättigung an Lösungsmittel im Raffinat kommt. Weiters ist es möglich, dass Grenzflächenladungen, die durch Belastung mit Tensiden auftreten können, die Koaleszenz unterbinden.
Die Verunreinigungen wirken sich in Raffinat und Extrakt unterschiedlich aus. Eine Kontamination der Extraktphase vermindert die Produktqualität wohingegen eine Trübung der Raffinatphase zu einer Verschlechterung der Abwasserqualität führt und die Wirtschaftlichkeit aufgrund von Verlusten an Lösungsmittel senkt. [1]
Im Zuge dieser Arbeit wird der Fokus auf die Enttrübung der Raffinatphase gelegt, da die Auflagen hinsichtlich der höchstzulässigen Konzentrationen von Kohlenwasserstoffen im Abwasser immer strenger werden und damit die Industrie zu neuen Ansätzen in der Aufreinigung dieser gezwungen wird. Bei der Enttrübung wird der Fokus in dieser Arbeit auf die Technologieentwicklung, insbesondere die elektrische Spaltung gelegt, da diese einen vielversprechenden Ansatz bei der Trennung von stabilen Emulsionen [2] darstellt.

Technologien zur Emulsionsspaltung

Es gibt verschiedene Möglichkeiten, Emulsionen zu spalten. Das mechanische Brechen von Emulsionen kann sehr einfach in einem Abscheider realisiert werden. Dieser benötigt allerdings vor allem bei der Trennung von Systemen, die sich langsam trennen, eine sehr große Abscheidefläche. Weiters wären auch Zentrifugen denkbar, die zwar den Flächenbedarf verringern, aber einen wesentlich höheren Energieeintrag notwendig machen. [2]
Ein weiterer Ansatzpunkt ist, den Einfluss der Temperatur zu nutzen, um die Viskosität der kontinuierlichen Phase zu reduzieren und damit die Sedimentationsgeschwindigkeit zu

erhöhen. [3] Allerdings ist darauf zu achten, dass die Emulsion nicht heterogen azeotrop verdampft.
Vor allem im Bereich der Analytik wird, um die organische Phase vermessen zu können, ein Lösungsvermittler zugesetzt. Dieser führt dazu, dass die Mischungslücke verlassen und ein einphasiges Gemisch erhalten wird. In der großtechnischen Anwendung ist dies allerdings nicht anwendbar, da sehr große Mengen an Lösungsvermittler benötigt werden, die in einem nachfolgenden Schritt wieder abgetrennt werden müssen.
Auch unter Verwendung eines elektrischen Wechselfeldes werden Emulsionen gespalten. Vor allem in der Rohölaufbereitung werden Hochspannungsfelder eingesetzt, um fein dispergiertes Wasser aus dem Rohöl zu entfernen. Grund dafür ist einerseits, dass die nachfolgenden Prozessschritte vereinfacht werden sollen, und andererseits, dass Korrosion von Rohrleitungen, Pumpen und anderem Equipment vermieden werden soll. [2] Weiters wird das elektrische Gleichstromfeld verwendet, um dichte Öl-in-Wasser Emulsionen zu spalten. [4] In der vorliegenden Arbeit soll dieser Ansatz auf O/W-Emulsionen erweitert werden, die eine geringe Konzentration an organischer Phase aufweisen, wie sie vor allem im Raffinat von Extraktionskolonnen auftreten.

Experimenteller Aufbau

Zur Untersuchung des Absetzverhaltens im elektrischen Gleichstromfeld wurde eine Apparatur entsprechend Abbildung 1 verwendet. An einer Glasapparatur (HxBxT: 127x60x105 mm) wurden Edelstahlelektroden (HxBxD: 169x50x1 mm) fixiert. Die Elektroden waren mit einer Gleichstromquelle verbunden. Die Isolierung im Apparat diente der Unterbrechung eines möglichen Fehlstromes durch die koaleszierte organische Phase. Unter Verwendung eines Amperemeters und eines Voltmeters wurden die korrekte Durchführung der Versuche und der Energieeintrag überprüft. Der Verlauf der Spaltung während eines Experiments wurde mithilfe einer Fotokamera, die vom PC aus gesteuert in definierten Abständen ausgelöst wurde, aufgenommen. Anhand der Fotoreihe konnten der Trennfortschritt analysiert und unterschiedliche Einstellungen verglichen werden.

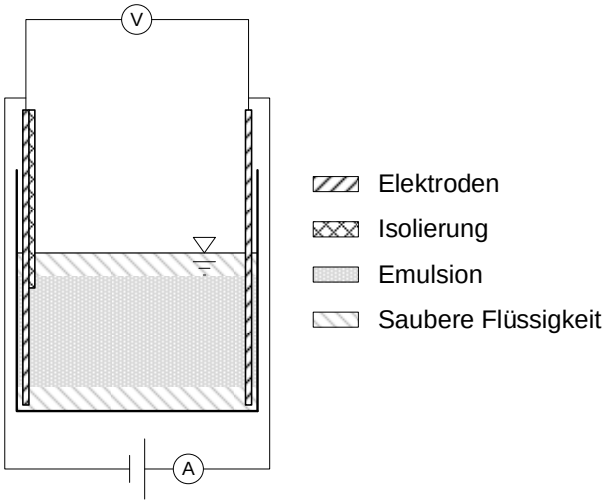

Abbildung 1: Schematischer Aufbau der Messzelle

Experimentelle Durchführung

Die Untersuchung des Spaltverhaltens von Emulsionen im elektrischen Gleichstromfeld wurde mit einer Emulsion aus 0,5 gew% mit Tensid beladener organischer Phase und entionisiertem Wasser durchgeführt. Grund für die geringe Konzentration an organischer Phase war, dass eine Feinsttrübung simuliert werden soll, die beispielsweise das Raffinat einer Extraktionskolonne verunreinigt.
Um den Einfluss von Tensiden auf das Spaltverhalten zu untersuchen, wurden Versuche mit je einem anionischen, kationischen und nichtionischen Tensid durchgeführt. Als anionisches Tensid wurde Dodecylbenzolsulfonsäure (DBSA) eingesetzt, Hexadecyltrimethylammonium Bromid (CTAB) wurde als kationisches Tensid eingesetzt und als nichtionisches Tensid kam Tween® 65 zum Einsatz. Dabei wurde ein Massenanteil von 0,001 g Tensid pro Gramm organische Phase vorgegeben.
Als organische Phase wurde in allen Versuchen ShellSol® K eingesetzt.

Ergebnisse

Nachfolgend sollen ausgewählte Versuche miteinander verglichen werden, um den Einfluss der Tenside und der angelegten Gleichspannung erkennbar zu machen.
Abbildung 2 zeigt verschiedene Zustände der Emulsion. In Bild A ist als Referenz eine Emulsion unter Verwendung von DBSA zum Zeitpunkt 0 dargestellt, also nach Erstellung der Emulsion bevor die Spannung angelegt wurde. Bild B zeigt den Referenzzustand einer Emulsion unter dem Einfluss des Erdschwerefeldes nach 3 h. Für diesen Versuch wurde zur Stabilisierung ebenfalls DBSA verwendet. In Bild C ist die Emulsion ebenfalls mit DBSA stabilisiert, allerdings wurde die Aufnahme nach 3 h bei 12 V Gleichspannung gemacht. Gleiches gilt für die Bilder D und E, wobei die Emulsion in D mit CTAB und in E mit Tween® 65 hergestellt wurde.
Im Vergleich der Bilder in Abbildung 2 ist deutlich ersichtlich, dass eine Enttrübung unter Einsatz einer elektrischen Gleichspannung eintritt. Der Vergleich zwischen den unterschiedlichen Tensiden zeigt, dass das elektrische Feld auf alle Tenside einen Einfluss hat, sogar jene Emulsion, die mit dem nichtionischen Tensid Tween® 65 stabilisiert wurde, zeigt eine Klärung in der Nähe der Elektroden. Interessant ist die Rückvermischung in Abbildung 2C. Diese mit DBSA stabilisierte Emulsion zeigt im Verlauf des Experimentes eine Klärung im Bereich der Kathode, die sich mit Fortdauer des Versuches wieder auflöst, wobei eine Klärung im Vergleich mit Bild A dennoch erkennbar bleibt.

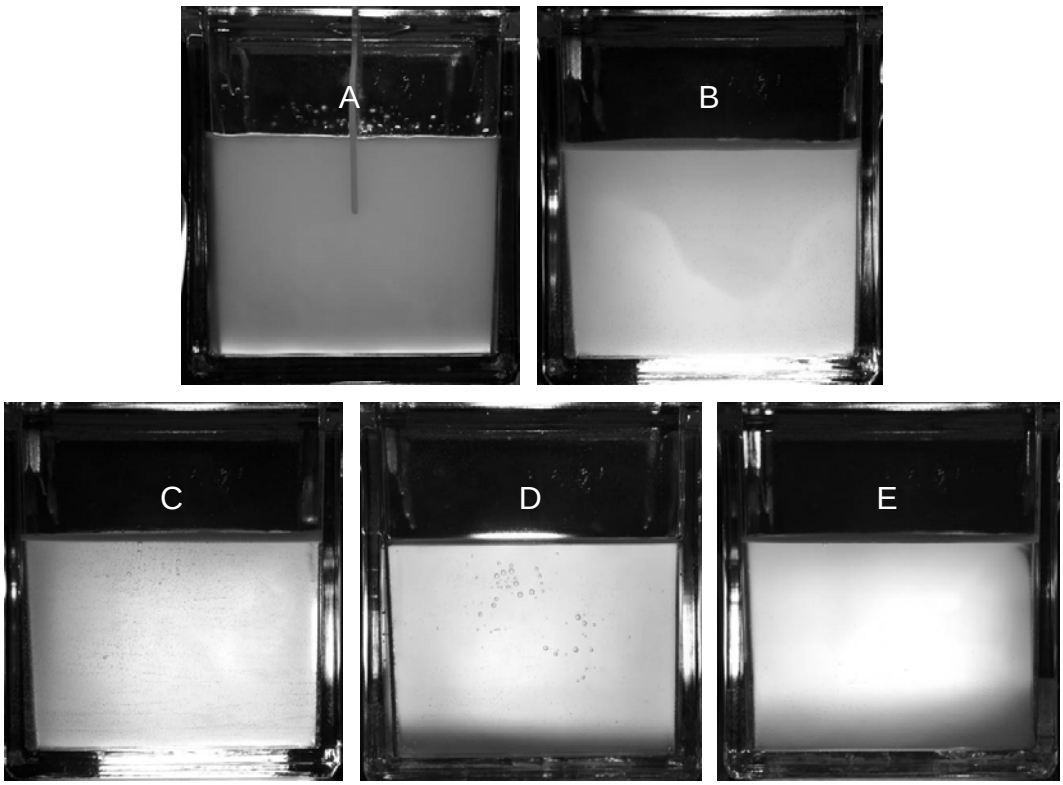

Abbildung 2: Referenzzustand A: anionisches Tensid zum Zeitpunkt 0;
Referenzzustand B: anionisches Tensid nach 3 h im Erdschwerefeld;
Bild C: Anionisches Tensid DBSA nach 3 h im Gleichspannungsfeld mit 12 V;
Bild D: Kationisches Tensid CTAB nach 3 h im Gleichspannungsfeld mit 12 V;
Bild E: Nichtionisches Tensid Tween® 65 nach 3 h im Gleichspannungsfeld mit 12 V
Für alle Bilder: Kathode rechts, Anode links

Zusammenfassung

In dieser Arbeit wird das Absetzverhalten von Feinsttrübungen, die durch verschiedene Tenside stabilisiert wurden, im elektrischen Gleichspannungsfeld untersucht. Dabei konnte festgestellt werden, dass die Enttrübung der Emulsion bei allen eingesetzten Tensiden vom elektrischen Feld beschleunigt wird. Dies bestätigt die vorteilhafte Wirkung des elektrischen Feldes.
Ziel dieser Arbeit sind der Technologievergleich und die Modellierung der Enttrübung.

Literatur

[1] Macher-Ambrosch R., Siebenhofer M.: Turbidity control. CEET Konkret, 2015, S. 18-19
[2] Draxler J.: Flüssige Membranen für die Abwasserreinigung, TU Graz, Habilitationsschrift, 1992
[3] Fang C.S., Lai P.M.C.: Microwave Heating and Separation of Water-in-Oil Emulsions. J. Microw. Power Electromagn. Energy 30, 1995, S. 46-57
[4] Ichikawa T., Itoh K., Yamamoto S., Sumita M.: Rapid demulsification of dense oil-in-water emulsion by low external electric field I. Experimental evidence. Colloids Surf., A 242, 2004, S. 21-26

Prozessintensivierung durch reaktive Trennverfahren in der Lösungsmittel-Rückgewinnung

Daniela Painer, Susanne Lux, Matthäus Siebenhofer
alle: TU Graz, Institut für chemische Verfahrenstechnik und Umwelttechnik, NAWI Graz
8010 Graz, Inffeldgasse 25c
d.painer@tugraz.at, susanne.lux@tugraz.at, m.siebenhofer@tugraz.at

Kurzfassung

Abwasserströme aus biobasierten Prozessen enthalten oft wertvolle Substanzen jedoch meist in geringer Konzentration. Diese sind nur durch aufwändige Prozessschritte isolierbar. Die Rückgewinnung kann aus rechtlichen und Umweltschutzgründen notwendig sein, kann aber auch zur nachhaltigen Produktion von Chemikalien beitragen. Die Abwasserbehandlung der Zellstoffindustrie beispielsweise ist mit dem ternären Gemisch Essigsäure/Ameisensäure/Wasser konfrontiert, welches ein ternäres Sattelpunktazeotrop und ein binäres Hochsiedeazeotrop aufweist. Die herkömmliche destillative Auftrennung ist durch diese Azeotrope und durch den großen Wasserüberschuss nicht möglich. Flüssig-flüssig-Extraktion eignet sich hervorragend für die Abtrennung dieser Carbonsäuren aus dem Abwasser, allerdings ist die Lösungsmittelrückgewinnung und Isolierung der Wertstoffe mit einem hohen apparativen und energetischen Aufwand verbunden. Reaktive Trennverfahren bieten durch Veränderung der Substanzeigenschaften alternative Prozesskonzepte für eine Auftrennung. Durch Veresterung der Carbonsäuren mit Methanol im beladenen Lösungsmittel werden leichtsiedende Ester gebildet, welche kontinuierlich mittels Destillation abgetrennt werden können. Dies verschiebt das Reaktionsgleichgewicht auf die Seite der Produkte und eine vollständige Veresterung der Carbonsäuren wird möglich. Die Überprüfung dieses reaktiven Trennkonzeptes wurde anhand von Batch-Reaktivdestillationsversuche erfolgreich durchgeführt.

Einleitung

Die Abtrennung von Verunreinigungen aus Abwässern stellt einerseits einen wichtigen Schutz für die Umwelt dar, kann aber zusätzlich zur Rückgewinnung von wertvollen Chemikalien und damit als weiteres wirtschaftliches Standbein dienen. Das Abwasser der Zellstoffindustrie enthält beispielsweise Essigsäure und Ameisensäure in geringer Konzentration. Bereits in den 1980er Jahren wurden Patente publiziert, welche Reaktivextraktion als Rückgewinnungsmöglichkeit der Carbonsäuren aus pflanzlichen Hydrolyseprodukten vorstellen. Das Patent von Kanzler und Schedler [1] beispielsweise verwendet als reaktives Extraktionsmittel Trioctylphosphinoxid in Undecan und zur Lösungsmittelregeneration Vakuum-Destillation. Die weitere Isolation der Carbonsäuren, Wasser und gegebenenfalls Furfural gestaltet sich aufgrund eines Hochsiedeazeotrops zwischen Ameisensäure und Wasser und eines ternären Sattelpunktazeotropes von Essigsäure, Ameisensäure und Wasser schwieriger. Hierfür schlagen Kanzler und Schedler eine Schleppmitteldestillation mit Di-n-propylether und/oder Ethyl-n-butylether für die Abtrennung des Wassers vor und weitere Destillationskolonnen für die Isolierung der Carbonsäuren und des Furfurals. In Abbildung 1 ist dieses Verfahrensschema dargestellt. Es ist ersichtlich, dass die Lösungsmittelregeneration und Isolierung der Wertstoffe den wesentlich größeren apparativen und energetischen Aufwand darstellen als die Abtrennung der Verunreinigungen aus dem Abwasser. Hier zeigt sich der Handlungsbedarf, um die Abwasseraufbereitung effizienter und kostengünstiger gestalten zu können.

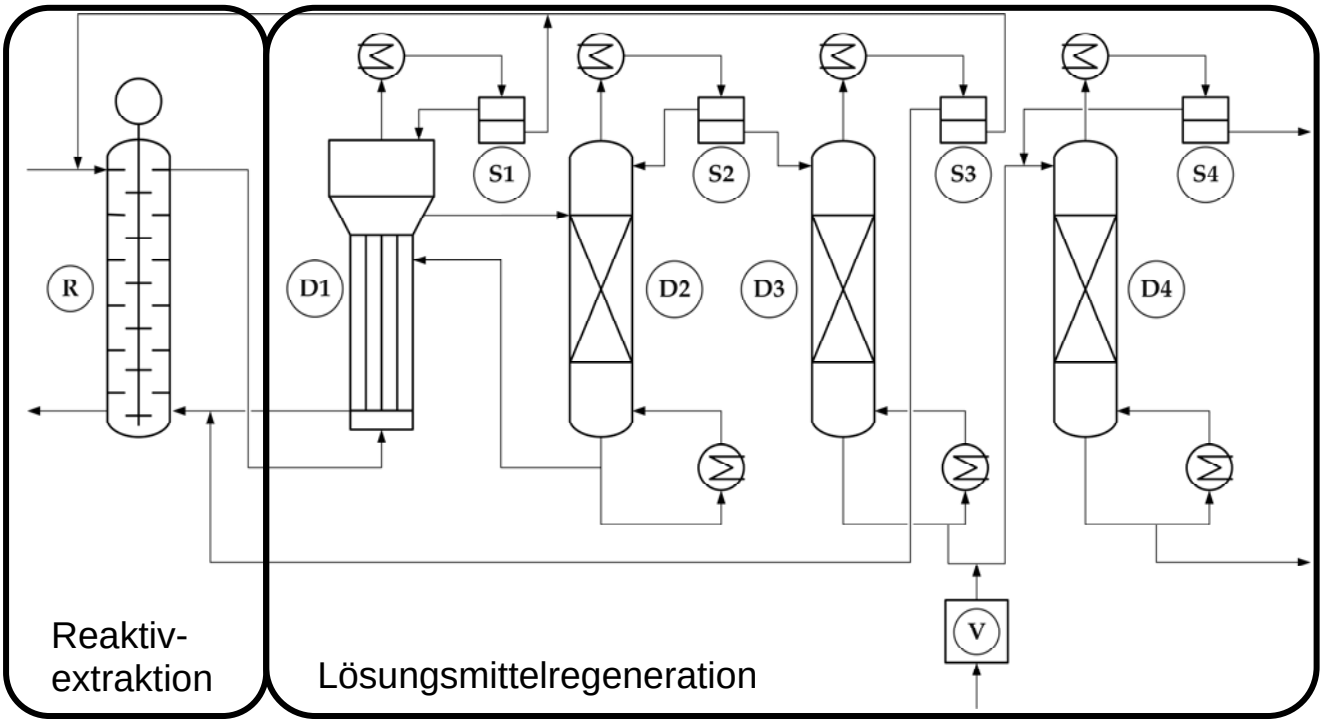

Abbildung 1: Verfahrensschema zur Extraktion von Essigsäure, Ameisensäure und gegebenenfalls Furfural aus wässrigen Lösungen von pflanzlichen Hydrolyseprodukten [1]

Reaktive Trennverfahren sind optimale Werkzeuge für die Prozessintensivierung. Durch die chemische Umwandlung der Carbonsäuren kann nicht nur die weitere Auftrennung wesentlich erleichtert, sondern auch der Marktwert der Produkte erhöht werden.

Reaktivdestillation zur Auftrennung des ternären Gemisches Essigsäure, Ameisensäure und Wasser wurde in Patenten von Hobbs und Bedford [2] und Aga und Debus [3] bereits diskutiert. In beiden Patenten war das Ziel reine Essigsäure als Sumpfprodukt abzuziehen und nur die Ameisensäure zu verestern. Hobbs und Bedford verwendeten dazu niedrigere Alkanole und Alkylacetate um das Alkylformiat als Kopfprodukt abzuziehen. Hingegen fanden Aga und Debus heraus, dass mit höheren Alkoholen und Estern mit mindestens drei Kohlenstoffatomen der Ameisensäureester gleichzeitig als Schleppmittel für das vorhandene Wasser dient und als Kopfprodukt abgezogen werden kann.
Bei vollständiger Veresterung beider Carbonsäuren aus einem wässrigen Gemisch mit Methanol und gleichzeitige Abtrennung der leichtflüchtigen Methylester als Kopfprodukt konnten 99,3 % der Ameisensäure und 71,5 % der Essigsäure ohne Zugabe eines Katalysators verestert werden [4].

Im Jahr 2013 wurde ein Patent veröffentlicht, das Veresterung kombiniert mit Destillation zur Lösungsmittelregeneration in der Extraktion organischer Säuren verwendet [5]. Dieses Patent weist auf den aktuellen Handlungsbedarf in der Lösungsmittelaufbereitung deutlich hin und zeigt das große Potential von reaktiven Trennverfahren.

Prozesskonzept

In der Zellstoffindustrie entsteht bei der Eindampfung der Schwarzlauge ein Brüdenkondensat mit Konzentrationen von bis zu 60 g/L Essigsäure und 30 g/L Ameisensäure, welche den Vorfluter belasten würden bzw. eine aufwändige biologische Abwasserreinigung erforderten. Die Abtrennung der Carbonsäuren aus dem

Brüdenkondensat kann aber mittels Reaktivextraktion erfolgen, beispielsweise mit Trialkylphosphanoxiden wie Cyanex®923, welche mit den Carbonsäuren ein Lewis-Säure/Base-Addukt bilden. Dieses Addukt wird durch Zugabe von Methanol gebrochen, da das Methanol mit den Carbonsäuren verestert. Die gleichzeitige Abtrennung der Methylester in einer Reaktivdestillation verschiebt das Reaktionsgleichgewicht auf die Seite der Produkte, wodurch eine vollständige Veresterung ermöglicht wird. Die leichtflüchtigen Methylester bilden mit dem überschüssigen Methanol das Destillat, welches beispielsweise mit Pervaporation aufgetrennt werden kann. Das regenerierte Lösungsmittel und Reaktionswasser wird zur Extraktion zurückgeführt. Durch Phasentrennung scheidet sich das Reaktionswasser vom Extraktionsmittel ab und wird über das Raffinat ausgetragen. In Abbildung 2 ist dieses reaktive Trennkonzept zur Lösungsmittelregeneration dargestellt.

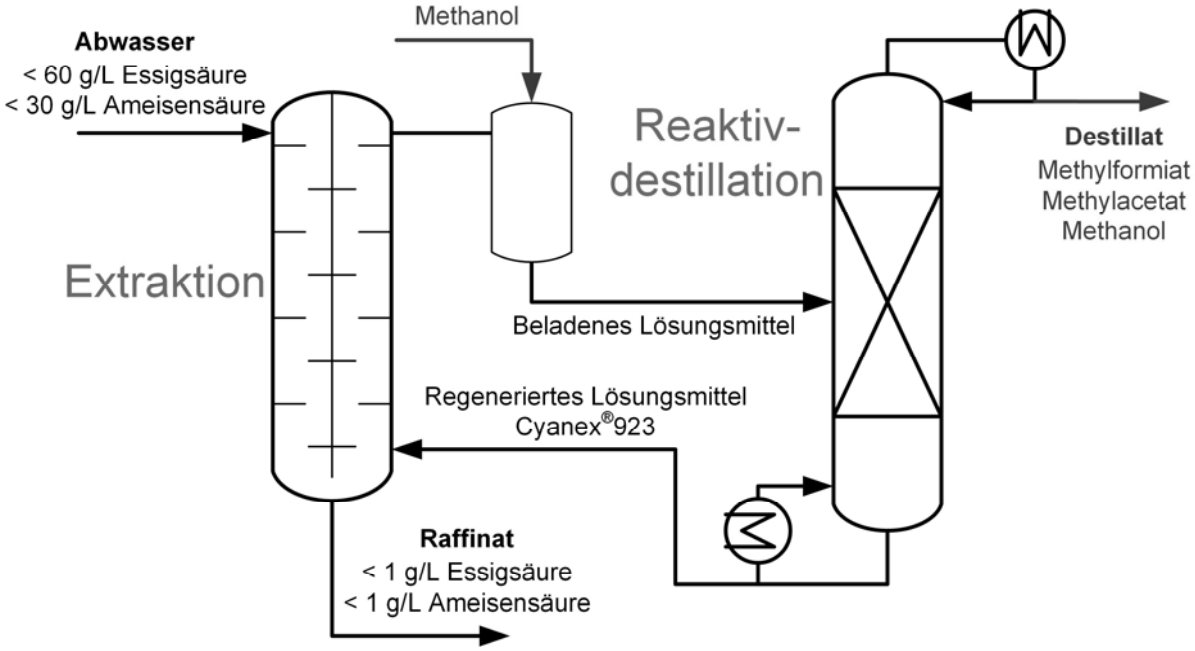

Abbildung 2: Reaktives Trennkonzept zur Rückgewinnung des Lösungsmittels

Proof of Concept

Zur Überprüfung des Trennkonzeptes wurden Batch-Reaktivdestillationsversuche durchgeführt. Die Versuche wurden in einem 500 ml Dreihalskolben mit einer 30 cm langen Vigreux-Kolonne und einem Rücklaufteiler durchgeführt. Das Rücklaufverhältnis wurde nach 1,5 h Reaktionszeit auf 10 eingestellt. Die Heizleistung wurde langsam entsprechend dem Siedepunkt des Sumpf-Gemisches erhöht, um eine kontinuierliche Abtrennung der Methylester zu gewährleisten. Es wurde ein äquimolares Verhältnis von Methanol zu beiden Säuren gewählt und kein Katalysator zugegeben.
Die Destillatzusammensetzung über die Versuchszeit ist in Abbildung 3 gezeigt. Zu Beginn der Destillatentnahme war die Konzentration an Methylformiat mit 0,8 mol/mol am höchsten. Die Ameisensäure ist die stärkere Säure im Vergleich zur Essigsäure und reagierte deshalb schneller mit dem Methanol. Erst als die Konzentration der Ameisensäure im Sumpf gering war, sank die Konzentration an Methylformiat im Destillat und die Konzentration von Methanol nahm zu. Die Methylacetatkonzentration stieg aufgrund der langsameren Essigsäureveresterung über die gesamte Versuchsdauer nur leicht bis 0,18 mol/mol. Es wurden Umsätze von Ameisensäure über 70 % und von Essigsäure von 13 % erreicht.

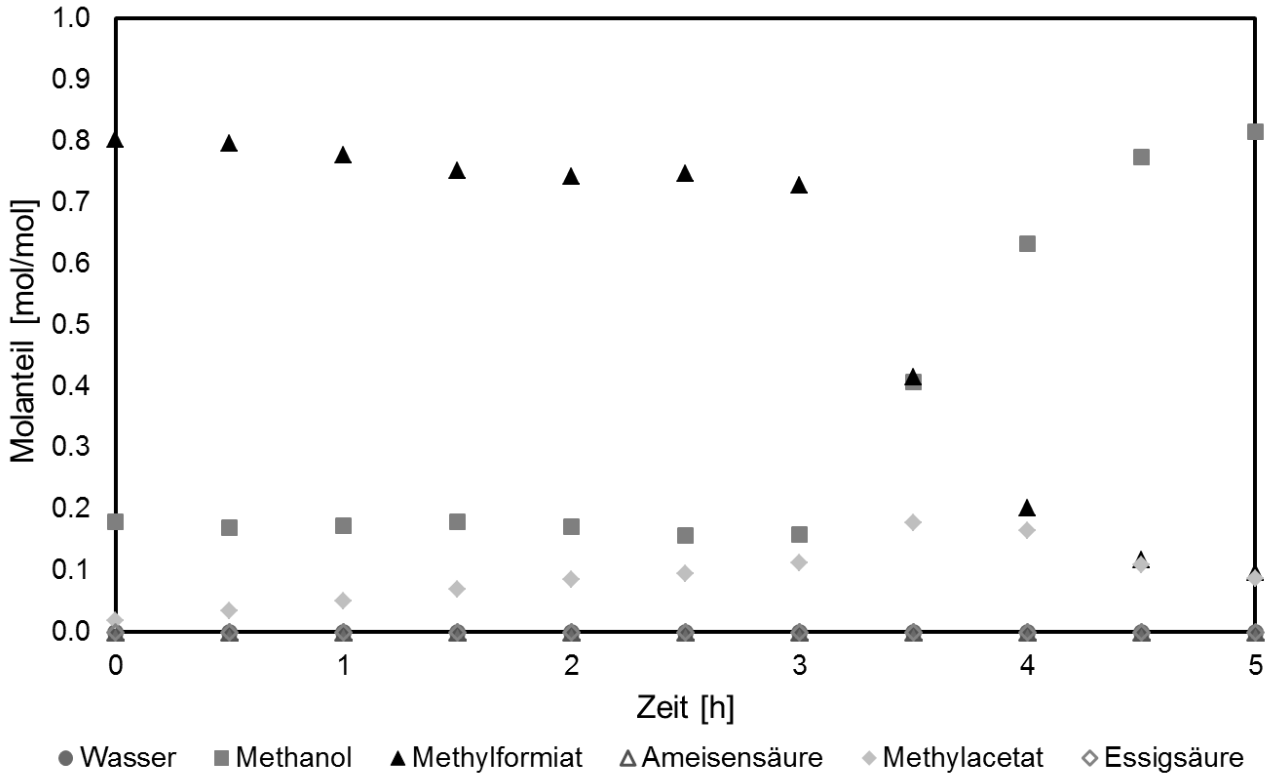

Abbildung 3: Destillatzusammensetzung der Batch-Reaktivdestillationsversuche der organische Phase 70 % Cyanex®923 in Undecan mit einem äquimolaren Verhältnis von Methanol zu beiden Carbonsäuren, Rücklaufverhältnis = 10, Umgebungsdruck

Zusammenfassung

Reaktive Trennverfahren haben großes Potential für die energieeffizientere und kostengünstigere Lösungsmittelregenerierung und Wertstoffisolierung. In Batch-Reaktivdestillationsversuche konnte das technologische Potenzial der Reaktivdestillation zur Abtrennung von Essigsäure und Ameisensäure aus Trialkylphosphanoxiden mit Methanol bestätigt werden.

Literatur

[1] W. Kanzler, J. Schedler; Verfahren zur Extraktion von Essigsäure, Ameisensäure, gegebenenfalls Furfurol. AT Patent 365 080, 1981.

[2] C. C. Hobbs, J. A. Bedford; Separation of formic acid from acetic acid. US Patent 3 660 483, 1972.

[3] R. L. Aga, H. R. Debus; Separation of acetic acid, water and formic acid. US Patent 3 801 629, 1974.

[4] D. Painer, S. Lux, M. Siebenhofer; Reaktive Trennung von Essigsäure/ Ameisensäure/Wasser-Gemischen aus der Bioraffinerie. Chem. Ing. Tech., Themenheft Reaktionstechnik, 2015. DOI: 10.1002/cite.201400130

[5] E. Tirronen, J. Hietala, R. Aksela; Method for recovery of organic acid from dilute aqueous solution. US Patent 2013/0331601 A1.

CFD-DEM Simulation of Wet Fluidized Beds: Evaporation Rates from the Spray and the Particle Surface

Maryam Askarishahi,[1,2] Mohammad-Sadegh Salehi, Stefan Radl[1]
[1]Graz University of Technology, Institute of Process and Particle Engineering, Inffeldgasse 13/III, 8010 Graz
[2]Research Center Pharmaceutical Engineering GmbH, Inffeldgasse 13/II, 8010 Graz
maryam.askarishahi@tugraz.at, sadegh.salehi1987@gmail.com, radl@tugraz.at

Abstract

CFD-DEM simulations were used to investigate particle-droplet-fluid interaction in a fluidized bed. Models were implemented in the CFDEM® simulation code to consider particle-droplet interaction, and droplet evaporation from (i) the particle surface, as well as (ii) from the spray. In detail, a model for predicting the deposition rate of droplets on the particles was added as a sink term to the transport equation for the droplet mass loading in the gas. The implemented models were verified for a packed bed at various particle Reynolds numbers and droplet Stokes numbers. Moreover, to consider the evaporation of droplets deposited on the particle surface, a source term was added to the transport equation for the vapour mass loading of the gas phase. Besides, the heat exchange between particle and fluid due to evaporation was taken into account in the heat balance equations. The implemented models can be used for the simulation of a wet fluidized bed. In fact, the developed models allow the prediction of the particle liquid content, which strongly affects the rate of agglomeration, as well as the moisture distribution in the gas phase. Most important, our predictions allow us to understand under which process conditions evaporation from the spray is important, and hence may lead to unwanted spray losses or dust formation.

Introduction

In various industries such as petrochemicals, food, and pharmaceutical, granulation figures prominently in the production of powder granules. Various phenomena are expected to occur in such systems: i) deposition of droplet on particles surface due to particle-droplet collision; ii) evaporation of liquid from particle surface stemming from flow of heated gas over wet particles; iii) particle agglomeration due to collision of wet particles. Since the process is complex and various physical phenomena interact (e.g., evaporation and wetting of particles), more experimental and numerical effort is needed for a complete understanding of these systems. The experimental studies presented in the open literature [1-3] are faced with several constrains, e.g., with respect to optimal access or image processing. Therefore, numerical simulation can be a strong tool to obtain worthwhile information about the phenomena occurring in the fluidized bed granulator.
The main objective of this study is to predict various quantities playing important roles in droplet evaporation and deposition phenomena in fluidized bed. To do so, additional modules for the CFDEM® package were developed to simulate particle-droplet fluid interaction in the fluidized bed.

Method

Simulations were performed after substantial extension of the CFDEM® code [4]. The momentum equation for the gas phase is solved based on a spatially-averaged form of the Navier-Stokes equations, and the motion of individual particles are solved using Newton's equation of translational and rotational motion. Due to temperature differences between the fluid phase, the injected droplets, and the particles, as well as evaporation phenomena, it is necessary to consider a differential heat and mass transport model for the air-vapor mixture. Furthermore, the local droplet content is predicted by solving a convection-diffusion equation for the corresponding droplet mass loading μ_{liq}. In order to compute the deposition rate of droplets on the particles, a clean-bed filter model was adopted (see Kolakaluri [5]). Thus, the droplet deposition rate is calculated as:

$$\dot{S_d} = -\lambda \left|\mathbf{u}_\mathrm{d} - \mathbf{u}_\mathrm{p}\right| \mu_{liq} \varphi_f \rho_f \tag{1}$$

Where $\left|\mathbf{u}_\mathrm{d} - \mathbf{u}_\mathrm{p}\right|$ is the slip velocity between the fluid phase (i.e., moist air) and the particles. λ is the filtration coefficient, which has dimensions [1/m], and which was modelled using the results of [Kolakaluri [5]] as a function of the droplet Stokes number and the particle diameter. Moreover, the rates of droplet evaporation from the particle surface and from droplets suspended in the gas phase were calculated based on the driving force for water vapour transport between particle and gas phase. This rate was estimated using the saturation density of water vapour at particle (or droplet) temperature, and appropriate Sherwood number correlations for dilute droplet and dense gas-particle flows. Note, that the droplet surface coverage of particles was assumed to not affect the evaporation rate, which clearly limits the current study to be explorative. Heat transfer rates were modelled using appropriate Nusselt correlations.

Results

In order to proof the correct implementation of the above models, several verification studies were performed. Here we show an example of such a test, namely the verification of the droplet deposition model (see Figure 1). This test models the deposition of droplets (which are injected at the inlet, i.e., *x* = 0) in a fixed bed of particles.

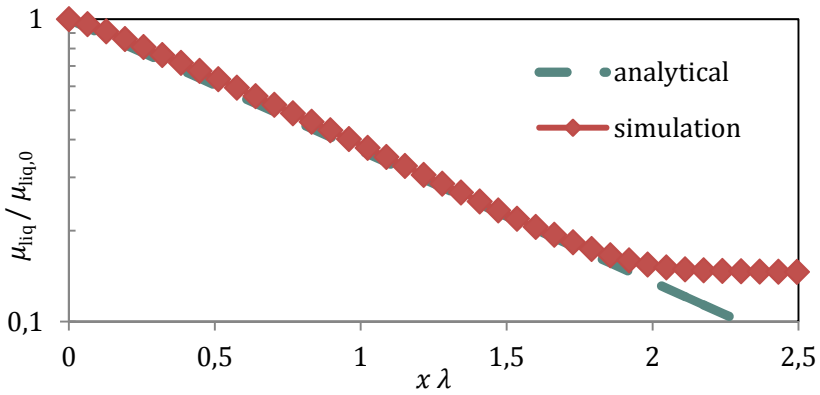

Figure 1: Comparison of the predicted droplet mass loading along a static particle bed (CFD-DEM simulation) and the corresponding analytical solution ($\lambda = 2.13 \cdot 10^2\ {}^{1}/_{m}$, $H_0 = 0.01$).

As seen in this figure, the predicted non-dimensional droplet mass loading is in excellent agreement with the analytical solution up to the height at which particles exist, i.e. $x = H_0$.

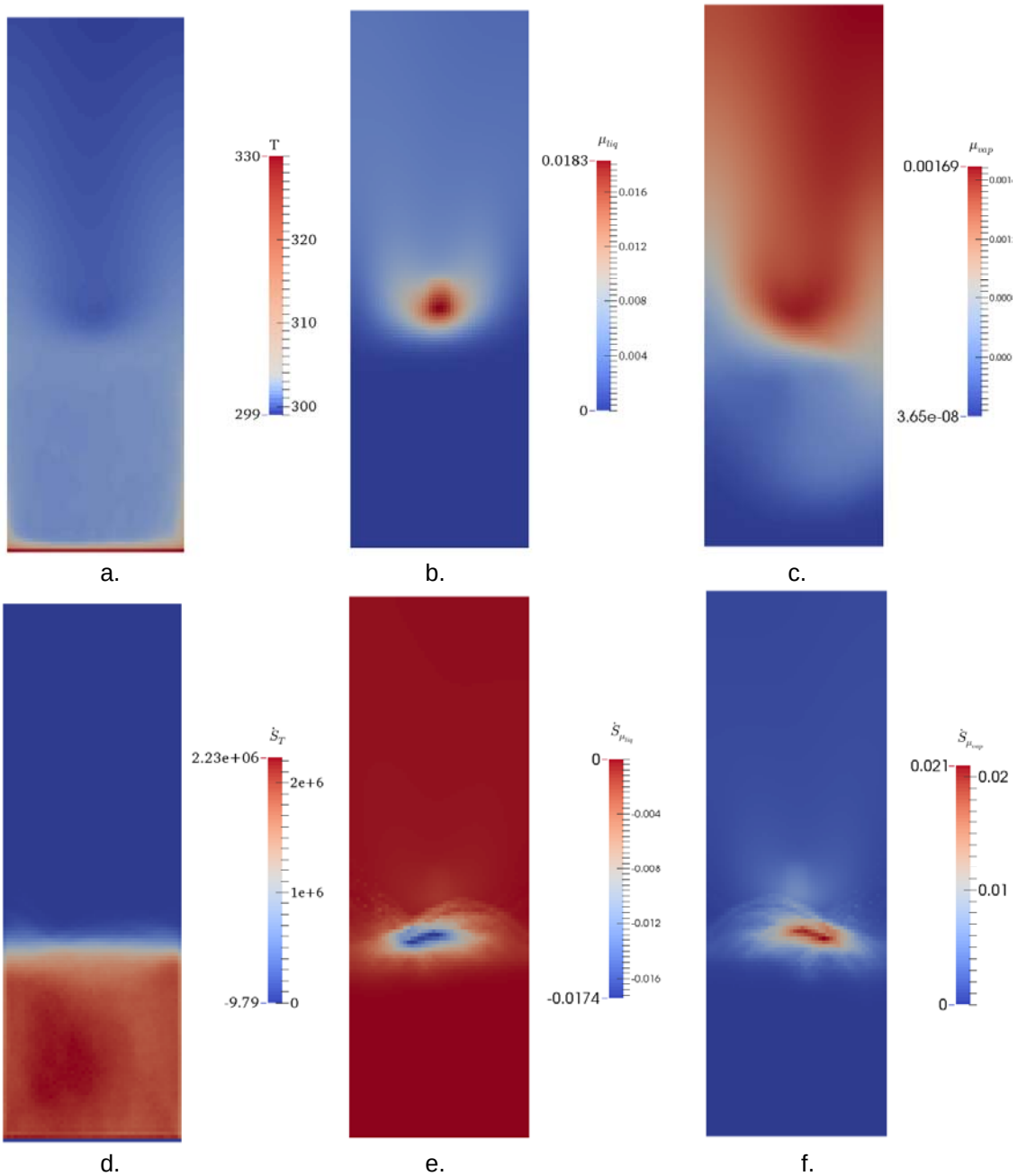

Figure 2: Contour plots of the a) gas temperature, b) liquid mass loading; c) vapour mass loading; d) heat source term; e) liquid source term; and f) vapour source term.

After successful implementation of all modes, we focussed on the simulation of particle-droplet-fluid interaction in a small fluidized bed. Therefore, a box was filled with $6 \cdot 10^4$ particles. Droplet injection (i.e., water) was modelled by adding a source term to the water droplet transport equation in a region located slightly above the particle bed. The contour-plots of key quantities were depicted in Figure 2. As seen in Figure 2.a, a large temperature gradient was predicted near the bed inlet, which can be attributed to the rapid cooling of the gas due to the presence of the particles. Also, efficient mixing of the particles in the fluidized bed leads to a virtually uniform particle temperature distribution. In the spray zone, a somewhat lower temperature was predicted due to droplet evaporation (see the distribution of the water vapour source

term $\dot{S}_{\mu_{vap}}$ in Figure 2f). However, the evaporation rate from wet particles is substantially higher, as can be seen from Figure 2f. Thus, it can be concluded that the rate of evaporation from the spray is smaller (at least in a local sense) in comparison with the corresponding evaporation rate from the particle surface. Another point discerned from this figure is that droplet deposition on particle mainly occurs on the bed surface since the sink term for liquid water $(-\dot{S}_{\mu_{liq}})$is higher (see Figure 2e).

In order to investigate the effect of evaporation on LoD (Loss on Drying, i.e., the water mass fraction), the liquid content of the particle was obtained for two cases with and without evaporation from the particle surface. As depicted in Figure 3, in case no evaporation occurs from the particle surface, the mean LoD increases over time and saturates only slowly. In contrast, when evaporation of deposited droplets is considered, the LoD reaches a statistical steady state after ca. 0.2 [s] and at approximately $5 \cdot 10^{-9}$. This clearly indicates that evaporation of liquid from the particle surface is the dominating effect. We argue that the high particle concentration, and hence the large specific interfacial area offered by the particles is the reason for this behaviour.

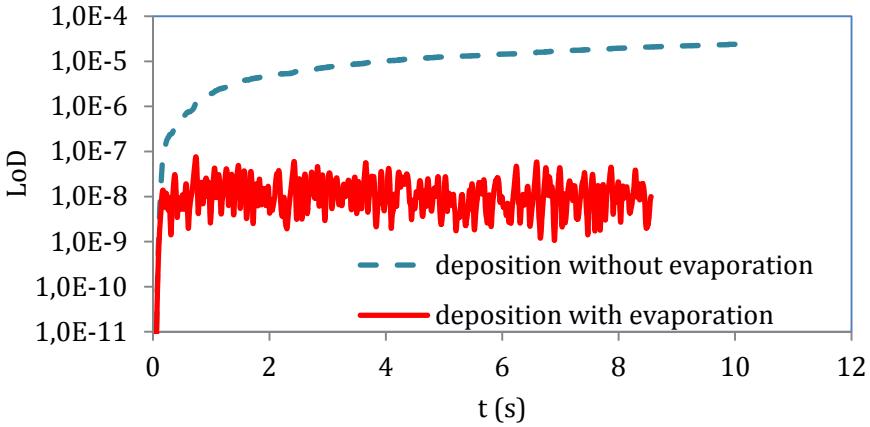

Figure 3: Variation of the mean particle wetness (indicated by the Loss On Drying value).

Acknowledgement

SR acknowledges funding from EC Grant 604656 (NanoSim). CFDEM® is a trade mark of DCS Computing GmbH.

Literature

[1] McDougall, S., et al., *Using dynamic pressure signals to assess the effects of injected liquid on fluidized bed properties.* Chemical Engineering and Processing: Process Intensification, 2005. vol. 44, no. 7, pp. 701-708.

[2] Ariyapadi, S., et al., *Digital X-ray imaging technique to study the horizontal injection of gas-liquid jets into fluidized beds.* International Journal of Chemical Reactor Engineering, 2003. vol. 1, no. 1, Article A56

[3] Briens, C., M. Dawe, and F. Berruti, *Effect of a draft tube on gas–liquid jet boundaries in a gas–solid fluidized bed.* Chemical Engineering and Processing: Process Intensification, 2009. vol. 48, no. 4, pp. 871-877.

[4] Kloss, C., et al., *Models, algorithms and validation for opensource DEM and CFD–DEM.* Progress in Computational Fluid Dynamics, an International Journal, 2012. vol. 12, no. 2-3, pp. 140-152.

[5] Kolakaluri, R., *Direct Numerical Simulations and Analytical Modeling of Granular Filtration.* 2013.

Process development strategies: Lactic acid isolation

Nuttakul Mungma, Marlene Kienberger, Matthäus Siebenhofer
TU Graz, Institute of Chemical Engineering and Environmental Technology,
Inffeldgasse25/C/II, 8010 Graz, Austria
n.mungma@tugraz.at

Abstract

Goal of the current work has been the evaluation of potential separation technology candidates for the separation of lactic acid via systematic approach using a decision matrix [1]. Due to the increasing demand of lactic acid for the production of poly-lactic acid, fermentation as well as downstream processing needs to be improved. Within this work a systematic approach on the basis of substance properties is applied to identify processes for the isolation of lactic acid from fermentation broth. In terms of costs the approach follows a strict sequence: mechanical unit operations were hierarchically evaluated before investigation of mass transfer unit operations. The decision matrix for mechanical unit operations results show that the most effective method in mechanical separation would be electrophoresis. Potential methods concerning mass transfer unit operations are permeation, pervaporation, electrodialysis and molecular sieving. Furthermore, lyophilysation may be of interest to look at.

Introduction

Due to the growing demand of L(+) lactic acid especially for the production of poly lactic acid, it is necessary to improve not only the fermentation process but also the purification processes [2]. Lactic acid is commercially produced via fermentation, it is used in the food, cosmetic and pharmaceutical industry, as preservative in flavors, and as monomer for the production of poly lactic acid. Worldwide the use of biopolymers is increasing, to produce poly lactic acid (PLA); lactic acid is needed in high purity. Global lactic acid demand in 2013 was 714.2 kilo tons, 360.8 kilo tons were used for PLA [3]. Currently, approximately 90% of lactic acid is produced in microbial fermentation. Due to impurities such as residual sugar, color, cell mass, nutrients and other organic acids purification, respectively product recovery is an important step in lactic acid production. Separation and purification of lactic acid from fermentation broth are major components of production expenditure [4].

The conventional lactic acid production process consists of the fermentation, the acidification, the purification and finally the concentration of the lactic acid. The pH value in fermentation is kept at around 5 - 6.8 depending on microorganisms used. The pH-value is adjusted with lime. At this pH-value lactate exists in dissociated form, most industrial processes add sulfuric acid to the broth to crystallize calcium sulfate (gypsum) [5], [6]. Different purification processes have been commercialized on industrial scale, in all cases the microorganisms of cells must be removed from the broth. Downstream process of lactic acid production is accounted to be 50 % of the total production cost [7]. Thus, the development of cost-effective and efficient downstream process should be studied.

The present work shows a tool which is well known from Theory of Inventive Problem Solving (TIPS). Every substance has specific properties such as heat capacity, acid dissociation constant, solubility, boiling point et cetera. These specific properties are taken into account in evaluation of downstream process with the example substance lactic acid. In this work, the preliminary study of the development of the decision matrix for the separation respectively purification of lactic acid is developed.

Methodology

In order to assess the suitability of lactic acid recovery process, a decision matrix was set up. For the development of the decision matrix it is assumed that a binary mixture of water and lactic acid has to be separated. The approach consists of three stages:

- Identification of substance properties for the target substance lactic acid
- Evaluation of the substance properties addressing mechanical unit operations
- Evaluation of the substance properties addressing mass transfer unit operations

The evaluation legends are "+" which represent the possibility to apply the mentioned processes in lactic acid recovery while "-" refers to the impossibility of using this technology as well as to irrelevant parameter which will not concern the separation process. At the bottom of the table the total amount of "+" is given. With the unit operations with the highest score the separation task may be accomplished. The total amount does not guarantee that the unit operation leads to a positive accomplishment of the separation task. The decision matrix does not rate the substance properties; it may be that even with a high total score a specific unit operation may not be useful for this separation task because the main substance property (e.g. difference in boiling point for distillation) is evaluated negative.

Result and Discussion

The decision matrix was designed to develop a systematic approach for the separation of lactic acid dissolved in water. Due to the costs of the unit operations a chronological approach from mechanical unit operations to mass transfer unit operations was applied. In **Fehler! Verweisquelle konnte nicht gefunden werden.** the decision matrix for mechanical unit operations is given.

Table 1: decision matrix for mechanical unit operations

properties of target substance		Sedimentation	Flocculation	Filtration	Mechanical sieving	Chromatography	Hydro cyclone	Flotation	Electrophoresis	Centrifuge
property	Value									
MW [g/mol]	90.08	-	-	-	-	+	-	-	+	-
MP [°C]	16.8	-	-	-	-	-	-	-	-	-
BP [°C]	122	-	-	-	-	-	-	-	-	-
Acidity (pKa)	3.86	-	-	-	-	-	-	-	+	-
Density [g/cm^3]	1.209	-	-	-	-	-	-	-	-	-
Dielectric constant	19.4	-	-	-	-	-	-	-	+	-
Solubilty in water	Very soluble	-	-	-	-	-	-	-	-	-
Enthalpy [kJ/mol]	1361.9	-	-	-	-	-	-	-	-	-
pH value	2	-	-	-	-	-	-	-	+	-
Flash point [°C]	113	-	-	-	-	-	-	-	-	-
Vapor pressure [mmHg] at 25 °C	0.0813	-	-	-	-	-	-	-	-	-
Heat of combustion [kJ/mol]	1361	-	-	-	-	-	-	-	-	-
Heat capacity [J/kg.K]	2.3	-	-	-	-	-	-	-	-	-
Entropy [kJ/mol.K)	192.05	-	-	-	-	-	-	-	-	-
Viscosity [Pa.s] 88.6%sol	0.037	-	-	-	-	-	-	-	+	+
Henry constant [atm-m ^{3} /mol]	9.6 x 10^{-9}	-	-	-	-	-	-	-	-	-
Freezing point [°C]	16.8	-	-	-	-	-	-	-	-	-
Molecular size [A]	7.5	-	-	-	-	+	-	-	+	-
Total		0	0	0	0	2	0	0	6	1

The table consists of all possibly applicable mechanical unit operations in dependence on the substance properties of lactic acid. The only mechanical separation technique which

may be applied for the separation of water/lactic acid is electrophoresis. The separation of the binary system can be achieved with the driving force „electrical potential“. Schober *et al* [8] claimed that high performance capillary electrophoresis (HPCE) can be used as a routine method to evaluate the production of lactic acid and other organic acids in fermentation broths.

According to the chronological approach, evaluation of the decision matrix for the mass transfer unit operations is given in **Fehler! Verweisquelle konnte nicht gefunden werden.**. The evaluations of mass transfer unit operations show that most of the unit operations may be used for the separation task. Referring to the value of Henry constant absorption/desorption is not the unit operation of choice. The targeted binary system contains lactic acid in a concentration of ~60 g/L. Hence if distillation would be used all the water has to be removed from the fermentation broth. Moreover, direct distillation is difficult as tendency to homopolymerization of lactic acid increases with increasing temperature [9]. For flash vaporization and evaporation the same arguments are effective as for the distillation. Lactic acid is poorly extracted by common organic solvent. Methods which may be used for the separation of the binary mixture are permeation, pervaporation, electrodialysis and molecular sieving. There are research studies about lactic acid separation from both synthetic fermentation broth and real fermentation broth, that use one or more of the methods evaluated positive in the decision matrix [10],[11],[12],[13].

In addition lyophilysation widely appears as an option method for preservation of bacteria and yeasts [14]. It is an interesting unit operation to separate lactic acid from water, as the difference in freezing points is 16.8°C.

Table 2: decision matrix for mass transfer unit operations

properties of target substance		Sorption	Desorption	Distillation	Flash vaporization	Extraction	Drying	Crystallization	Evaporation	Permeation	Pervaporation	Lyo-phillisation	Electrodialysis	Molecular sieve
property	Value													
MW [g/mol]	90.08	+	+	-	-	-	-	-	-	+	+	-	+	+
MP [°C]	18	-	-	-	-	-	-	-	-	-	-	-	-	-
BP [°C]	122	-	-	+	+	-	-	-	+	-	+	-	-	-
Acidity (pKa)	3.86	+	+	-	-	+	-	+	-	+	-	-	+	+
Density	1.209	+	+	-	-	+	-	+	-	+	-	-	-	+
Dielectric constant	19.4	-	-	-	-	-	-	-	-	-	-	-	+	-
Solubility in water	Very soluble	-	-	-	-	-	-	-	-	-	-	-	-	-
Enthalpy [kJ/mol]	1361.9	-	-	+	+	-	-	-	+	-	-	-	-	-
pH value	2	+	+	-	-	+	-	+	-	+	+	-	+	+
Flash point [°C]	113	-	-	-	-	-	-	-	-	-	-	-	-	-
Vapor pressure [mm.Hg] at 25 °C	0.0813	-	-	+	+	-	-	-	+	-	+	-	-	-
Heat of combustion [kJ/mol]	1361	-	-	-	-	-	-	-	-	-	-	-	-	-
Heat capacity [J/kg.K)	2.3	-	-	+	+	-	-	-	+	-	-	+	-	-
Entropy [kJ/mol.K]	192.05	-	-	+	+	-	-	+	+	-	+	-	-	-
Viscosity [Pa.s] 88.6%sol	0.0369	-	-	-	-	+	-	+	-	+	-	-	+	+
Henry constant [atm-m ^{3} /mol]	9.6 x 10^{-9}	-	-	-	-	-	-	-	-	-	-	-	-	-
Freezing point [°C]	16.8	-	-	-	-	-	-	-	-	-	-	+	-	-
Molecular size [A]	7.5	+	+	-	-	-	-	-	-	+	+	-	+	+
Total		5	5	5	5	4	0	5	5	6	6	2	6	6

Summary

The task has been to develop a decision matrix for the separation of the binary system water and lactic acid. A strategy concept according to TIPS [1], was applied for systematic technology screening. The outcome of this systematic approach showed that none of the

mechanical unit operations except electrophoresis is applicable for the separation task. With mass transfer unit operations the separation task can be accomplished. The decision for a specific unit operation is not only based on the validation, hence on the highest score, but also on experience.

Literature

[1] R. Stratton, D. Mann, and P. Otterson, “The Theory of Inventive Problem Solving (TRIZ) and Systematic Innovation-a Missing Link in Engineering Education?,” 2010.

[2] T. Ghaffar, M. Irshad, Z. Anwar, T. Aqil, Z. Zulifqar, A. Tariq, M. Kamran, N. Ehsan, and S. Mehmood, “Recent trends in lactic acid biotechnology: A brief review on production to purification,” *J. Radiat. Res. Appl. Sci.*, vol. 7, no. 2, pp. 222–229, 2014.

[3] S. James, “Lactic Acid and Poly Lactic Acid (PLA) Market to Reach $4,312.2 Million and $2,169.6 Million Respectively by 2020.” Grand View Research, Inc, 2015.

[4] M. Matsumoto, A. Panigrahi, Y. Murakami, and K. Kondo, “Effect of ammonium- and phosphonium-based ionic liquids on the separation of lactic acid by supported ionic liquid membranes (SILMs),” *Membranes (Basel).*, vol. 1, pp. 98–108, 2011.

[5] S. Taskila and H. Ojamo, “The current status and future expectations in industrial production of lactic acid by lactic acid bacteria,” *Lact. acid Bact. D food, Heal. …*, 2013.

[6] C. S. López-Garzón and A. J. J. Straathof, “Recovery of carboxylic acids produced by fermentation,” *Biotechnol. Adv.*, vol. 32, no. 5, pp. 873–904, 2014.

[7] M. A. Abdel-Rahman, Y. Tashiro, and K. Sonomoto, “Recent advances in lactic acid production by microbial fermentation processes,” *Biotechnol. Adv.*, vol. 31, no. 6, pp. 877–902, 2013.

[8] T. J. Schober, S. R. Bean, and D. Wang, “Capillary electrophoresis as a tool for evaluating lactic acid production from sorghum,” *Cereal Chem.*, pp. 117–121, 2009.

[9] P. Khunnonkwao, P. Boontawan, D. Haltrich, T. Maischberger, and A. Boontawan, “Purification of l-(+)-lactic acid from pre-treated fermentation broth using vapor permeation-assisted esterification,” *Process Biochem.*, vol. 47, no. 12, pp. 1948–1956, 2012.

[10] Y. Li, a Shahbazi, K. Williams, and C. Wan, “Separate and concentrate lactic acid using combination of nanofiltration and reverse osmosis membranes,” *Appl Biochem Biotechnol*, vol. 147, no. 1–3, pp. 1–9, 2008.

[11] I. H. Aljundi, J. M. Belovich, and O. Talu, “Adsorption of lactic acid from fermentation broth and aqueous solutions on Zeolite molecular sieves,” *Chem. Eng. Sci.*, vol. 60, no. 18, pp. 5004–5009, 2005.

[12] J. Quintero, A. Acosta, C. Mejía, R. Ríos, and A. M. Torres, “Purification of lactic acid obtained from a fermentative process of cassava syrup using ion exchange resins,” *Rev. Fac. Ing.*, no. 65, pp. 139–151, 2012.

[13] M. C. Duke, A. Lim, S. C. Da Luz, and L. Nielsen, “Lactic acid enrichment with inorganic nanofiltration and molecular sieving membranes by pervaporation,” *Food Bioprod. Process.*, vol. 86, no. 4, pp. 290–295, 2008.

[14] S. Kandil and M. El Soda, “Influence of Freezing and Freeze Drying on Intracellular Enzymatic Activity and Autolytic Properties of Some Lactic Acid Bacterial Strains,” no. June, pp. 371–382, 2015.

Herausforderungen der Technologie- und Verfahrensentwicklung und Lösungsalgorithmen

Andreas Toth, Susanne Lux, Daniela Painer, Matthäus Siebenhofer
alle: TU Graz, Institut für chemische Verfahrenstechnik und Umwelttechnik,
8010 Graz, Inffeldgasse 25C/II
andreas.toth@tugraz.at, susanne.lux@tugraz.at, d.painer@tugraz.at,
m.siebenhofer@tugraz.at

Kurzfassung

Steigende Anforderungen im Bereich der Ökonomie und der optimalen Nutzung von (begrenzten) Ressourcen erfordern die Entwicklungen zweckmäßiger verfahrenstechnischer Prozesse. Die Vielfalt an verfügbaren Technologien ermöglicht eine effiziente Lösung komplexer Trennprobleme, sofern es gelingt aus diesem Angebot die geeigneten Grundoperationen herauszufiltern. Die Anwendung strukturierter Lösungsalgorithmen (z.B. TRIZ) ermöglicht die Lösung von Problemen, wie zum Beispiel die Trennung von verdünnten Wasser/Essigsäure-Lösungen durch innovative Technologien.

Einleitung

Die Entwicklung von Technologien zur Optimierung der Ressourcennutzung und Verringerung von Abfallstoffen erlangt weltweit immer größere Bedeutung. Diesen Trend bestätigt auch das Klimaschutzabkommen, welches von den Vereinten Nationen am 12. Dezember 2015 in Paris ausgearbeitet wurde. In Artikel 10 dieses Abkommens [1] wird festgehalten, dass unter anderem die Förderung von Innovationen entscheidend ist, um dem globalen Klimawandel entgegenzuwirken. Prozesse mit hohem Energiebedarf, die exzessive Nutzung von fossilen Ressourcen und die thermische Verwertung von Wertstoffen leisten einen negativen Beitrag zum Klimawandel. Der Verfahrenstechnik kommt in allen diesen Bereichen eine tragende Rolle zu. Als Beispiele sind die Entwicklung von Technologien zur vollständigen Nutzung von Biomasse und die Optimierung bestehender verfahrenstechnischer Prozesse mit dem Fokus auf Ökonomie und Ressourcennutzung zu nennen. Die Rückgewinnung bzw. Isolierung von Stoffen, welche einer starken Dissipation unterliegen stellt eine große Herausforderung dar. Dies betrifft das Recycling von Edelmetallen aus Elektronikabfällen ebenso wie die Abtrennung von Kohlenwasserstoffverbindungen aus wässrigen Lösungen. Während für einfache Trennaufgaben eine große Palette an standardisierten Verfahren zur Verfügung steht, sind komplexere Trennprobleme bisher nur durch einen hohen Energie- und/oder Ressourcenaufwand lösbar. Um derartige Trennprobleme im Sinne des Pariser Klimaschutzabkommens bewältigen zu können, steht ein nahezu unerschöpflicher Pool an mechanischen, thermischen und chemischen Technologien zur Verfügung. In der Folge sollen verschiedene Herangehensweisen an die Verfahrensentwicklung am Beispiel der Isolierung von Essigsäure aus verdünnten wässrigen Lösungen erläutert werden.

Ansätze zur Verfahrensentwicklung

Die Auswahl und Kombination geeigneter verfahrenstechnischer Grundoperationen zur Lösung komplexer Trennprobleme stellt aufgrund der Vielfalt der Möglichkeiten eine Interpolationsbarriere dar. Die „Theorie des erfinderischen Problemlösens“ (TRIZ, engl. TIPS) [2] bietet die Möglichkeit strukturiert an Trennprobleme heranzugehen. Eines der

bekanntesten Werkzeuge des TRIZ ist eine Widerspruchsmatrix, in welche die Grundoperationen in den Spalten und die Eigenschaften des Stoffsystems in die Zeilen eingetragen werden. Diese Matrix ermöglicht es unter Berücksichtigung von wirtschaftlichen Randbedingungen, geeignete Grundoperation zu vergleichen, auszuwählen und zu kombinieren. In Tabelle 1 ist für das Trennproblem eines stark verdünnten Wasser/Essigsäure-Gemisches schematisch eine solche Matrix dargestellt.

Tabelle 1: Schematische Widerspruchsmatrix nach TRIZ für das Trennproblem eines stark verdünnten Wasser/Essigsäure-Gemisches

	Thermische Grundoperationen					Mechanische Grundoperationen			
	Destillation	Extraktion	Membran-trennverfahren	Kristallisation	. . .	Siebung	Agglomeration	Sedimentation	. . .
Schmelzpunkt				●					
Siedepunkt	●								
Dichte		●						●	
Dissoziationsgrad		●	●						
Molekülgröße			●			●	●	●	
Löslichkeit		●	●	●					
⋮									

Eine erste Analyse des Trennproblems mit diesem Ansatz zeigt, das mehrere Verfahren zur Lösung in Frage kommen. Die destillative Trennung ist aufgrund der Lage der Siedepunkte (siehe Tabelle 2) sehr energieaufwändig, da in einer stark verdünnten Lösung das gesamte Wasser verdampft werden müsste. Mit einem erheblich niedrigeren energetischen Aufwand kann die Isolierung der Essigsäure aus dem verdünnten Gemisch durch Kristallisation realisiert werden. Das Diagramm in Abbildung 1 zeigt das Fest-Flüssig-Gleichgewicht von Wasser/Essigsäure aus Datensätzen der Dortmund Data Bank [3]. Das System besitzt bei ca. 0,7 mol/mol Wasser und einer Temperatur von ca. 246 K einen eutektischen Punkt.

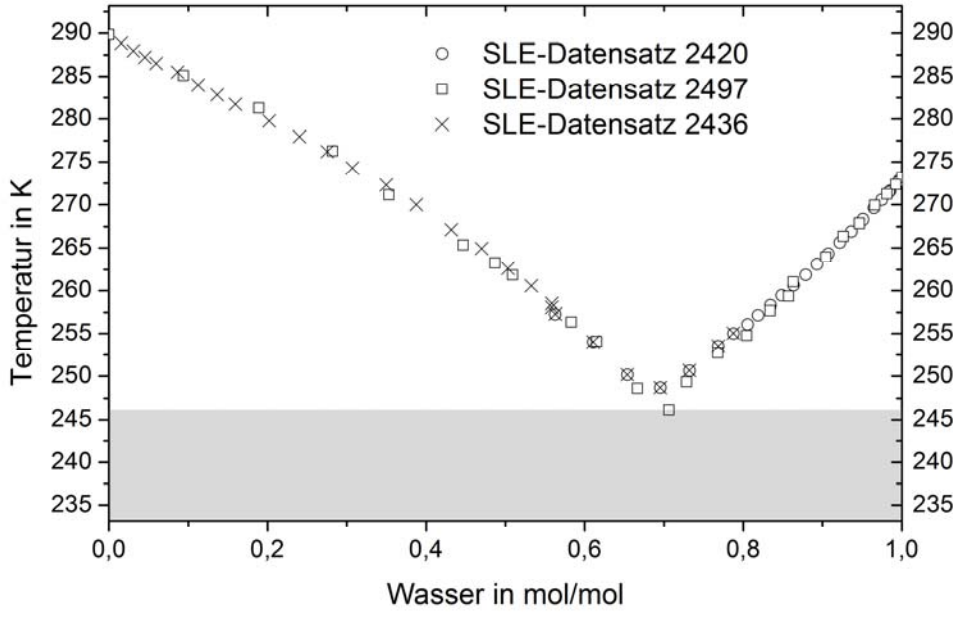

Abbildung 1: Fest-Flüssig-Gleichgewicht des binären Gemisches Wasser/Essigsäure [3]

Für den Fall der stark verdünnten Lösung ist der Bereich rechts dieses Punktes maßgeblich. Unterhalb der eutektischen Temperatur (grau hinterlegt) kristallisieren beide Komponenten gleichermaßen aus, während zwischen der Liquiduslinie (Messdaten) und der eutektischen Temperatur reines Wasser kristallisiert. Die Zusammensetzung der verbleibenden flüssigen Phase entspricht der Zusammensetzung auf der Liquiduslinie. Untersuchungen von Padhiyar et al. [4] bestätigen, dass eine Abtrennung der Essigsäure durch ein derartiges Verfahren möglich ist. Im Vergleich zu einer destillativen Trennung ergibt sich bei der Kristallisation ein Energieaufwand, welcher um Größenordnungen geringer ist. Die bisher gezeigten Ansätze nehmen die Eigenschaften des Stoffsystems als gegebene, unveränderliche Größen hin.

Kombinierte Verfahren

Ein weites Feld an Möglichkeiten eröffnet der Ansatz, die Eigenschaften des Stoffsystems zu verändern. Dies kann beispielsweise durch eine chemische Reaktion erreicht werden. Durch die Umwandlung der Essigsäure zu einem Ester unter Zugabe eines Alkohols können Dichte, Löslichkeit, Siedepunkt, etc. gezielt verändert werden. Die Wahl des Alkohols ist hierbei maßgeblich für die Wahl der Grundoperation. Ein positiver Nebeneffekt besteht darin, dass die abzutrennende Komponente in ein höherwertiges Produkt übergeführt werden kann. In Tabelle 2 sind die Wasserlöslichkeiten und Siedetemperaturen einiger Alkohole und ihrer Essigsäureester im Vergleich mit Wasser und Essigsäure angeführt.

Tabelle 2: Wasserlöslichkeiten und Siedetemperaturen ausgewählter Alkohole und ihrer korrespondierenden Essigsäureester im Vergleich mit Wasser und Essigsäure [5]

Komponente	Löslichkeit in Wasser	Siedetemperatur
Wasser	vollständig löslich	100 °C
Essigsäure	vollständig löslich	118 °C
Methanol	vollständig löslich	65 °C
n-Octanol	unlöslich	195 °C
Methylacetat	vollständig löslich	57 °C
n-Octylacetat	unlöslich	211 °C

Eine Veresterung mit Methanol hat zur Folge, dass eine destillative Auftrennung des Gemisches in Bezug auf den Energieaufwand deutlich verbessert wird, da der Siedepunkt von Methylacetat mit 57 °C gegenüber der Essigsäure halbiert werden kann. Die Kombination von Veresterung und Destillation in einem Verfahrensschritt führt als Reaktivdestillation zu einem geeigneten Verfahren zur Lösung des vorliegenden Trennproblemes [6]. Durch die Wahl des wasserunlöslichen, hochsiedenden *n*-Octanols als Reaktionspartner kann neben dem Siedepunkt auch die Wasserlöslichkeit gezielt verändert werden. Das ermöglicht in einem kombinierten Extraktions-/Reaktionsschritt eine effiziente und ökonomische Auftrennung des Gemisches.

Die beschriebene Herangehensweise an komplexe Trennprobleme ermöglicht auch die Optimierung bestehender Prozesse. Dies lässt sich anschaulich am Beispiel der Essigsäureisolierung durch eine Reaktivextraktion mit destillativer Lösungsmittel-rückgewinnung zeigen. Das vereinfachte Schema dieses Prozesses ist in Abbildung 2 dargestellt. Zusätzlich sind vier alternative Möglichkeiten für die Zugabe eines Alkoholes eingezeichnet. Die Senkung der Siedetemperatur ohne Veränderung des Löslichkeitsverhaltens – durch die Veresterung mit Methanol – würde sich dazu eignen, die destillative Lösungsmittelregeneration zu intensivieren und dadurch den Energiebedarf zu verringern [6].Im Gegensatz dazu hätte eine Erhöhung des Siedepunktes bei

gleichzeitiger, erheblicher Senkung der Löslichkeit – durch die Veresterung mit *n*-Octanol – eine Intensivierung des Extraktionsschrittes zur Folge, was durch eine Zugabe des *n*-Octanols zum regenerierten Lösungsmittel realisierbar wäre. Die destillative Abtrennung der Produkte kann so durch eine einfache Phasentrennung ersetzt werden, da aufgrund der Löslichkeiten die Produkte vollständig in die Lösungsmittelphase übergeführt werden. [7]

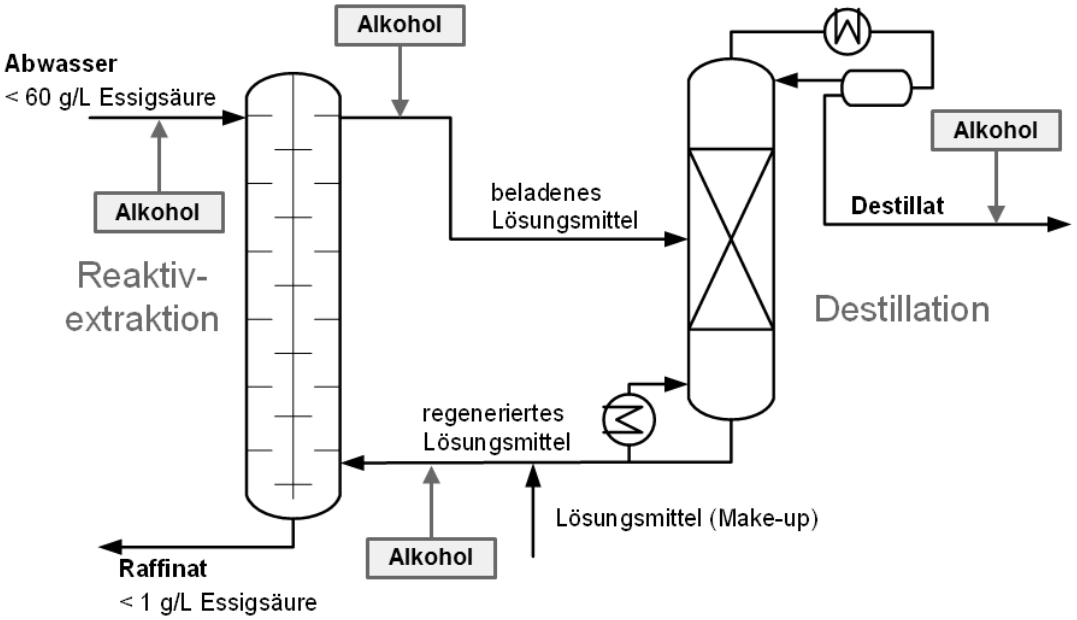

Abbildung 2: Vereinfachtes Prozessschema zur Isolierung von Essigsäure mit alternativen Intensivierungsoptionen [7]

Zusammenfassung

Die Förderung von Innovationen im Bereich der Technologie- und Verfahrensentwicklung ermöglicht die Lösung komplexer Trennprobleme. Durch eine strukturierte Analyse solcher Probleme – beispielsweise durch TRIZ – können ressourcen- und energieintensive Verfahren optimiert oder durch innovative Prozesse ersetzt werden. Als Beispiel dient die Isolierung von Essigsäure aus verdünnten, wässrigen Lösungen durch Kristallisation oder kombinierter Extraktion und Veresterung anstelle von konventioneller Destillation.

Literatur

[1] United Nations, *Adoption of the Paris Agreement*. Paris, 2015, S. 1–32.
[2] M. A. Orloff, *Grundlagen der klassischen TRIZ*. Springer Berlin Heidelberg, 2006.
[3] „Dortmund Data Bank.“ [Online]. Verfügbar unter: http://www.ddbst.com/en/EED/SLE/SLE Acetic acid%3BWater.php. [Zugegriffen: 26-Jan-2016].
[4] T. C. Padhiyar und S. B. Thakore, „Recovery of Acetic Acid From Effluent via Freeze Crystallization“, *Int. J. Sci. Eng. Technol.*, Bd. 2, Nr. 4, S. 211–215, 2013.
[5] Institut für Arbeitsschutz der Deutschen Gesetzlichen Unfallversicherung, „GESTIS-Stoffdatenbank“, 2015. [Online]. Verfügbar unter: http://gestis.itrust.de. [Zugegriffen: 28-Sep-2015].
[6] D. Painer, S. Lux, und M. Siebenhofer, „Reaktive Trennung von Essigsäure/Ameisensäure/Wasser-Gemischen aus der Bioraffinerie“, *Chemie Ing. Tech.*, Bd. 87, Nr. 6, S. 843–847, Juni 2015.
[7] A. Toth, „Intensivierung der Carbonsäureisolierung aus wässrigen Prozessströmen durch kombinierte Extraktion und Veresterung“, Technische Universität Graz, 2015.

NAWI Graz
Natural Sciences

Seit 2004 kooperieren Karl-Franzens-Universität und Technische Universität Graz im Rahmen der strategischen Partnerschaft NAWI Graz noch enger miteinander. Mit der Mission, eine österreichweit einzigartige Kooperation in den thematischen Überlappungsbereichen der Naturwissenschaften zu erschließen, wurden

- gemeinsame Studien implementiert,
- verstärkt kooperative Forschungsprojekte auf den Weg gebracht und durchgeführt, sowie durch gemeinsame Infrastrukturanschaffungen einerseits Duplizitäten vermieden und andererseits die Anschaffung finanziell erst ermöglicht. Zudem wurden in den Kooperationsbereichen die Entwicklungspläne beider Universitäten aufeinander abgestimmt und enthalten eine akkordierte Widmung der zur Besetzung anstehenden Professuren.

Grundsatz von NAWI Graz ist es, durch Bündelung von Ressourcen und Know-how den Standort Graz weiter zu stärken, eine kritische Masse im europäischen Kontext zu erzeugen und international sichtbarer zu machen.

Die Aktionsfelder sind dabei

- Betrieb und Weiterentwicklung gemeinsamer BA/MA-Studien und ihrer Organisation,
- die NAWI Graz Advanced School of Science (NAWI GASS)
- gemeinsame Forschungs- und Infrastrukturvorhaben
- Querschnittsthemen wie bspw. gemeinsame Berufungsverfahren oder Projekte zur Weiterentwicklung der Organisation von NAWI Graz

Umgesetzt werden die Inhalte in den fünf Fachgebiets-Arbeitsgruppen

- Molecular Bioscience, Biotechnology, Plant Science
- Chemistry and Chemical Technologies
- Earth, Space and Environmental Science
- Fundamental and Applied Mathematics und
- Physics

Bisherige Bilanz von NAWI Graz sind 18 gemeinsame Studien mit mehr 5.145 Studierenden (Stand WS 2015), eine verstärkte Forschungskooperation mit zahlreichen gemeinsamen Forschungsprojekte und einem Drittmittelvolumen von mehr als 29 Mio. Euro pro Jahr, eine Vielzahl von kooperativ angeschafften und genutzten Geräten, sowie zehn NAWI Graz Central Labs und Core Facilities. Darüber hinaus werden Berufungsverfahren gemeinsam durchgeführt.

from waste to value

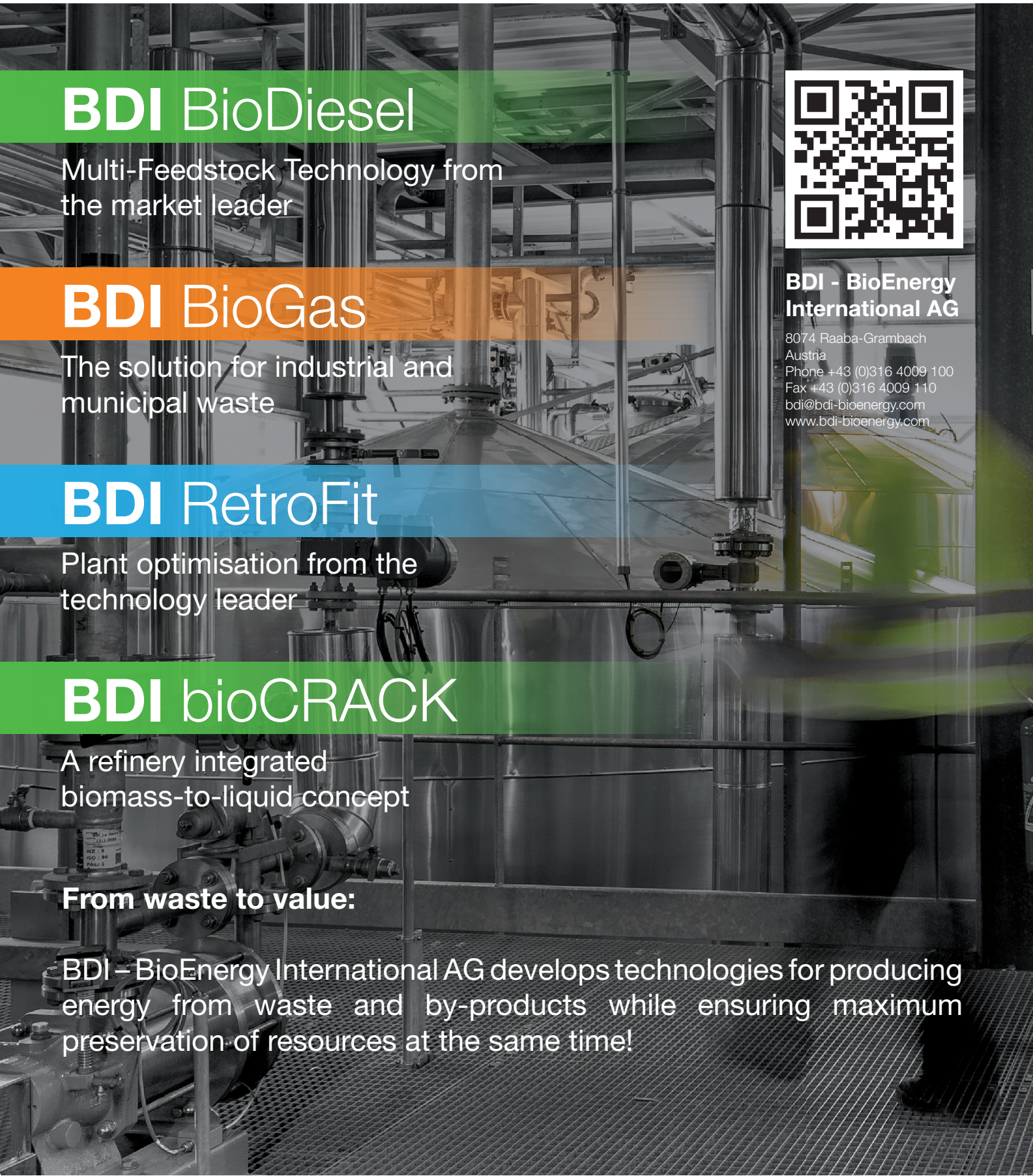

BDI BioDiesel

Multi-Feedstock Technology from the market leader

BDI BioGas

The solution for industrial and municipal waste

BDI RetroFit

Plant optimisation from the technology leader

BDI bioCRACK

A refinery integrated biomass-to-liquid concept

BDI - BioEnergy International AG

8074 Raaba-Grambach
Austria
Phone +43 (0)316 4009 100
Fax +43 (0)316 4009 110
bdi@bdi-bioenergy.com
www.bdi-bioenergy.com

From waste to value:

BDI – BioEnergy International AG develops technologies for producing energy from waste and by-products while ensuring maximum preservation of resources at the same time!

Innovation leben, Zukunft gestalten

In jedem dritten Smartphone weltweit sorgt ein Siliziummikrofon von Infineon Austria für den guten Ton.
Mehr als 3.300 Mitarbeiterinnen und Mitarbeiter aus rund 60 Nationen entwickeln und produzieren zukunftsweisende Technologien. Infineon Austria ist Österreichs forschungsstärkstes Industrieunternehmen.

www.infineon.com/austria

Infineon

natex

YOUR PARTNER
FOR SCALE UP

Industrial plants
Scale-up
R&D

from the

IDEA
to
PROCESS-DEVELOPMENT
and
REALIZATION

where innovation... meets experience

www.natex.at **office@natex.at** **Werkstraße 7, A-2630 Ternitz**

VTU engineering

Experience responsibility

Wir sind ein High-Tech-Unternehmen im Chemieanlagenbau. Unsere MitarbeiterInnen planen für Pharma, Chemie, Metallurgie und Umwelttechnik modernste Anlagen mit innovativen Werkzeugen. Know-how durch Erfahrung und ständige Weiterbildung, Offenheit für Alternativen und Mut zu Neuem sind prägende Eigenschaften unserer Unternehmenskultur.

Wir suchen:

Projektingenieure (m/w) für

- Verfahrenstechnik
- Qualifizierung
- Validierung
- Mess- und Regeltechnik
- Anlagenbau.

Pharma & Biotechnologie

Chemie & Metallurgie

Erdöl & Erdgas

www.vtu.com

Together with the global players in the pharmaceutical industry, the K1 Competence Center Research Center Pharmaceutical Engineering (RCPE) performs cutting-edge research in the field of process and product optimization.

The main focus is on the development of new drug delivery systems and the associated production processes and their monitoring. Thus, being a link between science and industry, RCPE carries out state-of-the-art business-oriented research, as witnessed by many experts in the field.

However, RCPE's successful performance during the last years is largely due to its experienced international team and to the close interaction with different Universities in Graz, Austria and on an international level.

RCPE is owned by Graz University of Technology (65%), University of Graz (20%) and Joanneum Research GmbH (15%).

We make tomorrow's drugs possible!

RCPE GmbH • 8010 Graz • Austria • www.rcpe.at


OMYA